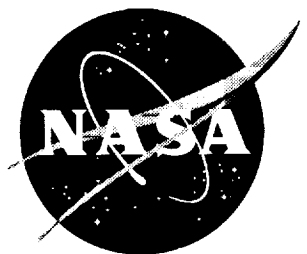


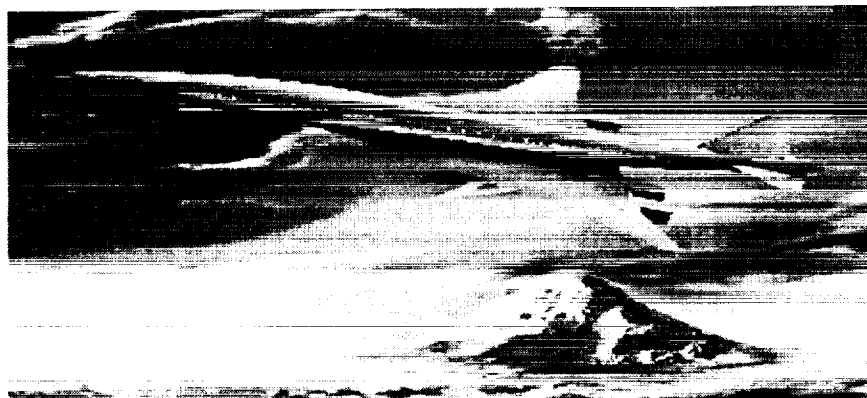
NASA/CP-1999-209692/VOL1/PT2



1998 NASA High-Speed Research Program Aerodynamic Performance Workshop

Volume I—Configuration Aerodynamics

Edited by
S. Naomi McMillin
Langley Research Center, Hampton, Virginia



December 1999

The NASA STI Program Office . . . in Profile

Since its founding, NASA has been dedicated to the advancement of aeronautics and space science. The NASA Scientific and Technical Information (STI) Program Office plays a key part in helping NASA maintain this important role.

The NASA STI Program Office is operated by Langley Research Center, the lead center for NASA's scientific and technical information. The NASA STI Program Office provides access to the NASA STI Database, the largest collection of aeronautical and space science STI in the world. The Program Office is also NASA's institutional mechanism for disseminating the results of its research and development activities. These results are published by NASA in the NASA STI Report Series, which includes the following report types:

- **TECHNICAL PUBLICATION.** Reports of completed research or a major significant phase of research that present the results of NASA programs and include extensive data or theoretical analysis. Includes compilations of significant scientific and technical data and information deemed to be of continuing reference value. NASA counterpart of peer-reviewed formal professional papers, but having less stringent limitations on manuscript length and extent of graphic presentations.
- **TECHNICAL MEMORANDUM.** Scientific and technical findings that are preliminary or of specialized interest, e.g., quick release reports, working papers, and bibliographies that contain minimal annotation. Does not contain extensive analysis.
- **CONTRACTOR REPORT.** Scientific and technical findings by NASA-sponsored contractors and grantees.

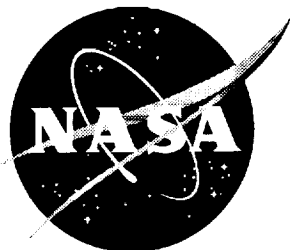
- **CONFERENCE PUBLICATION.** Collected papers from scientific and technical conferences, symposia, seminars, or other meetings sponsored or co-sponsored by NASA.
- **SPECIAL PUBLICATION.** Scientific, technical, or historical information from NASA programs, projects, and missions, often concerned with subjects having substantial public interest.
- **TECHNICAL TRANSLATION.** English-language translations of foreign scientific and technical material pertinent to NASA's mission.

Specialized services that complement the STI Program Office's diverse offerings include creating custom thesauri, building customized databases, organizing and publishing research results . . . even providing videos.

For more information about the NASA STI Program Office, see the following:

- Access the NASA STI Program Home Page at <http://www.sti.nasa.gov>
- Email your question via the Internet to help@sti.nasa.gov
- Fax your question to the NASA STI Help Desk at (301) 621-0134
- Telephone the NASA STI Help Desk at (301) 621-0390
- Write to:
NASA STI Help Desk
NASA Center for AeroSpace Information
7121 Standard Drive
Hanover, MD 21076-1320

NASA/CP-1999-209692/VOL1/PT2



1998 NASA High-Speed Research Program Aerodynamic Performance Workshop

Volume I—Configuration Aerodynamics

Edited by
S. Naomi McMillin
Langley Research Center, Hampton, Virginia

Proceedings of a workshop sponsored by the
National Aeronautics and Space Administration,
Washington, D.C., and held in
Los Angeles, California
February 9–13, 1998

National Aeronautics and
Space Administration

Langley Research Center
Hampton, Virginia 23681-2199

December 1999

Available from:

NASA Center for AeroSpace Information (CASI)
7121 Standard Drive
Hanover, MD 21076-1320
(301) 621-0390

National Technical Information Service (NTIS)
5285 Port Royal Road
Springfield, VA 22161-2171
(703) 605-6000

PREFACE

The High-Speed Research Program sponsored the NASA High-Speed Research Program Aerodynamic Performance Review on February 9-13, 1998 in Los Angeles, California. The review was designed to bring together NASA and industry High-Speed Civil Transport (HSCT) Aerodynamic Performance technology development participants in areas of: Configuration Aerodynamics (transonic and supersonic cruise drag prediction and minimization), High-Lift, and Flight Controls. The review objectives were to: (1) report the progress and status of HSCT aerodynamic performance technology development; (2) disseminate this technology within the appropriate technical communities; and (3) promote synergy among the scientist and engineers working HSCT aerodynamics. In particular, single- and multi-point optimized HSCT configurations, HSCT high-lift system performance predictions, and HSCT Motion Simulator results were presented along with executive summaries for all the Aerodynamic Performance technology areas. The HSR AP Technical Review was held simultaneously with the annual review of the following airframe technology areas: Materials and Structures, Environmental Impact, Flight Deck, and Technology Integration. Thus, a fourth objective of the Review was to promote synergy between the Aerodynamic Performance technology area and the other technology areas within the airframe element of the HSR Program.

The workshop was organized in three sections as follows:

Section I Independent Sessions

Section II Plenary Session

Section III Executive Summaries

The work performed in the Configuration Aerodynamics element of the High-Speed Research Program during 1997 was presented in the following sessions:

Analysis Methods and CFD Validation
Viscous Drag Predictions and Testing Methods
Aerodynamic Design Optimization Capability
Nacelle/Diverter Design and Airplane Integration
Configuration Assessments and Fundamental Studies
Technology Integration (TI) Studies related to Configuration Aerodynamics
(CA / TI Joint Session)

The work performed in the High Lift (HL) element of the High-Speed Research Program during 1997 was presented in the following sessions:

Concept Development
Test Programs and Techniques
Analytical Methods

The proceedings for the Aerodynamic Performance Annual Review are published in two volumes:

Volume I, Parts 1 and 2

Configuration Aerodynamics

Volume II

High Lift

AP Review Chairperson: Naomi McMillin
NASA Langley Research Center

CONTENTS

Preface.....	iii
---------------------	------------

Volume 1, Part 1 -- Configuration Aerodynamics

Configuration Aerodynamics ITD Summary	1
Propulsion Airframe Integration Working Group Summary	31

Analysis Methods and CFD Validation

Overview of Analysis Methods and CFD Validation	41
Shreekant Agrawal, <i>The Boeing Company</i>	

Cycle 2 Nonlinear Design Optimization Analytical Cross Checks	45
Dan Bencze, <i>NASA Ames Research Center</i>	

AIRPLANE Mesh Development with Grid Density Studies.....	75
Susan Cliff and Scott Lawrence, <i>NASA Ames Research Center</i> , Timothy Baker, <i>Princeton University</i> , Scott Thomas and Mark Rimlinger, <i>Sterling Software Inc.</i>	

High Reynolds Number Predictions for the Baseline Arrow Wing at Mach 2.48	147
Melissa Rivers and Richard Wahls, <i>NASA Langley Research Center</i>	

Applications of Parallel Processing in Configuration Analyses	171
Pichuraman Sundaram and James Hager, <i>The Boeing Company</i> , and Robert Biedron, <i>NASA Langley Research Center</i>	

TCA Full Configuration Performance and S&C Characteristics	205
Grant Martin, Raul Mendoza, Paul Kubiato, and Shreekant Agrawal, <i>The Boeing Company</i>	

Unstructured Grid Euler Method Assessment for Aerodynamic Performance Prediction of the Complete TCA Configuration at Supersonic Cruise Speed	287
Farhad Ghaffari, <i>NASA Langley Research Center</i>	

Unstructured Navier-Stokes Analysis of Full TCA Configuration	309
Neal Frink and Shahyar Pirzadeh, <i>NASA Langley Research Center</i>	

Viscous Drag Predictions and Testing Methods

Overview of Viscous Drag Predictions and Testing Methods	329
Robert Kulfan, <i>The Boeing Company</i>	

Skin Friction Drag Predictions: Summary of CFD Cross Checks, Wing/Body.....	333
Scott Lawrence and Goetz Klopfer, <i>NASA Ames Research Center</i>	

TCA and Symmetric Model Viscous Drag Predictions.....	355
Max Kandula, <i>Dynacs Engineering Co. Inc.</i>	

Feasibility Study of a TCA Symmetric Model for Accurate Skin-Friction Measurements	427
Raul Mendoza and Pichuraman Sundaram, <i>The Boeing Company</i>	

Historic Background on Flat Plate Turbulent Flow Skin Friction and Boundary Layer Growth.....	477
Robert Kulfan, <i>The Boeing Company</i>	
CA Testing Workshops: Process, Issues, Results.....	515
Robert Kennelly, <i>NASA Ames Research Center</i>	
High Reynolds Number Assessment of Boundary Layer Transition Trip Drag at Mach 2.48 on an HSCT Configuration	539
Richard Wahls and Melissa Rivers, <i>NASA Langley Research Center</i> , and Todd Magee and Michael Novean, <i>The Boeing Company</i>	
Experimental Bias and Precision Errors: Requirements, Analysis & Recommendations	571
Michael Novean and Todd Magee, <i>The Boeing Company</i>	
Aerodynamic Design Optimization Capability	
Overview of Aerodynamic Design Optimization Capability.....	621
Dan Bencze, <i>NASA Ames Research Center</i>	
BCAG Design Optimization Activities	625
Roy S. Conner, <i>The Boeing Company</i>	
SYN107-MB Aerodynamic Shape Optimization Method: Recent Improvements and Current Status	693
James Reuther, <i>RIACS</i> , Mark Rimlinger and David Saunders, <i>Sterling Software Inc.</i> , and Raymond Hicks, <i>MCAT</i>	
The AEROSHOP (AERodynamic Shape OPTimization) Toolkit.....	777
Eric Unger, Robert Narducci, James Hager, Peter Hartwich, Raul Mendoza, and Geojoe Kuruvila, <i>The Boeing Company</i>	
TCA6 Configuration Optimization.....	837
Raymond Hicks, <i>MCAT</i> , Mark Rimlinger, <i>Sterling Software Inc.</i> , and James Reuther, <i>RIACS</i>	

Volume 1, Part 2 -- Configuration Aerodynamics

Aerodynamic Design Optimization Capability - continued

Aerodynamic Gradients Using Three Methods.....	931
Geojoe Kuruvila, James Hager, and Pichuraman Sundaram, <i>The Boeing Company</i>	
CFD-Based Flap Optimization for the TCA in Transonic Flight Conditions	979
Robert Narducci, Eric Unger, David Yeh, Michael Novean, Pichuraman Sundaram, Todd Magee, Geojoe Kuruvila, Grant Martin, Alan Arslan, and Shreekanth Agrawal, <i>The Boeing Company</i>	
Viscous Design of TCA Configurations	1043
Steven Krist, Steven Bauer, and Richard Campbell, <i>NASA Langley Research Center</i>	
Progress Towards a Multipoint Optimization Procedure.....	1071
Robert Narducci and Shreekanth Agrawal, <i>The Boeing Company</i>	

Nacelle/Diverter Design and Airplane Integration

Overview of Nacelle/Diverter Design and Airplane Integration	1139
Francis Capone, <i>NASA Langley Research Center</i>	
Rigid Power Effects: Inlet Bleed, Spillage, and Bypass	1143
Mike Malone, Bryan Westra, Arsenio Dimanlig, Bill Bard, and Charlie Peavey, <i>Northrop Grumman</i>	
Propulsion Induced Effects (PIE) Test Program.....	1187
Gelsomina Cappuccio and Mark Won, <i>NASA Ames Research Center</i>	
Transonic Installed Nacelle Analyses.....	1241
Steve Chaney and Gordon Blom, <i>The Boeing Company</i>	
Nacelle Diverter Design and Nozzle Boattail Drag Studies	1365
Pichuraman Sundaram, Chih Shieh, Alan Arslan, Hoyt Wallace, and Shreekant Agrawal, <i>The Boeing Company</i>	

Configuration Assessments and Fundamental Studies

Overview of Configuration Assessments and Fundamental Studies.....	1457
Doug Wilson, <i>The Boeing Company</i>	
Model 2b Test Results.....	1461
Aga Goodsell, <i>NASA Ames Research Center</i>	
Nonlinear Cruise-pt. Validation (NCV) Model Wind Tunnel Test Summary and Posttest Analysis.....	1505
Kevin Mejia, <i>The Boeing Company</i>	
Aftbody Closure Model Design - Lessons Learned.....	1545
Francis Capone, <i>NASA Langley Research Center</i>	
HSR Model Deformation Measurements from Subsonic to Supersonic Speeds	1569
Al Burner, Gary Erickson, Wes Goodman, and G. Flemming, <i>NASA Langley Research Center</i>	
The Effect of Aeroelasticity on the Aerodynamic Performance of the TCA.....	1589
Geojoe Kuruvila, Peter Hartwich, and Myles Baker, <i>The Boeing Company</i>	
Initial TCA Stability and Control Assessment.....	1649
David Blake, Paul Glessner, Paul Kubiato, Brian Nishida, and Douglas Wilson, <i>The Boeing Company</i>	
Initial Predictions of Canard Integration	1671
Todd Magee, James Hager, and David Yeh, <i>The Boeing Company</i> , and Tim Haynes, <i>Dynacs Engineering Co. Inc.</i>	

Technology Integration (TI) Studies related to Configuration Aerodynamics (CA / TI Joint Session)

Overview of Technology Integration Activities Related to Configuration Aerodynamics.....	1757
Chester Nelson, <i>The Boeing Company</i>	

Cross-Discipline Evaluation of Optimized Designs and Features	1777
Chris Vegter and Greg Stanislaw, <i>The Boeing Company</i>	
TRANAIR Applications for Technology Integration Propulsion Trades.....	1797
Paul Dees, <i>The Boeing Company</i>	
CFD Data Generation Process for Nonlinear Loads	1817
Alan Arslan, Todd Magee, Eric Unger, Peter Hartwich, Shreekan Agrawal, Joseph Giesing, and Bala Bharadvaj, <i>The Boeing Company</i> , and Neal Chaderjian and Scott Murman, <i>NASA Ames Research Center</i>	

Volume 2 -- High Lift

High Lift ITD Summary	1873
-----------------------------	------

Concept Development

TCA High Lift Preliminary Assessment	1897
Paul Meredith, Gregory Wyatt, Mike Elzey, John Tran, David Yeh, and Ryan Polito, <i>The Boeing Company</i>	
TCA Planform and Leading-Edge Study at High-Lift Conditions	1933
David Yeh and Roger Clark, <i>The Boeing Company</i>	
Prediction of High-Lift Characteristics of the Preliminary Technology Concept (PTC)	2005
Keith Ebner, <i>The Boeing Company</i>	
Correlation of CFD Calculations and Wind Tunnel Measurements for the M2.4-7A Arrow Wing Configuration	2055
C. J. Woan, <i>The Boeing Company</i>	

Test Programs and Techniques

4% Arrow Wing Model Test in NASA Ames 12 Ft. Pressure Tunnel	2107
Robin Edwards, Ryan Polito, and Roger Clark, <i>The Boeing Company</i>	
Power Effects on the High-Lift S & C Characteristics of the TCA Model Tested in the LaRC 14x22 Wind Tunnel	2161
Paul Glessner, <i>The Boeing Company</i>	
Assessment of Boundary-Layer Transition Detection and Fixing Techniques	2187
Marvine Hamner and Roger Clark, <i>The Boeing Company</i>	
Experimental Study of Static and Dynamic Ground Effects for Low Aspect Ratio Wings	2233
Lewis Owens, <i>NASA Langley Research Center</i> , Arthur Powell, <i>The Boeing Company</i> , and Robert Curry, <i>NASA Ames Research Center</i>	

Analytical Methods

Potential Flow Analysis of Dynamic Ground Effect.....	2299
Winfried Feifel, <i>The Boeing Company</i>	

Dynamic Ground Effects Simulation Using OVERFLOW-D	2387
Bill Dwyer, <i>Northrop Grumman</i>	
Recent Results in the Study of Static Ground Effect Using an Inviscid Unstructured Grid Code	2471
Steve Yaros, <i>NASA Langley Research Center</i>	
Potential Flow Analysis of the Mark-XVI Flow Survey Probe	2509
Eric Roth, <i>The Boeing Company</i>	
Aerodynamic Design of Inboard Sealed Slats for the TCA-3 Wind Tunnel Test.....	2545
Robert Griffiths, <i>The Boeing Company</i>	
Navier-Stokes Results for HSCT High-Lift Configurations	2585
Anthony Saladino, <i>Dynacs Engineering Co. Inc.</i> , and Allen Chen, <i>The Boeing Company</i>	
Code Calibration Applied to the TCA High-Lift Model in the 14x22 Wind Tunnel (Simulation With and Without Model Post-Mount).....	2691
Wendy Lessard, <i>NASA Langley Research Center</i>	
Aerodynamic Analysis of TCA Wing/Body/Nacelle High-Lift Configurations	2735
Xuetong Fan and Paul Hickey, <i>ASE Technologies, Inc.</i>	
Canard Integration for CFD Analysis of HSCT High Lift Configurations	2765
David Yeh, <i>The Boeing Company</i>	
Comparison of CFL3D Results using Alternative Grid Interfacing Schemes	2831
Xuetong Fan and Paul Hickey, <i>ASE Technologies, Inc.</i>	



Aerodynamic Gradients using Three Methods

Geojoe Kuruvila

James O. Hager

P. Sundaram

Configuration Aerodynamics

The Boeing Company, Long Beach

HSR Airframe Technical Review

Los Angeles, California

February 9-13, 1998



This page is intentionally left blank.

Aerodynamic Gradients using Three Methods

Geojoe Kuruvila
James O. Hager
P. Sundaram

The Boeing Company
Long Beach, California 90807-5309

This paper investigates the relative merits of three methods for computing the gradients of aerodynamic forces with respect to shape design variables. The three methods considered in this study are the finite-difference, the sensitivity equation and the adjoint. The development cost, computing cost, accuracy and overall cycle-time for each of these approaches are addressed.

This page is intentionally left blank.

Outline



High Speed Aerodynamics, Long Beach

- Objective
- Methods for computing gradients
- Results
- Summary

Objective

In the HSR program, nonlinear aerodynamic shape optimization is considered very important in designing a viable HSCT. However, obtaining accurate gradients of the aerodynamic forces with respect to the design variables, at low overall cost and low cycle time, remains a challenge.

In this paper, three methods for computing gradients -- finite-difference, sensitivity equation and adjoint -- are presented and the gradients they produce, for a variety of shape design variables, are compared.

Objective



High Speed Aerodynamics, Long Beach

- Compute gradients of aerodynamic forces with respect to shape design variables using
 - Finite-difference method
 - Sensitivity equation method
 - Adjoint method
- Compare their relative merits
 - Accuracy
 - Cycle time
 - Cost

The Gradient

The objective of any optimization is to find the value of a set of design variables, b , such that the cost function, F , is a minimum. Any gradient based optimizer minimizes the cost function by searching for the location in the design space where the gradient of the F with respect to b vanishes. Therefore, obtaining accurate gradient is the most important part of the optimization.

In an aerodynamic shape optimization problem the design variables are, for example, amplitudes of shape functions and the cost function is, typically, drag or ratio of drag over lift. The cost function is a function of the flow variables, Q , and its position, X . For a discrete problem, X denotes the grid. For a given X , Q can be obtained by solving the governing equations of the flow (Euler or Navier-Stokes equations for example) with appropriate boundary conditions.

The Gradient



High Speed Aerodynamics, Long Beach

- Cost function : Drag, Drag/Lift,

Minimize $F(Q, X)$

$$Q = Q(X), \quad X = X(b), \quad b = [b_1, b_2, \dots, b_i, \dots, b_N]$$

- Analysis equation : Euler/Navier-Stokes

$$R(Q, X) = 0$$

- Gradient:

$$\frac{\partial F}{\partial b_i} = ? \quad i = 1, 2, \dots, N$$



Gradient using Finite-Difference Method

The finite-difference method is the easiest and the most straight-forward method for computing gradients. The cost function, F , is evaluated by solving the flow equations, $R=0$, (Euler or Navier-Stokes equations). Each design variable, b_i , is perturbed by an appropriate step-size, δb_i , and the new cost function value is determined by solving the flow equations again. From the cost functions at the two states of a design variable, the gradient of F with respect to b_i can be easily determined. This process is repeated for each design variable.

Determining the appropriate step-size is the most difficult part of this method. If the appropriate step-size is known, then the cost of finding each gradient could be as high as the cost of one flow solution. About 50-60% reduction in computing cost, for the flow solution, may be achieved by using a previous solution as the initial guess for the next solutions. However, the total cost of computing the gradients using this method is directly proportional to the number of design variables.

Gradient using Finite-Difference Method



High Speed Aerodynamics, Long Beach

- Gradient:

$$\frac{\partial F}{\partial b_i} = \frac{F(b + \delta b_i) - F(b)}{\delta b_i}; \quad i = 1, 2, \dots, N$$

- Step-size:

$$\delta b_i = ?$$

Gradient using Sensitivity Equation Method

In the sensitivity equation method, the gradients of the cost function with respect to the design variables are evaluated by computing the flow sensitivities, Q_i , where Q_i are the flow variables. The flow sensitivities are computed by solving the sensitivity equations. These equations are obtained by differentiating the flow equations and the grid generator. The sensitivity method eliminates the need to know the step-size for each design variable. However, for each design variable, the sensitivity equation has to be solved in order to compute the gradient. Therefore, the cost of computing the gradients is also directly proportional to the number of design variables.

Gradient using Sensitivity Equation Method



High Speed Aerodynamics, Long Beach

- Gradient:

$$\frac{\partial F}{\partial b_i} = \frac{\partial F}{\partial Q} \tilde{Q}_i + \frac{\partial F}{\partial X} \frac{\partial X}{\partial b_i}; \quad \tilde{Q}_i = \frac{\partial Q}{\partial b_i}; \quad i = 1, 2, \dots, N$$

- Sensitivity equations:

$$\frac{\partial R}{\partial Q} \tilde{Q}_i = - \frac{\partial R}{\partial X} \frac{\partial X}{\partial b_i}; \quad i = 1, 2, \dots, N$$

Automatic Differentiation of FORTRAN Codes

The sensitivity equations can be obtained by hand-differentiating the flow equations. This approach is very labor intensive. An easier approach is to use ADIFOR. ADIFOR takes a FORTRAN code (CFL3D for example) as input and generates a new FORTRAN code (CFL3D-AD) that computes the gradient of the specified dependent variable, F , with respect to the specified independent variable, b .

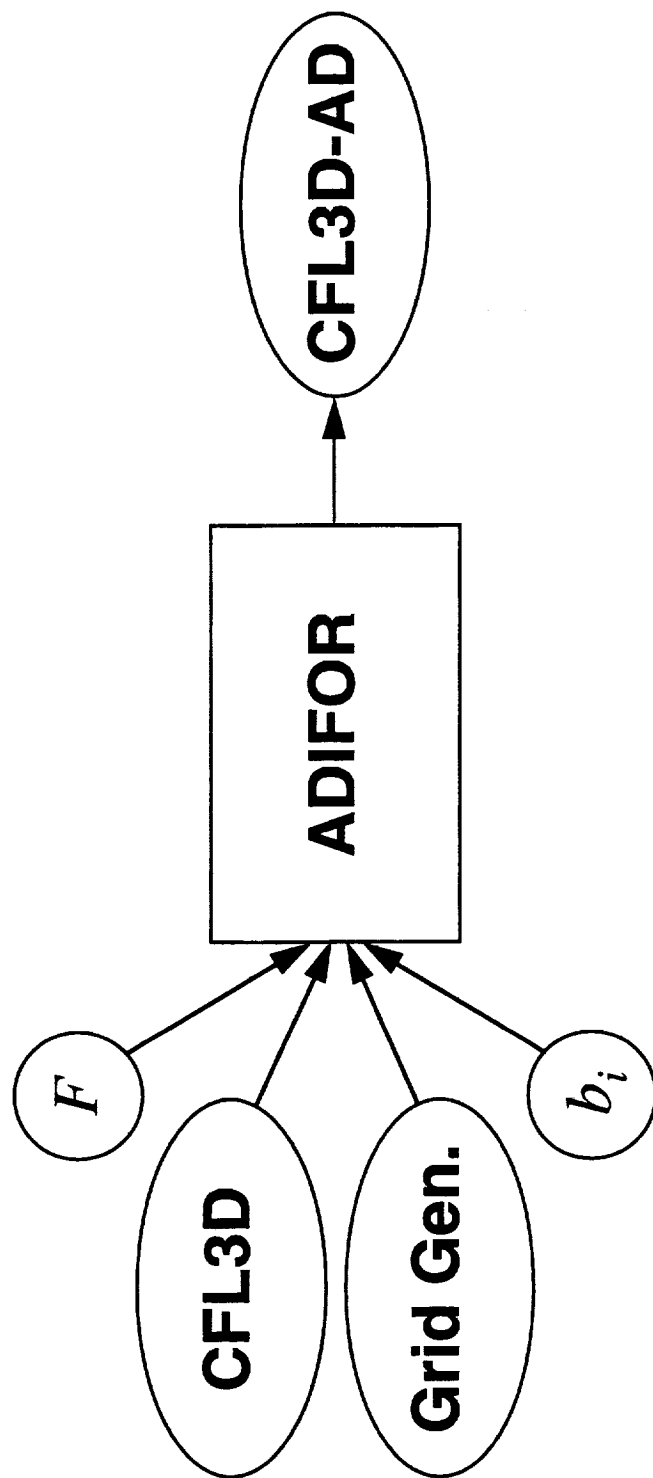
When CFL3D is treated as a “black-box” and differentiated using ADIFOR, it produces a very inefficient code.

Automatic Differentiation of FORTRAN Codes



High Speed Aerodynamics, Long Beach

The Black-Box Approach



CFL3D : F

CFL3D-AD : F, $\partial F / \partial b_i$



Automatic Differentiation of FORTRAN Codes

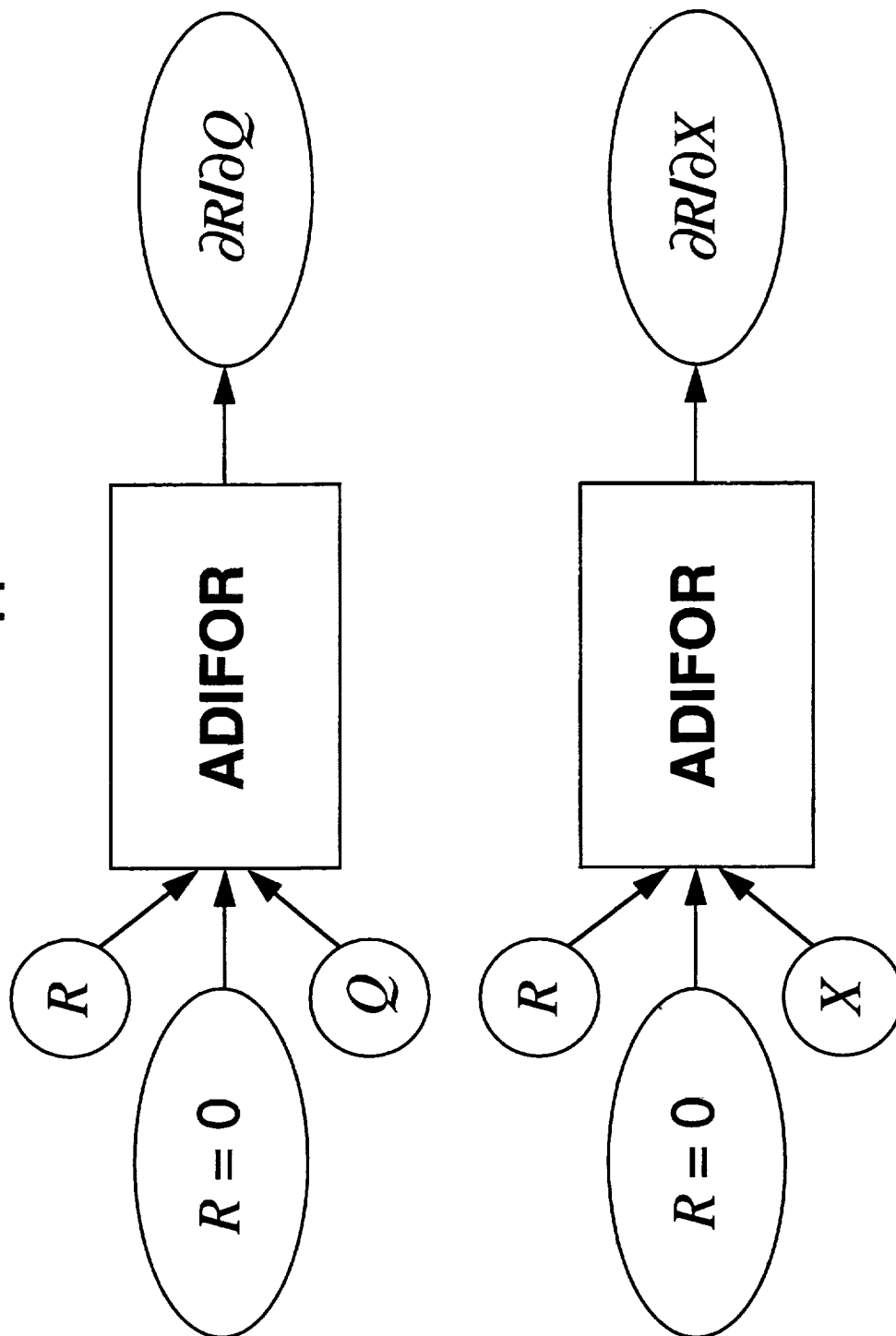
A smarter approach is to differentiate only the routines that are relevant for computing gradients and assembling them to create the differentiated code. The sensitivity equations obtained are solved using an incremental iterative approach. This approach, suggested by Newman and Taylor ("First- and Second-Order Aerodynamic Sensitivity Derivatives Via Automatic Differentiation with Incremental Iterative Methods"; Sherman, Taylor, Green, Newman, Hou and Korivi; Journal of Computational Physics, Vol 129, 1994, pp. 307-331), produces a code that is more efficient and practical to use for large design problems.

Automatic Differentiation of FORTRAN Codes



High Speed Aerodynamics, Long Beach

A Smarter Approach



CFL3Dhp-ADII

CFL3Dhp-ADII computes the sensitivities of CFL3Dhp, the parallel version of CFL3D. It was created using ADIFOR by differentiating only the routines that are relevant for computing gradients and assembling them into a code. At this time, only the Euler routines of CFL3D have been differentiated. The sensitivity equations are solved using the incremental iterative approach.

CFL3Dhp-ADII



High Speed Aerodynamics, Long Beach

- Parallel sensitivity equation code
- CFL3Dhp (Euler) differentiated using **ADIFOR**
- Solution using Incremental Iterative approach

Gradient using Adjoint Method

The adjoint method is the most efficient method for computing the gradients of cost function with respect to the design variables. In this method, the gradients are evaluated by solving the adjoint, λ , of the flow equations. The size of the adjoint system is the same as that of the flow equations. Therefore, the cost of computing the gradients is nearly independent of the number of design variables. Adjoint method also does not require the knowledge of the step-size.

Codes, that can automatically create the adjoint code for the flow codes are not available to HSR program today. Therefore, deriving and coding the adjoint equations is both labor and calendar time intensive.

Gradient using Adjoint Method



High Speed Aerodynamics, Long Beach

- Gradient:

$$\frac{\partial F}{\partial b_i} = \left\{ \left[\frac{\partial R}{\partial X} \right]^T \lambda + \left(\frac{\partial F}{\partial X} \right) \right\} \frac{\partial X}{\partial b_i}; \quad i = 1, 2, \dots, N$$

- Adjoint equation:

$$\left[\frac{\partial R}{\partial Q} \right]^T \lambda = - \frac{\partial F}{\partial Q}$$

TLNS3D-Adjoint

An adjoint code was created for the Euler part of the TLNS3D flow solver. This code, TLNS3D-Adjoint, has all the features of TLNS3D. The discretization of the adjoint equations together with the dissipation terms is consistent with that of TLNS3D. It is very efficient and can be soon used for fully integrated design of an HSCT.

TLNS3D-Adjoint



High Speed Aerodynamics, Long Beach

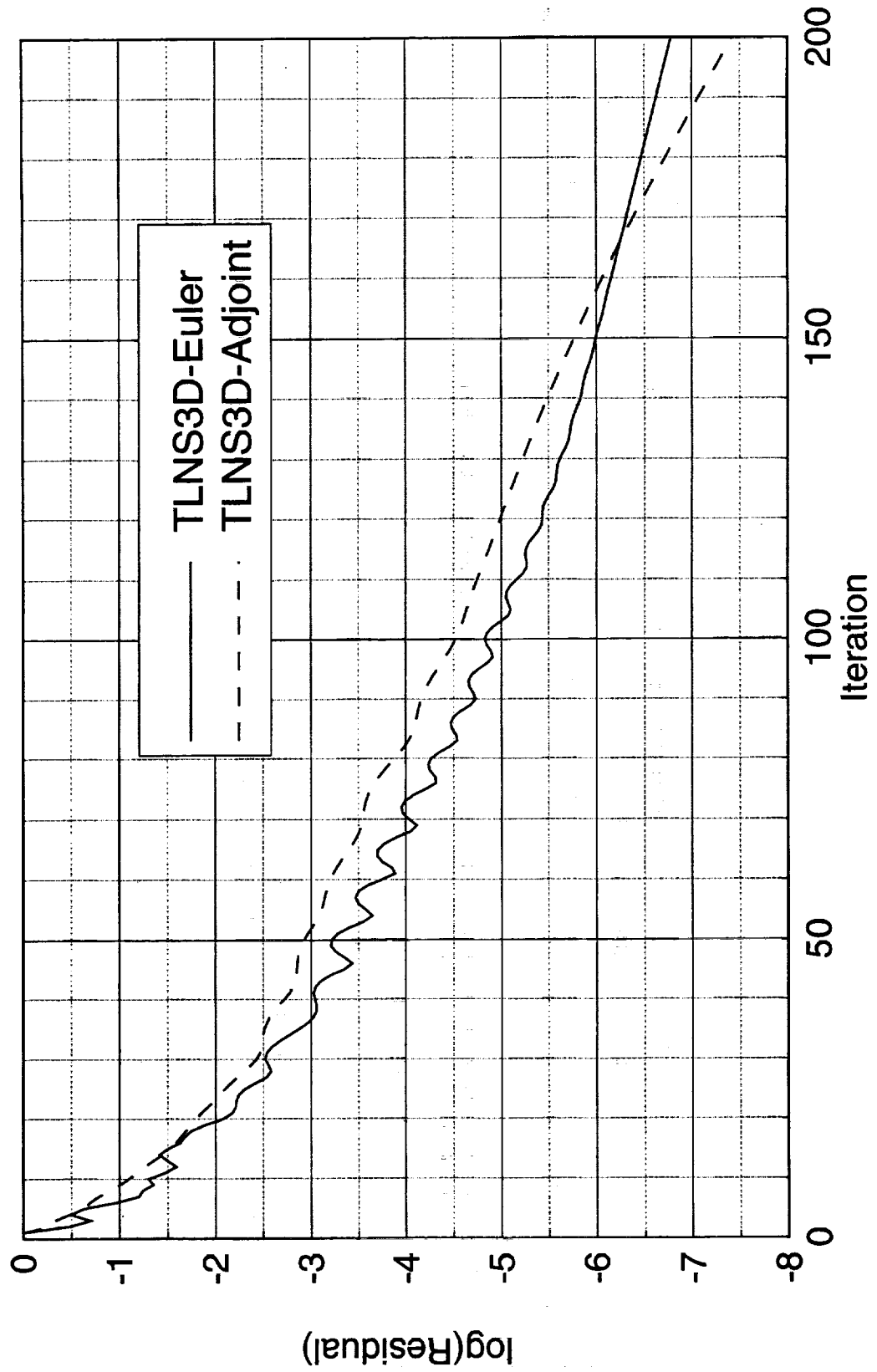
- Adjoint of TLNS3D (Euler) analysis code
- Central-difference discretization
- Blended 2nd and 4th order dissipation
- Runge-Kutta time stepping
- Multigrid acceleration
- Multiblock grids

Convergence Histories of Euler and Adjoint Solutions

The performance of TLNS3D-Adjoint is illustrated in this chart. For a typical Mach 2.4 wing/body design grid of 193x33x77 points, the residuals of both the flow and the adjoint equations drop by over 6 orders of magnitude in 200 iterations. Both the equations converge at about the same rate. Also, the various input parameters, for example the CFL number, the Runge-Kutta coefficients and the dissipation coefficients (vis0, vis2, vis4), are identical for both the equations.

Convergence Histories of Euler and Adjoint Solutions

TCA Baseline W/B, Grid: 193x33x73, $M_\infty=2.4$, $\alpha=3.518^\circ$



Comparison of the Three Methods

The comparative merits of the three methods for computing gradients are tabulated below. The development cost for the finite-difference method is negligible. It is relatively low for the sensitivity method if ADIFOR tool is used. Since tools to automatically generate adjoint codes are not available to the HSR program today, the development cost for adjoint methods is high. For the finite-difference method, the accuracy of the gradients depend on choosing appropriate step-size for each of the design variables. The other two methods are inherently accurate and do not require any step-size. While the finite-difference and the sensitivity methods both require the equivalent of $(N + 1)$ analyses, where N is the number of design variables, the adjoint method requires only the equivalent of 2 analyses. The CPU costs are about $(N + 1)\Psi C$, $(N + 1)\eta C$, and $2C + N\gamma$ for the finite-difference, sensitivity, and adjoint methods respectively, where, C is the CPU time required for one analysis. Ψ and η represent saving factors that can be achieved by using a solution as the initial guess for the next solution. Typically, Ψ and η range between 0.5 and 0.7. Once the flow and adjoint solutions are obtained, the cost for evaluating one gradient is denoted by γ . Generally, γ is much smaller than C . The memory required for the finite-difference and the adjoint methods are proportional to M , the number of grid points. However, for the sensitivity method, the memory requirement can be proportional to $(N + 1)M$.

Comparison of the Three Methods



High Speed Aerodynamics, Long Beach

	Finite-difference	Sensitivity eqn.	Adjoint
Development cost	Negligible	Low; using ADIFOR	High
Step-size	Required	Not required	Not required
Accuracy of gradient	Depends on step-size	Accurate	Accurate
No. of solutions	N+1 Analyses	1 Analysis N Sensitivities	1 Analysis 1 Adjoint
CPU cost	$(N+1)\psi C$	$(N+1)\eta C$	$2C + N\gamma$
Memory needed	∞M	$\infty (N+1)M$	∞M

N: No. of design variables; C : CPU time of 1 analysis

Ψ, η : Savings factor due to use of previous solution as initial guess

γ : Cost for evaluating one gradient ($\gamma < C$)

M : No. of grid points



Comparison of Adjoint with Finite-Difference

As a first test case, gradients of the TCA baseline wing/body configuration, with 193x33x77 grid points, at $M_\infty=2.4$, and $\alpha=3.5^\circ$ for a set of design variables were compared using adjoint and finite-difference methods. This set of design variables are representative of the design variables that are typically used in a wing/body optimization. Of the 26 design variables used, 18 were placed on the wing and 8 on the fuselage. The cost function was chosen to be drag/lift, D/L .

Comparison of Adjoint with Finite-Difference



High Speed Aerodynamics, Long Beach

- Test Case 1:
 - Wing/body, $M_{\infty}=2.4$, $\alpha=3.5^{\circ}$
 - Grid : 193x33x73
 - Cost function is drag/lift, D/L
 - 18 design variables on the wing
 - 8 design variables on the fuselage

Comparison of Adjoint with Finite-Difference

Since the finite-difference data was not generated specifically for this comparison, there are differences in the tools, in addition to the differences in the methodologies. While the finite-difference method used CFL3D for flow analysis, the adjoint-method used TLNS3D. The finite-difference method used FlexMesh for grid perturbations. For the adjoint method, since the analytical grid sensitivity modules were not ready, the grid sensitivities were computed using finite-differences. For this purpose, CSCMDO was used for grid perturbation.

Comparison of Adjoint with Finite-Difference



High Speed Aerodynamics, Long Beach

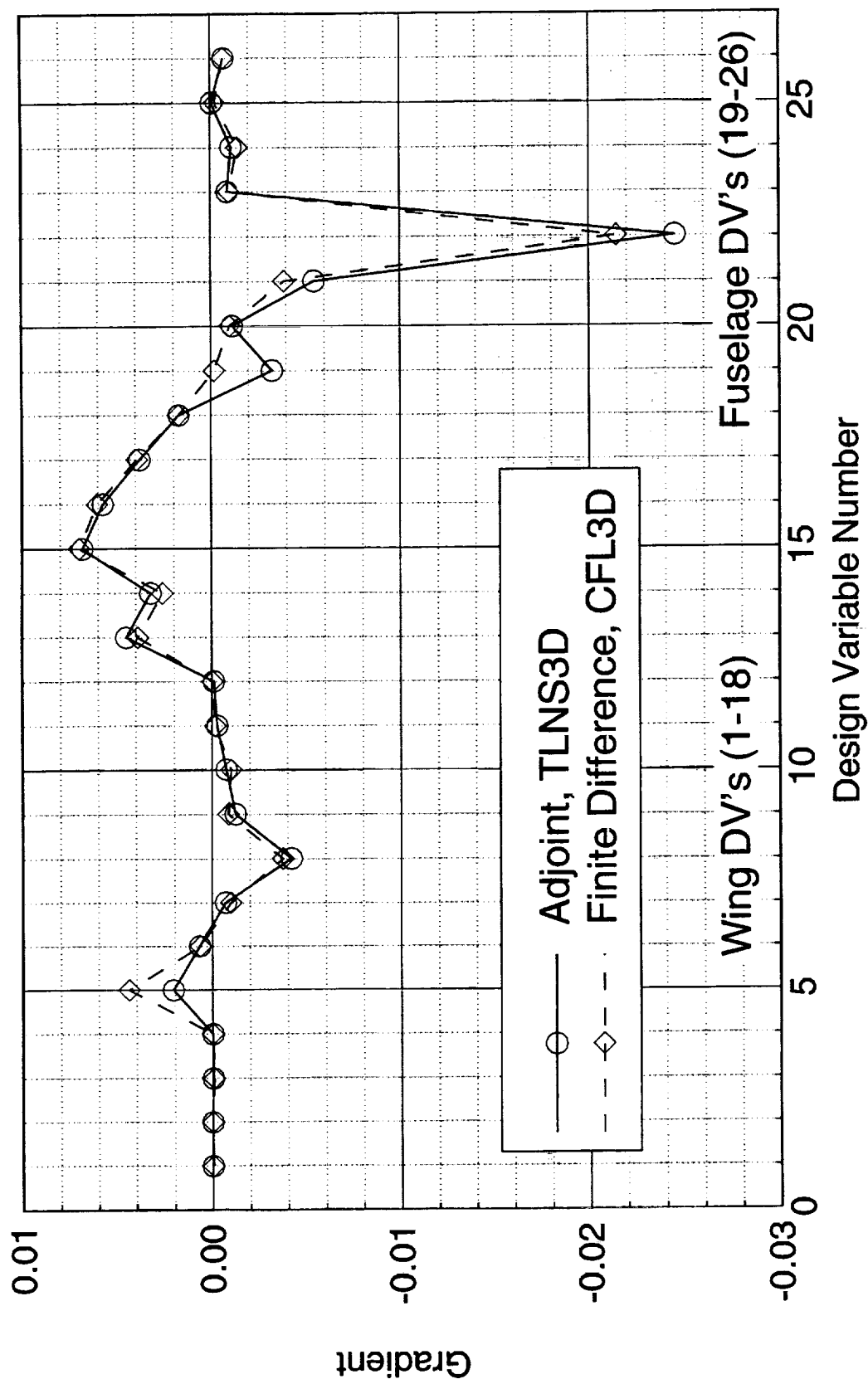
- Finite-difference
 - CFL3D
 - FlexMesh for grid perturbation
- Adjoint
 - TLNS3D
 - Finite-difference grid sensitivities
 - CSCMDO for grid perturbation

Gradients of Drag/Lift

The comparison of the gradients computed using the adjoint and the finite-difference methods are generally good. All of them have the same sign. The magnitudes of some, especially, design variables #5, #19, #21 and #22 show relatively large discrepancy. The step-sizes for the finite-difference gradients were determined from a step-size study. While most of the design variables showed reasonable trend for varying step-sizes, the behavior of some were erratic. This erratic behavior may have been due to insufficient convergence of the analysis problem. Thus, some of the step-sizes selected for this study may not have been the best. The other reasons for the discrepancies could be due to the differences in analysis codes (CFL3D vs. TLNS3D) and the grid perturbation/sensitivity approaches.

Gradients of Drag/Lift

TCA Baseline Wing/Body, $M_\infty=2.4$, $\alpha=3.518^\circ$



Comparison of Adjoint with Finite-Difference

The computational costs for this test case are tabulated here. For the wing/body configuration with only 26 design variables, the average cost of computing the gradients using finite-difference is about 7 minutes on a Cray C-90. For the adjoint method, once the flow solution and the adjoint solution are computed the cost of computing the gradient is about 1 minute per design variable. Note that the cost of computing gradients for a more complex geometry (wing/body/nacelle/diverter), using finite-differences, will increase at a faster rate than the ones using adjoint method.

Comparison of Adjoint with Finite-Difference



High Speed Aerodynamics, Long Beach

	Finite-difference	Adjoint
Code	CFL3D	TLNS3D-Adjoint
Machine	Cray C-90	Cray C-90
CPU time	3.2 hrs.	1.3 hrs.
Memory	24 MW	35 MW

Comparison of the Three Methods

As a second test case, gradients of the TCA baseline wing/body configuration, with 193x33x77 grid points, at $M_\infty=2.4$, and $\alpha=3.5^\circ$ for a set of 50 design variables were compared using all three methods; 16 of these design variables were placed on the wing and the remaining 34 of them on the fuselage. The cost function was chosen to be drag, D. The memory requirements are reasonable.

Comparison of the Three Methods



High Speed Aerodynamics, Long Beach

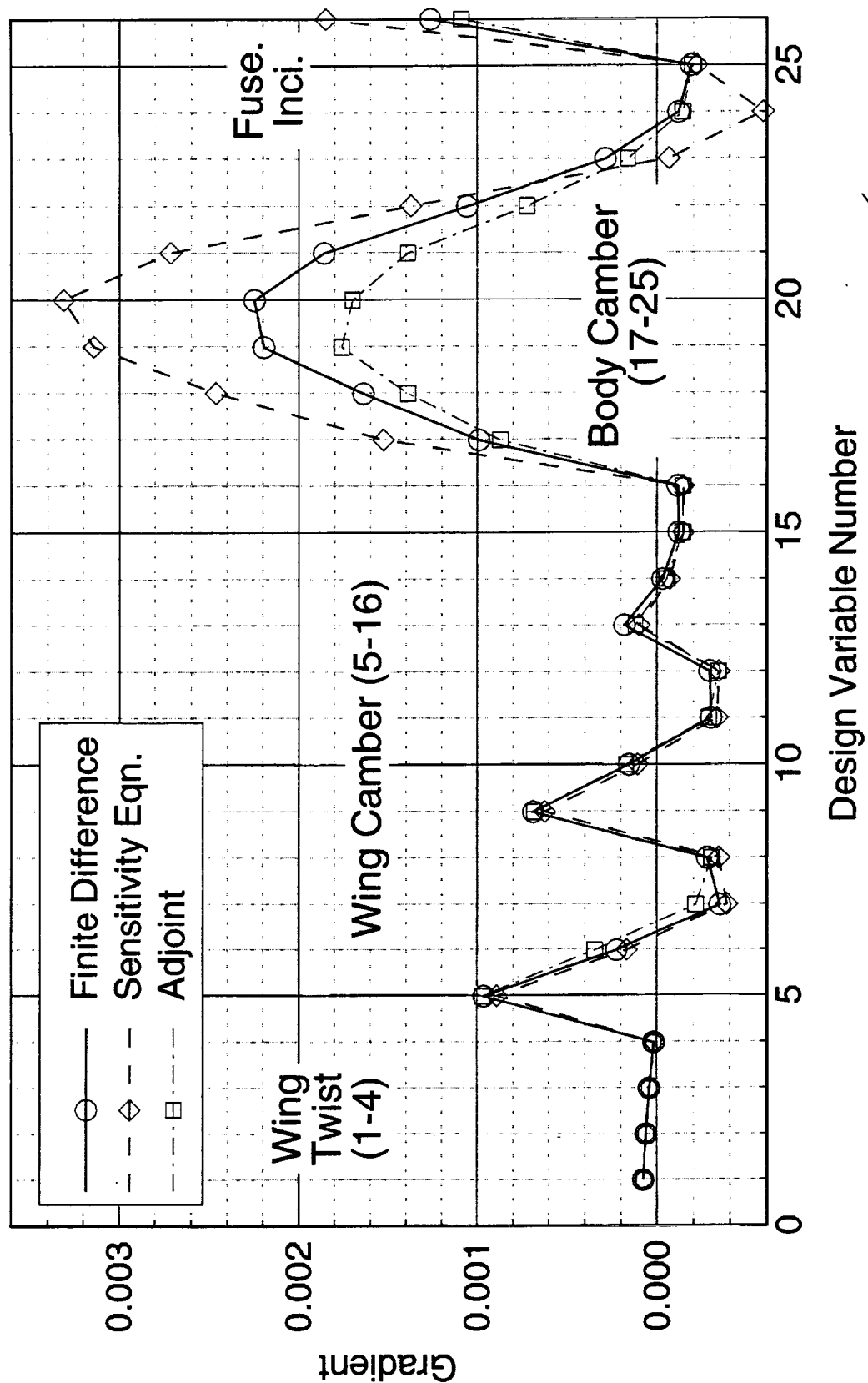
- Test Case 2:
 - Wing/body, $M_\infty=2.4$, $\alpha=3.5^\circ$
 - Grid : 193x33x73
 - Cost function is drag, D
 - 16 design variables on the wing
 - 34 design variables on the fuselage

Gradient of Drag

The comparison of the most of the gradients computed using the finite-difference, sensitivity equation and adjoint methods are generally good. Note that a step-size study was not conducted in this case. However, reasonable step-sizes were selected based on past experiences. The magnitudes of design variables #17 to #24, and #26 show large discrepancies. The sign of the gradient for design variable #23, obtained using the sensitivity equation method is different from the ones obtained using the other two methods. One of the reasons for the discrepancies between the adjoint and the other two methods could be the use of different analysis codes (CFL3D vs. TLNS3D). Another reason could be the grid perturbation and sensitivity process. Although the adjoint method does not require the step-size, it needs the grid sensitivity. Since an analytical grid sensitivity was not available, it was computed using finite-differences. To compute the finite-difference grid sensitivities, the adjoint method used the CSCMDO code to perturb the grid, while the finite-difference used FlexMesh to perturb the grid.

Gradients of Drag

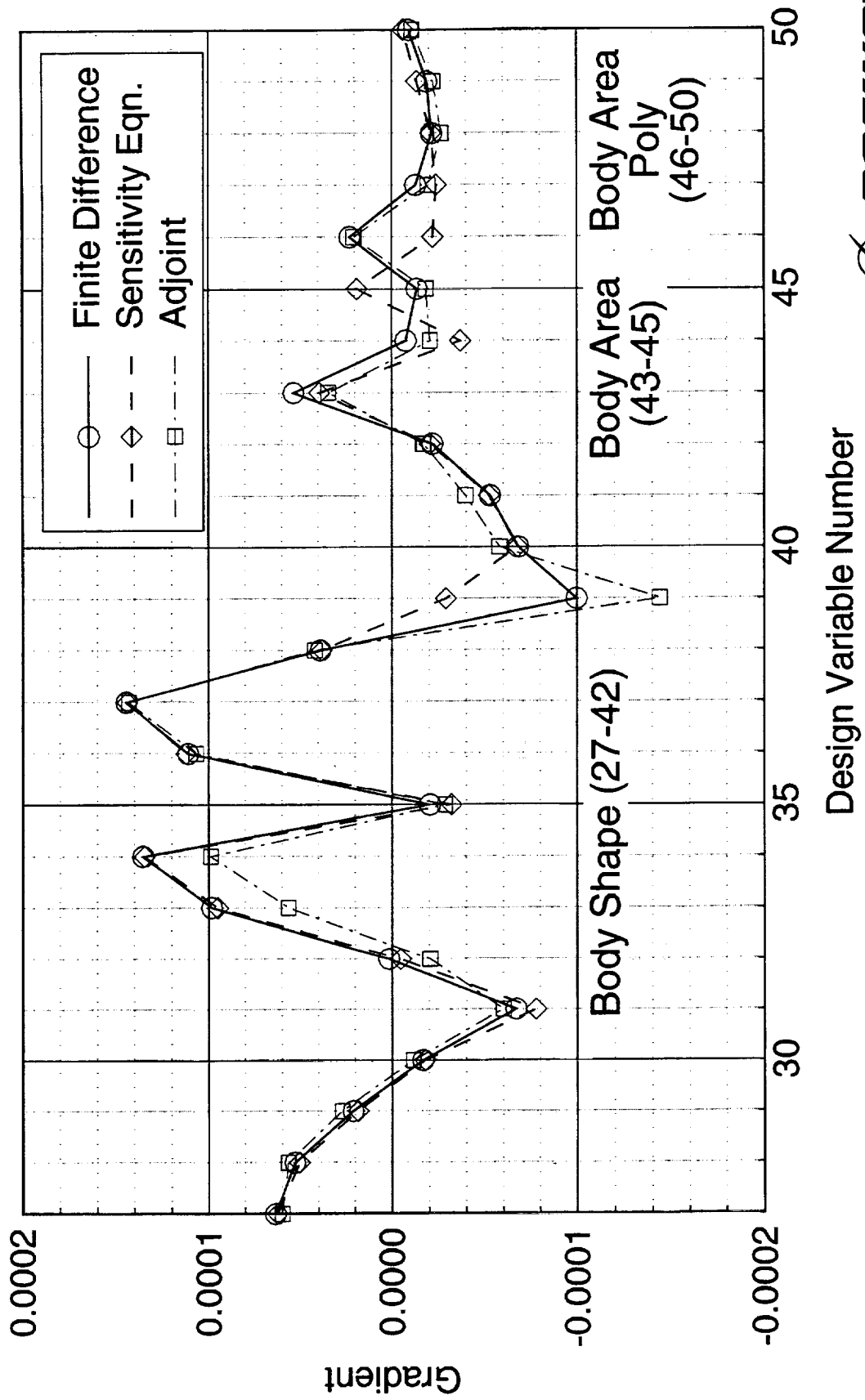
TCA Baseline Wing/Body, $M_\infty=2.4$, $\alpha=3.518^\circ$



This page is intentionally left blank.

Gradients of Drag

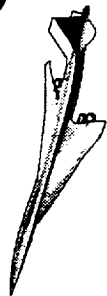
TCA Baseline Wing/Body, $M_\infty=2.4$, $\alpha=3.518^\circ$



Comparison of the Three Methods

The computational costs for this test case are tabulated below. For the wing/body configuration with 55 design variables, using finite-differences requires about 5.8 hours on a Cray C-90, while the adjoint method need only 1.8 hours. The sensitivity method required about 20 hours of equivalent C-90 hours. This may not be a fair comparison, since IBM SP-2 is a parallel computer and by using large numbers of processors CFL3Dhp-ADII can compute gradients in reasonable wall clock time. The memory required for the finite-difference and adjoint methods are reasonable. The memory required on SP-2 is also considered reasonable since each of the 24 processors used only 10 MW.

Comparison of the Three Methods



High Speed Aerodynamics, Long Beach

	Finite-difference	Sensitivity eqn.	Adjoint
Code	CFL3D	CFL3Dhp-ADII	TLNS3D-Adjoint
Machine	Cray C-90	IBM SP2	Cray C-90
CPU time	5.8 hrs.	20 [*] hrs.	1.8 hrs.
Memory	24 MW	24x10 MW	35 MW

* Equivalent C-90 hours

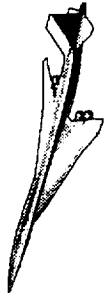
Summary

Finite-difference gradient codes are easy to develop. However, the accuracy of the gradients depends on picking the appropriate step-size. The cost of computing the gradients is directly proportional to the number of design variables and the cost of one analysis. Therefore, for large number of design variable the cost is high.

Sensitivity equation codes, CFL3Dhp-ADII for example, are easy to develop using ADIFOR. Step-size is not an issue. Therefore, the gradient it computes is considered accurate. However, the cost of computing the gradients is directly proportional to the number of design variables and the cost of one analysis. Therefore, for large number of design variable the cost is high. Since CFL3Dhp-ADII runs on parallel computers, the wall time required to compute gradients for large number of design variables can be made reasonable by using large number of processors. Efforts are currently underway to improve the efficiency of CFL3Dhp-ADII on parallel platforms.

Adjoint codes (TLNS3D-Adjoint) takes significant labor and calendar time to develop. Since the adjoint method does not require a step-size the gradient is considered accurate. However, due to the lack of a grid sensitivity code, TLNS3D-Adjoint uses finite-difference grid sensitivities which requires a step-size. This deficiency will be removed, in the near future, by creating a grid sensitivity code using ADIFOR. The cost of computing gradients is nearly independent of the number of design variables. Therefore, this is the most practical approach when the number of design variables is large.

Summary



High Speed Aerodynamics, Long Beach

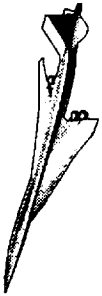
- Finite-difference (CFL3D)
 - Easy to develop
 - Experience required to pick appropriate step-size
 - Accuracy is an issue
 - Cost is high for large no. of design variables
- Sensitivity equation (CFL3Dhp-ADII)
 - Easy to develop using ADIFOR
 - Step-size is not needed
 - Accurate
 - Cost is high for large no. of design variables
 - Effort underway to improve efficiency



This page is intentionally left blank.

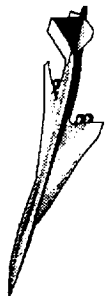
Summary

High Speed Aerodynamics, Long Beach



- Adjoint (TLNS3D-Adjoint)
 - Time-consuming to develop
 - Step-size is not required
 - Grid sensitivity using ADIFOR
 - Accurate
 - Cost is nearly independent of the no. of design variables

This page is intentionally left blank.



CFD-based Flap Optimization of the TCA in Transonic Flight Conditions

Robert P. Narducci, Eric R. Unger, David T. Yeh, Michael G. Novean,
P. Sundaram, Todd E. Magee, Geojoe Kuruvila, Grant L. Martin,
Alan E. Arslan, and Shreekant Agrawal

Configuration Aerodynamics
The Boeing Company, Long Beach

HSR Airframe Technical Review
Los Angeles, California
February 9-13, 1998



This page is intentionally left blank.

CFD-based Flap Optimization of the TCA in Transonic Flight Conditions

**Robert P. Narducci, Eric R. Unger, David T. Yeh, Michael G. Novean,
P. Sundaram, Todd E. Magee, Geojoe Kuruvila, Grant L. Martin,
Alan E. Arslan, and Shreekant Agrawal**

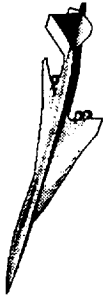
**The Boeing Company
Long Beach, California 90807-5309**

Until recently, the emphasis of non-linear aerodynamic shape design for HSCT configurations has been on drag minimization at the supersonic cruise condition. The performance of the aircraft at the transonic flight condition, as well as for the acceleration and deceleration through the subsonic and low supersonic flight regimes, can be much improved with flap deflections. The primary objective of this study was to incorporate CFD simulations and a grid perturbation tool to model flap deflections with optimization theory to determine the flap deflections for least drag at a given flight condition. The procedure leveraged lessons learned from an earlier procedure developed under an Independent Research and Development (IRAD) project at Boeing Long Beach for flap optimization of the M2.4-7A HSCT configuration. Optimization runs were performed at a series of Mach numbers using Euler analyses on a coarse grid. Fine grid Navier-Stokes analyses were performed on baseline and finalized flap configurations to measure a drag reduction. The optimization procedure was validated through testing at the NASA Langley 16-foot transonic wind tunnel.

Outline

The paper begins with an overview of an earlier transonic flap optimization procedure developed under IRAD for the M2.4-7A Opt5 configuration. An outline of the current optimization procedure is given next. Results of the optimization including a presentation of Navier-Stokes results follows. The optimization was applied at five Mach numbers: $M_\infty=0.6, 0.8, 0.9, 1.1, 1.8$. The next section contains data from the NASA Langley 16-ft Transonic Wind Tunnel which is used to compare with the predicted optimization results. Areas of process improvement and a summary of major accomplishments concludes this paper.

Outline



High Speed Aerodynamics, Long Beach

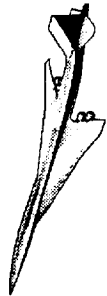
- Introduction to TCA flap optimization
- Background work with the M2.4-7A Opt 5
- Optimization methodology
- Optimization results
- Experimental validation
- Conclusions

Introduction

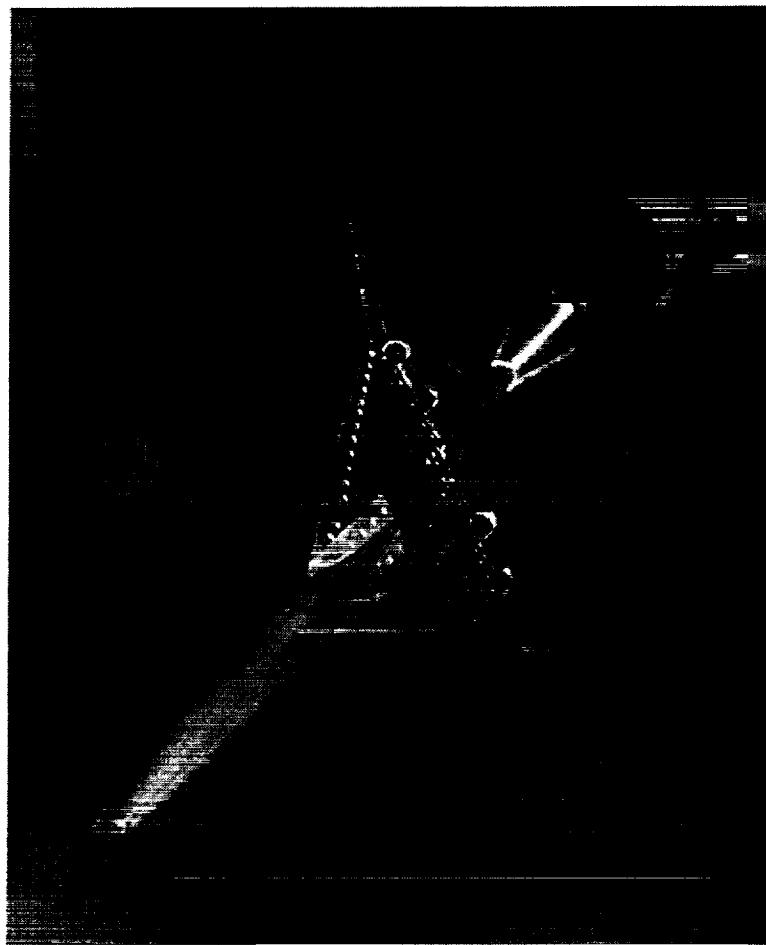
Until recently, nonlinear aerodynamic shape design within Configuration Aerodynamics has focused mainly on optimization for supersonic cruise. At Boeing Long Beach, new shapes for the wing, fuselage, and nacelles have been defined with an Euler-based optimization scheme and the supersonic cruise performance benefits have been, in certain instances, experimentally validated in wind tunnels. The HSCT, designed primarily for supersonic cruise, must rely on flaps for subsonic, transonic, and low supersonic flight. Obtaining flap deflection angles for minimum drag at off-design Mach numbers can have a significant impact on aircraft sizing.

In this work, a technology is developed that builds from the supersonic cruise point optimization methodology to obtain optimum flap deflections at a series of off-design conditions. The technology, based on Euler analyses, is applied on the TCA configuration. Drag improvements are verified with a detailed N-S analysis of the baseline and optimized flap configurations. Finally, improvements are experimentally validated through extensive wind-tunnel testing.

Introduction



High Speed Aerodynamics, Long Beach



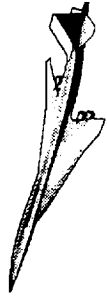
- Euler optimization
- Navier-Stokes analysis for verification
- Experimental validation



Terminology

The terminology defined in this chart is used throughout the paper.

Terminology



High Speed Aerodynamics, Long Beach

- Throughout the presentation, “Baseline” refers to the TCA zero-flap configuration
- “Current” refers to flap deflections consistent with the TI or BCAG parametric study
- Flap settings are indicated by the convention:

$$vv^\circ / ww^\circ / xx^\circ / yy^\circ / zz^\circ$$

vv°	Inboard leading-edge deflection
ww°	Outboard leading-edge deflection
xx°	Inboard trailing-edge deflection
yy°	Middle trailing-edge deflection
zz°	Outboard trailing-edge deflection

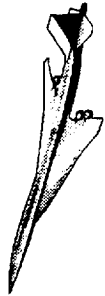


Objectives

The main objective of this work was to develop a technology to determine optimum flap deflection angles for HSCT configurations. The philosophy behind the technology was to pool together existing software and integrate past experience. The technology combined a Boeing Long Beach grid generator, CFL3D, and a Boeing proprietary optimization package. The technology was applied at several Mach number conditions using the TCA geometry. Results of the optimization were compared against data obtained in the NASA Langley 16-ft Transonic Wind Tunnel.

Validation of this technology inherently generates a large quantity of CFD and experimental data for the TCA configuration at off-design Mach numbers. This invites an investigation into the flowfield to better understand flow phenomena over the wing, with and without flaps.

Objectives



High Speed Aerodynamics, Long Beach

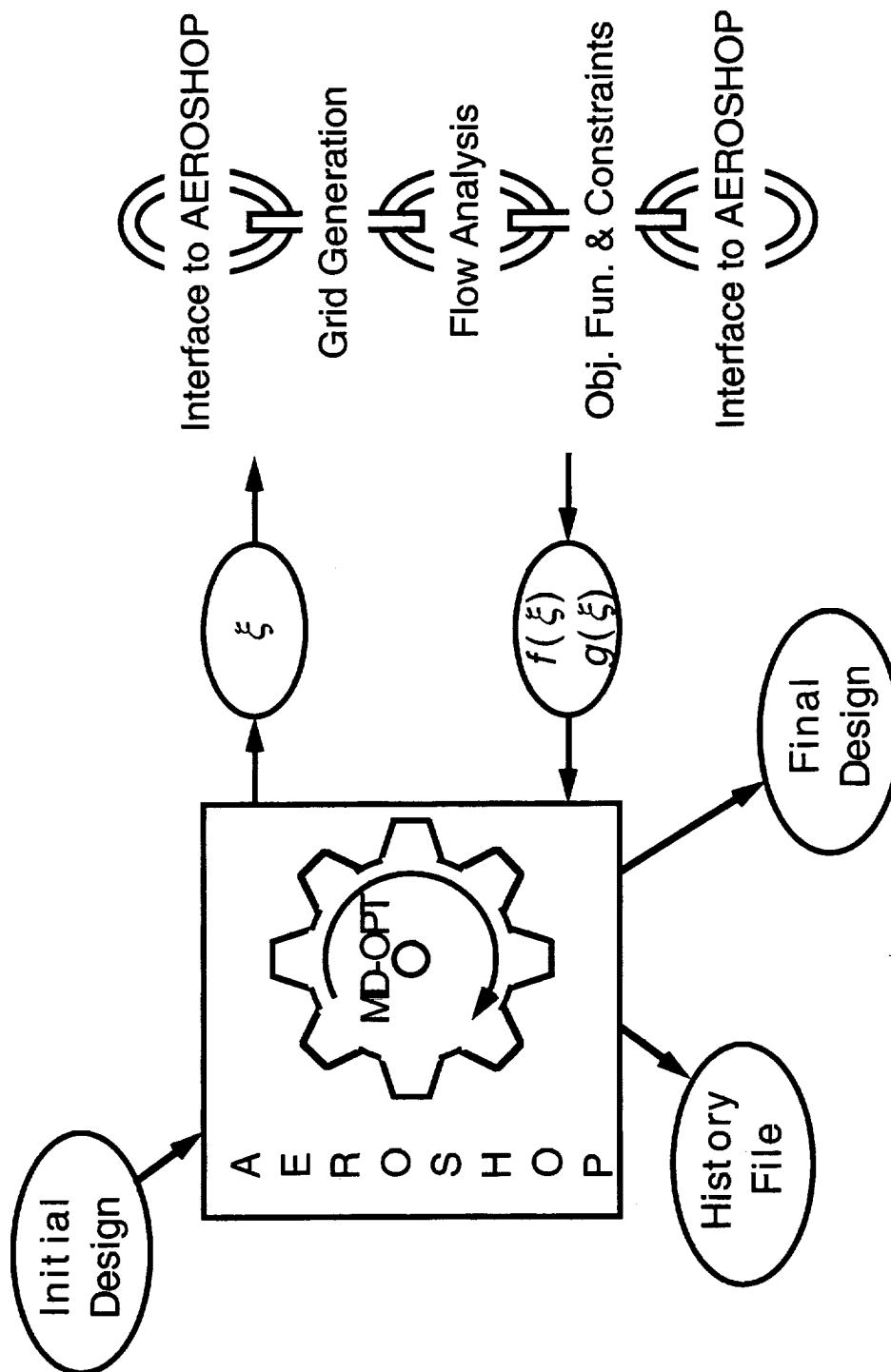
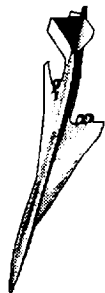
- Develop a technology to incorporate nonlinear aerodynamics into a procedure to determine optimal flap settings for flights at off-design Mach numbers
- Apply the technology to the TCA at several given Mach numbers
- Validate the optimization results in the wind tunnel
- Understand the nature of the flow on the wing with and without flaps to refine the optimization process

Approach for CRAD Study

The flap optimization software was restructured when applied to the TCA, however the methodology closely follows that used under the IRAD work. The software used to perform the TCA optimization is AEROSHOP. AEROSHOP was designed with a modular philosophy to take advantage of existing, stand-alone codes which can easily be interchanged, one of another so that many types of optimization problems can be solved. AEROSHOP sends a UNIX shell command whenever it needs flow analysis information. In this way, a UNIX script can be written to chain together a series of codes to perform the grid generation and flow analysis of a particular configuration. The first step of the UNIX script is to interpret the design variables and modify appropriate input files used in the remainder of the script. The second link is a sequence of programs that modifies an existing grid to model the desired flap deflection. The next link is the CFD analysis. The fourth and final links compute the objective function and the constraints and places the values in a file for AEROSHOP to read. The optimization is driven by MDOPT, a proprietary version of the commercially available NPSOL software.

Approach for CRAD Study

High Speed Aerodynamics, Long Beach



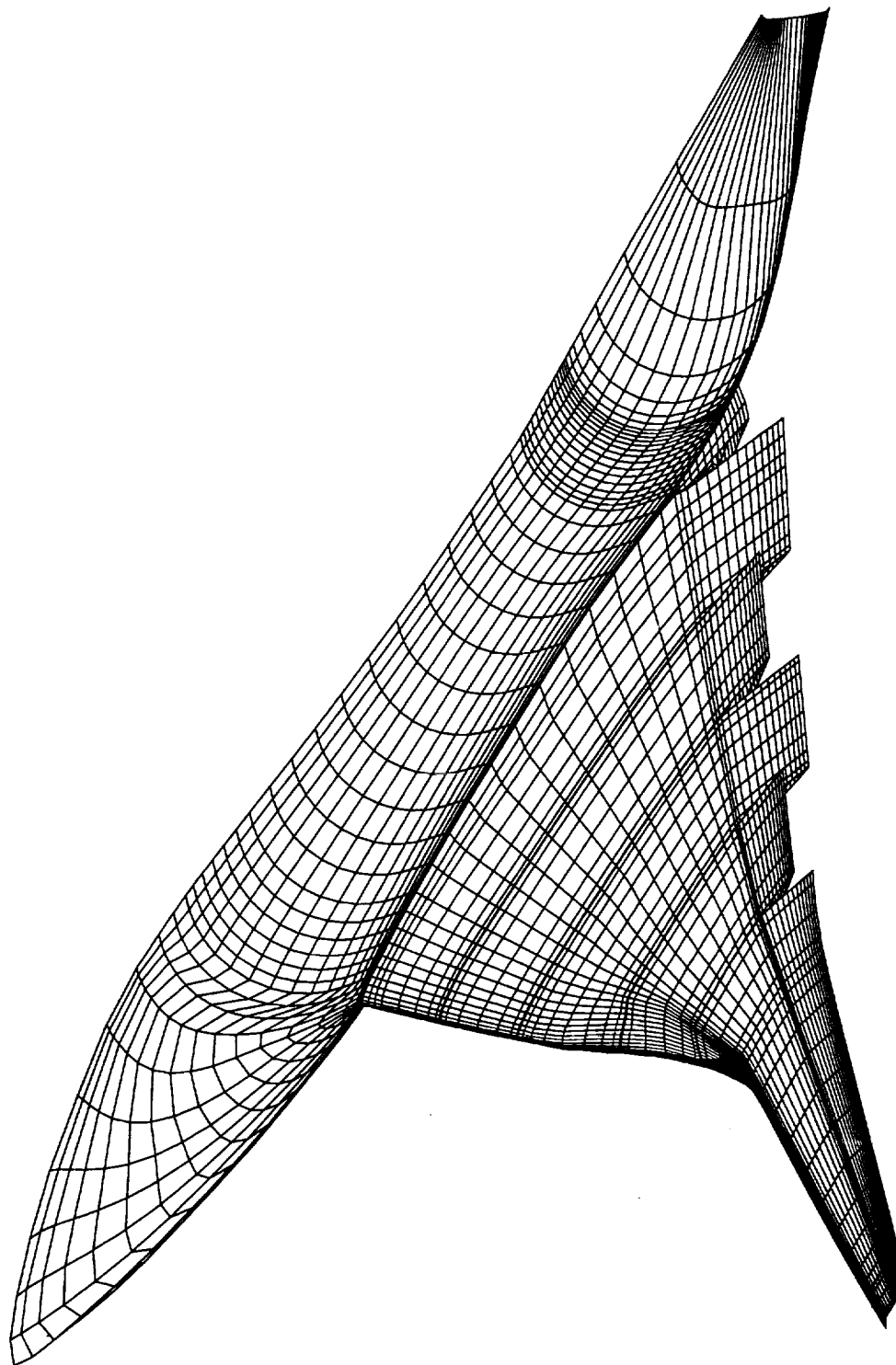
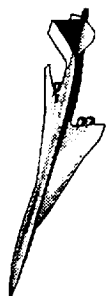
Grid Generation

Another hurdle in the problem is the need for a rapid and robust grid generation tool. For this, a process developed by Yeh and Clark¹ under the high-lift element of HSR was incorporated into the design procedure. From an existing single-block grid, the process adds grid lines corresponding to flap hinge lines and spanwise width definitions. Additional grid lines are introduced to model flow between the wing and flap sections. In a relatively small region near the surface, grid lines are straightened, normal to the surface, so that cross-sides and negative volumes are not introduced with the flap deflection. Flaps are then rotated about a hinge line. Cubic splines are used to smooth the streamwise transition from wing to deflected flap.

1. Yeh, David & Clark, Roger, "Assessment of Computational Methods Applied to HSCT High-Lift Configurations with Multiple Flap Surfaces," HSR 1997 High-Lift Workshop Conference Proceedings, February, 1997.

Grid Generation

High Speed Aerodynamics, Long Beach

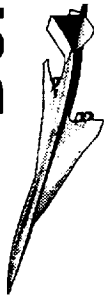


BDEING

Definition of the Optimization Problem

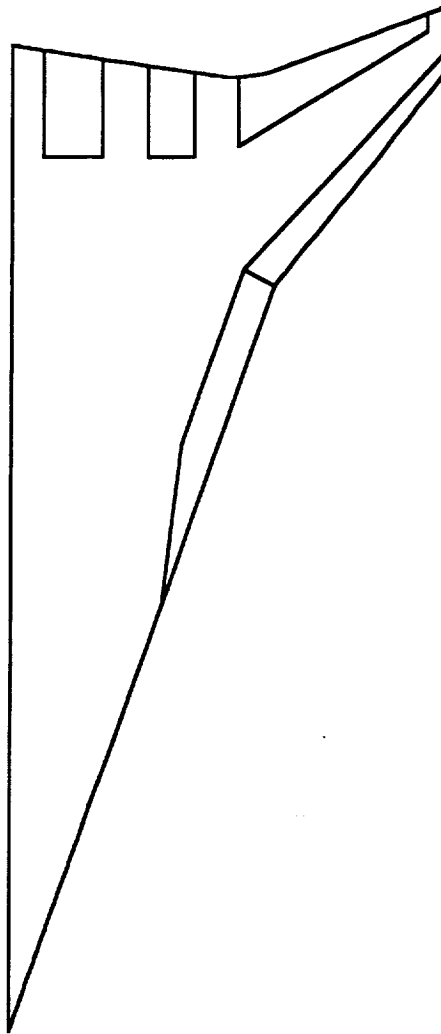
The objective of this work is to minimize D/L at a given Mach number and lift condition. With the flaps already defined, no attempt was made to optimize the shape of the flaps (i.e., the leading-edge radius, length or width of the flaps). The optimization problem is a relatively simple one. There are five flaps on each wing. Assuming symmetry, this leads to five design variables. Angle-of-attack was added to the design variable list to assist in maintaining the only constraint, lift.

Definition of the Optimization Problem



High Speed Aerodynamics, Long Beach

- Minimize D/L using Euler analysis complemented with flat-plate skin friction obtained for the flight Reynolds number
- Constrain lift to the 1-g cruise condition
- Six design variables include 5 flaps and the angle-of-attack

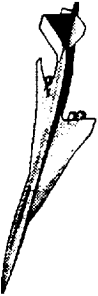


BOEING

Navier-Stokes Assessments

Numerous Navier-Stokes analyses were obtained to confirm improvements of the Euler-based optimization and better understand flow over the TCA wing. All solutions were obtained with a consistent process using CFL3D or its parallel version, CFL3Dhp. The Baldwin-Lomax turbulence model with the Degani-Schiff modification was used to close the system of governing flow equations. Grids were obtained using the procedure described earlier. They contained 3.4 million points (289 streamwise, 65 normal, 181 spanwise) and were clustered to achieve a $y^+ = 1.5$. All solutions were run at $Re_c = 6.36 \times 10^6$, the nominal wind-tunnel Reynolds number. All forces and moments quoted in this report are integrated to a fuselage station of 3148 in. to be consistent with the wind-tunnel model.

Navier-Stokes Assessment



High Speed Aerodynamics, Long Beach

- Optimization improvements are verified with CFL3D (or CFL3Dhp) Navier-Stokes analyses
- All Navier-Stokes solutions are run consistently with the following features:
 - Baldwin-Lomax turbulence model with Degani-Schiff modification
 - All grids contain 3.4 million points (289x65x181) and are clustered to achieve $y^+=1.5$
 - All solutions were run at a nominal wind-tunnel Reynolds number ($Re_c=6.36 \times 10^6$)
 - Forces and moments are integrated to FS 3148” to be consistent with wind-tunnel measurements

$M_{\infty}=0.6$ Convergence History

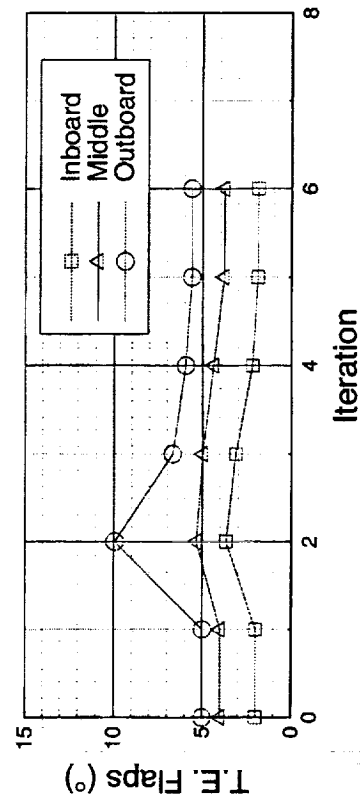
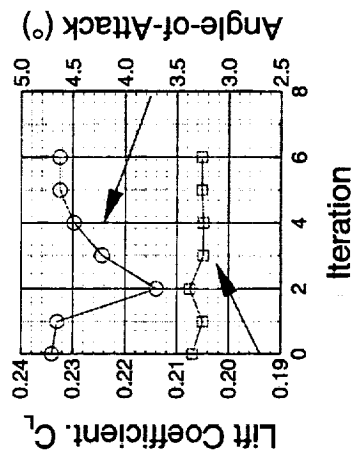
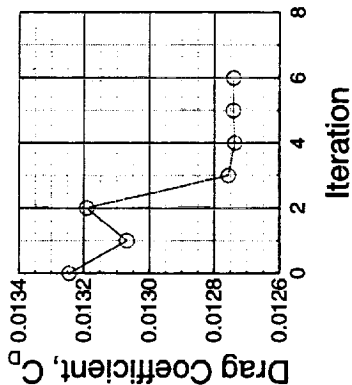
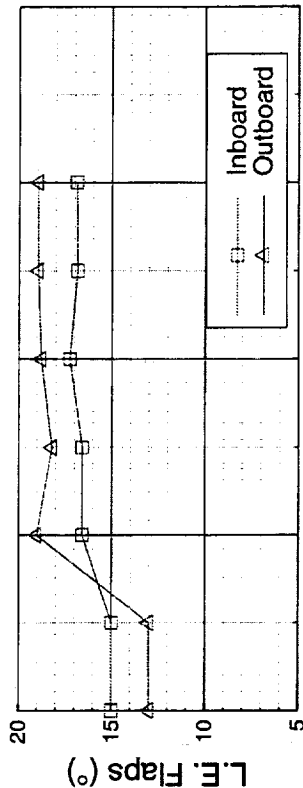
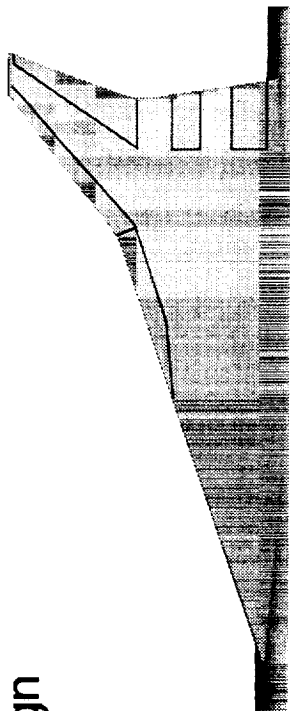
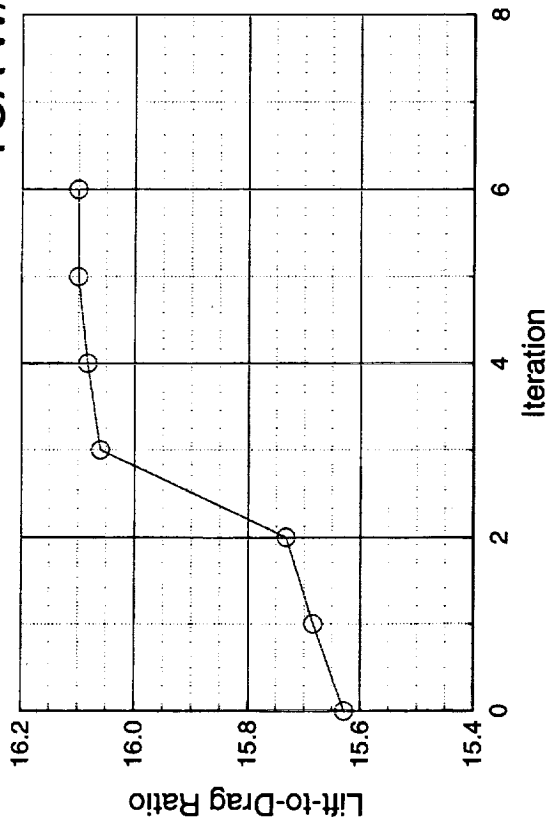
Shown below is the convergence history for the optimization performed at $M_{\infty}=0.6$. For this case, the lift is constrained to $C_L=0.205$. The initial flap setting was chosen as the final flap setting obtained from the optimization performed at $M_{\infty}=0.8$. The optimization was considered converged when the variations in design variables from iteration to iteration were small and changes in lift and drag settled to small levels.

M_∞=0.6 Convergence History



High Speed Aerodynamics, Long Beach

AEROSHOP with CFL3D Euler
TCA W/B/F Design



Upper Surface Streamlines and Cp Contours, $M_\infty=0.6$

Colored shading corresponding to upper surface pressures and streamlines for the baseline and optimized configurations are shown below. The figure was generated from Navier-Stokes solutions at $M_\infty=0.6$ ($C_L=0.205$) using CFL3D. A vortex is formed from the leading edge at roughly the mid-span on the baseline configuration. Deploying the inboard leading-edge flap, in this case 16.9° , removes the vortex resulting in less spanwise flow. The optimized configuration is also characterized by straight streamlines on the outboard panel, however a small bubble of hingeline separation is evident from the 19° outboard leading-edge flap deflection. The overall drag reduction at the cruise C_L from the baseline configuration to the optimized configuration as predicted from the Navier-Stokes solutions is 46.4 counts.

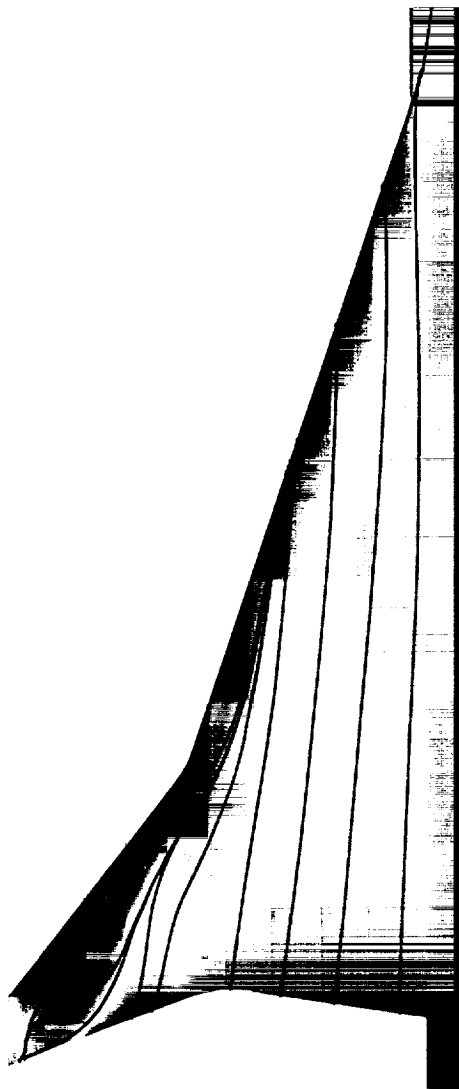
Upper Surface Streamlines and Cp Contours, $M_\infty=0.6$



High Speed Aerodynamics, Long Beach

CFL3D Navier-Stokes (Baldwin-Lomax with D-S), $C_L=0.205$, $Re_c=6.36 \times 10^6$

Baseline Configuration
 $0^\circ/0^\circ/0^\circ/0^\circ$



Optimized Configuration
 $16.9^\circ/19^\circ/1.9^\circ/3.8^\circ/5.6^\circ$



BOEING

$M_\infty=0.8$ Convergence History

The history of the optimization at $M_\infty=0.8$ is shown below. For this case, the lift is constrained to $C_L=0.19$. The initial flap setting was chosen as the final flap setting obtained from the optimization performed at $M_\infty=1.1$ (The $M_\infty=0.9$ result was not available at the time this design started). This history is characterized by a sudden increase in the lift-to-drag ratio from iteration 4 to 5. The reason of this and the corresponding sudden changes in the design variable values is unknown.

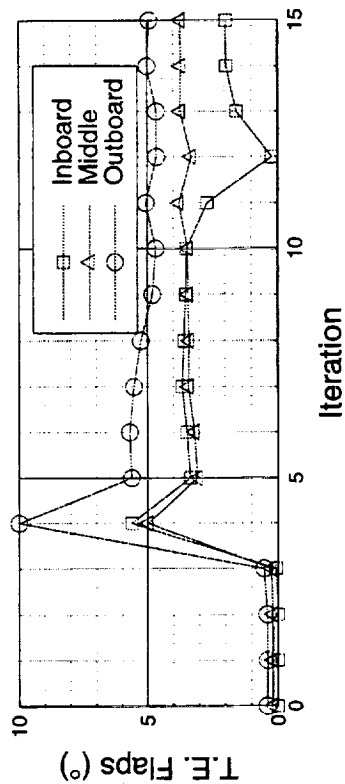
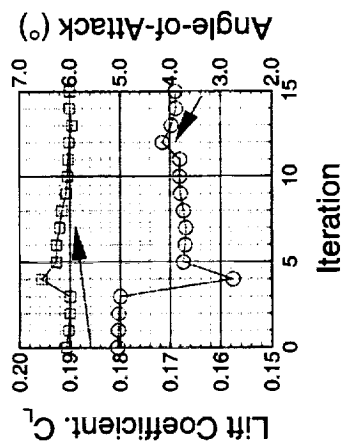
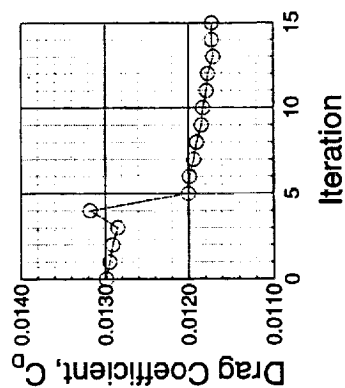
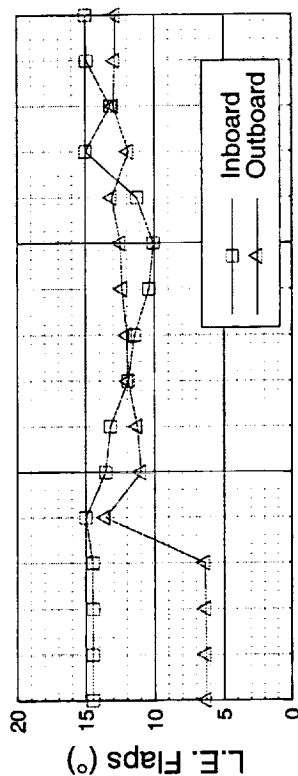
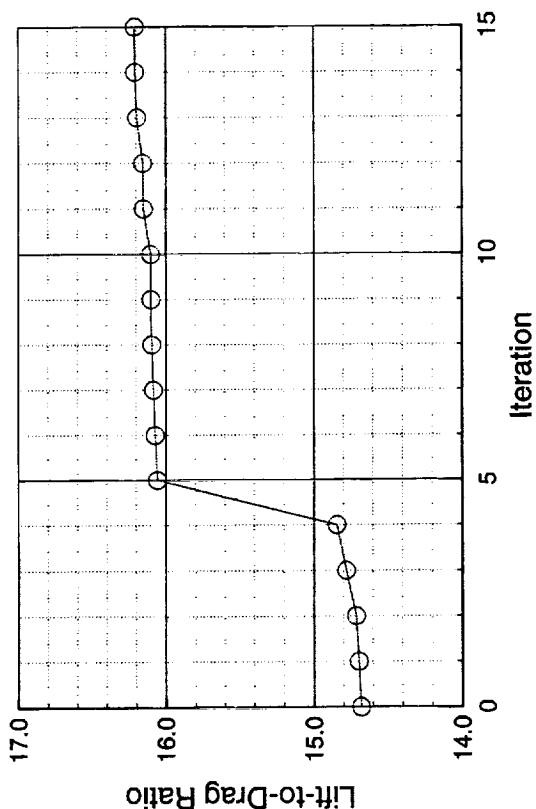
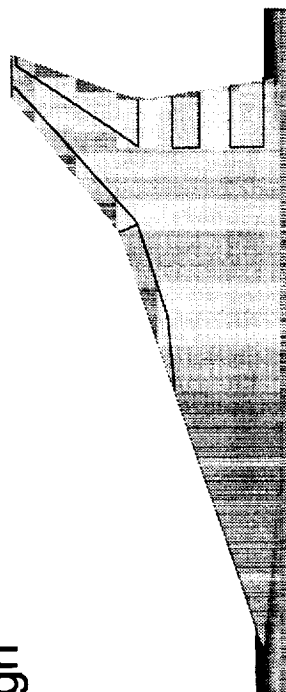
A Navier-Stokes assessment of the baseline and optimized flap configurations was not performed at the cruise lift condition for this Mach number. However, from solutions neighboring the cruise condition, the predicted Navier-Stokes increment between the baseline and optimized configurations, interpolated to $C_L=0.19$, is 40.0 count.

$M_{\infty}=0.8$ Convergence History



High Speed Aerodynamics, Long Beach

AEROSHOP with CFL3D Euler
TCA W/B/F Design



$M_{\infty}=0.9$ Convergence History

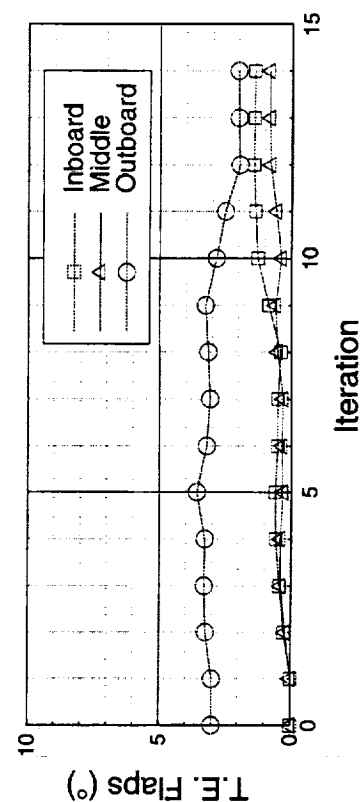
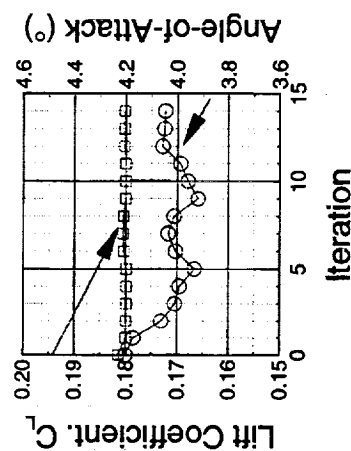
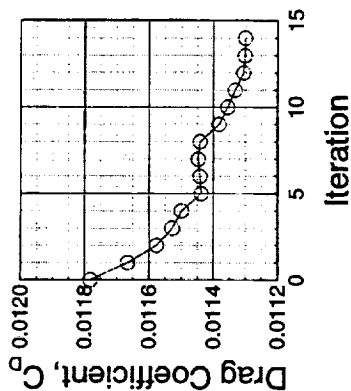
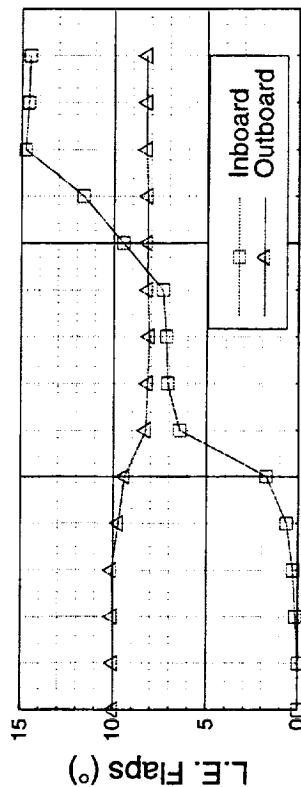
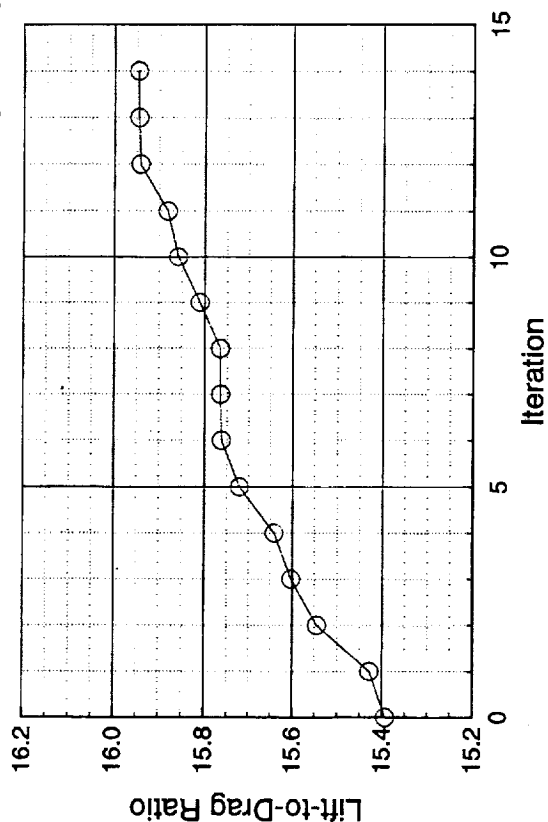
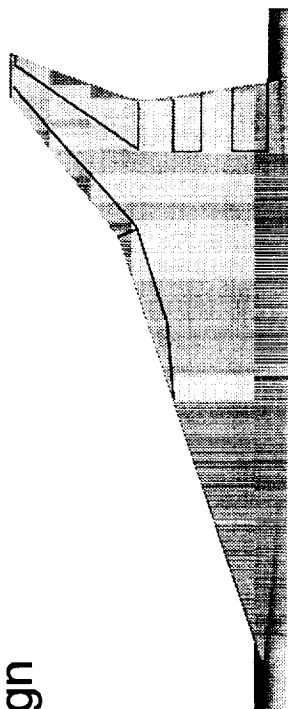
The design history for the $M_{\infty}=0.9$ optimization is shown below. Lift was constrained to $C_L=0.18$. The initial flap deflections for this design was arbitrarily selected to be $0^\circ/10^\circ/0^\circ/3^\circ$. The design proceeded 14 iterations before the design variables, lift and drag settled to optimum values.

$M_{\infty}=0.9$ Convergence History



High Speed Aerodynamics, Long Beach

AEROSHOP with CFL3D Euler
TCA W/B/F Design



Upper Surface Streamlines and Cp Contours, $M_\infty=0.9$

Shown below are upper surface pressure contours and streamlines from Navier-Stokes solutions of the baseline and optimized configurations at $M_\infty=0.9$. As in the $M_\infty=0.6$ case, the baseline is characterized by a vortex generated from the leading-edge near the mid span. The outboard panel has separated spanwise flow. The leading-edge deflections clean the flow over the wing significantly as can be seen from the straighter streamlines. The overall drag reduction at the cruise C_L from the baseline configuration to the optimized configuration as predicted from the Navier-Stokes solutions is 26.3 counts.

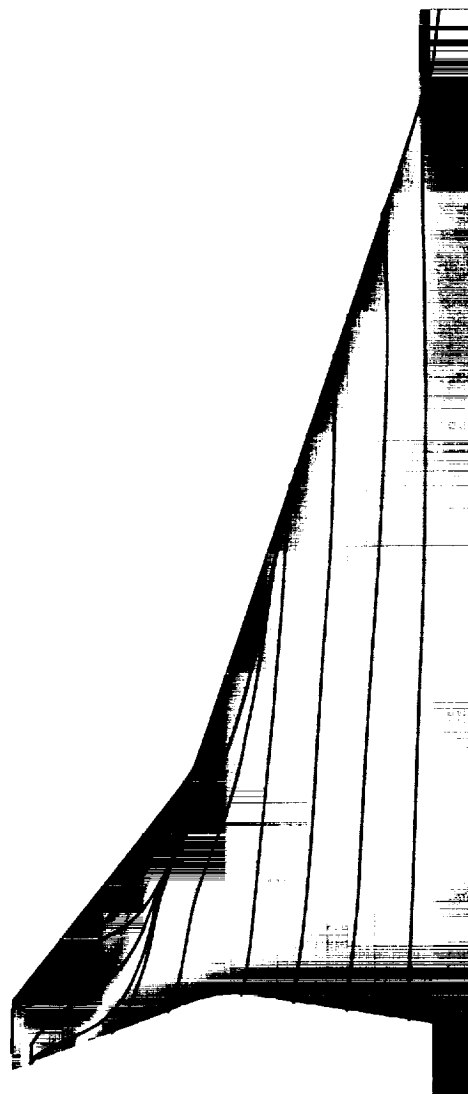
Upper Surface Streamlines and Cp Contours, $M_\infty=0.9$



High Speed Aerodynamics, Long Beach

CFL3D Navier-Stokes (Baldwin-Lomax with D-S), $C_L=0.18$, $Re_c=6.36 \times 10^6$

Baseline Configuration
 $0^\circ/0^\circ/0^\circ/0^\circ$



Optimized Configuration
 $14.5^\circ/8.2^\circ/1.4^\circ/0.8^\circ/2.0^\circ$

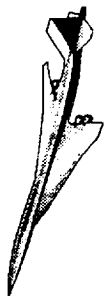


BOEING

$M_\infty=1.1$ Convergence History

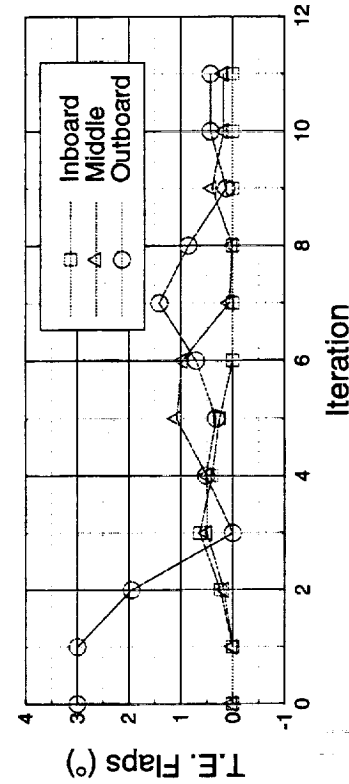
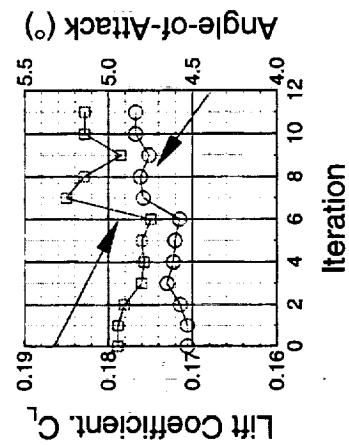
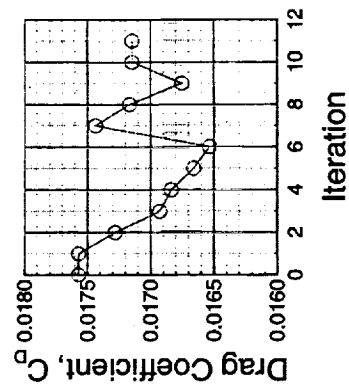
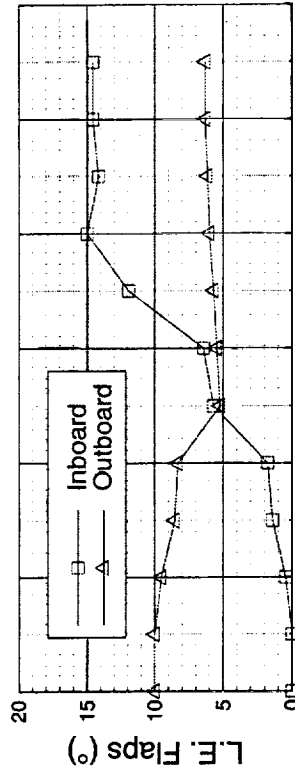
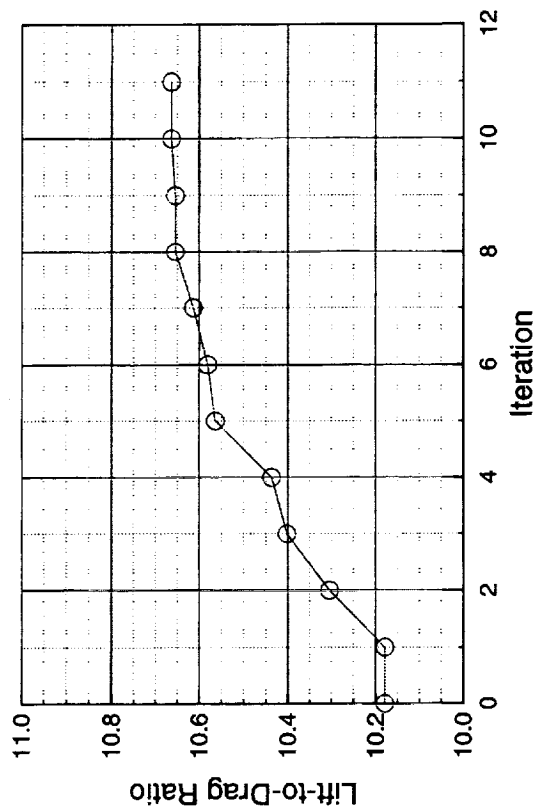
The convergence history for flap optimization at $M_\infty=1.1$ is shown below. For this case, the lift is constrained to $C_L=0.175$. The starting flap deflections are consistent with the starting conditions for the $M_\infty=0.9$ case. The design converged in 11 iterations requiring little trailing-edge flap deflections.

$M_{\infty}=1.1$ Convergence History



High Speed Aerodynamics, Long Beach

AEROSHOP with CFL3D Euler
TCA W/B/F Design



Upper Surface Streamlines and Cp Contours, $M_\infty=1.1$

Shown below are upper surface pressure contours and streamlines from Navier-Stokes solutions of the baseline and optimized configurations at $M_\infty=1.1$. The baseline and optimized streamlines follow similar trends shown in earlier figures for $M_\infty=0.6$ and $M_\infty=0.9$. The overall drag reduction at the cruise C_L from the baseline configuration to the optimized configuration as predicted from the Navier-Stokes solutions is 10.4 counts.

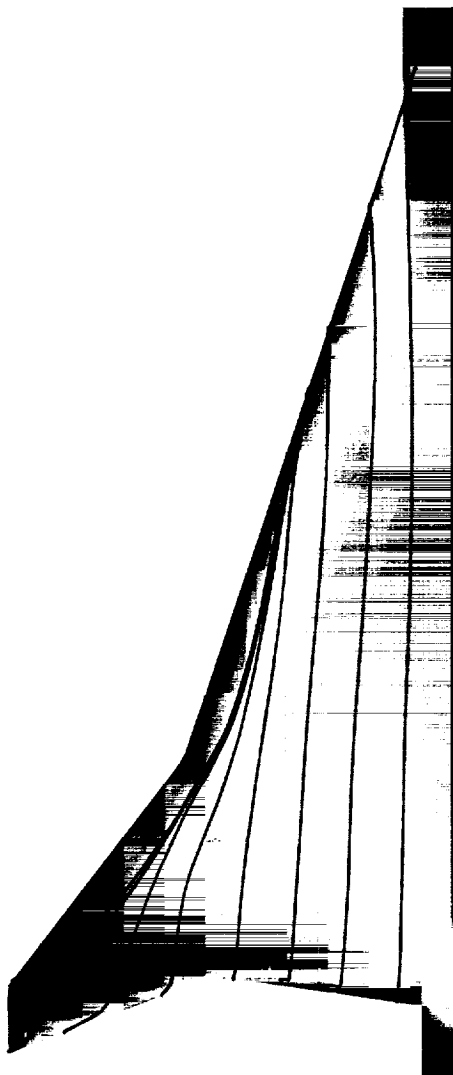
Upper Surface Streamlines and Cp Contours, $M_\infty=1.1$



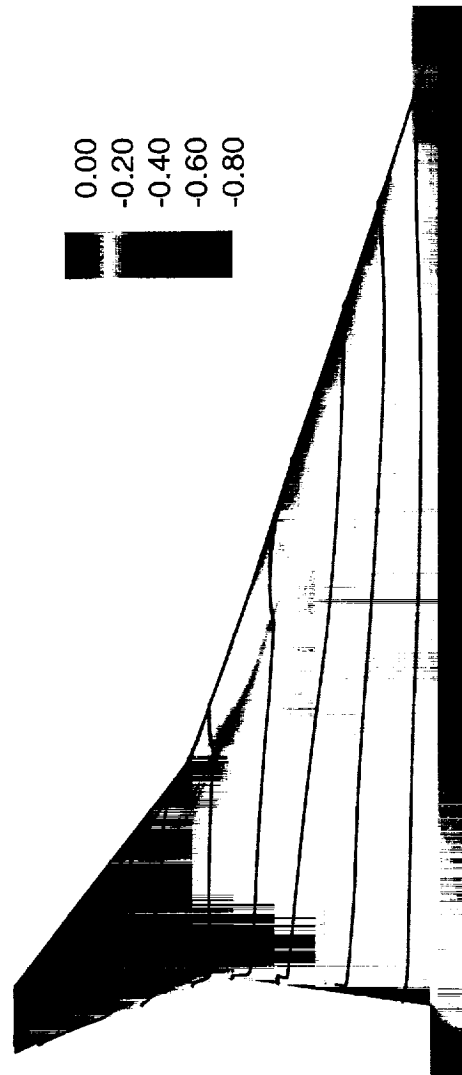
High Speed Aerodynamics, Long Beach

CFL3D Navier-Stokes (Baldwin-Lomax with D-S), $C_L=0.175$, $Re_c=6.36 \times 10^6$

Baseline Configuration
 $0^\circ/0^\circ/0^\circ/0^\circ$



Optimized Configuration
 $14.5^\circ/6.3^\circ/0.2^\circ/0.4^\circ$



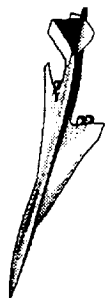
0.00
-0.20
-0.40
-0.60
-0.80



$M_\infty=1.8$ Convergence History

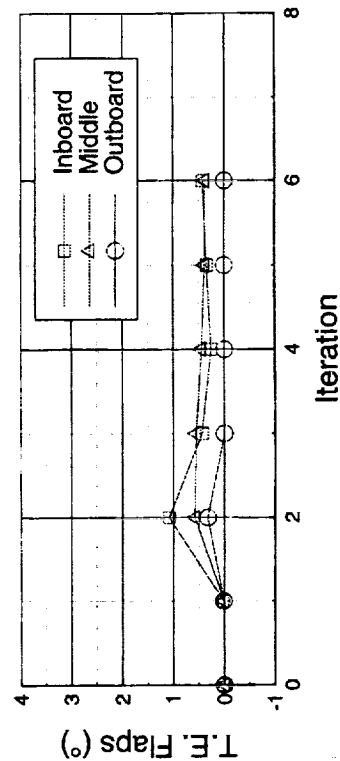
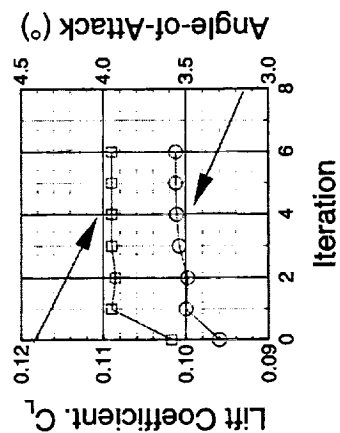
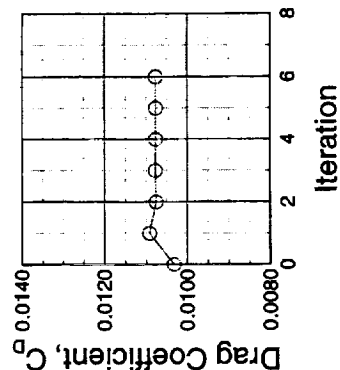
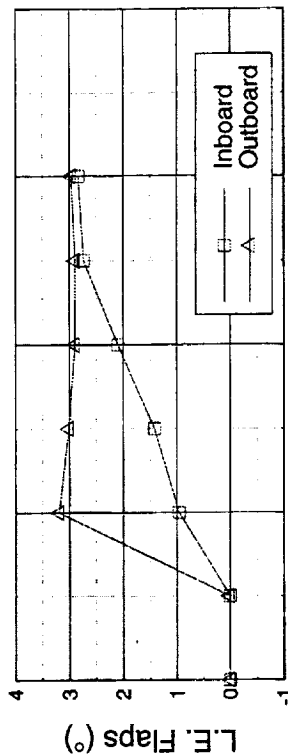
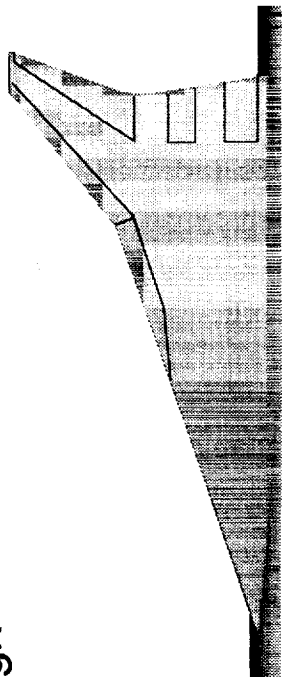
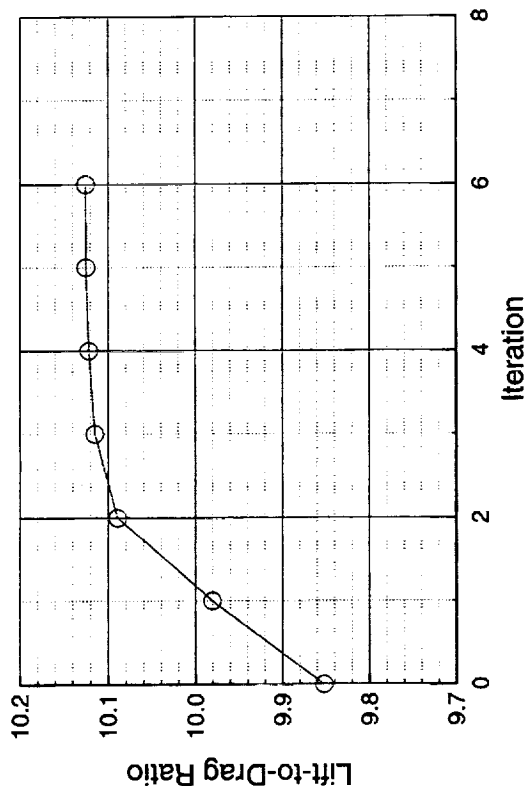
Shown below is the convergence history for the optimization performed at $M_\infty=1.8$. For this case, the lift is constrained to be above $C_L=0.099$. Zero degree flap deflections were chosen as the initial conditions for the optimization. The design converged in less iterations than the two previous cases. As the Mach number approaches the supersonic cruise Mach number of 2.4, the flaps become less effective, and the optimization can be expected to converge quicker.

$M_{\infty}=1.8$ Convergence History



High Speed Aerodynamics, Long Beach

AEROSHOP with CFL3D Euler
TCA W/B/F Design



Upper Surface Streamlines and Cp Contours, $M_\infty=1.8$

Colored shading corresponding to upper surface pressures and streamlines from Navier-Stokes solutions at $M_\infty=1.8$ ($C_L=0.099$) for the baseline and optimized configurations are shown below. As expected, the flow is relatively well behaved and flaps do little to improve the performance. The overall drag reduction at the cruise C_L from the baseline configuration to the optimized configuration as predicted from the Navier-Stokes solutions is 2.6 counts.

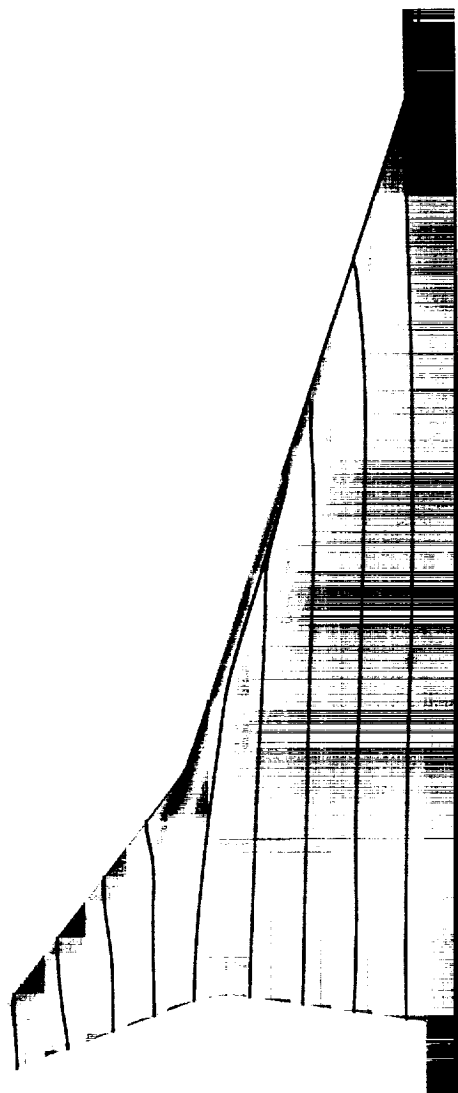
Upper Surface Streamlines and Cp Contours, $M_\infty=1.8$

High Speed Aerodynamics, Long Beach

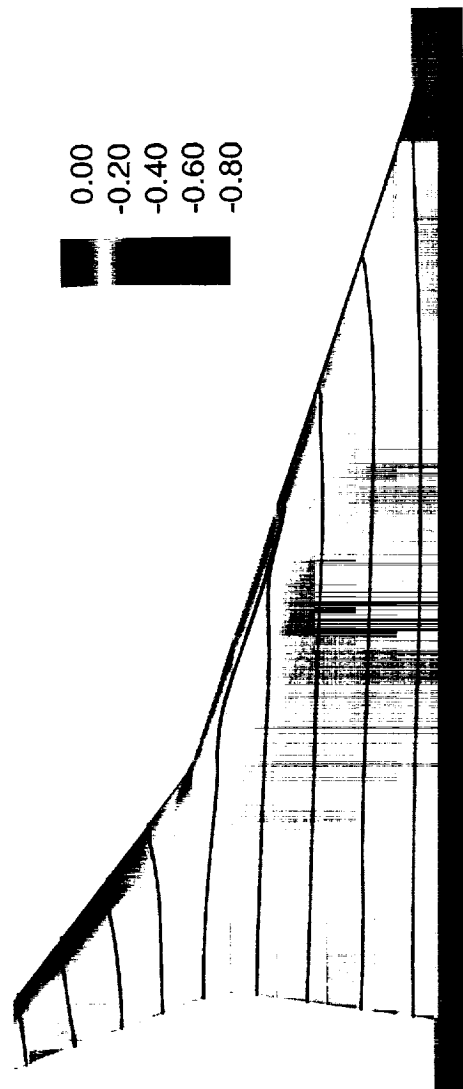


CFL3D Navier-Stokes (Baldwin-Lomax with D-S), $C_L=0.099$, $Re_c=6.36 \times 10^6$

Baseline Configuration
 $0^\circ/0^\circ/0^\circ/0^\circ$



Optimized Configuration
 $2.8^\circ/3.0^\circ/0.4^\circ/0.4^\circ/0^\circ$

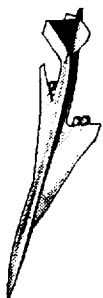


BOEING

Summary of Flap Optimization

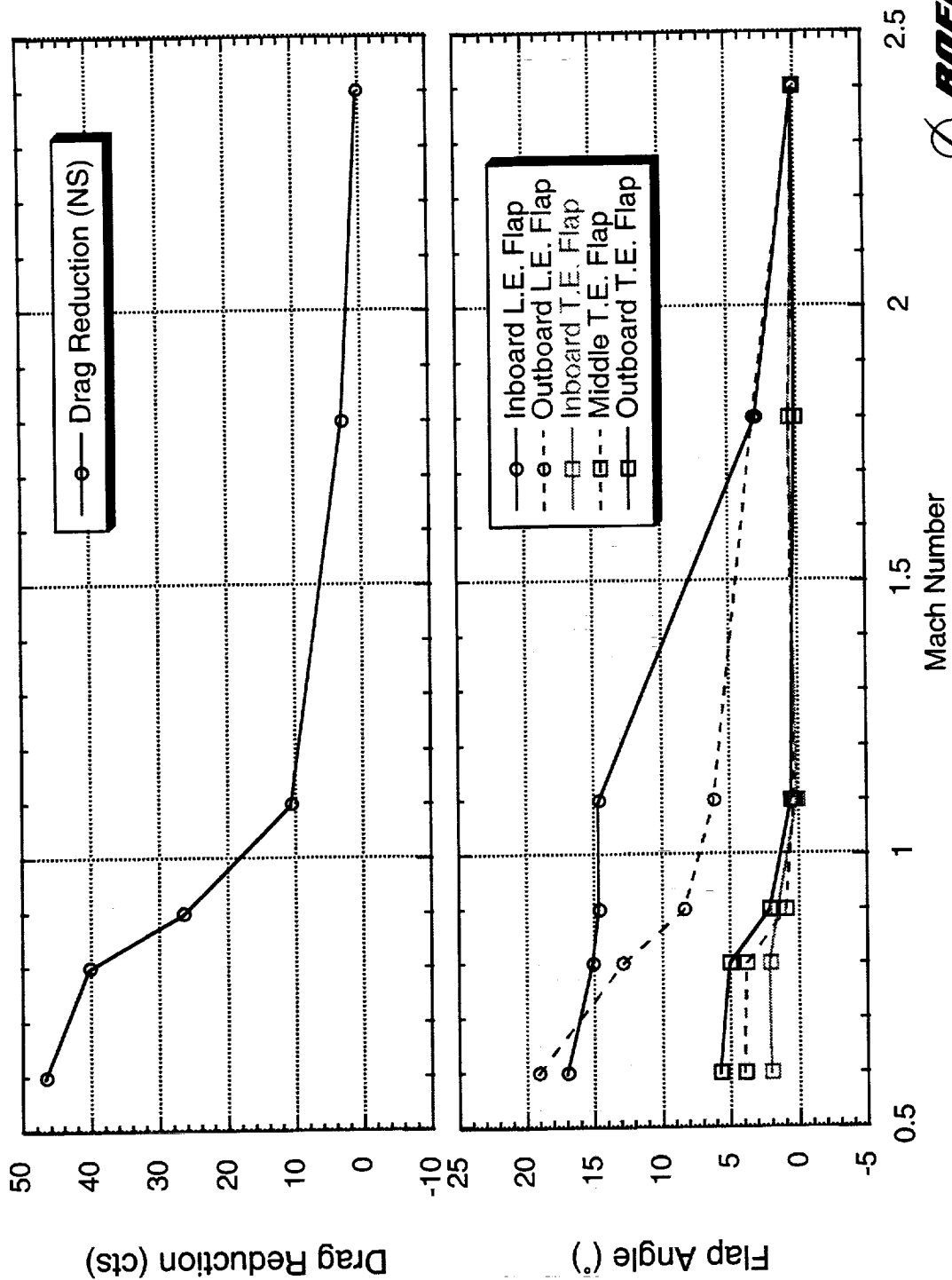
A summary of the drag reduction and flap settings versus Mach number is given in this figure. The drag reduction is computed at the cruise lift condition for the given Mach number and represents the drag decrement between the baseline configuration (zero flaps) and the optimized flap configuration. As the Mach number increases, the drag reduction decreases since the wing approaches the supersonic design condition and flaps become less helpful. Flap deflections generally decrease with Mach number. Above Mach 1, the trailing-edge flaps are not needed.

Summary of Flap Optimization



High Speed Aerodynamics, Long Beach

$Re_c = 6.36 \times 10^6$



Improvement Over Current Flap Schedule

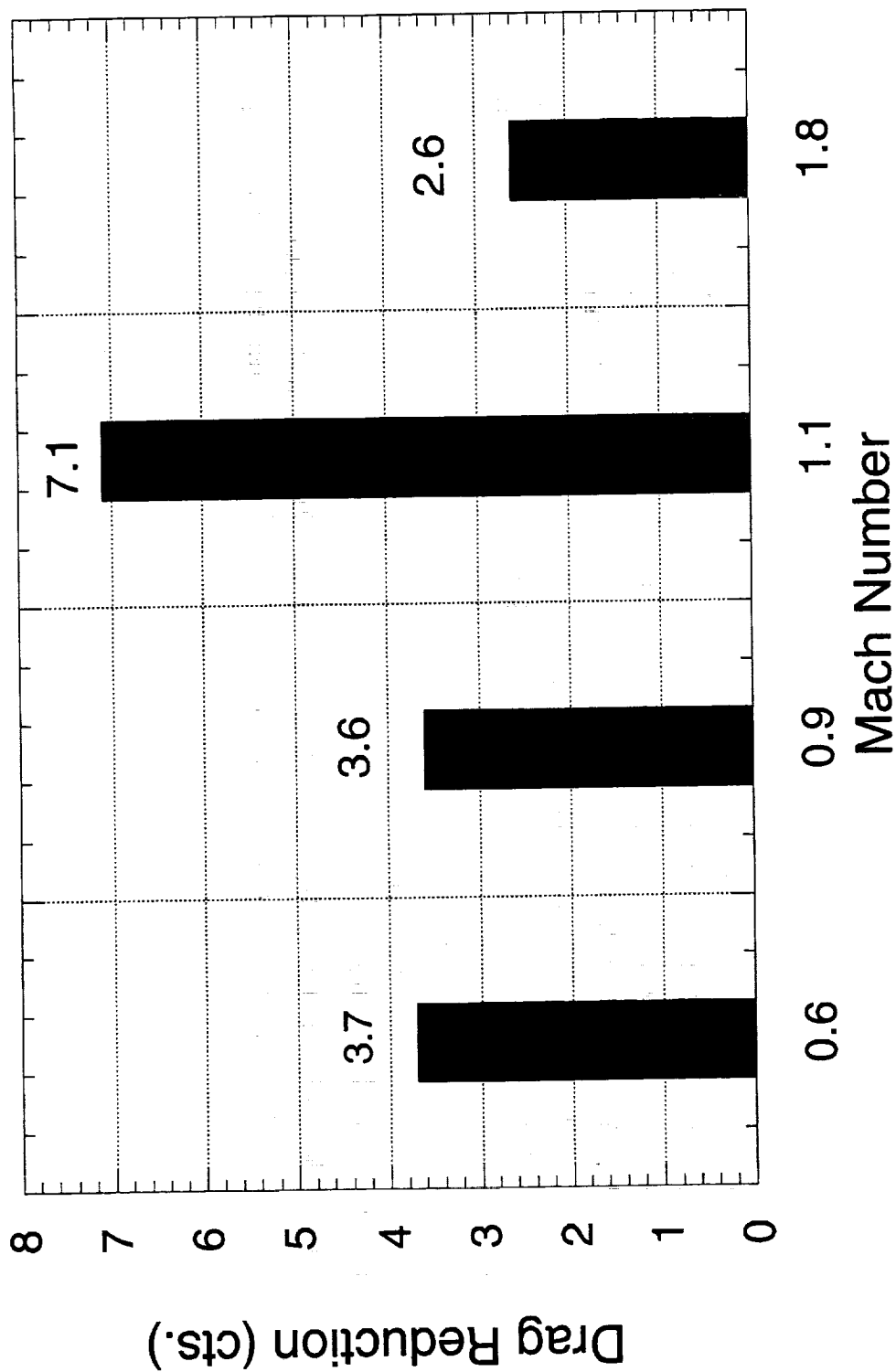
The current flap schedule for the TCA was determined by either the Technology Integration element of HSR (using linear aerodynamic methods) or by Dynacs (using a Navier-Stokes parametric study). In both of these methods, the use of flaps other than those existing on the outboard wing panel were not considered. The bar chart below compares the drag reduction obtained from the optimized flap settings over the current flap schedule. The increments are obtained from CFL3D Navier-Stokes solutions at the cruise lift condition for the given Mach number.

Improvement Over Current Flap Schedule

High Speed Aerodynamics, Long Beach



CFL3D Navier-Stokes Predictions (Baldwin-Lomax with D-S), $Re_c = 6.36 \times 10^6$

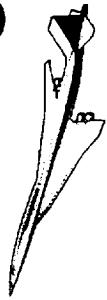


Summary of Experimental Testing

The NASA Langley 16-ft Transonic Wind Tunnel was chosen for the facility to conduct the experimental test. The objectives of the wind-tunnel test (Test 496) were to 1) validate the performance of the optimized flap schedule at $M_\infty=0.6, 0.9$, and 1.1 , 2) obtain data to understand the nacelle/diverter effects on the performance of the optimized flaps settings, and 3) understand the nature of the flow over the wing with and without flap deflections. For this, force, moment, and pressure data were obtained for the W/B, W/B/F, W/B/N/D and W/B/N/D/F configurations. Flow visualization data, including PSP, colored oil flows, and UV oil were also obtained. Though not directly supporting the objectives of the test, visual model deformation (VMD) data were also obtained. The NASA Langley test engineers were Wes Goodman and Dan Cler. Al Burner was responsible for the VMD data.

Wind-tunnel data shown in this report has not been finalized and is subject to change under the review of the test engineers. A report documenting all Test 496 results is in progress.

Summary of Experimental Testing



High Speed Aerodynamics, Long Beach

- Test 496, Transonic Flap Optimization Validation, was conducted for 5 weeks in the NASA Langley 16-ft Transonic Wind-Tunnel facility
- The 1.675% TCA Model 2a was modified to include an inboard leading-edge flap (became Model 5)
- Force, moment and pressure data for W/B, W/B/F, W/B/N/D, and W/B/N/D/F at $M_\infty=0.6, 0.9, 1.1$
- Flow visualization data included:
 - PSP (pressure)
 - Colored oil flow (stream traces)
 - UV oil flow (transition)
- Model deformation



CFL3D Navier-Stokes and Test Results

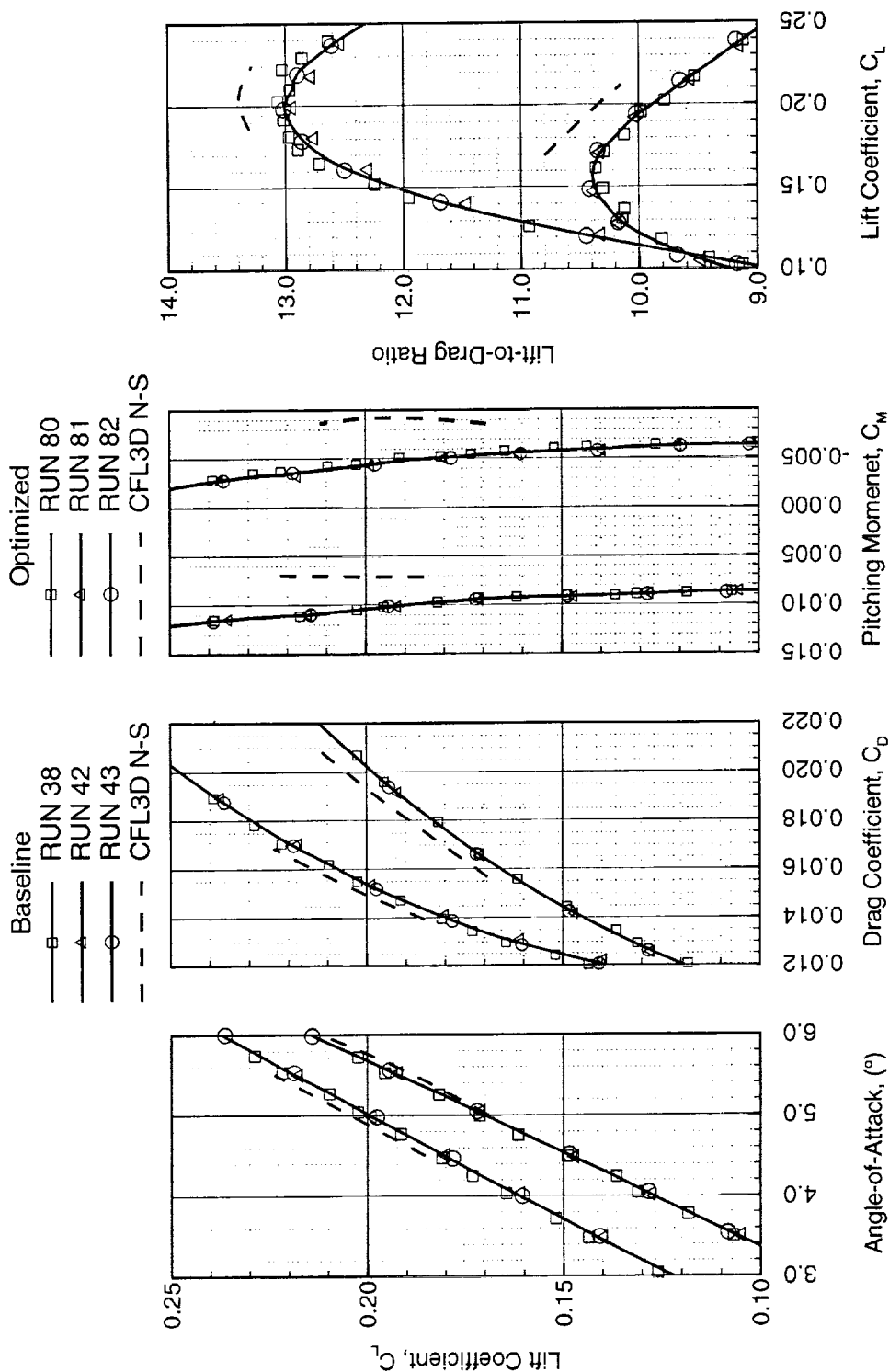
Absolute force and moment predictions are compared with the test data in the following three charts. Selected experimental runs for the baseline and optimized configurations are splined together and compared to CFL3D Navier-Stokes predictions (from solutions presented earlier). Shown below is the comparison at $M_\infty=0.6$. The optimized flap configuration is shown in red and the baseline configuration is in black. The lift is over-predicted in the optimized case, while under-predicted for the baseline configuration. For both configurations, the drag is under-predicted, thus resulting in an over-prediction in the lift-to-drag ratio. The pitching moment is also inaccurately captured, though much of this can be attributed to aeroelastic deformation of the wind-tunnel model.

CFL3D Navier-Stokes and Test Results



High Speed Aerodynamics, Long Beach

W/B Navier-Stokes Solution at $M_\infty=0.6$, $Re_c=6.36 \times 10^6$
(Baldwin-Lomax with Degani-Schiff)



BOEING

CFL3D Navier-Stokes and Test Results

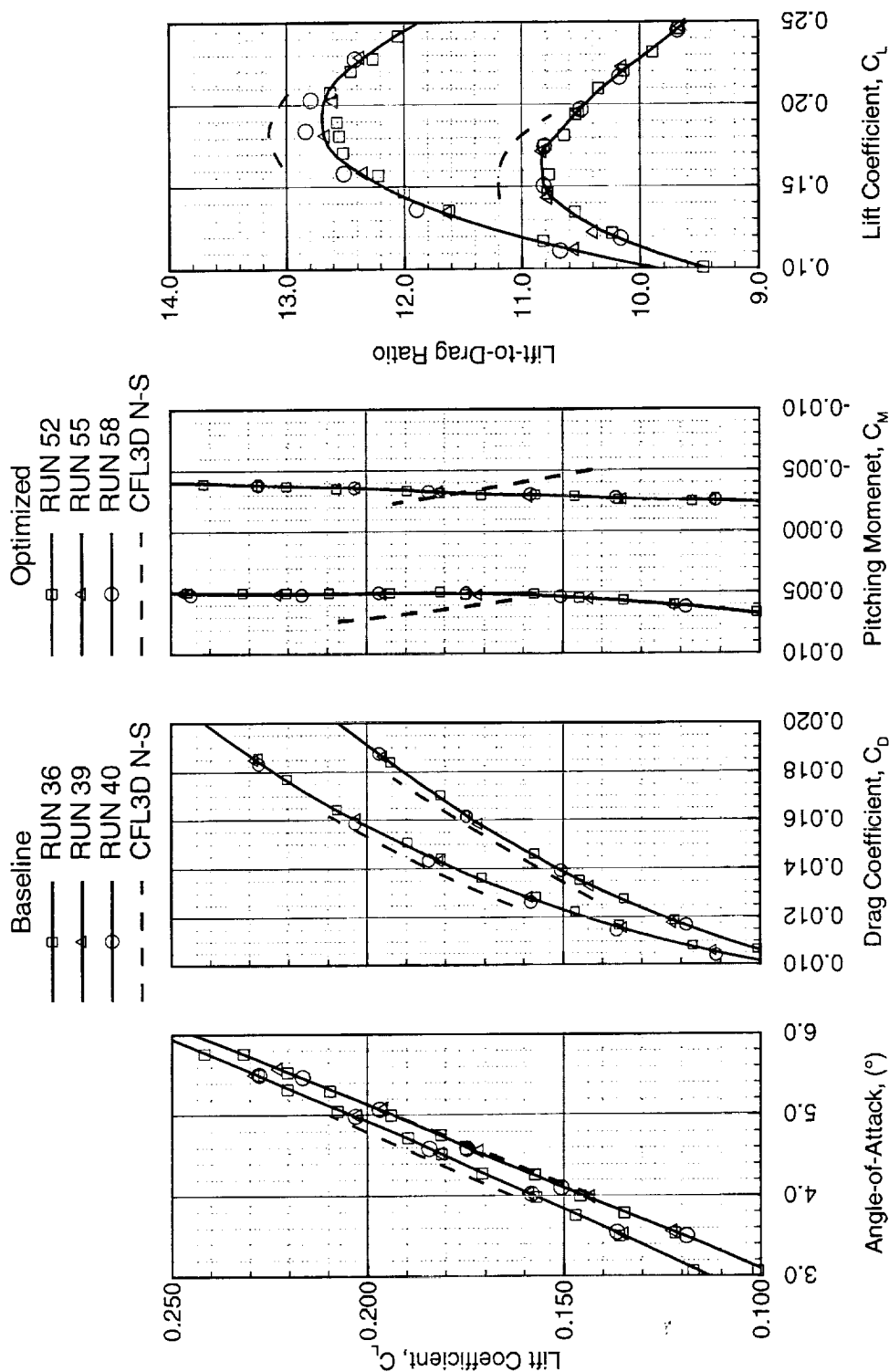
As before, the optimized configuration is shown in red, the baseline is shown in black. The comparison at $M_\infty=0.9$ is similar to that at $M_\infty=0.6$. The lift is over-predicted in the optimized case, while slightly under-predicted for the baseline configuration. For both configurations, the drag is under-predicted, thus resulting in an over-prediction in the lift-to-drag ratio. The pitching moment is also inaccurately captured.

CFL3D Navier-Stokes and Test Results



High Speed Aerodynamics, Long Beach

W/B Navier-Stokes Solution at $M_\infty=0.9$, $Re_c=6.36 \times 10^6$
(Baldwin-Lomax with Degani-Schiff)



CFL3D Navier-Stokes and Test Results

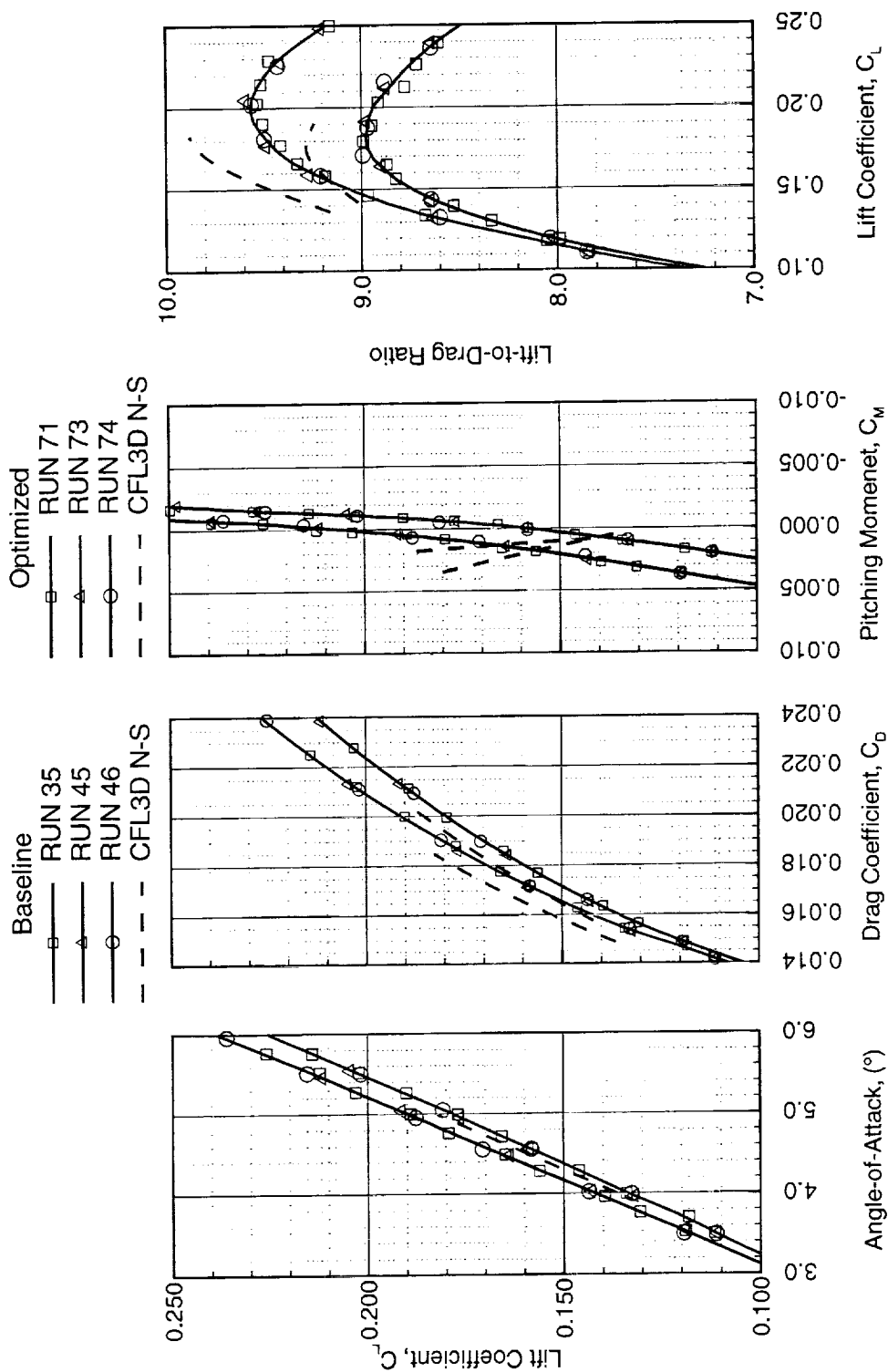
Again, the optimized configuration is shown in red, the baseline is shown in black. The comparison at $M_\infty=1.1$ generally follows that of the two earlier Mach numbers. The lift is over-predicted in the optimized case, but agrees well for the baseline configuration. For both configurations, the drag is under-predicted, thus resulting in an over-prediction in the lift-to-drag ratio. The pitching moment is also inaccurately captured.

CFL3D Navier-Stokes and Test Results



High Speed Aerodynamics, Long Beach

W/B Navier-Stokes Solution at $M_\infty=1.1$, $Re_c=6.36 \times 10^6$
(Baldwin-Lomax with Degani-Schiff)



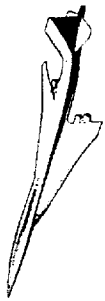
Comparison of Predicted and Measured Drag Increments

Though absolute force levels were not accurately captured by the application of CFL3D, drag increments between flap configurations at a given lift condition were reasonably predicted above $M_\infty=0.6$. This chart compares the predicted drag reduction between the baseline and optimized flap configurations at the cruise lift condition for the given Mach number. Though the process for predicting overall forces and moments using CFL3D needs improvement, the consistent application is adequate to judge one flap configuration over another. Also included in this chart are the Euler-predicted increments as computed from the optimization process. The consistency between the Euler, Navier-Stokes and experimentally measured increments yields credibility to the design process.

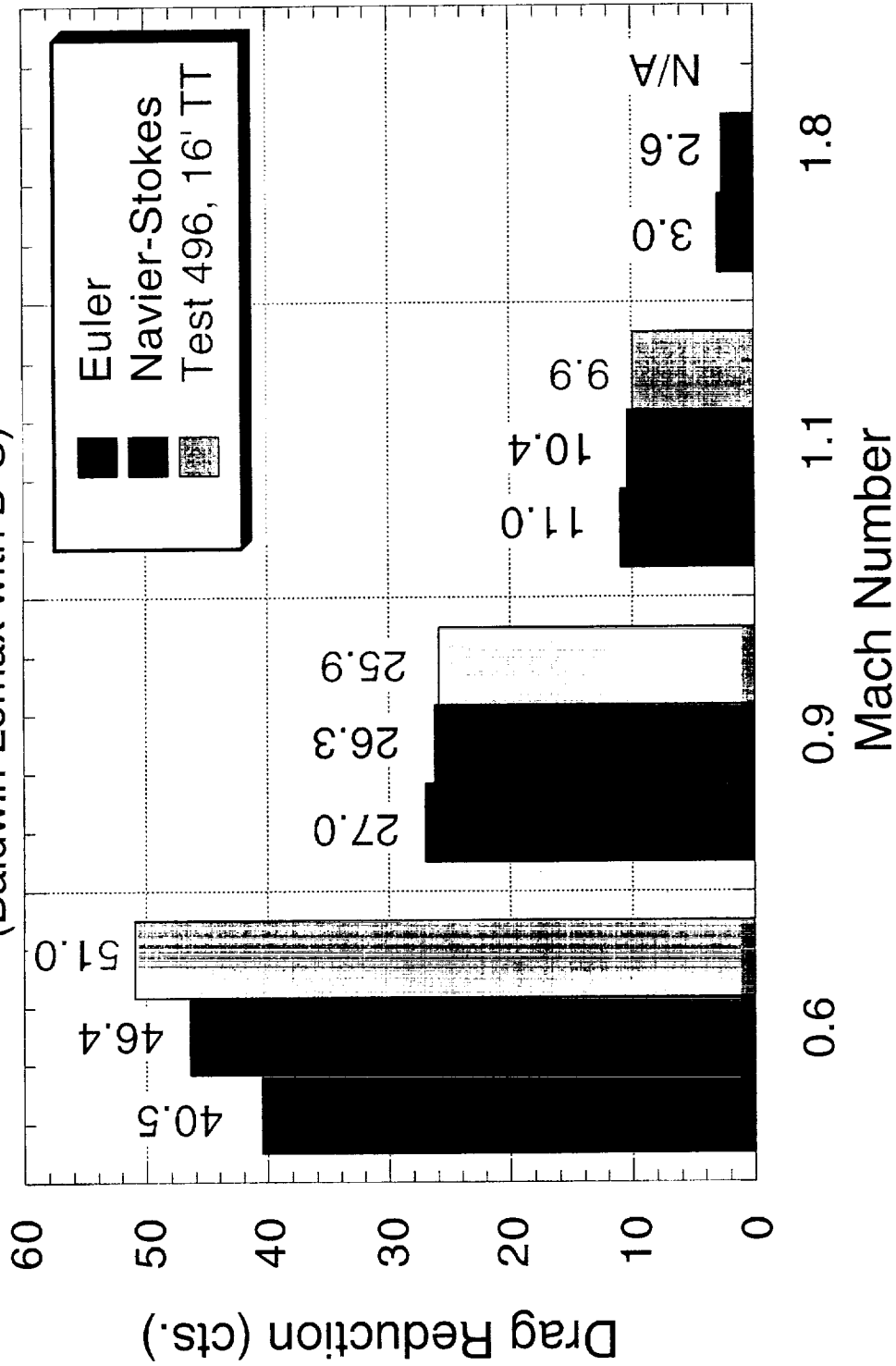
Comparison of Predicted and Measured W/B

Drag Increments

High Speed Aerodynamics, Long Beach



Navier-Stokes Solutions at $Re_c = 6.36 \times 10^6$
(Baldwin-Lomax with D-S)

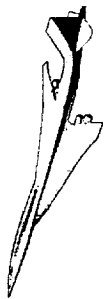


Predicted Streamlines and Oil Flow Traces

The following 3 figures compare surface streamlines on the upper surface of the optimized configurations at $M_\infty=0.6$, 0.9, and 1.1. The upper figures are snapshots of colored oil flow patterns from the 16-ft wind-tunnel test. The lower picture is from CFL3D Navier-Stokes solutions near the tunnel Reynolds number condition. The tunnel can take a few minutes to reach condition once air starts to blow and frequently the oil drifts over the model before the desired conditions are set. Patterns on the front section of the wing do not tend to accurately represent the desired flow condition. Generally, the CFD simulation agrees well with the experiment.

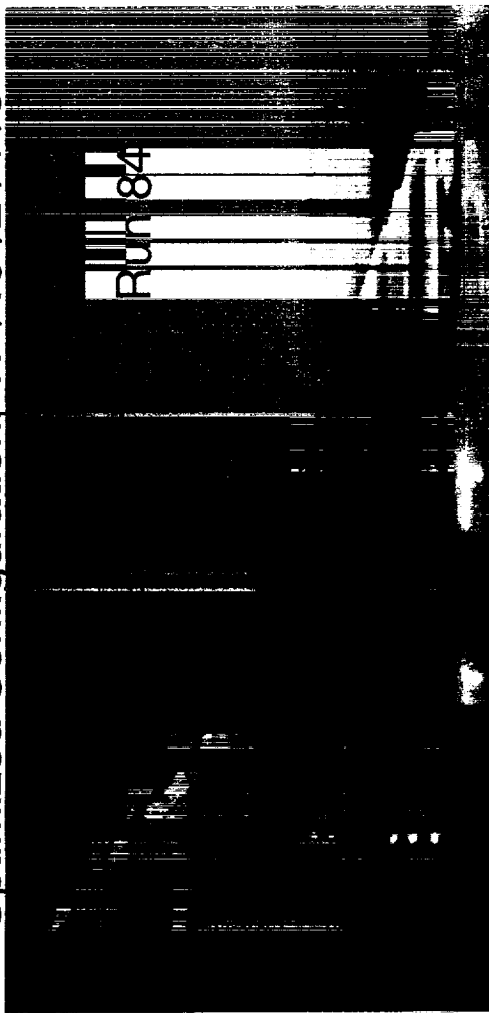
Colored oil flow patterns were also documented for the baseline configuration, however due to the vortical flow inherent in these configurations, the runs were not very successful.

Predicted Streamlines and Oil Flow Traces, $M_\infty=0.6$

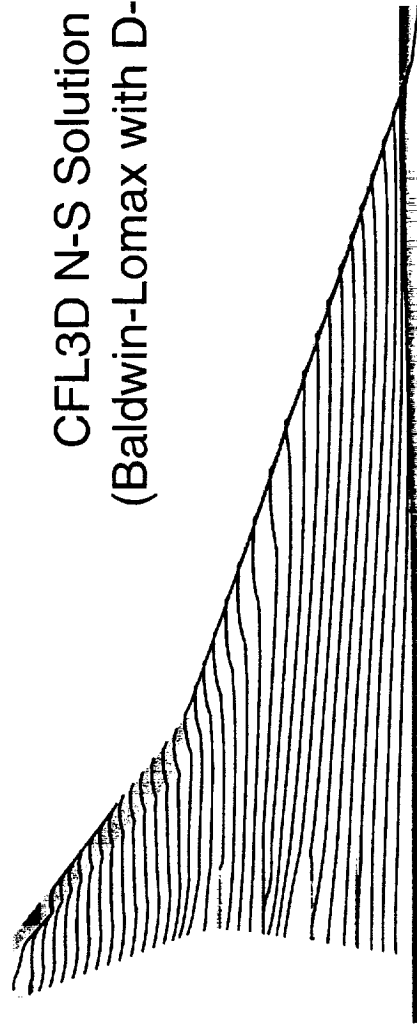


High Speed Aerodynamics, Long Beach

Upper Surface, $C_L=0.205$, $Re_c=6.36 \times 10^6$
Optimized Configuration, $17^\circ/19^\circ/2^\circ/4^\circ/5^\circ$



CFL3D N-S Solution
(Baldwin-Lomax with D-S)



BOEING

Predicted Streamlines and Oil Flow Traces

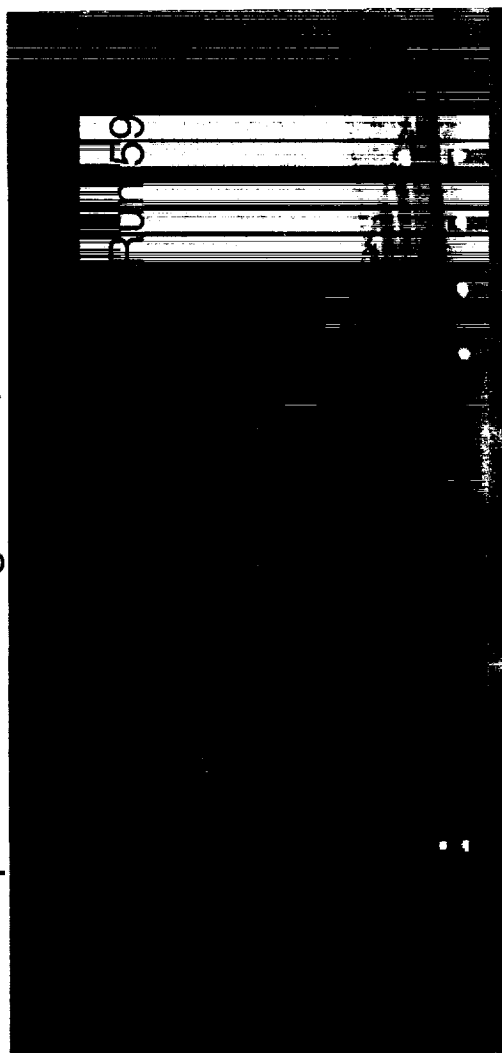
This page is intentionally left blank.

Predicted Streamlines and Oil Flow Traces, $M_\infty=0.9$

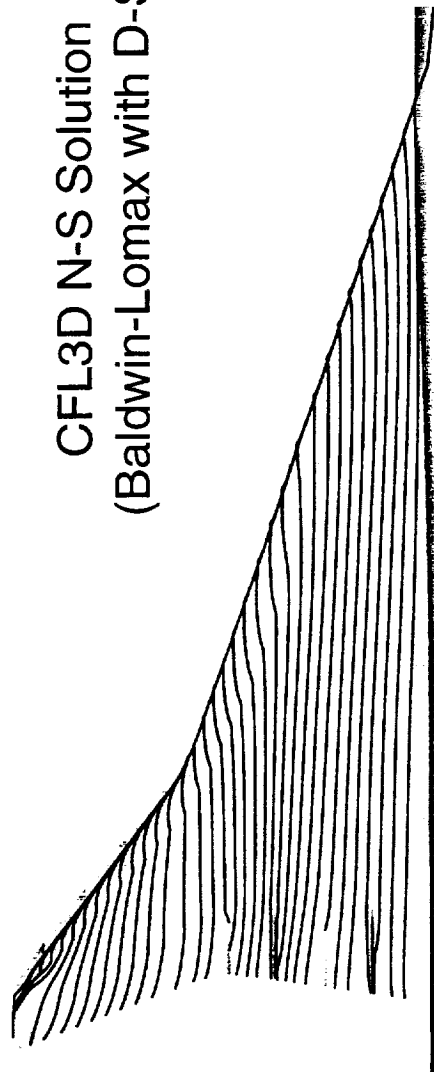


High Speed Aerodynamics, Long Beach

Upper Surface, $C_L=0.18$, $Re_c=6.36 \times 10^6$
Optimized Configuration, $15^\circ/8^\circ/1.5^\circ/1^\circ/2^\circ$



CFL3D N-S Solution
(Baldwin-Lomax with D-S)



BOEING

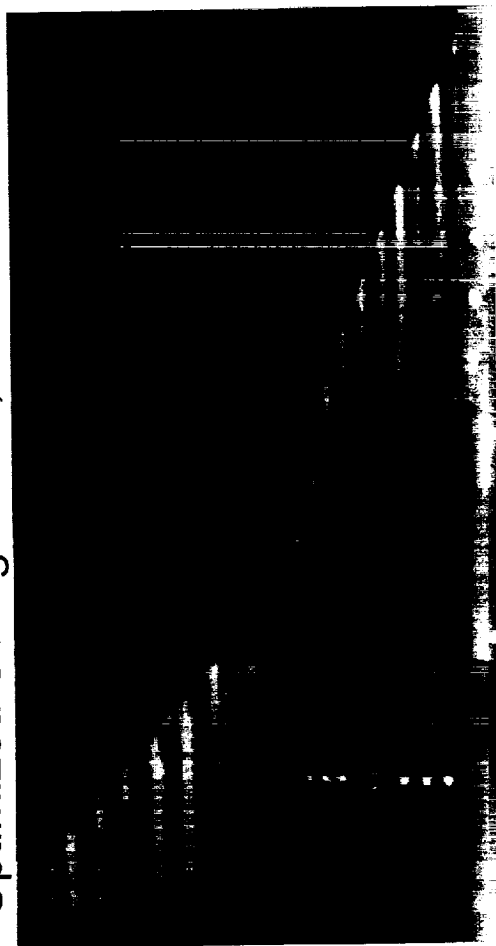
Predicted Streamlines and Oil Flow Traces

This page is intentionally left blank.

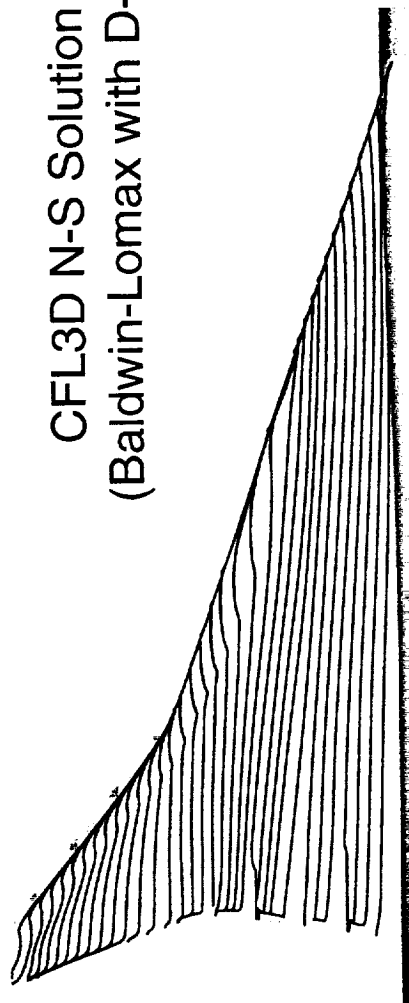
Predicted Streamlines and Oil Flow Traces, $M_\infty=1.1$

High Speed Aerodynamics, Long Beach

Upper Surface, $C_L=0.175$, $Re_c=6.36 \times 10^6$
Optimized Configuration, $15^\circ/6^\circ/0^\circ/0.5^\circ$



CFL3D N-S Solution
(Baldwin-Lomax with D-S)



BOEING

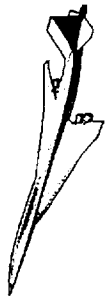
Off-design Flap Deflections

The validation of predicted Navier-Stokes drag reductions are very encouraging, and the Euler increments are also reasonable considering that transonic flows feature many viscous phenomena. Yet, a question still remains whether the Euler-based optimization has yielded the best flap settings for viscous-dominated flowfield. To answer this question, configurations with flap deflections near the Euler-based optimum were tested in the wind tunnel. The results are shown below in the bar chart.

At $M_\infty=0.9$, the trailing-edge flaps have been modified from their optimized deflections to 3° setting and 0° settings. Within the experimental accuracy of the data, the configurations show similar benefits with perhaps a slight edge going to the 3° flap deflection. Euler optimization does not account for boundary layer growth. In this case, the flow over the wind-tunnel model may experience a flap deflection slightly less than the actual deflection due to the presence of the boundary layer. The wind-tunnel flow over the 3° trailing-edge flap deflection may be a closer representation of inviscid flow over the optimized trailing-edge flaps than the wind-tunnel flow over the optimized trailing-edge flaps.

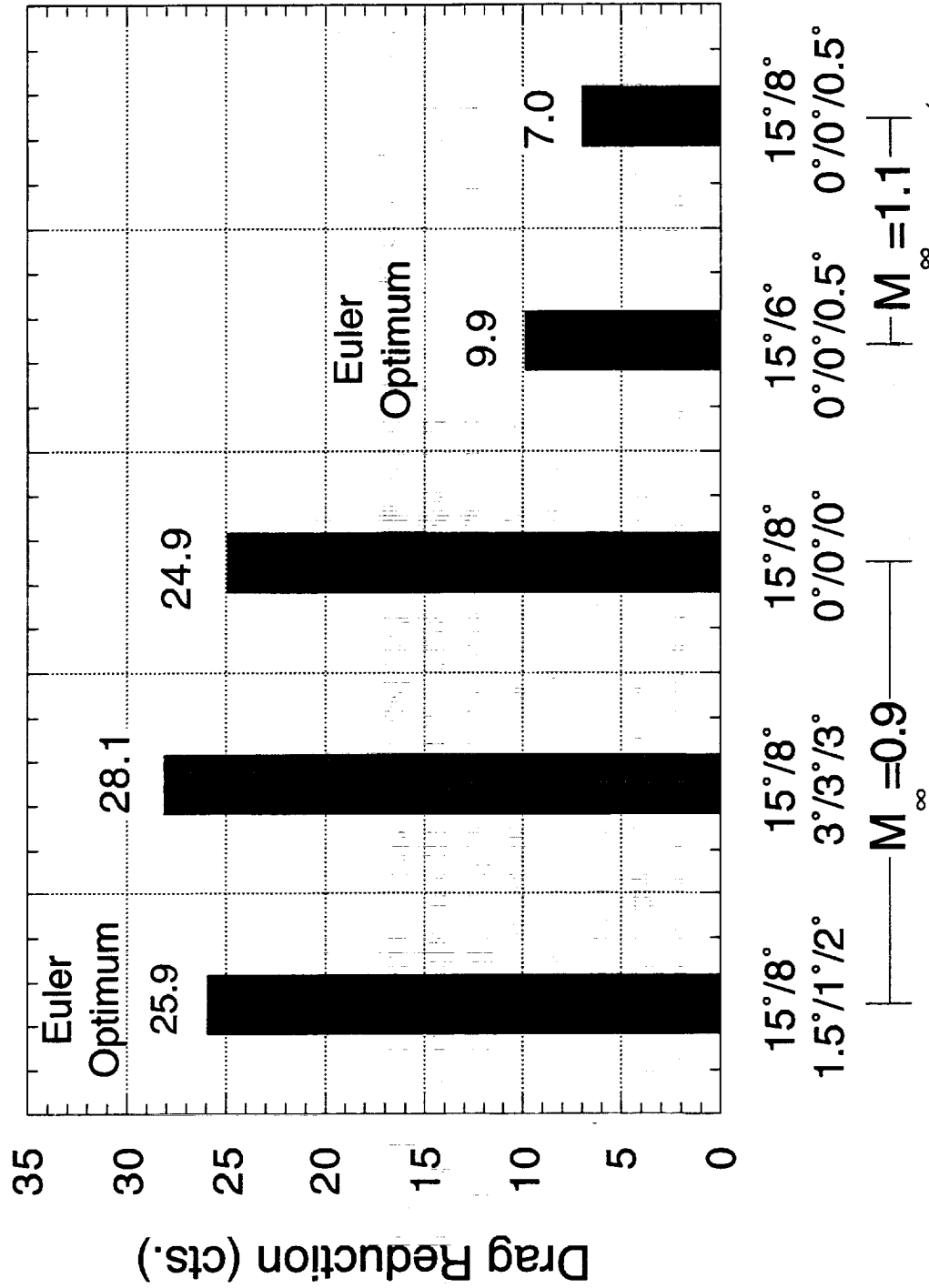
At $M_\infty=1.1$, the outboard leading-edge flap was deflected an additional 2° down. In this case, the drag increment was lessened by 3 counts lending credibility to the optimization process. The boundary layer growth on the outboard wing panel is expected to have a much smaller effect on flap optimization as the chord length is much smaller. A more exhaustive study varying all flaps individually would further strengthen the validation, though tunnel time restrictions are prohibitive.

Off-design Flap Deflections



High Speed Aerodynamics, Long Beach

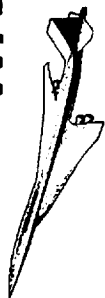
1.675% TCA Model 5 Test 496 in the NASA Langley 16' TT, $Re \approx 4 \times 10^6/ft$



W/B/F Versus W/B/N/D/F Optimization

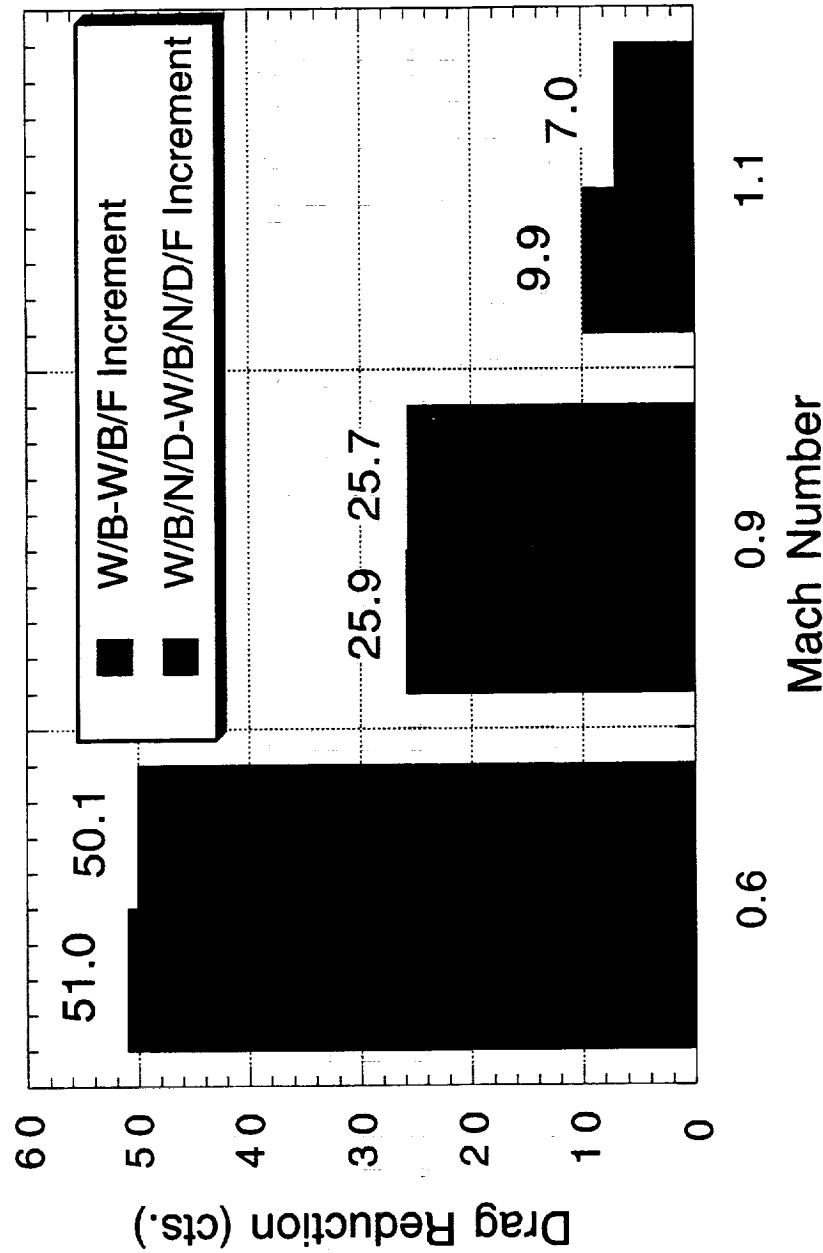
Transonic flap optimization using the W/B configuration offers an attractive simplification to W/B/N/D/F optimization because of the relative ease in geometry manipulation and lower cost in CPU associated with CFD analyses. However, it has yet to be determined if this simplification is acceptable. During the wind-tunnel test, force and moment measurements of the baseline and optimized flap configurations with nacelles installed were made to compare the effects of the nacelles on the predicted increment. The measured increment between the optimized and baseline configurations with and without nacelles is summarized in the chart below for the 1-g cruise condition. Though the measurements cannot definitively justify the simplification to W/B/F optimization, the fact the the addition of nacelles had little effect on the increment is encouraging.

W/B/F Versus W/B/N/D/F Optimization



High Speed Aerodynamics, Long Beach

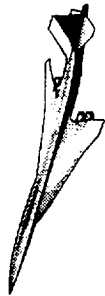
1.675% TCA Model 5 Test 496 in the NASA Langley 16' TT, $Re \approx 4 \times 10^6/\text{ft}$



Conclusions

This paper summarizes an exhaustive study performed at Boeing Long Beach to develop, apply and validate a transonic flap optimization procedure. The workhorse optimization code at Long Beach, AEROSHOP, was adopted for the task, pooling together existing technologies into a single process for the optimization. The optimization was performed at five Mach numbers for the baseline TCA geometry. Drag benefits were obtained from the Euler-based optimization, and verified with detailed Navier-Stokes assessments of the baseline and optimized flap configurations. It was observed from the optimizations that above $M_\infty=1$, trailing-edge flaps are not needed. Also, for the given leading-edge radius on the TCA, the use of an inboard leading-edge flaps further reduces drag. The optimization was validated with wind-tunnel tests at three Mach numbers, $M_\infty=0.6$, 0.9, and 1.1. Though all test results confirmed significant drag reduction, the most encouraging validation of the predicted drag increments were observed for Mach numbers of 0.9 and 1.1.

Conclusions



High Speed Aerodynamics, Long Beach

- AEROSHOP was adopted, connecting existing technologies for transonic flap optimization
- Optimization was performed at $M_\infty=0.6, 0.8, 0.9, 1.1,$ and 1.8
 - No trailing-edge flaps needed above $M_\infty=1$
 - Inboard leading-edge flap further reduces drag
- Performance improvements with Euler-based optimized flaps were verified with Navier-Stokes analyses
- Recommended flap settings for Model 5 were tested in the NASA Langley 16-ft TT; this validated the procedure at $M_\infty=0.6, 0.9, 1.1$



This page is intentionally left blank.



Viscous Design of TCA Configuration

Steven E. Krist, Steven X. S. Bauer, Richard L. Campbell
NASA Langley Research Center

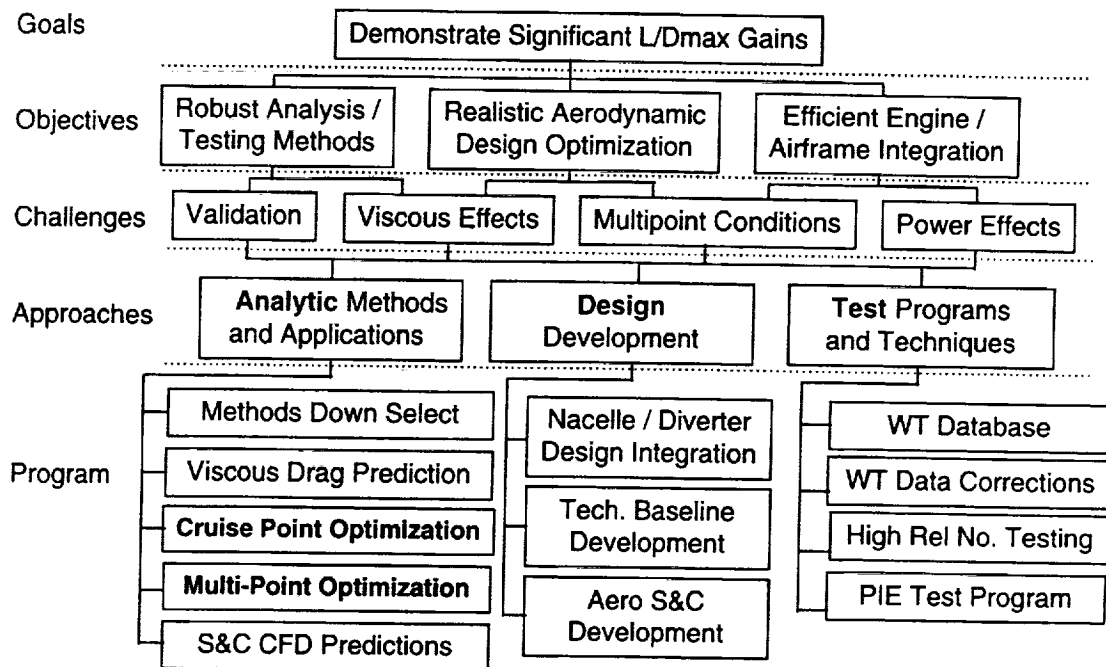
Aerodynamic Performance Workshop
HSR Annual Airframe Review
Los Angeles, CA
February 9 - 11, 1998

Viscous Design of TCA Configuration

The goal in this effort is to redesign the baseline TCA configuration for improved performance at both supersonic and transonic cruise. Viscous analyses are conducted with OVERFLOW, a Navier-Stokes code for overset grids, using PEGSUS to compute the interpolations between overset grids. Viscous designs are conducted with OVERDISC, a script which couples OVERFLOW with the Constrained Direct Iterative Surface Curvature (CDISC) inverse design method.

Configuration Aerodynamics Technology Development

Session 3: Aerodynamic Design Optimization Capability



Configuration Aerodynamics Technology Development

This work was performed under the Configuration Aerodynamics element of the High Speed Research program. The specific milestones addressed are Cruise Point Optimization and Multi-Point Optimization.

Outline

- Automated Griding For TCA Designs
- OVERDISC Inverse Design Procedure
- Dual-Point Redesign of BCAG TCA Optimized Configuration
- Natural Flow Wing Design of TCA

Outline

The successful execution of any computational fluid dynamics (CFD) based aerodynamic design method for complex configurations requires an efficient method for regenerating the computational grids to account for modifications to the configuration shape. The first section of this presentation deals with the automated regidding procedure used to generate overset grids for the fuselage/wing/diverter/nacelle configurations analysed in this effort. The second section outlines the procedures utilized to conduct OVERDISC inverse designs. The third section briefly covers the work conducted by Dick Campbell, in which a dual-point design at Mach 2.4 and 0.9 was attempted using OVERDISC; the initial configuration from which this design effort was started is an early version of the optimized shape for the TCA configuration developed by the Boeing Commercial Airplane Group (BCAG), which eventually evolved into the NCV design. The final section presents results from application of the Natural Flow Wing design philosophy to the TCA configuration.

Automated Gridding of TCA Designs

- Modifications to TCA Baseline Overset Grids Supplied by BCAG
 - Wall spacings for transonic cruise
 - Topology modifications for regridding and PEGSUS41–46
- Wing/Body script to generate volume grids from fuselage and wing surface grids
- Rerig Nacelles Satisfying Constraints
 - Fixed inboard and outboard nacelle hard points on wing t.e.
 - Clearance between nacelle lip and wing lower surface
 - Avoid nacelle protrusion through rear spar
- Regrid nacelle component grids
- Run PEGSUS

Automated Gridding of TCA Designs

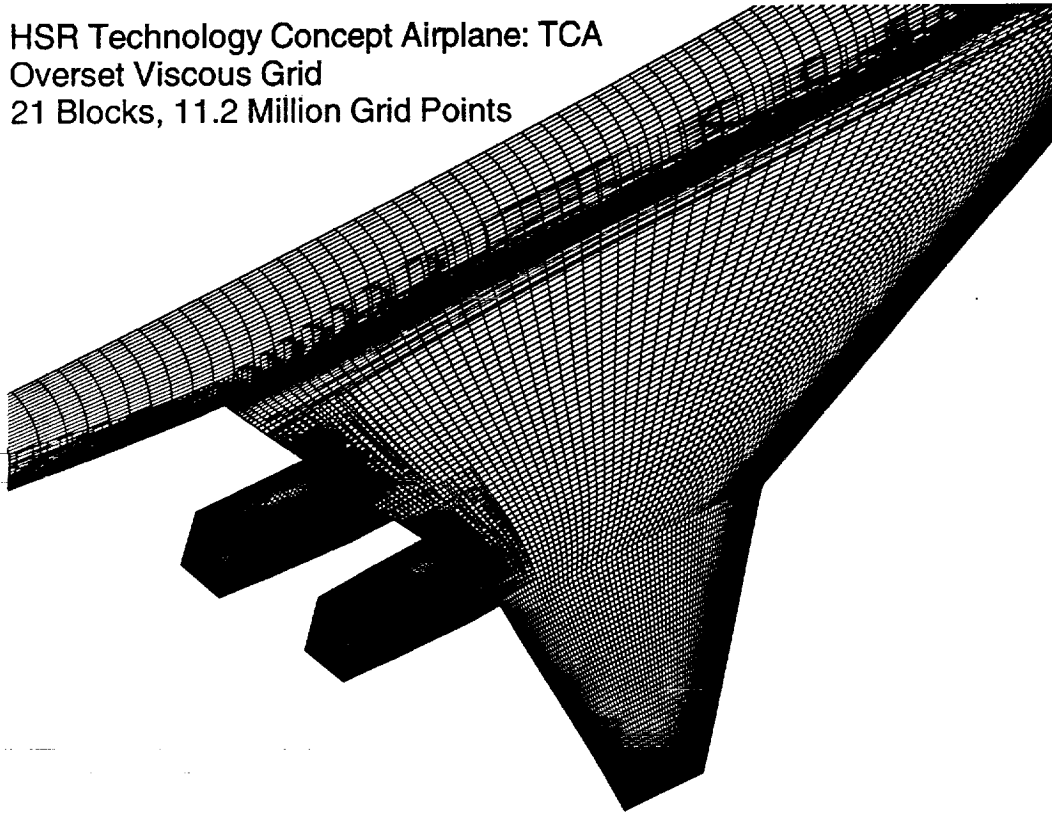
The initial overset grids utilized in this effort were developed by Steve Chaney and Steve Ogg at BCAG. While the grids were initially sized for the Mach 2.4 cruise condition, they were modified for the Mach 0.90 cruise condition by decreasing the wall-normal spacing to a third of its original value, thereby maintaining a y^+ value of one. A slight change to the topology was also made to the nacelles. This change permits the use of PEGSUS version 41–46, which is roughly seven times faster than version 41–36, which was required for the successful interpolation of the initial set of overset grids.

The intent in the regridding procedure is to automatically generate the complete set of overset volume grids for the fuselage/wing/diverter/nacelle configuration, starting from fuselage and wing surface grids, for any fuselage/wing configuration shape on the TCA planform. At this point in the effort, the diverters and nacelles are not being redesigned.

The first step in the regridding procedure is to generate the fuselage/wing volume grids using a modified version of the Wing/Body script developed in the Advanced Subsonic Transport (AST) program. The second step is to rerig the nacelles on the configuration. Constraints on the nacelle positioning are utilized to ensure clearance between the nacelle upper surface ejector port and the wing upper surface (the nacelles protrude through the upper surface of the wing near the wing trailing edge), to provide sufficient clearance between the wing lower surface and the nacelle inlet lip to avoid boundary layer ingestion, and to prevent the nacelle surface from cutting into the rear spar of the wing. Once the nacelles are positioned correctly, the overset component grids are restretched and reprojected onto the appropriate surfaces to ensure consistency between the grid blocks. Further details of the nacelle installation procedure are presented on the following 3 pages.

The last step in the procedure is to run PEGSUS to compute the interpolations between the new system of overset grids. The entire regridding procedure, from generation of the fuselage/wing grids to completion of PEGSUS is implemented with a unix script. Through numerous designs, this fully automated procedure has been found to be quite robust, typically generating on the order of 10 orphan points for new configurations.

HSR Technology Concept Airplane: TCA
Overset Viscous Grid
21 Blocks, 11.2 Million Grid Points



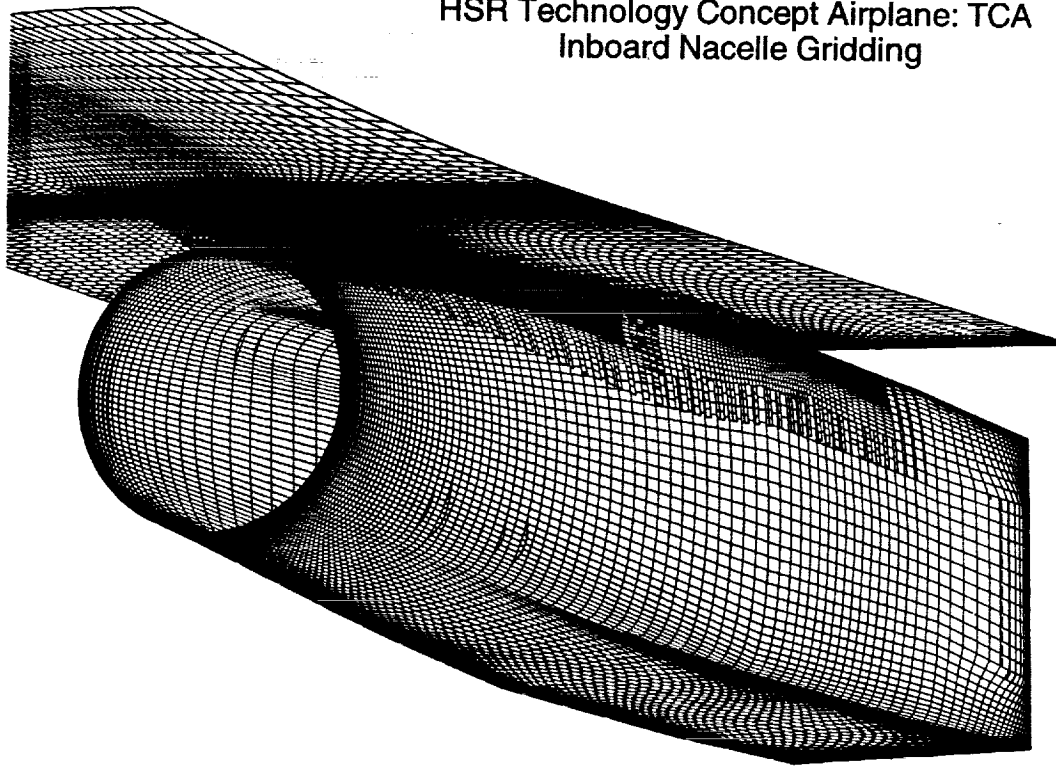
TCA Overset Viscous Grid

The fuselage/wing/diverter/nacelle system of overset grids utilized throughout this work is comprised of 21 blocks containing a total of 11.2 million grid points. Several of the surface grids for the configuration are shown in the figure, where the view is from above, outboard, and behind the wing.

The advantage to using overset rather than abutting structured grids is that each component of the configuration can be gridded independently. In this case, independent grids are generated for the wing and fuselage, and a third grid, referred to as the collar grid, is automatically generated to handle the intersection of the wing with the fuselage. To grid the diverters and nacelles, a total of 8 grids are used for each nacelle/diverter combination. The internal and external nacelle surfaces are each handled with one grid, while each side of the diverter is treated with a forward and aft grid which differ somewhat in topology. Since the nacelles protrude through the upper surface of the wing, an additional fairing grid is used to handle the intersection of the wing upper surface with the nacelle. The eighth grid is a box-like grid which encloses most of the nacelle, but has one surface lying on the wing lower surface; the box-like grid runs well downstream of the end of the nacelle.

While overset methods allow for relatively simple gridding procedures as compared to the procedures for constructing abutting grids, it presents additional difficulties in that invalid portions of a grid must be cut out (e.g. that portion of the nacelle external volume grid which runs through the wing and diverter), and appropriate interpolations between grids must be computed. Construction of the PEGSUS input file to perform these tasks can be quite formidable. Moreover, special care is required in design problems to keep the hole cutting specifications flexible enough to handle significantly different configurations.

HSR Technology Concept Airplane: TCA Inboard Nacelle Gridding



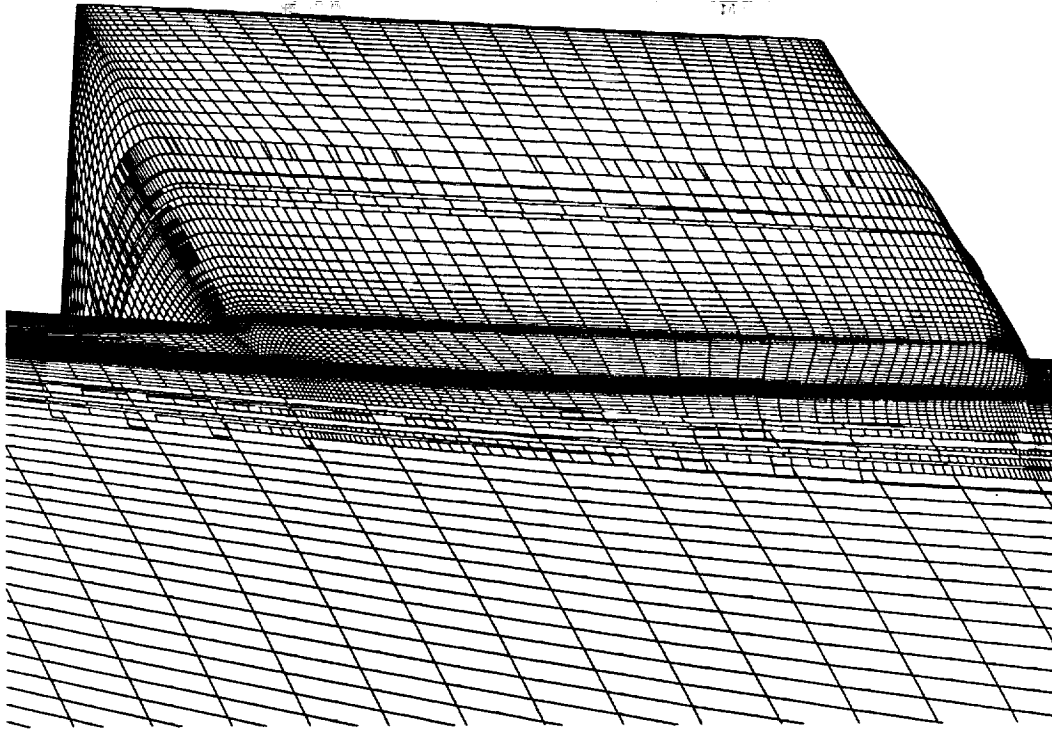
TCA Inboard Nacelle Gridding

Surface grids from several components of the inboard nacelle are shown in the figure, where the view is from inboard and below the inboard nacelle. The upper most grid is the surface of the box-like grid which lies on the lower surface of the wing, which has only been represented up to the trailing edge of the wing. The forward inboard diverter grid contains three viscous surfaces, lying on the lower wing surface, the diverter, and the nacelle. The aft diverter grid contains two viscous surfaces; separate surfaces for the diverter and nacelle are not required near the trailing edge since the angle between the two surfaces is quite shallow.

In rigging the nacelle, the ejector port clearance with the wing upper surface is maintained in approximate fashion, namely, fixed points on the aft inboard and outboard diverter grids are required to lie on the wing trailing edge at a specific span station. After a configuration change, the hard point on the inboard diverter is translated to lie on the wing trailing edge. The nacelle is then rotated to position the outboard hard point onto the wing trailing edge, adding both yaw and roll to the nacelle orientation. The lip of the nacelle is then positioned to meet a distance constraint between the lip and the lower surface of the wing, which changes the inclination of the nacelle. A check is then made to ensure that the nacelle does not cut into the lower spar of the wing; if it does, the lip is rotated down until the constraint is met. With the nacelle properly positioned, all of the nacelle component volume grids are subjected to the same series of translations and rotations.

At this point, all that remains to finish the gridding is to ensure that the surfaces of the diverter, upper surface fairing, and box-like grids lie on the appropriate overlapping surfaces of the wing, diverter, and nacelle. This is done through a series of surface projections with appropriate stretching of the volume grids. Treatments for the diverter and box-like component grids are fairly straight forward. Treatment of the upper surface fairing is not.

HSR Technology Concept Airplane: TCA Nacelle Fairing Grid



TCA Nacelle Fairing Grid

The nacelle fairing surface grid is shown in the figure, where the view is from on top of the wing slightly upstream of the fairing. The upstream portion of the fairing lies on the wing upper surface until it reaches the horizontal intersection line of the wing with the nacelle (the horizontal region of compressed grid spacing). At that point, the sides of the fairing surface grid continue on the wing upper surface, while the center of the grid lies on the nacelle. Downstream of the trailing edge, the sides of the fairing surface grid are treated like a wake, while the center of the surface grid remains on the nacelle. To regrid the fairing, three intersection lines between the wing and nacelle surfaces must be computed, and the surface grid must be restretched and reprojected appropriately, with particular care required at the corners of the intersection lines. Details are left to the readers imagination.

OVERDISC Inverse Design Procedure

Script to loop through the design process using:

- CDISCRUN: runs CDISC with a pre-processor to extract design information and a post-processor to output modified surface grids
- Grid Manipulation Script: rerig nacelles to meet design constraints and perturb volume grids to maintain grid continuity between overlapping blocks
- PEGSUS: recompute interpolations between overset grids
- MIXSUR: recompute force and moment interpolation stencils
- OVERFLOW: Update solution for modified configuration

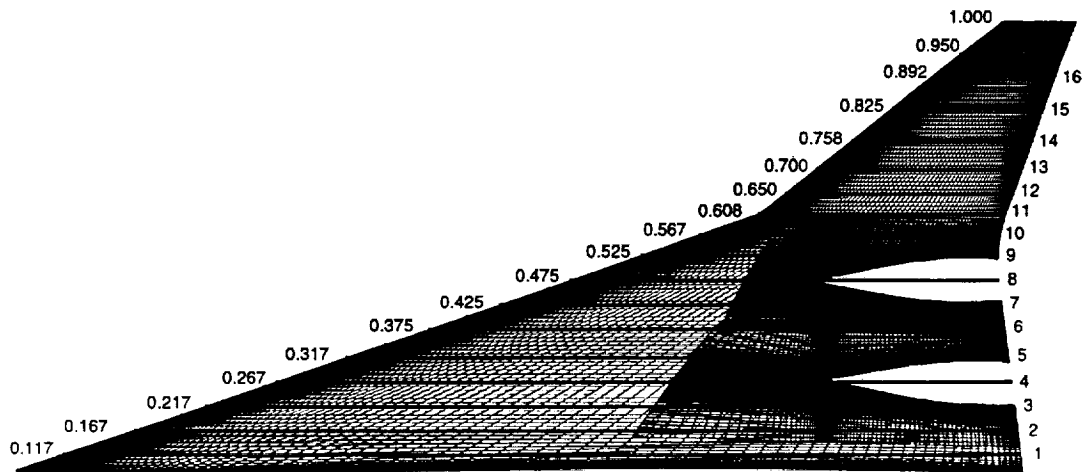
OVERDISC Inverse Design Procedure

OVERDISC is a unix script which couples the CDISC inverse design method with the OVERFLOW analysis code. The coupling is implemented by extracting information from the OVERFLOW solution and grid files for use in CDISC, regenerating the overset volume grids to conform to the configuration modifications output from CDISC, and running PEGSUS to compute the interpolations between the new system of overset grids. In order to maintain a history of the configuration forces and moments through the course of the design, an additional step is required, namely, running MIXSUR to compute the interpolation stencils for the overset surface grids.

Typical OVERDISC designs at the Mach 2.4 cruise condition were run for 10 design cycles with 40 multigrid iterations per design cycle and 150 multigrid iterations to obtain convergence of the final design. The computation time required for a complete design was on the order of 24 hours on a C90, which is nearly equivalent to the time it takes to obtain a converged solution of the initial configuration. The time spent on running CDISC, the automated regidding script, PEGSUS, and MIXSUR was roughly 1 hour per design cycle, or about the same time required to run OVERFLOW for 40 multigrid iterations. The time spent on the design portion of the script can be reduced by skipping the PEGSUS run, for all but the final design, and using the initial interpolation file in analyzing the intermediate designs. This procedure saved about 2/3 of an hour per design cycle and proved to be quite robust; it was used extensively. Nevertheless, runs of the OVERDISC script in the multitask mode averaged less than 2 CPU's on the C90, whereas OVERFLOW runs average about 6 CPU's;

While the automated gridding script and PEGSUS runs proved to be quite robust, computation of the surface grid interpolation stencils in MIXSUR were not; particularly troublesome was the lower surface of the wing, which contains 12 overlapping surface grids. In fact, the input file to MIXSUR had to be modified for most of the designs before the final forces and moments could be computed. This difficulty suggests that in developing automated regidding scripts for designs, surface projections should always be implemented with parametric projections.

TCA Design Stations Wing Lower Surface



TCA Design Stations

A crucial element in utilizing OVERDISC is creation of the CDISC "target" file, in which design stations, as well as flow and geometry constraints at those stations, are specified. CDISC is a knowledge-based approach to design for which the typical mode of operation is to use flow constraints to modify the current analysis pressure distributions at the design stations to develop target pressure distributions. Differences between the analysis and target pressure distributions are then related to surface curvature changes along the design stations. Geometry constraints are directly imposed on the new surface shapes. Multiple passes are made through both the flow and geometry constraints in an attempt to satisfy all the requirements. Grid lines lying between design stations are modified by linear interpolation of the surface increments computed at the encompassing design stations.

Flow and geometry constraints are grouped into three general categories. Global constraints influence multiple design stations (e.g. spanload or twist distribution). Section constraints affect both surfaces on, say, an airfoil (e.g. section lift coefficient or minimum thickness at a spar). Surface constraints are applied to a single aerodynamic surface (e.g. shock strength or surface curvature restrictions).

The design stations utilized in a typical OVERDISC design of the TCA configuration, superimposed on the lower surface of the wing, are illustrated in the figure. Note that CDISC design stations must lie along grid lines; in this case they lie along grid lines of the wing. The coupling with OVERFLOW is such that a design station can run through a blanked out section of the grid; the preprocessor PREDISC is used to interpolate information from the appropriate overlapping grid to grid points along the specified grid line. In instances where the design station runs through a solid surface (e.g. stations 4 and 8 which run through the diverters), options are available to turn off the flow constraints in the invalid section of the station, but geometry constraints are still applied.

As suggested by the figure, in this work, OVERDISC was only used to design the wing. In order to prevent discontinuities in the grid, the 1st design station was always held fixed.

TCA Design Constraints Imposed on the Wing

- Forward and Rear Spar Thickness Distributions
- 2.4% Maximum Thickness/Chord Ratio as a Minimum
- Leading Edge Radius Constraint
- Volume Constraint Between Inboard Spars

TCA Design Constraints Imposed on the Wing

Constraints on redesigns of the wing for the TCA configuration are as follows:

- Minimum wing thickness distribution along the forward and rear spars
- 2.4% maximum thickness/chord ratio, as a minimum
- Minimum leading edge radius: the spanwise distribution is only specified inboard of the wing leading edge break
- Minimum volume between the forward and rear spars, for the section of the wing inboard of the wing leading edge break

All of the constraints were satisfied in all of the OVERDISC redesigns of the wing.

OVERDISC Dual-Point Design of TCA

- Weighted Average of Geometries (WAG)
 - Use CDISC to generate independent single point designs at multiple design points
 - Blend the geometries at each surface grid point based on a weighted average to minimize an objective function
- Two-point design procedure:
 - Design for reduced drag at $M=0.95$ and 2.4
 - Analyze point designs at opposing conditions
 - Compute geometry weighting factor based on objective function and constraints
 - Blend point design geometries and re-analyze at the two design points
 - Continue last two steps until minimum of objective function is determined

OVERDISC Dual-Point Design of TCA

The attempt in this effort was to take one of the TCA configurations generated with an aerodynamic optimization code and redesign the wing for improved performance at both supersonic and transonic cruise. The design method used is the Weighted Average of Geometries (WAG) method embodied in CDISC. In this method, CDISC is used to generate independent single point designs at multiple design points. The geometries from the various designs are then blended at each surface grid point using a weighted average, in an attempt to minimize an objective function.

Status of TCA Dual-Point Design

- Start from BCAG Optimized Configuration (Early Design), with modified diverter/nacelle topology
- Initial Single Point Designs with OVERDISC
 - $M=2.4$
 - << design objective: reduce shock strength
 - << 0.7 count drag reduction
 - $M = 0.95$
 - << design objective: recamber for larger L/D
 - << 11.0 count drag reduction
- Evaluate Single Point Designs at Opposing Conditions
 - $M = 0.95$ design never converged at $M = 2.4$
- Status: Switch Effort to Look at Flap Scheduling and Design

Status of Dual-Point Design

The starting point for the dual-point design of the TCA configuration was from an optimized configuration developed by BCAG which showed a 5.6 count drag reduction over the TCA baseline configuration; the optimized configuration is actually a precursor to the NCV design developed by BCAG.

The first step in the WAG method was to redesign the configuration at Mach 2.4. The attempt in this design was merely to reduce the strength of the compression seen on the wing lower surface resulting from the shocks emanating from the diverters and nacelles. The design provided an additional 0.7 count drag reduction over that of the optimized configuration; further details of the design are provided on the following two pages.

The second step was to redesign the configuration at Mach 0.95. The attempt in the design was to recamber the wing in order to improve the L/D ratio. The design led to an 11.0 count drag reduction over that of the optimized configuration.

The third step was to evaluate the single point designs at the opposing conditions. While the evaluation was not a problem for the Mach 2.4 design at Mach 0.95, the solution for the Mach 0.95 design at Mach 2.4 never did converge. However, it was apparent that the Mach 0.95 design would show large deteriorations in performance at the Mach 2.4 condition. Since 1 count of drag reduction at supersonic conditions is weighted equal to 4 counts of drag reduction at the transonic condition, it was evident that the WAG procedure would lead to use of the Mach 2.4 design solely, rather than blending the two designs. Hence, the dual-point design effort was terminated at this point.

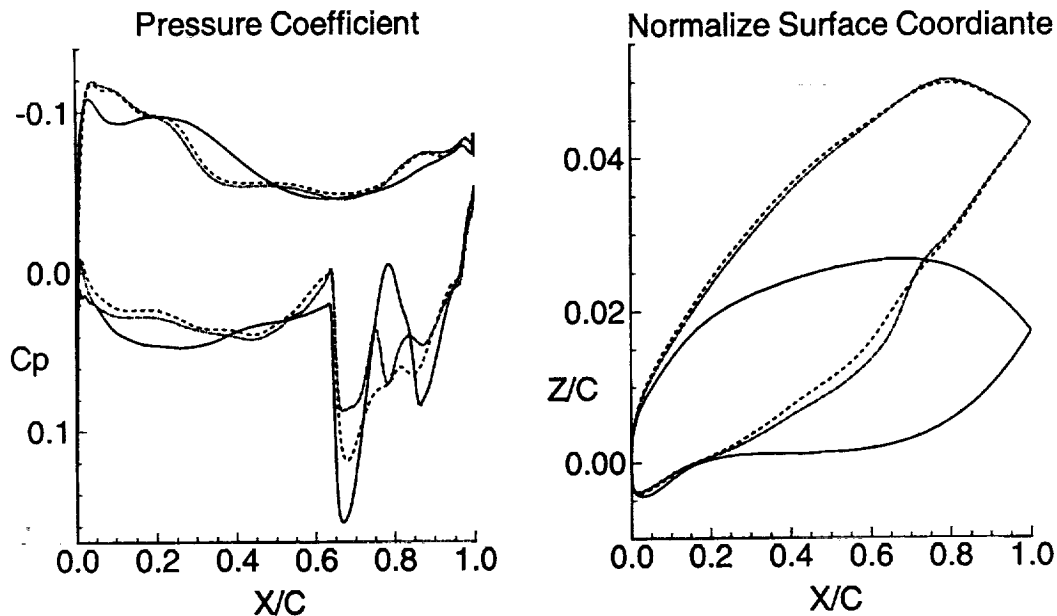
It is apparent from this effort that starting a multi-point design from a single point supersonic cruise design, without considering flap deflections at the transonic conditions, is impractical for the TCA configuration.

TCA Designs

$M = 2.40$
 $Re = 4.0 \times 10^6$

———— baseline $\alpha = 3.00^\circ$
 - - - - - BCAG $\alpha = 3.98^\circ$
 - · - · - BCAG + OVERDISC $\alpha = 3.98^\circ$

$\eta = 0.416$



TCA Designs: Surface Pressure Coefficient and Normalized Coordinate at 0.416

The attempt in the Mach 2.4 redesign of the optimized configuration was to reduce the compression on the wing lower surface resulting from the shocks emanating off the nacelles and diverters. In CDISC, this was implemented by "constraining" the pressure coefficient in the vicinity of the shock to remain above some specified level, with varying levels used at the different design stations.

The figure shows the surface pressure coefficient and normalized coordinate at the 41.6% span station, which lies just inboard of the outboard nacelle, for the TCA baseline, BCAG optimized, and OVERDISC redesigned configurations. The constraint applied within CDISC was to limit the pressure coefficient at the design station to be below 0.08 in the vicinity of the shock. This leads to the addition of a convex increment in the surface coordinate in the vicinity of the shock. In order to close the airfoil at the leading and trailing edges, regions forward and aft of the shock are modified with concave increments to the surface curvature. Geometry constraints on the spar thickness and maximum thickness are then applied, leading to the changes seen in the upper surface shape.

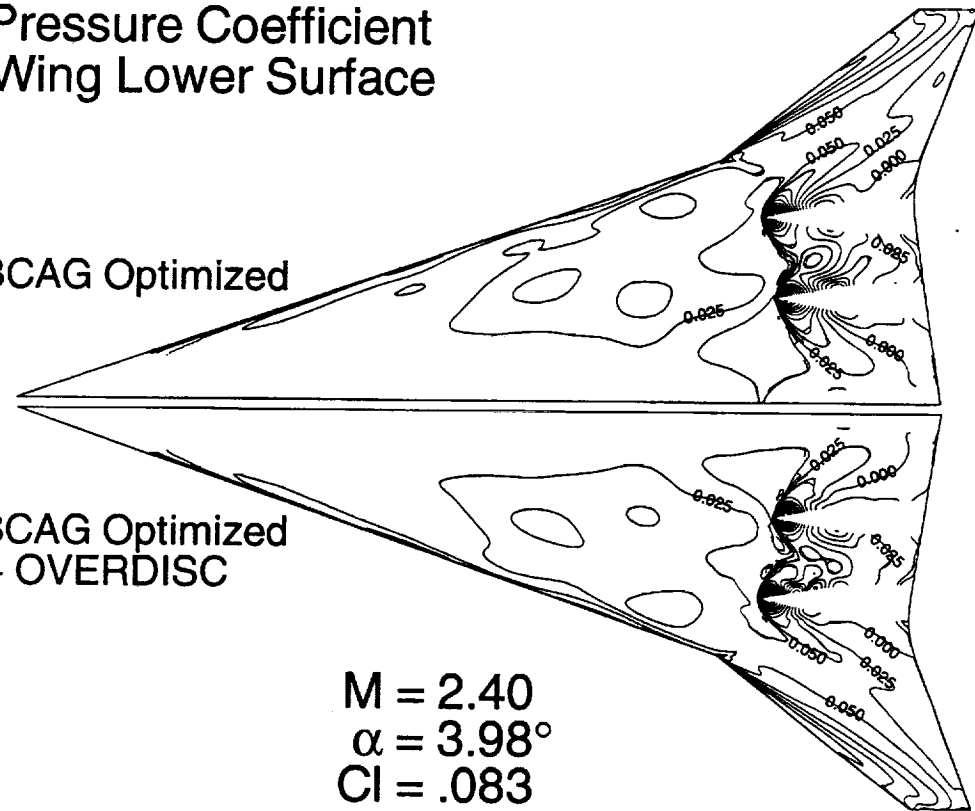
The results indicate that the strength of the compression has been significantly reduced with the OVERDISC design, but that the pressure recovery aft of the shock is somewhat less favorable than that for the optimized configuration.

Pressure Coefficient Wing Lower Surface

BCAG Optimized

BCAG Optimized
+ OVERDISC

$M = 2.40$
 $\alpha = 3.98^\circ$
 $C_l = .083$



Lower Surface Pressure Coefficient on the Optimized and OVERDISC designs at Mach 2.4

Pressure Coefficient distributions on the lower surface of the BCAG optimized and OVERDISC redesigned configurations at Mach 2.4 are shown in the figure. It is evident that the shock footprints on the lower surface have been reduced with the OVERDISC redesign.

Natural Flow Wing Design Procedure

- Apply NFW Concept and Conduct Euler Analyses of Wing/Body Configuration at $M=2.4$ to Refine Thickness, Camber, Etc.
 - Blunt leading edge outboard of leading edge break
 - Landing gear incorporated into fuselage
- OVERFLOW Analyses of NFW W/B/N/D Configurations at Supersonic and Transonic Cruise
- OVERDISC Inverse Design The Best Configuration

Natural Flow Wing Design Procedure

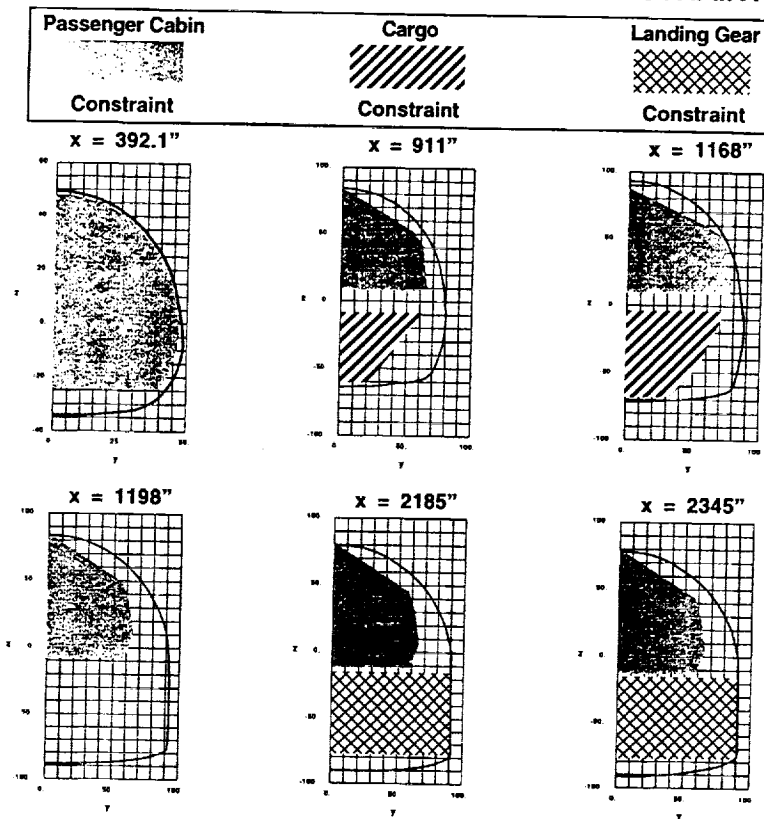
The Natural Flow Wing (NFW) Design philosophy was developed by Rick Woods and Steve Bauer to provide multipoint performance improvements for fighter aircraft over a range of transonic and supersonic flight conditions. Details of the design philosophy are reported in the 1996 HSR workshop proceedings under the title "Application of the Natural Flow Wing Design Philosophy to the HSR Arrow Wing Configuration".

Initial application of the NFW design philosophy to the TCA configuration was implemented through Euler analyses of the fuselage/wing configuration at Mach 2.4. Parametric studies were utilized to refine thickness, camber and twist distributions. There are two aspects of the resulting NFW designs which differ significantly from both the TCA baseline and the optimized configurations developed by other participants in the HSR program. First, the entire landing gear constraint is incorporated into the fuselage, rather than incorporating it into both the fuselage and wing; details of the fuselage shape are illustrated on the following page. Second, as a means for improving transonic performance, the airfoil sections outboard of the wing leading edge break are blunt rather than sharp.

The more promising NFW configurations developed in the initial study were analyzed at both the Mach 2.4 and 0.90 cruise conditions using OVERFLOW. Grids for the fuselage/wing/diverter/nacelle configurations were generated using the automatic regidding procedure discussed in the first section of this presentation.

The most promising NFW configuration, referred to as NFW701, provided drag reductions of 1.4 and 10.2 counts at the supersonic and transonic cruise conditions, respectively, over that of the TCA baseline. OVERDISC was then used to redesign the NFW701 configuration at Mach 2.4.

NASA LaRC TCA-NFW FUSELAGE AND CONSTRAINTS



TCA-NFW Fuselage and Constraints

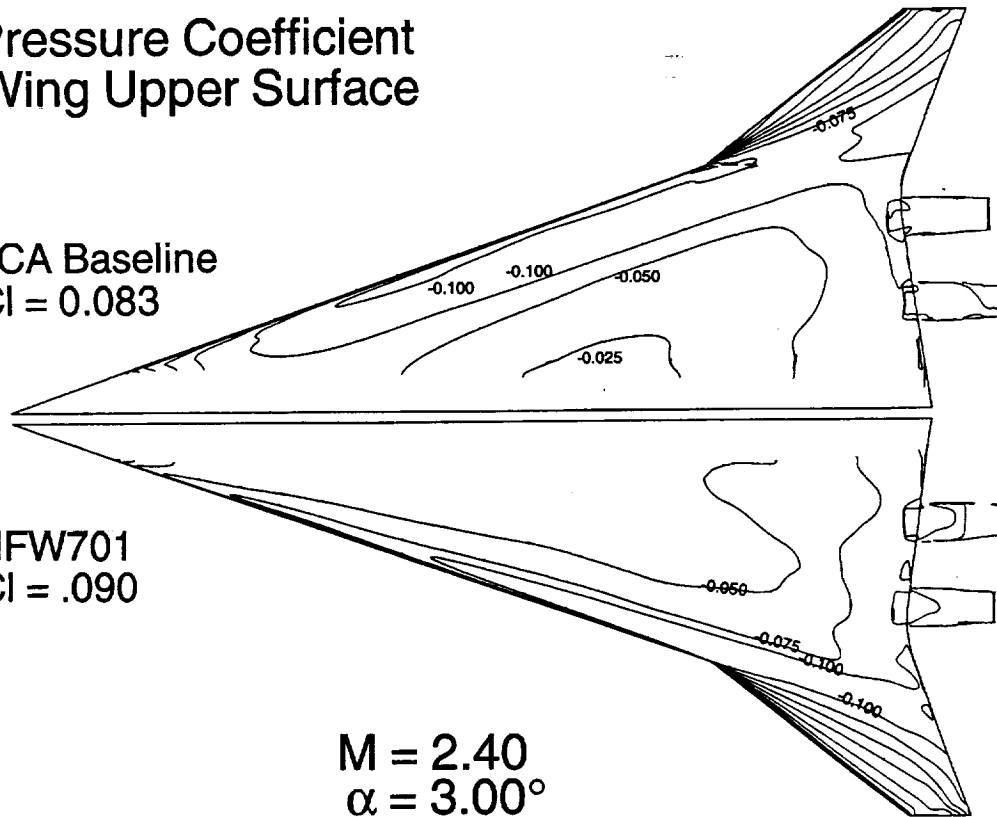
The figure shows the NFW fuselage outer mold line and TCA constraints at six cross-sections; note that the scales at station 392.1 differ from the scales used at the other five stations. The most significant aspect of the NFW fuselage design is that the entire landing gear constraint is incorporated into the fuselage. Due to the spanwise extent of the landing gear, the passenger cabin constraint applied at stations 2185 and 2345 is the same constraint applied at station 1198, rather than applying the specified TCA constraint which is much less severe. Application of the larger passenger cabin constraint would allow for an additional seat or two per row over the mid section of the fuselage.

Pressure Coefficient Wing Upper Surface

TCA Baseline
 $C_l = 0.083$

NFW701
 $C_l = .090$

$M = 2.40$
 $\alpha = 3.00^\circ$



Upper Surface Pressure Coefficient on the TCA Baseline and NFW701 at Mach 2.40

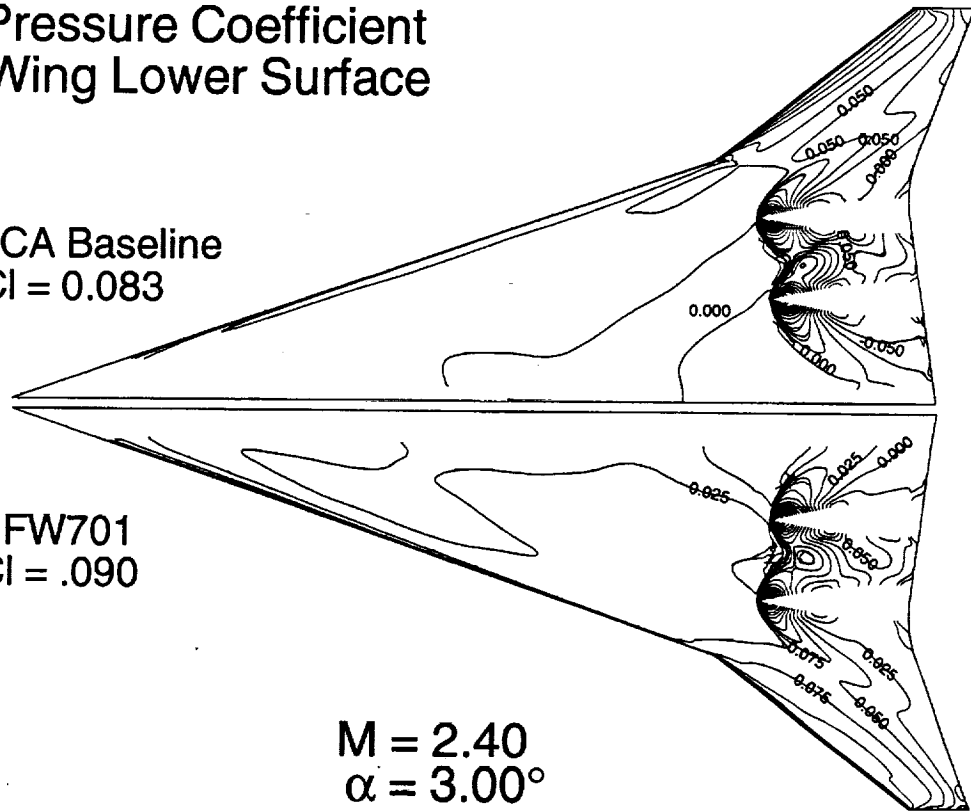
Pressure coefficient distributions on the upper surface of the wings for the TCA baseline and NFW701 configurations at Mach 2.4 are shown in the figure. Note that the configurations are run at the same angle of attack, but the NFW701 lift coefficient is 0.90 rather than 0.83. It is evident that the NFW701 design embodies significantly less leading edge suction along the entire span. The effect of using blunt airfoil sections outboard of the leading edge break in the NFW701 design is indicated by the higher pressures near the leading edge.

Pressure Coefficient Wing Lower Surface

TCA Baseline
 $C_l = 0.083$

NFW701
 $C_l = .090$

$M = 2.40$
 $\alpha = 3.00^\circ$



Lower Surface Pressure Coefficient on the TCA Baseline and NFW701 at Mach 2.40

Pressure coefficient distributions on the lower surface of the wings for the TCA baseline and NFW701 configurations at Mach 2.4 are shown in the figure; blank regions near the wing trailing edge are the diverter cut-outs. The pressure coefficient for NFW701 is marginally higher over most of the inboard wing in front of the nacelles; the shock foot prints are somewhat larger as well, but expansions in the shock recovery regions have been reduced. Outboard of the leading edge break, the NFW701 design sees significantly higher pressures.

Pressure Coefficient Wing Upper Surface

TCA Baseline

$C_l = 0.161$

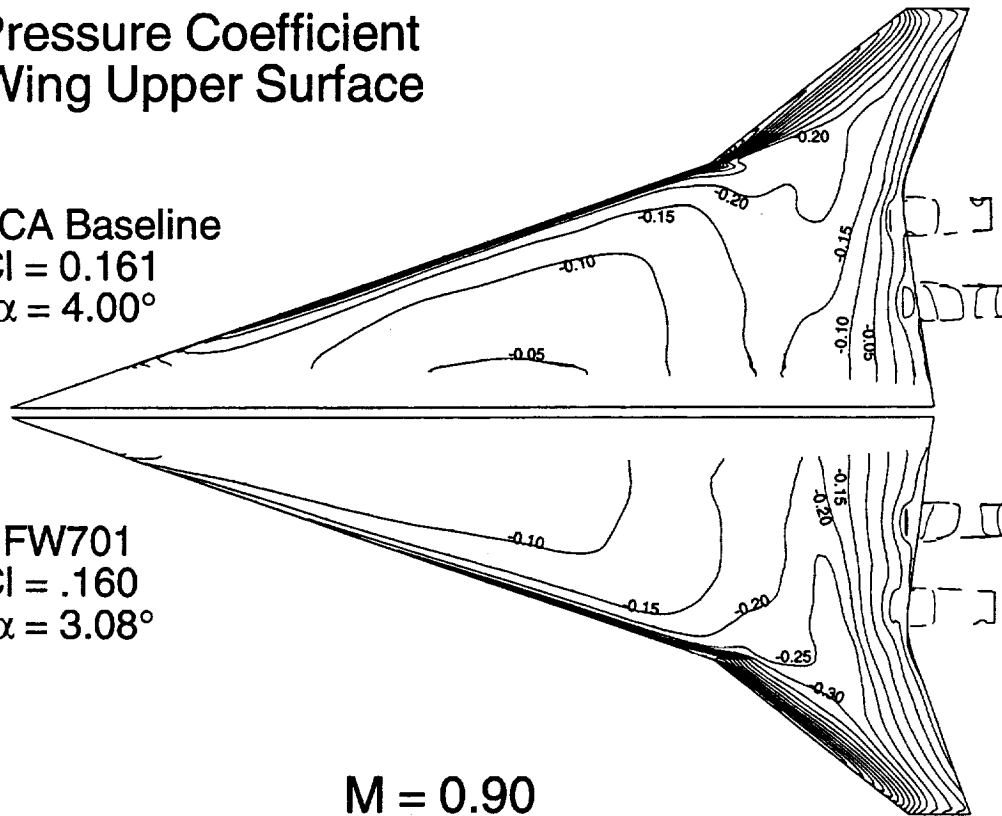
$\alpha = 4.00^\circ$

NFW701

$C_l = .160$

$\alpha = 3.08^\circ$

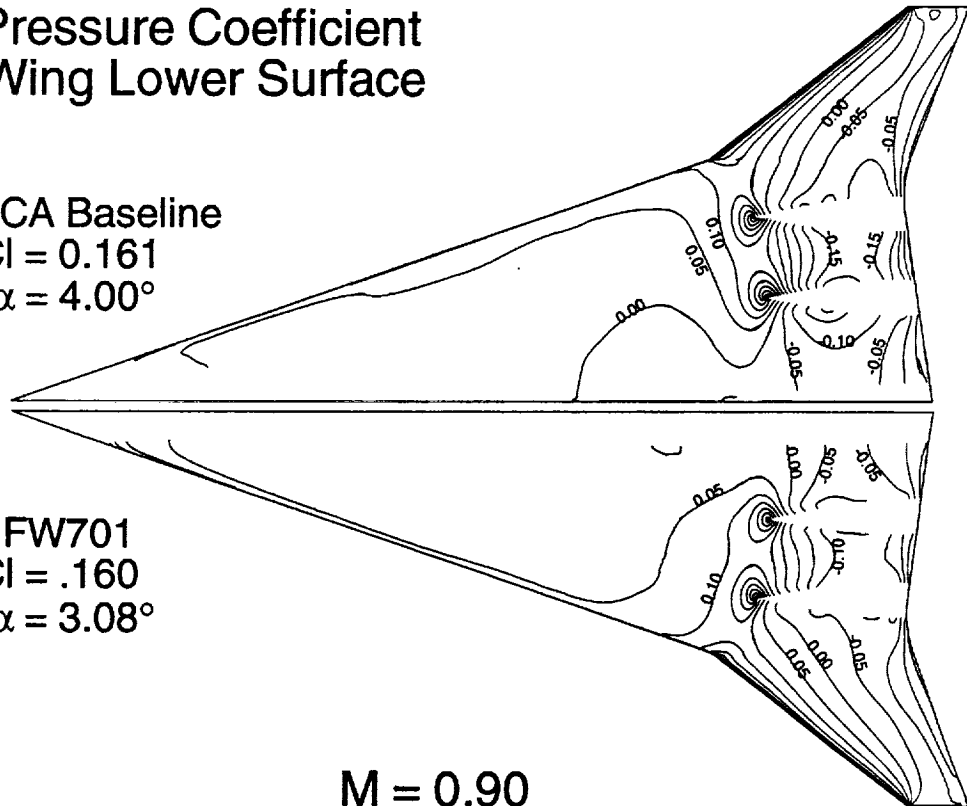
$M = 0.90$



Upper Surface Pressure Coefficient on the TCA Baseline and NFW701 at Mach 0.90

Pressure coefficient distributions on the upper surface of the wings for the TCA baseline and NFW701 configurations at Mach 0.9 are shown in the figure. Both configurations are run at a design C_l of 0.16, but the angle of attack for the baseline and NFW701 configurations are 4.0 and 3.08 degrees, respectively. Once again, the NFW701 design embodies significantly less leading edge suction along the entire span. However, it sees significantly more expansion over the inboard aft section of the wing, with the aft shock further downstream.

M = 0.90



Pressure coefficient distributions on the lower surface of the wings for the TCA baseline and NFW701 configurations at Mach 0.9 are shown in the figure. While the pressure distributions for the two configurations are similar forward of the diverters and outboard of the leading edge break, the NFW701 design sees significantly less expansion aft of the nacelles, particularly between the nacelles.

OVERDISC Design Objectives

- Maintain Leading Edge Bluntness of Initial NFW Design
- Reduce Shock Strength
- Generate Additional Leading Edge Suction Inboard of Inboard Nacelle
- Unload Outboard Wing
- Reduce Upper Surface Trailing Edge Expansion

OVERDISC Design Objectives

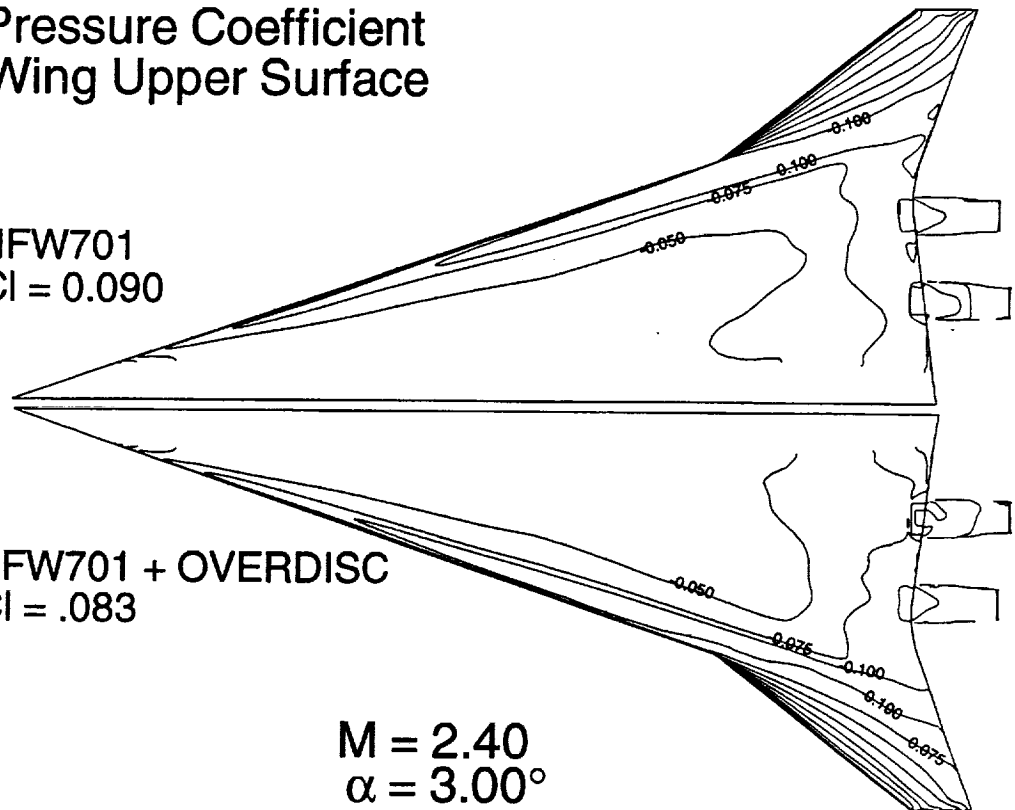
Upon selection of the NFW701 design as the most promising of the configurations developed using the NFW design philosophy, the configuration was redesigned at Mach 2.4 using OVERDISC, and the redesigned configuration was evaluated at Mach 0.90 as well. One of the major constraints applied in the redesign was to maintain the leading edge bluntness of the NFW701 design in an attempt to preserve the transonic performance. Additional flow constraints were applied to reduce the shock strength on the lower surface, generate additional leading edge suction on the upper surface inboard of the inboard nacelle, reduce the loading on the mid and outboard wing sections, and reduce the upper surface expansions near the wing trailing edge.

Pressure Coefficient Wing Upper Surface

NFW701
 $C_l = 0.090$

NFW701 + OVERDISC
 $C_l = .083$

$M = 2.40$
 $\alpha = 3.00^\circ$



Upper Surface Pressure Coefficient on NFW701 and the OVERDISC Redesign at Mach 2.40

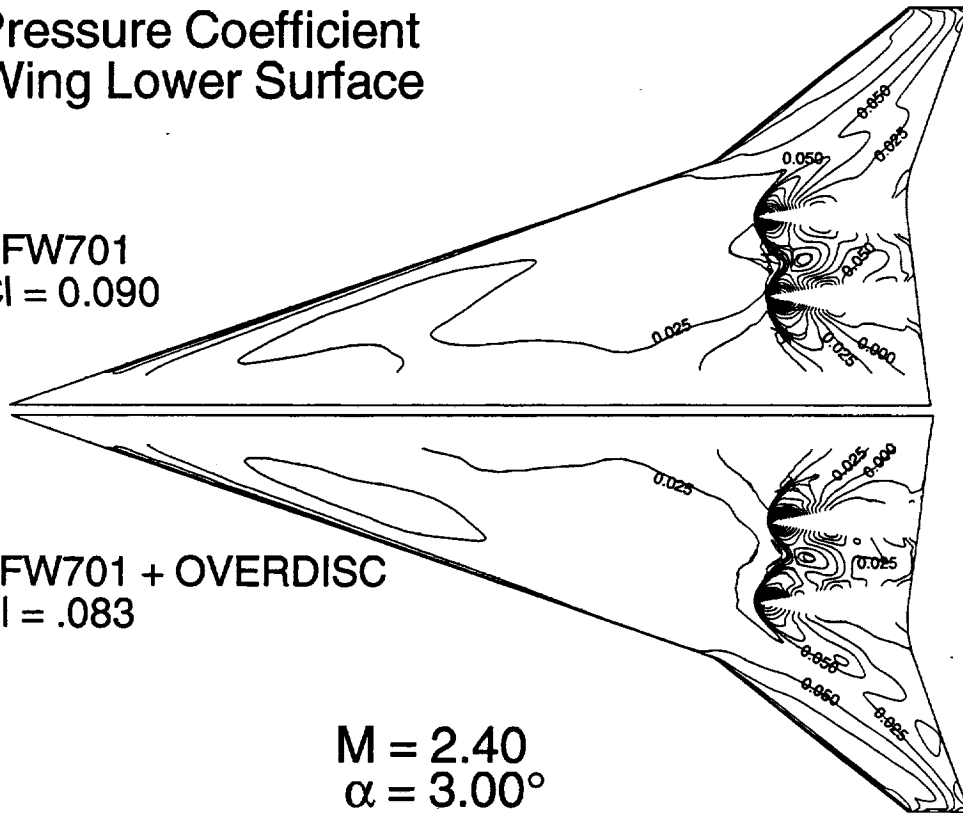
Pressure coefficient distributions on the upper surface of the wings for the NFW701 and OVERDISC redesigned configurations at Mach 2.4 are shown in the figure. Note that both configurations are run at a 3 degree angle of attack, but the lift coefficient for the redesign has dropped down to the specified design C_l . The extension of the leading edge pressure contours upstream of their initial position (see for example the -0.1 contour) indicates that a moderate amount of additional leading edge suction was obtained with the redesign. Similarly, contours at the trailing edge indicate that there is moderately less expansion of the flow in this region.

Pressure Coefficient Wing Lower Surface

NFW701
 $C_l = 0.090$

NFW701 + OVERDISC
 $C_l = .083$

$M = 2.40$
 $\alpha = 3.00^\circ$



Lower Surface Pressure Coefficient on NFW701 and the OVERDISC Redesign at Mach 2.40

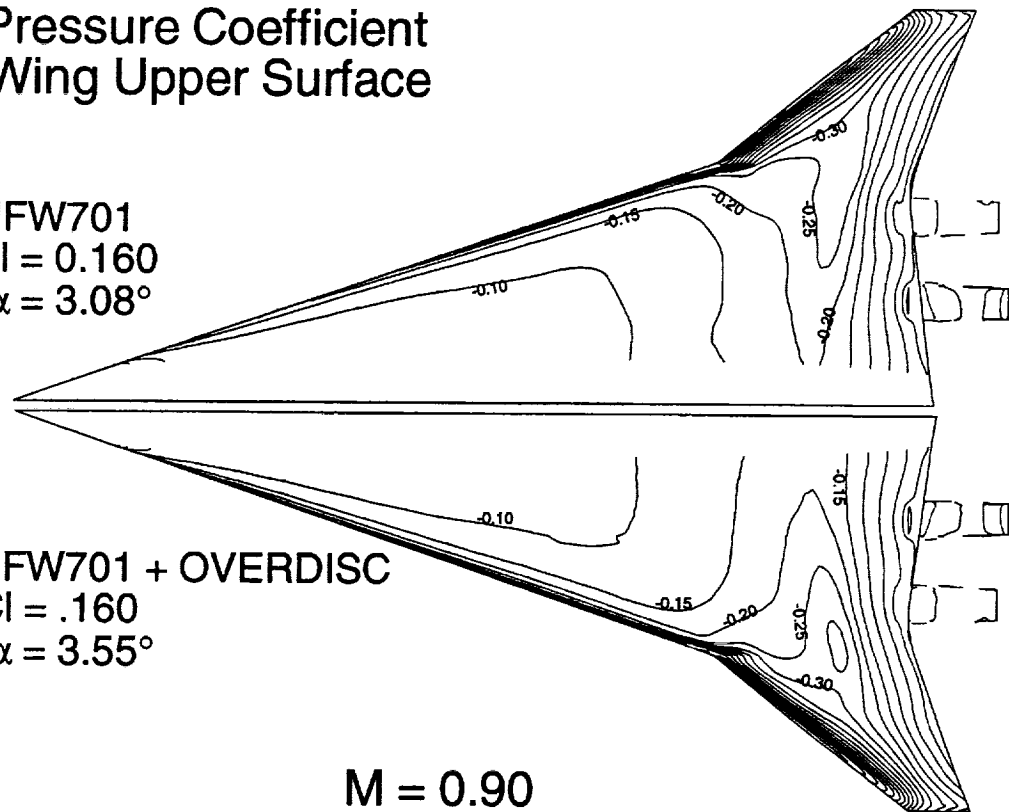
Pressure coefficient distributions on the lower surface of the wings for the NFW701 and OVERDISC redesigned configurations at Mach 2.4 are shown in the figure. While the redesign provided a moderate reduction in the shock strength on the lower wing surface, the reduction was not nearly as large as expected based on the experience in redesigning the BCAG optimized configuration. The reason for this appears to be that significantly more smoothing was utilized in the NFW701 redesign to prevent discontinuities in the surface at the spar locations; that smoothing reduced the degree to which the shock was attenuated.

Pressure Coefficient Wing Upper Surface

NFW701
 $C_l = 0.160$
 $\alpha = 3.08^\circ$

NFW701 + OVERDISC
 $C_l = .160$
 $\alpha = 3.55^\circ$

$M = 0.90$



Upper Surface Pressure Coefficient on NFW701 and the OVERDISC Redesign at Mach 0.90

Pressure coefficient distributions on the upper surface of the wings for the NFW701 and OVERDISC redesigned configurations at Mach 0.9 are shown in the figure. Note that both configurations are run at the design C_l of 0.16, but the redesign angle of attack is 3.55 degrees rather than 3.08. There is little to distinguish between the pressure distributions for the two configurations.

Pressure Coefficient Wing Lower Surface

NFW701
 $C_l = 0.160$
 $\alpha = 3.08^\circ$

NFW701 + OVERDISC
 $C_l = .160$
 $\alpha = 3.55^\circ$

$M = 0.90$

Lower Surface Pressure Coefficient on NFW701 and the OVERDISC Redesign at Mach 0.90

Pressure coefficient distributions on the lower surface of the wings for the NFW701 and OVERDISC redesigned configurations at Mach 0.9 are shown in the figure. The most notable difference between the two configurations is on the outboard wing panel, where the redesign has been unloaded to some extent. Note that somewhat larger expansions are beginning to appear between the nacelles with the redesign.

TCA Performance Predictions

$$Re = 4.0 \times 10^6$$

Configuration	α	CL	CD	ΔCD
---------------	----------	----	----	-------------

M = 2.40

Baseline	3.00	0.8300	0.01207	—
NFW701	3.00	0.8964	0.01252	-0.00014
NFW701 CDISC	3.00	0.8325	0.01176	-0.00034

M = 0.90

Baseline	4.00	0.1608	0.01567	—
NFW701	3.07	0.1599	0.01457	-0.00102
NFW701 CDISC	3.55	0.1601	0.01456	-0.00106

TCA Performance Predictions

Performance predictions for the TCA baseline, NFW701, and OVERDISC redesigned NFW701 configurations are shown in the figure. The results indicate that the redesigned configuration provides an additional 2 count drag reduction over that of NFW701 at supersonic cruise while maintaining the same transonic performance improvement over that of the TCA baseline. However, the transonic performance improvement of 10.6 counts does not compare well with flap optimization studies, which indicate that a 26 count drag reduction is obtainable at transonic cruise for the TCA configuration with optimized flaps.

While the NFW design provided significant improvements in transonic performance over that of the TCA baseline, it is apparent that the benefits of the NFW design at transonic cruise cannot be properly evaluated without considering optimal flap settings in the assessment. Moreover, while the viscous analysis of the NFW design indicated a 3.4 drag count reduction over that of the TCA baseline at supersonic cruise, the reduction is significantly less than the roughly 6 drag count reduction obtained in the various optimizations conducted by other participants in the HSR program.

Nevertheless, the NFW design has two unique features which merit further consideration, namely, incorporation of the entire landing gear constraint into the fuselage and the utilization of a blunt rather than sharp leading edge outboard of the wing leading edge break. At the least, the NFW design provides an intriguing alternative starting point (rather than starting from the baseline configuration) for the aerodynamic optimization methods used elsewhere within the HSR program.

Future Plans

- HSR
 - Wind up NFW design of TCA
 - Nacelle/Diverter Redesigns
 - << CDISC redesign of diverter/nacelle
 - << procedures for satisfying inlet flow constraints
 - Powered Effects
- Couple OVERFLOW with an aeroelastics module
 - ELAPS
 - Utilize an OVERDISC type script for regridding

Future Plans

One of the unresolved issues with the NFW designs is determination of the penalty and benefit of utilizing a blunt rather than sharp leading edge outboard of the wing leading edge break at the supersonic and transonic cruise conditions, respectively. This issue will be addressed by modifying the outboard leading edge of the OVERDISC redesigned NFW701 configuration to be sharp and analyzing the resulting configuration at Mach 2.4 and 0.9. While it is believed that additional supersonic performance improvements are obtainable with moderate modifications to the NFW configuration, further redesigns of the wing using OVERDISC are not anticipated at this time. Instead, effort will be spent on redesigning the nacelles and diverters and investigating methods for satisfying constraints on the engine inlet flow.

An additional area of investigation which has been initiated is the analysis of powered effects at transonic cruise. Overset grids for a configuration with the nozzle flaps deflected are currently under construction.

One additional effort which is worthy of note is the coupling of OVERFLOW with an aeroelastics module in order to account for aeroelastic deformations. In this work, OVERFLOW is to be coupled with the ELAPS code using an automated regridding procedure similar to that used with OVERDISC.

This page is intentionally left blank.



Progress Towards a Multipoint Optimization Procedure

1071

Robert P. Narducci and Shreekant Agrawal

Configuration Aerodynamics
The Boeing Company, Long Beach

HSR Airframe Technical Review
Los Angeles, California
February 9-13, 1998



This page is intentionally left blank.

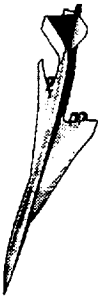
Progress Towards a Multipoint Optimization Procedure

Robert P. Narducci and Shreekanth Agrawal
The Boeing Company
Long Beach, California 90807-5309

This paper investigates the relative merits of two multipoint design approaches for the HSCT. In the first, a supersonic cruise point design is used as initial conditions for a flap optimization at the transonic cruise condition. In the second approach, the shape of the HSCT is optimized with considerations of aerodynamic performance at the supersonic and transonic cruise conditions weighed according to its impact on the maximum take-off gross weight (MTOGW). Results using the first approach are presented using the Boeing Long Beach (BLB), and NASA Ames Cycle 2 designs. The impact of the initial configuration shape on transonic cruise performance and flap deflection angles is addressed. An intermediate multipoint design using the second approach is also presented and compared with designs from the first approach.

Motivation

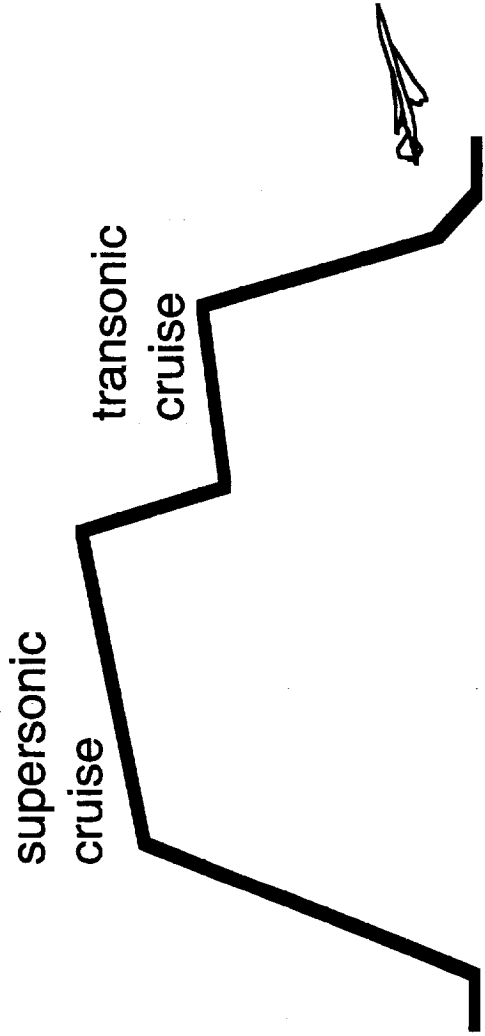
The mission of an HSCT is made up of many legs: taxi-out and take-off, climb, supersonic cruise, descent, subsonic cruise, descent, approach, and taxi-in. In Configuration Aerodynamics, the focus of design thus far has been on the longest part of the mission, the supersonic cruise. Yet, supersonic considerations may not be sufficient to meet the program goal of an overall aerodynamically efficient design. Features that are introduced to increase the aerodynamic efficiency at the supersonic cruise point may incur large drag penalties at off-design flight conditions. Likewise, features that greatly decrease the drag at off-design conditions with little adverse impact on the supersonic cruise point design would be missed in current single point design methods. To avoid single point specific design features and incorporate beneficial features for off-design flight conditions, the HSCT must be designed with a multipoint optimization process.



Motivation

High Speed Aerodynamics, Long Beach

- HST design with only supersonic cruise point considerations may not be sufficient to meet program goals for aerodynamically efficiency
- Configuration changes may exist that have large drag benefits at off-design Mach numbers with only minimal impact at the supersonic condition



 **BOEING**

Objectives

The primary focus of this work is to investigate several approaches to multipoint design and implement the most promising of these into AEROSHOP. AEROSHOP is the Boeing Long Beach design environment for shape optimization of HSCT configurations with non-linear aerodynamic considerations. The next objective is to evaluate the methods by obtaining and evaluating designs using each approach. The evaluation should lead to a recommendation for a multipoint optimization strategy for future HSCT designs. To meet the secondary objective, an assessment of the impact of different supersonic cruise point designs on the transonic cruise performance will be made. Here, if all designs with appropriate flap deflections can reach the same level of performance at the transonic cruise condition, it may not be necessary to have multipoint design considerations during shape optimization since the performance at off-design Mach numbers is insensitive to a variety of designs.

Objectives



High Speed Aerodynamics, Long Beach

- Primary objectives
 - Develop and apply several approaches to multipoint design
 - Compare optimization experiences and designs to recommend a strategy for future multipoint designs
- Secondary objective
 - Assess the impact of different supersonic cruise point designs on the transonic cruise performance

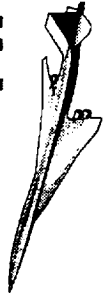
Two Approaches to Multipoint Design

Two approaches are currently being investigated for multipoint design at Boeing Long Beach. In the first, optimization is performed to determine flap settings for minimum drag at the transonic cruise condition for a non-linearly optimized supersonic cruise point configuration. In the second approach, the transonic and supersonic performance are optimized simultaneously.

The assumption in Approach 1 is that the transonic performance level is not heavily dependent on the wing camber, twist, and thickness and fuselage area distribution, cross-sectional shape, and camber line. These are the geometric features optimized for supersonic cruise and the assumption implies that whatever drag penalty might be incurred at the transonic cruise condition can be regained with the optimized flap deflections.

The second approach removes the major assumption made in the first approach. Here, the optimization of the configuration is carried out by integrating inputs from both the supersonic and transonic cruise conditions, thus requiring a supersonic and transonic solution for every inquiry made by the optimizer.

Two Approaches to Multipoint Design



High Speed Aerodynamics, Long Beach

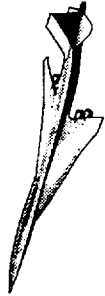
- Approach 1 - Sequential supersonic/transonic designs
 - Supersonic cruise point shape optimization
 - Flap schedule optimization at transonic cruise conditions
- Approach 2 - Combined supersonic/transonic design
 - Weighing of supersonic and transonic drag in a single objective function for shape and flap optimization

Comparison of Approaches

In the current implementation, where gradients are computed by finite-differences, significant savings in CPU resources can be achieved with Approach 1 over that of Approach 2. Concentrated optimization with large sets of design variables and a full complement of constraints can be applied at the supersonic condition. After a supersonic optimized design has been lofted, a simpler optimization with a few design variables representing flap deflections can be done at the transonic condition. Only a few constraints are needed in this step. Additionally, since the flap optimization at transonic conditions is relatively inexpensive and does not feedback to the supersonic cruise shape, assessments at several Mach numbers can be easily achieved.

Approach 2 is more comprehensive since it does allow for wing and fuselage shape to change according to supersonic and transonic requirements. Approach 2 will not allow single-point design features that have large adverse effects at other design conditions. Likewise, beneficiary features at the transonic condition that have little impact on the supersonic cruise point performance may be introduced into the design.

Comparison of Approaches



High Speed Aerodynamics, Long Beach

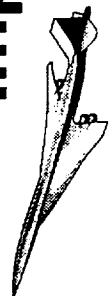
- Approach 1
 - Less computationally intensive
 - More amenable to investigating performance at more Mach numbers
- Approach 2
 - Allows for geometric changes that may provide large drag benefits at off-design Mach numbers for little penalty at the supersonic cruise condition
 - May avoid features specifically for supersonic cruise point performance benefits

Implementation of Approach 1

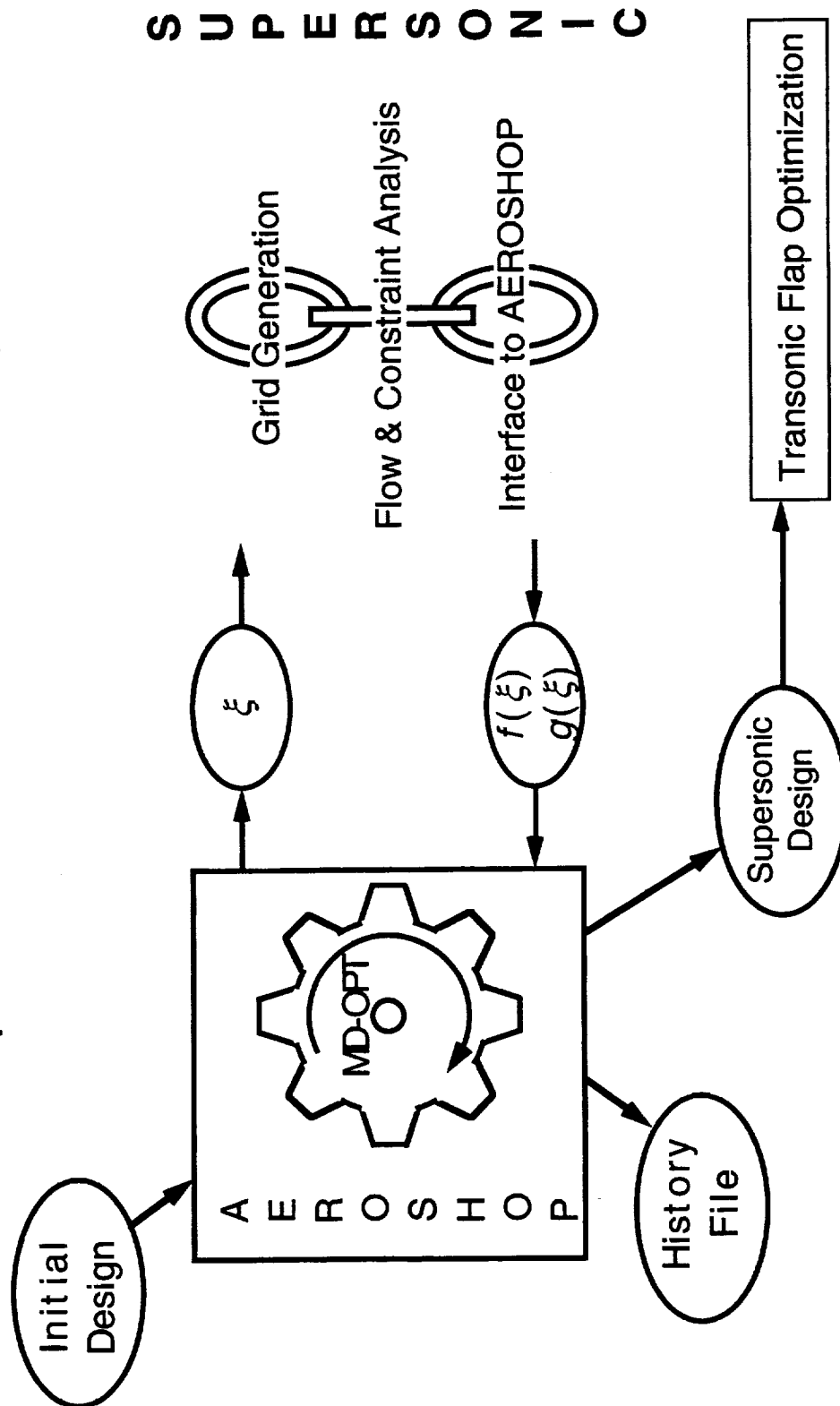
The implementation of Approach 1 is a simple matter since the process is a sequential merger of two existing processes: single supersonic cruise point design and transonic flap optimization. The AEROSHOP design tool is a program that make a system call to a UNIX shell script, sometimes referred to as the AEROSHOP chain. The AEROSHOP chain is the sequence of commands that links together the grid generator, flow solver, and constraint analysis codes. The final code in the script collects the objective function and constraint information and passes it to AEROSHOP. Communication between the optimizer and the AEROSHOP chain is done via data files. The design variables, represented by ξ in the figure, are written to a file for the grid generator to interpret. The objective function, f , and the constraints, g , are likewise written to a file for the optimizer to read. The optimizer in AEROSHOP is MD-OPT, a proprietary version of the commercially available NPSOL software. The AEROSHOP chain for supersonic cruise point design is used first. Here codes for W/B/N/D integrated optimization are used to obtain a supersonic cruise point design. The AEROSHOP chain is then replaced with one for transonic flap optimization. The W/B geometry of the supersonic cruise point design is fitted with flap definitions for the TCA baseline geometry. The final product is the supersonic cruise point design with a flap schedule at one or more Mach numbers lower than the supersonic cruise.

Implementation of Approach 1, Part 1

High Speed Aerodynamics, Long Beach



Supersonic Cruise Point Design



S U P E R S O N I C



Implementation of Approach 1

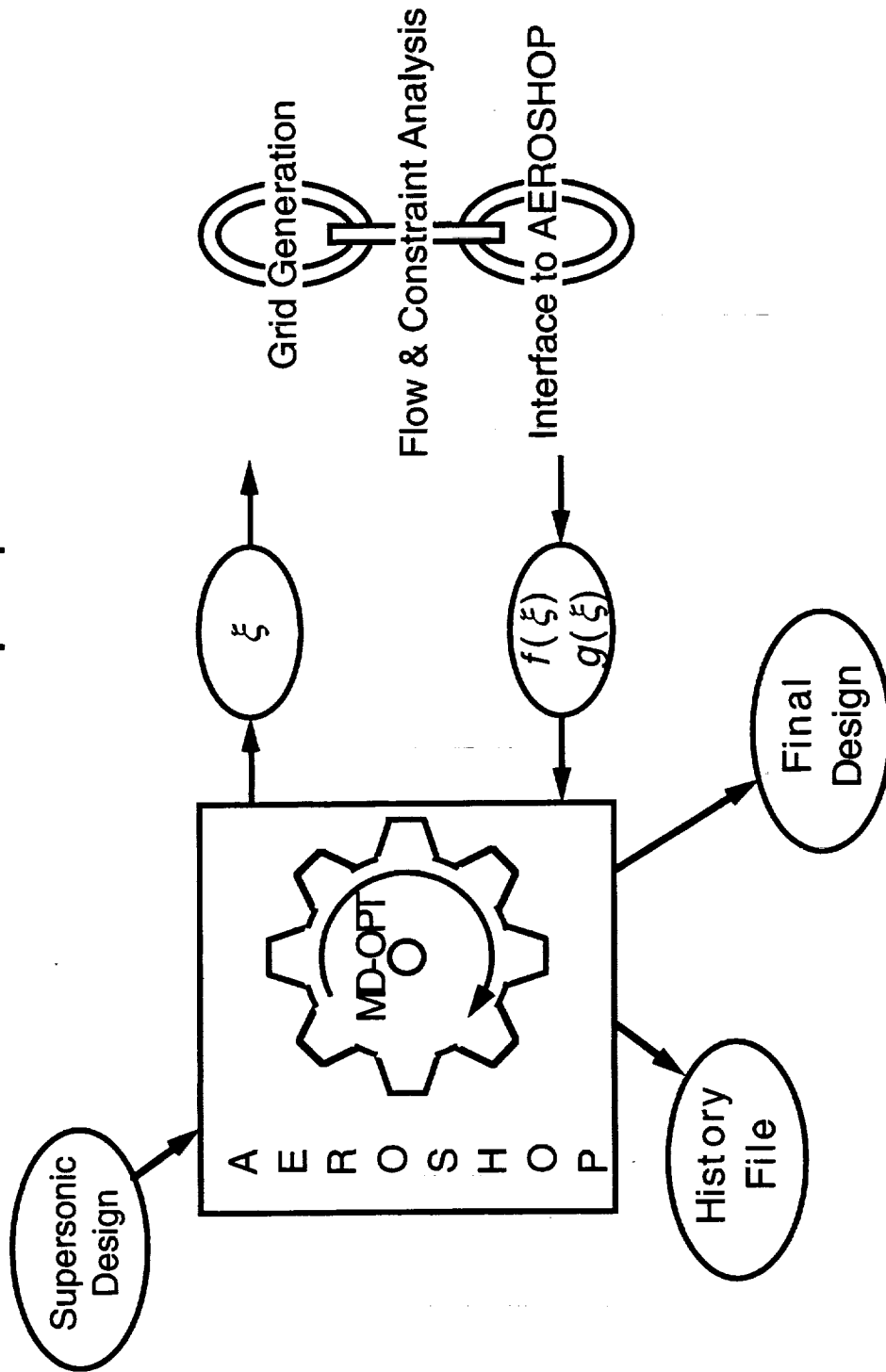
This slide is intentionally left blank.

Implementation of Approach 1, Part 2

High Speed Aerodynamics, Long Beach



Transonic Flap Optimization



T R A N S O N I C



Application of Approach 1

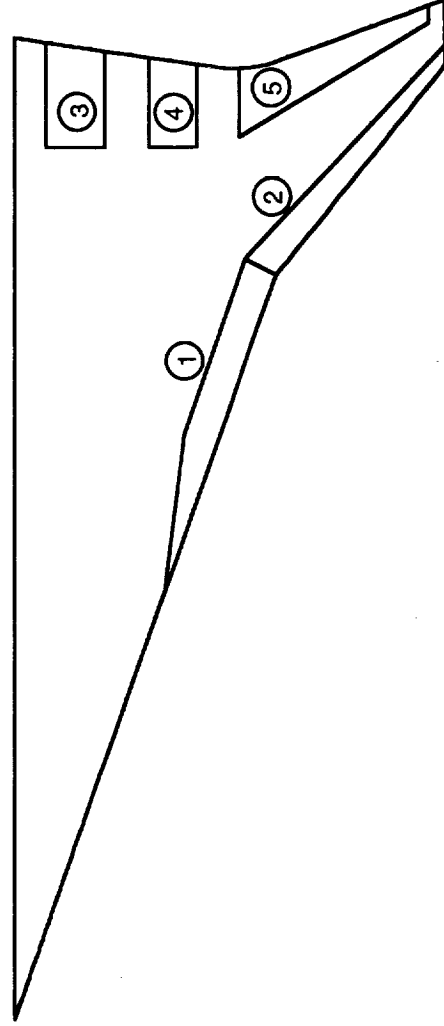
Approach 1 is applied to the BLB Cycle 2 and Ames Cycle 2 designs. Although strictly speaking, neither one of these designs were obtained using AEROSHOP, they do represent supersonic cruise point designs. The BLB design was obtained using MDO3D, a precursor to AEROSHOP, and the Ames design was obtained primarily using SYN87. The transonic flap optimization minimized the ratio of drag-to-lift at $M_\infty=0.9$ subject to a constraint on the cruise lift condition ($C_L=0.18$). The design variables for the optimization are the five TCA flap deflection angles and the angle-of-attack. The optimizations for both supersonic cruise point designs are identical to that performed for the Baseline TCA configuration except the inboard trailing-edge flap was narrowed to accommodate the increase fuselage girth at the wing trailing-edge station.

Application of Approach 1



High Speed Aerodynamics, Long Beach

- Obtained supersonic cruise point design from Cycle 2 effort
- Optimized flap deflections at $M_\infty=0.9$ starting from the BLB Cycle 2, and Ames Cycle 2 designs (BCAG Cycle 2 flap optimization not available at the time of this writing)
- Constrain lift to the 1g cruise condition
- Six design variables include 5 flaps and the angle-of-attack



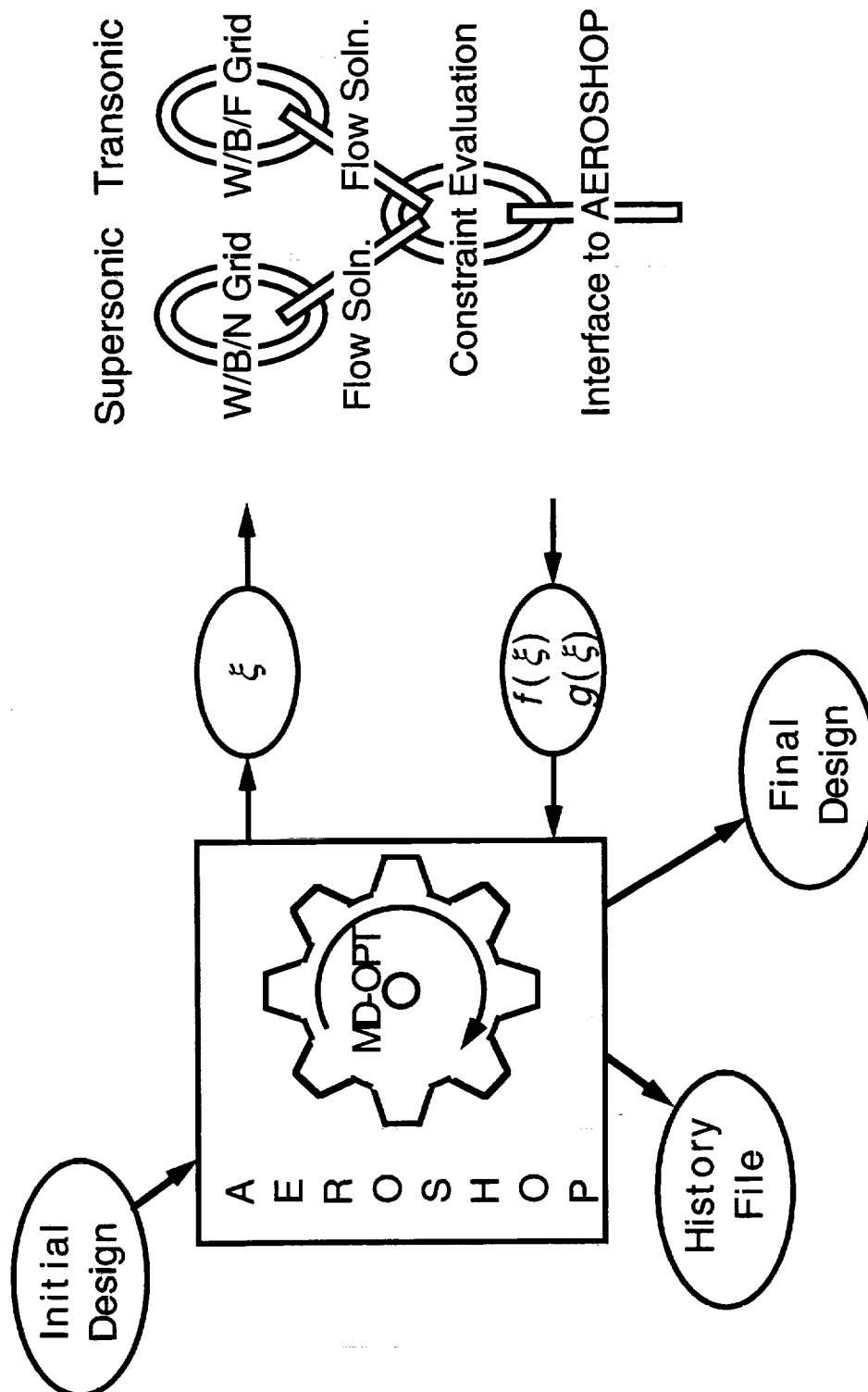
BOEING

Implementation of Approach 2

The implementation of Approach 2 also used the AEROSHOP design tool. This implementation, however, was more complicated than its predecessor since it required a merger of the AEROSHOP shell scripts rather than the sequential use of them. Separate grids are generated for the supersonic and transonic flow analyses, though each represents the same wing and fuselage geometry. The supersonic grid models the W/B/N/D configuration; the transonic grid represents the W/B/F configurations and features an extended far field. CFL3D is run in separate applications for the supersonic and transonic analysis. The objective function and constraint evaluation codes take information from the aerodynamic analyses and the geometry definition and pass the multipoint evaluation to AEROSHOP. The final product is a multipoint design with a flap schedule for $M_\infty=0.9$ cruise. Flaps are not deflected in the supersonic cruise segment.

Implementation of Approach 2

High Speed Aerodynamics, Long Beach



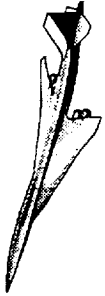
Application of Approach 2

The AEROSHOP design tool can run with any definition of an objective function. The multipoint objective function must intelligently weigh supersonic cruise performance with transonic cruise performance for the multipoint design to have a meaningful impact. Several objective functions have been identified as viable candidates for multipoint optimization, though here we investigate only one. We use

$$F = -(W_s \Delta C_{Ds} + W_t \Delta C_{Dt}),$$

where W_s and W_t are weights associated with the supersonic and transonic segments of the HSCT mission, and ΔC_{Ds} and ΔC_{Dt} are the drag reductions with respect to the baseline configuration at the supersonic and transonic straight and level cruise conditions, respectively. The value of the weights, W_s and W_t , are subject to further investigation. Current thinking has identified the weights as 8000 and 2000 for the supersonic and transonic drag reduction, respectively. These weights have been determined through inputs from the Technology Integration (TI) element of HSR Program where the Take-Off Gross Weight (TOGW) is 4 times as sensitive to a count of supersonic drag as it is to a count of transonic drag.

Application of Approach 2



High Speed Aerodynamics, Long Beach

- Supersonic and transonic cruise performance are weighted according to TOGW considerations

$$F = -(W_s \Delta C_{Ds} + W_t \Delta C_{Dt})$$

$s \rightarrow$ Supersonic cruise
 $t \rightarrow$ Transonic cruise

- Example: $W_s = 8000 \text{ lbs/ct}$ @ supersonic cruise
 $W_t = 2000 \text{ lbs/ct}$ @ transonic cruise



Application of Approach 2

Approach 2 was applied using the BLB Cycle 2 design as an initial geometry. Optimization was applied in three applications of design variable sets, though nothing would prevent a single application of an all inclusive design variable set (AEROSHOP can accommodate hundreds of design variables at a time). Details of the design variable sets follow in the next few charts. In all, 144 different design variables are defined for the multipoint design. Some variables, such as angle-of-attack and flap deflections have been repeated in the sets, hence the total number of design variables is not additive. Constraints for the design are applied according to the requirements set forth by TI for the supersonic cruise point design effort.

Application of Approach 2



High Speed Aerodynamics, Long Beach

- Design variables are applied in three sets
 - Angle-of-attack, wing twist, camber and thickness, fuselage camber, and flaps 58
 - Angle-of-attack, wing thickness in the nacelle region, and trailing-edge flaps 54
 - Angle-of-attack, fuselage area, shape and camber 44

(some variables are repeated) Total: 144

- Constraints are applied as per TI requirements for the TCA supersonic point design

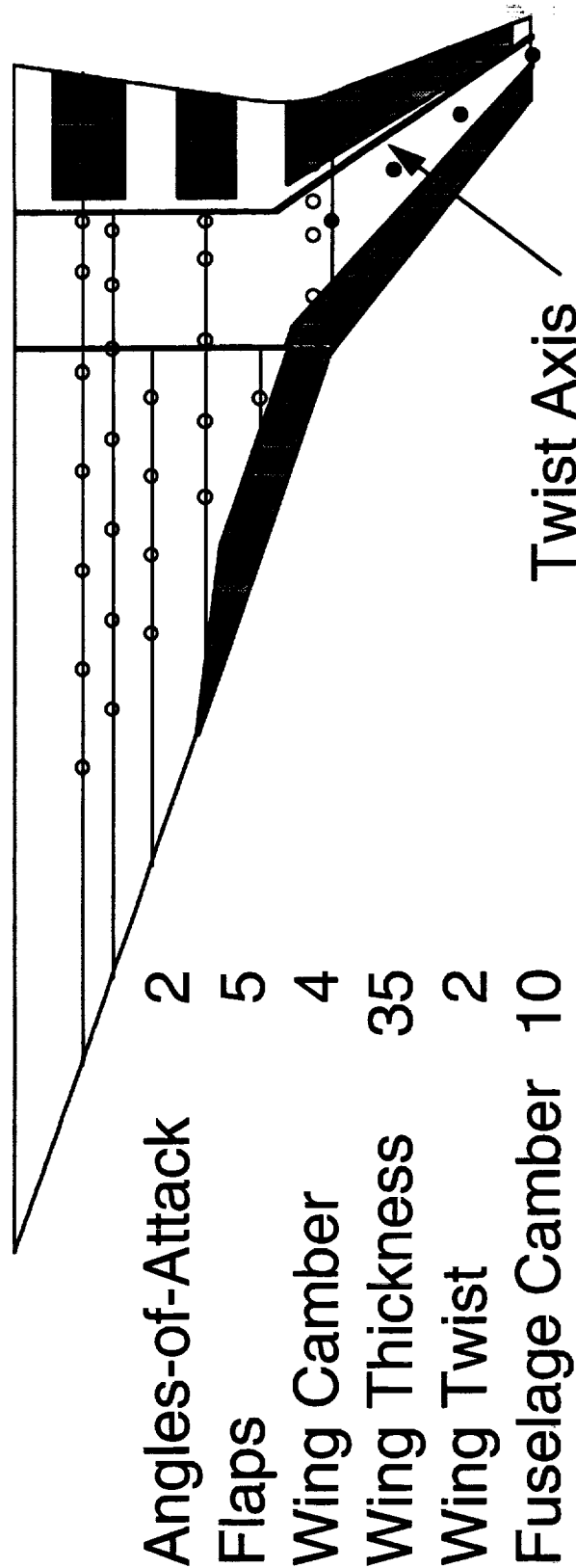
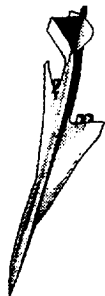


Design Variable Set #1

The first set of design variables represents the most general application of design variables, working on both wing and fuselage. The hollow circles on the planform represent the location of the thirty-five lower surface thickness variables. By operating strictly on the lower surface, these variables also modify the camber. The wing camber variables are placed on the outboard wing panel and are represented by the solid circles. Wing twist perturbations are applied along the rear spar. The four of the ten fuselage camber design variables vary the fuselage camber; the remainder modify the deck and vertical wing placement. Two angle-of-attack design variables are required, one for supersonic analysis, the other for transonic analysis. The flap design variables are only applied for transonic analysis and are represented by the shaded region.

Design Variable Set #1

High Speed Aerodynamics, Long Beach



Total 58

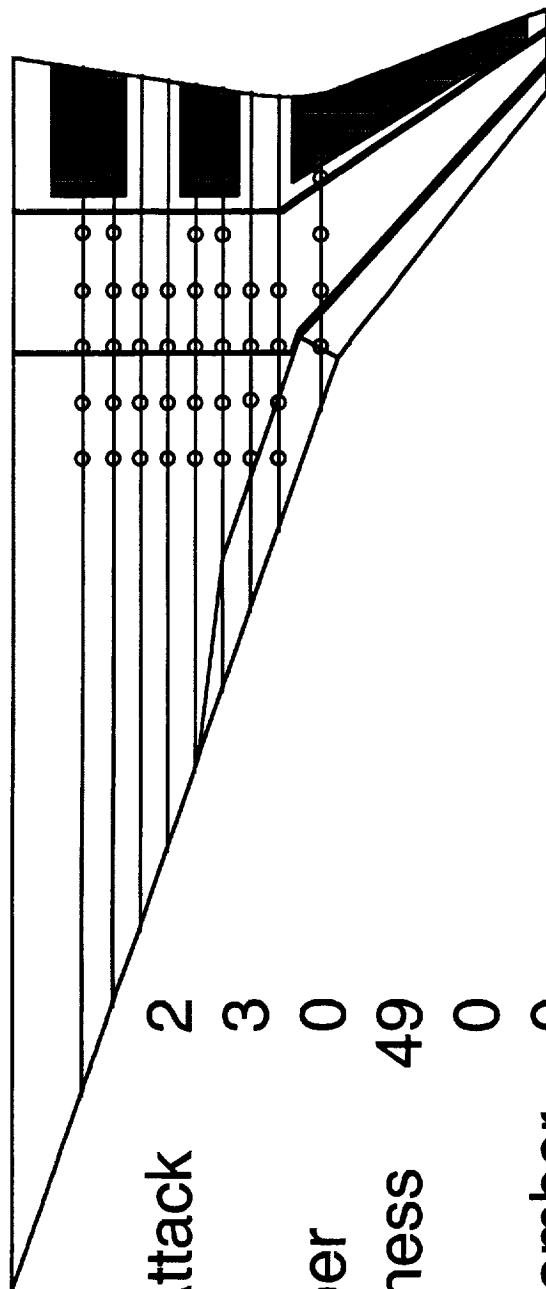


Design Variable Set #2

The second set represents a detailed refinement of the wing lower surface in the nacelle region. Forty-nine thickness variables are used here. As in the previous set, two angle-of-attack design variables are required, one for supersonic analysis, the other for transonic analysis. In this set, only the trailing-edge flaps are used for optimization.

Design Variable Set #2

High Speed Aerodynamics, Long Beach



Angles-of-Attack	2
Flaps	3
Wing Camber	0
Wing Thickness	49
Wing Twist	0
Fuselage Camber	0
Fuselage Area	0
Fuselage Shape	0

Total 54



Design Variable Set #3

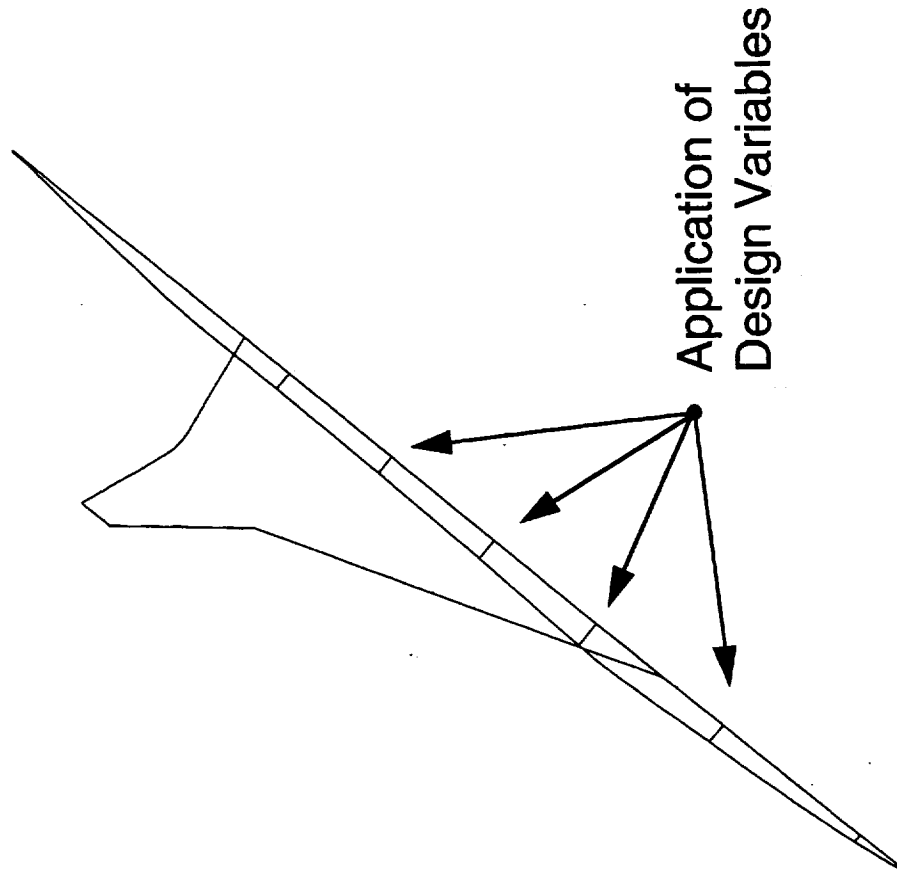
The objective of the final design variable set is to refine the fuselage. The angle-of-attack and the fuselage camber design variables from the first set are repeated here. The remaining variables allow the cross-sectional area to scale and change shape in the section from the forebody to just ahead of the trailing-edge flaps.

Design Variable Set #3

High Speed Aerodynamics, Long Beach



Angles-of-Attack	2
Flaps	0
Wing Camber	0
Wing Thickness	0
Wing Twist	0
Fuselage Camber	14
Fuselage Area	8
Fuselage Shape	<u>20</u>
Total	44



Benchmark Flap Optimization for Baseline TCA

For the purpose of comparisons, the results of the transonic flap optimization of the baseline configuration are included here. The Euler-based design proceeded for fourteen iterations before variations in the design variables, lift and drag settled. At the subsonic cruise condition ($M_\infty=0.9$), the minimal obtainable drag for this configuration as determined by Euler analysis and a flat-plate skin-friction prediction is 113 counts.

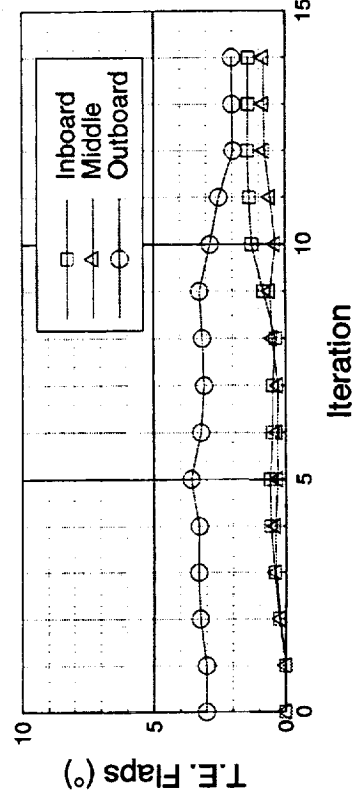
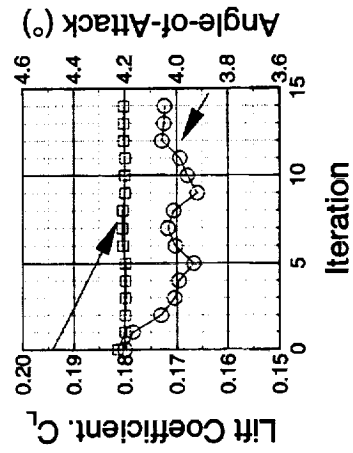
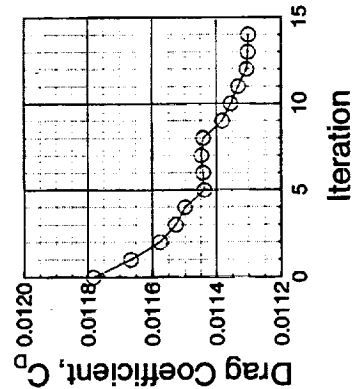
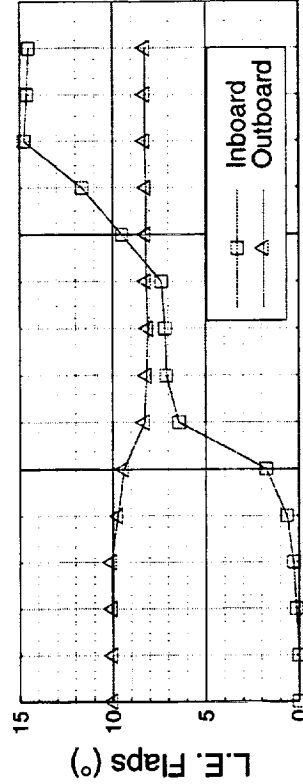
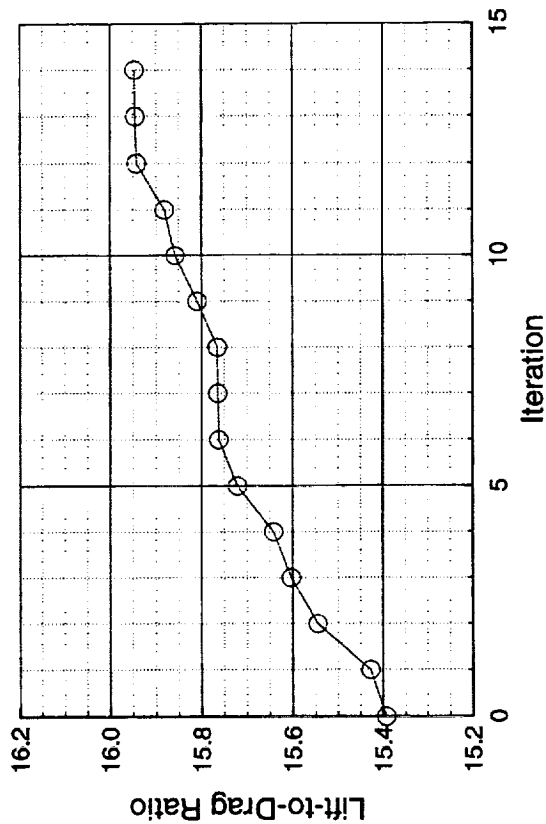
Benchmark Flap Optimization for Baseline TCA



High Speed Aerodynamics, Long Beach

AEROSHOP with CFL3D Euler, $M_\infty=0.9$

TCA Baseline Design



Results from Approach 1

The history of the flap optimization associated with the BLB Cycle 2 design is shown below. One noticeable difference between this optimization and that of the baseline TCA is the lack of a large inboard leading-edge flap deflection. For this configuration, the Euler and flat-plate prediction method shows the transonic cruise drag level to be 116 counts.

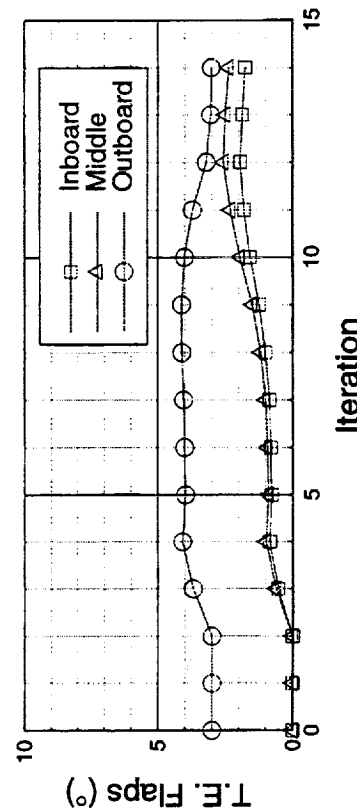
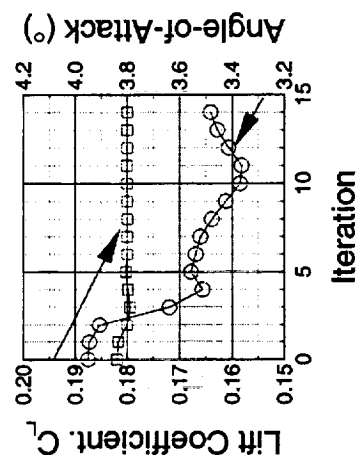
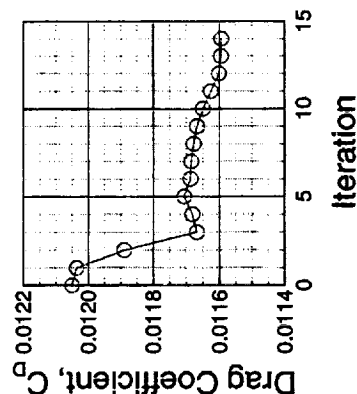
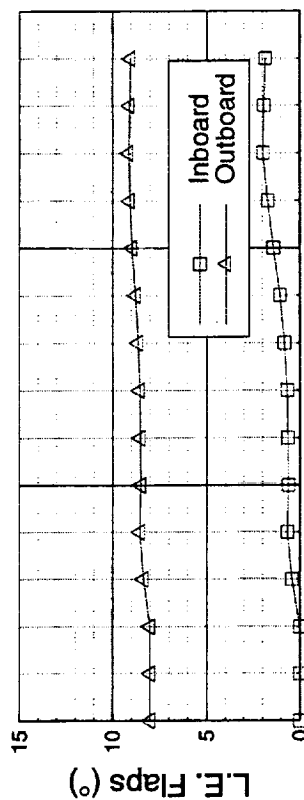
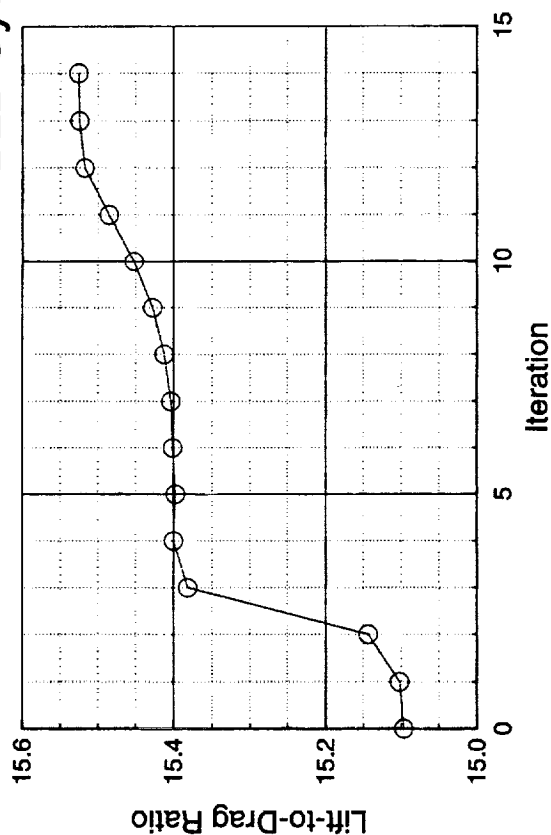
Results from Approach 1



High Speed Aerodynamics, Long Beach

AEROSHOP with CFL3D Euler, $M_\infty=0.9$

BLB Cycle 2 Design



Results from Approach 1

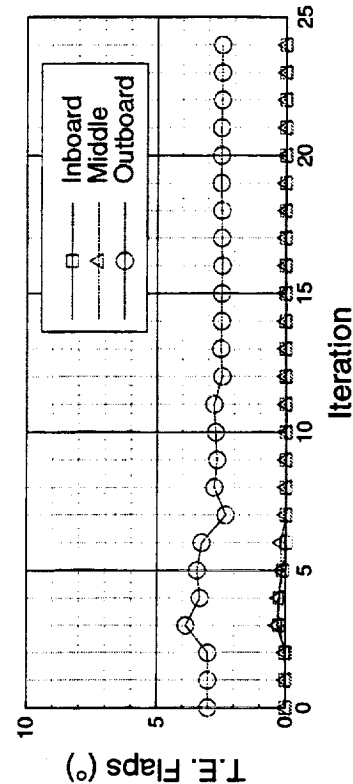
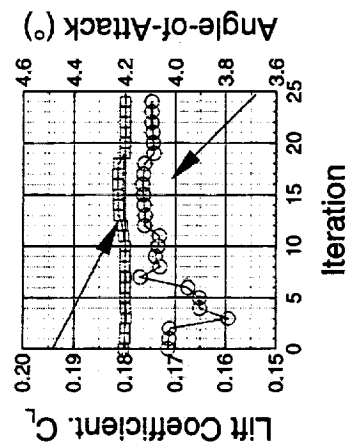
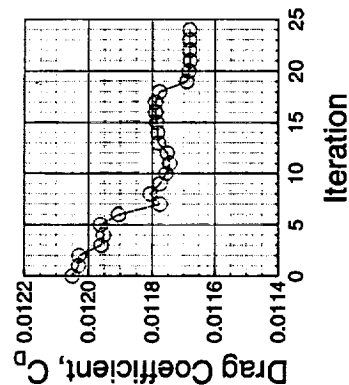
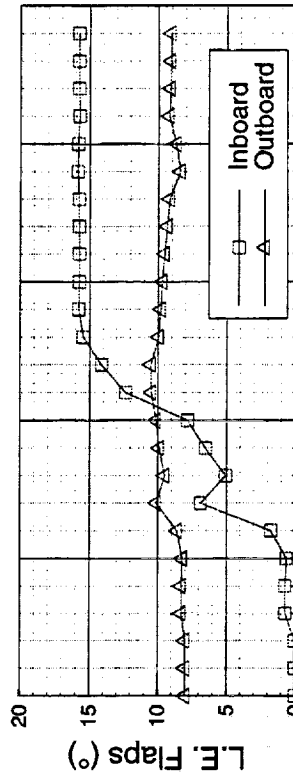
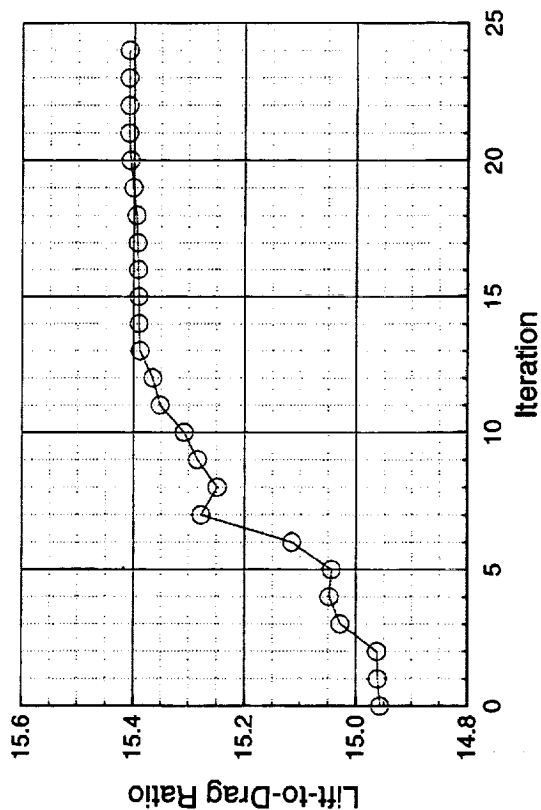
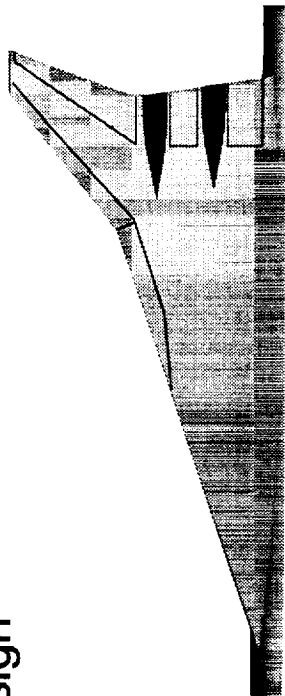
The history of the flap optimization associated with the Ames Cycle 2 design is shown below. The optimized flap settings are similar to the Baseline configuration. For this configuration, the Euler and flat-plate prediction method shows the transonic cruise drag level to be 116.8 counts.

Results from Approach 1



High Speed Aerodynamics, Long Beach

AEROSHOP with CFL3D Euler, $M_\infty=0.9$
Ames Cycle 2 Design



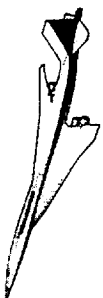
BOEING

Comparison of Approach 1 Designs

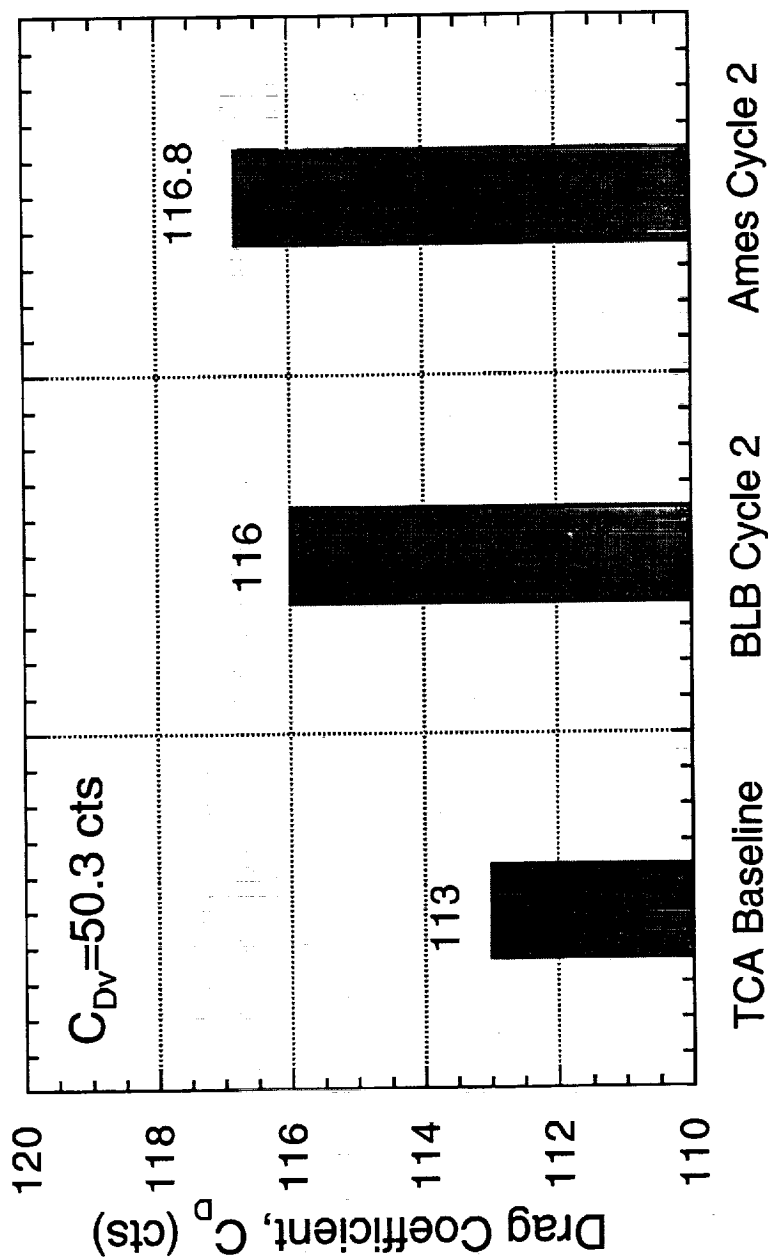
The bar chart below shows a comparison of the predicted drag level at the transonic cruise ($M_\infty=0.9$, $C_L=0.18$) portion of the HSCT mission. The predictions are made using CFL3D in the Euler mode on the design grid (113x33x91). An estimate of 50.3 counts of skin friction are added to all Euler predictions. The design with the lowest drag at the transonic cruise condition is the TCA baseline configuration. The BLB and Ames Cycle 2 designs have features that improve the performance at the supersonic condition, but hurt the transonic performance. All designs are analyzed with optimized flap settings. At the supersonic condition, the Euler improvements of the BLB Cycle 2 and Ames Cycle 2 designs over the baseline are 3.5 and 7 counts, respectively.

Comparison of Approach 1 Designs

High Speed Aerodynamics, Long Beach



Transonic Cruise W/B Performance at $M_\infty=0.9$, $C_L=0.18$
CFL3D Euler & Flat-plate Skin-Friction



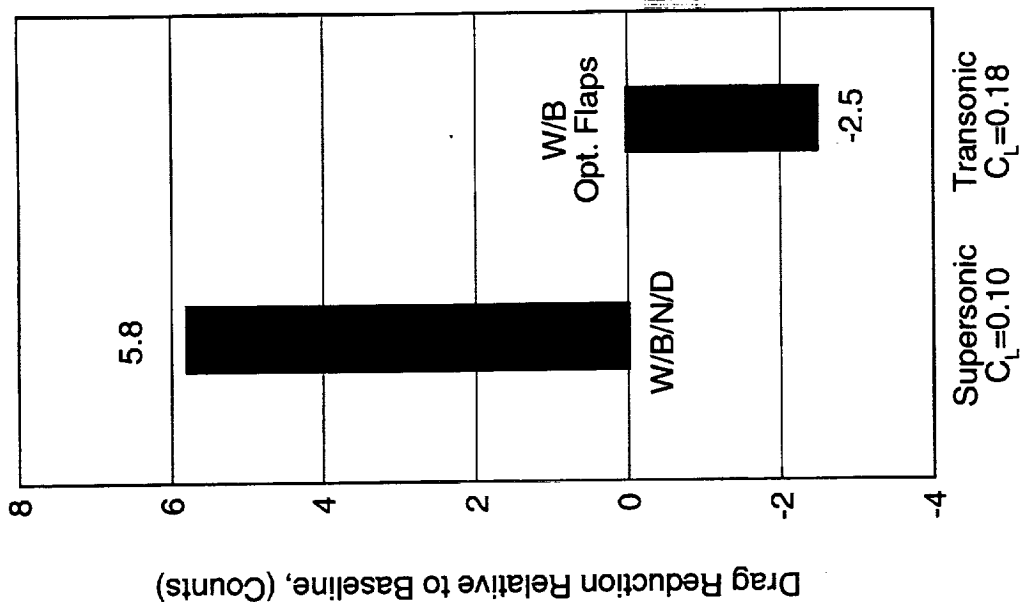
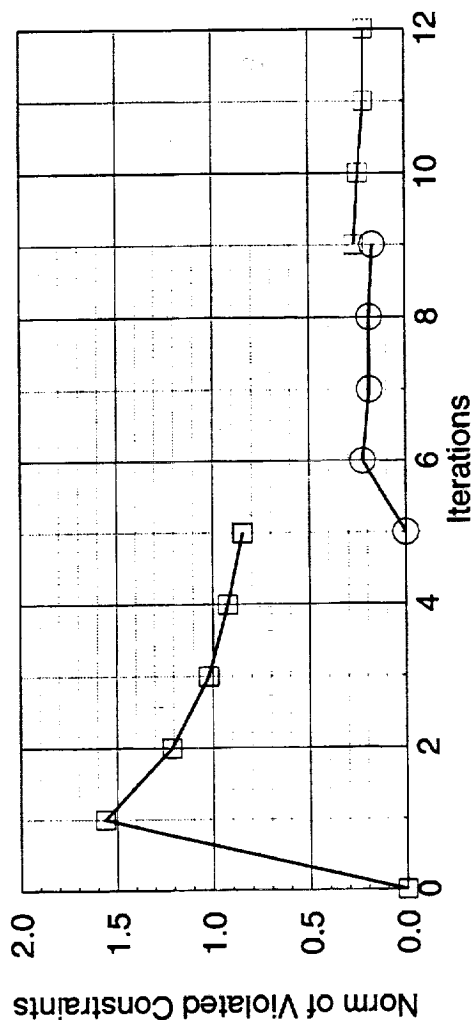
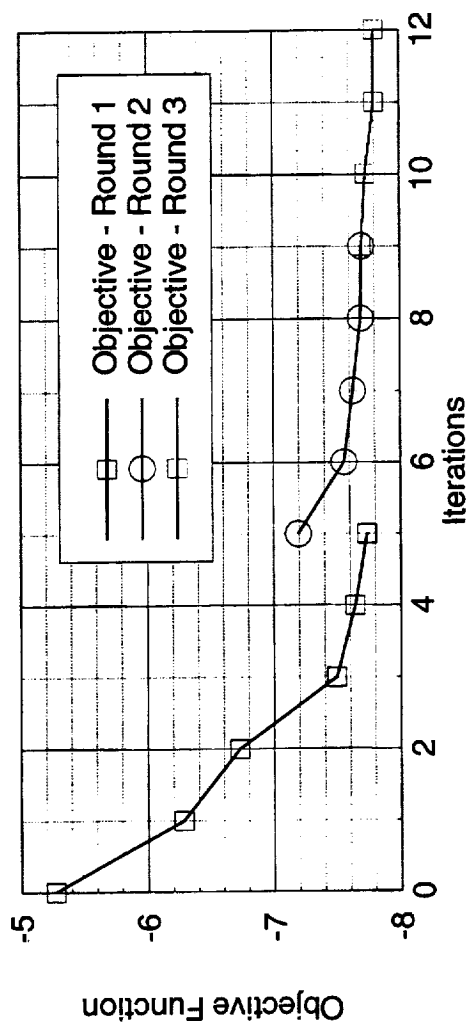
Results from Approach 2

The chart below shows a convergence history of the optimization using Approach 2. The optimization using the first set of design variables covers the first 5 iterations (black); the second set of variables covers iterations 5-9 (red); the third variable set covers iterations 9-12 (blue). To save time, thickness constraints that became violated during the first application of design variables were manually satisfied by adding thickness to the upper and lower surface at the spars. This resulted in a small jump in the objective function at iteration 5. The chart tracks the history of the objective function (upper left), the norm of violated constraints (lower left). Typically, a multipoint design would display a decrease in performance relative to a single point design at the supersonic cruise point, but an increase in total performance. In this case, the Approach 2 design has better supersonic performance due to an improvement in supersonic cruise point design process. The TCA baseline still has the best transonic performance when nonlinear optimization is applied to determine flap deflections.

Results of Approach 2



High Speed Aerodynamics, Long Beach



Supersonic $C_L=0.10$
Transonic $C_L=0.18$



Multipoint Approach 2 Design

Below is a comparison of the Baseline TCA and the multipoint design obtained using Approach 2. The optimized configuration has not been processed since the optimization, but nevertheless features a generally smooth surface.

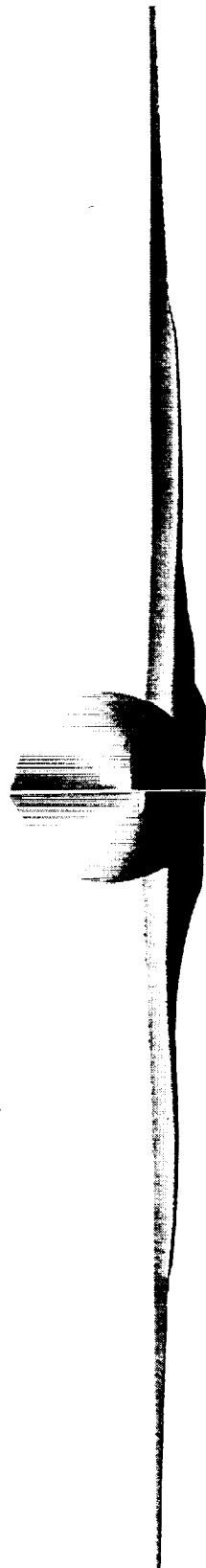
Comparison of the TCA and Multipoint Approach 2 Designs



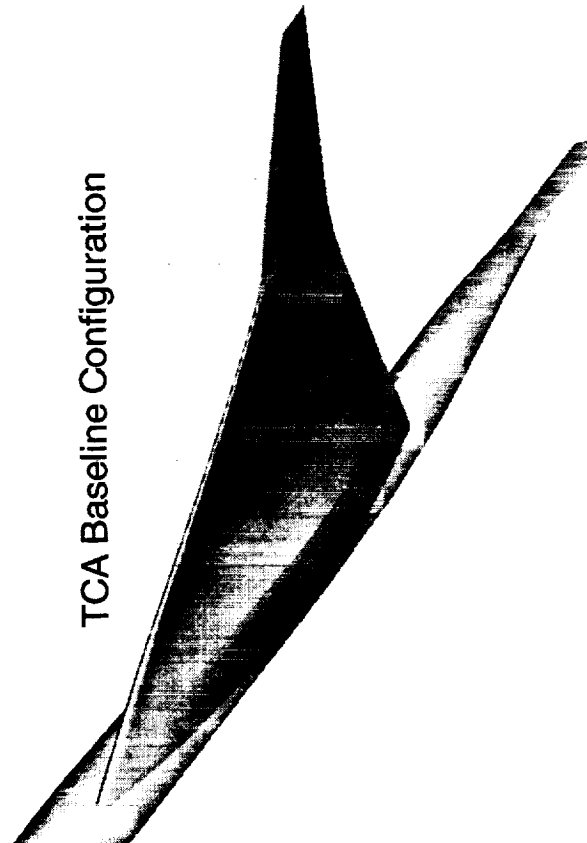
HSCT Aerodynamics, Long Beach

AEROSHOP w/ CFL3D Euler, $M=2.4$

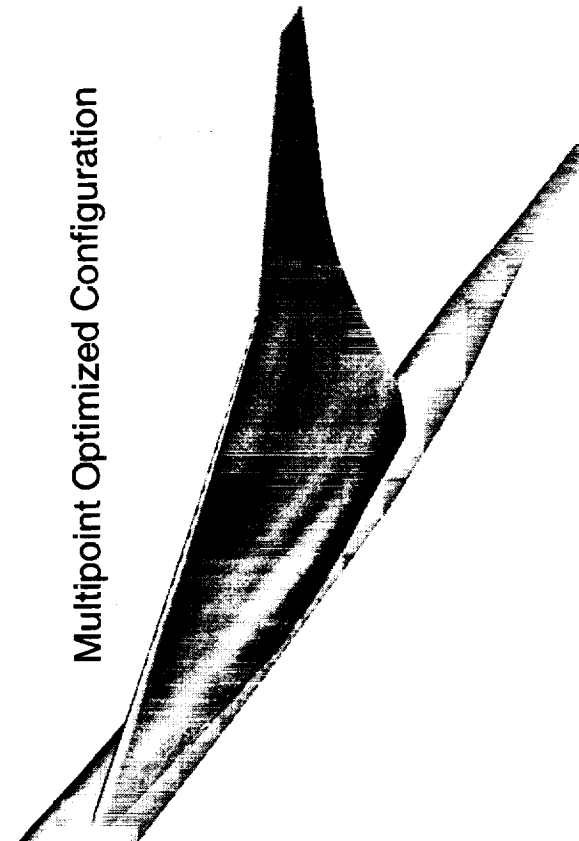
TCA Baseline Configuration



Multipoint Optimized Configuration



TCA Baseline Configuration



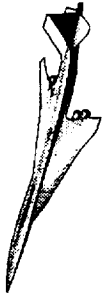
Multipoint Optimized Configuration



Active and Violated Constraints

The optimizer within AEROSHOP often violates constraints during the design process and tends to recover violations in the later stages of optimization. It is often cheaper to fix violated constraints by the hand of an experienced designer. For the purpose of demonstrating the multipoint design capability, small constraint violations were ignored. These violations occurred in maximum fuselage radius of curvature allowable, minimum spar thickness allowable, and minimum fuel volume required. It is thought that the penalty on performance to satisfy these small violations is minimal. Constraints that are active, but not violated include allowable space for the empennage carry-through and main landing gear, and trailing-edge closure angle.

Active and Violated Constraints



High Speed Aerodynamics, Long Beach

Approach 2 Multipoint Design

- Minor maximum radius of curvature violations on fuselage
- Empennage carry-through is active
- Main landing gear bay clearance is active
- Very minor front and rear spar thickness violations
- Fuel volume is violated by 0.5% (3.7' cubic box)
- Trailing-edge closure angle is active

Comparison of Designs

Force comparisons of the TCA baseline, and Approach 1 and 2 multipoint designs are shown on the figure below for the supersonic cruise evaluation condition. The Approach 1 design in this figure and all subsequent figures is the BLB Cycle 2 design. The forces are computed using CFL3D in the Euler mode using the design grid. Flat-plate skin friction estimated for the TCA baseline design ($Re_c=6.36 \times 10^6$) have been added to all designs.

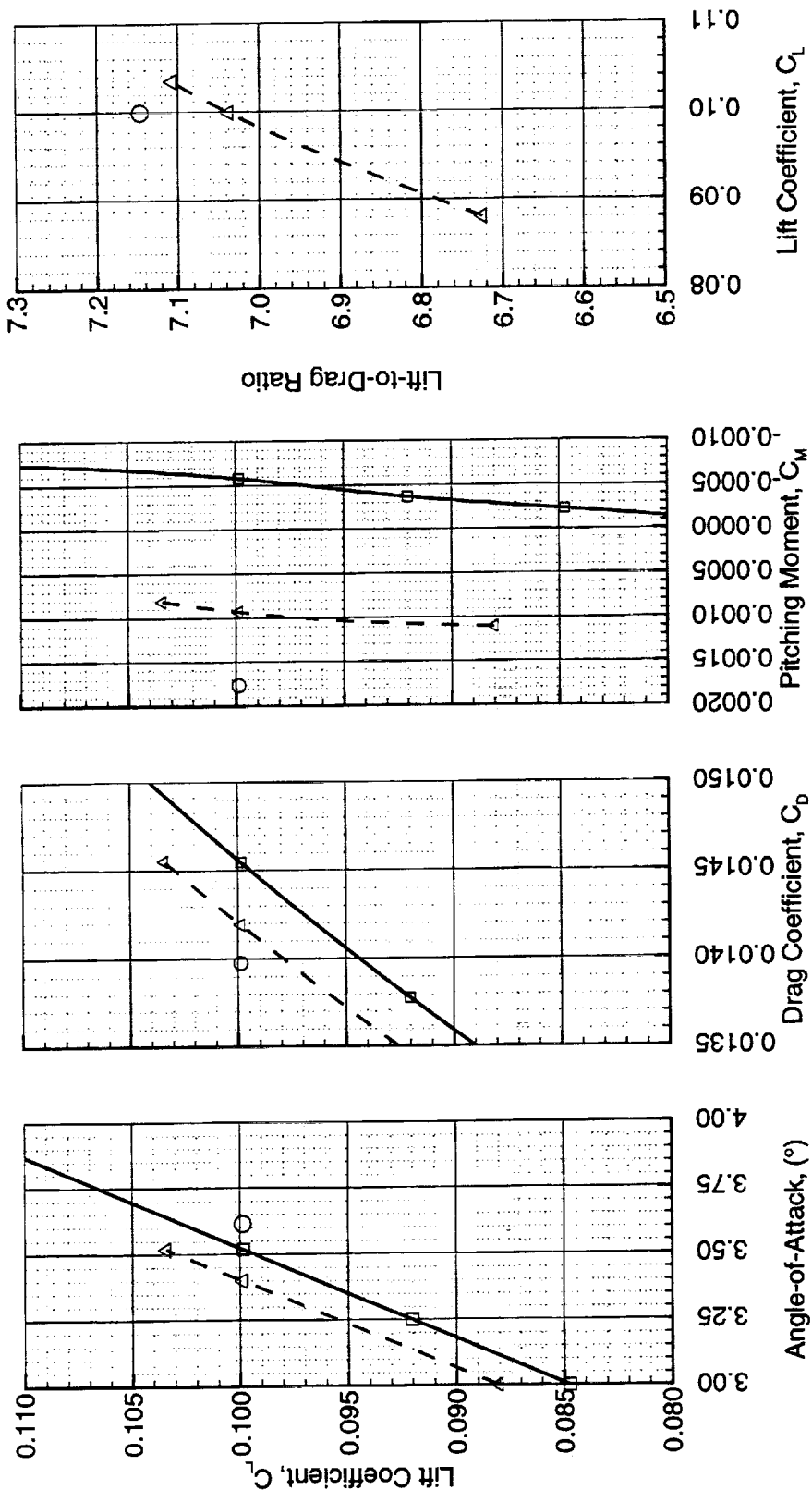
Comparison of Designs



High Speed Aerodynamics, Long Beach

Supersonic Force Assessment of Multipoint Designs
CFL3D Euler, W/B/N/D Configuration, $M_\infty=2.4$ (Design Grid)

—□— Baseline —△— Approach 1 —○— Approach 2



Comparison of Designs

Force comparisons of the TCA baseline, and Approach 1 and 2 multipoint designs are shown on the figure below for the transonic cruise evaluation condition. The forces are computed using CFL3D in the Euler mode using the design grid. Flat-plate skin-friction estimated for the TCA baseline design (50.3 counts for $Re_c=163 \times 10^6$) have been added to all designs.

Comparison of Designs

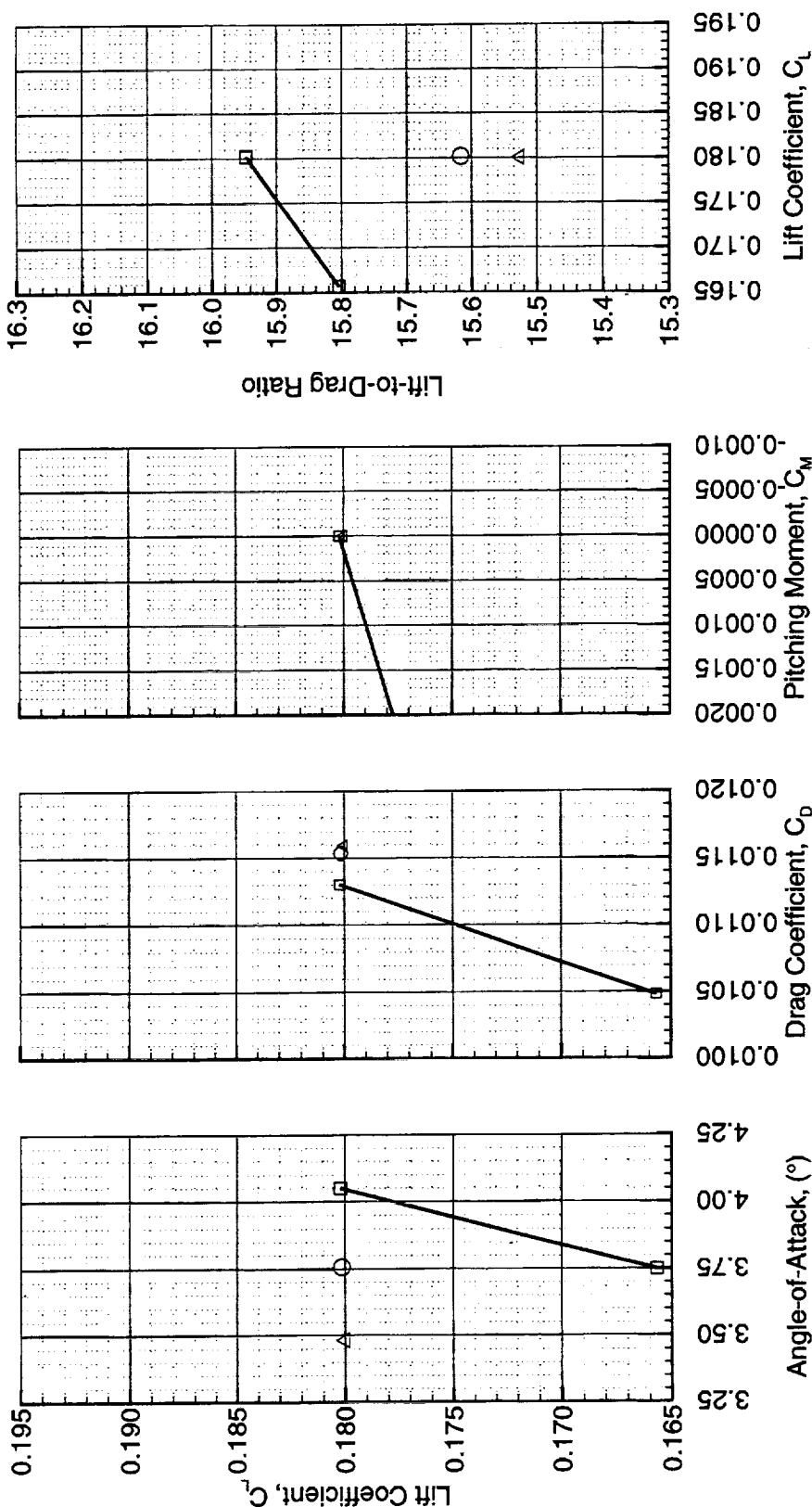


High Speed Aerodynamics, Long Beach

Transonic Force Assessment of Multipoint Designs

CFL3D Euler, W/B/N/D Configuration, $M_\infty=0.9$ (Design Grid)

—□— Baseline —△— Approach 1 —○— Approach 2

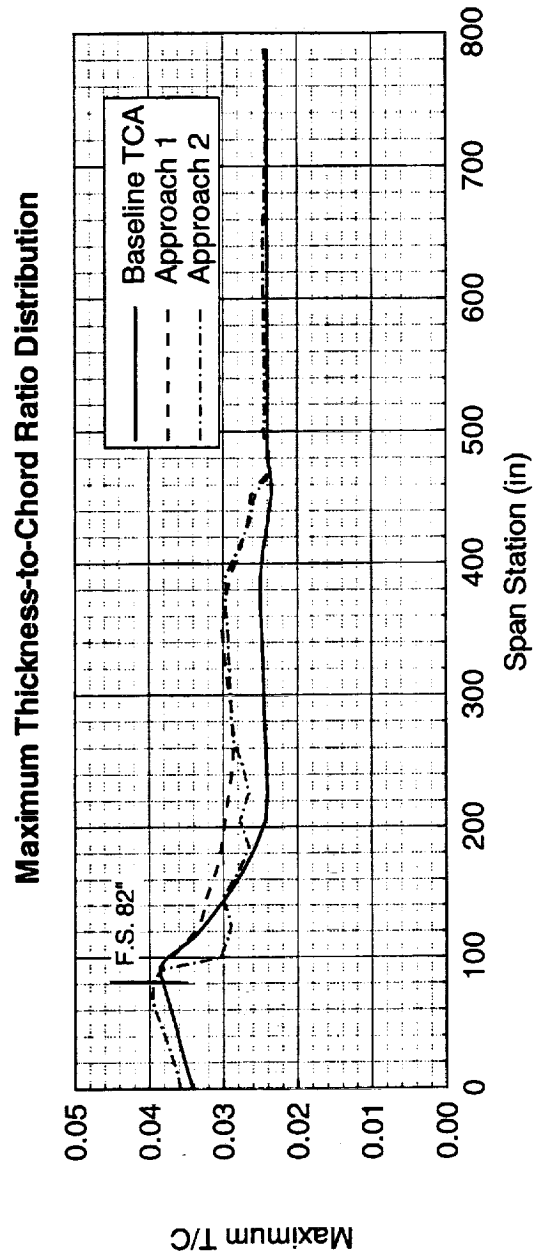
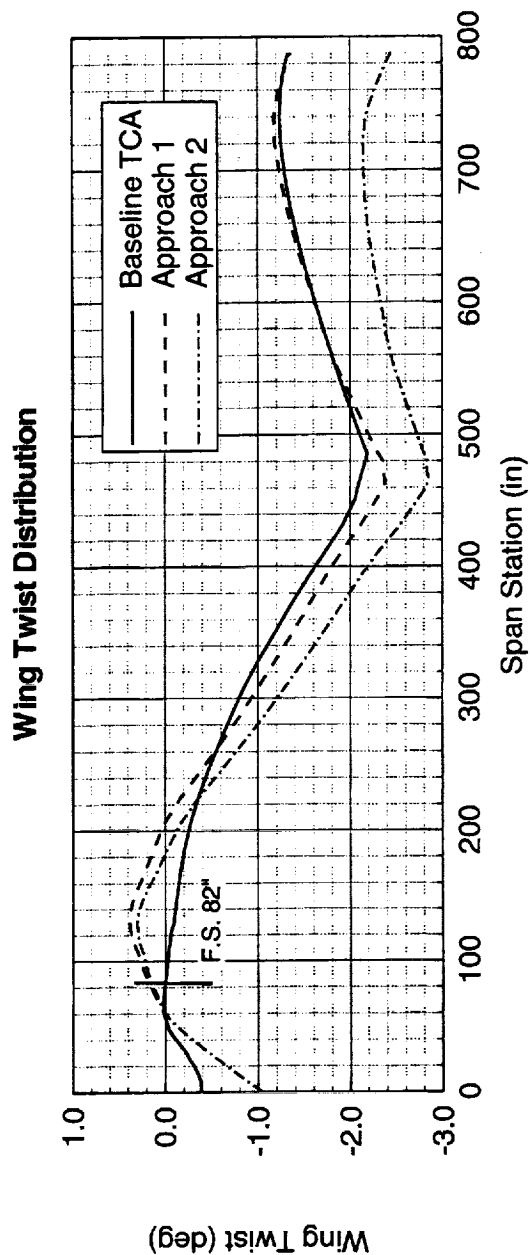


Comparison of Designs

Shown below is the twist and maximum thickness-to-chord ratio for the TCA baseline and multipoint designs.

Comparison of Designs

High Speed Aerodynamics, Long Beach

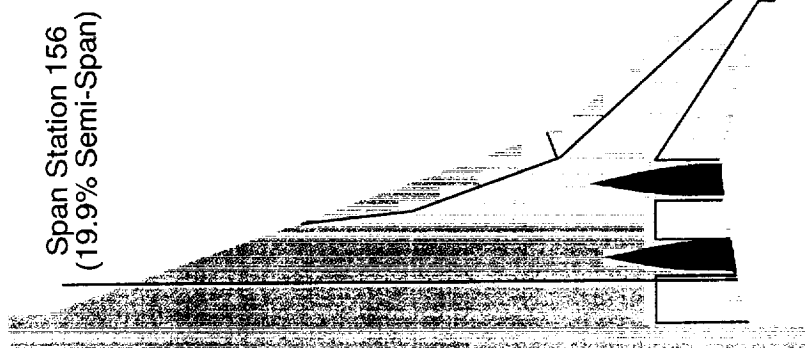
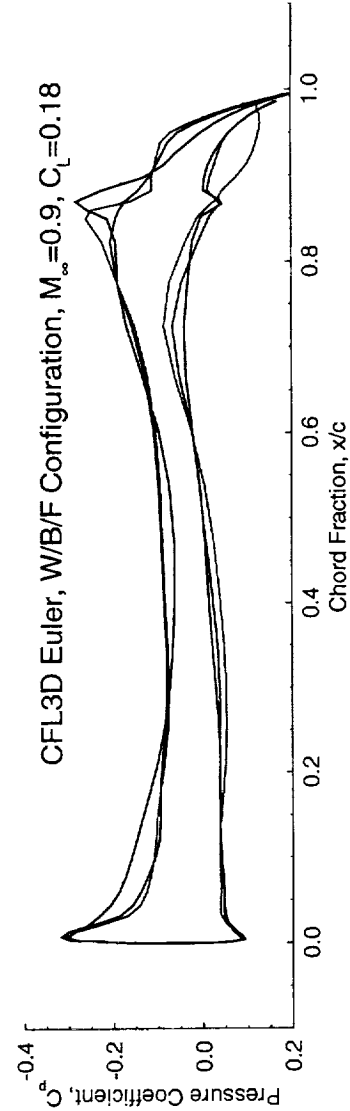
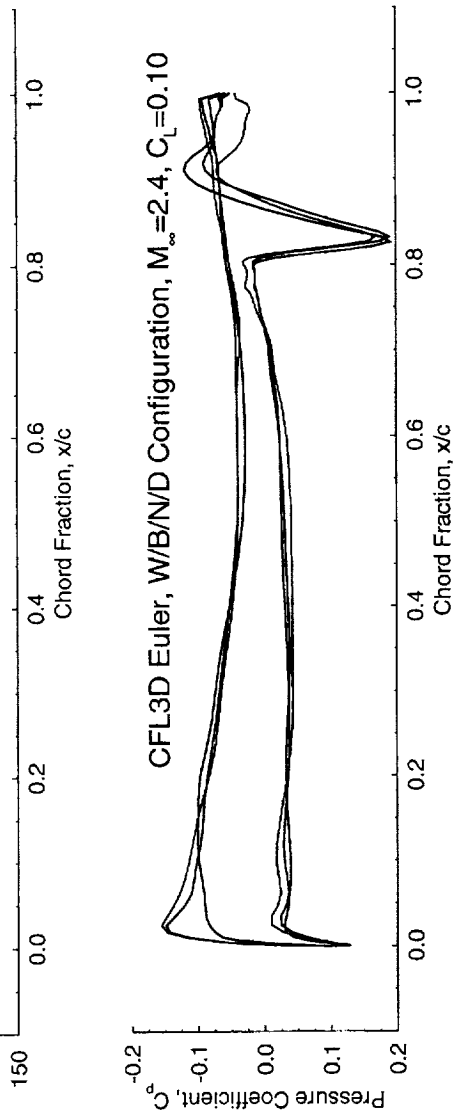
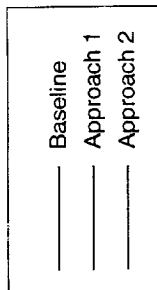
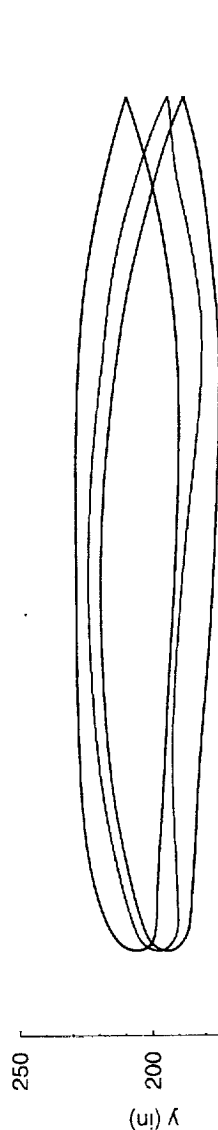


Comparison of Designs

Wing sections and pressure coefficient distributions at the supersonic and transonic cruise conditions are shown in the next several slides. The pressure coefficients are computed from CFL3D in the Euler mode.

Comparison of Designs

High Speed Aerodynamics, Long Beach

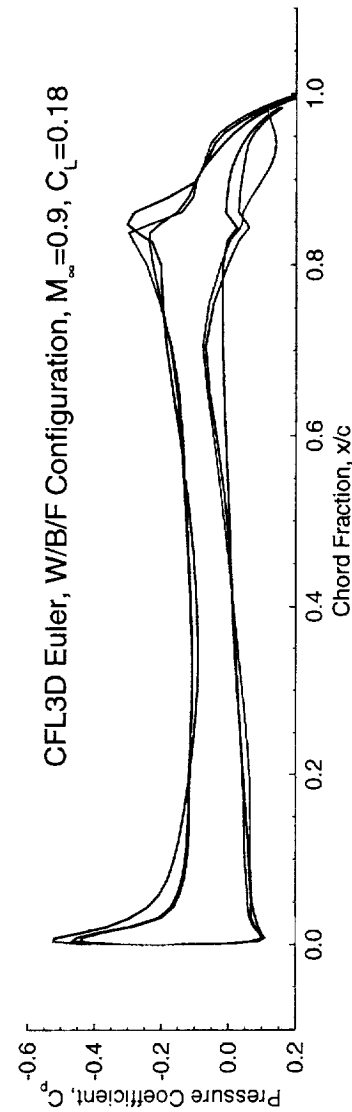
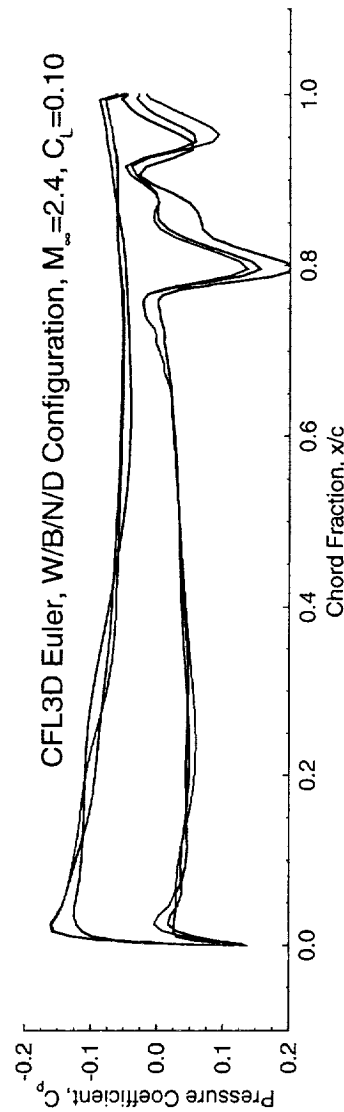
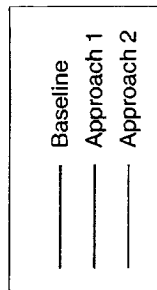
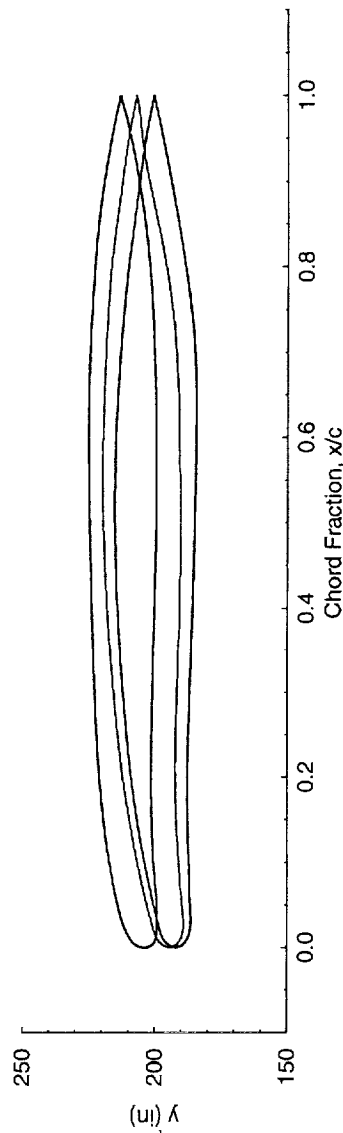


Comparison of Designs

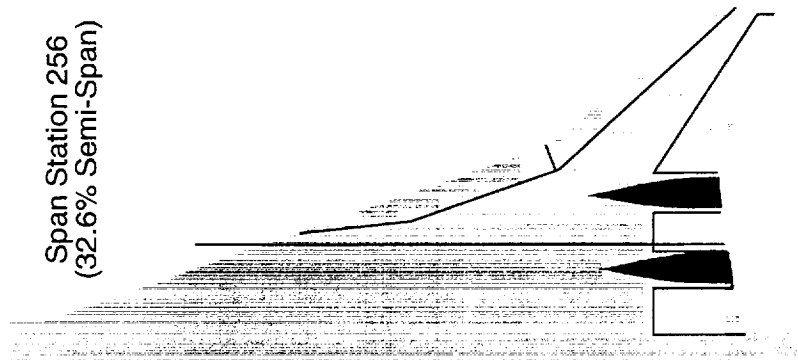
This page is intentionally left blank.

Comparison of Designs

High Speed Aerodynamics, Long Beach



Span Station 256
(32.6% Semi-Span)

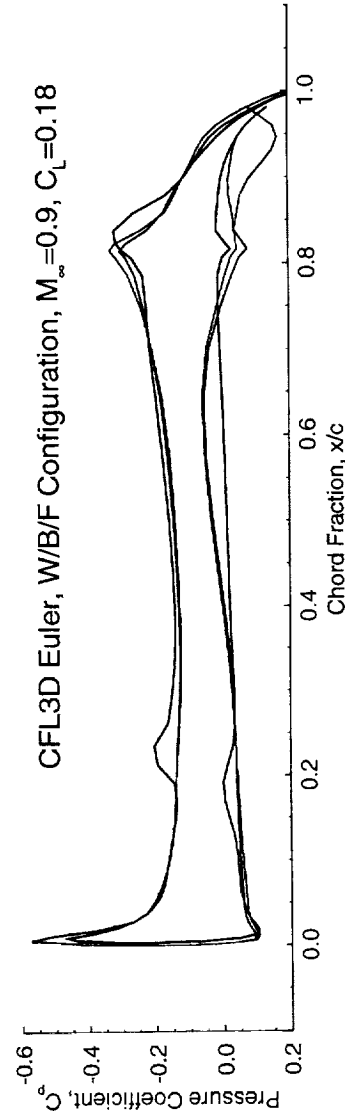
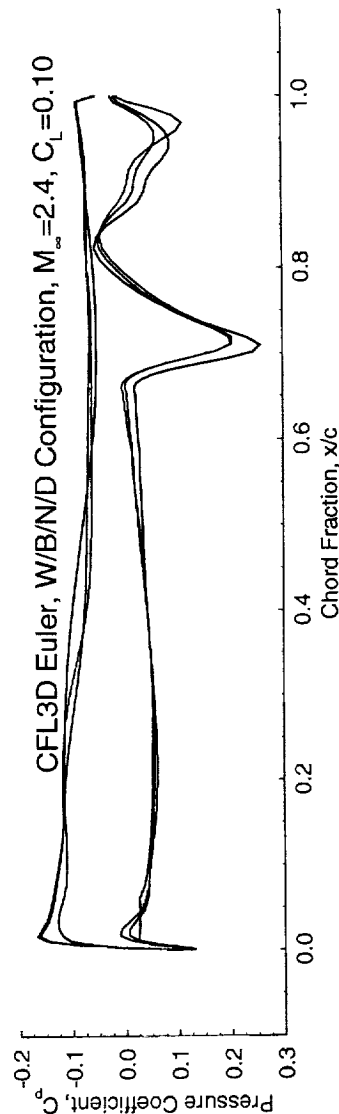
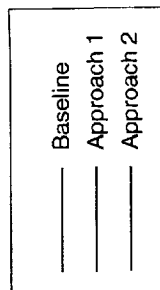
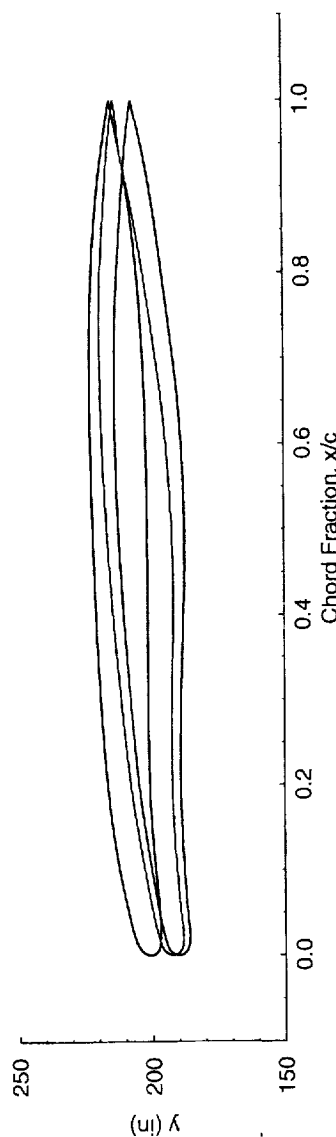


Comparison of Designs

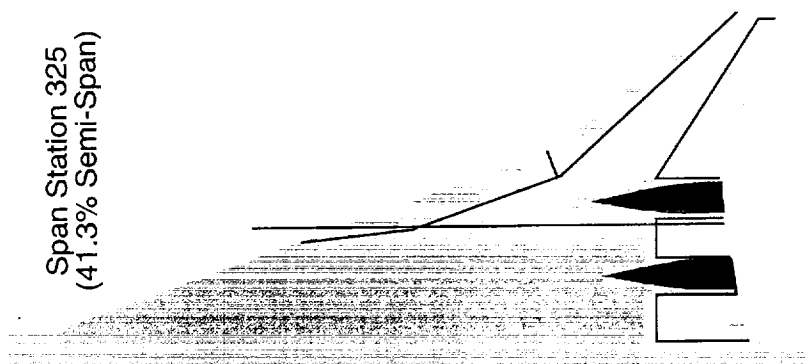
This page is intentionally left blank.

Comparison of Designs

High Speed Aerodynamics, Long Beach



Span Station 325
(41.3% Semi-Span)

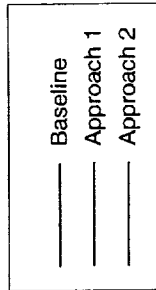
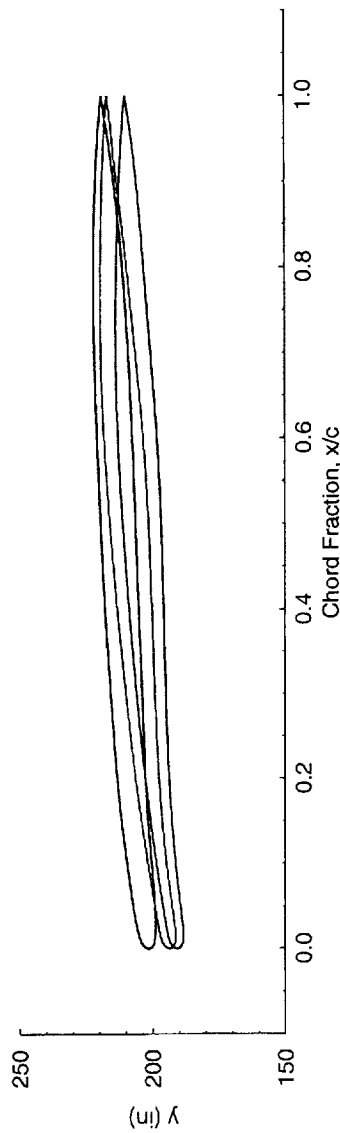


Comparison of Designs

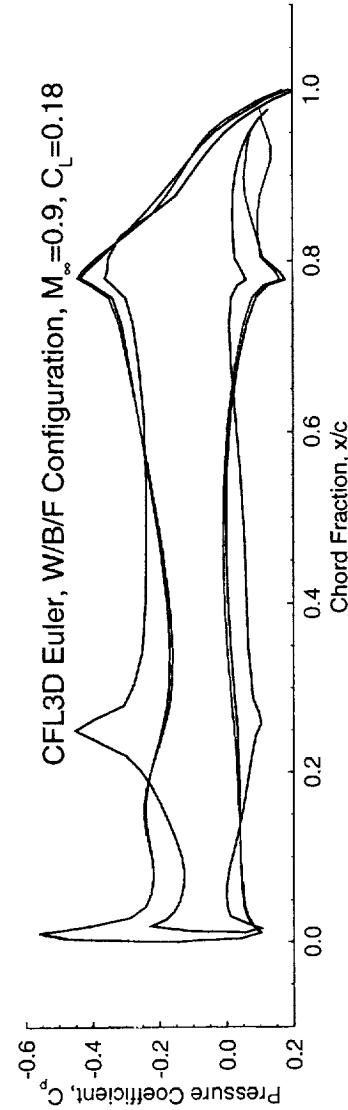
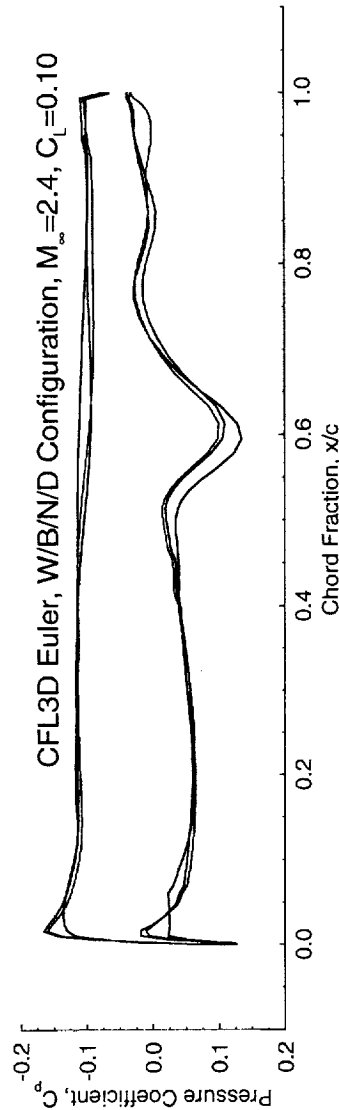
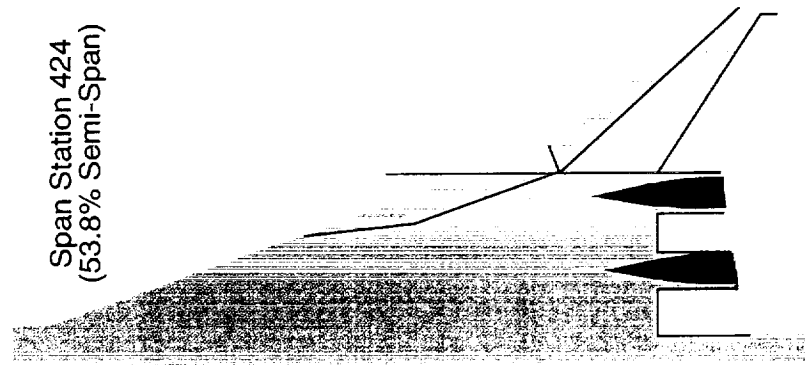
This page is intentionally left blank.

Comparison of Designs

High Speed Aerodynamics, Long Beach



Span Station 424
(53.8% Semi-Span)

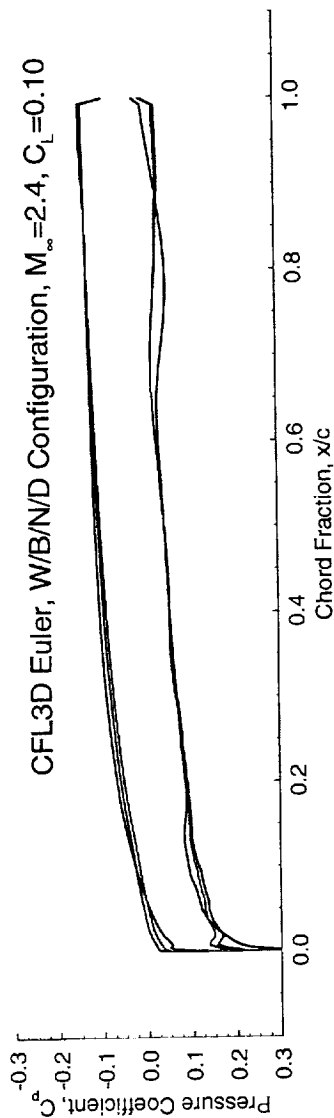
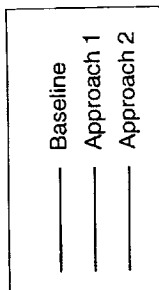
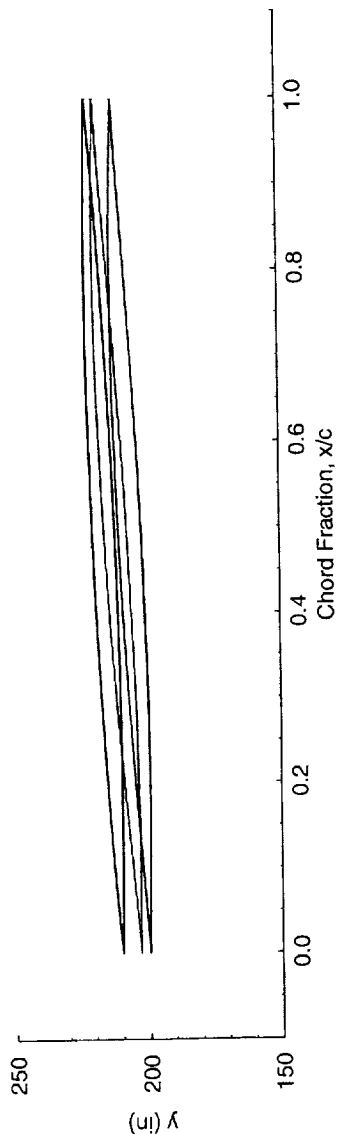
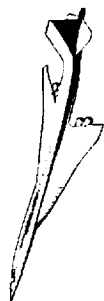


Comparison of Designs

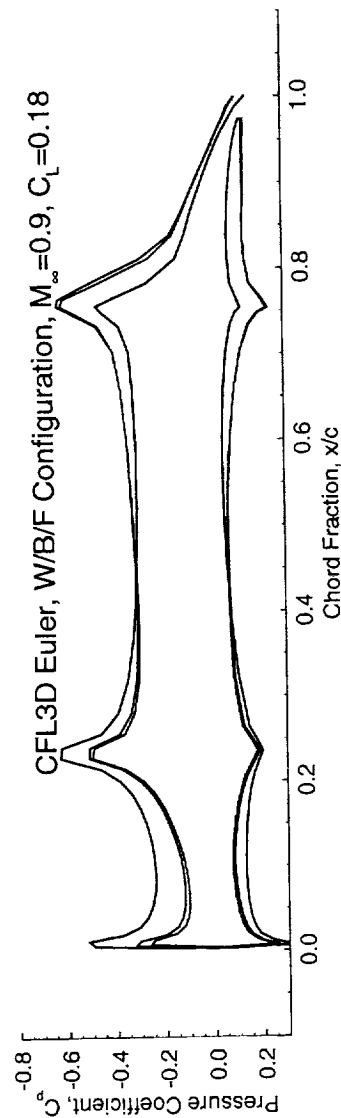
This page is intentionally left blank.

Comparison of Designs

High Speed Aerodynamics, Long Beach

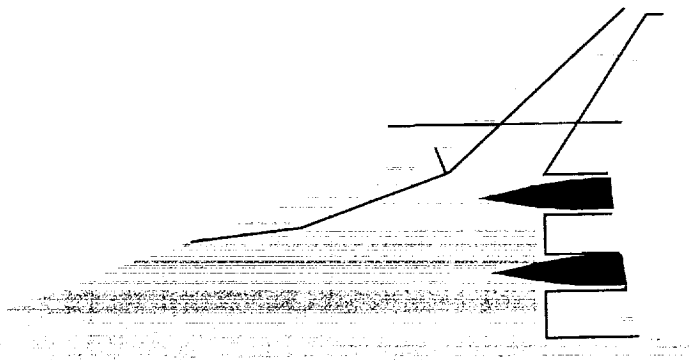


CFL3D Euler, W/B/N/D Configuration, $M_\infty=2.4$, $C_L=0.10$



CFL3D Euler, W/B/F Configuration, $M_\infty=0.9$, $C_L=0.18$

Span Station 535
(67.9% Semi-Span)

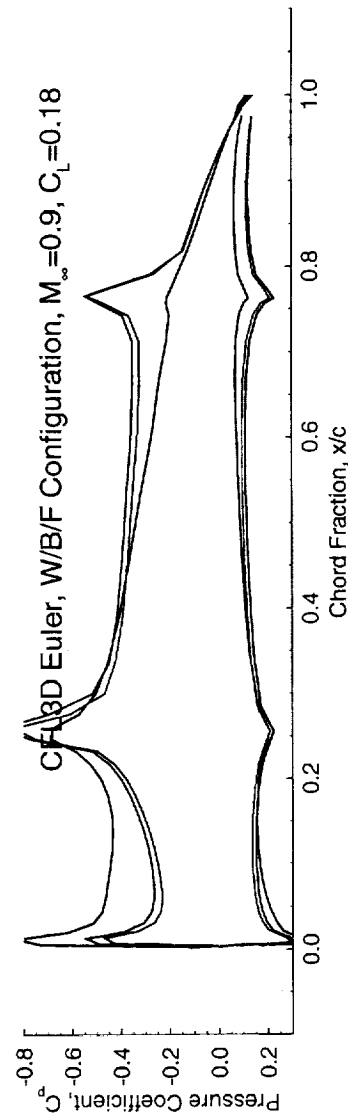
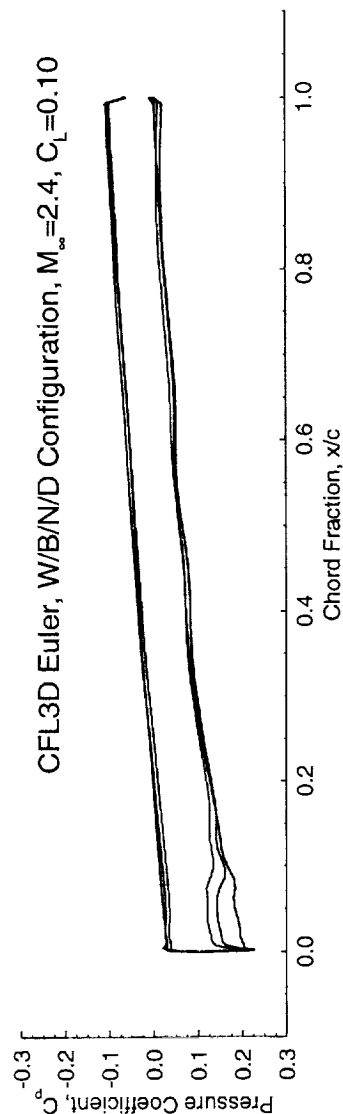
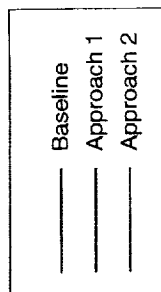
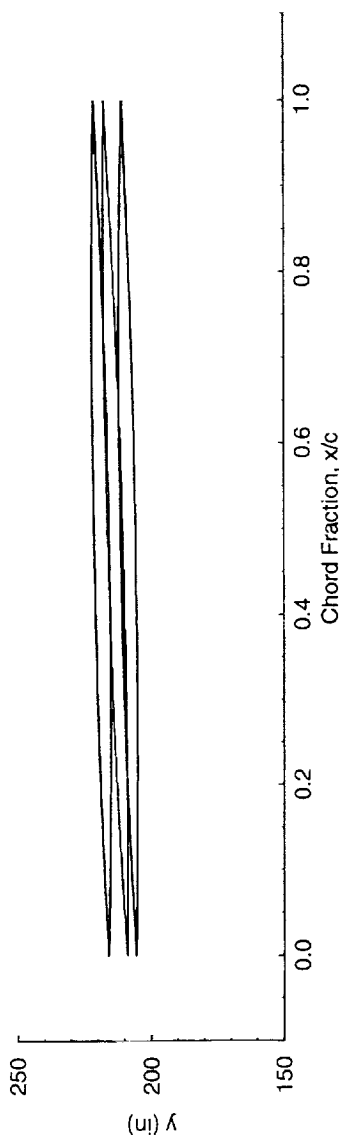


Comparison of Designs

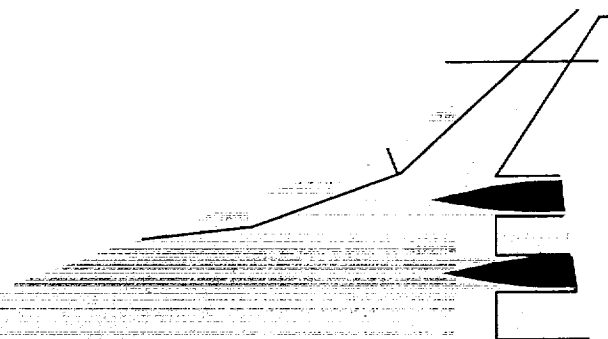
This page is intentionally left blank.

Comparison of Designs

High Speed Aerodynamics, Long Beach



Span Station 669
(85.0% Semi-Span)



Comparison of Designs

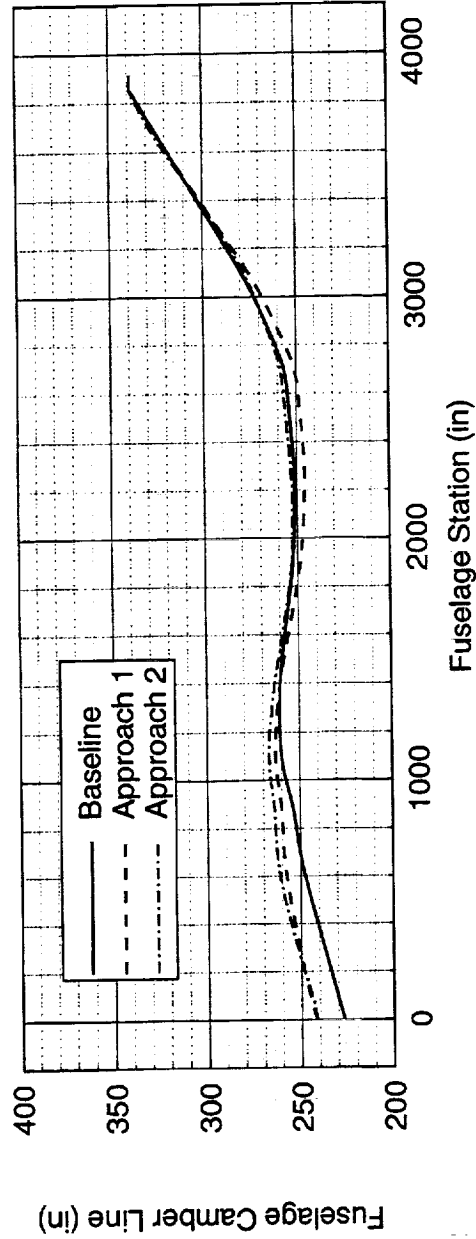
Shown below is the fuselage camber line and area distribution for the TCA baseline and multipoint designs.

Comparison of Designs

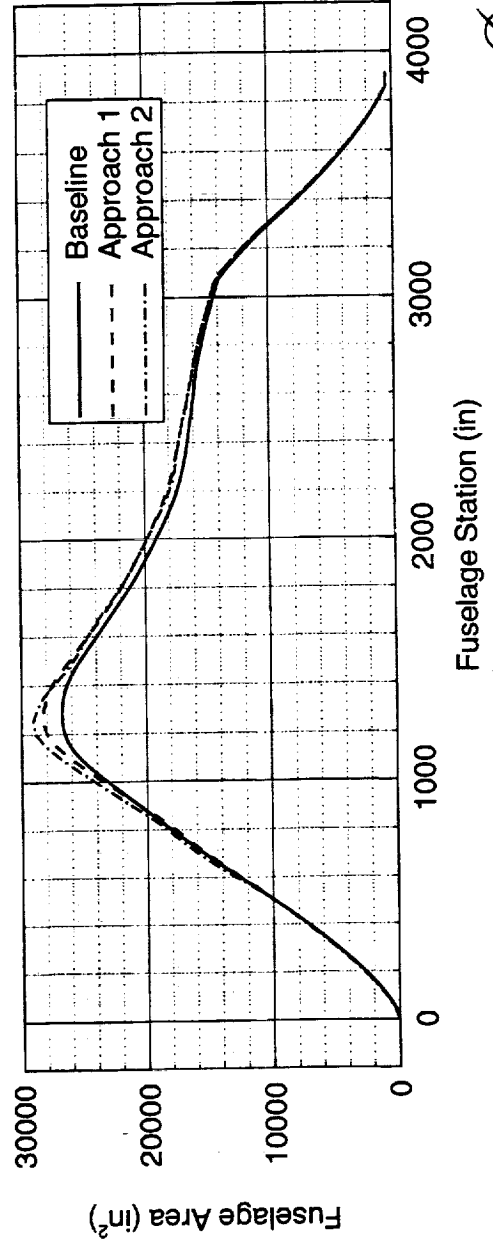
High Speed Aerodynamics, Long Beach



Fuselage Camber Distribution



Fuselage Area Distribution



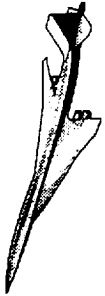
Conclusions

Two approaches to multipoint design have been investigated in this paper. The first involves a supersonic cruise point optimization, followed by a transonic flap optimization. The second integrates supersonic and transonic performance requirements into the wing twist, thickness, and camber, fuselage area, shape, and camber, and flap settings. Both methods were adopted into the AEROSHOP environment.

The first approach was applied using the BLB and Ames Cycle 2 supersonic cruise point designs. The second approach was applied starting from the BLB Cycle 2 design and improved this design at both the supersonic and transonic conditions. A comparisons of designs at the transonic cruise point show about a 4 count variation in drag level depending on the configuration shape.

The Ames Cycle 2 design and the multipoint design using Approach 2 have comparable multipoint performance characteristics. Based on Euler predictions, the Ames Cycle 2 design has about a 1.5 count advantage at $M_\infty=2.4$, while the Approach 2 design has a similar advantage at the transonic condition. Weighed appropriately the Ames Cycle 2 design has a slight edge, though Navier-Stokes assessments are needed to fairly compare the designs.

Conclusions



High Speed Aerodynamics, Long Beach

- Two approaches to multipoint optimization have been implemented and demonstrated in AEROSHOP
- Depending on the initial cruise shape, the transonic performance with optimum flap deflections varied by about 4 counts
- Simultaneously optimizing for supersonic and transonic cruise performance resulted in a smooth, conservative design with significant supersonic drag savings and little penalty at the transonic cruise condition

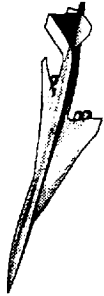
Areas of Future Work

A definitive assessment of the multipoint design requires Navier-Stokes flow analyses at the appropriate evaluation points. A Cycle 2 supersonic assessment has already been done, however not at the transonic cruise condition. Additionally, the multipoint design from Approach 2 has yet to be evaluated with Navier-Stokes analyses.

The multipoint design process is resource intensive in the way gradients are approximated. The current method of using finite-differences is inefficient even when restart solutions are used to start solutions of perturbations. Recent advancements in the adjoint formulation of TLNS3D has shown promising results for supersonic, single-block cases. Once the method is enhanced to include multi-block and transonic cases, significant savings in process turn-around can be expected.

A final area of process improvement is to replace the W/B/F modeling at the transonic condition with W/B/N/D/F modeling. Though this increases the fidelity between the supersonic and transonic modeling, preliminary results from the optimized flap wind-tunnel test (NASA Langley Test 496) show similar drag increments between baseline and flap configurations for W/B and W/B/N/D models.

Areas of Future Work



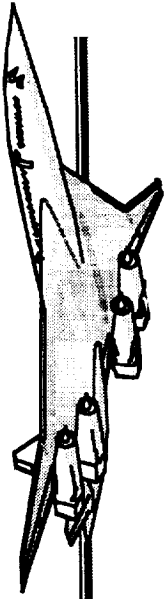
High Speed Aerodynamics, Long Beach

- Navier-Stokes assessments of Approach 1 and Approach 2 multipoint designs at all evaluation points
- Implement adjoint sensitivity method for computing the gradients during optimization
- Implement W/B/N/D/F configuration analyses during the transonic portion of the optimization process

This page is intentionally left blank.

HSR

High Speed Research



Configuration Aerodynamics ITD Team Year End Technical Review

February 9 - 11, 1998

Session 4: Nacelle/Diverter Design and Airplane Integration

Session Chairman: Francis Capone

Configuration Aerodynamics Technology Development

Session 4: Nacelle/Diverter Design and Airplane Integration

Goals

Demonstrate Significant L/Dmax Gains

Objectives

Robust Analysis /
Testing Methods

Realistic Aerodynamic
Design Optimization

Efficient Engine /
Airframe Integration

Challenges

Validation

Viscous Effects

Multipoint Conditions

Power Effects

Approaches

Analytic Methods
and Applications

Design
Development

Test Programs
and Techniques

Program

Methods Down Select

Viscous Drag Prediction

Cruise Point Optimization

Multi-Point Optimization

S&C CFD Predictions

Nacelle / Diverter
Design Integration

Tech. Baseline
Development

Aero S&C
Development

WT Database

WT Data Corrections

High Rel No. Testing

PIE Test Program

Configuration Aerodynamics Technology Development

Nacelle/Diverter Design and Airplane Integration

Objectives:

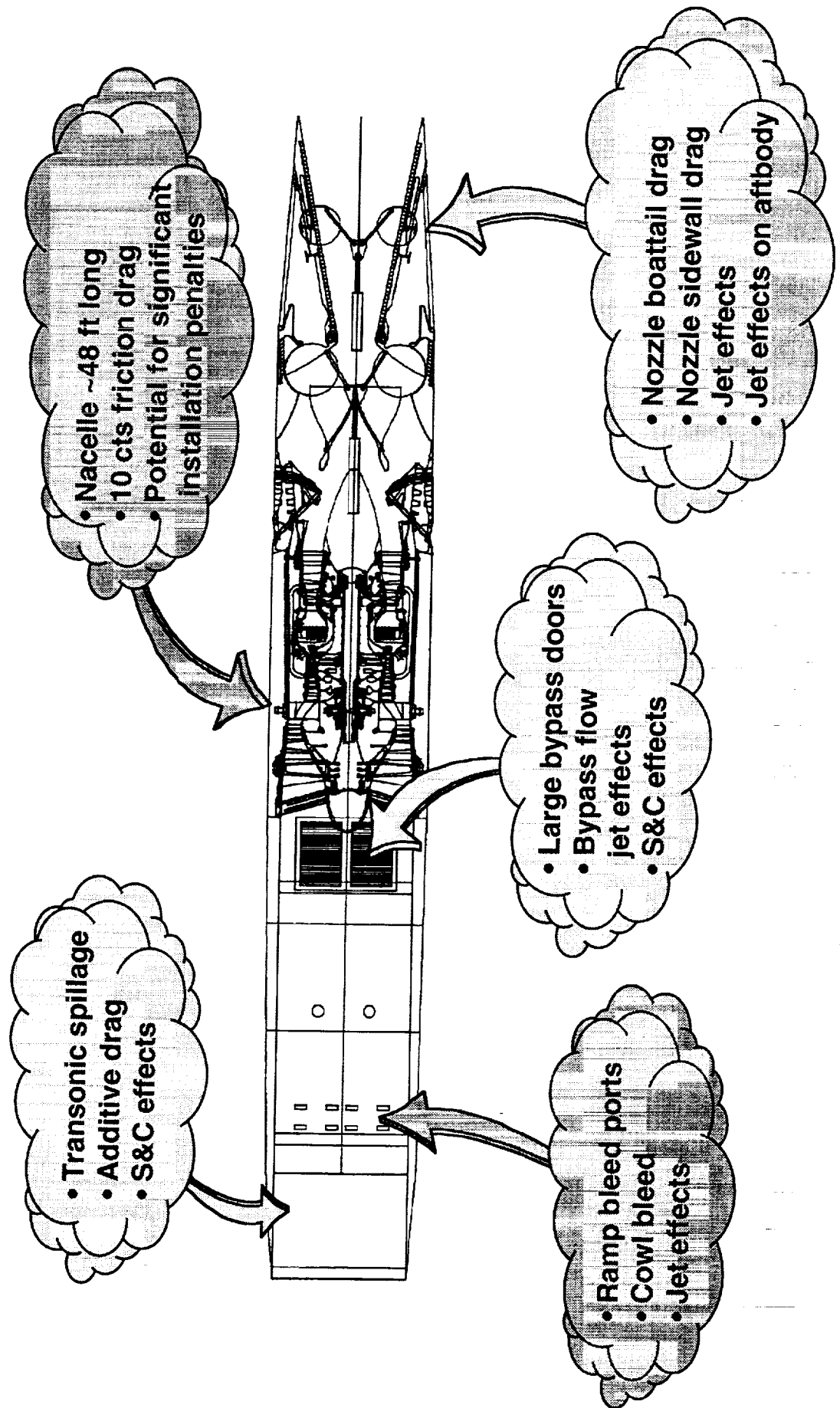
- Adapt, apply, validate and select nacelle design methods and codes based on their ability to improve the supersonic and transonic aerodynamic performance of HSCT aircraft configurations
- Develop methods for evaluating propulsion effects

Issues:

- Lots of issues

HSR Nacelle Installation Issues

Propulsion Induced Effects MUST be Beneficial to Meet L/D_{\max} Projections



Nacelle Airframe Integration Aerodynamic Performance HSR Task 32

**Rigid Power Effects 4.3.1.1.4
Final Review
February 1998**

1143

This page is intentionally left blank.

Northrop Grumman Team

Task Manager:

Charlie Peavey

CFD Analysis:

**Michael Malone
Bryan Westra
Arsenio Dimanlig**

Propulsion Integration:

Bill Bard

**Flight Sciences
Research and Technology Engineering
Military Aircraft Systems Division**

Rigid Power Effects (Inlet Bleed, Spillage, and Bypass) – Final Review

The 1997 Bleed Exhaust and Inlet Spillage Assessment study was initiated to develop an understanding of how the propulsion/inlet system affects the aerodynamic performance of the High Speed Civil Transport Technology Concept Airplane (TCA). Boeing subcontracted Northrop Grumman Corporation (NGC) to perform this analysis.

The objective of the task was to perform a parametric, viscous, CFD analysis to determine the effects of bleed exhaust and inlet spillage on the external aerodynamics of the TCA. The amount of bleed air exhaust is not significant in the transonic regime and was not included in the subsonic cruise ($M=0.9$) or transonic climbout ($M=1.2$) conditions where the spill effects dominate. Likewise, the inlet operates on design (i.e. shock-on-lip) at the supersonic cruise condition ($M=2.4$) without spillage, yet has significant bleed exhaust. Thus two separate investigations could be made. By analyzing the nacelles isolated and the TCA configuration with flow-through nacelles (wind tunnel configuration), a detailed drag build-up could be performed. The first section of this presentation details the bleed exhaust study and the following section discusses the effect of inlet spillage. There was no bypass flow for any of the cases in this study.

Objectives

- **Perform a Parametric, Viscous CFD Analysis on the Technology Concept Aircraft (TCA)**
- **Assess Inlet Spillage, and Bleed and Bypass Interference Effects**
 - Cowl and Centerbody Bleed at Supersonic Cruise ($M=2.4$)
 - Inlet Spillage at Transonic Cruise ($M=0.9$) and Climbout ($M=1.2$)
- **Provide Detailed Drag Buildup**

Rigid Power Effects (Inlet Bleed, Spillage, and Bypass) – Final Review

The Northrop Grumman in-house CFD code, GCNSfv, employing the one-equation Spalart-Allmaras turbulence model, was used for all of the analyses presented. While other turbulence models are available in GCNSfv the Spalart-Allmaras model was chosen to be consistent with the Boeing Company's CFD analysis using OVERFLOW and the Spalart-Allmaras model and to reduce computation time (about 10% compared to using a two-equation model).

The baseline TCA geometry was used in this study, including the axi-inlet/blunt-base nacelles. For the cases where a flow-through nacelle was analyzed, the constant area flow-through duct geometry was used. For the cases with inlet spillage, the actual inlet geometry was used up to the AIP (Aerodynamic Interface Plane) where a Mass Flow Ratio (MFR) boundary condition was used to set up the proper spill condition. The aft half of the flow through duct was used to set a similar nozzle exit condition to the flow-through cases.

In an analysis performed on the Ref. H wing/body (last years task) it was shown that the viscous drag predictions improved by using constant grid spacing off solid walls (first four cells). For this reason, four-cell constant spacing was used off of all solid surfaces.

A transpiration boundary condition was used to model the cowl bleed exhaust. The use of this B.C. was validated in a separate 2D analysis and is presented in detail later in the presentation.

The force and moment integrations were performed using FOMOCO, and the post-processing of the solutions were performed using FAST. Both codes were developed at the NASA-Ames Research Center.

Approach

- **Solver: GCNSfv on the NAS Cray C-90**
- **Turbulence Model: Spalart-Allmaras**
- **TCA Geometry, Axisymmetric Inlets with 2D Nozzle Nacelles, Inlet Spikes for Spill, Simplified Nacelle Cowl Bleed Model, NGC-Designed Center Body Bleed Ports per Boeing Specifications**
- **Incorporated 4 Constant Off-Body Cells in Grids**
- **Implemented Transpiration B.C. for Nacelle Cowl Bleed**
- **Post Processing: FOMOCO, FAST**

Rigid Power Effects (Inlet Bleed, Spillage, and Bypass) – Final Review

The CFD code used was GCNSfv developed by Northrop Grumman Corporation. It is based on the ARC3D thin-layer Navier-Stokes algorithm created at NASA Ames. The solution method is an implicit, node-based finite-volume scheme. Complex geometries are analyzed by using multi-block structured grids. The boundary conditions between blocks can be specified as patched class 1 through 4, where class 1 is point-to-point matching, class 2 is incremental point-to-point matching, class 3 is arbitrary face matching, and class 4 is arbitrary sub-face matching. A Chimera overlapping grid block option is also available. To speed convergence, grid sequencing and multigrid schemes can be used. GCNSfv provides four turbulence models to the user: Baldwin-Barth and Spalart-Allmaras one-equation models, Menter's $k-\omega$ SST 2-equation model, and Girmaji's Algebraic Reynolds Stress Model. GCNSfv offers a wide variety of boundary conditions including propulsion specific conditions such as characteristic inflow (mass flow ratio and corrected mass flow, inlet bleed) and outflow (nozzle pressure ratio, nozzle temperature ratio, transpiration) conditions. The code runs at approximately 12 μ s/iteration/grid-point on the Cray C-90 and parallelization allows the code to utilize six of the available sixteen processors allowing effective use of the multi-task batch queue.

Generalized Compressible Navier–Stokes Code

- **NASA Ames ARC3D Thin–Layer Navier–Stokes Algorithm**
- **Implicit, Node–Based Finite–Volume Scheme**
- **Multi–Block Structured Grids for Complex Geometries**
- **Class 1, 2, 3, & 4 Patched Block Interface Mappings**
- **Chimera Overlapping Grid Block Option**
- **Grid Sequencing & Multigrid Convergence Acceleration**
- **Menter’s $k-\omega$ SST 2–Equation, Spalart–Allmaras, 2–Equation Algebraic Reynolds Stress, & Baldwin–Barth Turbulence Models**
- **Extensive Boundary Condition Menu**

Rigid Power Effects (Inlet Bleed, Spillage, and Bypass) – Final Review

The following table shows the run matrix developed for the current study. All of these runs were at flight Reynolds number conditions. Runs 1–7 are part of the bleed assessment study. Runs 8–9 and 24–31 were initially assigned to include wind tunnel Reynolds number conditions, but were not run due to time constraints and slow throughput on the NAS Cray C–90. Runs 10–23 are concerned with the spill assessment study.

Each grid number corresponds to a particular nacelle configuration. For instance, the GRID 1 represents the baseline or flow-through nacelle configuration. The right twelve columns reflect the various components and/or modifications that are included in a particular nacelle geometry. A two-number grid number, such as GRID61, correspond to a full aircraft or full configuration geometry. The first number, 6, defines the type of nacelle used for the inbound nacelle; for this case, the inbound nacelle has an inlet spike, while the outboard nacelle is a baseline configuration.

Rigid Power Effects (Inlet Bleed, Spillage, and Bypass) – Final Review

Run Matrix

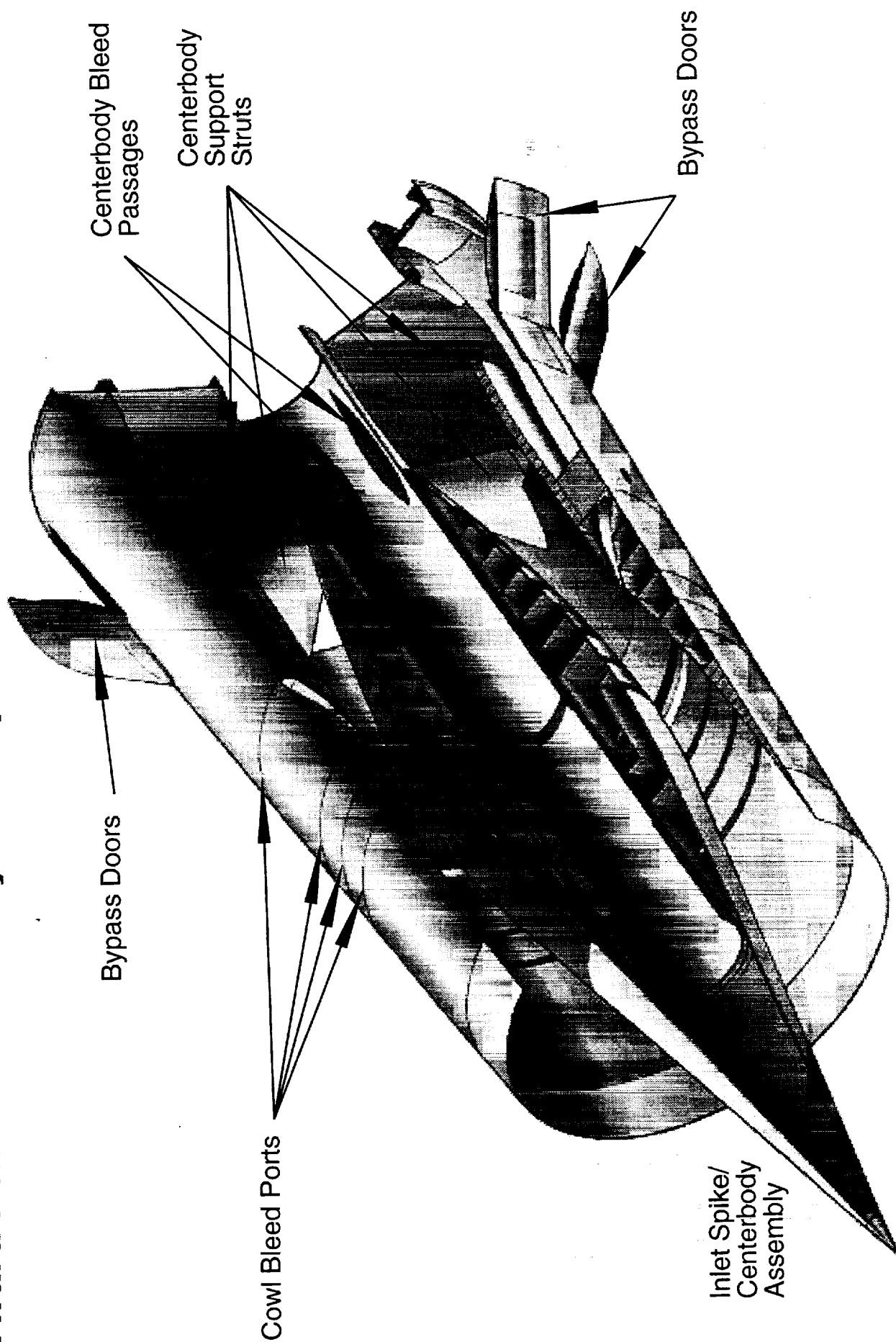
RUN #	GRID #	Mach		Isolated Nacelle					Full – Config. Inboard				Full – Config. Outboard			
		0.9	1.2	2.4	Inlet Spike	Flow-Through	Cowl Bleed	Centerbody Bleed Ports	Inlet Spike	Flow-Through	Cowl Bleed	Centerbody Bleed Ports	Inlet Spike	Flow-Through	Cowl Bleed	Centerbody Bleed Ports
1	1			✓		✓										
2	2			✓		✓	✓									
3	3			✓		✓		✓								
4	4			✓		✓		✓								
5	5			✓		✓	✓	✓								
6	11			✓						✓				✓		
7	55			✓						✓	✓	✓		✓	✓	✓
10	1	✓														
11	6	✓			✓											
12	7	✓			✓			✓								
13	1		✓			✓										
14	6		✓		✓											
15	7		✓		✓			✓								
16	11	✓								✓				✓		
17	61	✓							✓					✓		
18	16	✓								✓			✓			
19	66	✓							✓				✓			
20	11		✓							✓				✓		
21	61		✓						✓					✓		
22	16		✓							✓			✓			
23	66		✓						✓				✓			

Rigid Power Effects (Inlet Bleed, Spillage, and Bypass) – Final Review

Shown here is a cutaway view of the forward portion of the TCA axisymmetric nacelle configuration. Details revealed in this conceptual drawing include the boundary layer bleed zones on the translating centerbody and the internal cowl surfaces. These draw the boundary layer flow into plenums which in turn are vented to the external surfaces of the nacelle. The cowl bleed exhausts through a series of four circumferential slots on the external surfaces. The centerbody bleed is ducted through the centerbody supports to several large, cowed exit ports, not visible in this particular view. The large open doors are for inlet bypass flow, used only at particular flight conditions. The task objective was to quantify the effects of the bleed exhaust flows and the spillage from the inlet lip.

At the time this task began, extensive details of the exhaust exits were not defined. As will be seen, NGC created a slightly different model geometry, including the centerbody bleed exits.

Forward Nacelle Geometry Concept

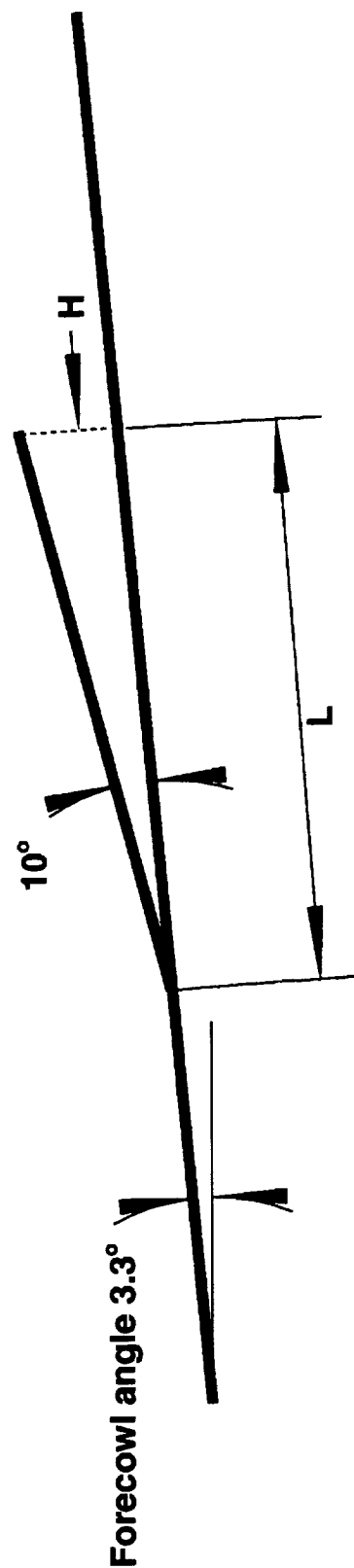


Rigid Power Effects (Inlet Bleed, Spillage, and Bypass) – Final Review

To improve main engine performance, boundary layer air is bled off the inlet cowl and the centerbody spike. This air is exhausted on the outside surfaces of the engine nacelle through a series of ports.

There are 4 rows of cowl bleed ports around the circumference of the nacelle. These ports discharge at a ten degree angle relative to the cowl mold line. The exit heights are inside the boundary layer with the first three ports 0.150" high and the fourth port at 0.290" high. The centerbody bleed exhaust ports are also oriented at a ten degree discharge angle, but consist of three 15-degree arc length sections. These sections are centered at the centerbody struts (since the centerbody bleed flow plumbing travels through the strut). Actual centerbody bleed port geometry will be shown later in this report.

Bleed Exhaust – Port Geometry



Cowl Ports

Port 1: $H=0.150"$. $X_{start}=112.1"$
Port 2: $H=0.150"$. $X_{start}=118.8"$
Port 3: $H=0.150"$. $X_{start}=125.7"$
Port 4: $H=0.290"$. $X_{start}=136.2"$

θ = Entire Circumference
(Outboard Diverter to Inboard Diverter)

Centerbody Ports

Port 5: $H=3.23"$. $X_{start}=169.2"$
Port 6: $H=1.57"$. $X_{start}=199.8"$

$\theta = 3 \times 15\text{deg. sections}$
($90\text{ deg.}, 180\text{ deg.}, 270\text{ deg.}$)

Rigid Power Effects (Inlet Bleed, Spillage, and Bypass) – Final Review

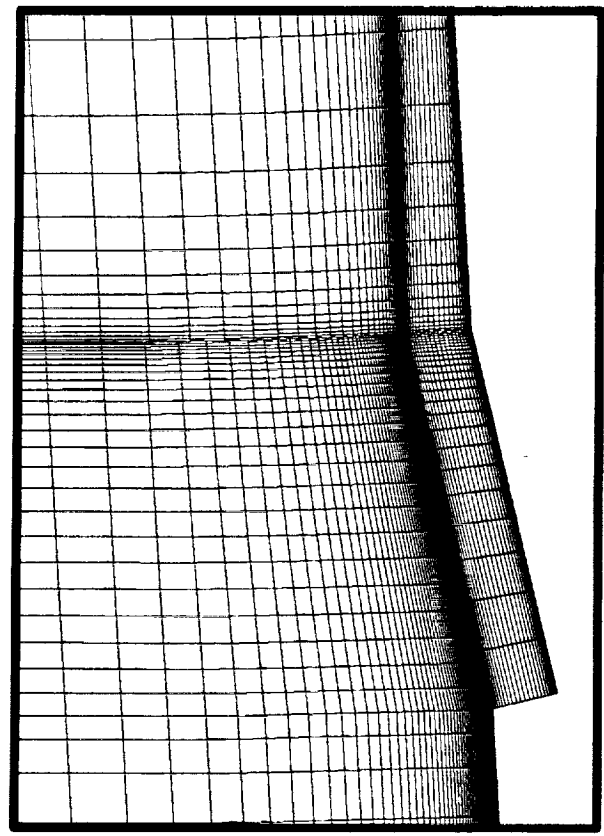
Due to the small size of the cowl bleed ports and the large number of grid points required to fully model the port geometry (plenum, ramp), a transpiration boundary condition was used to model the cowl bleed ports (ports 1–4). A 2D study, modeling the first three ports, was performed to validate the use of the transpiration B.C.

Three models for the cowl bleed ports were investigated: (1) the actual port geometry, including the ramp and plenum, (2) a single transpiration B.C. covering all three ports, and (3) three separate transpiration B.C.'s, one for each port. Shown here are close-ups of the two-dimensional grid topologies used for models 1 and 3. For the model 3 grid, the geometry of the port is overlaid for reference. Note the the finer grid required for model 1 to capture the viscous walls and shear layer. The calculated velocity from the transpiration B.C. is prescribed at the surface with the proper flow angle (10° from the surface) to give the same (equivalent) exit flow area as the port geometry. This is required to match the port mass flow rate.

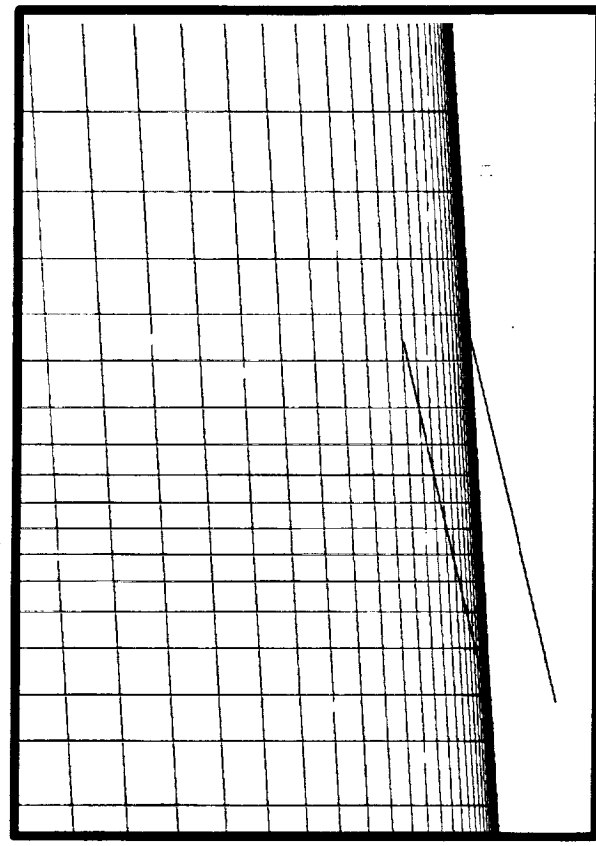
Rigid Power Effects (Inlet Bleed, Spillage, and Bypass) – Final Review

Bleed Exhaust – Port Modeling Study

Actual Port Model



Transpiration Model



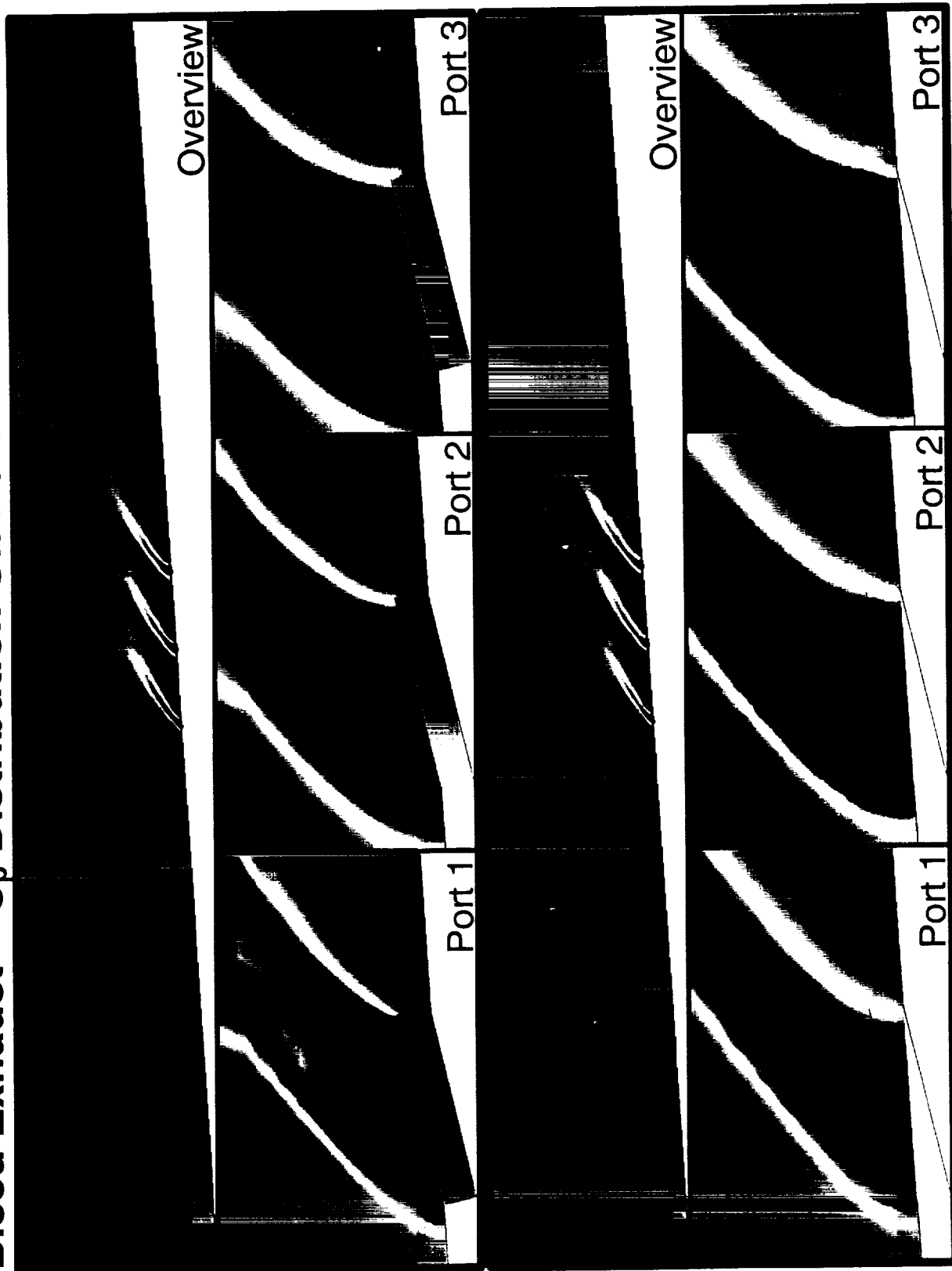
Rigid Power Effects (Inlet Bleed, Spillage, and Bypass) – Final Review

Boeing provided the plenum pressures for each of the cowl bleed ports on the nacelles. These specified plenum pressures, which increased from port 1 to port 3, were used for the boundary conditions in this part of the study.

The next figure shows the solutions obtained for port configurations 1 and 3. The overall Cp distributions look very similar. The close-ups compare each individual port and show remarkable similarities. The bow shock off the ramp is reproduced in the transpiration B.C. due to the flow exiting at the prescribed 10° angle. The surface pressures between the ports also compare well. Qualitatively the transpiration B.C. looks like an acceptable substitute.

Rigid Power Effects (Inlet Bleed, Spillage, and Bypass) – Final Review

Bleed Exhaust – C_p Distribution On Port Models



Rigid Power Effects (Inlet Bleed, Spillage, and Bypass) – Final Review

The next figure shows the wall pressure distribution plot on all three models. The peaks from all three ports look similar between the actual and multi-patch transpiration port models, while the single port model only has one long peak across all three ports. The single port model also suffers from a low pressure prediction downstream of the last port.

The pressure peak for the multi-patch model at the first individual port appears lower than the actual port model's result. Both solutions at the second port match closely. The multi-patch leading edge pressure peak at the third port is higher, but the shape of the rest of the solution looks similar. The extreme pressure lows from the actual port solution are due to the sharp turning of the flow as it exits the port. This cannot be reproduced with the transpiration B.C., but the peak is over such a small area that it will not affect the overall forces. The total mass flow

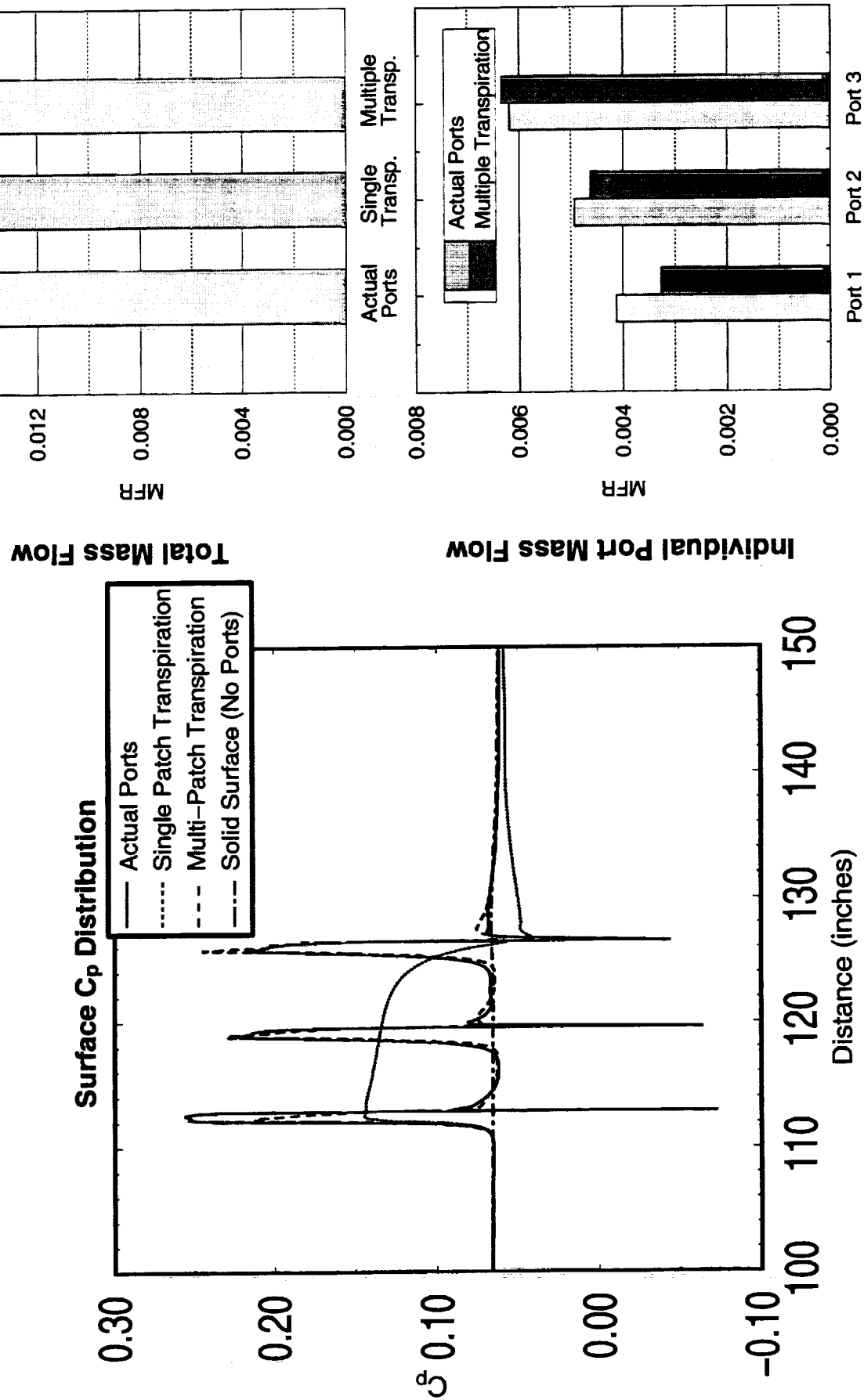
The total mass flow (as a ratio to the inlet mass flow rate) out of all the ports is also compared in the figure. The mass flow rate from the transpiration B.C. is within 6% of the actual port solution. Comparing individual port mass flow rates shows that the bulk of the error is from the first bleed port.

Overall, the results from the multiple transpiration B.C. were quite encouraging and were deemed an acceptable substitute to modeling each individual port.

Rigid Power Effects (Inlet Bleed, Spillage, and Bypass) – Final Review

Bleed Exhaust – Port Models Results

$M = 2.4$



Rigid Power Effects (Inlet Bleed, Spillage, and Bypass) – Final Review

Five different nacelle configurations were examined in the bleed study. For the isolated nacelle cases, all five geometries shown in the figure were considered. The GRID1 geometry or baseline geometry, which is used in RUN 1 is a flow-through ducted nacelle. The GRID2 geometry, used in RUN 2, consists of the four cowl bleed ports, modeled as transpiration boundary patches. GRID3 has non-flowing centerbody bleed ports so the interior nozzle blocks are excluded from the grid. It is used in RUN 3. The GRID4 geometry, which is similar to the GRID3 geometry, has flowing centerbody bleed ports. This grid is applied in RUN 4. Finally, the GRID5 geometry, which has both the cowl bleed ports and flowing centerbody bleed ports are used in RUN 5.

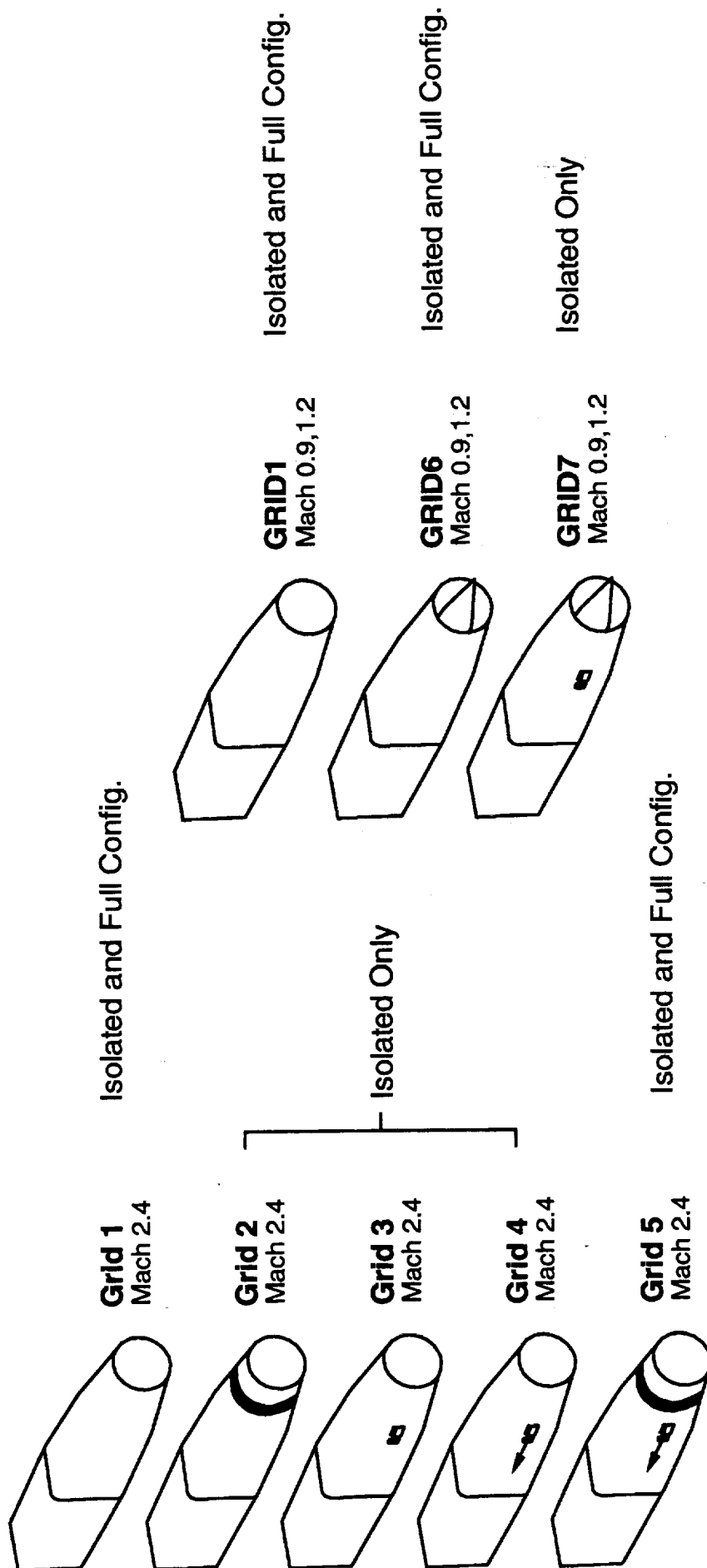
For the full configuration, flight Reynolds number cases, only two of the nacelle configurations were considered. The GRID1 geometry, used on both inboard and outboard nacelles, combined to form the GRID11 or baseline geometry. This was used in RUN 6. The GRID55 geometry, both nacelles using the GRID5 nacelle geometry, was used in RUN 7.

Three nacelle geometries were examined for various inlet spillage cases. For the isolated nacelle cases, all three geometries shown in the figure were considered. The GRID1 geometry or baseline nacelle geometry, which is used in RUN 10 and RUN 13, is a flow-through nacelle. The GRID6 geometry, used in RUN 11 and RUN 14, consists of an inlet spike and an aft duct. The GRID7 geometry, which is similar to the GRID6 geometry, also has the same non-flowing centerbody bleed ports seen previously in the bleed section of this study. This grid is applied in RUN 12 and RUN 15.

For the full configuration, flight Reynolds number cases, four different combinations of the first two isolated nacelle geometries are implemented. GRID11, the baseline geometry, has flow-through nacelles for both inboard and outboard nacelles. This grid is used in RUN 16 and RUN 20. GRID61's inboard nacelle has an inlet spike and a flow-through outboard nacelle (used in RUN 17 and RUN 21), while GRID16 is vice versa (RUN 18 and RUN 22). Both nacelles have inlet spikes in GRID66. This grid is used in both RUN 19 and RUN 23.

Rigid Power Effects (Inlet Bleed, Spillage, and Bypass) – Final Review

Nacelle Geometry



Key:	Cowl Bleed Ports	Centerbody Port Geometry	Centerbody Ports Flowing	Centerbody/ Spike Geometry

Rigid Power Effects (Inlet Bleed, Spillage, and Bypass) – Final Review

Shown here is the overlapping grid topology used for the GRID55 geometry. The centerbody bleed port grids are situated within the second nacelle section (yellow grids). The cowl bleed ports, modeled with grid clustering for the transpiration boundary condition, are in the nacelle forward section (red grids).

For the full configuration, as seen here, the first three nacelle blocks (red, yellow, and magenta) have C-mesh topologies, where both ends map onto the lower surface of the wing. The fourth block (green) is an O-mesh topology. The duct (cyan) is a slit-O-mesh, where instead of a pole the face is folded over itself.

There are five standard blocks used for the wing-body. The third and fourth nacelle blocks (magenta and green), the nozzle block (not shown), and the fairing that connects the top surfaces of both nacelles and the wing (not shown) are standard blocks as well. The flow-through duct blocks (cyan) were not changed either. Hence, a total of 15 blocks used from the previous year's study were unchanged. The first outer nacelle block (red) was varied according to the required configuration. The old block was used if the cowl bleed ports were not included. The second block (yellow) had to be redone from last year by increasing the number of grid points to allow proper communication with the centerbody bleed ports. The same block was used still, even if the ports were not included.

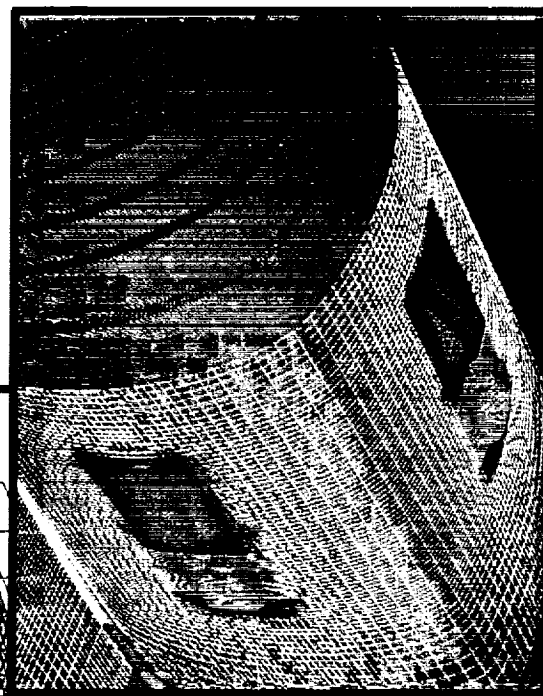
Here, the grid topology for the centerbody bleed ports (5 and 6) and cowl bleed ports (1-4) are shown. The same topology is applied for both isolated and full configuration geometries. This topology is similar to the one used for the actual port model from the port model study. Each centerbody bleed port requires three grids: the outer block (orange and green), the nozzle block (interior, not shown), and the exhaust block (blue). A part of the forward face (xmin face) of each exhaust block maps onto a corresponding nozzle block's aft face (xmax face), the rest of the face maps onto a corresponding outer block's aft face (orange or green). The secondary outer nacelle block (yellow) is clustered appropriately to accommodate each set of centerbody bleed ports. Each set of two centerbody bleed ports require 516,464 points. With six sets required for both nacelles, the total number of points required for the full configuration becomes 3,098,784. The final grid consisted of 55 blocks and approximately 11 million grid points.

Rigid Power Effects (Inlet Bleed, Spillage, and Bypass) – Final Review

Bleed Exhaust – Grid Topology



**55 Blocks
11M Grid Points
Chimera/Patched**



NORTHROP GRUMMAN

Rigid Power Effects (Inlet Bleed, Spillage, and Bypass) – Final Review

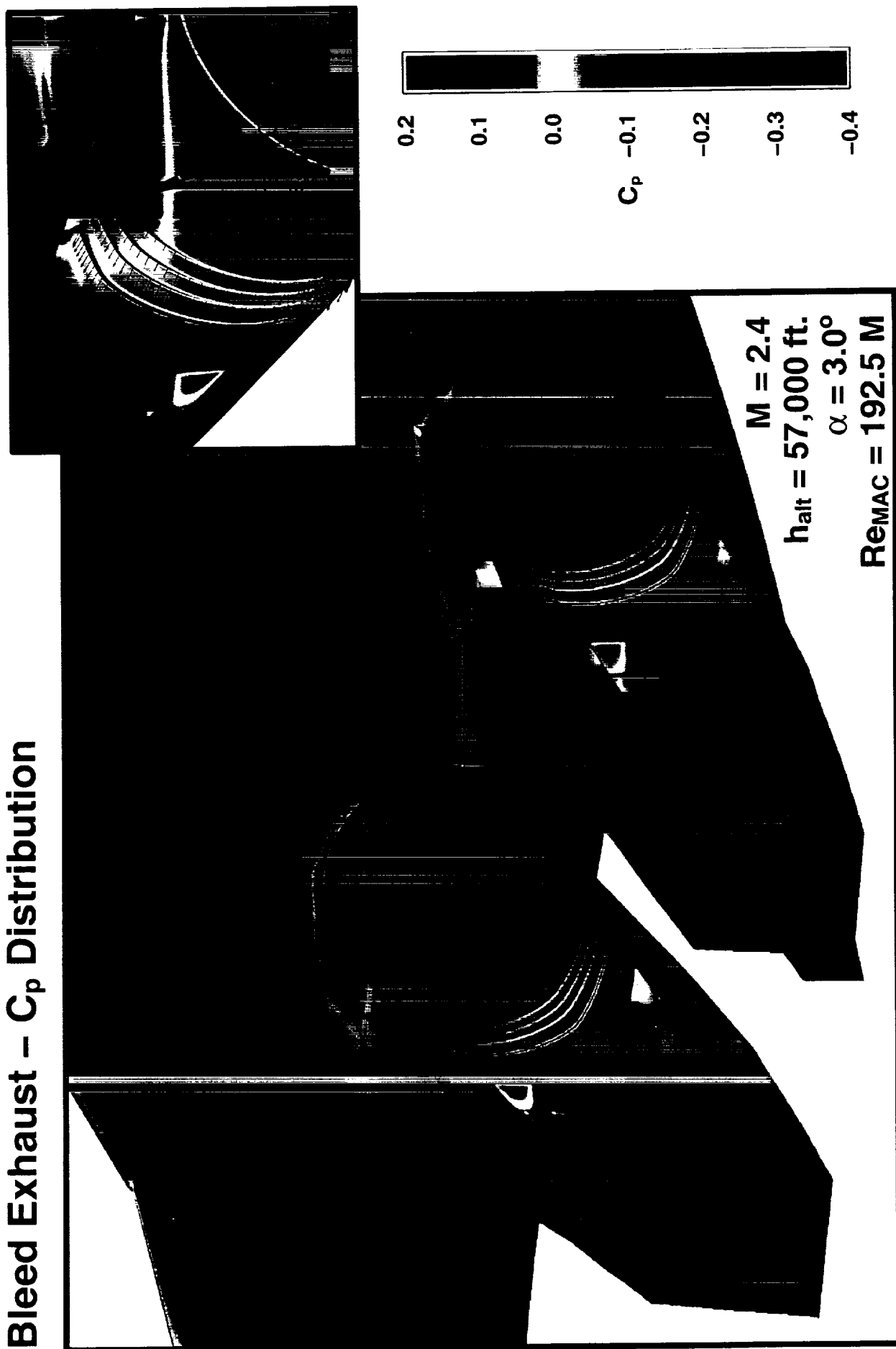
The surface pressure distribution for the GRID55 (RUN 7) solution is shown from a view point looking up at the nacelles from under the right wing. The transition to the supersonic outboard wing panel and fuselage are also visible. The high pressure due to the bow shock off of the diverter can be seen on the nacelle and wing lower surface. Also note the high pressure band on the wing lower surface due to the cowl bleed ports. The is most evident near the outboard nacelle due to the closer proximity to the lower wing surface. The area of the cowl bleed ports can be seen on the nacelle surface as the high pressure stripes, most notably port 4 which has a larger area and higher plenum pressure (and resulting mass flow rate) than ports 1–3.

The inset figure is a closeup of the inboard nacelle with part of the wing surface removed in order to see the upper surface of the nacelle. Velocity vectors from the cowl bleed ports are plotted showing that the high pressure behind the diverter shock causes the first cowl bleed port to backflow. This could be alleviated by limiting the circumference of the first cowl bleed port.

This case required approximately 450 MW of memory on the NAS Cray C-90. The maximum allowable job size for the multi-task batch queue on the C-90 is 256 MW. In order to run in this queue, GCNSfv was modified to include the option of an out-of-core solver, writing some data to disk to save memory. The fast IO (\$FASTDIR) was used to keep IO time to a minimum and reduce wallclock time for job completion. Each run required approximately 40 CPU hours to run.

Rigid Power Effects (Inlet Bleed, Spillage, and Bypass) – Final Review

Bleed Exhaust – C_p Distribution



Rigid Power Effects (Inlet Bleed, Spillage, and Bypass) – Final Review

Total lift and drag are compared between the RUN 6 (GRID11, baseline) and RUN 7 (GRID55) cases. Each of the nacelles in GRID55 utilizes the GRID5 nacelle geometry, which includes all three sets of the centerbody bleed ports and four bleed cowls for each nacelle.

The total forces, which includes the pressure, viscous, and momentum forces, were calculated over all the external surfaces of the aircraft. Only the internal duct and the flat nozzle base are excluded from the force integration.

The plot shows that both lift and drag improved for the GRID55 geometry over baseline. Drag alone improved by about 4.5 counts; lift by 1.5. Naturally, these improvements are attributed to the momentum forces exerted by all the bleed ports. Recall from the isolated nacelle study, that the drag decreased by about 1.5 counts between the GRID5 and GRID1 geometry. By superposition, with four nacelles, drag should decrease by 6 counts, which is just about the same effect seen in the GRID55 case.

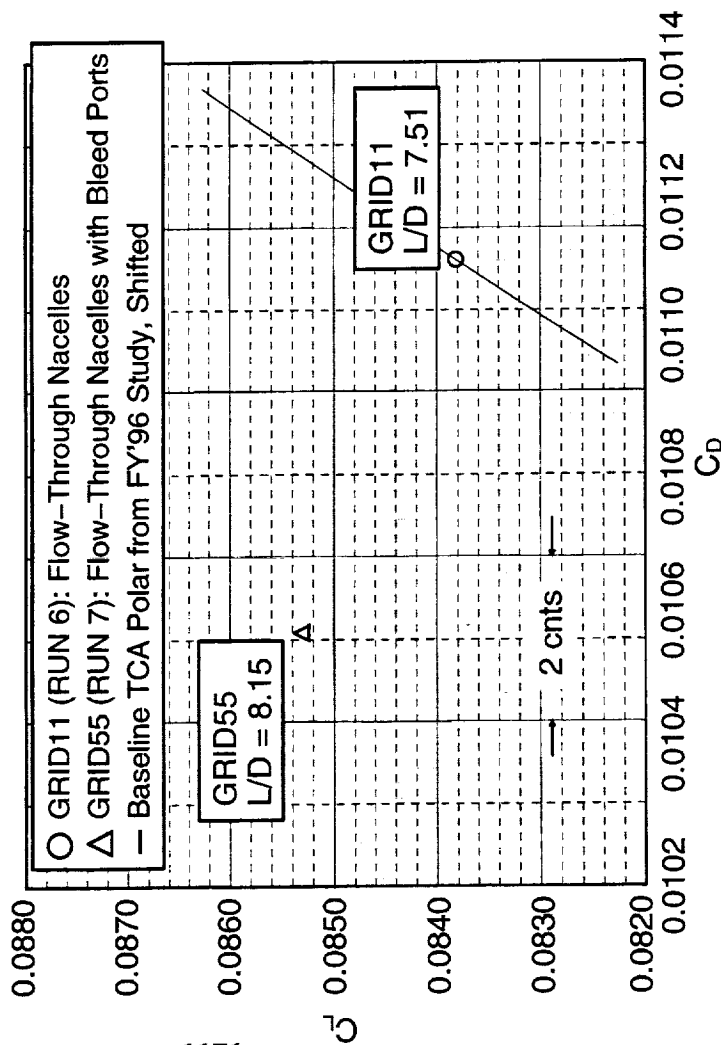
The lift increase of about 1.4 counts can similarly be accounted for due to the bleed ports. It is easy to assume immediately that the momentum generated by the bottom centerbody bleed ports from both nacelles, each having a downward component, created the additional lift. The momentum from the bottom half of the cowl bleed ports from each nacelle also has a downward component that could add to the lift. However, as seen in the isolated nacelle cases, lift changes were negligible between geometries. Further, it will be shown later that the cowl bleed ports' interaction with the wing is its one way of adding lift to the total.

The next set of graphs compares the total lift and drag for each nacelle. For the isolated nacelle cases, the drag was evidently reduced by about 0.75 count due to the bleed forces. About the same (1 count) effect is seen between the GRID11 and GRID55 inbound and outboard nacelles.

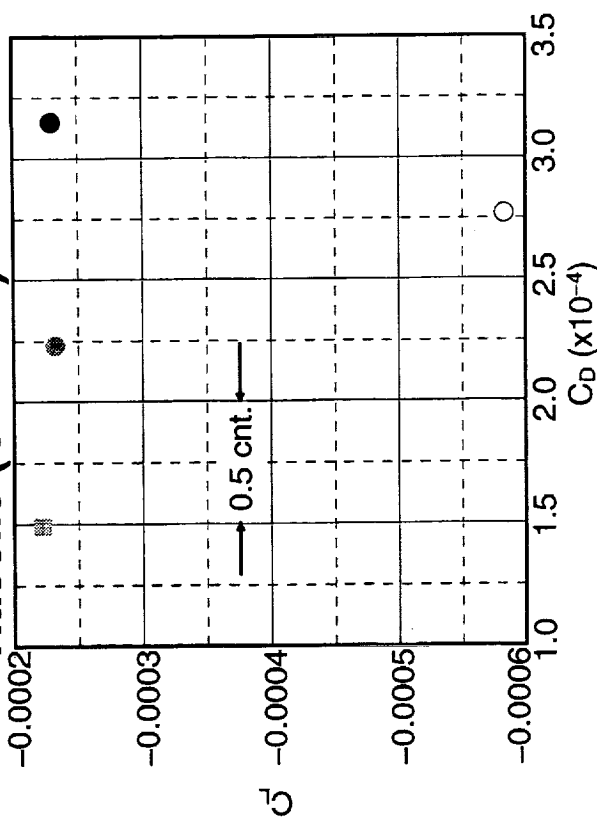
Additionally, both configurations show lower lift and drag for the inbound nacelle than the outboard nacelle. Due to the proximity of the installed nacelles to the leading edge of the wing, the outboard nacelle has similar lift and drag to the isolated nacelle. The inbound nacelle has larger negative lift due to its relative negative angle of attack when installed under the wing.

Bleed Exhaust – Lift and Drag

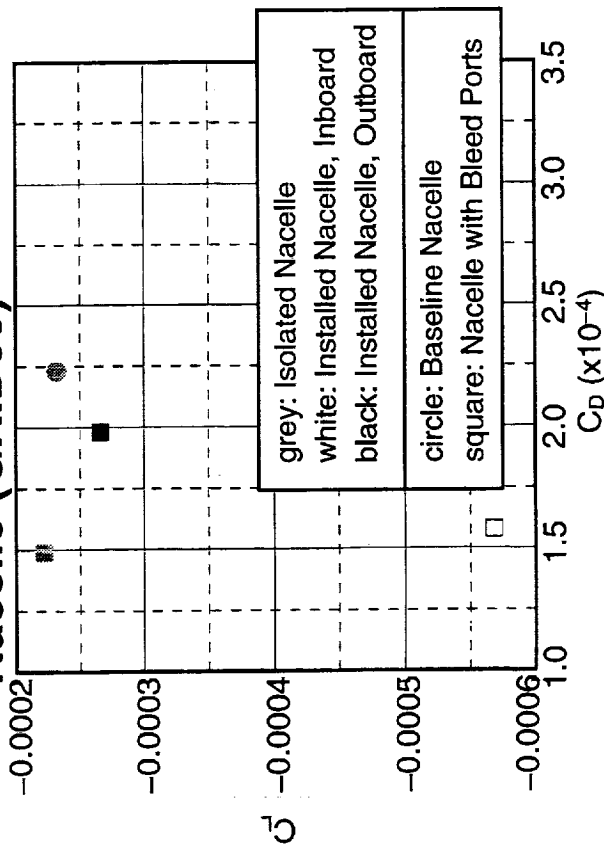
Full Configuration



Nacelle (GRID11)



Nacelle (GRID55)



Flow-Through Duct Forces and Base Area Excluded

Rigid Power Effects (Inlet Bleed, Spillage, and Bypass) – Final Review

The mass flux distribution plot for the RUN 5 (GRID5, isolated nacelle) case is compared with similar plots for the inbound and outbound nacelles of RUN7 (GRID55)

Upon examination, note how the mass flux distribution at the first three bleed cowls for both inbound and outbound nacelles drop at both ends, unlike those shown for the GRID5 case. Especially at port one, there is even negative flux at both ends for both nacelles, and a slight negative flux on the inbound side of the outbound nacelle's second port. This indicates back flow at these areas of the cowl ports, close to the diverter. A high pressure region exists close to the diverter, which is caused by a shock emanating from the diverter's leading edge. The isolated nacelle does not have a diverter so no high pressure regions are generated around its cowls' ends, resulting in an almost linear distribution.

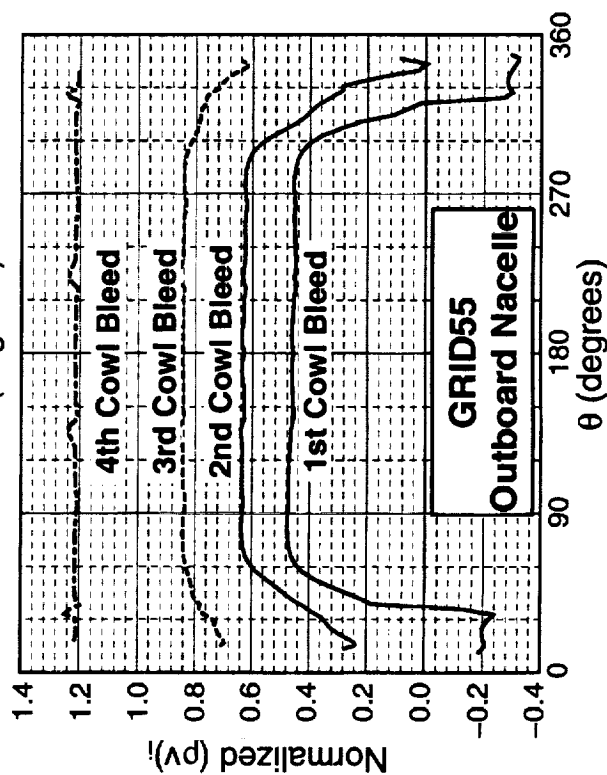
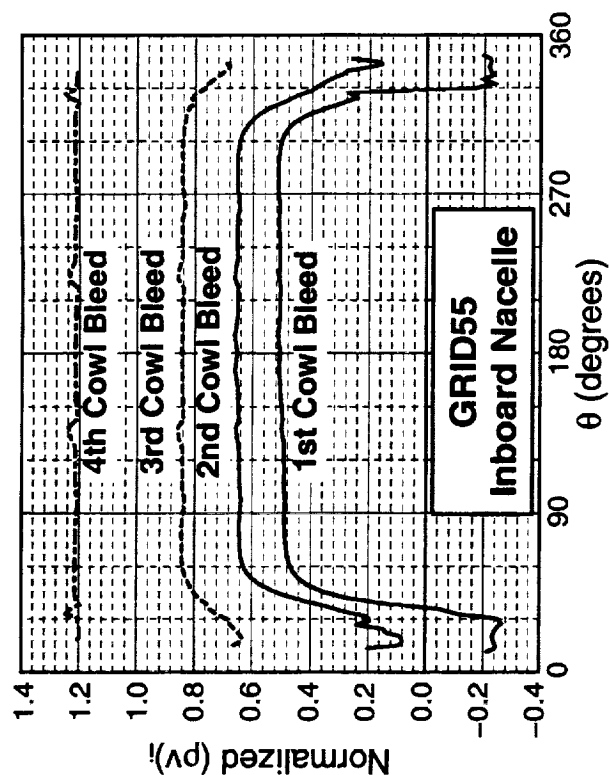
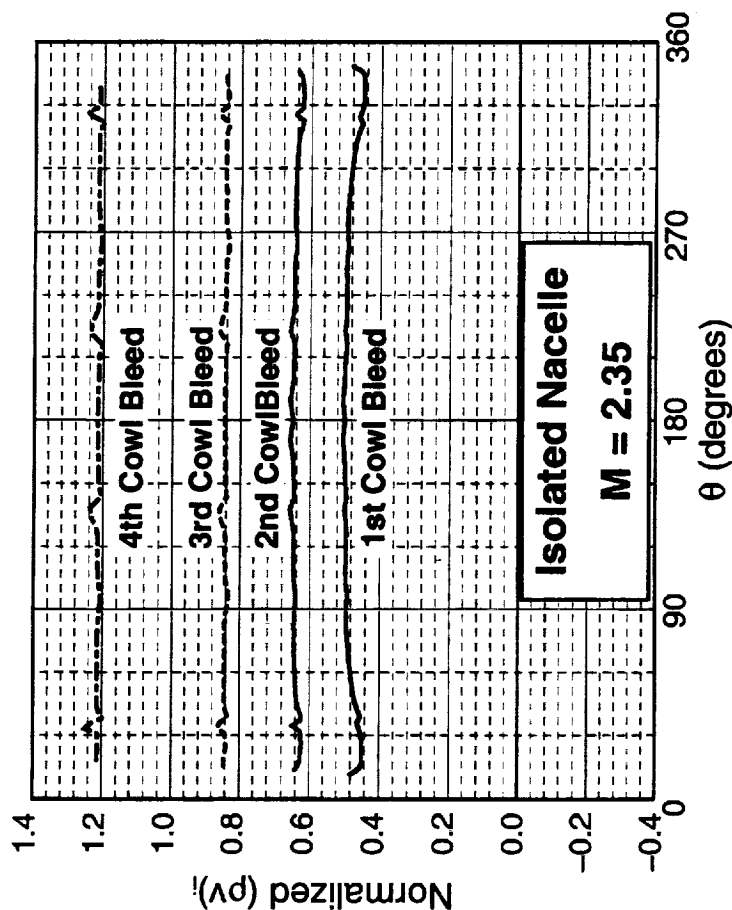
At some point, the high pressure region weakens such that at port four, both inbound and outbound nacelles match the GRID5 solution.

Rigid Power Effects (Inlet Bleed, Spillage, and Bypass) – Final Review

Bleed Exhaust – Mass Flux on Cowl Bleeds

GRID55, RUN 7

M = 2.4



NORTHROP GRUMMAN

Rigid Power Effects (Inlet Bleed, Spillage, and Bypass) – Final Review

The following figure illustrates the topology applied to the GRID66 geometry. The wing-body blocks are the same ones used from the bleed exhaust study. The blocks that define the middle and aft part of each nacelle (yellow, magenta, and green), along with the fairing block above the wing and nacelle and the nozzle base block (both not shown) are unchanged too. The flow-through duct and forward outer nacelle block (red) used for the GRID11, GRID61, and GRID16 geometries are the same blocks used in the bleed exhaust study (GRID11).

With the introduction of the inlet spike (cyan), the forward outer nacelle block (red) is stretched further forward to match the inlet spike block's length. The inlet spike block is an O-mesh topology, while the outer nacelle block is of a C-mesh topology. Both blocks' length and the clustering required at the tip of the nacelle spike are reasons why 790,347 points more are required for each nacelle.

The geometry for all four full configuration cases are shown in the inset figures. The grid topology for the inlet spike geometry are the same between inboard and outboard nacelles. The same is true for the flow-through nacelles.

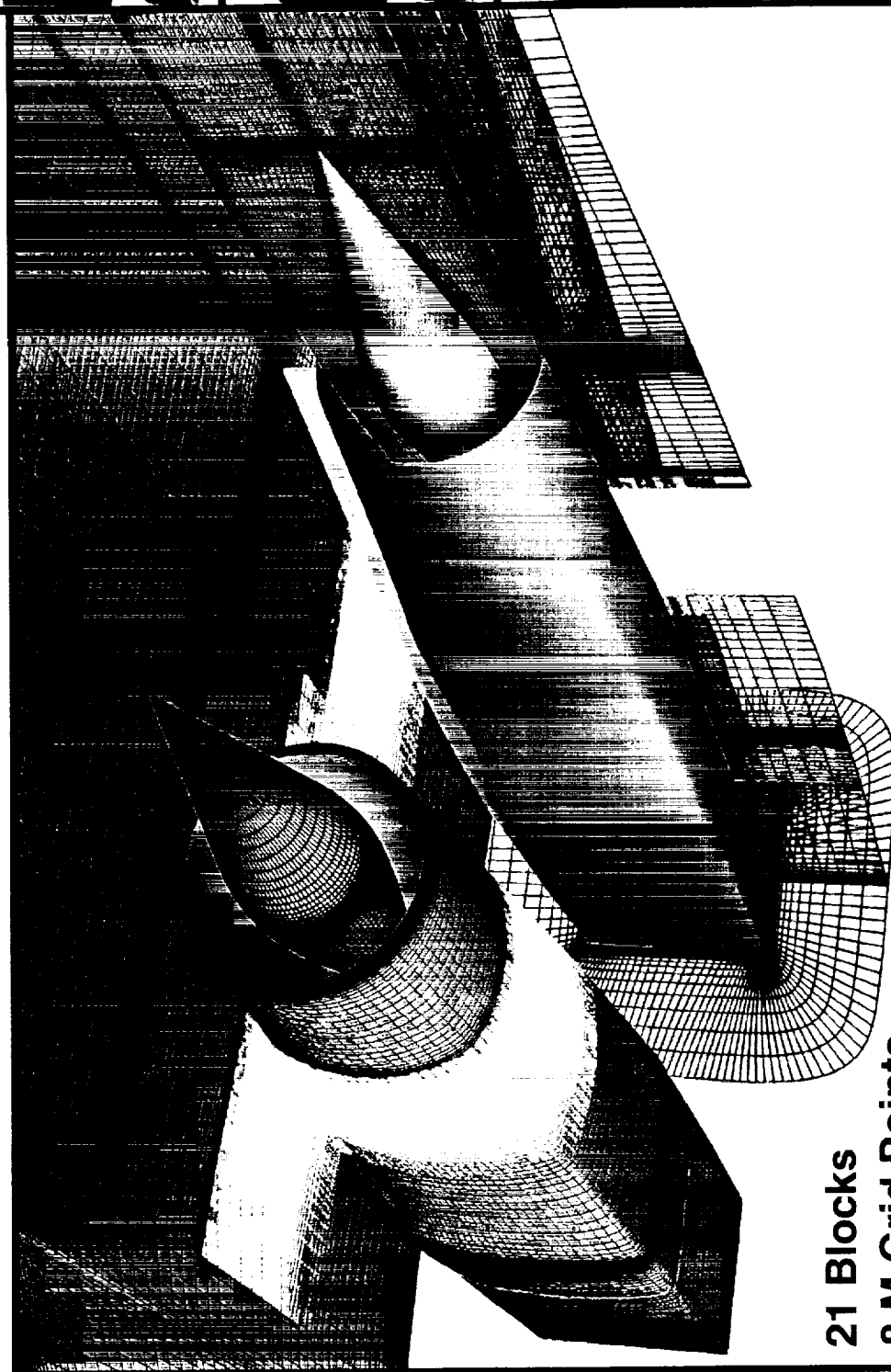
GRID11, or the baseline grid, has flow-through nacelles. In GRID61, the inboard nacelle has an inlet spike. The outboard nacelle has an inlet spike in GRID16. GRID66 has inlet spikes on both nacelles.

Note from the grid point totals that the addition of a spike adds 790,347 points to each nacelle grid. The complexity of the spike geometry naturally results in the addition of points due to clustering at critical areas such as the inlet spike tip and the inlet lip.

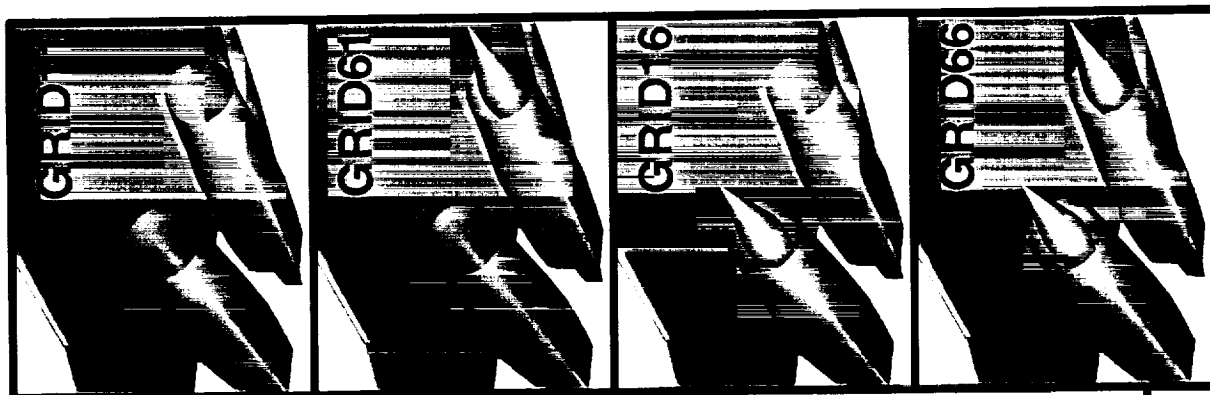
The final grid shown consisted of 21 blocks and approximately 8 million grid points.

Rigid Power Effects (Inlet Bleed, Spillage, and Bypass) – Final Review

Inlet Spillage – Grid Topology



**21 Blocks
8 M Grid Points
Chimera/Patched**



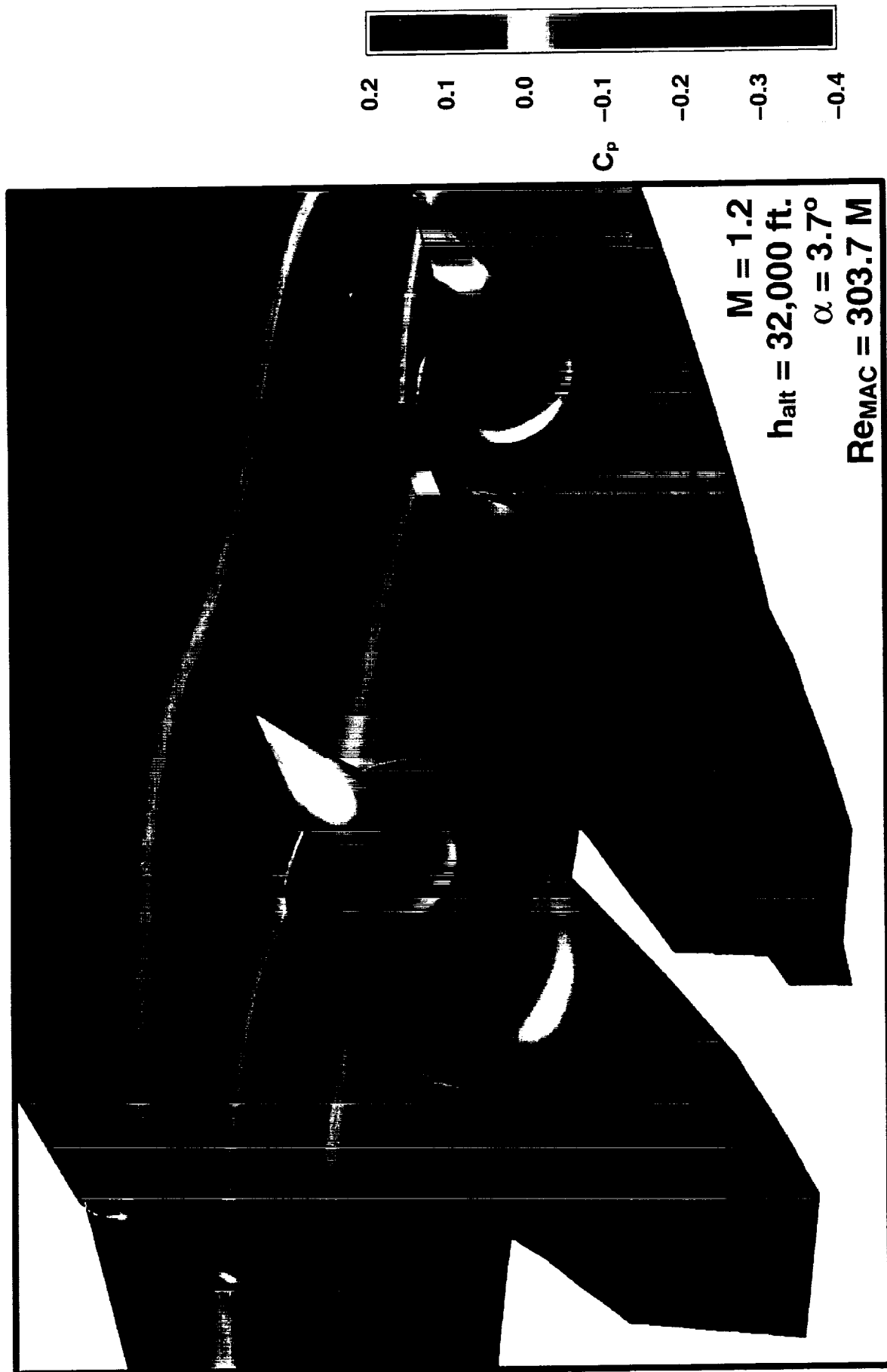
Rigid Power Effects (Inlet Bleed, Spillage, and Bypass) – Final Review

The solution for the GRID66 configuration is shown for RUN23 ($M=1.2$, $h=32,000$ ft, $Re=303.7 \times 10^6$, $a=3.7^\circ$). The surface is colored by pressure coefficient (C_p). The contours show the high pressure behind the shock off of the spikes hitting the wing lower surface. Both engines are operating at a MFR of 0.654 and the spill flow is evident by the dark blue (low C_p) regions near the cowl. Note that the spill patterns for the inboard and outboard nacelle are different due to their orientation to the flow. Also note that due to the wing presence the nacelles are forced to spill down, unlike the isolated nacelles which had a more uniform spill pattern. The surface contours on the centerbodies show the normal shock that develops at the inlet lip. The channeling of the flow between the nacelles results in the low pressure region between the nacelles.

This run required approximately 330 Mwords of memory on the Cray C-90 and anywhere from 40 CPU hours (for the $M=1.2$ cases) to 100 CPU hours (for the $M=0.9$ cases). Again the out-of-core solver in GCNSfv was used to keep the main memory requirement below 256 Mwords. The transonic ($M=0.9$) cases were difficult to converge to steady state, requiring significantly more iterations than the supersonic cases. Care was taken to ensure that the deltas between the $M=0.9$ cases were converged.

Rigid Power Effects (Inlet Bleed, Spillage, and Bypass) – Final Review

Inlet Spillage – C_p Distribution



Rigid Power Effects (Inlet Bleed, Spillage, and Bypass) – Final Review

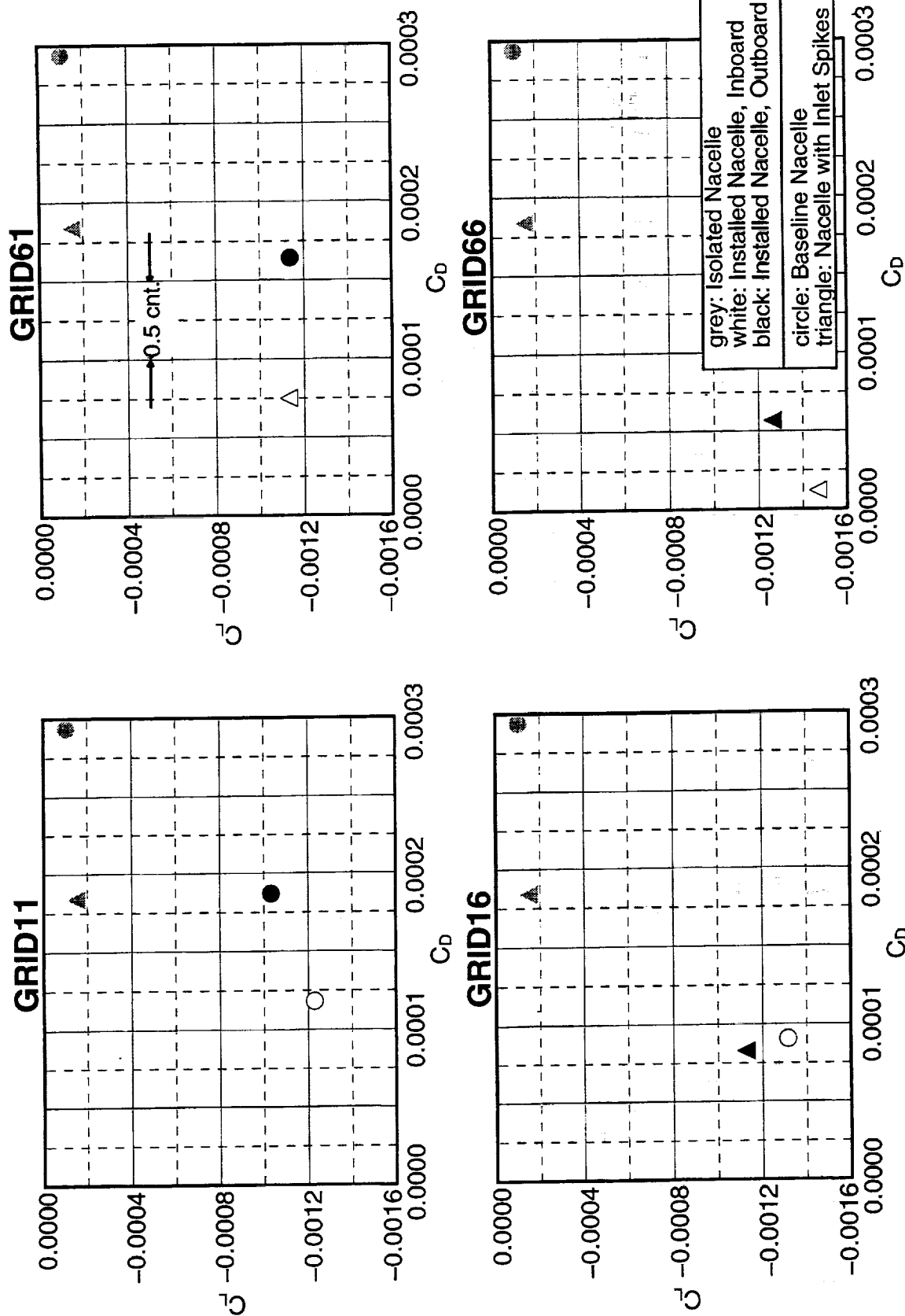
The following set of graphs compare each nacelle's lift and drag in full configuration against the isolated nacelle (GRID1 and GRID6) results. Note that the internal duct, nozzle base area and centerbody are excluded from the force integration. Immediately apparent from these plots is that the lift for each nacelle is reduced when installed under the wing. This can simply be attributed to a combination of wing-nacelle interaction and each nacelle's (inboard and outboard) different orientations from the isolated version.

Second, as is shown by the isolated nacelle result, there is a consistent reduction in its drag when an inlet spike (and the eventual result of spilling) is installed. Except for GRID61's inboard nacelle, lift is also consistently reduced when the inlet spike is present. With the air around each nacelle's forward cowl accelerated by spilling, pressure in this part is reduced, thereby reducing the drag. Since the diverter takes up space on the upper part of each nacelle, most of the pressure reduction due to spilling is only affecting the lower surface of each nacelle, hence the reduction in lift.

Finally, interaction between the nacelles is also affected by their geometry. Specifically, lift and drag on one nacelle is consistently reduced when the other is spilling. Clearly, this is a product of the inlet spike generating shocks that interact with the flow around the other nacelle.

Inlet Spillage – Nacelle Lift And Drag

$M = 0.9$



Inlet Duct, Spike, and Nozzle Forces Excluded

Rigid Power Effects (Inlet Bleed, Spillage, and Bypass) – Final Review

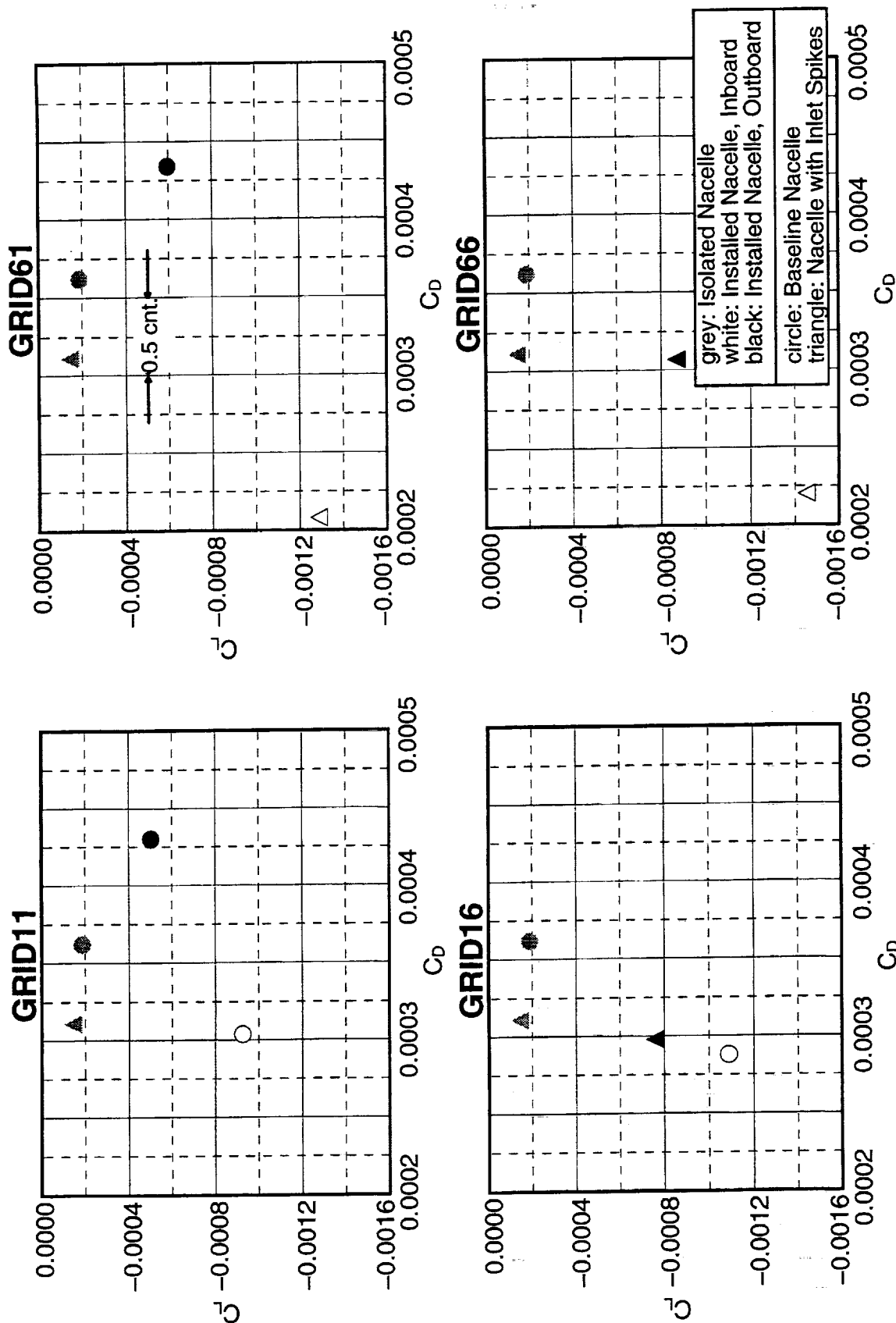
The following set of graphs compare each installed nacelle's lift and drag against the isolated nacelle (GRID1 and GRID6) results. Similar to what was seen in the Mach 0.9 cases, the lift for each nacelle is reduced when installed under the wing.

Second, as is shown by the isolated nacelle results, there is a consistent reduction in installed nacelle drag when an inlet spike (and the eventual result of spilling) is present. However, unlike the isolated nacelle, lift decreases when there is spillage. With the air around each nacelle's forward cowl accelerated by spilling, pressure in this part is reduced, thereby reducing the drag. Since the diverter takes up space on the upper part of each nacelle, most of the pressure reduction due to spilling is only affecting the lower surface of each nacelle, hence the reduction in lift.

Lift for one nacelle is also consistently reduced when the other has an inlet spike. Except for the inboard nacelle drag for GRID11 and GRID16, a nacelle's drag consistently increases when the other nacelle is spilling. Evidently, the shock emanating from the spike's leading edge is interfering with the flow around the other nacelle.

Inlet Spillage – Nacelle Lift And Drag

M = 1.2



Rigid Power Effects (Inlet Bleed, Spillage, and Bypass) – Final Review

In this figure, the total lift and drag results for all four spill configurations (GRID11, GRID61, GRID16, GRID66) are plotted for both the subsonic ($M=0.9$) condition (runs RUN 16, RUN 17, RUN 18, and RUN19) and the transonic ($M=1.2$) condition (runs RUN 20, RUN 21, RUN 22, and RUN23).

For the $M=0.9$ condition, the L/D increases with the addition of the centerbody (and spill) and the combined effect of both centerbodies (GRID66) shows a pronounced changes in L/D . This results in roughly a four count drag reduction compared to the flow-through ducts (wind tunnel geometry).

For the $M=1.2$ condition, the combined effect of both centerbodies (GRID66) is nearly a linear superposition of the GRID16 and GRID61 solutions. Again the L/D increases with the addition of the centerbody. The net change in drag is a 2–3 count reduction.

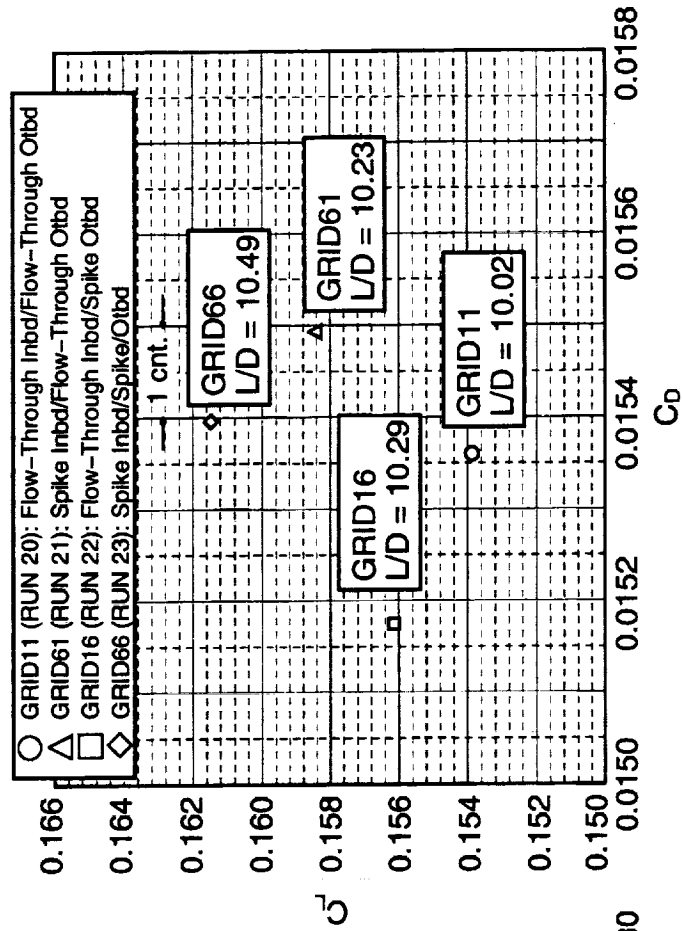
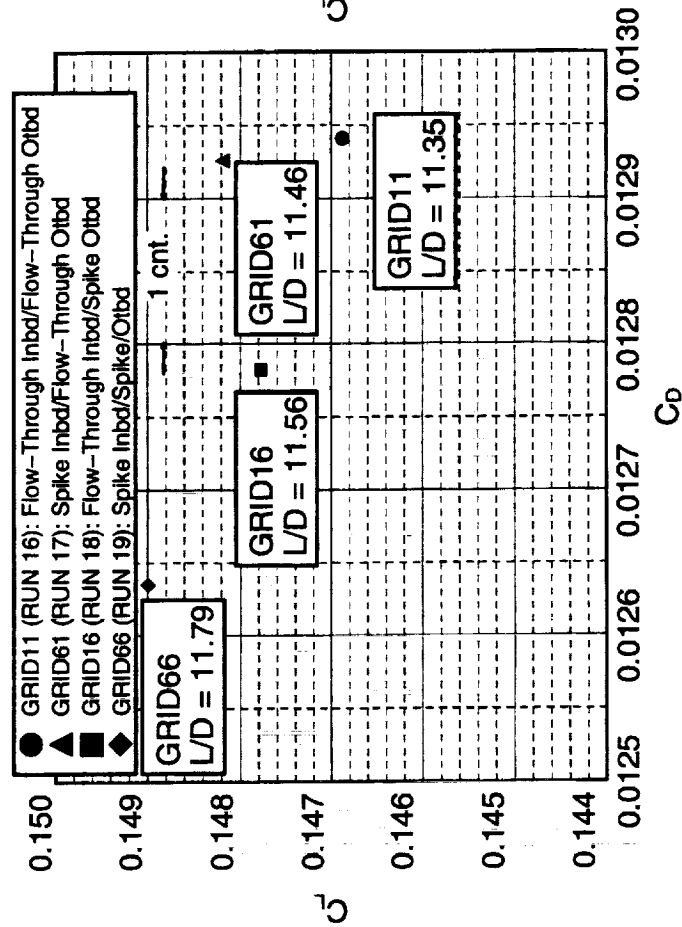
Note again that the internal duct, nozzle base and centerbody are excluded from the force integration.

Rigid Power Effects (Inlet Bleed, Spillage, and Bypass) – Final Review

Inlet Spillage – Full Configuration Lift And Drag

M = 0.9, $\alpha = 3.7^\circ$
Re_{MAC} = 163.0 M
h_{alt} = 40,000 ft.

M = 1.2, $\alpha = 3.7^\circ$
Re_{MAC} = 303.7 M
h_{alt} = 32,000 ft.



Inlet Duct, Spike, and Nozzle Forces Excluded

Rigid Power Effects (Inlet Bleed, Spillage, and Bypass) – Final Review

It was determined from the 2-D port analysis that using a transpiration boundary condition to model cowl bleed ports whose exits' heights are significantly smaller than the nacelle diameter is sufficient. Other than momentum being generated to reduce total drag, the rest of the external drag forces (viscous and pressure) are essentially unaffected by bleed. The cowl ports (especially those sections on the upper half of the nacelle) create flow conditions that give a beneficial interaction with the lower surface of that wing to improve L/D . Finally, given the plenum pressure at the appropriate bleed port, the desired mass flow was achieved at the centerbody bleed ports and by simply using a transpiration boundary condition for the cowl bleed ports.

Unlike the Mach 1.2 cases, the Mach 0.9 solutions for the full configuration geometries proved difficult to obtain. Residuals and forces were slow to converge. Additional runs, though needed would have been too costly. However, solutions from each geometric case taken at various intermediate iteration levels and processed appear to maintain some appreciable consistency in its results. This in turn, results in consistent relative differences in solutions between geometries at a certain iteration level. Since differences in geometry basically amount to which nacelle has an inlet spike, each nacelle's effect to the overall solution can be sufficiently accounted for.

Results have also shown, for both Machs 0.9 and 1.2 cases, that L/D improves with the addition of inlet spikes, especially lift. The improvements to the lift was mostly due to inlet spikes providing an additional source for compression shocks.

Throughout all the nacelle cases, isolated and full configuration, the nacelle drag decreased if spillage occurred. With spilling causing flow to accelerate around the forward part of the nacelle thereby reducing pressure, and the nacelle's pointed shape (from the midsection to the lip, excluding the inlet spike), a propulsive component is produced on this part of the nacelle thereby reducing external drag. In addition, the inlet spike on the outboard nacelle has consistently reduced drag to the overall geometry mainly due to the flow spilling over onto the leading edge of the wing. This effect is more pronounced since the outboard inlet is located close to the leading edge of the wing. However, it must be noted that external lift and drag forces do not include the forces on the internal nacelle surfaces, including the spike/centerbody.

Conclusion/Accomplishments

- **2D Analysis Shows That Cowl Bleed Exhaust Can be Simulated Accurately Using a Simplified Transpiration Model**
- **Successfully Evaluated Effects of Bleed That Cannot be Tested in the Wind Tunnel Due to Scaling**
- **Effects of Bleed Exhaust on External Drag is Negligible**
- **Can Achieve Desired Cowl and Center Body Bleed Mass Flows With Expected Plenum Pressures**
- **At Transonic Regime ($M = 0.9$), Solution Convergence is Slow, But Relative Differences in Solutions Between Geometric Cases are Consistent**
- **Nacelle and Inlet Spike Interaction Improves External L/D**
- **Generated Versions of Grids for Wind Tunnel Reynolds Number Cases**

This page is intentionally left blank.



Propulsion Induced Effects (PIE) Test Program

**Gelsomina Cappuccio, Mark J. Won
NASA Ames Research Center**

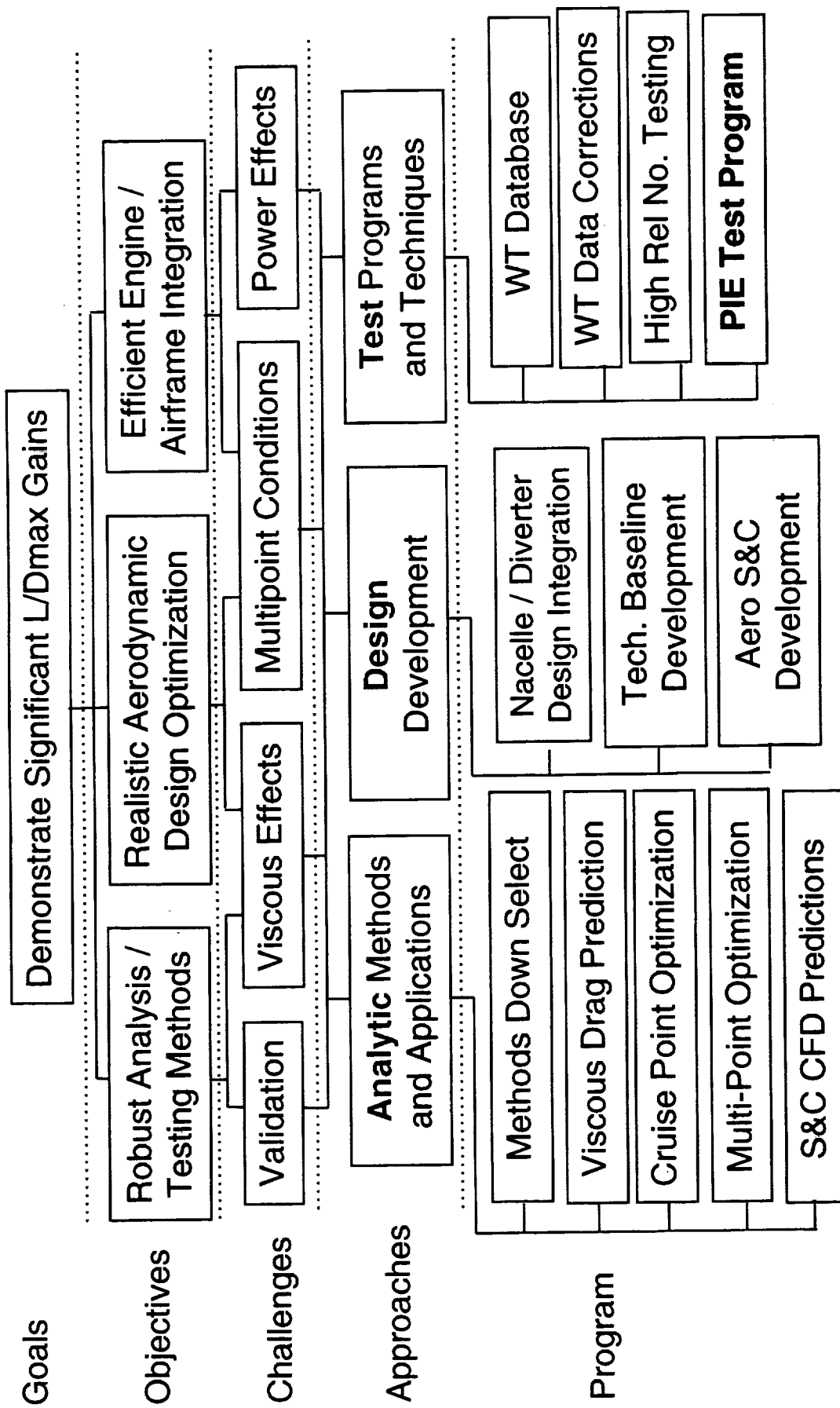
**Year End Technical Review
Configuration Aerodynamics ITD Team**

**Los Angeles, CA
February 9 - 13, 1998**

Program Hierarchy Chart - No Facing Page Description

Configuration Aerodynamics Technology Development

Session 4: Nacelle/Diverter Design and Airplane Integration



The PIE program is currently represented by several core representatives from Ames, Boeing and Micro Craft, Inc (Tulahoma Division). These individuals are primarily involved in the detailed planning and development aspects of the test program.



Core PIE Program Players

Ames - Program Lead

- Mina Cappuccio (POC)
- Mark Won (Applied Test)

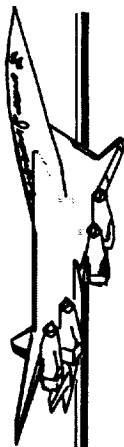
Boeing - Industry Input

- Eric Adamson (TI)
- Chih Shieh (CFD)
- Hoyt Wallace (CPC Nozzle)

Micro Craft - Tullahoma (Model Development)

- Glenn Hardin
- Jon Lines

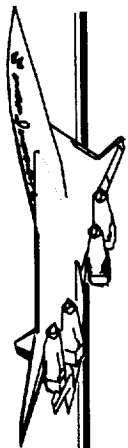
The Propulsion Induced Effects (PIE) test program is being lead by NASA Ames for Configuration Aerodynamics (CA). Representatives from CA, Technology Integration (TI), Inlet, and the Nozzle ITD's are working with Ames in defining and executing this test program. The objective of the CA 4-14 milestone is to assess the propulsion/airframe integration characteristics of the Technology Concept Airplane (TCA) and design variations using computational and experimental methods. The experimental aspect includes static calibrations, transonic and supersonic wind tunnel testing. The test program will generate a comprehensive database that will include all appropriate wind tunnel corrections, with emphasis placed on establishing the propulsion induced effects on the flight performance of the TCA.



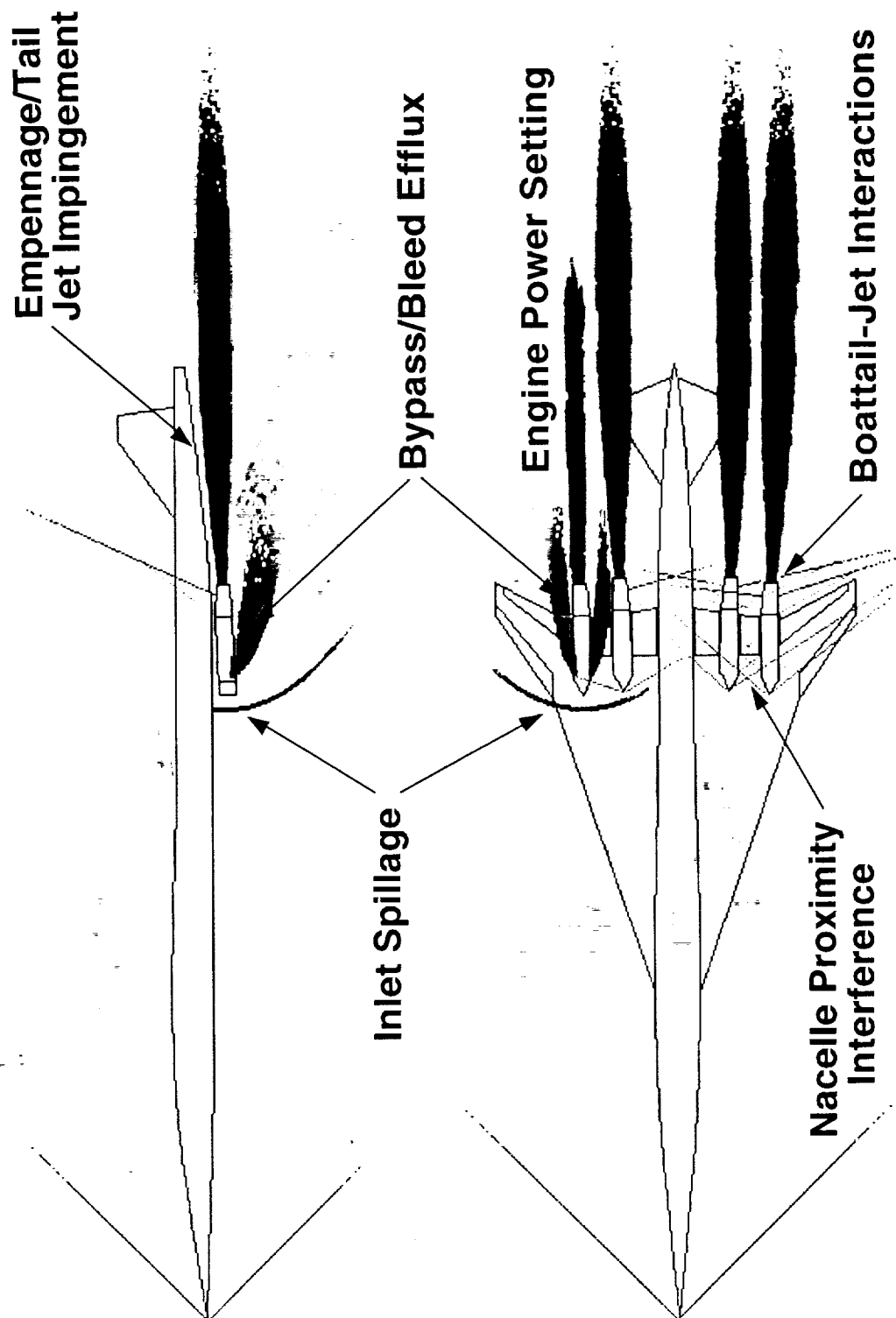
CA Milestone 4-14 Mission Statement:

- The objective of this milestone is to assess the propulsion/airframe integration characteristics of the Technology Concept Airplane and design variations through computational analysis and experimental subsonic through supersonic wind tunnel testing
- The milestone will generate a comprehensive CFD and wind tunnel database of baseline and design variations
- Emphasis will be placed on establishing the propulsion induced effects on the flight performance of the Technology Concept Airplane with all appropriate wind tunnel corrections

The predominant propulsion/airframe interactions considered for PIE generally include: inlet spillage; bypass and bleed efflux discharge from the nacelles; inlet spillage variation with engine power setting; jet impingement on the empennage and tail; nacelle-nacelle and nacelle-wing proximity flow interference; and nozzle boattail-jet flow interactions.

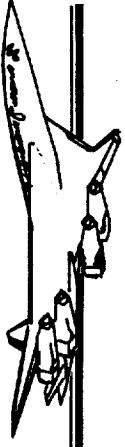


PIE Flow Physics on TCA



PIE testing is required due to the lack of information and understanding of PIE-generated forces and moments (with respect to airplane performance, stability and control). Not much is known about how PIE varies with TCA configuration changes and how much it impacts the design optimization process.

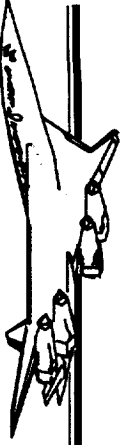
There is a lack of confidence in relying on computational methods, alone, to predict PIE behavior. CFD to experimental data comparisons are rarely in agreement with each other, and discrepancies are often left unresolved. If CFD or other empirical tool is utilized to predict PIE increments, relevant experimental data must be available to develop the numerical methods and validate the computed results.



Why Do PIE Testing?

- 1. Lack sufficient information & understanding of PIE on:**
 - **TCA forces & moments (performance, S & C)**
 - **TCA configuration changes & design optimization**
- 2. Cannot rely on CFD alone to determine PIE increments (CFD to test data comparisons on TCA are frequently mismatched & unresolved)**
- 3. Developing and validating empirical, CFD, or hybrid PIE prediction methods require test data**

The PIE program is challenged with the task of developing a comprehensive experimental approach to obtain the PIE magnitudes on TCA forces and moments. Sufficient airplane configuration fidelity must be retained and preserved to meet performance and selected stability and control requirements. Additional work should include CFD validation and design trade studies to complement and enhance the PIE test data to extend the range of applicability beyond the experimental envelope.

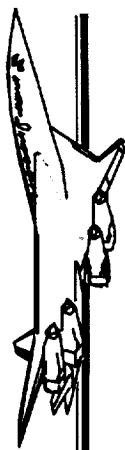


The CHALLENGE

- **Develop a comprehensive experimental approach to obtain PIE magnitudes on TCA forces & moments**
- **Preserve sufficient model configuration fidelity to address performance and selected S & C requirements**
- **Perform CFD validation & design trade studies to complement & enhance PIE test data**

The program's framework rests on determining the PIE magnitudes on the TCA forces and moments, while preserving sufficient configuration fidelity to focus on performance and selected stability and control requirements. At transonic speeds, inlet spillage drag, installed nozzle boattail drag and nozzle plume-aft body/tail interactions are of primary interest, with the goal of resolving drag increments to within ± 1.5 counts.

At supersonic speeds, inlet bypass/bleed interference and nozzle plume-aft body/tail interactions are considered to be the dominant effects. It is anticipated that these may yield PIE drag increments greater than the targeted experimental accuracy of ± 0.5 counts at or around supersonic cruise conditions.



Specific Test Program Thrusts

Obtain PIE force, moment & pressure data on TCA by:

Transonic Testing ($0.9 \leq M \leq 1.2$):

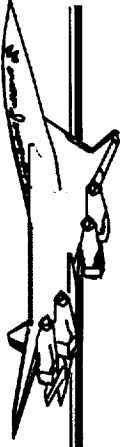
- inlet spillage/additive drag
- installed JE nozzle boattail/flap effects
- nozzle plume-aft body/tail interactions
- Δ drag uncertainty $\leq \pm 1.5$ cts

Supersonic Testing ($1.6 < M \leq 2.4$)

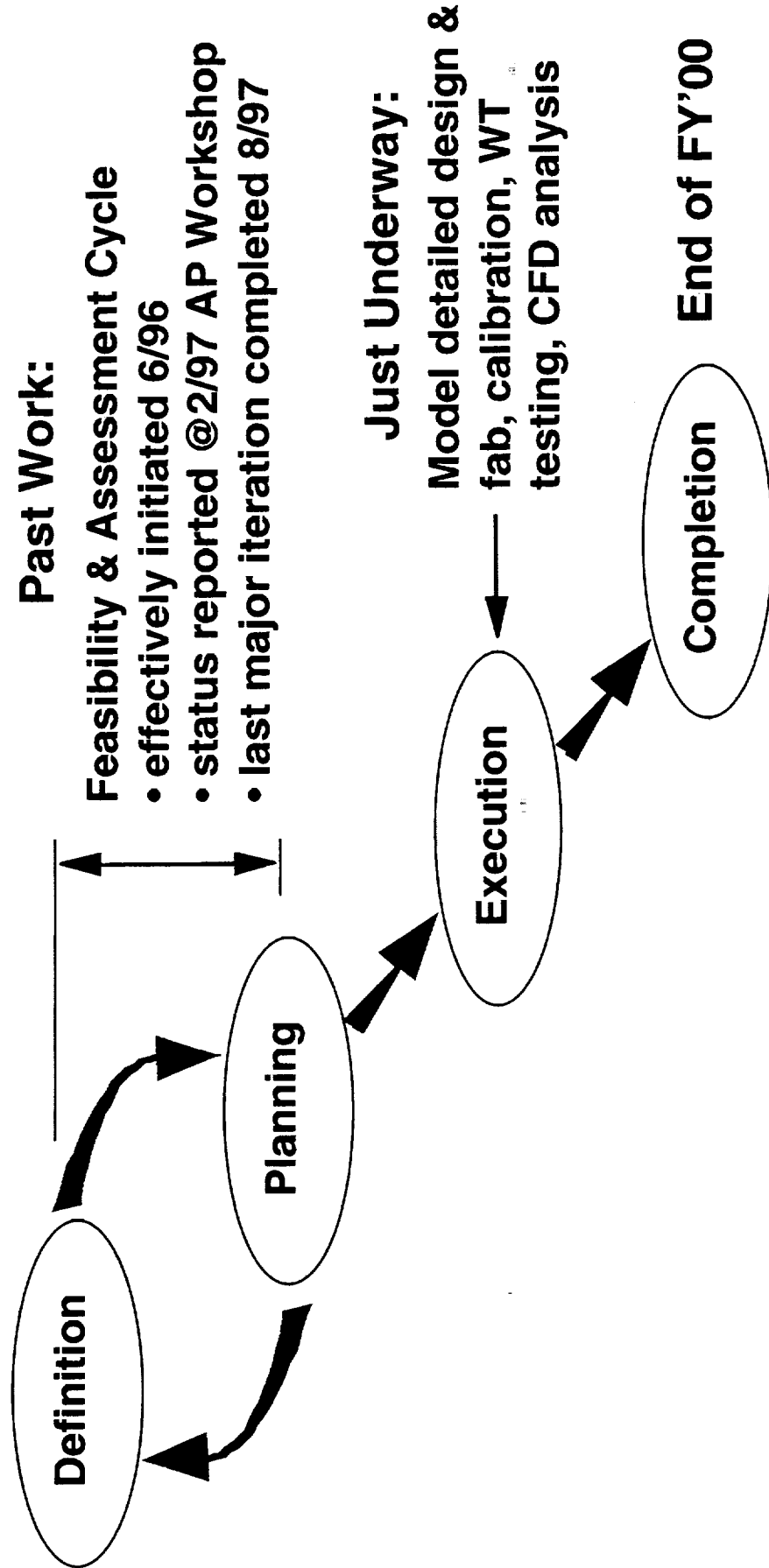
- inlet bypass efflux interference
- ramp/cowl bleed efflux interference
- nozzle plume-aft body/tail interactions
- Δ drag uncertainty $\leq \pm 0.5$ cts

The current activity has evolved from a series of feasibility and assessment studies, which essentially began in June 1996. This scoping effort initially centered on defining and ranking those critical technologies that would derive the most benefit from the PIE program. Conceptual model design and preliminary test planning were coupled with anticipated funding profiles to establish the likelihood of program completion within a mandated timeframe. Much of the work was presented at the 1997 Aero Performance Workshop.

Chronologically speaking, the PIE program has recently entered into the execution phase, commencing with detailed model design work. The impetus for the present effort stems from the findings of the last overall evaluation cycle, completed in August 1997. The recent feasibility and assessment defined and projected a program path for model fabrication, wind tunnel testing, CFD analysis and other related activities that will meet the CA 4-14 objectives by the end of FY00.



Program Evolution



The program plan, as presented at the February 1997 Aero Performance Workshop, set several working objectives. For maximum model fidelity, the model would be sized as large as possible to obtain the best data accuracy. The test approach would concentrate on obtaining performance data, rather than expanding into the stability and control aspects of the TCA configuration. The majority of the testing would be focused in the transonic regime, where little performance data has been obtained. Since nacelle inlet bleed is activated at supersonic speeds above Mach 1.6, it was given a low priority for model development and testing. To take advantage of its operating cost benefits and operational range, the Ames 11-Ft wind tunnel was the primary choice for conducting transonic testing in FY99.



Program Plan Presented to 2/97 AP Wkshp

- Use largest possible model scale for best configuration fidelity & data accuracy
- Emphasis on performance over S & C requirements
- Focus on transonic testing (fill gap in TCA perf. data base)
- Consider installed supersonic bleed testing as a low priority
- Develop model & plan transonic testing around ARC 11-Ft entry in FY99 ("free tunnel")

The PIE test program, as of one year ago, was defined by a model concept, test plan and cost schedule. The wind tunnel model was conceived as a 5.7% scale platform to conduct powered testing with force and pressure measurements. The model featured a sting-supported, full-span wing assembly and an open-ended flared aft body with tail. Three types of nacelles were considered: two flow-through axisymmetric inlet nacelles, representing an aero reference and an inlet reference geometry, both containing a single nozzle/boattail configuration; the third nacelle was powered for jet-effects testing four nozzle/boattail combinations. The inlet reference nacelle contained an inlet centerbody and offered blown bypass and bleed capabilities.

One crucial feature of this earlier program was the implementation of a pilot nacelle to explore and evaluate the various calibration and bookkeeping methodologies anticipated for spillage testing. Testing would be conducted on selected flow-through and jet-effects nacelles at Boeing's Flight Simulator Chamber (FSC) and thrust stand facilities. Based on prior planning work, emphasis was placed on transonic testing in the Ames 11-Ft, with AEDC's 16T serving as a back-up - both facilities offered variable tunnel pressure capability required for powered testing by the 5.7% PIE model. For supersonic testing, AEDC's 16S and NASA Lewis' 10 X 10 were the only facilities that could accommodate a model of this scale.

The program funding profile was established for a base cost of approximately \$4 million to cover model design, fabrication and non-operations related testing expenses at Ames and Lewis - this figure included industry support for testing and data analysis activities. Factoring test costs at AEDC, additional funds would be required for 16T (~\$3.3 million) and 16S (~\$3 million).



Program Highlights 1 Yr Ago...

Model concept

- 5.7% scale, powered, force & pressure model
- full-span, sting mounted, removable flared aft-body w/ tail
- 3 nacelle types: aero ref & inlet ref flow-through, JE
- axisymmetric inlet w/ removable centerbody
- 1 ref + 4 operating JE nozzle/boattail configurations
- parametric blown bypass hardware

Test plan

- implement pilot nacelles to explore & evaluate throttle-dependent measurement techniques (test @ Boeing FSC, thrust stand)
- transonic testing: ARC 11-Ft, AEDC 16T as alt. (< 1 atm required)
- supersonic testing: AEDC 16S or LeRC 10 X 10

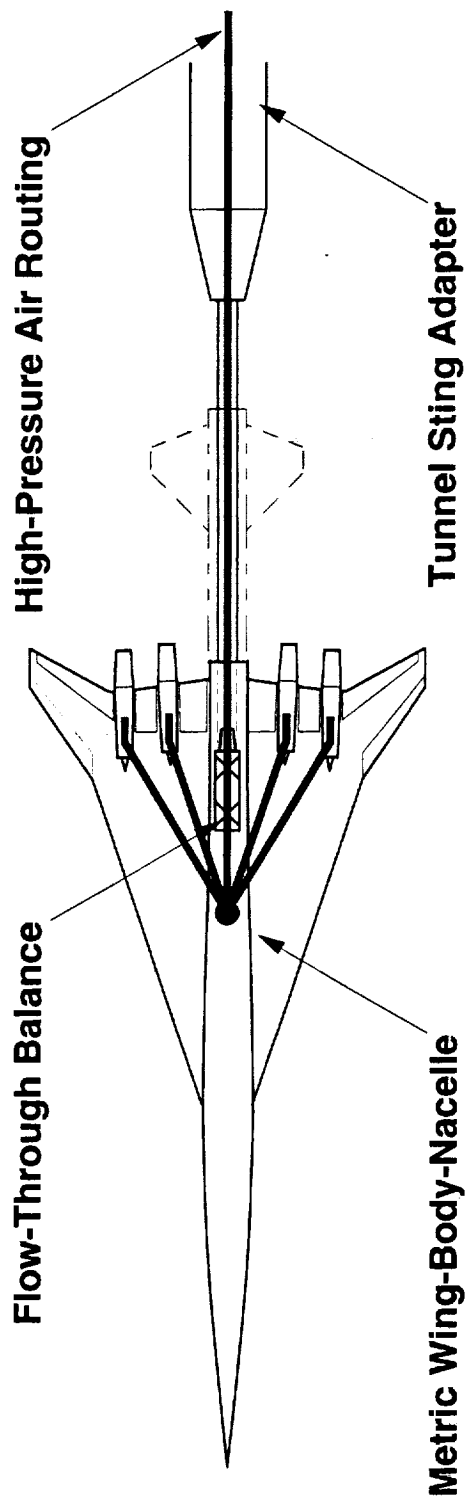
Projected program costs

- model des & fab, test, indust. support ~ \$4M (NASA WT)
- AEDC testing @16T: ~ \$3.3M; @16S ~ \$3M

The principal features of the 5.7% PIE model included: a flow-through balance; on-board high-pressure air handling capability for jet-effects testing; an all-metric wing-body-nacelle model construction; and an aft body extension with a vented posterior and a generic tail geometry to accommodate rear-sting entry into the model.



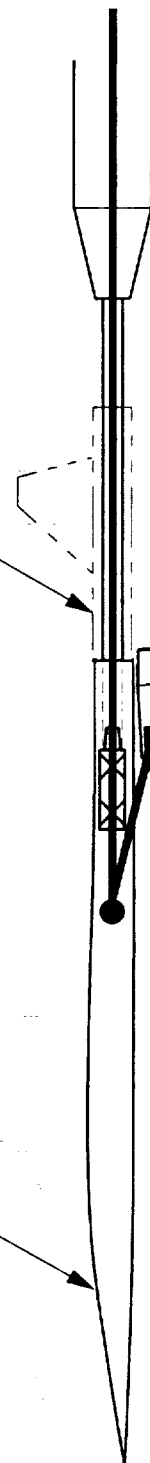
5.7% PIE Model Testing



Aft Body Configurations:

- truncated
- open-extended & tail (in phantom)

Full-length Forebody



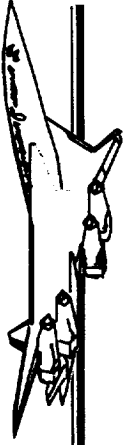
Discussions between PIE and CA representatives between May and July 1997 lead to an overall reassessment of the then-established program path. From a technical perspective, complications arising from tunnel flow quality and wall interference were anticipated for 5.7% model testing in the 11-Ft and AEDC 16T. These included tunnel Mach instability, shock reflections and buoyancy. The ability of applied computational-empirical techniques to correct for these effects and accurately resolve PIE force and moment increments was perceived to be questionable; relying on such methods to derive useful data was deemed to be extremely risky for the program.

Delays in the Ames 11-Ft Modernization schedule were expected to impact the PIE program by either slipping the 11-Ft entry to a later date or testing at the AEDC 16T; either alternative would adversely extend the projected transonic entry beyond FY00.

The appropriateness and relevancy of the PIE model configurations being considered for testing were also brought into question. Updates to the inlet design, nozzle geometry and engine cycle made the baseline axisymmetric-centerbody PIE nacelle obsolete for TCA implementation and development. The latest configuration changes at the time included a 2-D bifurcated inlet geometry and a higher aspect ratio nozzle boattail.

The open-ended empennage and generic tail were not representative of the true aft body geometry (which has complete closure and upsweep). Measured aft body force and moment increments would be arbitrary with respect to the TCA empennage geometry, and would be of little value without testing an empennage with the correct closure geometry.

The likelihood of not being able to test and evaluate transonic data from the 11-Ft before FY00 implied that testing would have to be conducted at AEDC, potentially requiring a total expenditure in excess of \$10 million to complete PIE testing work.



Feasibility & Assessment (~5/97)

Technical concerns

- 11-Ft data quality at 5.7% scale is questionable (Mach stability, shock reflections, buoyancy, etc)
- lack of confidence in CFD-empirical methods to correct transonic data or accurately assess interference effects on F & M increments

Projected 11-Ft operational status

- ARC 11-Ft production readiness during FY99 unlikely
- delay requires slide in transonic entry beyond FY00 or test at AEDC

Usefulness of configurations represented

- use updated engine inlet/nozzle/cycle? (2-D inlet, bigger AR nozzle)
- generic empennage & tail geometry (lack “true” aft body & tail)

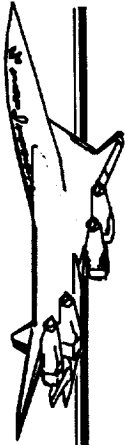
Potential +\$10M pricetag due to 11-Ft & PCD schedule conflict

The combined technical, scheduling and cost risks associated with developing and testing a 5.7% scale PIE model far exceeded the funding and time constraints imposed on the CA ITD. This precipitated discussions in May-June 1997 between CA and PIE team representatives to seek other alternatives that would meet the PCD objectives at substantially lower cost and shorter timeframe than those anticipated for the 5.7% model concept.

Options included using one or a combination of existing HSR models to perform a portion of the PIE testing. These included the 1.5 and 1.7% TCA models, as well as the 1.7 and 2.7% Ref H models. Since none of these models are equipped for on-board blowing, they would be used predominantly for flow-through nacelle testing purposes to investigate spillage and aspirated bypass/bleed effects.

For jet effects testing, a large scale isolated blown nacelle rig was proposed to evaluate nozzle plume on aft body and wing in-proximity effects. Another approach for powered testing included modifying the 1.5% scale TCA (Model 23) aft body design to include high-pressure air blowing capability, at a scale comparable to the 1.7% TCA wing-body models. By combining data from either of these powered models with the unpowered TCA or Ref H models, one could possibly construct PIE increments if scale, geometry and nacelle-nacelle interaction considerations were deemed negligible.

The ultimate alternative involved the building and testing of a moderately scaled model that could be used for both wing-body-nacelle and aft body PIE testing. If carefully scaled, this model could be tested transsonically and supersonically in a NASA wind tunnel.



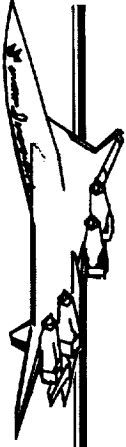
Program Redirection Options (~6/97)

BIG (\$\$ + Delay + Technical Risk) @5.7% scale = need to explore other alternatives:

- use or modify existing models (1.5, 1.7% TCA, 1.7 & 2.7% Ref H) for PIE testing
- build & test isolated in-proximity blown nacelle on aft body, wing
- integrate other aft body tests into PIE model
- build a moderately scaled model for powered WBN & aft body PIE testing

In August 1997, the PIE team evaluated the alternatives for PIE testing. The team concluded that the most logical approach to meeting the program's objectives, while retaining technical viability at reasonable cost, is to build and test a powered 3% scale wing-body-nacelle-aft body model.

This model arrangement will provide the most comprehensive composite "picture" of the PIE contributions. With a common model configuration and scale to serve as a reference, obtaining incremental PIE force and moment increments are relatively straightforward (linear superposition principles apply), unlike the other proposed alternatives which involved models with different scales and geometries. Since four powered nacelles can be afforded, the installed jet effects interactions are included in the PIE simulation, unlike the proposed isolated blown nacelle rig approach.



Outcome of 8/97 Planning Cycle

Best approach to meet program objectives, retain technical viability at reasonable cost: Build a new powered WBN/aft body TCA model at 3% scale

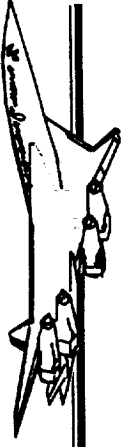
- gives the most comprehensive composite “picture” of PIE contributions
- common model baseline to reference PIE F & M increments
- avoids uncertainties associated with applying PIE data from models of different scales (1.7 vs. 2.7%) & geometries (Ref H vs. TCA)
- overall installed JE interactions are included in PIE simulation (unlike large scale isolated blown nacelle rigs)

The 3% scale PIE model includes: the addition of a strut-supported model for refined aft-body testing with a closed upswept empennage and tail; incorporating the 2-D bifurcated inlet nacelle geometry (in place of the axisymmetric-centerbody); increasing the variety of nozzle/boattail configurations for combined flow-through and jet-effects nacelle testing, with input from the CPC Nozzle team; and blown bypass and bleed capabilities.

With the reduction in model scale, tunnel pressure variability is no longer required for either unpowered or powered transonic testing; therefore, the Langley 16-Ft. has been selected for PIE testing (up to Mach 1.2). The smaller model scale will also permit supersonic PIE testing in the Ames 9 X 7, with the Lewis 10 X 10 serving as an alternate test site.

Program integration with other HSR wind tunnel activities was introduced as a risk-reduction measure. PIE configurations and test methods will be applied to other models to gain distance on the "learning-curve" for eventual PIE testing and model development work. Near term work will include building and testing separate PIE nacelles for the 1.7% scale TCA at cruise Mach to gain insight into the nacelle's design, construction, calibration and application of correction methods for the 3% scale version. Another risk mitigating measure will involve the comparison of PIE model aft body development and test techniques with a 1.5% scale TCA model, scheduled for testing later this year.

The projected program cost for the revised PIE program using a 3% model is estimated to be under \$4 million, including model design, fabrication, testing and support from industry.



3% PIE Model & Test

Model concept

- supplement metric wing-body with strut-mounted metric aft-body
- augment open aft-body with “true” geometry (closed upswept) & tail
- incorporate 2-D bifurcated inlet
- increase nozzle/boattail configurations w/ CPC Nozzle input
- include blown bypass & bleed simulations

Test plan

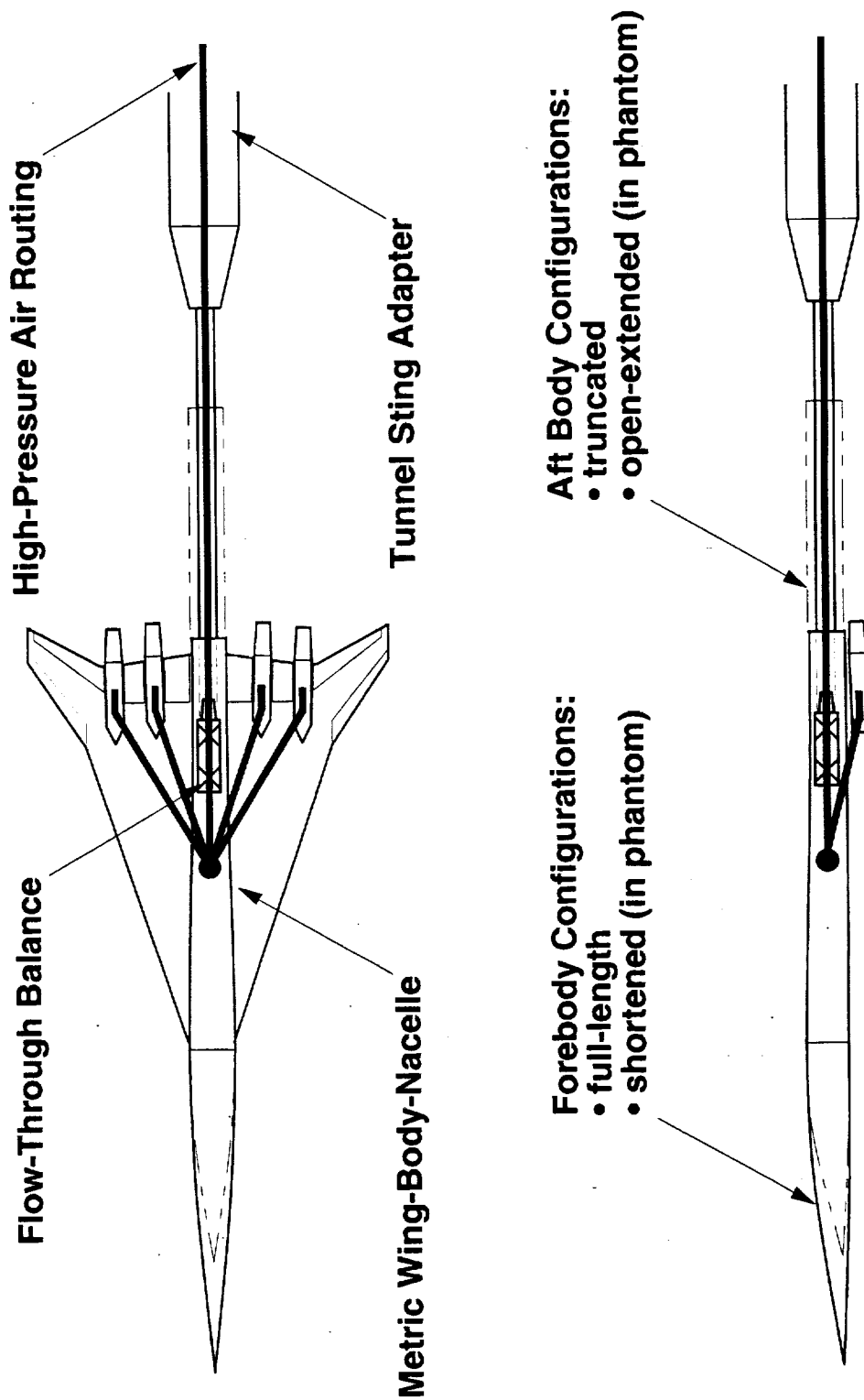
- transonic testing: LaRC 16-Ft (~ 1 atm OK @3% scale)
- supersonic testing: ARC 9 X 7 (LeRC 10 X 10 as alternate)
- mitigate risk by exercising PIE test elements on near-term CA WT activities: 2-D inlet nacelles, WT corrections, aft body testing methods

Program cost: < \$4M (model des & fab, test, indust. support)

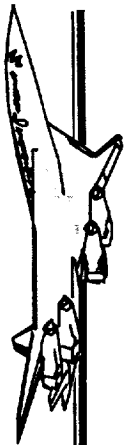
Wing-body-nacelle PIE interactions will be obtained using a metric, rear-entry sting supported model arrangement. Force and moment data will be measured using a special flow-through balance that is being designed to pass high-pressure air from the facility to the nacelles. To properly obtain aft body increments from the metric wing-body-nacelle configuration, the sting model will be tested with two forebody-aft body fuselage combinations: a full-length forebody mated to a truncated aft body; and a shortened forebody paired with a generic open-extended aft body. In addition to the balance, the model will be instrumented with external and internal (diagnostic) static pressure taps.



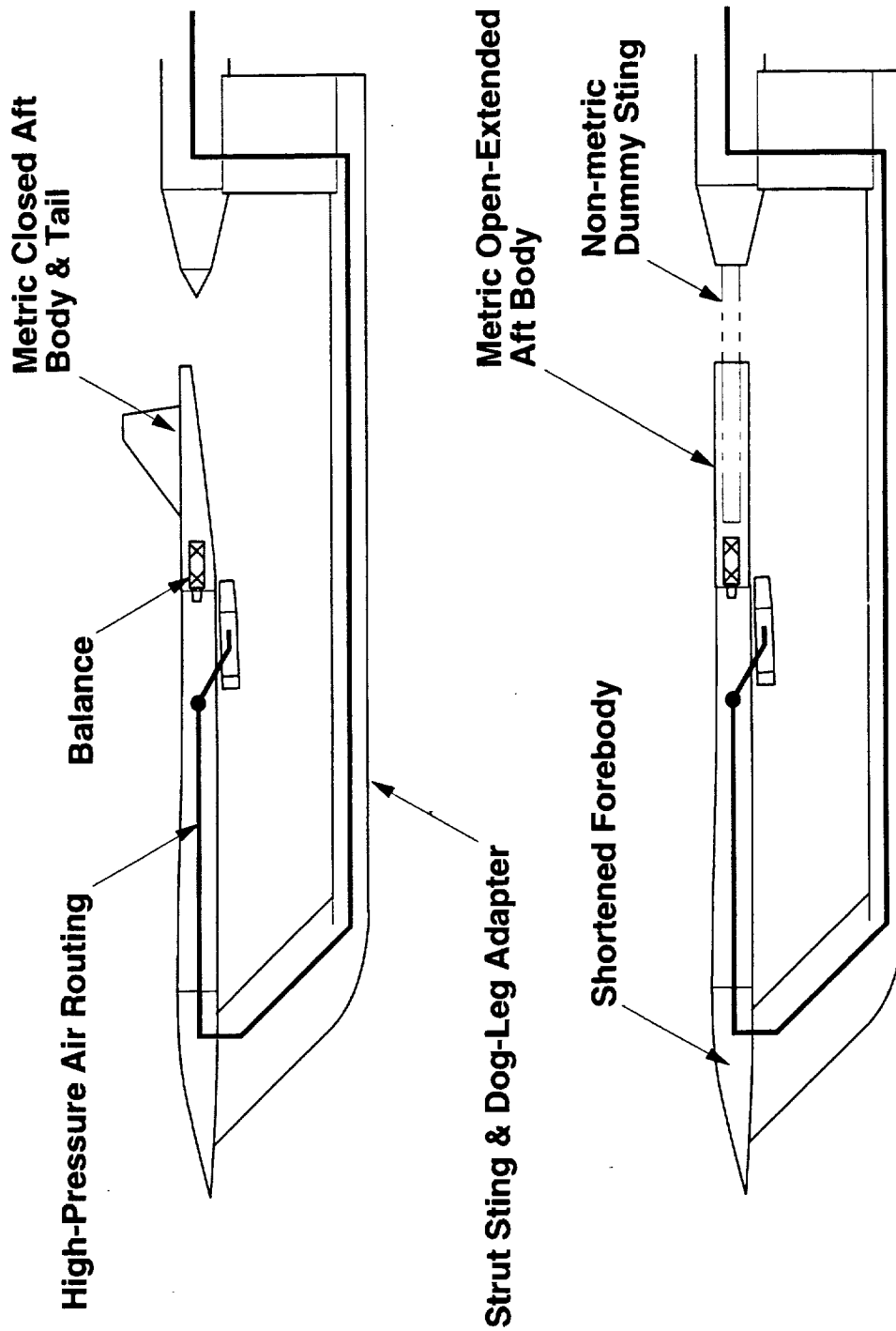
3% PIE Sting-Mounted Model Testing



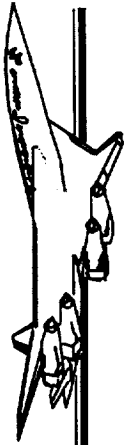
Aft body incremental data will be obtained using a strut supported model arrangement, where only the aft body is metric. Two empennage configurations will be tested: the open-extended and the closed upswept aft body with tail. The non-metric model will include the shortened fuselage, wing and nacelle portion of the model assembly. High-pressure air from the facility will be routed through the sting strut and into the non-metric wing-body for discharge by the nacelles. The aft body will be bridged to the rest of the fuselage by a conventional force and moment balance, and will include both external and internal (diagnostic) static pressure taps. In addition to the strut support hardware, a dummy sting will be tested with the metric open-extended aft body to determine if the measured pressures and forces vary in the presence of the rear-entry sting.



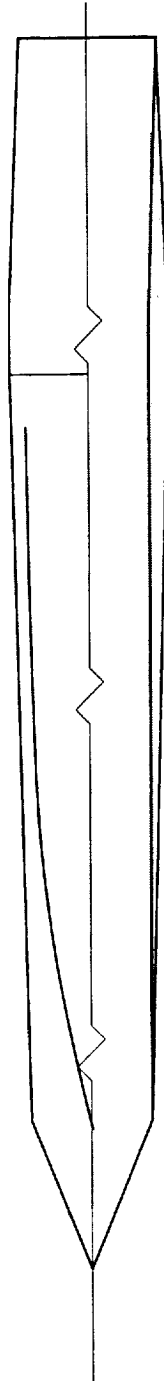
3% PIE Strut-Mounted Model Testing



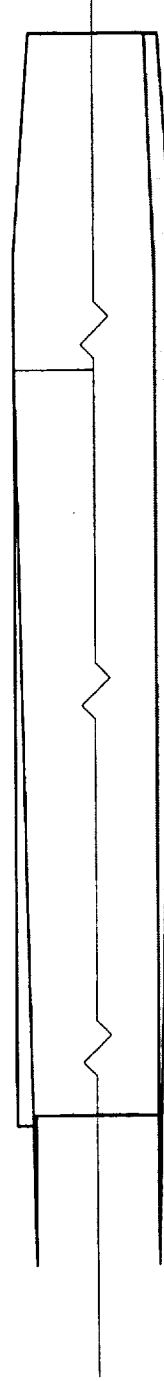
The baseline nacelle geometry for all aerodynamic testing is defined by an aero reference nacelle with a rectangular 2-D inlet and exit shape. This nacelle features a constant area flow-through duct featuring a supersonic-cruise boattail configuration, with the upper and lower flaps truncated at the nozzle sidewall trailing edge. Nacelle instrumentation is limited to internal and external static pressure taps.



Aero Reference Nacelles



top external/centerline sheer view

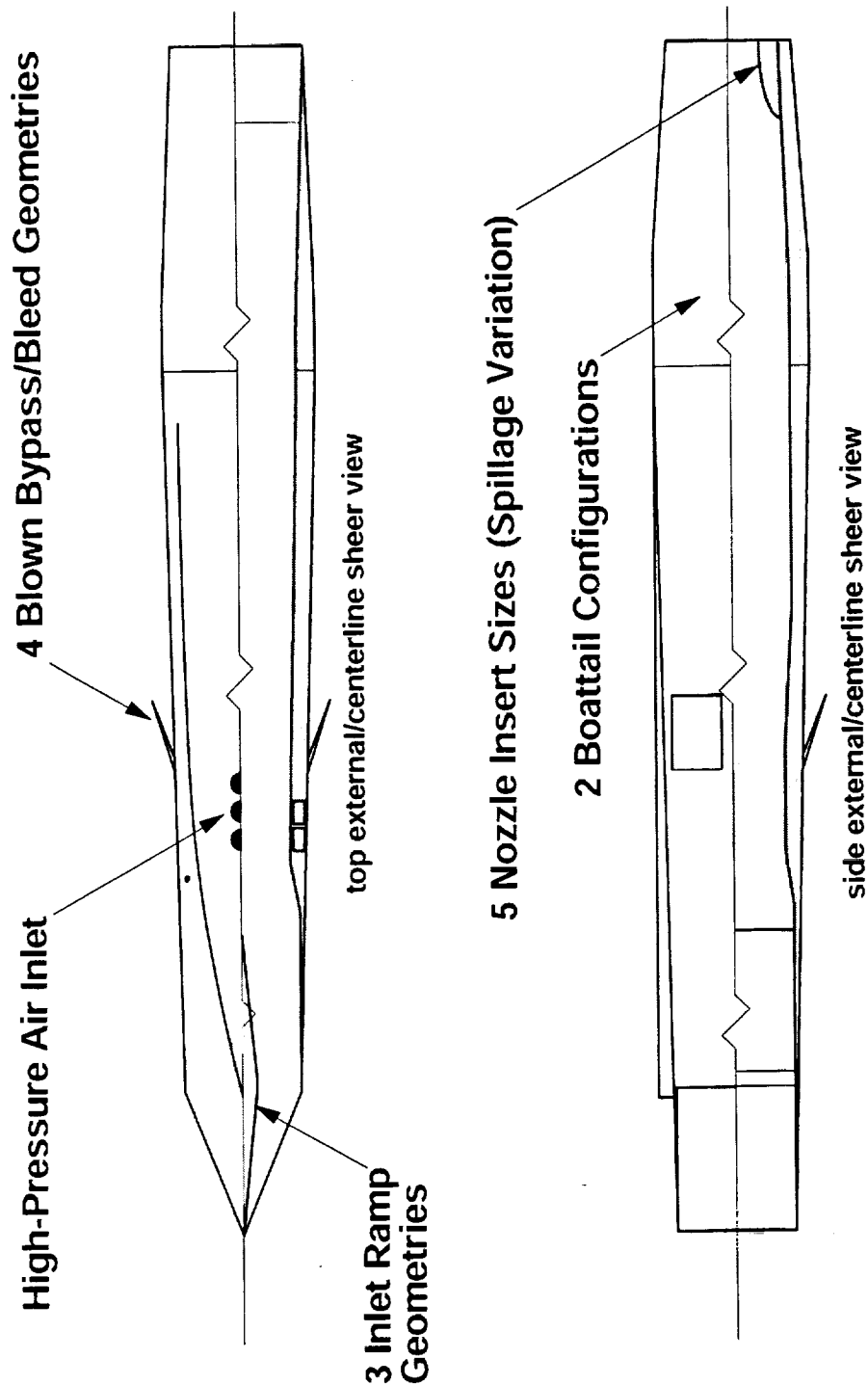


side external/centerline sheer view

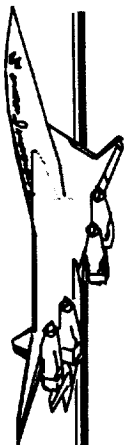
The inlet reference nacelle serves as a platform for conducting flow-through spillage and blown bypass/bleed testing. The inlet includes three interchangeable ramp configurations for 2-D inlet bifurcation. Bypass and bleed are defined by flapped doors, louver doors, porous surfaces and slotted surfaces which are all interchangeable. Bypass/bleed flow simulation is performed by directing facility high-pressure through the model and into the nacelle cowl for discharge through the bypass/bleed nozzles. To adjust the inlet spillage rate, removable inserts will be parametrically installed in the nacelle duct exit to vary inlet mass flow. In addition to the aero reference boattail and nozzle, a second parametric boattail configuration will be also tested on the inlet reference nacelle assembly. Nacelle instrumentation is limited to internal and external static pressure taps (no rakes used in the duct).



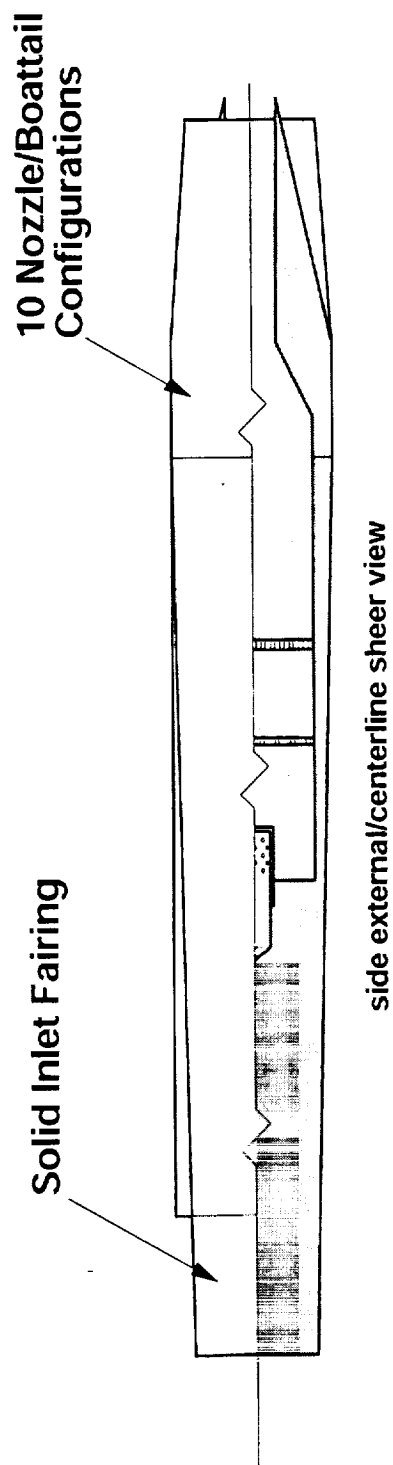
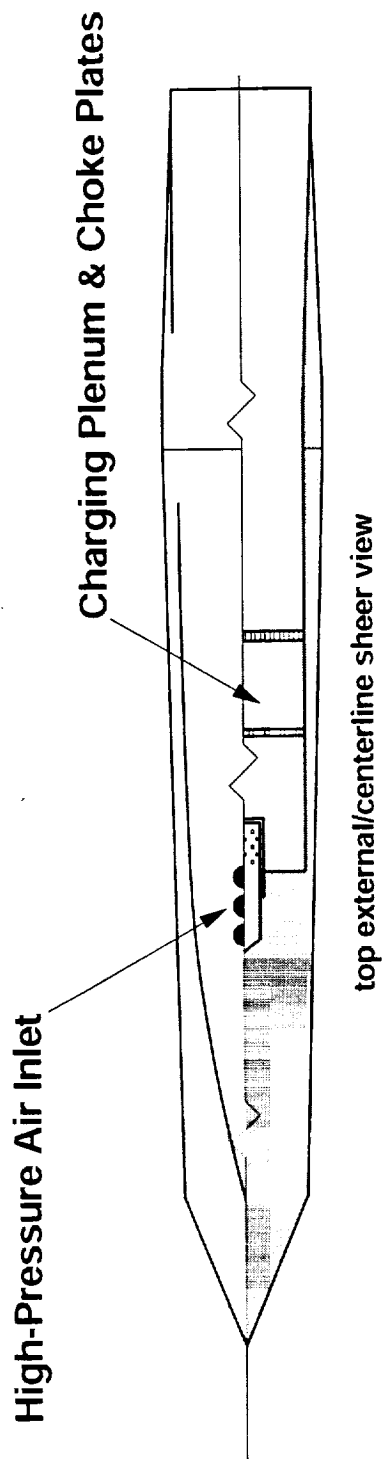
Inlet Reference, Bypass/Bleed Nacelles



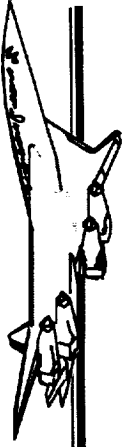
The jet effects nacelle is used for installed nozzle testing. Unlike the flow-through nacelles, the inlet aperture is covered by a solid inlet fairing. High-pressure air from the facility is directed into the nacelle, where it is then conditioned through charging plenums and choke plates before being discharged by the nozzle. In addition to the aero reference boattail and nozzle, nine additional geometries representing operating nozzle/boattail configurations (defined by the CPC nozzle team) will be also tested on the jet effects nacelle assembly



Jet Effects Nacelles



The present 3% PIE model includes element that are representative of the current and projected TCA design. The model will allow the parametric testing of geometric variables: inlet ramps; bypass & bleed covers; nozzle/boattail flap sidewall and flap angles with alternate trailing edge shapes; nozzle internal geometry; wing leading and trailing edge flap deflections; forebody length; aft body closure; and tail installation/stabilizer deflections. The test program will utilize these features to determine PIE increments over a range of transonic and supersonic Mach numbers, model angles of attack and sideslip, inlet spill rates, engine power settings, and bypass/bleed flow rates.



3% Model Test Variables Available

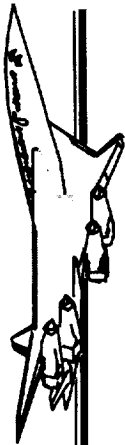
Geometry:

- inlet ramp
- bypass & bleed door
- nozzle boattail sidewall & flap angles, TE shaping
- LE, TE wing flaps
- forebody length
- aft-body closure
- vertical & horizontal stabilizer

Flow

- Mach (transonic, supersonic)
- attitude (alpha, beta)
- inlet spillage (A0/AC)
- power setting (\geq design NPR)
- bypass & bleed efflux simulation

The direct costs associated with the design, fabrication and testing of the 3% PIE model and related systems have been estimated and projected through the end of FY00 (program termination). Some of the funded activities have been already identified as part of the CA PCD over-guideline request made in FY97. The CPC Nozzle team has funded the design and fabrication of the blown nacelle nozzles for FY98. Several noteworthy estimates that have not been yet firmly established due to their premature nature include the flow-through balance calibration work and facility operational costs related to Ames 9 X 7 supersonic testing. Total PIE test program cost at this time is estimated to be \$3.911 million.



Funding/Activity Profile

Direct Costs (\$K)

Source	Supported Activity	FY98	FY99	FY00	Comments
CA ITD	Model design & initial fab.	320			full accrual @end of FY98
	Model fab. completion		1,246		full accrual @mid-FY99
	Balance fab. & static calib.		515		fab. & calib. by Boeing
	Balance flow calib.		100		calib. by Boeing @FSC, LaRC 16T
	Nacelle calib.		342		calib. by Boeing @FSC
	WT test support		300	400	includes pre-test, test, post-test work
CPC Nozzle	Nozzle design & fab.	400			full accrual @end of FY98
Others?	LaRC 16T operation			108	9 wks @\$12K/shift wk
	ARC 9X7 operation			180	3 wks @\$60K/shift wk
FY totals:		720	2,503	688	

Projected Activity Totals:

Model design & fab.	1,966
Balance fab. & calib.	615
Model calib. & WT test support	1,042
WT operations	288

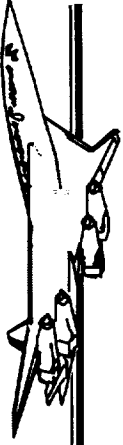
estimates not firmly established
costs included in CA PCD OGL request

Program total: 3,911

Many calculated risks and challenges are or will be faced in the PIE test program. One of these is the ability to accurately determine the internal drag correction for the flow-through nacelles. The currently envisioned approach relies on correlating static pressure measurements with CFD predictions. Due to the relatively small scale of this model, the impact of utilizing a limited quantity and type of instrumentation to determine the internal drag is uncertain. Testing a smaller version of the PIE nacelles on a 1.675% scale TCA wind tunnel model later this summer will help refine and validate this measurement technique.

One critical aspect of PIE testing is the measurement accuracy of the new flow-through balance. Since the balance axial force capacity is essentially sized for the nominal static thrust produced by the nozzles (which is nearly four times the maximum drag load), balance sensitivity may be compromised during unpowered model testing. The quality of the balance data obtained from blown nacelle testing is influenced by the ability to accurately correct errors associated with balance stream momentum, pressure and temperature variations.

Due to the onboard flow-distribution capability within the model for blown nacelle testing, balancing the flow rates and thrust levels between the left and right wing nacelles poses additional complications. Any imbalance in model flow and thrust will be an artifact of model design tolerances and fabrication/assembly quality control processes. Manual trim valves will be incorporated into the model's air-distribution network, and should help compensate for these discrepancies.

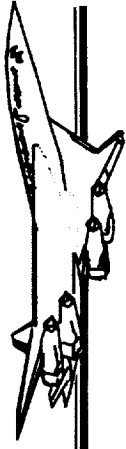


Calculated Challenges & Risks

- **Internal duct drag correction**
 - method relies on “rake-less” instrumentation and good CFD correlation
 - influence of model fidelity on data quality is uncertain
 - testing of PIE nacelles on 1.7% TCA (7/98) will serve as learning tool
- **New flow-through balance**
 - blown balance accuracy may not be sufficient for all PIE F&M data
 - sensitivity partially compromised to accommodate JE nozzle testing
 - corrections for internal momentum, pressure & temperature effects
- **Model flow & thrust balancing control**
 - depends on model fabrication & assembly quality control
 - compensate for inter-nacelle imbalances w/ manual trim valves

There are other risks and challenges that the PIE test program is or will be facing:

- The Ames 9 X 7 operational status for FY00 is still in question - CA has not had much recent experience testing at the Lewis 10 X 10 tunnel
- Until aft body data for the TCA is obtained, there is some suspicion that the PIE increments may be coupled with model support interference at high transonic speeds, mainly from shocks from the strut sting body impinging on the wing-body-nacelle
- The selection of scale may compromise measurements that are sensitive to model fidelity. This includes the effect of nacelle diverter gap height, which may choke prematurely at transonic and supersonic speeds, and bias measured spillage or bypass/bleed drag increments. Due to finite material thickness, a limited quantity of pressure taps will be installed on the nacelles, and may not be sufficiently adequate to sense the pressure variations required for accurate flow measurements or correlations (mass flow, momentum, etc). Also, boundary layer trip devices may not provide effective, uniform turbulent boundary layer transition around the leading edges of the model surface
- The scatter or deadband of the measured data may larger than the required drag increment resolution (± 1.5 counts transonically, ± 0.5 counts supersonically)
- The present model configuration may be prematurely frozen at the time of model fabrication, such that the TCA configuration is no longer represented in the PIE data



Calculated Challenges & Risks (cont'd)

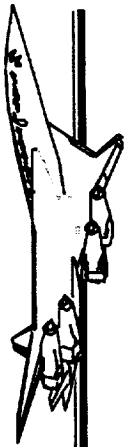
- **ARC 9 X 7 availability before mid-FY00, no recent CA experience at LeRC 10 X 10**
- **Model support interference coupling w/ PIE increments**
- **Effect of model fidelity on data quality & desired test performance**
 - **nacelle diverter choking (relatively low test RN)**
 - **quantity, placement of instrumentation on measurements**
 - **effective BL transition methods**
- **Increments buried in data scatter/deadbands > 1.5 cts (transonic); > 0.5 cts (supersonic)**
- **Premature configuration freeze (wing planform, nacelle geometry, empennage closure)**

The risks are not unique to the PIE program or its approach. The 5.7% scale PIE model, with other HSR high-speed models, have or will face similar technical and program difficulties. Despite these hurdles, many substantial benefits will be derived from the 3% PIE test. An understanding of the PIE magnitudes on TCA performance and stability and control will be learned to an appreciable extent. Valuable insight will be gained into how PIE influences configuration variability and design optimization.

The PIE effort will demonstrate how to test a four-engined HSR/HSCT type of airplane to obtain propulsion/airframe data. Unique experimental simulation and measurement techniques will be validated, such as the use of blown bypass/bleed and non-intrusive nacelle duct instrumentation.

A wealth of data will be generated for CFD calibration and development work. The experimental data base will provide the groundwork for performing design trade studies and constructing performance decks for the TCA.

The technical approach should reflect the best utilization of funds and resources to achieve the program's objectives. In the long run, the PIE test effort will serve as a risk-reduction measure for any future propulsion/integration work beyond FY00 involving an HSR/HSCT airplane configuration.



Program Risks = Value, Knowledge

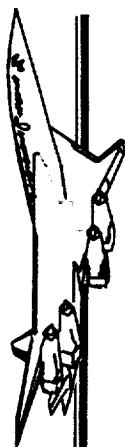
Risks are not unique to PIE program or approach currently employed - substantial benefits will be gained:

- understanding of PIE magnitudes on performance, S & C
- valuable insight into impact of PIE on overall TCA configuration variability, design optimization
- how to do future tests
 - powered 4 engine WBN/aft body configurations
 - blown bypass/bleed simulation
 - non-intrusive flow-through duct measurements
- large, comprehensive experimental data base for CFD calibration & development
- best (technical approach)/(\$\$ & resources)
- reduces technology risk for any HSR/HST-type propulsion airframe integration/development work beyond FY00

Several PIE program activities are currently in progress. Micro Craft is performing the detailed design for the 3% model, and will begin fabrication work very shortly to deliver hardware and assemblies to Ames before the middle of FY99. Micro Craft is also tasked to perform the detail design for the 1.675% PIE nacelles that will be tested on TCA Model 2b, later this summer. Boeing has been tasked to perform the detailed design, fabrication and calibration of two flow-through by the end of FY99.

Testing work is scheduled to commence with the static nacelle calibration in April-July 1999, followed by the transonic wind tunnel entry at the Langley 16-Ft in October-December 1999, and ending with the supersonic entry in the Ames 9 X 7 in January 2000.

In the meantime over-guideline funds are being sought for PIE program work beyond FY98 to support continued model fabrication, testing, CFD and data analysis through FY00.



Current Program Status

Model work

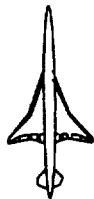
- Micro Craft tasked to perform 3% PIE model detailed design & fab for model delivery before mid-FY99
- Micro Craft tasked to detail design PIE 2-D nacelles for 1.675% scale TCA model (Model 2b) to aid 3% model design
- Boeing tasked to design, fab & calibrate (static + momentum) flow-through force-moment balance for WT use at end of FY99

Projected 3% PIE test entries

- Boeing FSC static flow-through & blown nacelle calibration: 4/99-7/99
- LaRC 16T testing: 10/99-12/99
- ARC 9 X 7 testing: 1/00

OGL funding for PIE program activities through FY00

This page is intentionally left blank.



Transonic Installed Nacelle Analyses

Nacelle / Diverter Design and Airframe Integration (4.3.1.3)

Team

BCAG: Steve Chaney

Gordon Blom

Northrop–Grumman



February 1998 HSR Airframe Technical Review



HSCT High Speed Aerodynamics - BCAG

The primary objective for propulsion/airframe integration (PAI) work stated in the planning and control document (PCD) is to develop technology required to support the development of the High Speed Civil Transport (HSCT). The technology development includes:

- 1) Developing computational and empirical based tools for the aerodynamic design & analysis of complex geometry configurations. This development consists primarily of adapting current state-of-the-art computational fluid dynamics (CFD) codes to the HSCT PAI configurations and conditions. This is followed by validation with wind tunnel or flight aerodynamic data.
- 2) Identifying the key design variables for HSCT PAI installations with the tools described above. Exercising these variables in parametric or direct design optimization studies in order to develop design guidelines for efficient nacelle installations.

These overall three year objectives for sub-task 3 lead to the specific objectives for 1997 as described below.



Objective

- Configuration aero PAI objectives as stated in PCD:
 - Develop, adapt, apply, validate, evaluate computational and empirical based aerodynamic design/analysis tools
 - Identify key design variables and develop design guidelines for efficient nacelle installations
-
- Specific objectives for 1997:
 - Transonic viscous CFD analysis method validation for W/B/N/D
 - Verify methodology for viscous evaluation of multi-point optimization designs
 - Continue drag assessment of bifurcated inlet vs. axisymmetric inlet
 - Evaluate analysis methods for propulsion induced effects and scope magnitude of PIE forces:
 - Inlet spillage (transonic)
 - Supersonic cruise inlet bleed flow



The approach taken in the 1997 PAI contract studies was to continue computational studies of inlet geometries and propulsion related effects. At the conclusion of the 1996 studies a bifurcated inlet installation had been designed and analyzed at the supersonic cruise condition. The results indicated no drag penalty compared to the TCA baseline axisymmetric inlet. This study was continued in 1997 at transonic conditions.

Up to this point very little wing/body transonic CFD work had been completed and no wing/body/nacelle/diverter studies had been done. It was first necessary to conduct a validation effort of the chosen analysis method (OVERFLOW) at the Mach numbers of interest (0.9 and 1.2). The TCA wind tunnel data from the NASA LaRC 16-ft tunnel was chosen for this task.

The wind tunnel configuration has flow-through internal duct nacelles which have very low spillage rates at transonic conditions. The actual flight airplane spills 40% of the inlet flow at Mach 0.9. In order to accurately model this condition a boundary condition must be set inside the inlet duct that controls the massflow rate. OVERFLOW had a pressure b.c. for accomplishing this; it was necessary to add the ability to measure the massflow in the duct and iterate on the pressure in order to obtain a desired massflow rate.

Both the bifurcated and TCA baseline axisymmetric inlets were analyzed with flight spillage conditions at transonic cruise (Mach 0.9) and transonic climb (Mach 1.2). The Boeing analysis was at the propulsion induced effects (PIE) test condition: 3%-scale TCA in LaRC 16-ft wind tunnel. Northrop-Grumman was subcontracted to analyze the axisymmetric inlet at flight Reynolds Number in 1997 and the bifurcated inlet in 1998.



Approach

TRANSONIC STUDIES

- Validate viscous CFD analysis of TCA W/B/N/D at Mach 0.9 and 1.2 with NASA LaRC 16 ft wind tunnel data (BCAG)
- Complete implementation of boundary conditions in OVERFLOW for spillage control (BCAG)
- Analyze TCA W/B/N/D/Centerbody with flight spillage rates at transonic cruise (Mach 0.9) and transonic climb (Mach 1.2)
 - Wind tunnel Reynolds Number: PIE test condition (BCAG)
 - Full scale flight Reynolds Number (NGC)
- Viscous transonic analysis of TCA bifurcated inlet nacelle installation at Mach 0.9 and 1.2 for comparison to axisymmetric baseline
 - Flow-through duct and inlet with compression ramp (BCAG)



February 1998 HSR Airframe Technical Review

HSCT High Speed Aerodynamics - BCAG



In addition to the transonic spillage analyses, Northrop-Grumman (NGC) performed a supersonic analysis of cowl and centerbody bleed effects at flight Reynolds Number. Both of these NGC studies are contained in a separate report.



Approach

SUPERCUISE STUDIES

- CFD assessment of effect of cowl and centerbody bleed flow on external aerodynamics of TCA axisymmetric baseline installation
- Flight Reynolds Number condition (NGC)



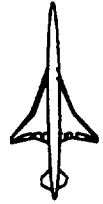
February 1998 HSR Airframe Technical Review



HSCT High Speed Aerodynamics - BCAG

The Boeing (Seattle) portion of the PAI contract work that follows is broken down into several sections:

- 1) Transonic OVERFLOW validation results for the TCA,
- 2) Spillage results for the baseline TCA axisymmetric inlet,
- 3) Spillage results for the bifurcated inlet nacelle on the TCA,
- 4) Comparison of the two inlet concepts.



Outline

- **Transonic CFD validation**
- **Inlet spillage CFD analysis**
 - **Axisymmetric inlet**
 - **Bifurcated inlet**



February 1998 HSR Airframe Technical Review

HSCT High Speed Aerodynamics - BCAG

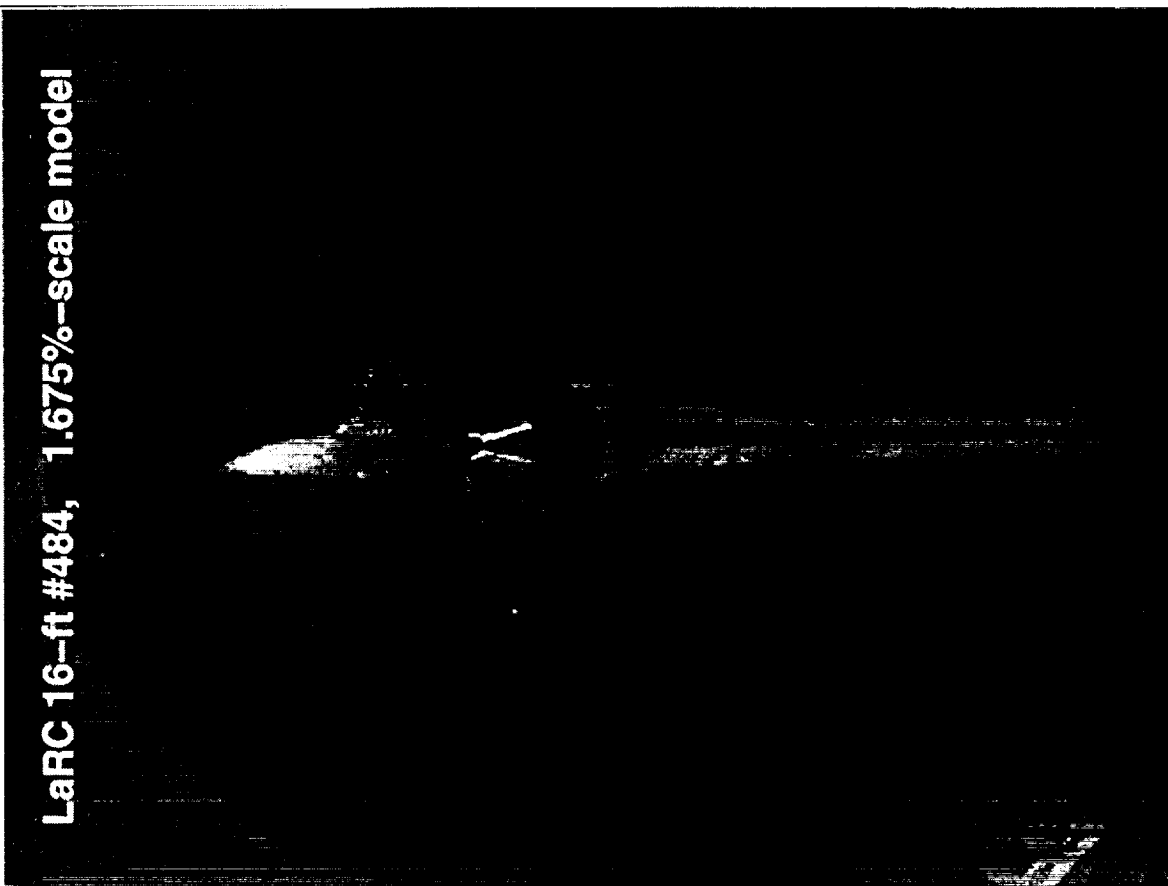


The CFD validation data was from the wind tunnel test of the baseline TCA model 2a at the NASA Langley 16-ft transonic wind tunnel data. Test #484 was four weeks long and began on October 15, 1996. A total of 209 runs were completed during approximately 304 hours of occupancy time. Force data were acquired for the baseline, flaps-up configuration, as well as, for combinations of leading edge (+4, +8, +10 deg.) and trailing edge (+3 and +6 deg.) outboard flap deflections over a range of Mach numbers (0.3 to 1.2). Pressure data were acquired for the baseline configuration (zero flap deflection) only. Short and near term repeatability were very good over the entire Mach range with 80% confidence intervals at or below 0.50 drag counts. The nose, wing upper and lower leading edge, and nacelle external and internal leading edge, had trip discs applied to induce boundary layer transition to turbulent flow. The nacelles had flow-through constant area internal ducts for which skin friction drag values were calculated pre-test and applied to the test data in order to obtain an external only drag values.

The data used for the OVERFLOW validation were the baseline zero flap deflection data at Mach 0.90, 0.95, and 1.20, with and without the nacelles.



Baseline TCA Transonic Validation Test Data





February 1998 HSR Airframe Technical Review

HSCT High Speed Aerodynamics - BCAG



OVERFLOW grids of the TCA wing/body and wing/body/nacelle/diverter were built for the test condition described in the previous page. Some of the geometry details are outlined in the chart given here. The OVERFLOW cases were all run with the Spalart-Allmaras turbulence model.



Baseline TCA OVERFLOW Validation Analyses

- **Geometry W/B, W/B/N/D**
 - Flow-through internal duct**
 - Wing upper surface nacelle bump on**
 - Outboard wing LE, nacelle lip, infinitely sharp**
 - Wing LE planform break transition in 1 inch**
 - No nozzle flap extensions (flat base as on WT model)**
 - No nozzle flap deflections (reference configuration)**
 - No outboard flap deflections**
 - No wind tunnel walls**
- **NASA LaRC 16-ft WT Reynolds Number (~ 4 million/ft)**
 - **$\Delta y \sim 0.003$ inches, $y^+ \sim 0.6$**
- **Spalart–Allmaras turbulence model**
- **No-slip walls are all turbulent**
- **Central difference**
- **Multi-gridding**

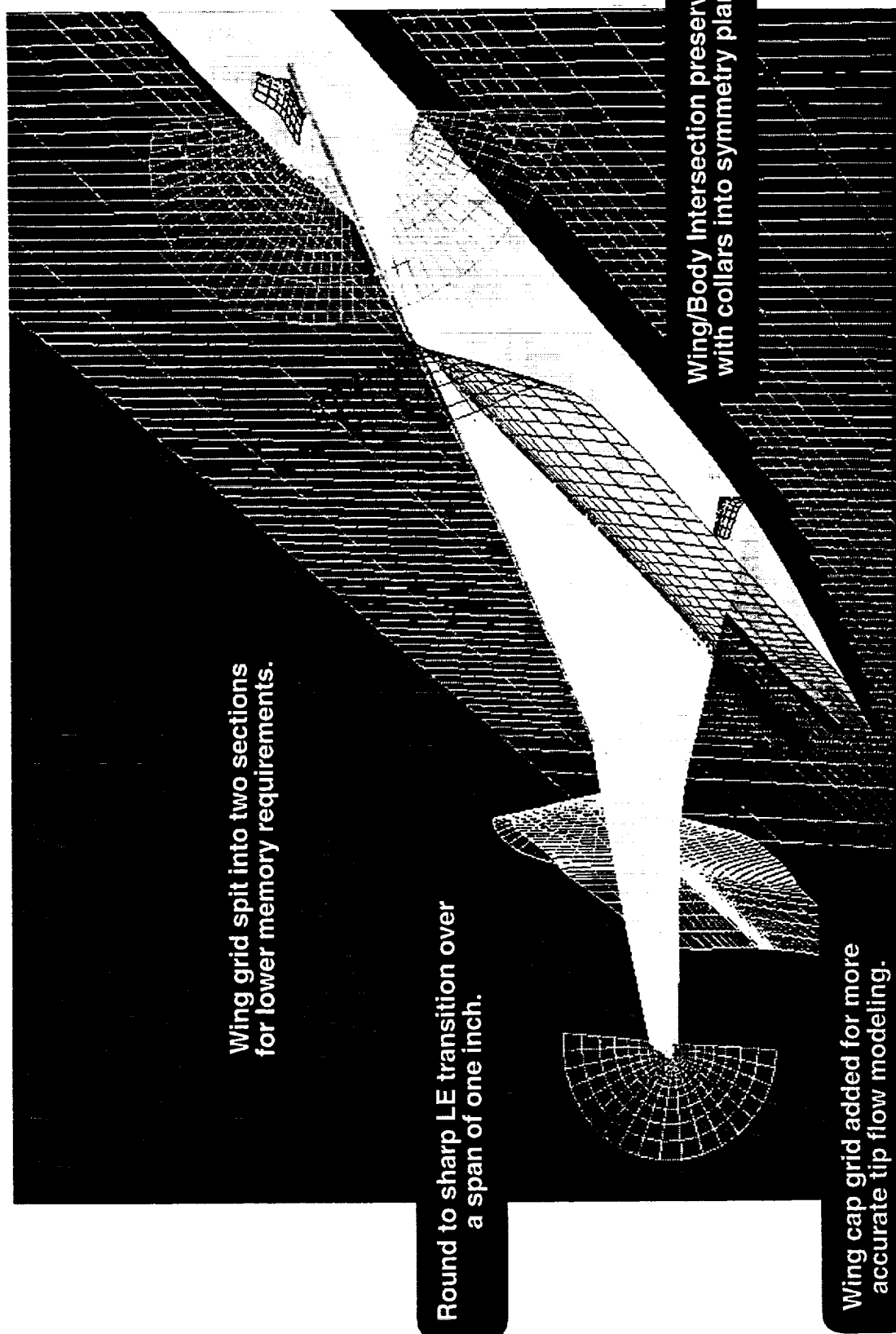


The OVERFLOW wing/body grid for the TCA configuration is shown. The topology was atypical in that there are two collars connecting the wing and the body, instead of the usual one. This was due to the fact that the TCA wing/body intersection line was not continuous. The wing lower surface actually crossed the symmetry plane below the body so that the intersection lines end on the symmetry plane. Collars were built to follow these intersection lines; the collars overlapped aft of the wing TE instead of forming the usual C-grid wake boundary condition. The wing, body, and collar grids were surrounded by a single box grid and an outer boundary ellipsoid grid.

For the 1997 transonic work several modifications were made to the grid. The wing grid was split just inboard of the planform break to reduce the size of the largest grid and therefore reduce memory requirements. This often resulted in faster movement through the queue when larger memory jobs were waiting ahead of the OVERFLOW TCA job. The actual wing tip geometry was modeled with a cap grid. Previously the wing grid had just been extended spanwise and a c-grid averaging boundary condition used. The wing tip cap grid was included in order to insure the most accurate communication of data between the upper and lower surface. All grid to grid communication regions were double-fringed and the minimum interpolation quality was increased from 0 to 0.3.



TCA Wing/Body OVERFLOW Grid



Wing grid spit into two sections
for lower memory requirements.

Round to sharp LE transition over
a span of one inch.

Wing cap grid added for more
accurate tip flow modeling.

Wing/Body Intersection preserved
with collars into symmetry plane.

Grid points removed for clarity



The OVERFLOW TCA wing/body grid had 4.2 million grid points for the LaRC 16-ft wind tunnel condition. The grid stretching strategy from the surface developed on Reference H OVERFLOW analyses of using 3 equally spaced cells was employed on the TCA configuration as well. The wing had 106 points chordwise on the upper and lower surfaces. A stretching ratio limit of 1.2 was adhered to strictly.



TCA Wing/Body OVERFLOW Grid Dimensions Transonic Wind Tunnel Condition Analysis

Component	j _{max}	k _{max}	l _{max}	points
Body	208	91	57	1,078,896
Wing1	271	66	54	965,844
Wing2	271	45	54	658,530
Cap	163	37	63	379,953
Collar1	221	25	45	248,625
Collar2	53	25	45	59,625
Box	220	52	64	732,160
Ellipsoid	78	45	31	108,810
TOTAL				4,232,443

NASA LaRC 16 ft, Mach 0.3 to 1.2, Re/ft = 4 million,

Test 484, 1.675%-scale, Re_{MAC} = 6.1 million,

PIE test, 3.0 %-scale, Re_{MAC} = 11 million,

$$y^+ = 0.6 \rightarrow dy_{\text{surface}} = 0.003 \text{ in.}$$

$$y^+ = 1.0 \rightarrow dy_{\text{surface}} = 0.003 \text{ in.}$$

NOTES:

Three equidistant points from surface.

Stretching ≤ 1.2

Wing surface has 106 points from LE to TE:

$\Delta s_{LE} = .01\%$ to $.02\%$ chord, $\Delta s_{TE} = .4\%$ to $.5\%$ chord.



February 1998 HSR Airframe Technical Review



HSCT High Speed Aerodynamics - BCAG

The OVERFLOW gridding around the nacelles is shown. Each nacelle requires 7 additional grid blocks. Three blocks to do the nacelle external and internal geometry, two blocks on either side of the diverter, fairing grid spanning the wing TE and upper nozzle area, and a box grid (fitted to wing lower surface) to help tie all the blocks together. The nacelle leading edge lips were modeled by overlapped external and internal grid blocks that started forward of the lip by about 20 inches. A single grid block wrapped around the nacelle base region. The grid blocks on either side of the diverter overlapped ahead of the diverter LE and protruded forward ahead of the nacelle LE.

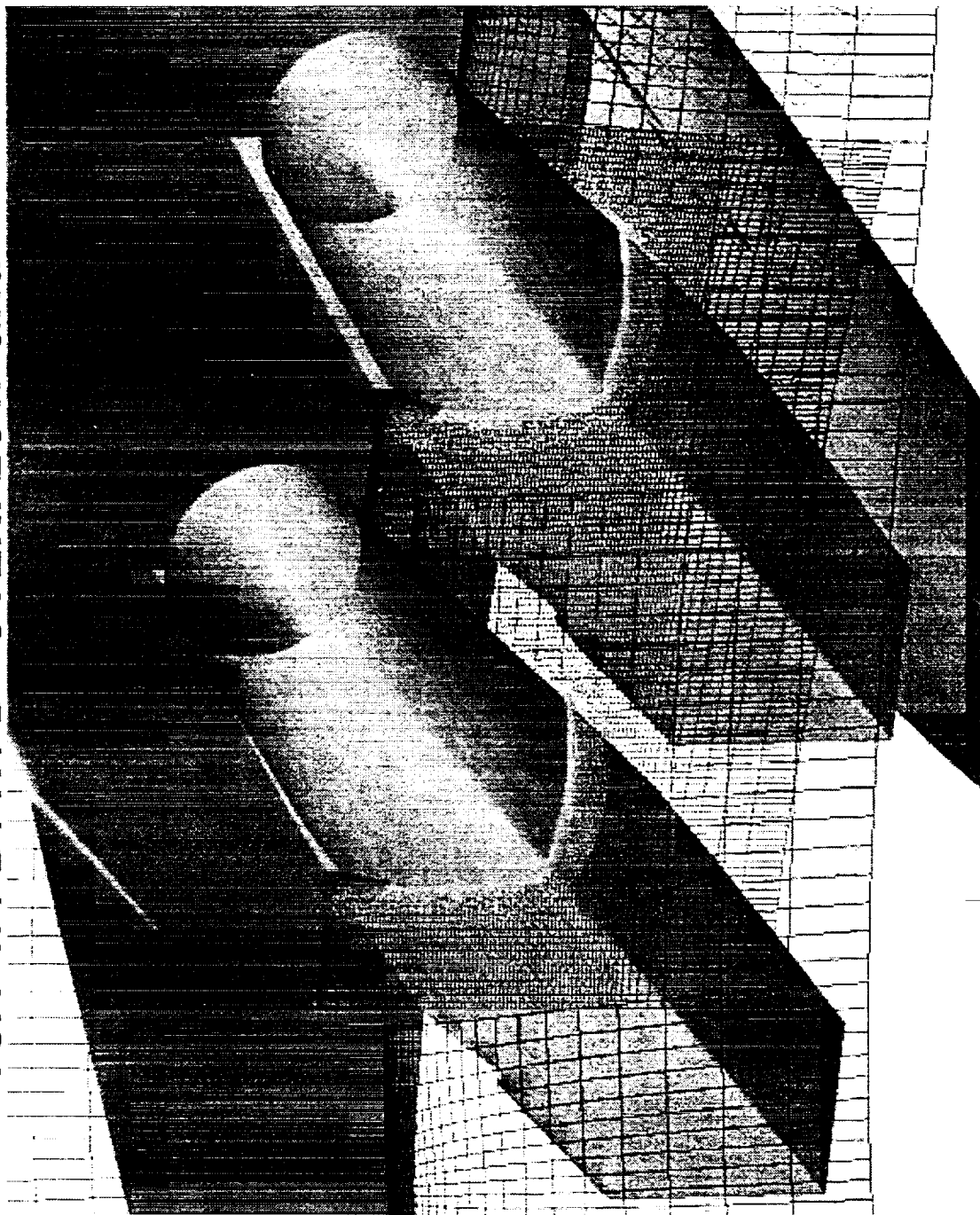


February 1998 HSR Airframe Technical Review



HSCT High Speed Aerodynamics - BCAG

TCA W / B / N / D OVERFLOW GRID





February 1998 HSR Airframe Technical Review



HSCT High Speed Aerodynamics - BCAG

Each nacelle added a total of 4.3 million grid points, yielding a total wing/body /nacelle/diverter grid size of 12.9 million points for the flow-through internal duct configuration.



TCA Wing/Body/Nacelle/Diverter OVERFLOW Grid Dimensions Transonic Wind Tunnel Condition Analysis

Component	l_{\max}	k_{\max}	l_{\max}	# points
Wing/Body INBOARD	-	-	-	4,232,443
Nacelle Box	131	67	107	1,269,918
Nac Cowl	80	161	45	586,845
Nac Nozzle A	47	161	45	340,515
Nac Nozzle B	30	161	45	217,350
Nac Internal	57	161	45	412,965
Diverter Left	176	45	73	581,445
Diverter Right	176	45	73	581,445
Div Fairing	113	59	45	300,015
OUTBOARD	-	-	-	4,259,988
Nac / Div	-	-	-	12,861,795
TOTAL				

NASA LaRC 16 ft, Mach 0.3 to 1.2, $Re/ft = 4$ million,

Test 484, 1.675%-scale, $Re_{MAC} = 6.1$ million,

PIE test, 3.0 %-scale, $Re_{MAC} = 11$ million,

$$y^+ = 0.6 \rightarrow dy_{\text{surface}} = 0.003 \text{ in.}$$

$$y^+ = 1.0 \rightarrow dy_{\text{surface}} = 0.003 \text{ in.}$$

NOTES: Three equidistant points from surface.
Stretching ≤ 1.2



February 1998 HSR Airframe Technical Review

HSCAT High Speed Aerodynamics - BCAG



The residual and force history for a typical transonic OVERFLOW run are shown. This particular case was run out past 2300 steps. The runs were usually stopped at 1800 steps where 3 orders of magnitude residual reduction was achieved for all 24 grid blocks, the lift was varying less than 0.1 % over the last 100 steps, and both pressure and viscous drag were varying less than 0.1 drag count over the last 100 steps.

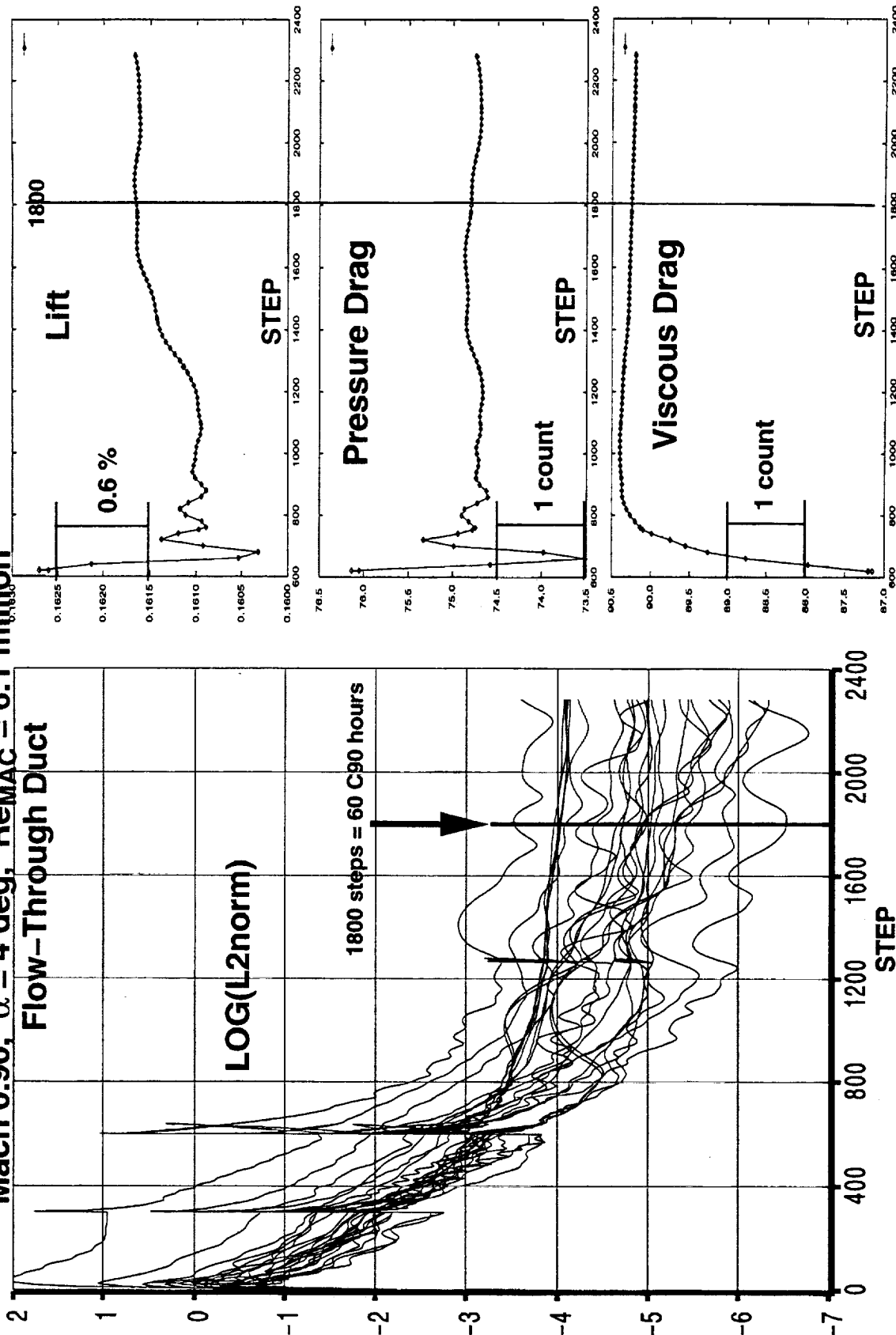


HSCT High Speed Aerodynamics - BCAG

OVERFLOW W/B/N/D Transonic Convergence

Mach 0.90, $\alpha = 4$ deg, $Re_{MAC} = 6.1$ million

Flow-Through Duct



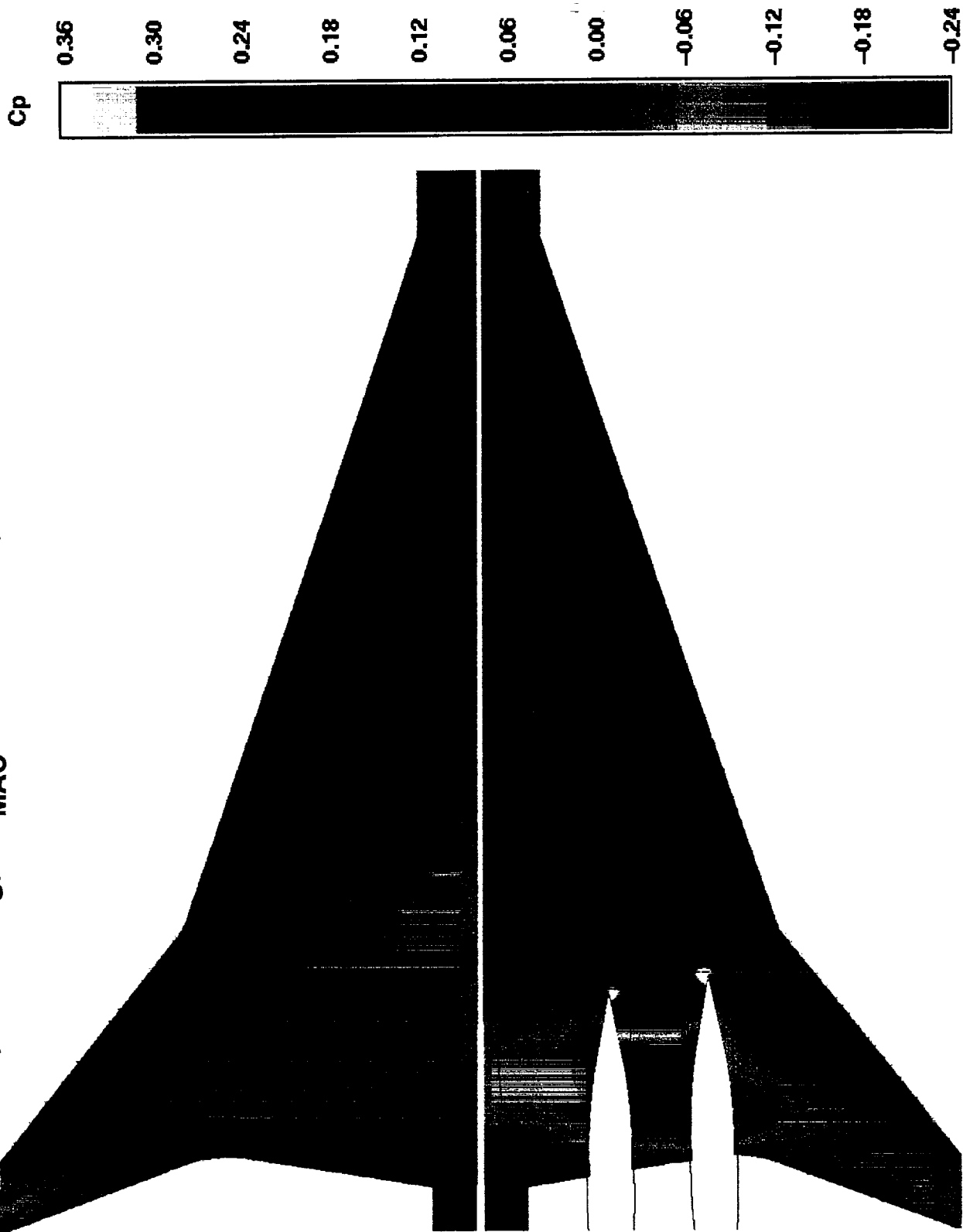


The wing lower surface pressure distribution from the OVERFLOW analysis of the TCA at transonic cruise is shown. The forward extent of the nacelle pressure field can be clearly seen when compared to the nacelles-off case. Other features to note are the increased positive and negative pressures between the nacelles (when compared to the opposite sides of either the inboard or outboard nacelles) due to mutual interference between the two nacelles. The positive pressure field from the nacelles extended spanwise to such an extent that it impinged on the wing leading edge and wrapped around to effect the upper surface pressures (plots illustrating this will be shown later).



HSCT High Speed Aerodynamics - BCAG

TCA Wing/Body/Nacelle/Diverter Wing Pressure Contours
Mach 0.90, $\alpha = 4$ deg, $Re_{MAC} = 6.1$ million, OVERFLOW Solutions





February 1998 HSR Airframe Technical Review

HSCT High Speed Aerodynamics - BCAG



Nacelle region close-up

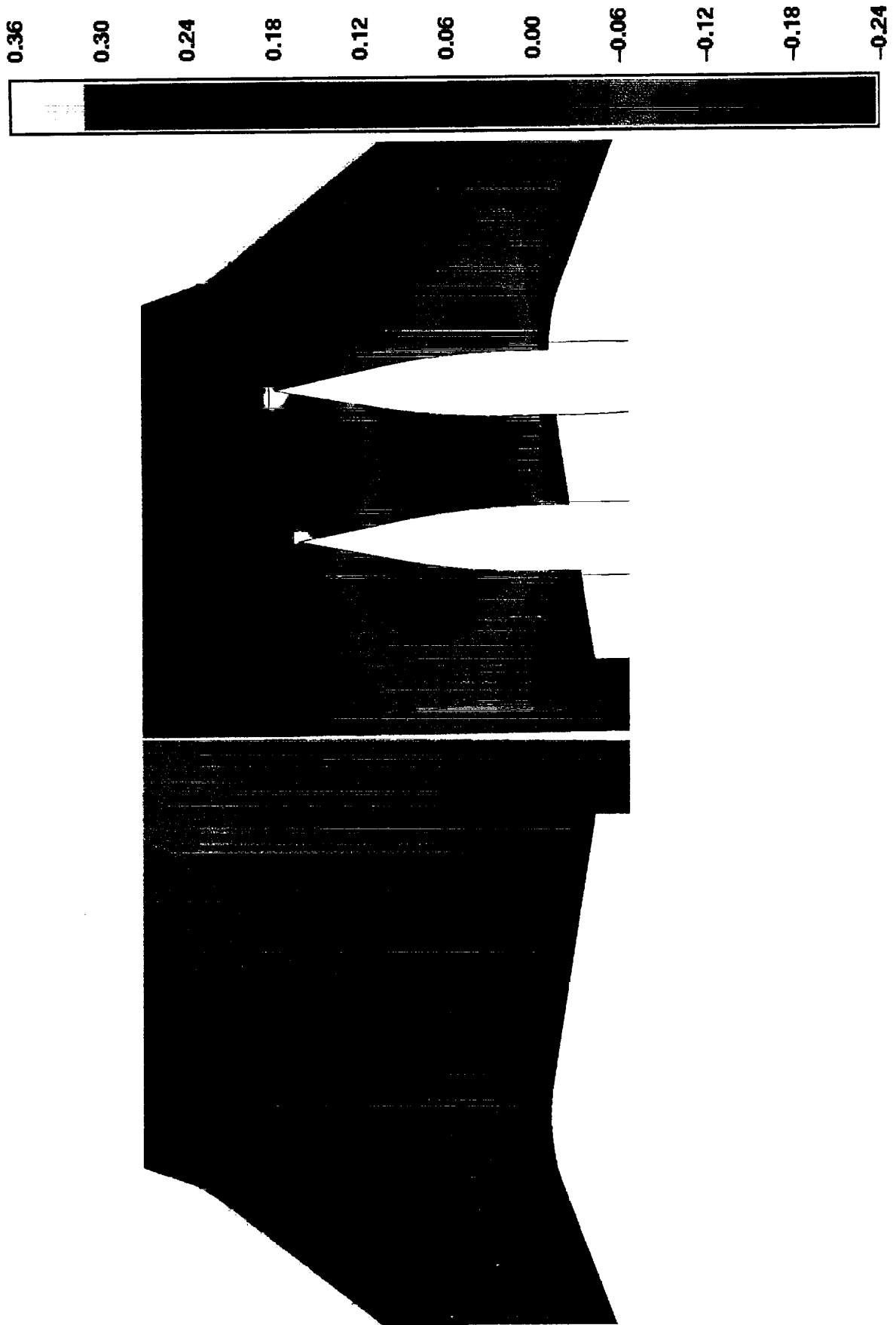
---See text for previous page---



HSCT High Speed Aerodynamics - BCAG

**TCA Wing/Body/Nacelle/Diverter Wing Pressure Contours
Mach 0.90, $\alpha = 4$ deg, $Re_{MAC} = 6.1$ million, OVERFLOW Solutions**

Cp





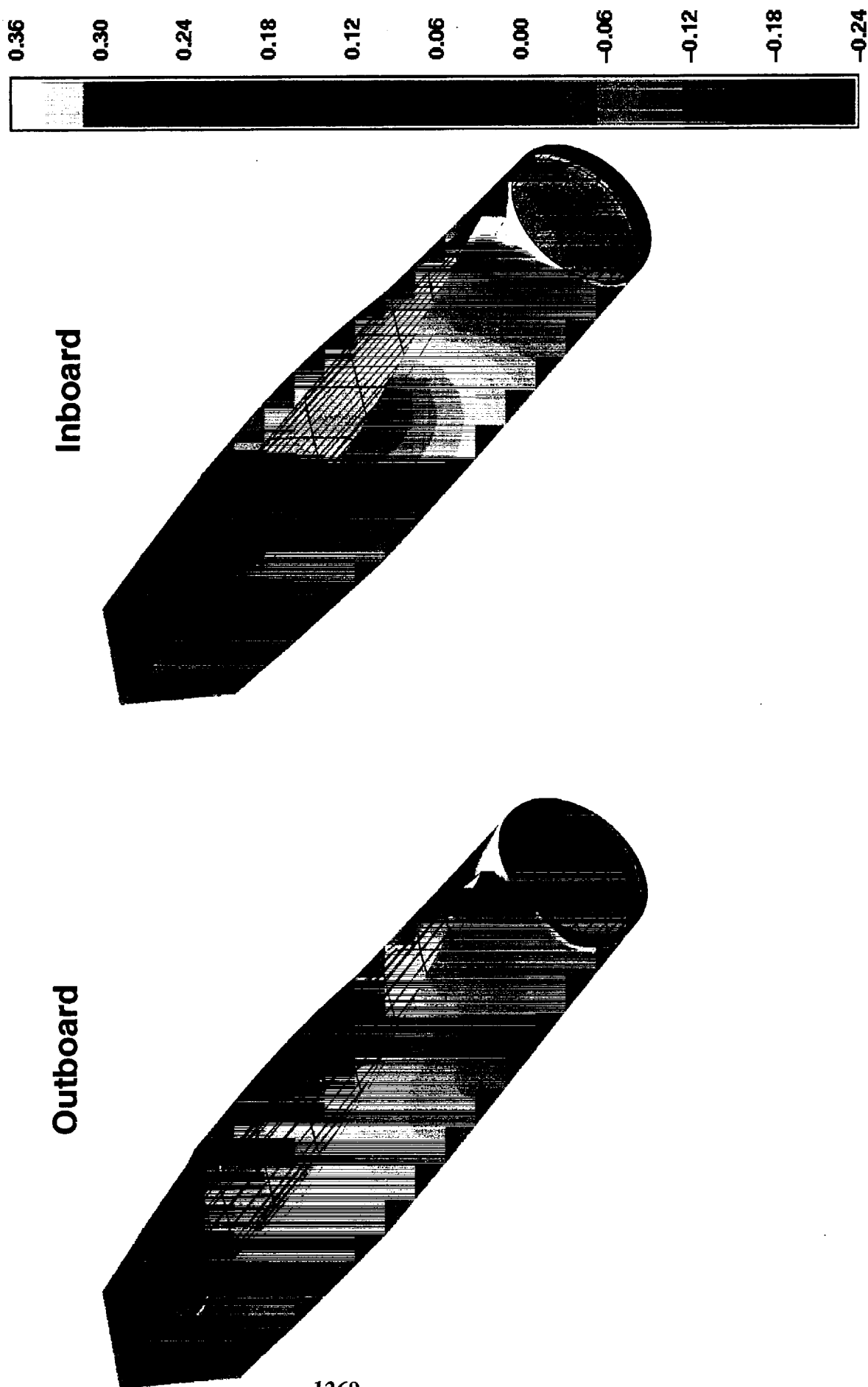
The nacelle/diverter surface pressure distribution from the Mach 0.9 OVERFLOW solution is shown here. Only the external surface pressures are shown; the pressures seen through the internal duct grid are external surface pressures. The increased positive pressures on the side toward the adjacent nacelle are clearly evident, as is a region of negative pressure around a large portion of the lip of each nacelle. This was evidence of the internal duct spilling. All though the duct was constant area and flow-through, the boundary layer buildup resulted in the duct choking and as a result spilling around the inlet lip resulting in an expansion field. An interesting feature was the non-symmetric characteristics of this phenomenon. No inlet flow was spilled at the crown of the nacelle. The spill rate was also reduced on the nacelle lip side toward the adjacent nacelle where the local external pressures were increased due to the mutual interference discussed earlier. A mass flow measurement plane was inserted into the internal duct in order to measure the inlet flow rate from the CFD solution exactly; the results are shown in the next figure.



**TCA Wing/Body/Nacelle/Diverter Nacelle Pressure Contours
Mach 0.90, $\alpha = 4$ deg, $Re_{MAC} = 6.1$ million, OVERFLOW Solution**

Outboard

Inboard



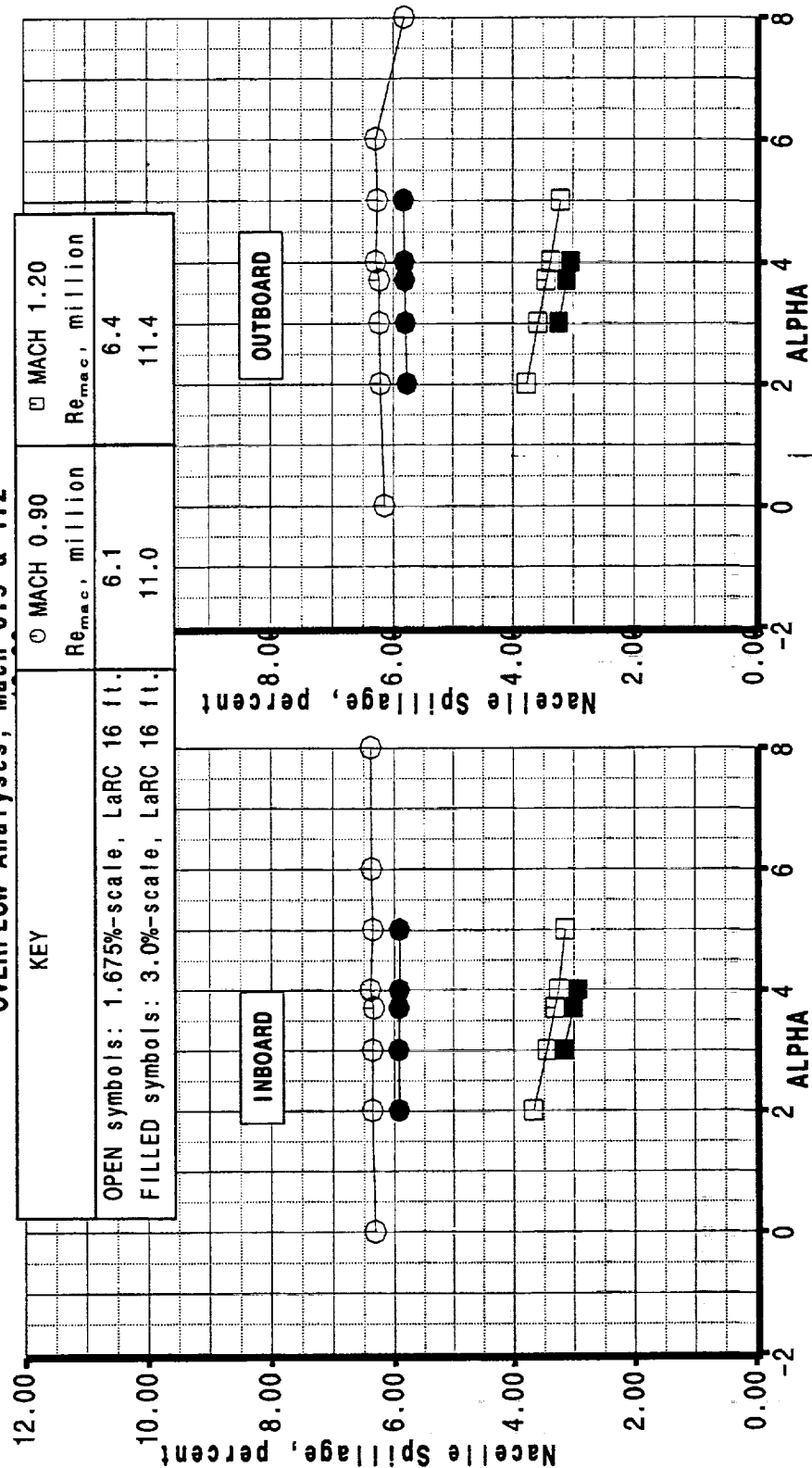


The spill rates for the inboard and outboard nacelles for all the OVERFLOW analyses of the flow-through duct configuration are shown. At Mach 0.9 the analyses indicated that the 1.675%-scale model was spilling about 6.2 %, with very little variation with angle of attack. The filled symbols show the spill rate for a slightly higher Reynolds Number corresponding to a 3%-scale TCA in the LaRC 16-ft tunnel. As expected, the higher Reynolds Number thinned the boundary layer enough that a measurable reduction in spill was achieved. The Mach 1.20 analyses indicated a reduced spill rate around 3% and slightly more variation with angle of attack.



TCA Nacelle Spillage (Wind Tunnel Flow-Through Duct)

OVERFLOW Analyses, Mach 0.9 & 1.2



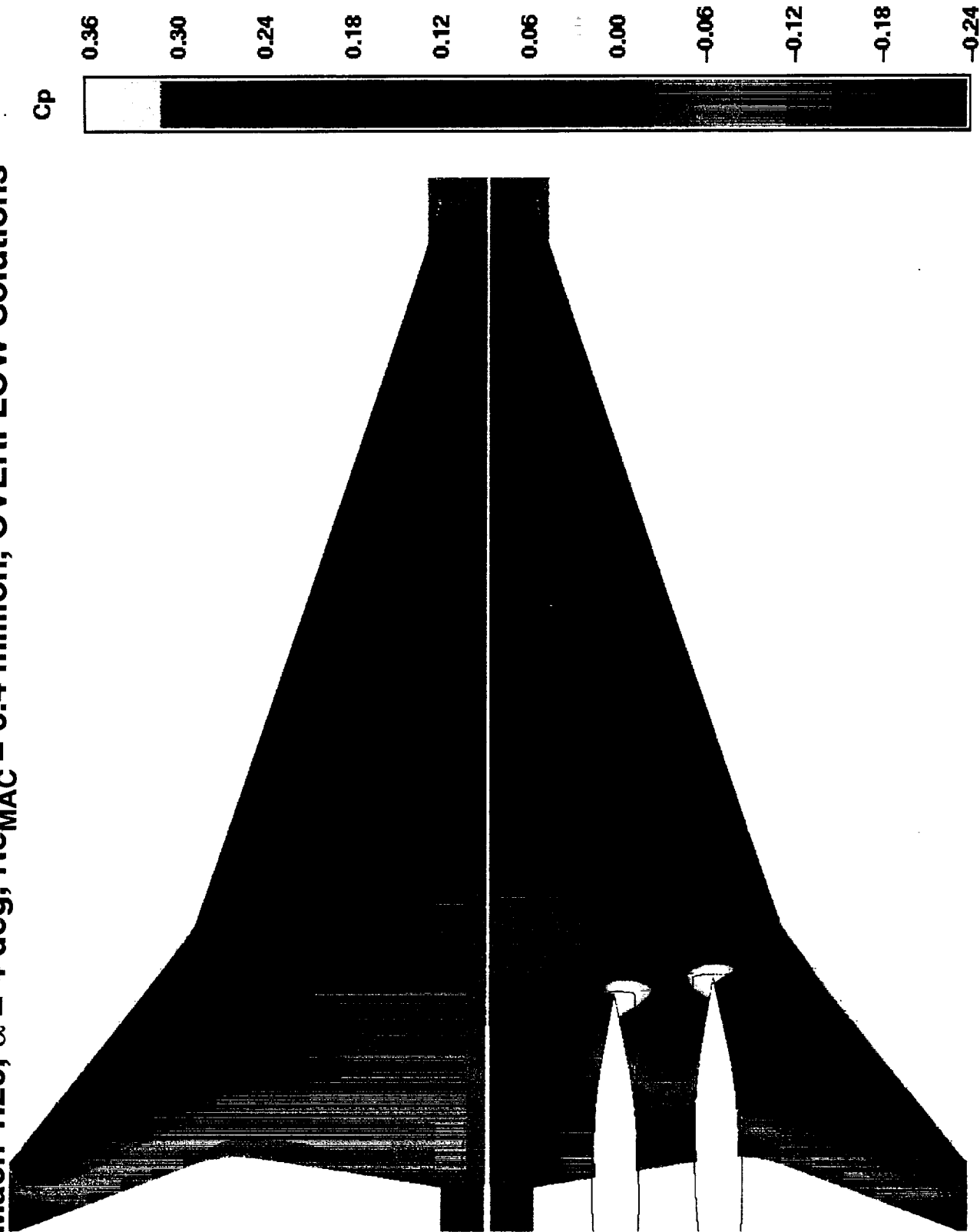


The wing lower surface pressure distribution from the OVERFLOW analysis of the TCA at transonic climb is shown. A comparison to the Mach 0.90 pressure distribution discussed earlier indicated the expected result for this supersonic Mach Number of a much reduced forward extent area of the nacelle pressure field. The positive pressures around the forward part of the nacelle were increased in both magnitude and spanwise area of influence when compared to the Mach 0.9 data, probably due to the presence of normal shocks. The spanwise influence of the nacelle positive pressure field extended all the way across the body and to the wing leading edge.



HSCT High Speed Aerodynamics - BCAG

TCA Wing/Body/Nacelle/Divorter Wing Pressure Contours Mach 1.20, $\alpha = 4$ deg, $Re_{MAC} = 6.4$ million, OVERFLOW Solutions





February 1998 HSR Airframe Technical Review

HSCT High Speed Aerodynamics - BCAG



Nacelle region close-up

---See text for previous page---



**TCA Wing/Body/Nacelle/Diverter Wing Pressure Contours
Mach 1.20, $\alpha = 4$ deg, $Re_{MAC} = 6.4$ million, OVERFLOW Solutions**





February 1998 HSR Airframe Technical Review



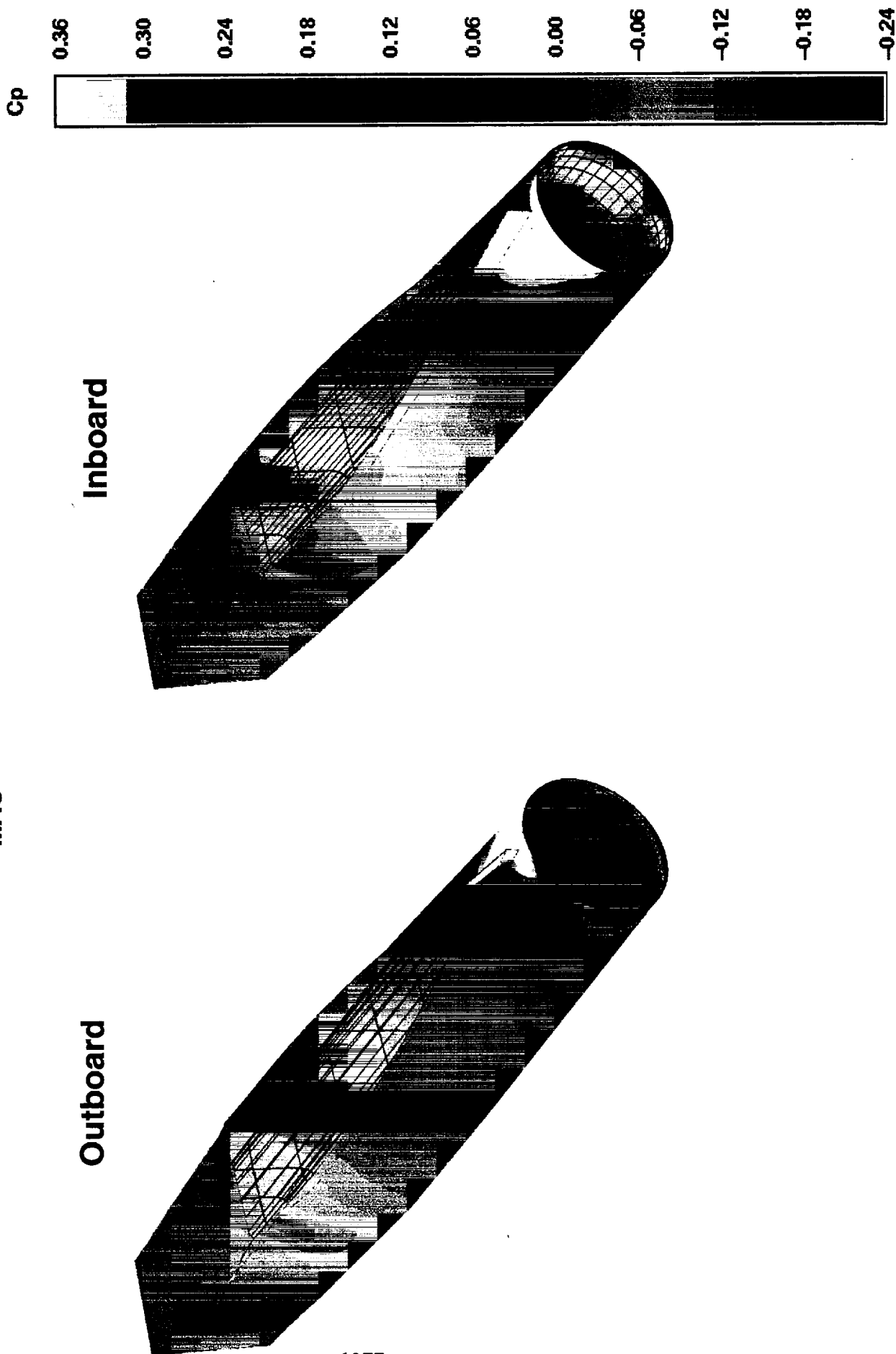
HSCT High Speed Aerodynamics - BCAG

The nacelle/diverter surface pressure distribution from the Mach 1.2 OVERFLOW solution is shown here. Only the external surface pressures are shown; the pressures seen through the internal duct grid are external surface pressures. The asymmetry of the inlet lip spill flow was even more pronounced than for the Mach 0.9 case discussed earlier (although the spill rate is lower as shown in the earlier plot: 3% compared to 6%).



HSCT High Speed Aerodynamics - BCAG

**TCA Wing/Body/Nacelle/Diverter Nacelle Pressure Contours
Mach 1.20, $\alpha = 4$ deg, $Re_{MAC} = 6.4$ million, OVERFLOW Solution**





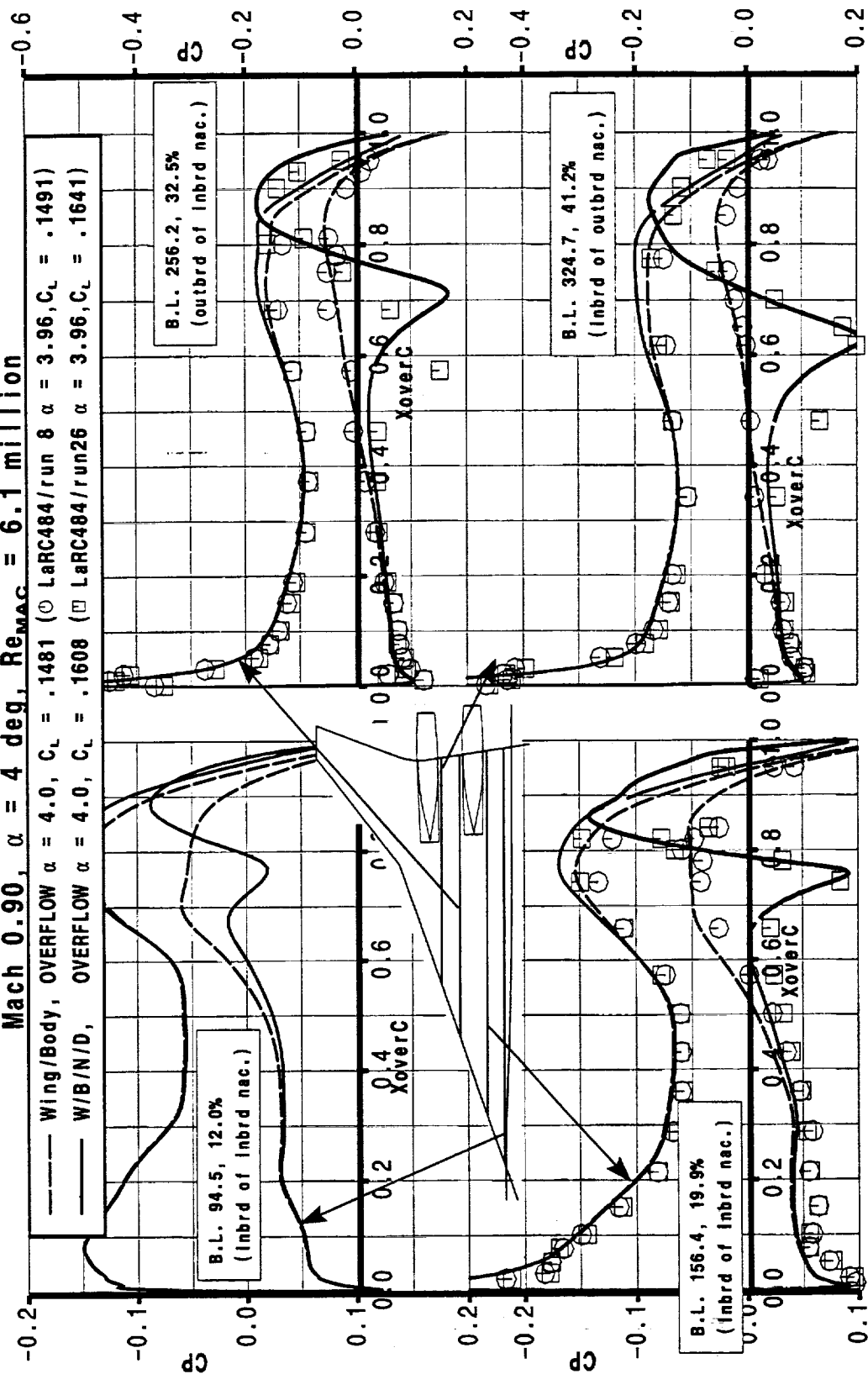
The next two figures show the wing pressure coefficient distribution at the transonic cruise condition of Mach 0.9 compared to the test data. The computational predictions appear to adequately match the test data (but not quite as well as has been reported previously for supersonic comparisons) except at two locations on the wing lower surface. Pressure taps on the wing lower surface ahead of the nacelles at $Y = 256$ and 324 inches indicated a higher positive pressure than OVERFLOW is predicting. These results were identical to those shown by Steve Krist (of NASA LaRC) at the February 1997 workshop. Examination of the W/B pressure data in this same region indicated some erratic behavior in a region that should be relatively smooth. Location of these pressures on the pressure contour plots shown earlier indicated the magnitude of the flow phenomena that would be need to be occurring for these pressures to be real. The consensus of the HSR community is that this phenomena was the result of a pressure measurement problem.

Although there are some regions where the absolute pressure prediction was slightly off, in almost all cases the incremental pressure of the nacelles was still captured very accurately.



TCA Wing/Body/Nacelle/Diverter Chordwise Pressure Distributions

Mach 0.90, $\alpha = 4$ deg, $Re_{MAC} = 6.1$ million





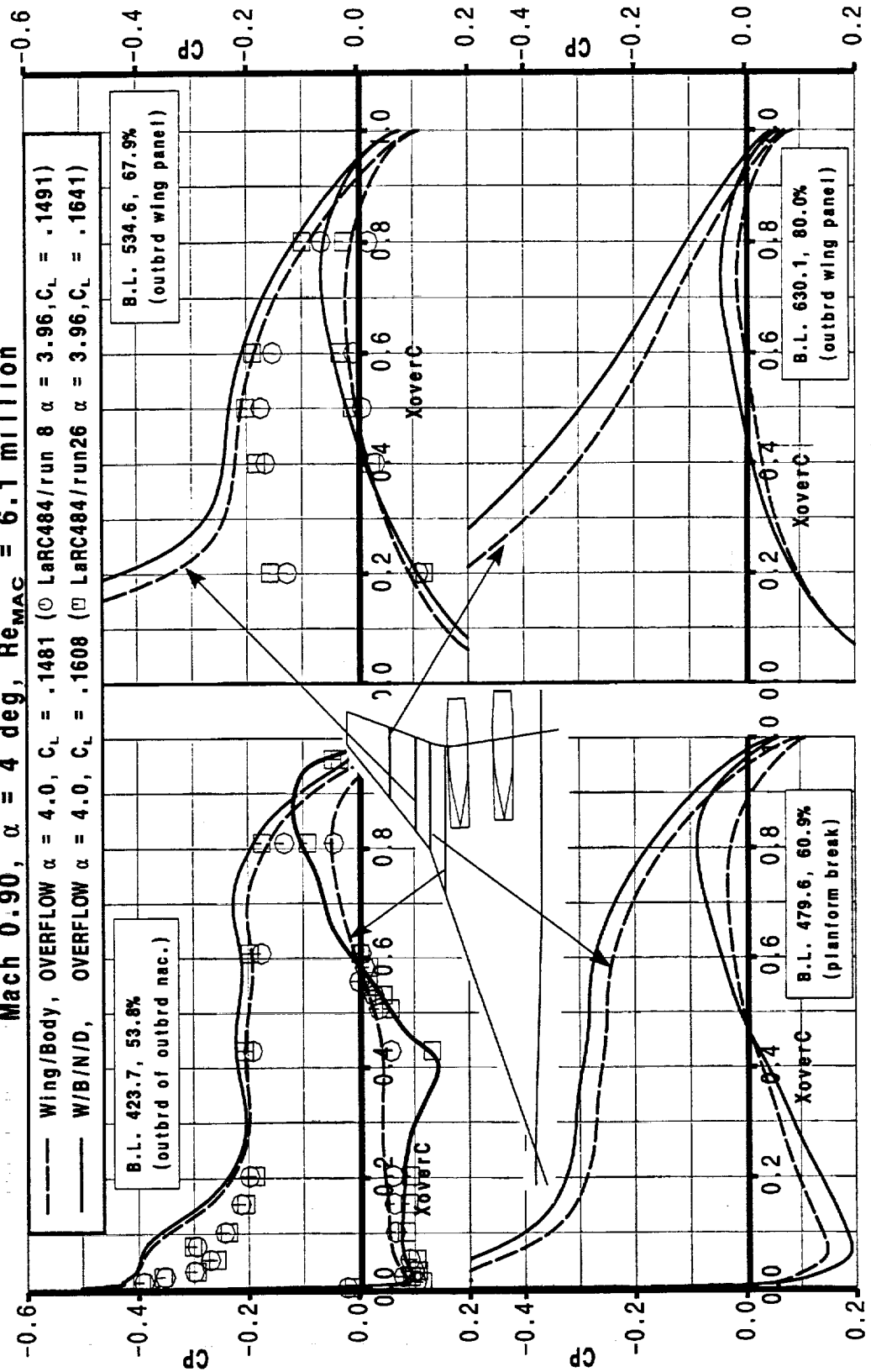
It was interesting to note the very large effect the nacelles had on the outboard wing panel; the negative C_p level of the upper surface appears to be raised from LE to TE outboard of the planform break. A discrepancy between test and analysis that was consistent with other HSR team member computations of the same condition was the pressure predictions on the upper surface of the wing outboard panel. The CFD data indicated a large region of negative pressure extending aft to 30 % chord at BL534.6; the test data showed no indication of this phenomena. It was anticipated that the wing leading edge (outboard panel) would be separated at this condition with the zero-flap-deflection configuration. The actual flight airplane will have the flaps deflected to maintain attached flow on the outboard panel.



HSCT High Speed Aerodynamics - BCAG

TCA Wing/Body/Nacelle/Diverter Chordwise Pressure Distributions

Mach 0.90, $\alpha = 4$ deg, $Re_{MAC} = 6.1$ million





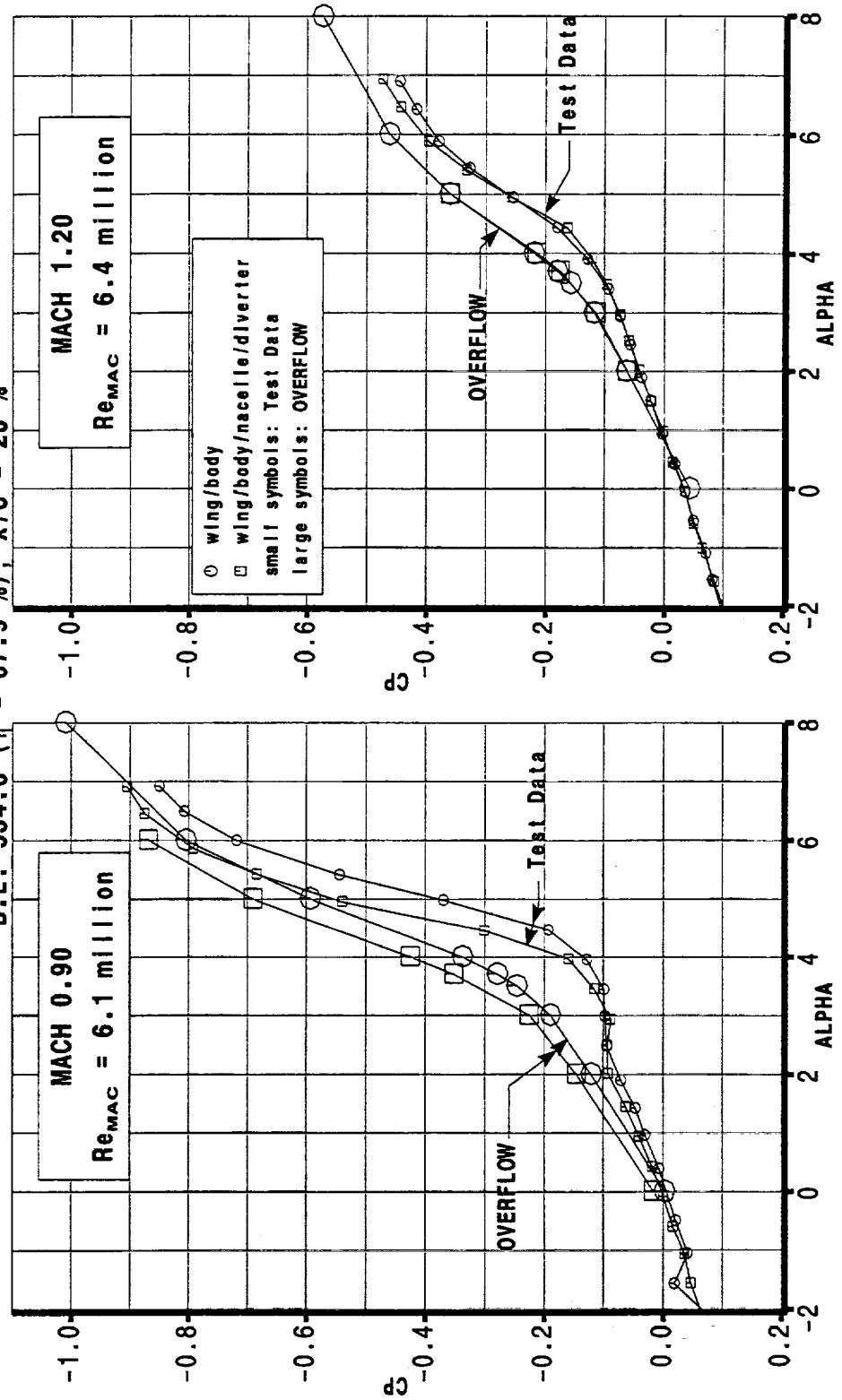
OVERFLOW pressure data was extracted at the 20% X/C location on the B.L.534.6 chordwise cut to match the pressure tap location on the wind tunnel model. The results are plotted here versus angle of attack for the both Mach 0.90 and 1.20. Based on the change of slope of the curves it appeared that the OVERFLOW calculations were predicting the separation at the leading edge at a lower angle of attack than occurred in the wind tunnel test (~ 3 deg vs 4 deg). So that at the angle of attack for which the previous pressure distributions were shown (4 deg) the leading edge separation bubble in the test data had not yet reached the pressure port. The data shown here indicate that between this alpha of 4 deg and a value of 4.8 the test data pressure changed rapidly to the level predicted by the OVERFLOW simulation as the separation bubble reaches the port. It is also possible that the OVERFLOW simulation and the test had the separation occur near the same angle of attack but the separation bubble in the test grew in the chordwise direction more slowly. Areas of investigation for resolving this discrepancy are:

- 1) Sharp leading edge grid topology. Currently using a c-grid around the LE which undoubtedly induces numerical error due to the skewing necessary to make a grid do this. Overlapping upper and lower surface grids similar to the nacelle sharp LE gridding are an option.
- 2) Turbulence model. Its not clear that a different turbulence model would effect the sharp LE separation, but it very likely could effect reattachment location (the size of the separation bubble).
- 3) Aeroelastic deflection of the wind tunnel model outboard panel leading to unloading could be effecting the separation characteristics.



**TCA W/B & W/B/N/D Pressure Coefficient Aft of Sharp Leading Edge
OVERFLOW vs Test Results**

B.L. 534.6 ($\eta = 67.9\%$), $X/C = 20\%$





February 1998 HSR Airframe Technical Review



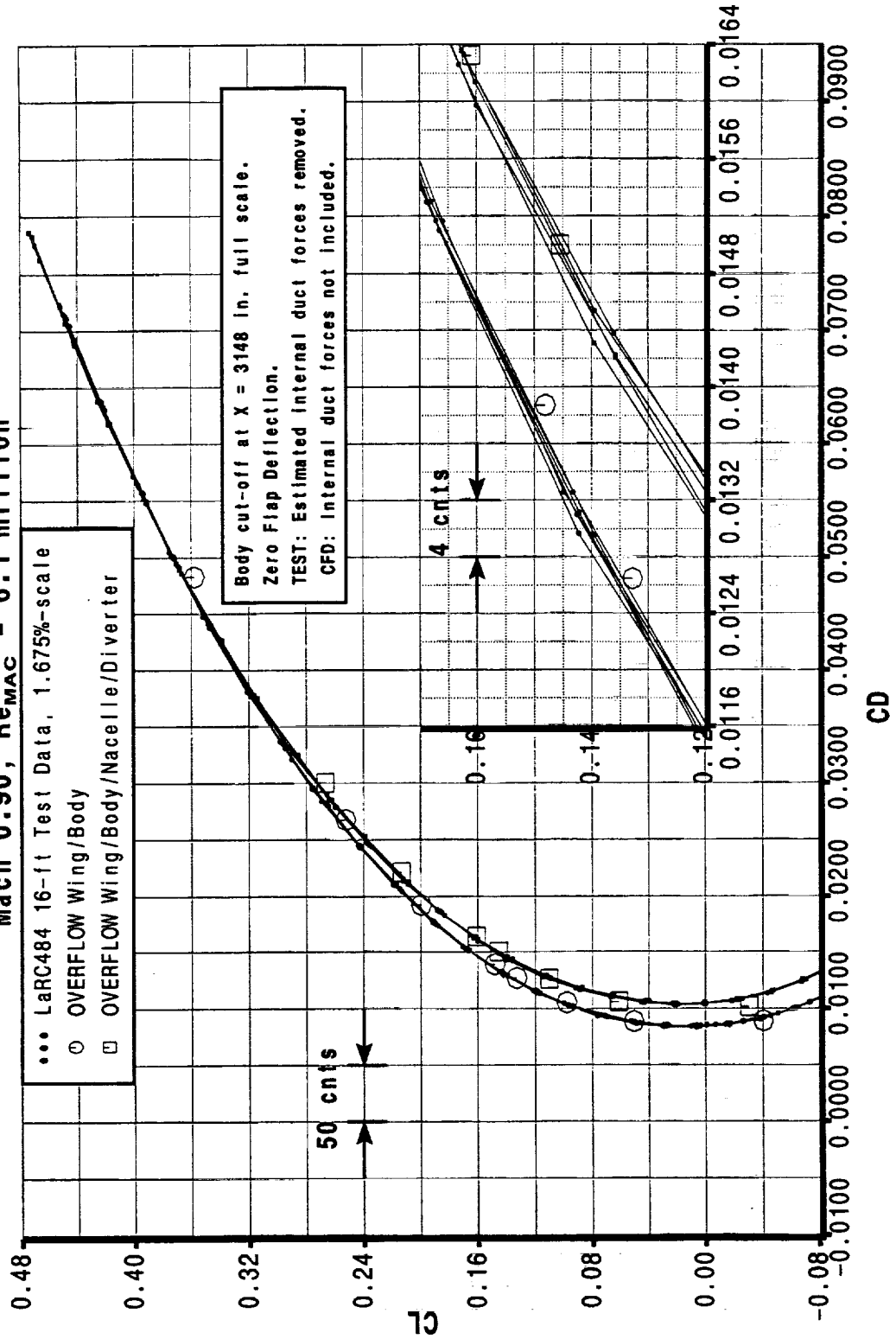
HSCT High Speed Aerodynamics - BCAG

The TCA drag polar for Mach 0.9 is shown in this figure. The solution data are 1 to 2 counts higher than the test data at the transonic cruise condition.



TCA Wing/Body/Nacelle/Diverter Drag Polar

Mach 0.90, $Re_{MAC} = 6.1$ million

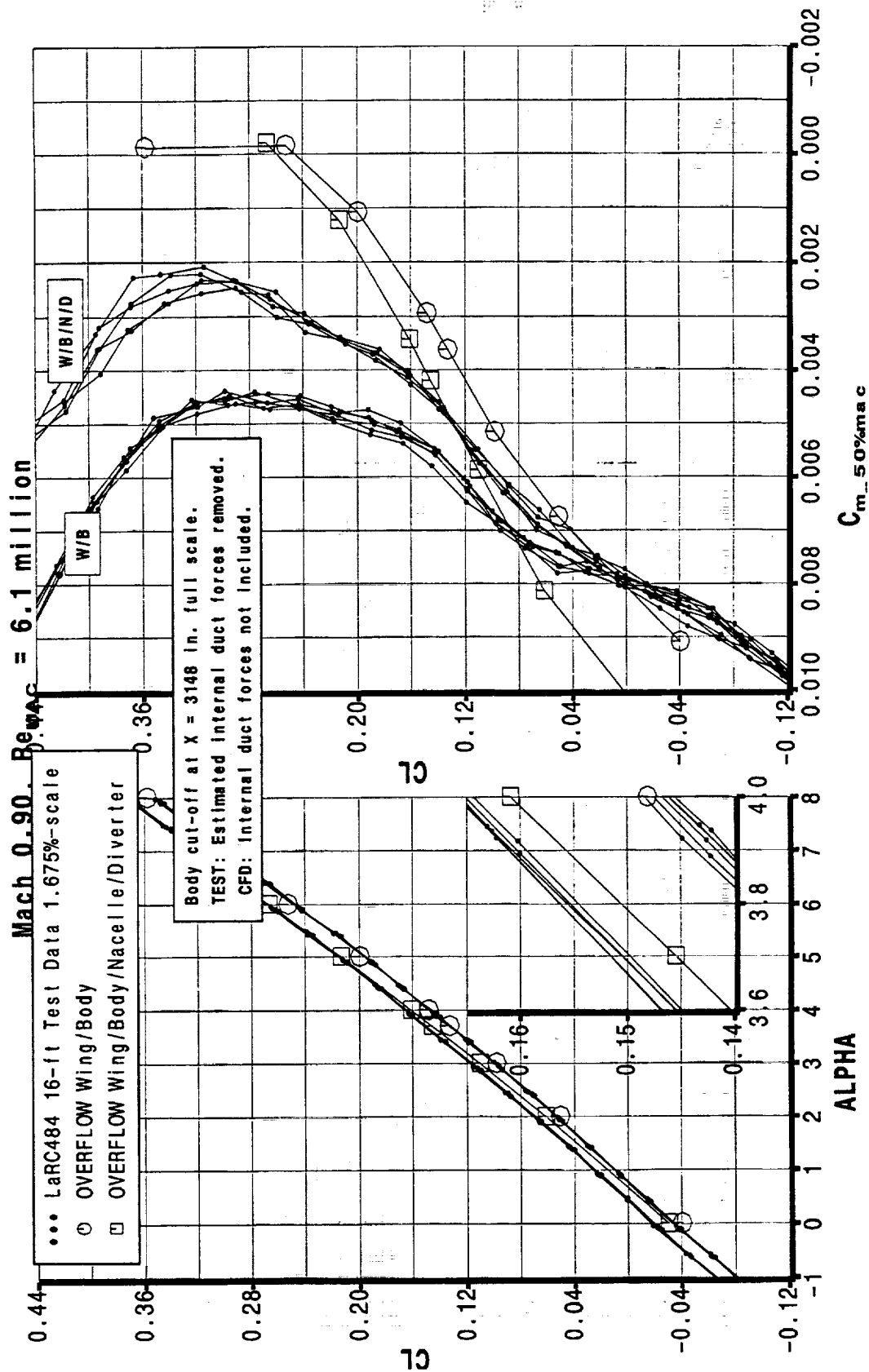




The lift and pitching moment test/CFD comparisons shown in this figure indicated typically good lift curve agreement for the W/B but the OVERFLOW W/B/N/D lift is 3% lower than test. Also, the incremental effects of the nacelles on the pitching moment prediction were substantially different than the test data. The break in the pitching moment curve at angle of attack of 6 degrees appears to have been modeled accurately but at perhaps a slightly lower alpha than for the test data (possible due to premature separation of the sharp LE in the OVERFLOW simulation discussed earlier). The absolute pitching moment predictions also appeared to be rotated from the test data very similarly to that seen in previous supersonic validation studies. Rotating the transonic pitching moment data by the same amount as was tried for the supersonic data (0.013 MAC) yielded very good agreement with test.



TCA Wing/Body/Nacelle/Diverter Lift & Pitching Moment





HSCT High Speed Aerodynamics - BCAG

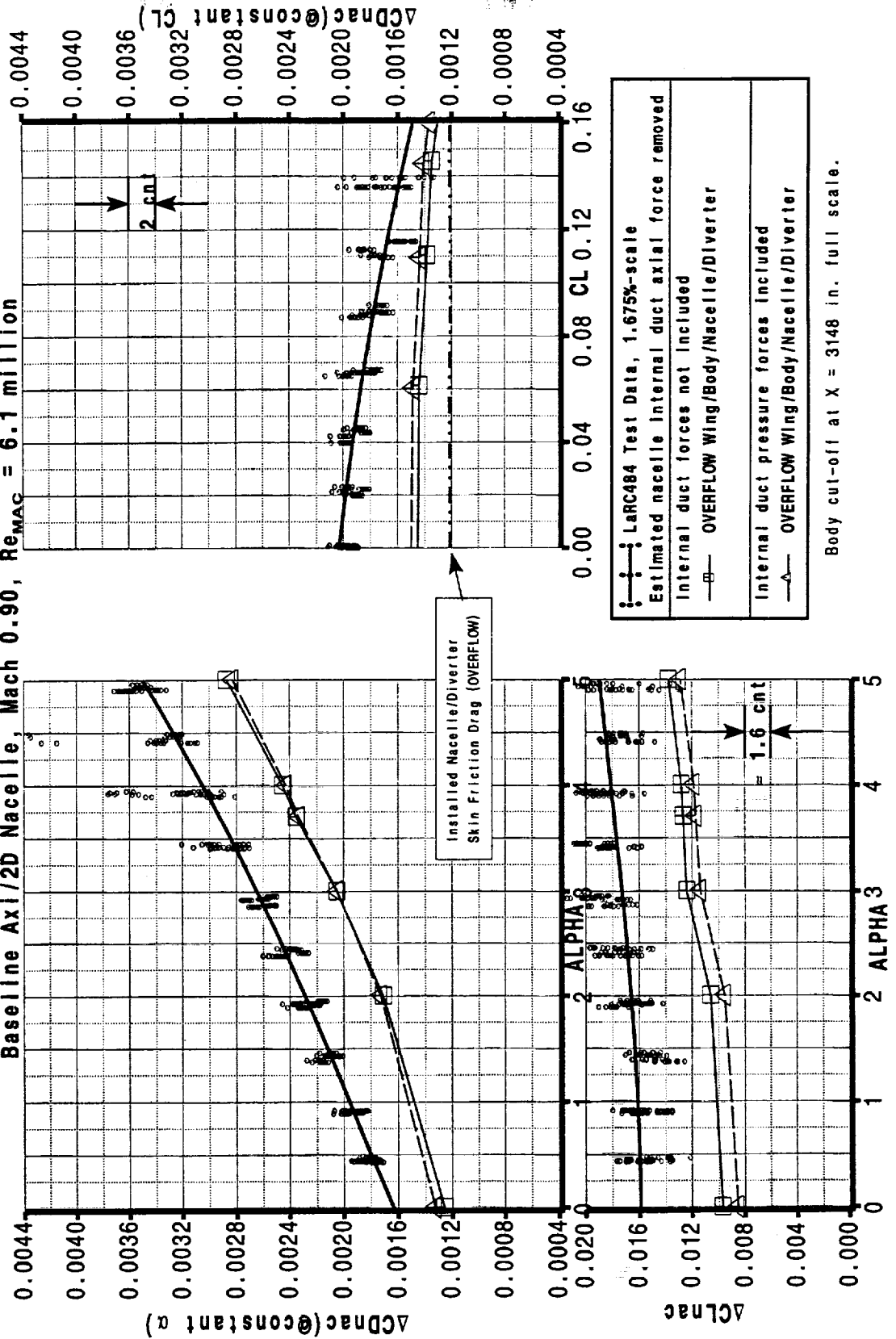
The nacelle/diverter force increments are shown in this figure. On the left, the drag and lift increments at constant angle of attack are shown. The plot on the right shows the final installed drag increment of the nacelle/diverter versus the lift of the wing/body/nacelle/diverter. The OVERFLOW data is shown with and without the internal duct lift included. The test data is shown both as a scatter band and as a curve fit to all data. The scatter data was obtained by simply calculating all deltas combinations possible from the 5 wing/body/nacelle/diverter runs and the 9 wing/body runs. This method gives a rudimentary presentation of the scatter in the data: ± 2.0 counts at transonic cruise.

The OVERFLOW nacelle/diverter drag at constant angle of attack was about 5 counts less than the test data. However, the lift increment was also under-predicted so that the OVERFLOW nacelle/diverter drag at constant lift was less than 2 counts low at the transonic cruise condition ($CL \sim 0.15$). There are several phenomena that could be effecting these comparisons:

- 1) The spillage condition simulated in the OVERFLOW data may not be matching the wind tunnel spillage condition correctly.
- 2) The wind tunnel data did not have the internal duct pressure forces (primarily lift) removed, so the OVERFLOW data was shown with this component included in the data. This effect was worth about 0.6 count.
- 3) The wind tunnel data had estimated internal duct skin friction removed. The next figure compares this estimated term to the OVERFLOW calculated value. There was very little difference; using the same correction for both would move the OVERFLOW nacelle/diverter drag increment 0.13 counts closer to the wind tunnel data.
- 4) The nacelle boundary layer trip drag may be on the order of several counts.



TCA Wing/Body/Nacelle/Diverter PAI Force Increments
Baseline Axi/2D Nacelle, Mach 0.90, $Re_{MAC} = 6.1$ million





February 1998 HSR Airframe Technical Review

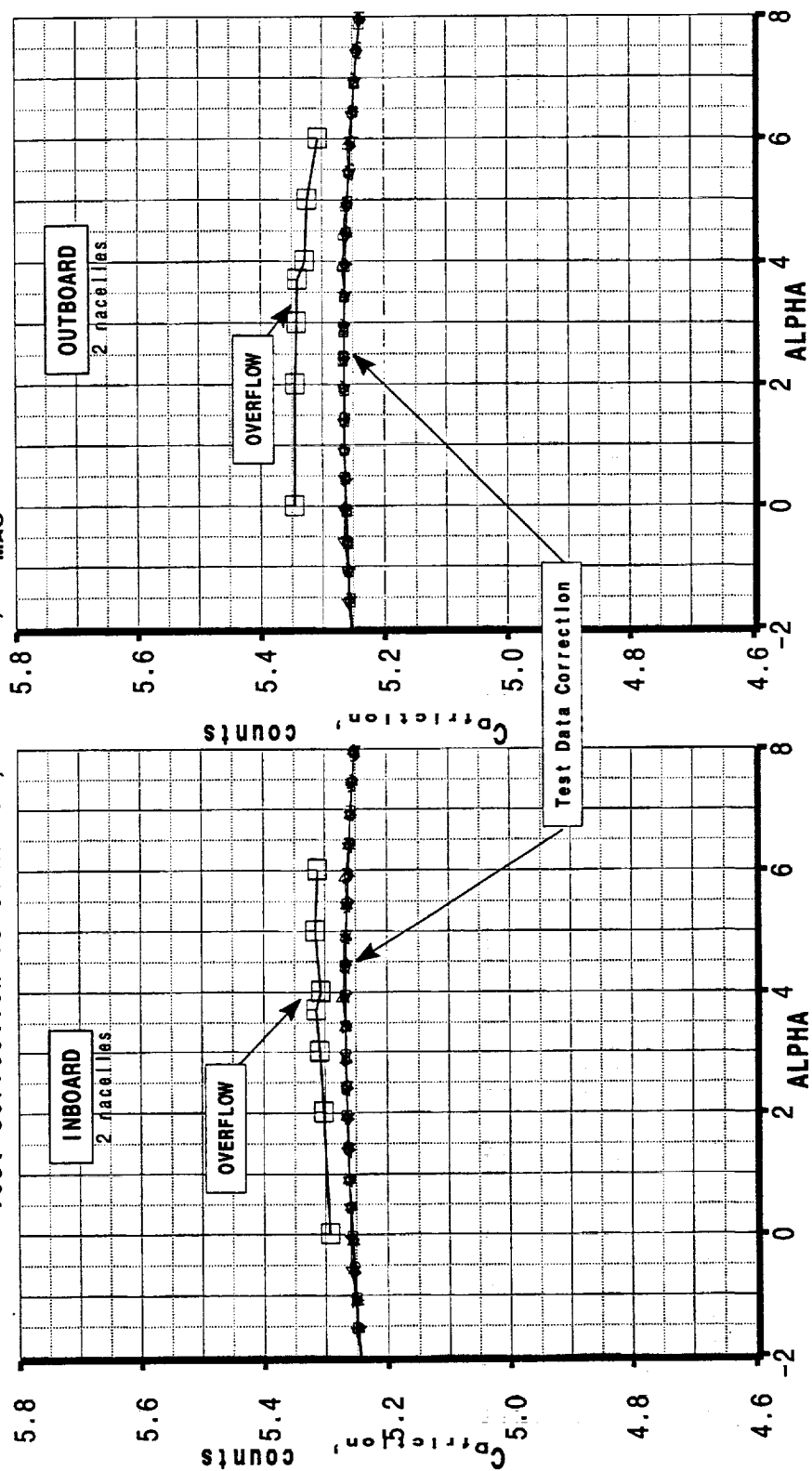


HSCT High Speed Aerodynamics - BCAG

This figure shows the wind tunnel estimated nacelle internal duct drag correction contained in the test data file compared to the OVERFLOW results. The comparison illustrated no significant difference.



TCA Nacelle Internal Duct Friction Drag
Test Correction vs OVERFLOW, Mach 0.9, $Re_{MAC} = 6.1$ million





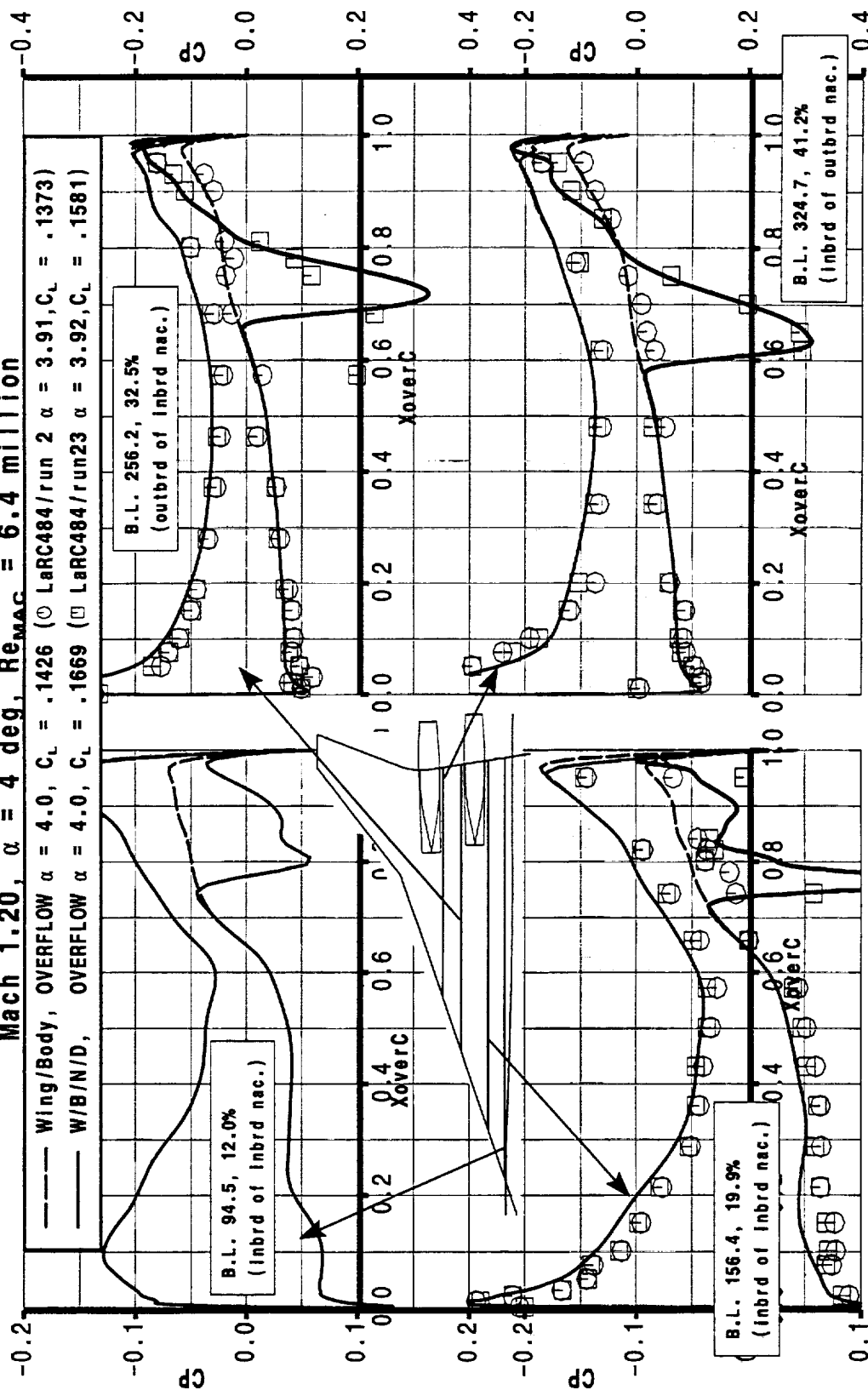
The transonic validation effort was repeated at Mach 1.2 (transonic climb). Pressure distributions at Mach 1.2 and angle of attack of 4 degrees are shown in the next two figures. These plots indicated very similar trends to those seen in the Mach 0.90 pressure data comparisons. The OVERFLOW results matched the nacelle/diverter shock accurately except for the B.L. 256.2 row; this row of data has shown similar discrepancies at every Mach number for which data has been taken on this model.



HSCT High Speed Aerodynamics - BCAG

TCA Wing/Body/Nacelle/Diverter Chordwise Pressure Distributions

Mach 1.20, $\alpha = 4$ deg, $Re_{MAC} = 6.4$ million





February 1998 HSR Airframe Technical Review



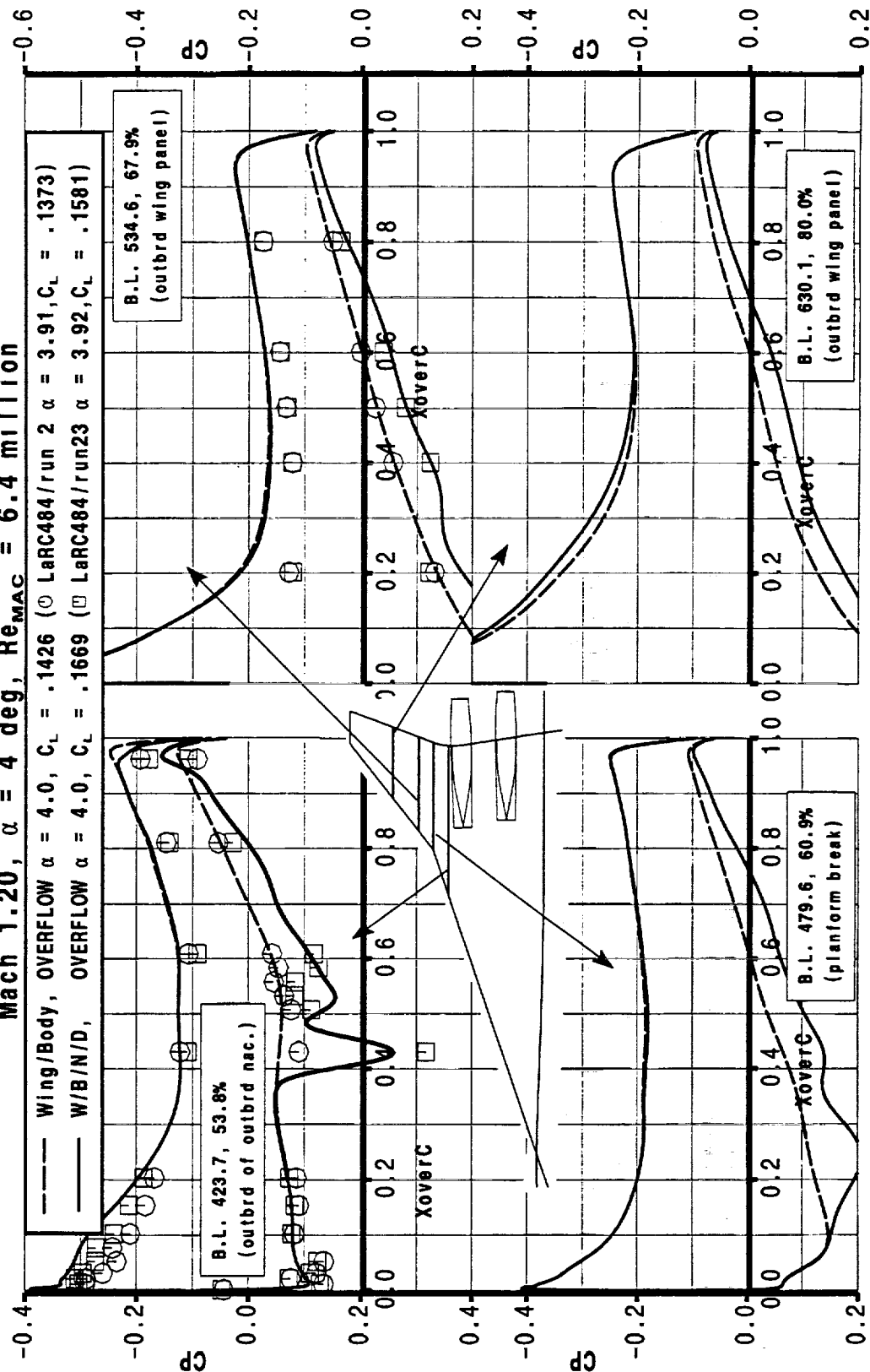
HSCT High Speed Aerodynamics - BCAG

The outboard panel pressure data on the upper surface near the leading edge indicated the same discrepancy between the OVERFLOW computation and the test data as was seen in the Mach 0.90 case, although the pressure differences were smaller. The same data was plotted versus angle of attack and is shown in the figure contained in the Mach 0.90 section. See the discussion in that section for possible causes of this discrepancy associated with the sharp leading edge separation.



TCA Wing/Body/Nacelle/Diverter Chordwise Pressure Distributions

Mach 1.20, $\alpha = 4$ deg, $Re_{MAC} = 6.4$ million





February 1998 HSR Airframe Technical Review



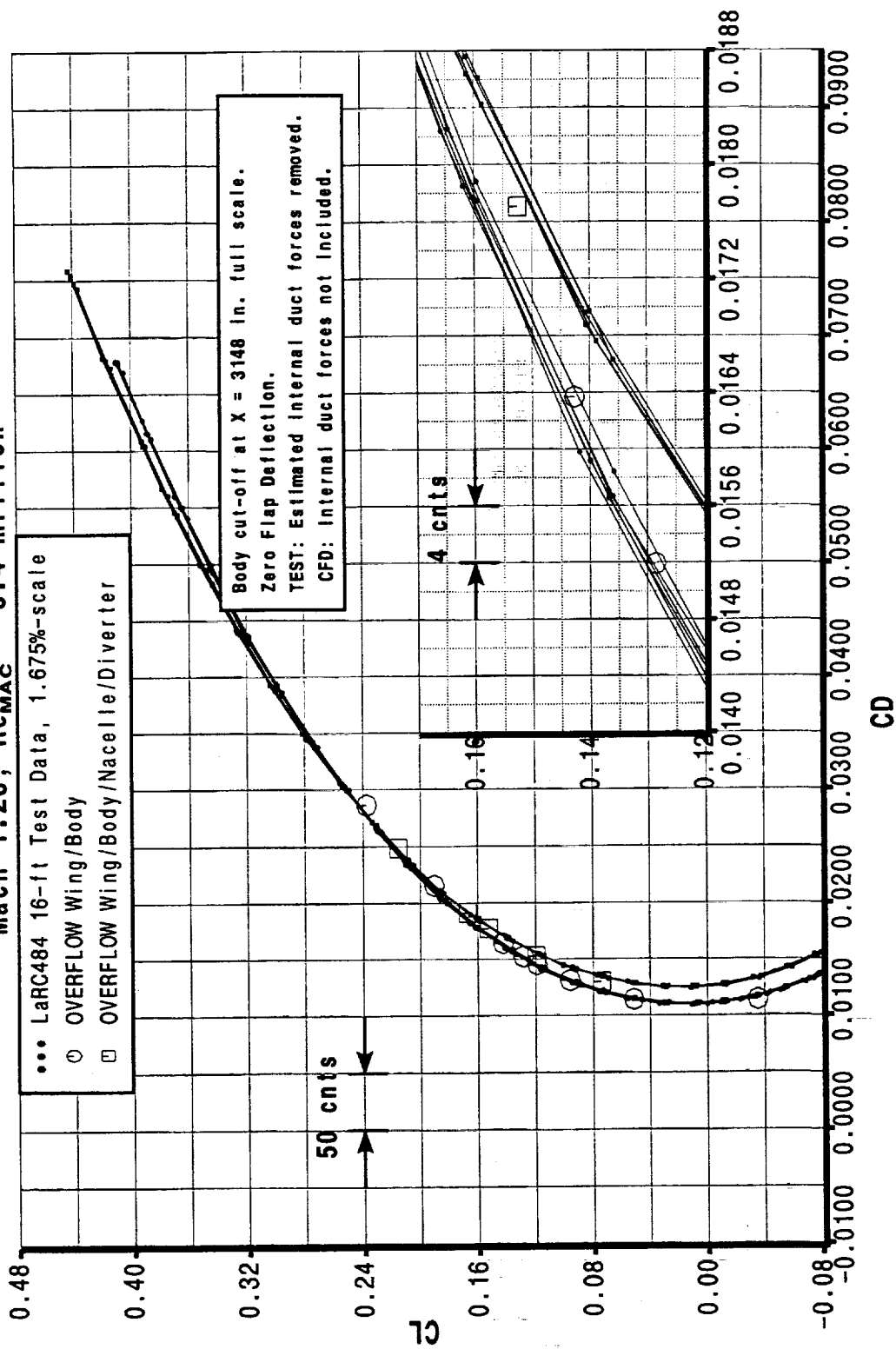
HSCT High Speed Aerodynamics - BCAG

A drag polar plot is shown comparing OVERFLOW results to LaRC 16 ft data for the TCA (Mach 1.20, no flap deflections). The wing/body OVERFLOW results were 1 to 2 counts higher than the mean test data result. The wing/body/nacelle/diverter OVERFLOW results were about 2 counts lower than test at constant lift.



TCA Wing/Body/Nacelle/Diverter Drag Polar

Mach 1.20, $Re_{MAC} = 6.4$ million





February 1998 HSR Airframe Technical Review



HSCT High Speed Aerodynamics - BCAG

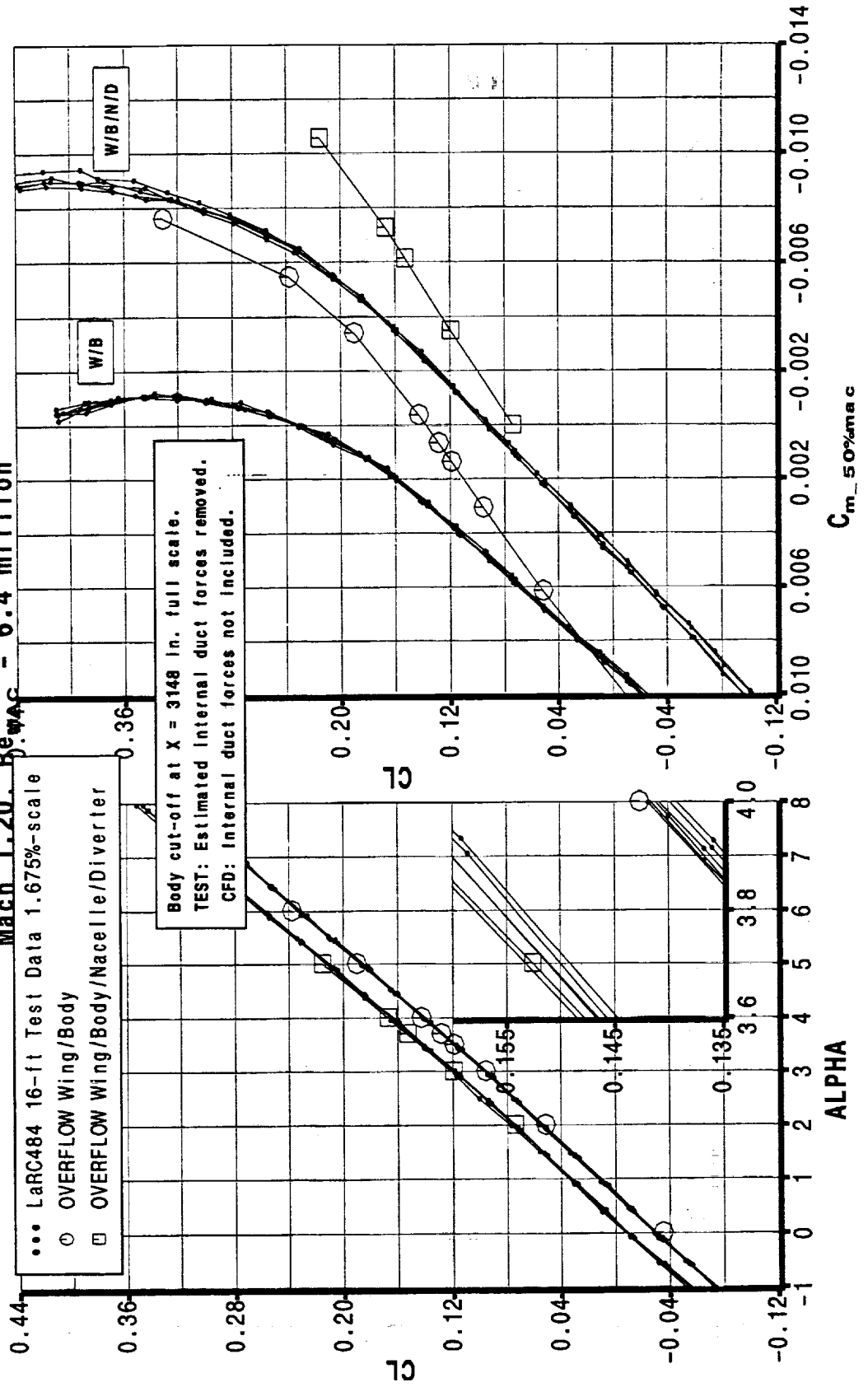
A lift & pitching moment plot is shown comparing OVERFLOW results to LaRC 16 ft data for the TCA (Mach 1.20, no flap deflections). The pitching moment increment due to the nacelles was calculated much more accurately in this case than for Mach 0.90. This was reflected in the lift data where both the wing/body and the wing/body/nacelle/diverter cases were predicted accurately. This was in contrast to the Mach 0.90 case where the wing/body was prediction was accurate but the wing/body/nacelle/diverter lift was 3% low.



HSCT High Speed Aerodynamics - BCAG

TCA Wing/Body/Nacelle/Diverter Lift & Pitching Moment

Mach 1.20, $Re_{MAC} = 6.4$ million





The nacelle/diverter force increments for Mach 1.20 are shown. As described in the previous figure's text the nacelle lift increment was modeled very accurately. The OVERFLOW nacelle/diverter drag at constant angle of attack was about 3 counts less than the test data. The OVERFLOW nacelle/diverter drag increment at constant lift was about 3.5 counts less than test data at the transonic climb condition ($CL \sim 0.15$). There are several phenomena that could be effecting these comparisons:

- 1) The spillage condition simulated in the OVERFLOW data may not be matching the wind tunnel spillage condition correctly.
- 2) The wind tunnel data did not have the internal duct pressure forces (primarily lift) removed, so the OVERFLOW data was shown with this component included in the data. This effect was worth about 0.5 count (bringing OVERFLOW closer to test).
- 3) The wind tunnel data had estimated internal duct skin friction removed. Figure 6 compares this estimated term to the OVERFLOW calculated value. There is a small discrepancy. Using the same internal drag correction for both CFD and test would move the OVERFLOW nacelle/diverter drag increment 0.25 counts closer to the wind tunnel data.
- 4) The nacelle boundary layer trip drag may be on the order of several counts. Only points 1) and 4) above are open issues.

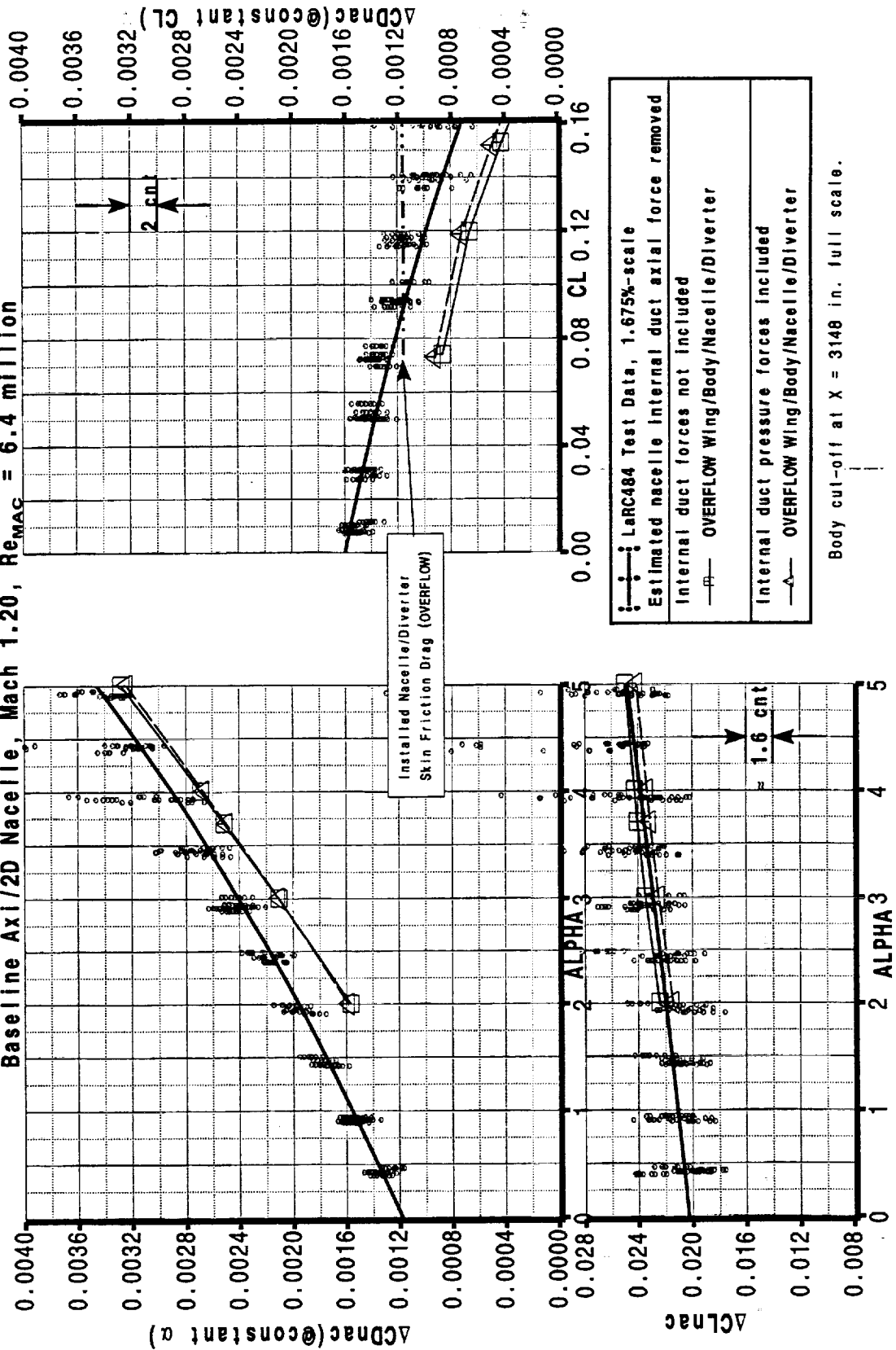
It was concluded that for the purpose of determining nacelle/diverter force increments with and without spillage that these predictions indicated adequate accuracy in the OVERFLOW method.



HSCT High Speed Aerodynamics - BCAG

TCA Wing/Body/Nacelle/Diverter PAI Force Increments

Baseline Ax1/2D Nacelle, Mach 1.20, $Re_{MAC} = 6.4$ million





February 1998 HSR Airframe Technical Review

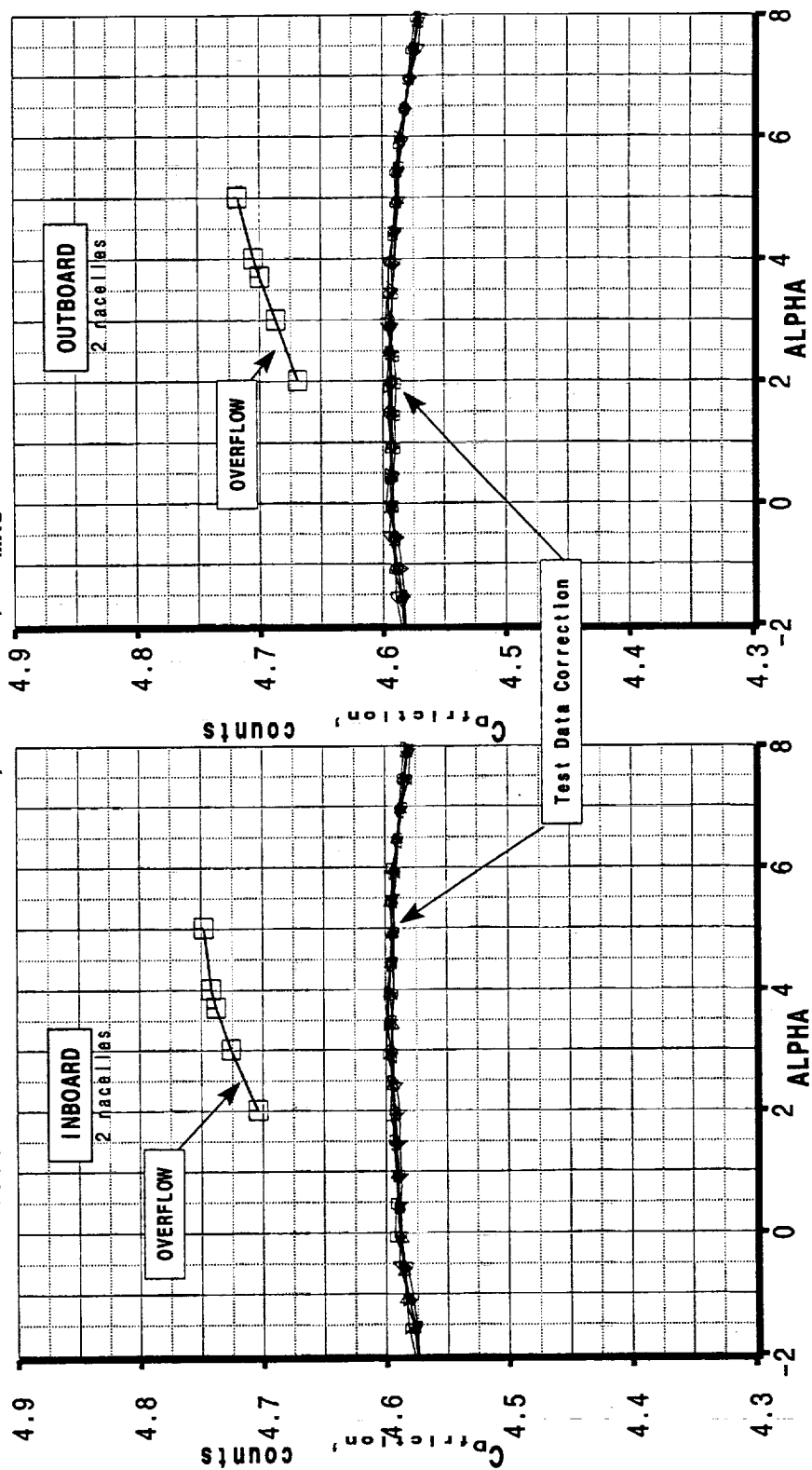


HSCT High Speed Aerodynamics - BCAG

This figure shows the wind tunnel estimated nacelle internal duct drag correction contained in the test data file compared to the OVERFLOW results. The comparison indicated a small difference between them of 0.14 count for the two inboard nacelles and 0.11 count for the two outboard nacelles (for total of 0.25 mentioned in previous page).



TCA Nacelle Internal Duct Friction Drag
Test Correction vs OVERFLOW, Mach 1.2, $Re_{MAC} = 6.4$ million





The HSR community has spent several years validating and refining CFD methods for supersonic design and analysis. It will take a similar effort to reach the same level of accuracy for transonic conditions. This task will be modified somewhat by several factors:

- 1) Applying what has been learned from supersonic analyses has already provided a higher level of accuracy for these initial transonic cases then was achieved on the first supersonic analyses.
- 2) Achieving the same level of accuracy for transonic conditions as for supersonic may not be necessary due to the relatively smaller amount of time spent at transonic conditions (an exception is the case of transonic climb sizing the engines).
- 3) The high speed reference wind tunnel configuration that represents the supersonic flight configuration (i.e. centerbody shock is on the nacelle lip, zero spillage), does not model the actual transonic condition very accurately. As discussed earlier the flow through nacelles spill about 6 % at Mach 0.9; in flight, not only is there a centerbody in place, but the spillage is 40%. The transonic data taken with the supersonic reference configuration will probably be a component of the total drag defined by the thrust-drag bookkeeping system. The next section will show that the flight spillage levels have a large impact on airplane performance characteristics.
- 4) The undeflected leading edge flap configuration investigated here introduces a more difficult simulation problem because of the sharp leading edge separation. This may become important for S&C type conditions, but transonic cruise studies will incorporate deflected flaps and therefore eliminate the separation problem. The effect of the deflected onboard panel flaps on the ability to model the transonic PAI effects will also need to be investigated.



Transonic Validation Conclusions

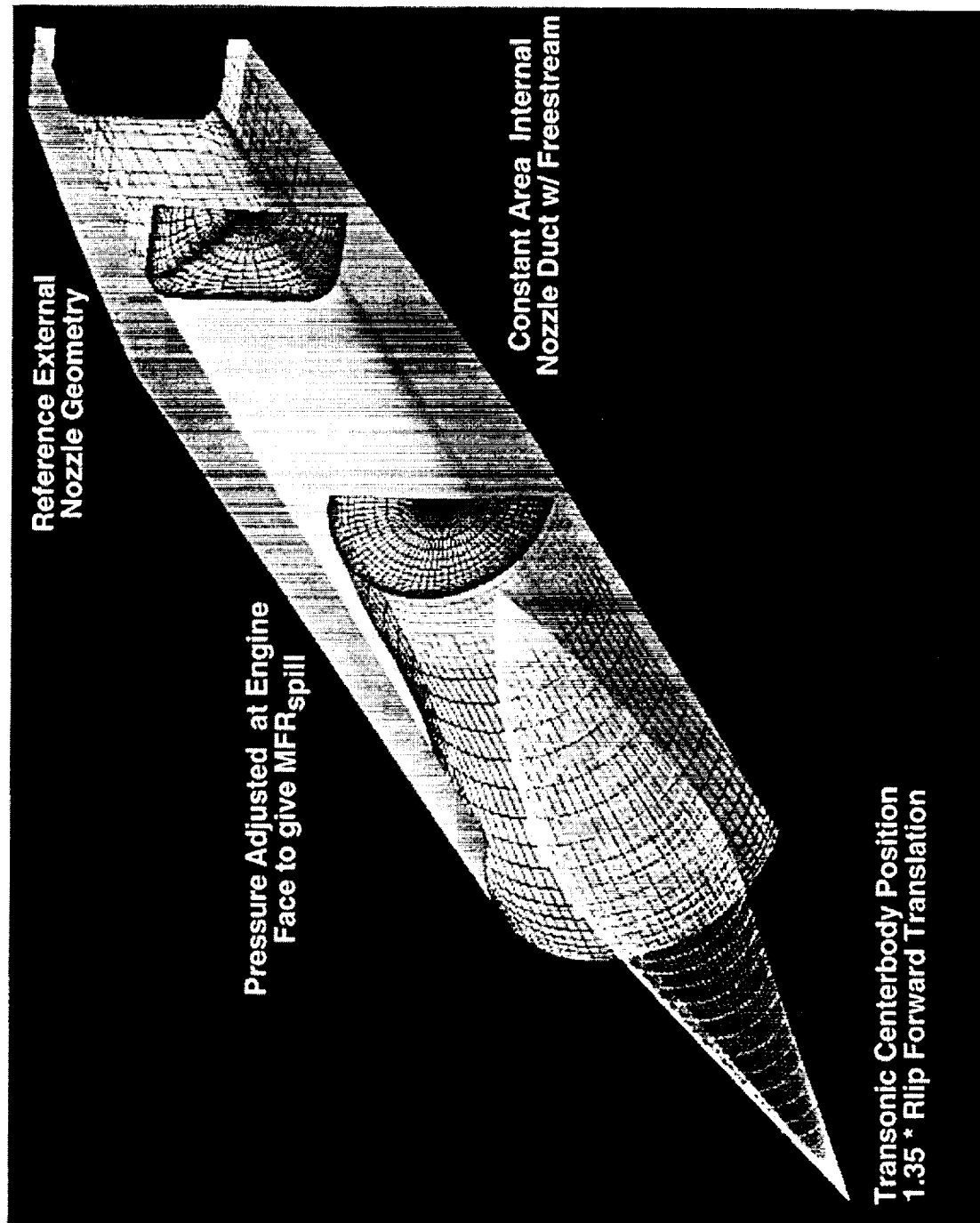
- Initial validation of OVERFLOW for transonic PAL effects successful
 - Absolute drag predictions within 3 counts of test
 - Nacelle drag increments within 3 counts of test
- Pressure discrepancy forward of nacelles: bad pressure port
- Outboard panel pressures near wing LE: separation modeling
- Pitching moment rotation: approximately 0.013 MAC
- Transonic trip drag: not yet determined
- CFD flow-through duct spill vs. WT spill: measure in wind tunnel ?
- Outboard flap effects on transonic PAL (and vice versa)
- Flow-through duct spillage is a function of Reynold Number with implications for:
 - Tunnel to tunnel comparisons
 - T-D bookkeeping
 - Wind tunnel to flight extrapolation



The grid system for OVERFLOW analysis of the isolated TCA nacelle with centerbody and controlled spillage is shown; this same set of grids was applied to the installed nacelles as well. The actual inlet internal lines as defined by propulsion were modeled up to the engine face where a pressure boundary condition was imposed that could be varied during the run in order to achieve the desired mass flow rate. The centerbody was placed at the transonic full forward position. The reference supersonic nozzle configuration was retained and the aft portion of the wind tunnel constant area duct was used as the internal nozzle with freestream conditions imposed at the forward face.



TCA Transonic Inlet Spillage



Reference External
Nozzle Geometry

Constant Area Internal
Nozzle Duct w/ Freestream

Pressure Adjusted at Engine
Face to give MFR_{spill}

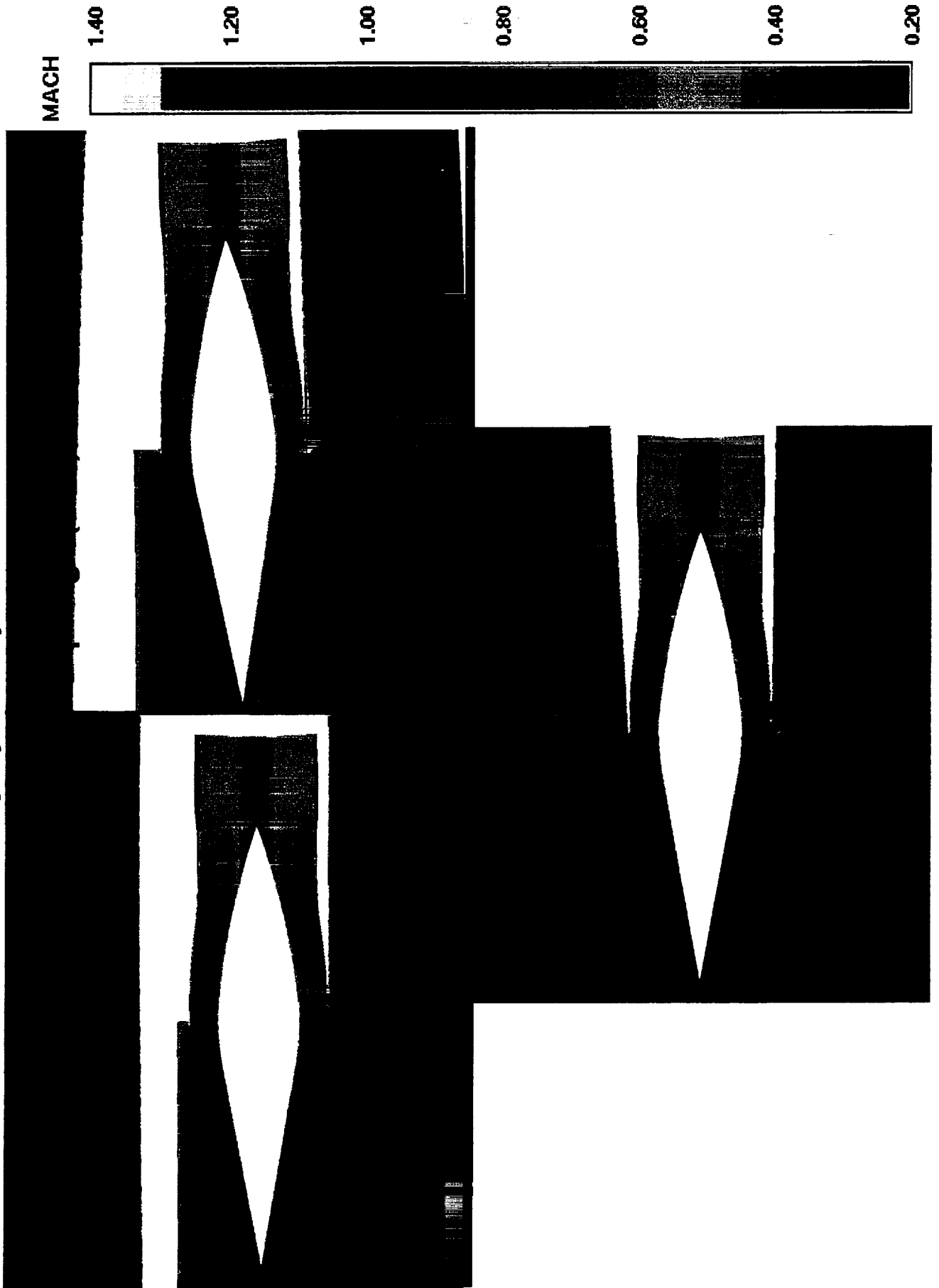
Transonic Centerbody Position
1.35 * Rlip Forward Translation



Symmetry plane Mach contours from the OVERFLOW solutions are shown below for the transonic cruise conditions (40 % spillage). The two top figures are the inboard and outboard installed nacelles; the bottom figure is the isolated case. The flow field for all three cases was similar with one primary difference between the installed nacelles and the isolated nacelle: the installed nacelle flow fields indicated no spillage at the crown of the nacelle. This same phenomena was observed for the flow-through nacelles discussed in the previous section.



TCA Inlet/Centerbody Symmetry Plane Mach Contours



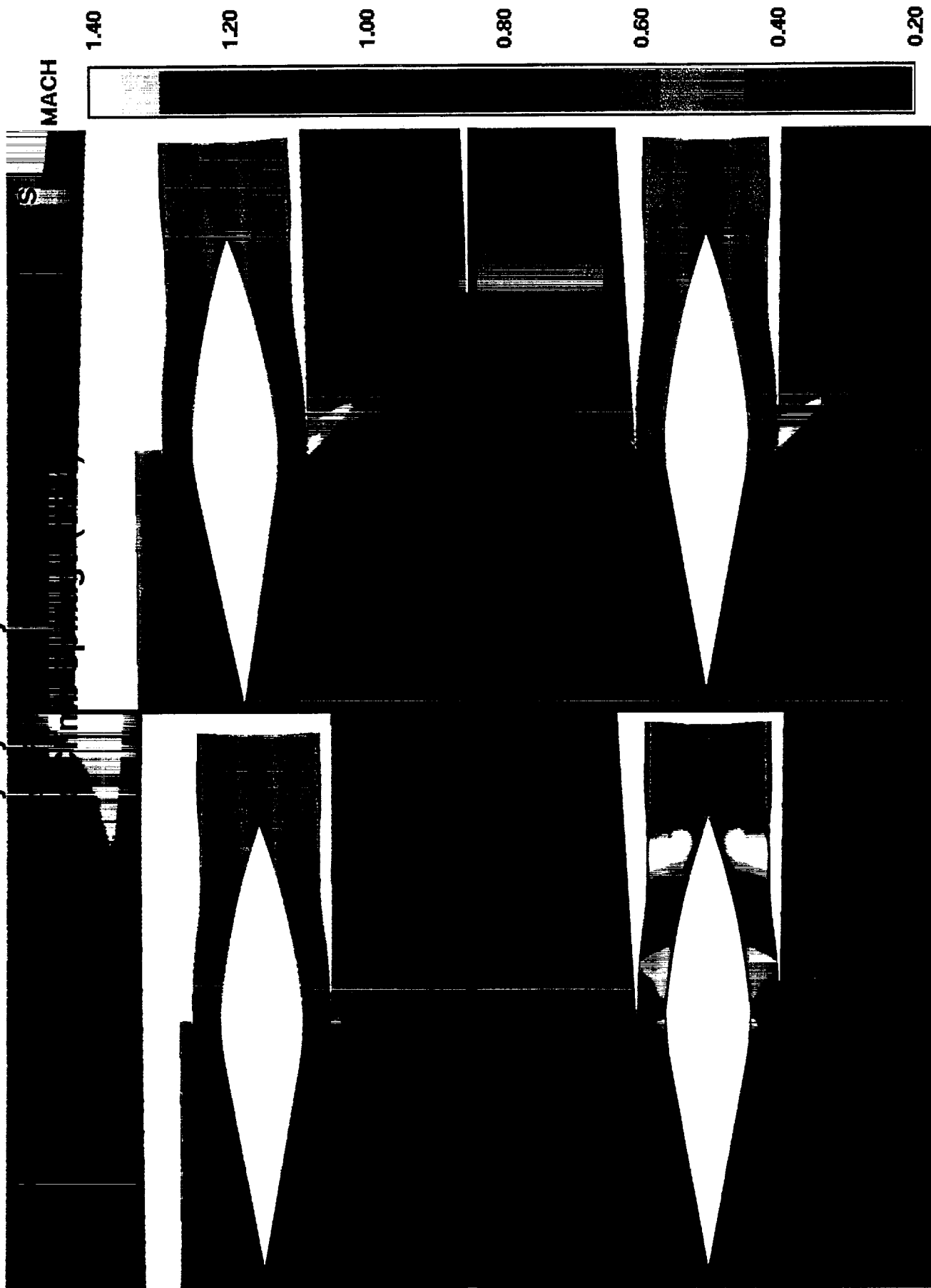


Symmetry plane Mach contours from the OVERFLOW solutions are shown below for the transonic climb conditions at Mach 1.20 (35 % spillage). The two top figures are the inboard and outboard installed nacelles; the bottom figures are isolated cases at two different spillage levels. In contrast to the Mach 0.90 case the installed nacelle case exhibited very different flow field characteristics then the isolated nacelle. It appears that the shock from the centerbody separated the wing boundary layer and the flow remained subsonic the rest of the way back to the inlet. The isolated nacelle with the same spillage as the installed (bottom left) had supersonic flow to the inlet lip and did not shock down to subsonic until the end of the centerbody. In order to achieve a subsonic inlet internal flow field for the isolated nacelle it was necessary to increase the spillage to 38 %, in which case, as shown in bottom right figure, the flow went through a normal shock before entering the inlet. This situation was illustrative of a condition where the spillage flow field was very different between the isolated and installed nacelles, and in addition, was very sensitive to both the approach flow field and the engine flow rate.



HSCT High Speed Aerodynamics - BCAG

TCA Inlet/Centerbody Symmetry Plane Mach Contours





The residual and force history for a typical transonic OVERFLOW run with flight spillage levels is shown. This particular case was run out past 4000 steps. The runs were usually stopped at 3000 steps where 3 orders of magnitude residual reduction was achieved for all 32 grid blocks, the lift was varying less than 0.2 % over the last 100 steps, and both pressure and viscous drag were varying less than 0.2 drag count over the last 100 steps.

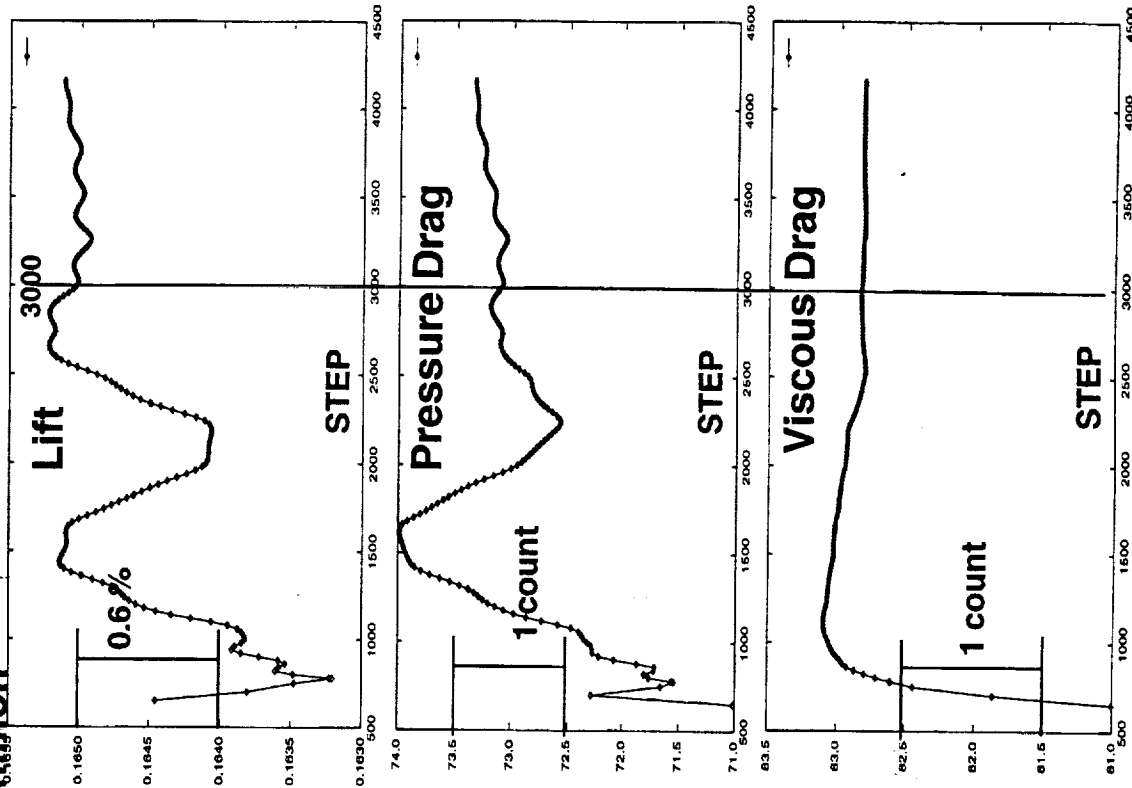
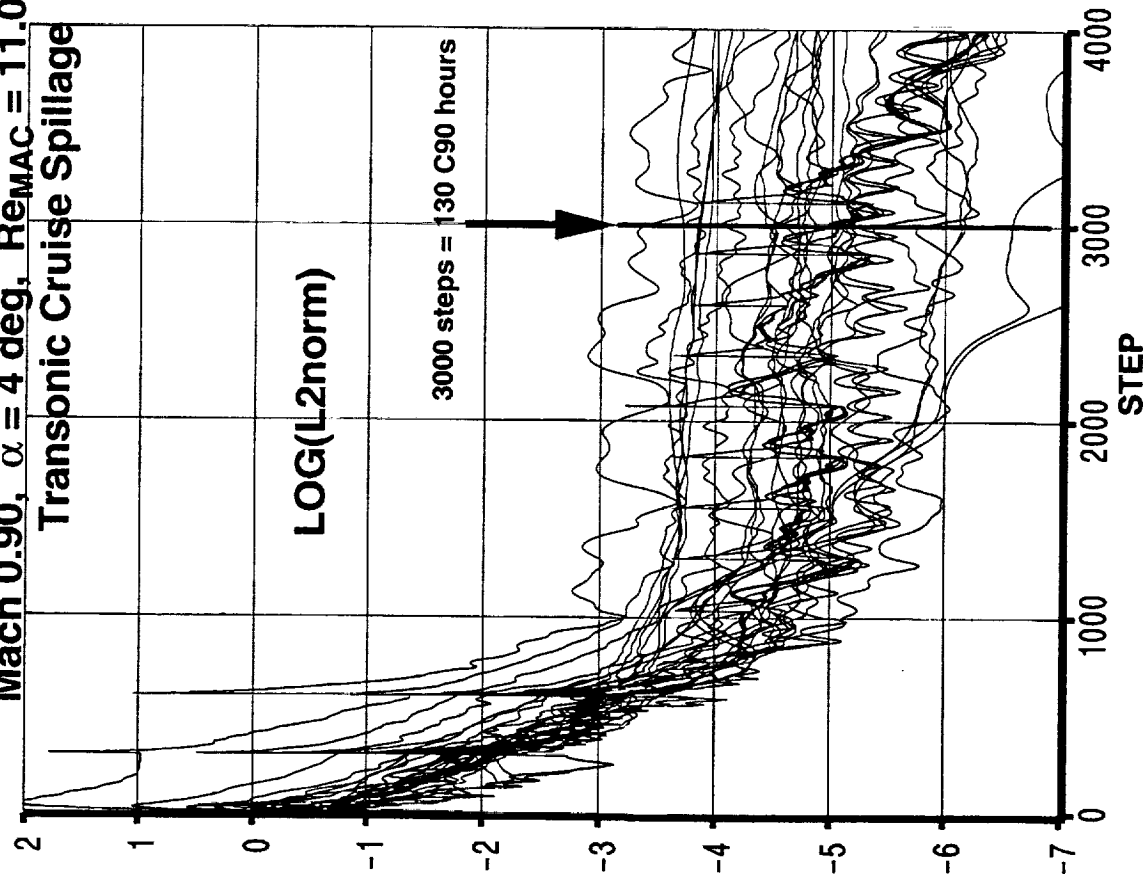


HSCT High Speed Aerodynamics - BCAG

OVERFLOW W/B/N/D/CB Transonic Convergence

Mach 0.90, $\alpha = 4$ deg, $Re_{MAC} = 11.0$ million

Transonic Cruise Spillage





February 1998 HSR Airframe Technical Review



HSCT High Speed Aerodynamics - BCAG

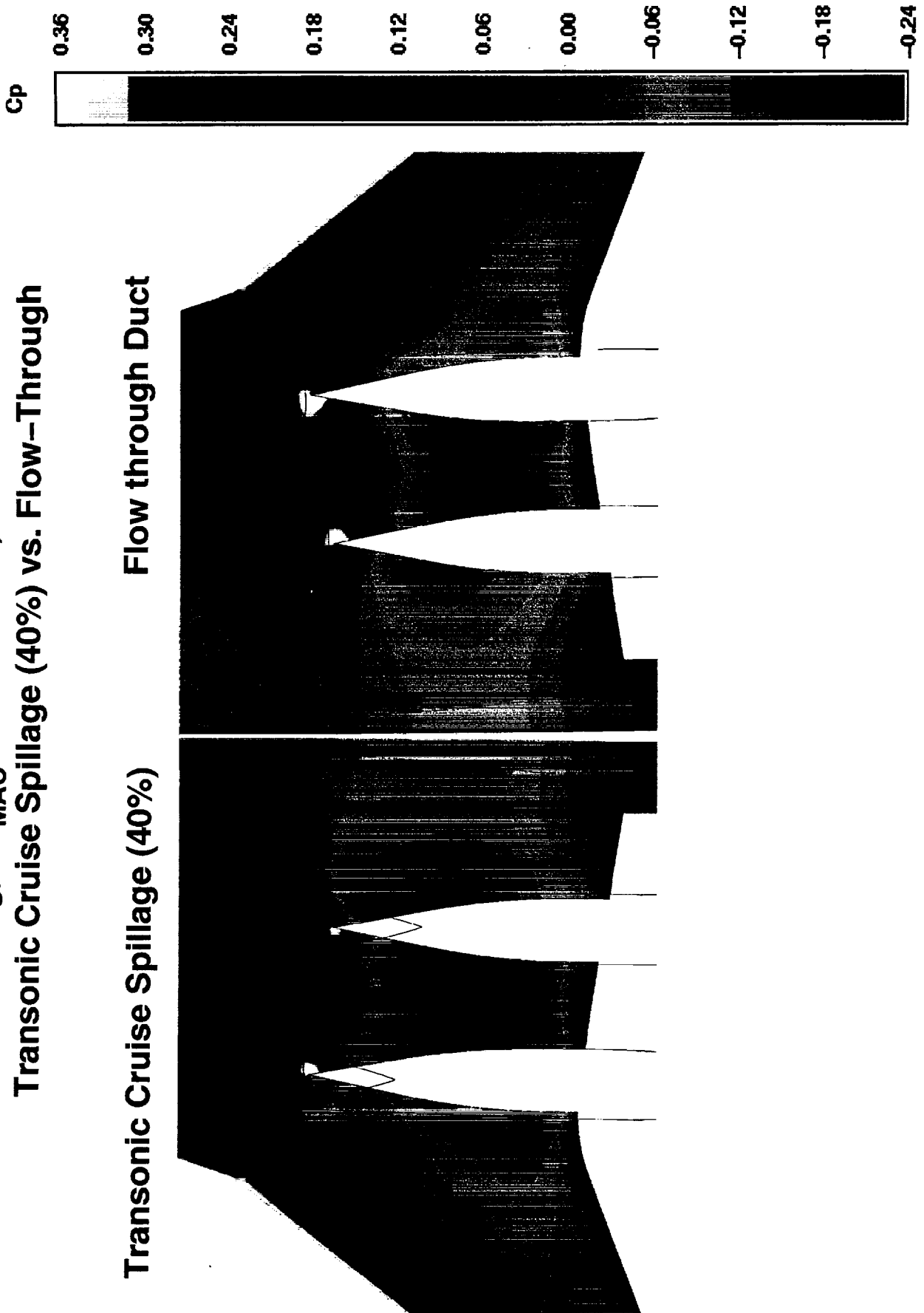
The next several figures show surface pressure contours on the wing lower surface and on the nacelles for the Mach 0.90 and 1.20 flight spillage OVERFLOW simulations (compared to flow-through nacelle calculations).

The figure below shows the wing lower surface pressure contours for the transonic cruise condition with 40 % spillage. The presence of the centerbody and the higher spillage (40% vs 6%) resulted in a larger footprint of positive pressure forward of the nacelle inlets. The spilled flow also increased the magnitude of the expansions downstream of the inlets.



HSCT High Speed Aerodynamics - BCAG

**TCA Wing/Body/Nacelle/Diverter Wing Pressure Contours
Mach 0.90, $\alpha = 4$ deg, $Re_{MAC} = 11.0$ million, OVERFLOW Solutions
Transonic Cruise Spillage (40%) vs. Flow-Through**





The next two figures show nacelle surface pressure contours for the inboard and outboard installations from Mach 0.90 OVERFLOW simulations. The asymmetry of the spillage around the inlet lip noted earlier for the flow-through case was clearly evident for the flight spillage case with centerbody. In addition, the effect of the much higher spillage level resulted in a larger region of negative pressure around the inlet lip (where the flow was spilling). The 40% spillage also appeared to reduce the magnitude of the positive pressure region at the crown of the nacelle.



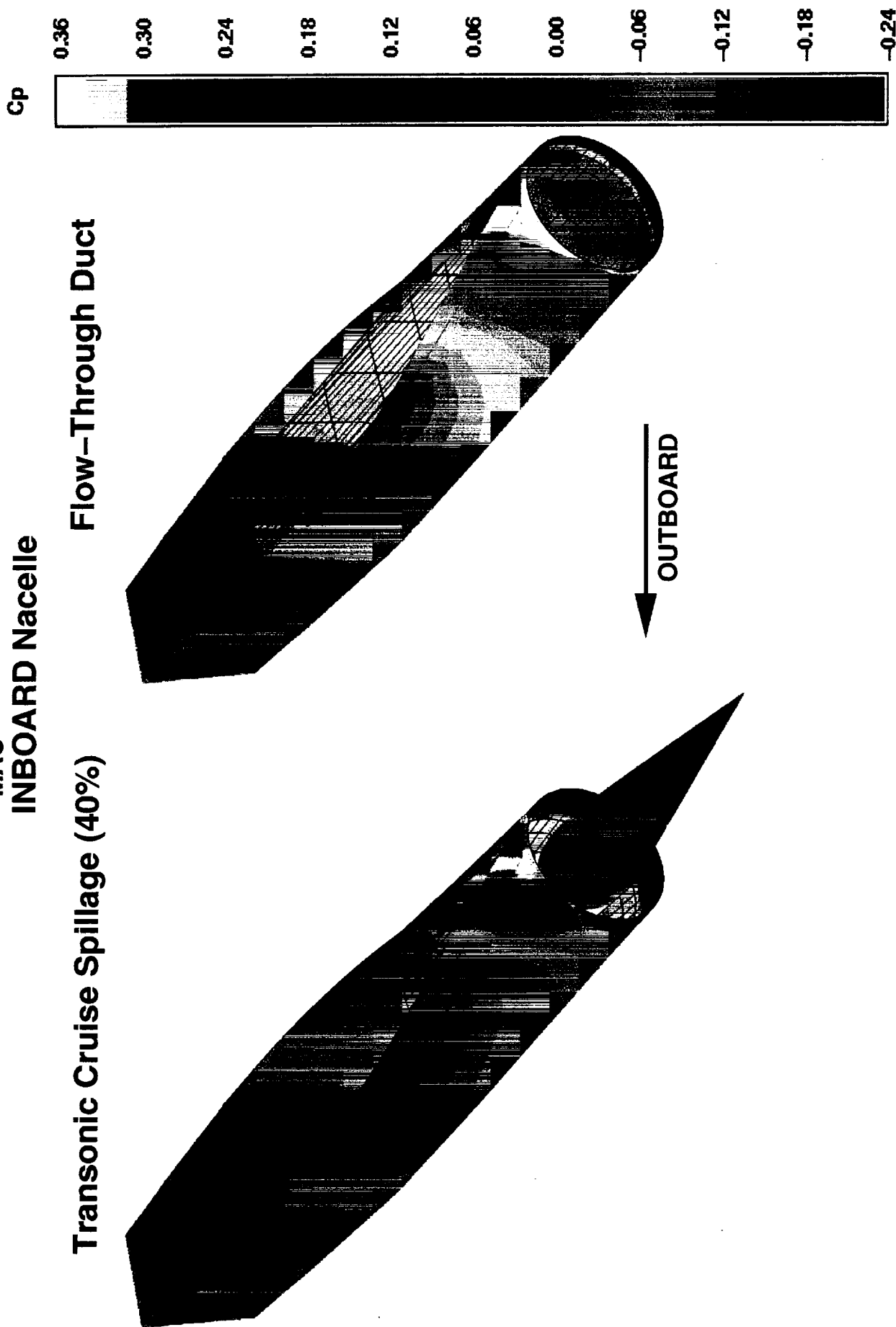
TCA Wing/Body/Nacelle/Diverter Nacelle Pressure Contours

Mach 0.90, $\alpha = 4$ deg, $Re_{MAC} = 11.0$ million, OVERFLOW Solution

INBOARD Nacelle

Transonic Cruise Spillage (40%)

Flow-Through Duct





February 1998 HSR Airframe Technical Review

HSCT High Speed Aerodynamics - BCAG



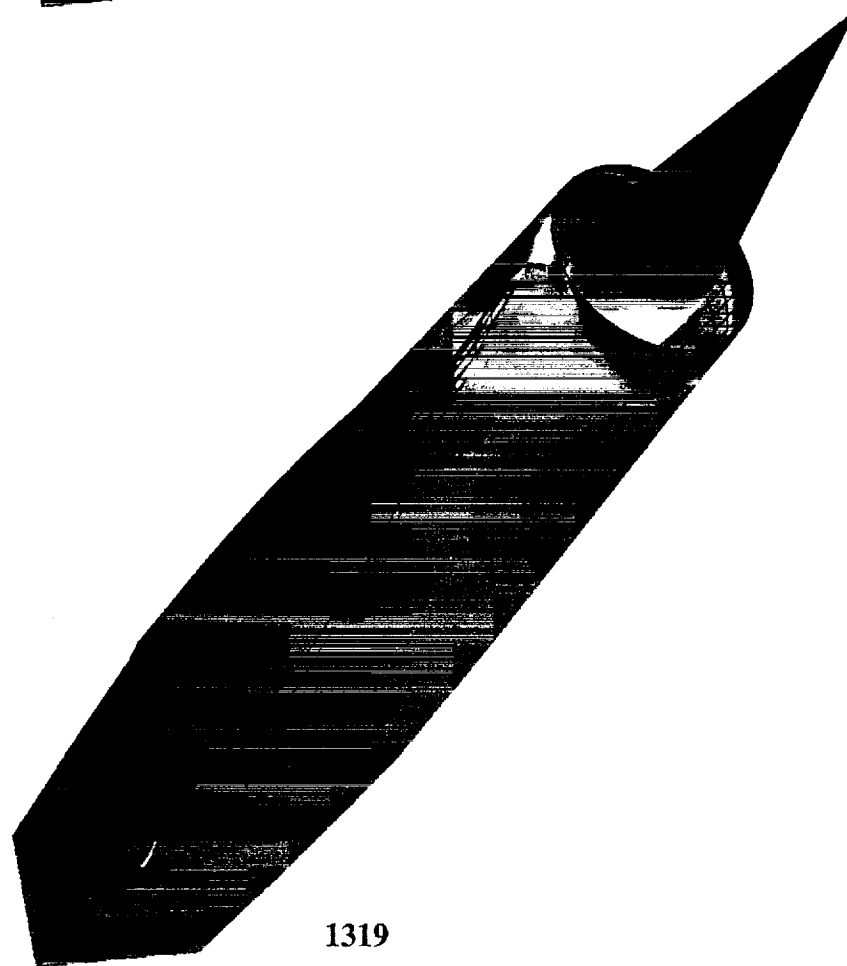
---See text for previous page---



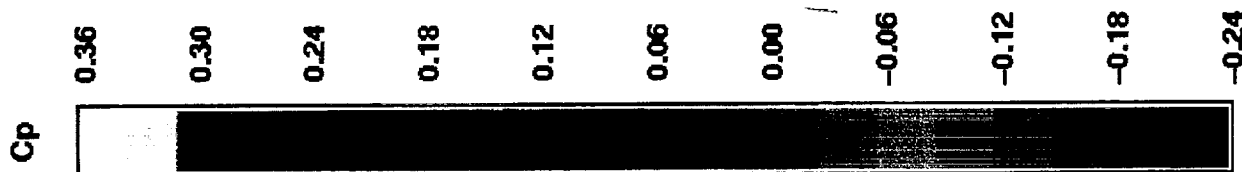
**TCA Wing/Body/Nacelle/Diverter Nacelle Pressure Contours
Mach 0.90, $\alpha = 4$ deg, $Re_{MAC} = 11.0$ million, OVERFLOW Solution
OUTBOARD Nacelle**

Transonic Cruise Spillage (40%)

Flow-Through Duct



OUTBOARD





February 1998 HSR Airframe Technical Review

HSCT High Speed Aerodynamics - BCAG



The transonic climb spillage is slightly lower than cruise (35% vs 40%) but results in a larger impact on the wing lower surface pressures due to the supersonic Mach Number. The figure shows the normal shock near the tip of the centerbody extending nearly across the entire wing lower surface. The pressure contours under the centerbodies had larger regions where the positive pressure scale maximum was exceeded. The outboard wing leading edge region also had higher pressure levels.



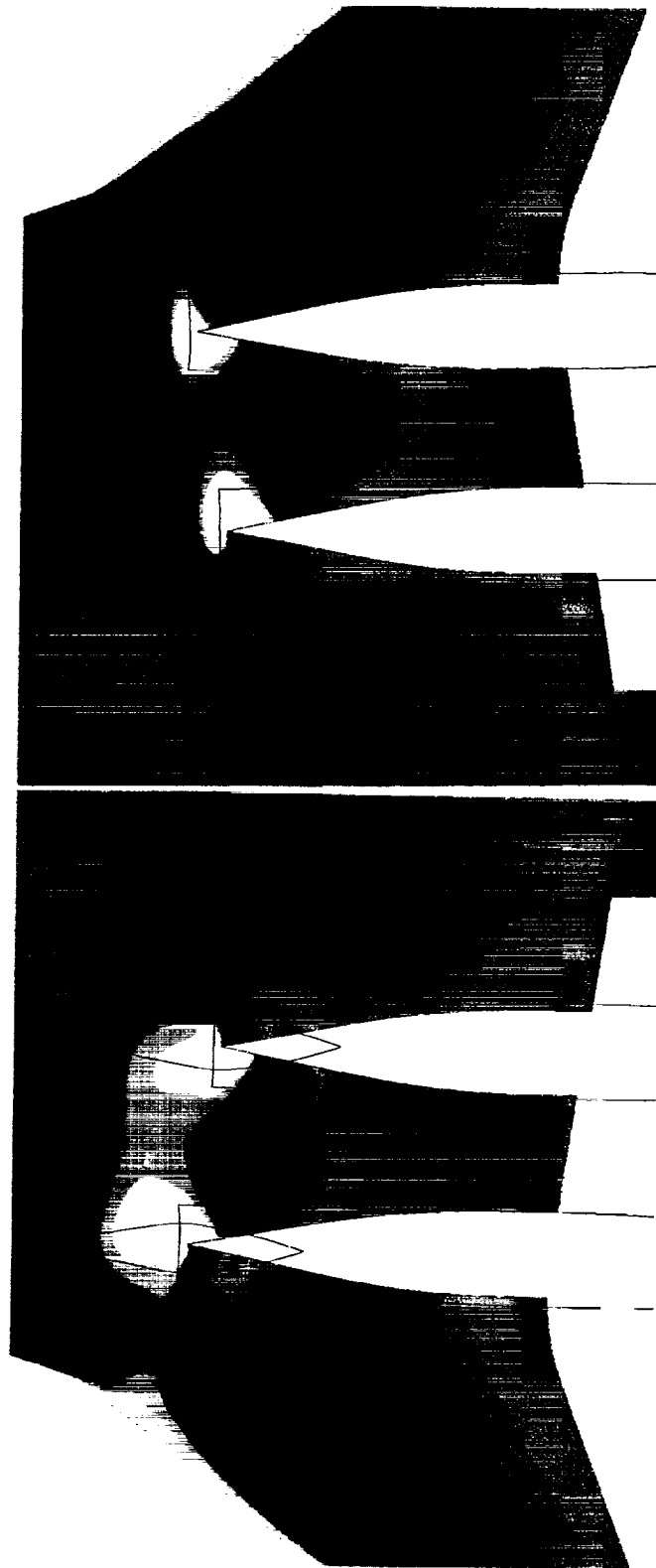
TCA Wing/Body/Nacelle/Diverter Wing Pressure Contours

Mach 1.20, $\alpha = 4$ deg, $Re_{MAC} = 11.4$ million, OVERFLOW Solutions

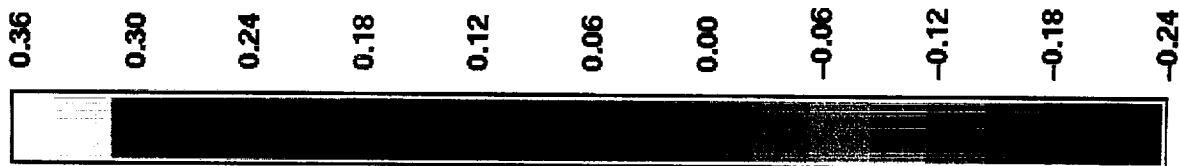
Transonic Climb Spillage (35%) vs. Flow-Through

Transonic Climb Spillage (35%)

Flow-Through Duct



Cp





February 1998 HSR Airframe Technical Review



HSCT High Speed Aerodynamics - BCAG

The effect of the flight transonic climb spillage on the nacelle pressures was very similar to that shown previously for the Mach 0.90 case. Comparison of the flow-through (3 % spillage) and the climb (35 % spillage) cases indicated that the negative pressure regions were larger around the inlet lip where the flow was being spilled and the positive pressure regions were somewhat reduced in size (but to a lesser extent than for Mach 0.90).



HSCT High Speed Aerodynamics - BCAG

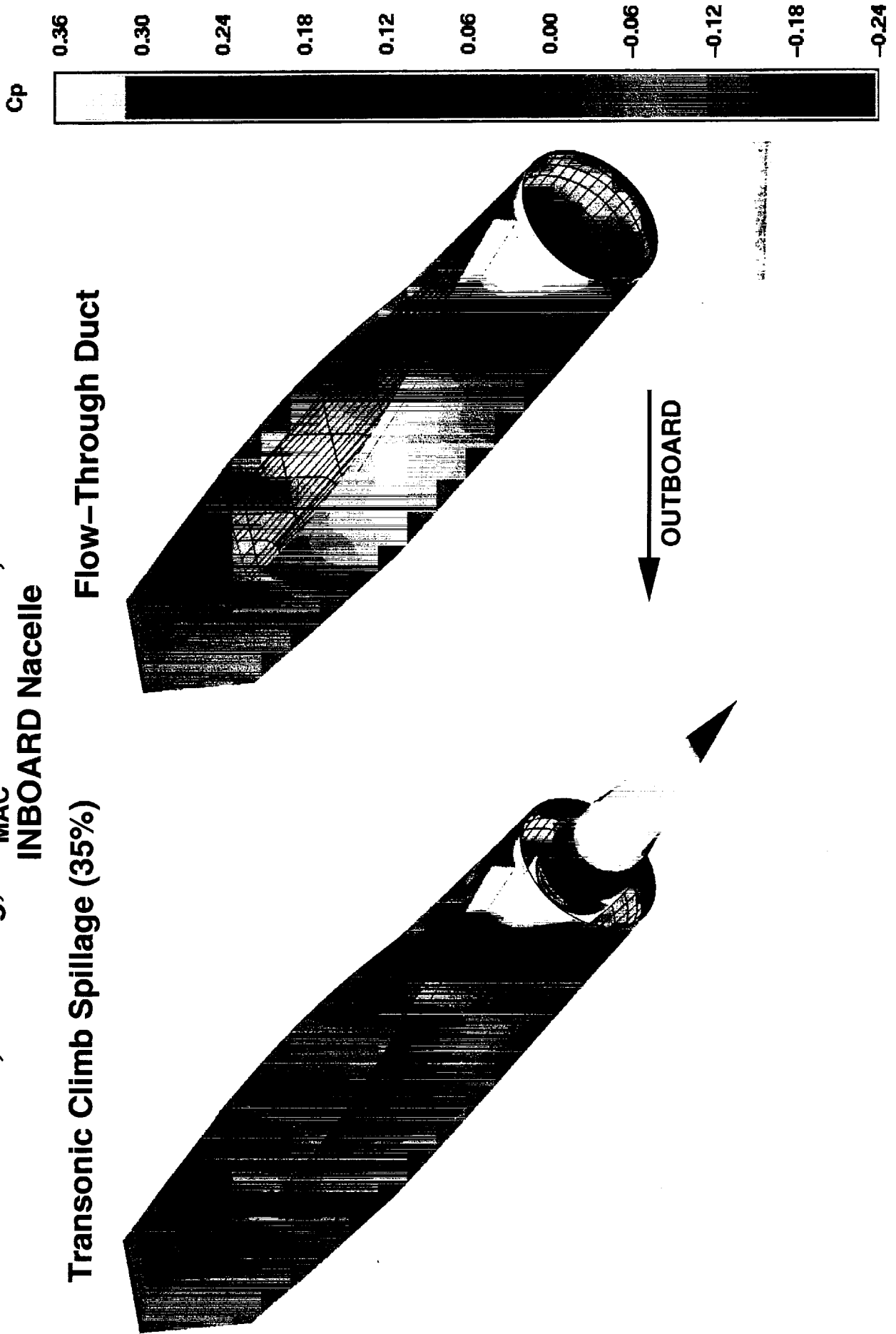
TCA Wing/Body/Nacelle/Diverter Nacelle Pressure Contours

Mach 1.20, $\alpha = 4$ deg, $Re_{MAC} = 11.4$ million, OVERFLOW Solution

INBOARD Nacelle

Transonic Climb Spillage (35%)

Flow-Through Duct





February 1998 HSR Airframe Technical Review

HSCT High Speed Aerodynamics - BCAG



---See text for previous page---



HSCT High Speed Aerodynamics - BCAG

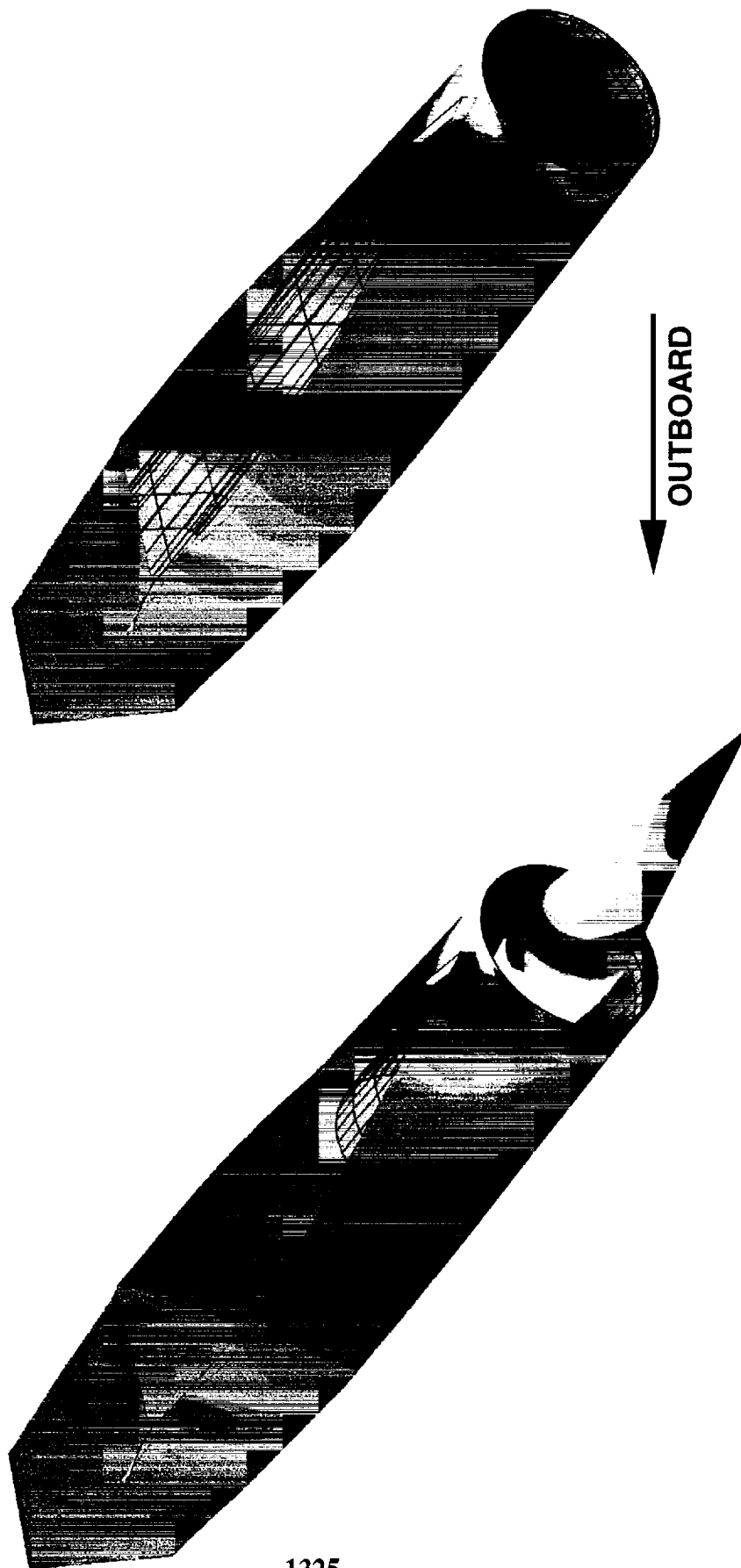
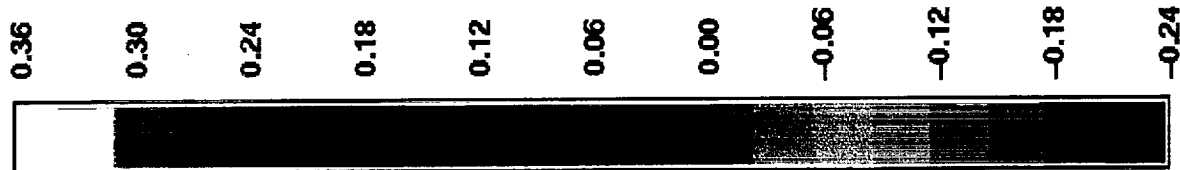
TCA Wing/Body/Nacelle/Diverter Nacelle Pressure Contours

Mach 1.20, $\alpha = 4$ deg, $Re_{MAC} = 11.4$ million, OVERFLOW Solution

Transonic Climb Spillage (35%)

Flow-Through Duct

Cp





February 1998 HSR Airframe Technical Review

HSCT High Speed Aerodynamics - BCAG



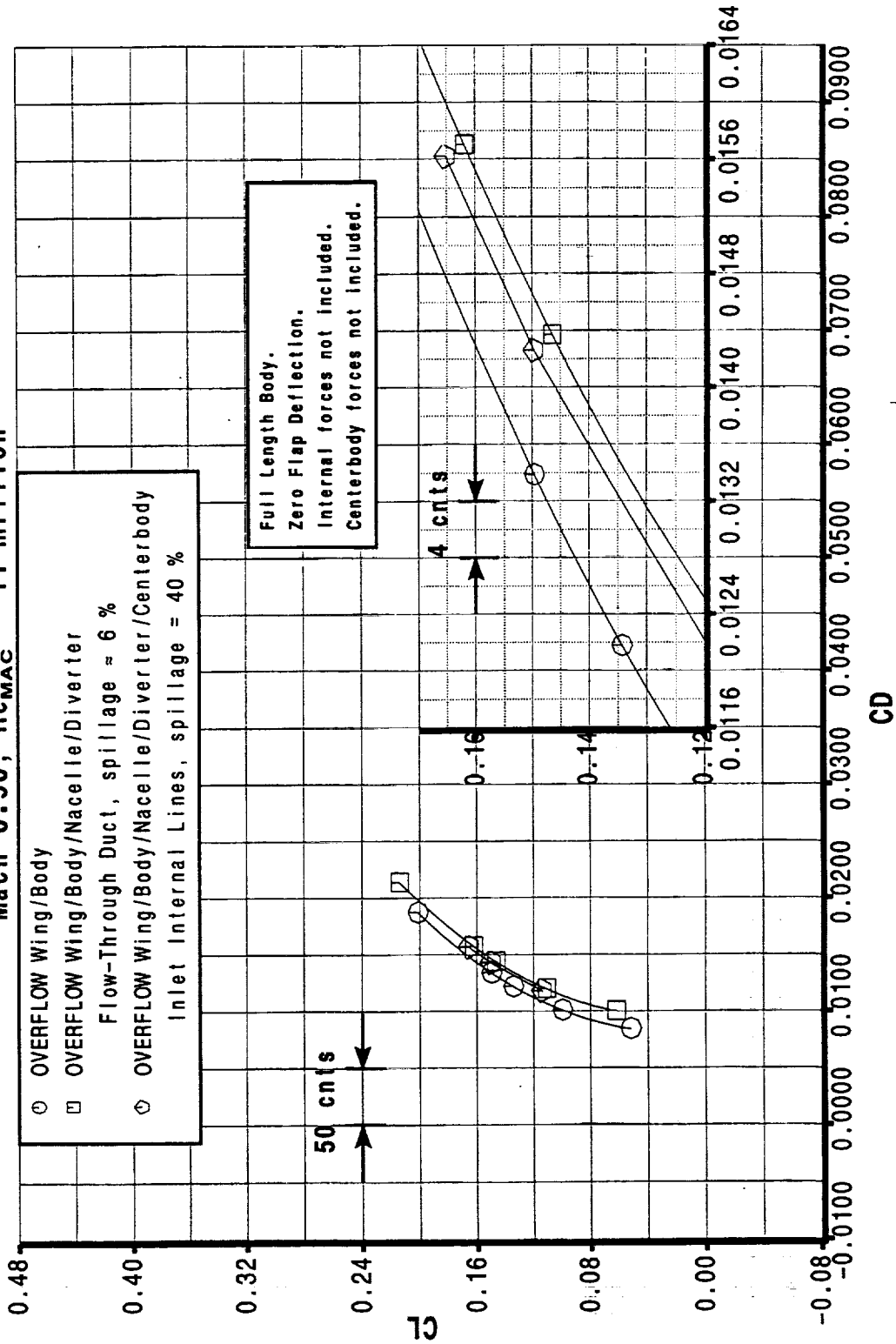
The figure shows the drag polar data for the OVERFLOW simulation of the TCA with the centerbody installed and the spillage controlled to the transonic cruise level (40 %). Based on the pressures shown previously the results are not unexpected: the increase in positive pressure on the lower surface of the wing resulted in a lift increase and the negative pressure increase around the inlet lip resulted in a drag reduction.



HSCT High Speed Aerodynamics - BCAG

TCA Wing/Body/Nacelle/Diverter/Centerbody Drag Polar

Mach 0.90, $Re_{MAC} = 11$ million





February 1998 HSR Airframe Technical Review



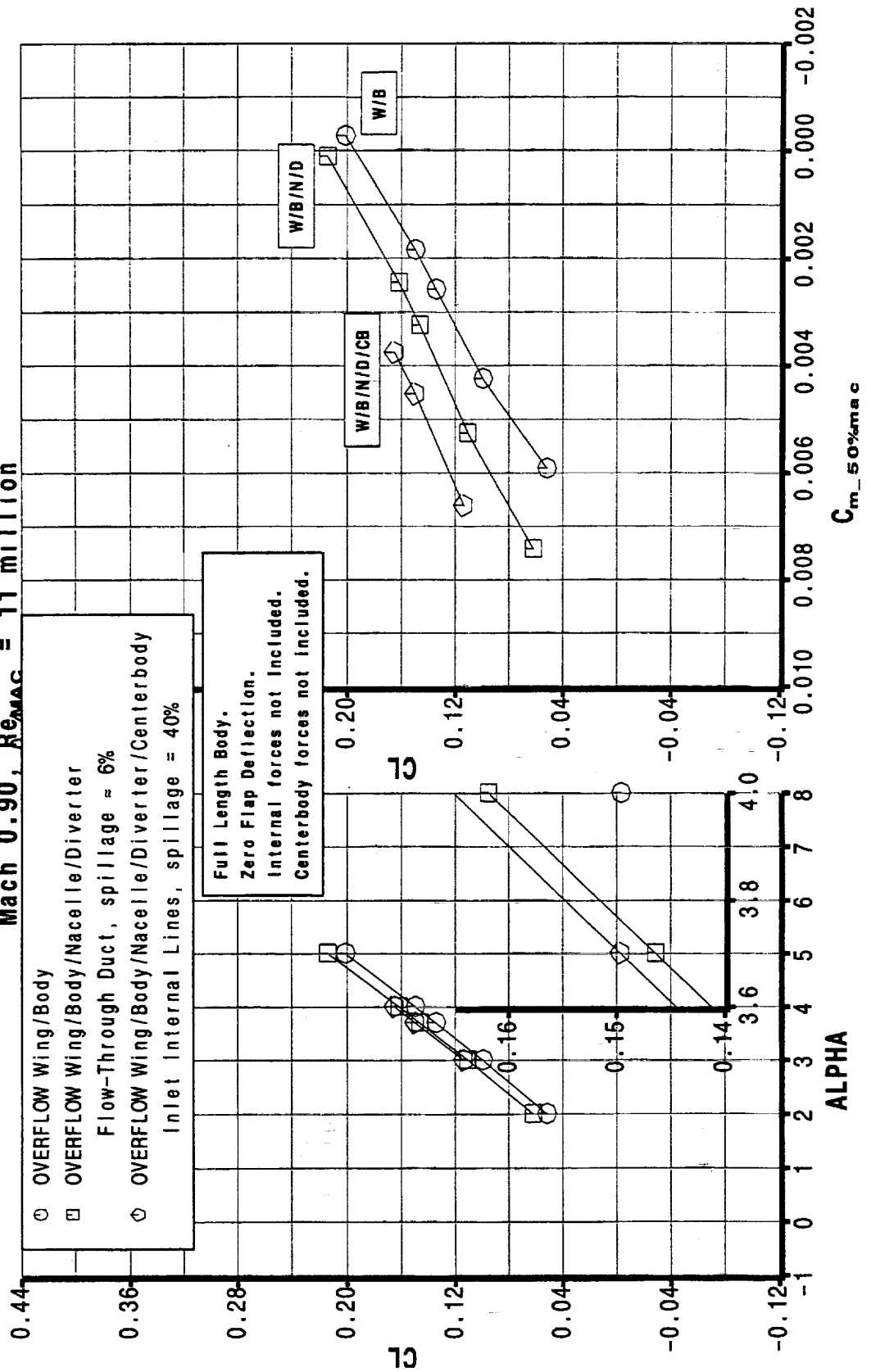
HSCT High Speed Aerodynamics - BCAG

The lift and pitching moment data are shown in this figure. The addition of the flow-through duct nacelles and the spilling nacelles with centerbody did not effect the pitching moment slope but there was a constant positive shift of the whole curve (in this low angle of attack region). The increase in lift relative to the flow-through case is evident.



TCA Wing/Body/Nacelle/Diverter/Centerbody Lift & Pitching Moment

Mach 0.90, $Re_{MAC} = 11$ million





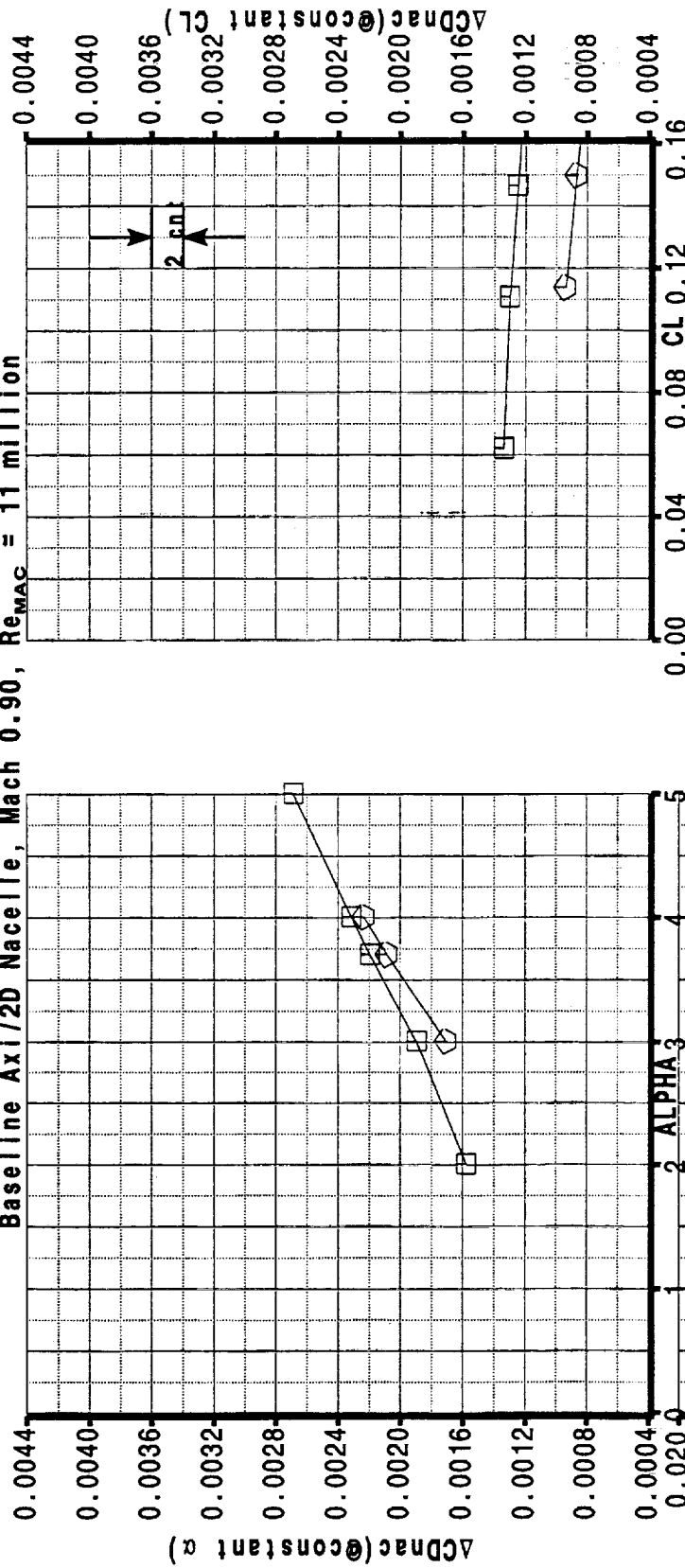
The Mach 0.90 data shown in the previous two figures are recast here in terms of nacelle force increments. This presentation serves to highlight how large an impact the increased lift of the 40 % spill case had on the installed drag of the nacelle. At constant angle of attack the spillage increase from 6 % to 40 % decreased the nacelle drag increment by ~ -1 counts, but the lift increase of ~ +0.0031 (2% of total lift) resulted in the installed drag increment decreasing by 4 counts (from 12 to 8 counts). These deltas between the nacelle force increments are essentially what could be called spillage increments; the problem is that the baseline was not a zero spillage case (the flow-through case spills 6%). These 'spillage increments' can be compared to the NGC results for flight Reynolds Number: spillage lift increment +0.0021 spillage drag increment -3.1 counts

A comparison of these values to the OVERFLOW wind tunnel Reynolds Number data (+0.0031 and -1 respectively) was clouded by the fact that the baseline for the two cases has two different spillage levels. The NGC flow-through case had lower spillage due to the higher Reynolds Number (thinner boundary layer).



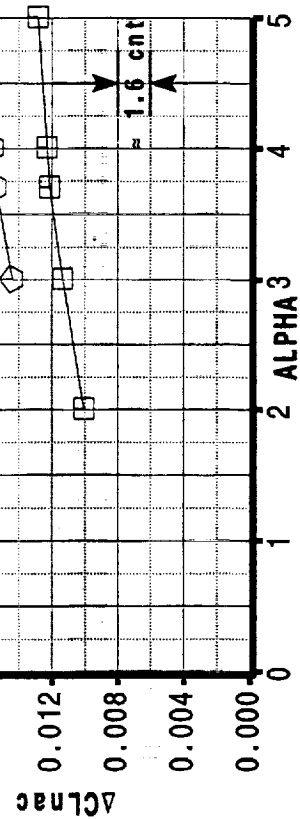
TCA Wing/Body/Nacelle/Diverter PAI Force Increments

Baseline Axi/2D Nacelle, Mach 0.90, $Re_{MAC} = 11$ million



- OVERFLOW Wing/Body/Nacelle/Diverter
Flow-Through Duct, spillage = 6 %
- ◇ OVERFLOW Wing/Body/Nacelle/Diverter/Centerbody
Inlet Internal Lines, spillage = 40 %

Full Length Body.
Zero Flap Deflection.
Internal forces not included.
Centerbody forces not included.





February 1998 HSR Airframe Technical Review

HSCT High Speed Aerodynamics - BCAG



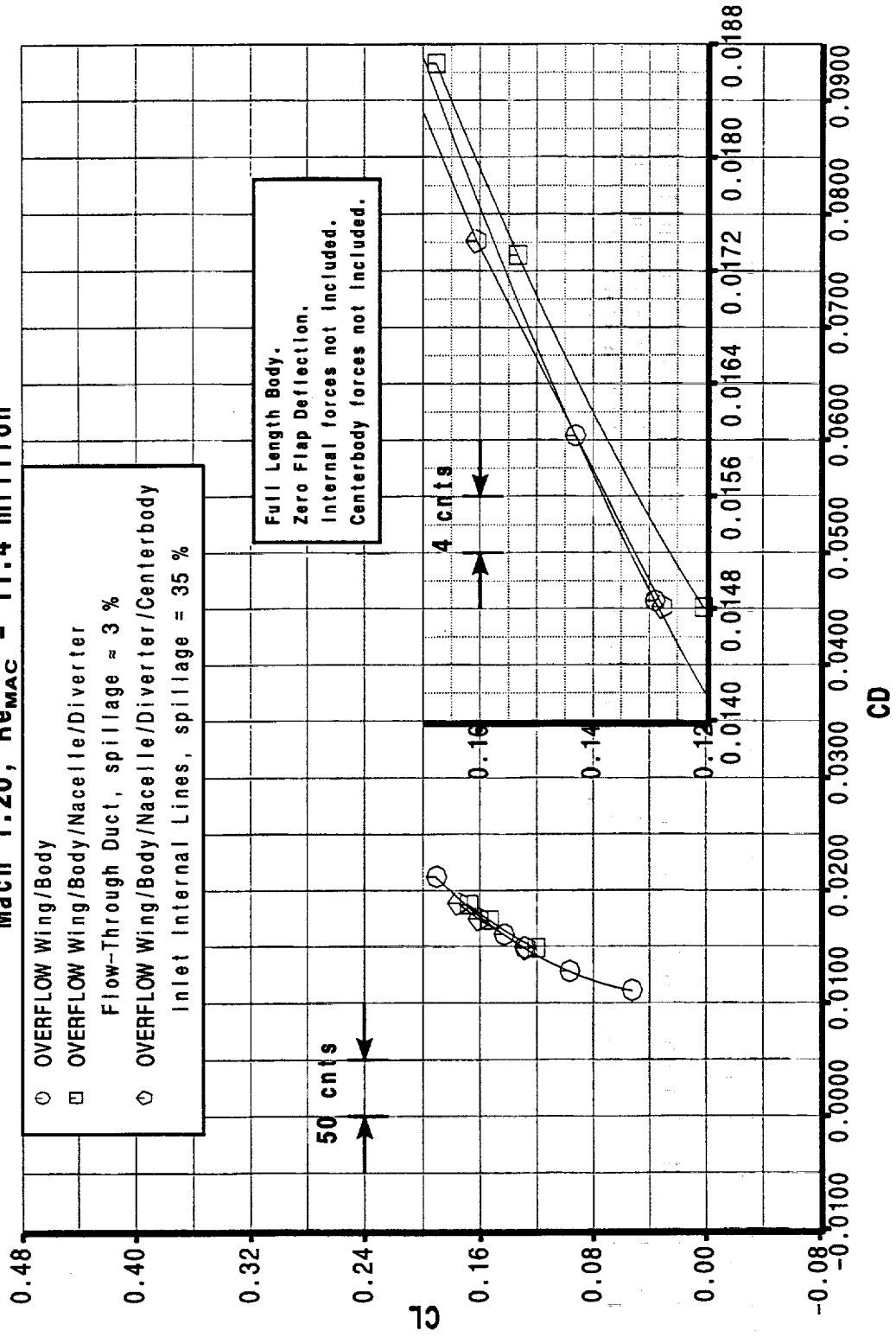
The figure shows the drag polar data for the OVERFLOW Mach 1.2 simulation of the TCA with the centerbody installed and the spillage controlled to the transonic climb level (35%). The large increase in the wing lower surface positive pressure shown in a previous figure was clearly evident as an increase in lift that shifted the W/B/N/D polar to the other side of the wing/body polar curve.



HSCT High Speed Aerodynamics - BCAG

TCA Wing/Body/Nacelle/Diverter/Centerbody Drag Polar

Mach 1.20, $Re_{MAC} = 11.4$ million





February 1998 HSR Airframe Technical Review

HSCT High Speed Aerodynamics - BCAG

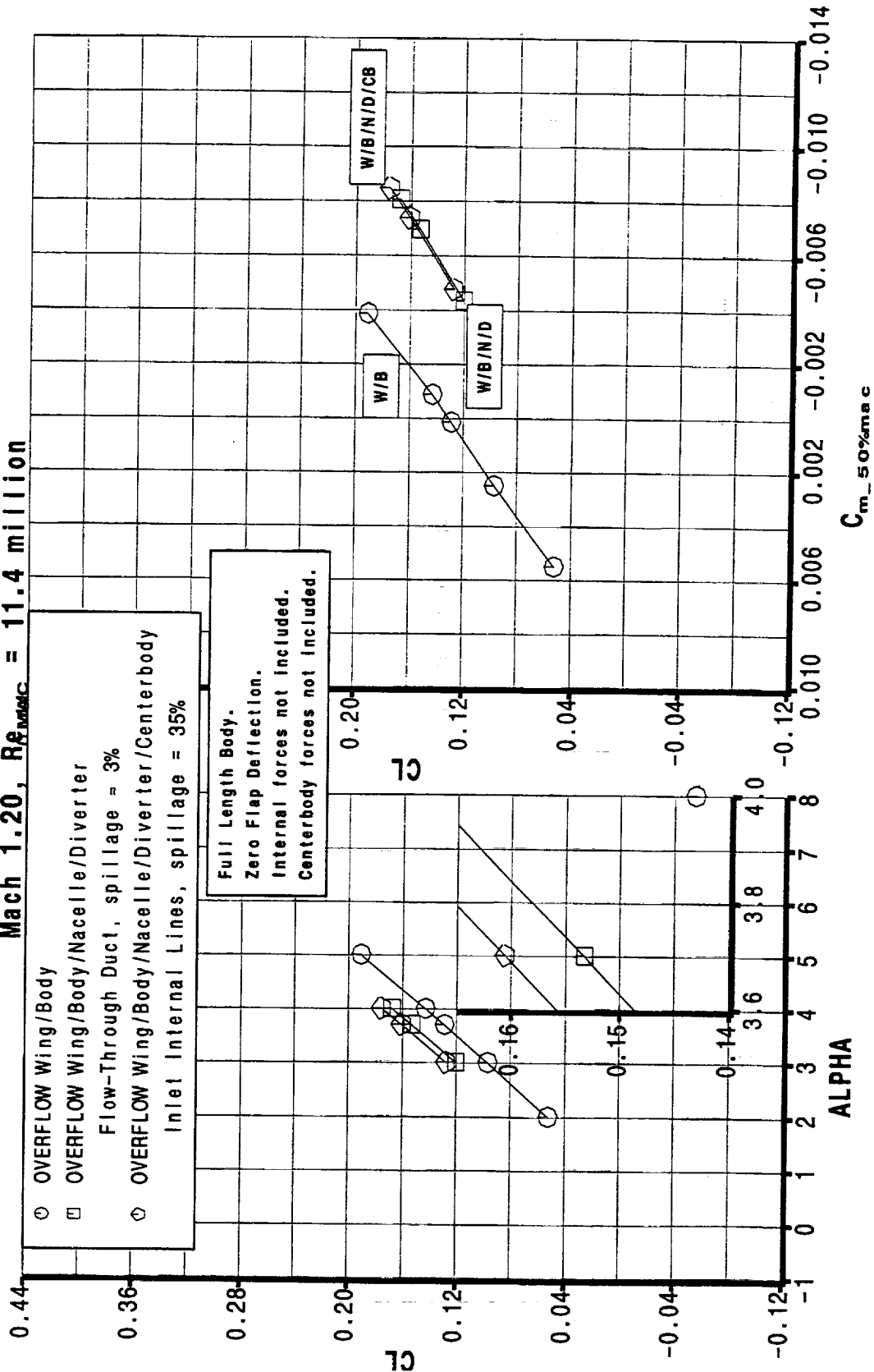


The Mach 1.2 lift and pitching moment data are shown in this figure. The addition of the flow-through duct nacelles and the spilling nacelles with centerbody had a small effect on the pitching moment slope but in contrast to the Mach 0.9 results (positive shift) there was a negative shift of the whole curve (in this low angle of attack region).



TCA Wing/Body/Nacelle/Diverter/Centerbody Lift & Pitching Moment

Mach 1.20, $Re_{MAC} = 11.4$ million



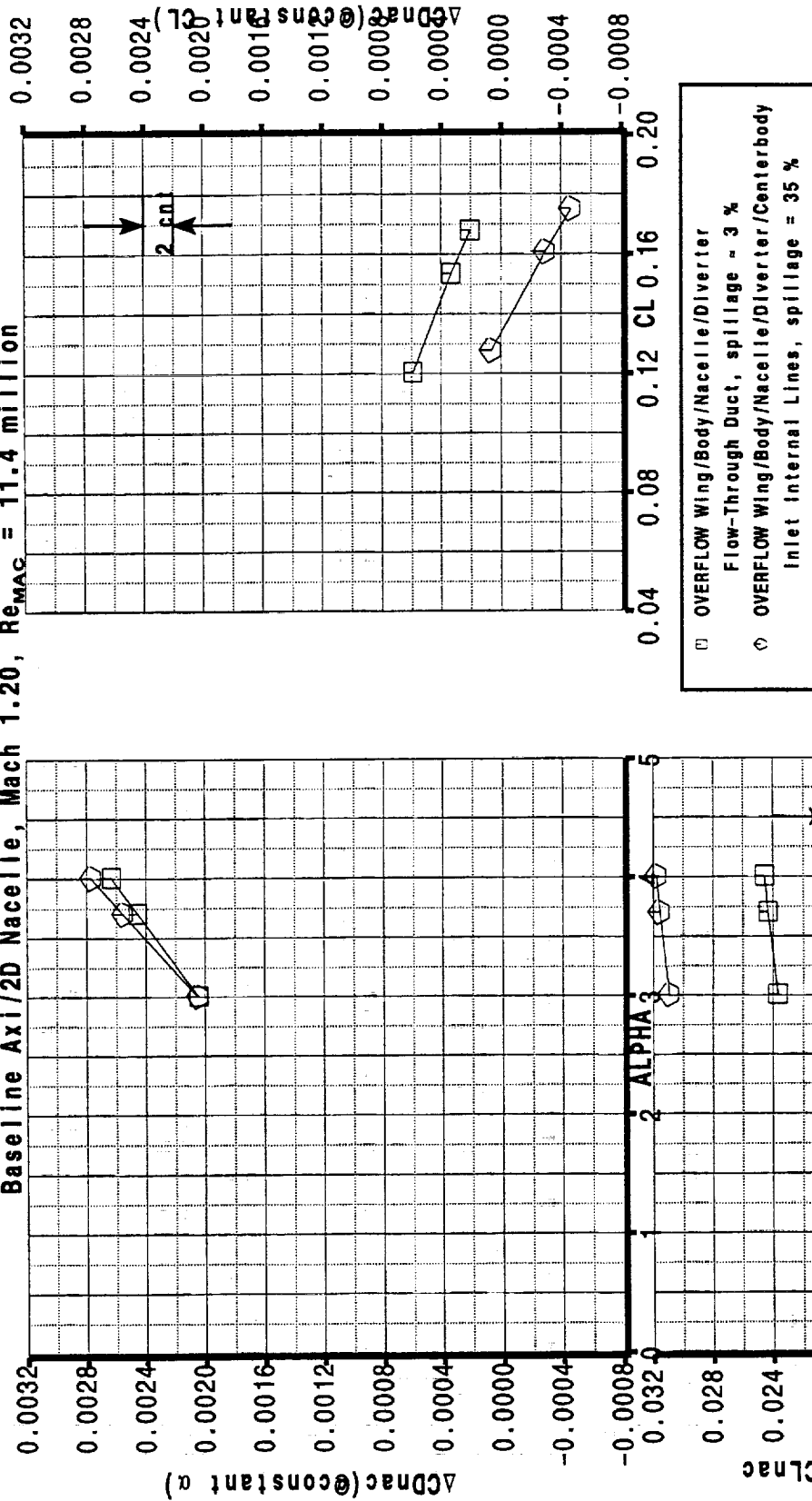


The Mach 1.20 data shown in the previous two figures are recast here in terms of nacelle force increments. This presentation serves to highlight how the increased lift of the 35 % spill case had an even larger effect on the installed drag of the nacelle than for the Mach 0.90, 40 % spillage case. At constant angle of attack the spillage increase from 3 % to 35 % increased the nacelle drag increment by ~ 1 counts, but the lift increase of ~ +0.007 (4% of total lift) resulted in the installed drag increment decreasing by 6 counts (from +2 to -4 counts). The NGC flight Reynolds Number results for these spillage increments were:

- spillage lift increment +0.0076
- spillage drag increment +0.35 count



TCA Wing/Body/Nacelle/Diverter PAI Force Increments
Baseline Axi/2D Nacelle, Mach 1.20, $Re_{MAC} = 11.4$ million





Bifurcated inlet installation

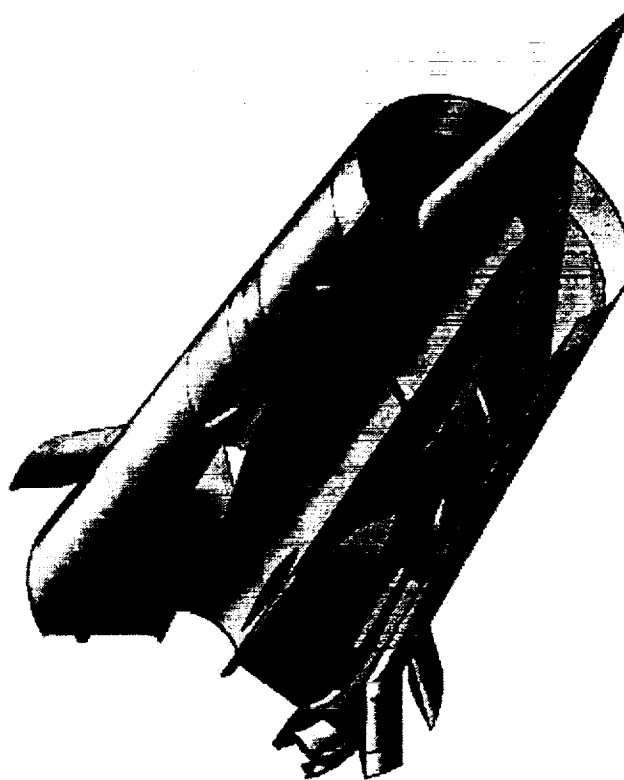
A bifurcated inlet nacelle was configured and installed on the TCA in 1996. This configuration was the result of a joint effort of high speed aerodynamics and propulsion design staffs. The normal nacelle installation guideline for diverter height was adhered to while also matching the end of the nacelle forecowl to the current TCA baseline nacelle nozzle. For the outboard nacelle this was possible without moving the current nozzle position. On the inboard installation it was necessary to rotate the nozzle slightly (nose up 0.3 deg). This inlet has a much larger lip bevel than the baseline TCA axisymmetric, but the bevel is smaller than previous bifurcated inlets as the result of some structural analyses and material studies allowing a redesign. The baseline TCA axisymmetric inlet has a 12 deg lip bevel that extends aft until the wall thickness is ~ 0.04 inches. The bifurcated inlet lip bevel extends aft along a 12 deg angle until the wall thickness is 0.2 - 0.3 inches.

The diverter LE was slid forward slightly ahead of the cowl lip station. This was done in order to try to start pushing the diverter channel flow out before it could choke as it did on the Ref H installation. In addition the nacelle top shoulders were rounded as quickly as possible aft of the lip bevel in order to provide some relief to the diverter channel area. The diverter planform half-angle at the diverter LE was the same as the baseline TCA (11 deg). However, on the bifurcated installation this half-angle went immediately into a large radius to fair into the maximum diverter width at the rear. This was in contrast to the baseline diverter planform which held the 11 deg half-angle on a straight line before starting a smaller radius and fairing into max width.

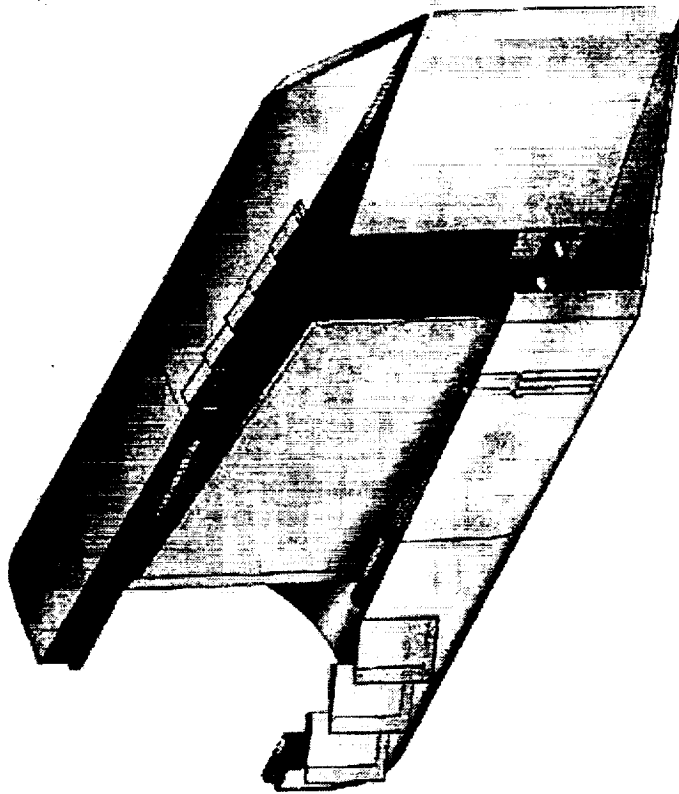


TCA Baseline and Alternate Inlets

Axisymmetric



Bifurcated

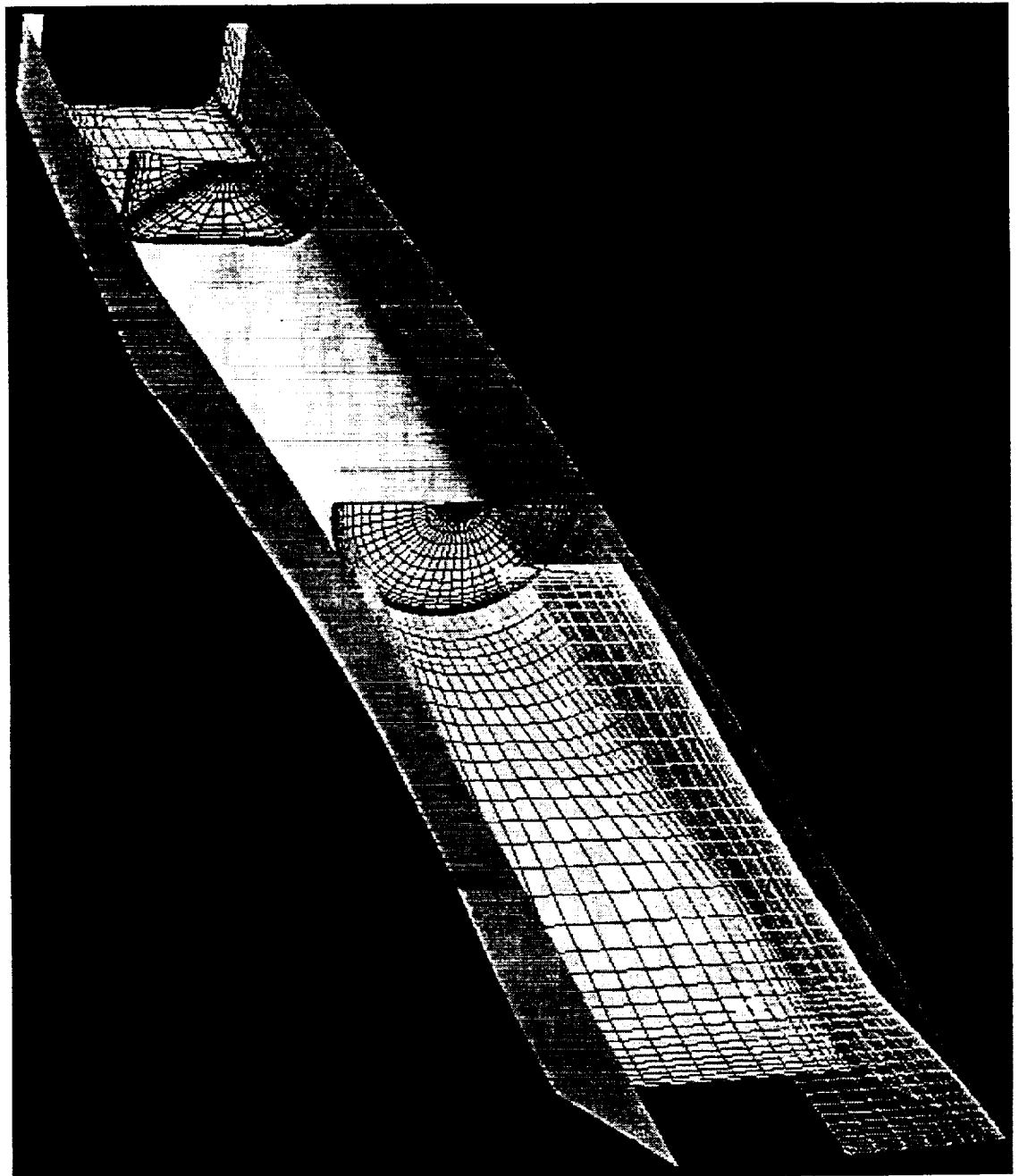




The OVERFLOW bifurcated inlet internal grid system is shown in this figure. The topology was very similar to the axisymmetric inlet except for the replacement of the centerbody grid by the compression ramp grid. Only the bottom half of the ramp surface grid is shown (yellow). Also, grid points have been removed for clarity. The inlet internal lines as defined by propulsion were used up to the engine face (blue). The mass flow was controlled at that station by adjusting pressure. The ramp was in the fully collapsed transonic configuration.



TCA Bifurcated Transonic Inlet Spillage

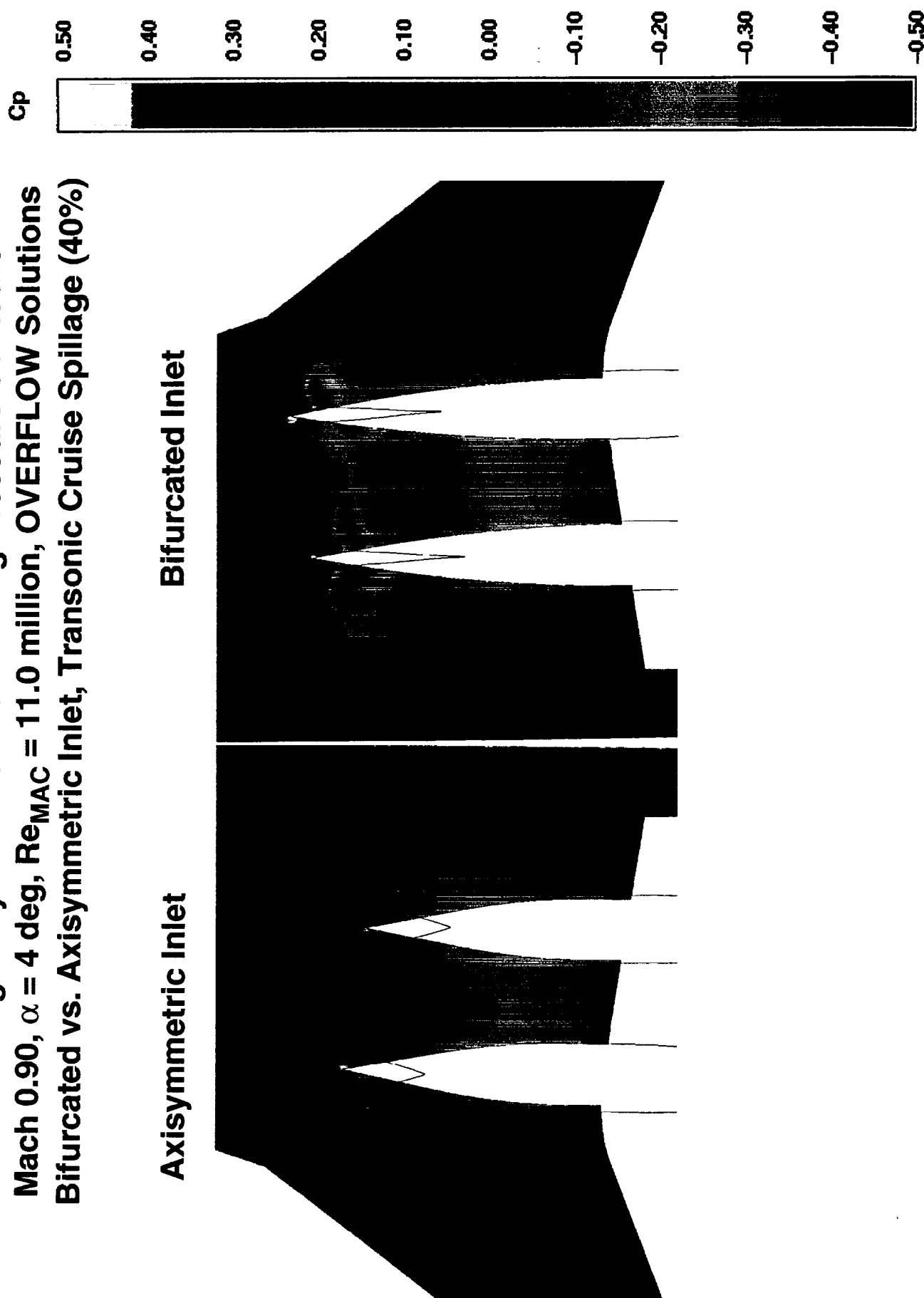




The wing lower surface pressure contours are compared at Mach 0.90, transonic cruise spillage, for the axisymmetric and bifurcated inlet installations. The pressure distribution characteristics were similar but the bifurcated had both higher positive pressures and lower negative pressures. Note that the pressure coefficient scale has been changed from the that used in previous figures in order to be able to assess the bifurcated pressure values. The very localized negative pressures generated on the wing lower surface by the bifurcated installation are probably due to the fact that the bifurcated inlet spills only to the sides creating much higher localized spill effects (expansion) than for the axisymmetric inlet.



TCA Wing/Body/Nacelle/Diverter Wing Pressure Contours Mach 0.90, $\alpha = 4$ deg, $Re_{MAC} = 11.0$ million, OVERFLOW Solutions Bifurcated vs. Axisymmetric Inlet, Transonic Cruise Spillage (40%)





February 1998 HSR Airframe Technical Review

HSCT High Speed Aerodynamics - BCAG



The next two figures show the nacelle surface pressures for the inboard and outboard nacelles (again comparing the bifurcated and axisymmetric inlet at Mach 0.90, 40% spillage). The large expansion around the bifurcated inlet cowl leading edge was clearly evident, as was, the spreading of this expansion around the inlet.



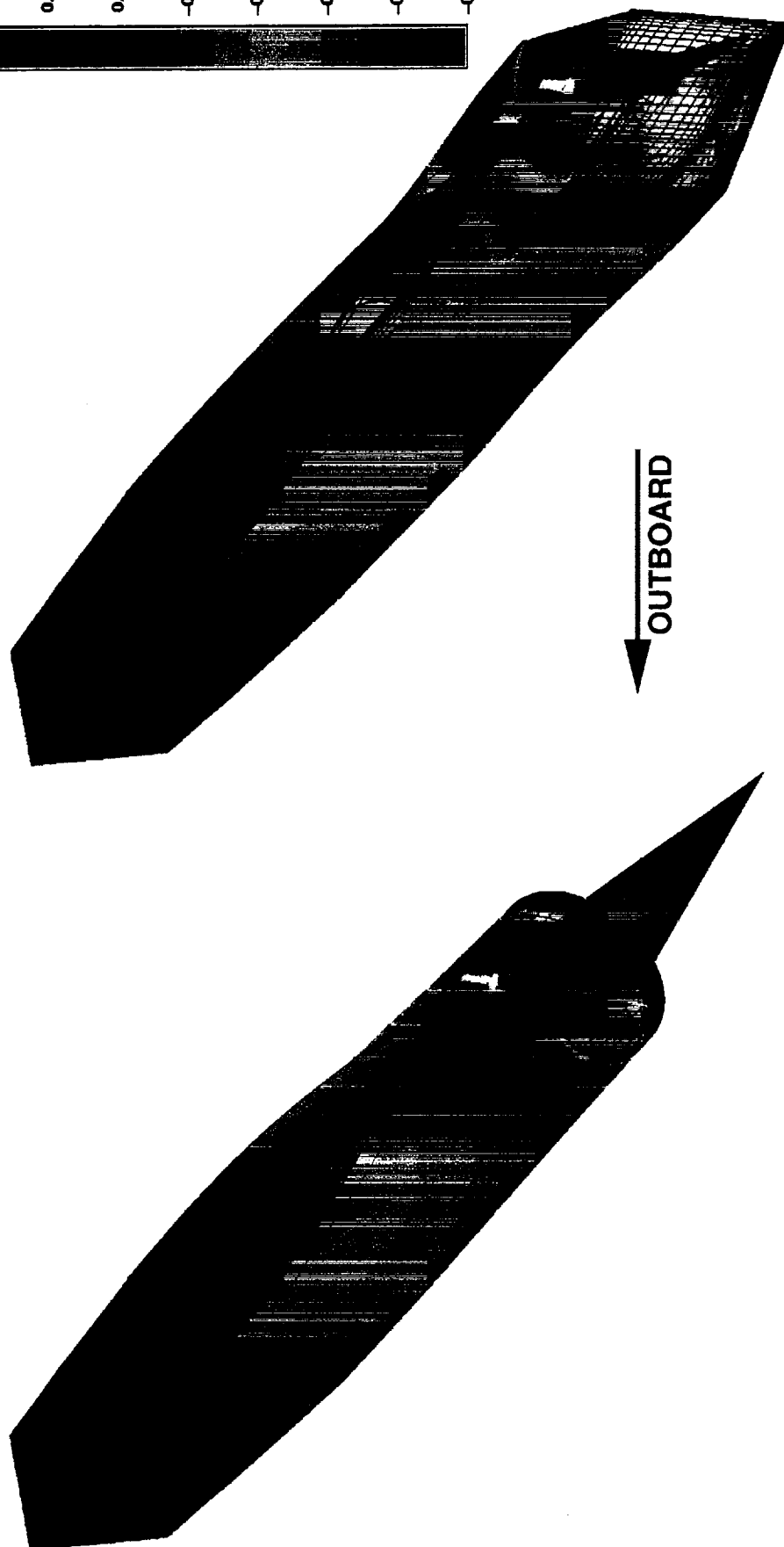
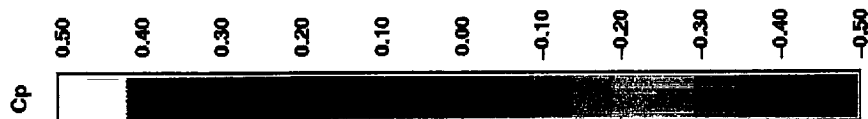
TCA Wing/Body/Nacelle/Diverter Nacelle Pressure Contours

Mach 0.90, $\alpha = 4$ deg, $Re_{MAC} = 11.0$ million, OVERFLOW Solution
 Bifurcated vs. Axisymmetric Inlet, Transonic Cruise Spillage (40%)

INBOARD Nacelle

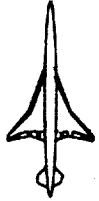
Axisymmetric Inlet

Bifurcated Inlet





February 1998 HSR Airframe Technical Review



HSCT High Speed Aerodynamics - BCAG

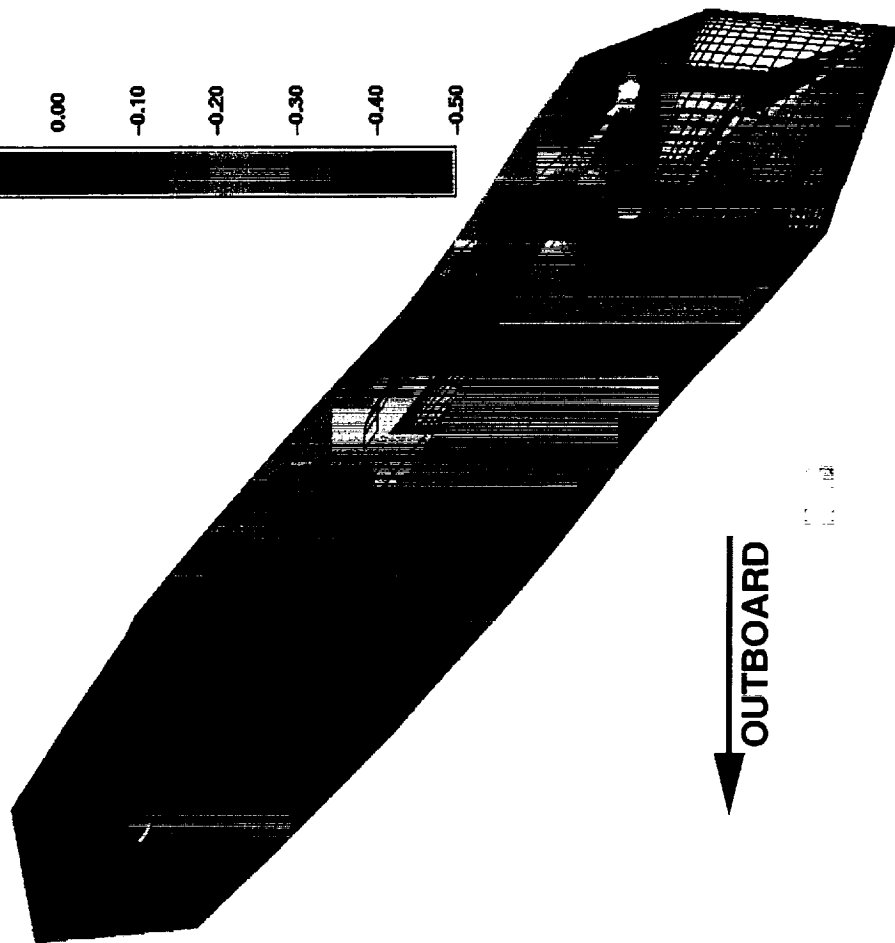
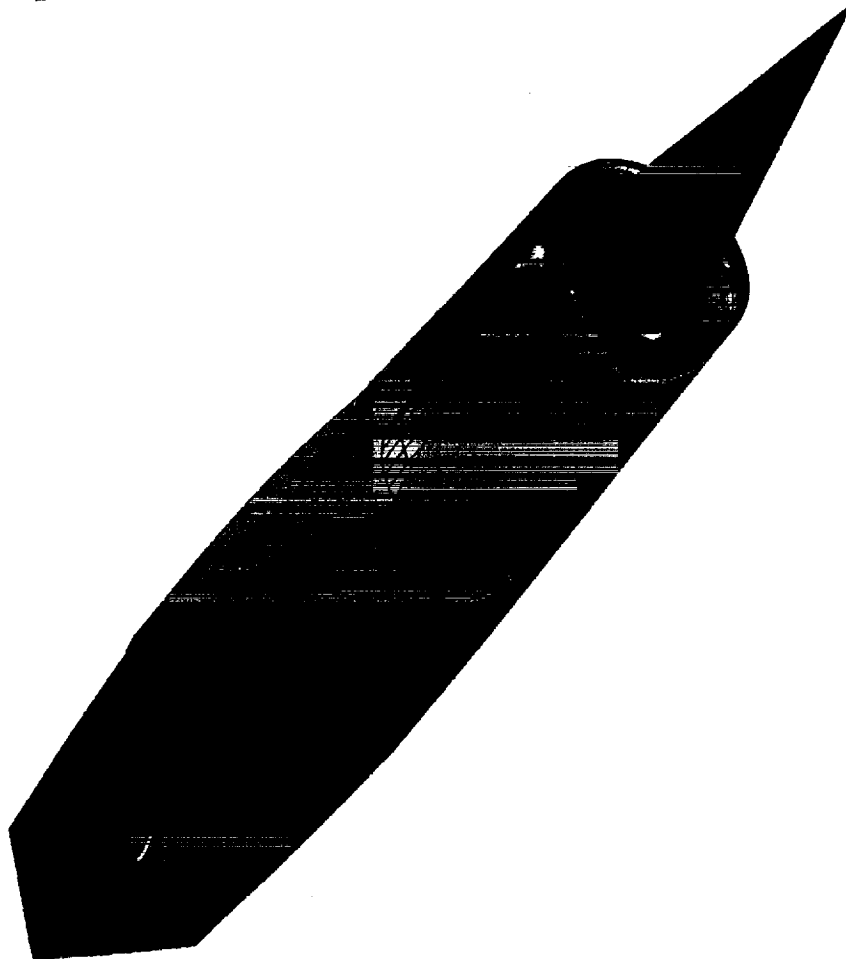
---See text for previous page---



TCA Wing/Body/Nacelle/Diverter Nacelle Pressure Contours
Mach 0.90, $\alpha = 4$ deg, $Re_{MAC} = 11.0$ million, OVERFLOW Solution
Bifurcated vs. Axisymmetric Inlet, Transonic Cruise Spillage (40%)
OUTBOARD Nacelle

Axisymmetric Inlet

Bifurcated Inlet





February 1998 HSR Airframe Technical Review

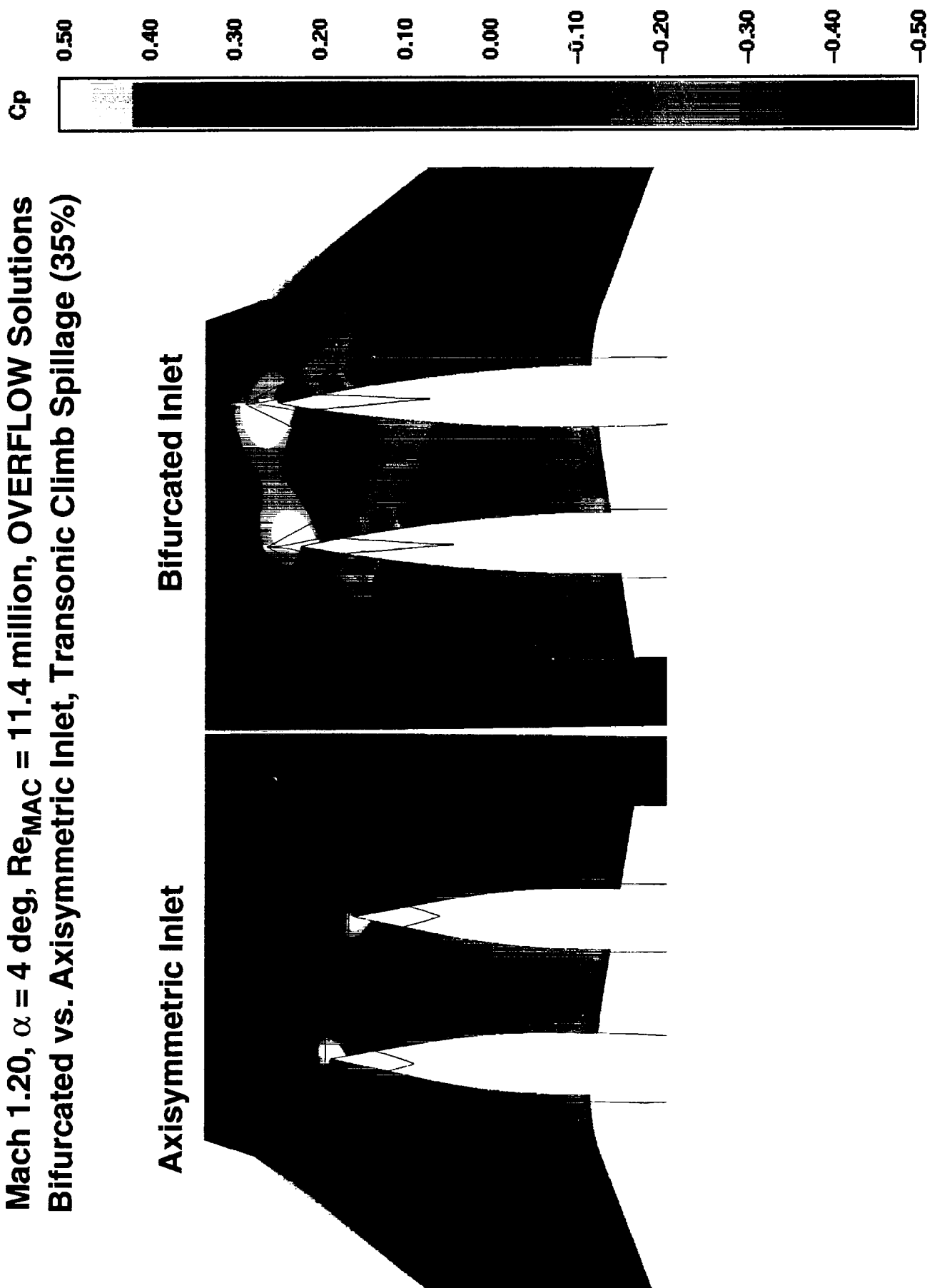


HSCT High Speed Aerodynamics - BCAG

The wing lower surface pressure contours are compared at Mach 1.20, transonic climb spillage, for the axisymmetric and bifurcated inlet installations. The pressure distribution comparison was similar to the Mach 0.90 comparison. The bifurcated inlet appeared to be generating an even stronger normal shock than the axisymmetric inlet and the resulting pressures again required a pressure coefficient scale change from that used for the axisymmetric.



**TCA Wing/Body/Nacelle/Diverter Wing Pressure Contours
Mach 1.20, $\alpha = 4$ deg, $Re_{MAC} = 11.4$ million, OVERFLOW Solutions
Bifurcated vs. Axisymmetric Inlet, Transonic Climb Spillage (35%)**





The next two figures show the nacelle surface pressures for the inboard and outboard nacelles comparing the bifurcated and axisymmetric inlet at Mach 1.20, 35% spillage. The most evident difference between the pressure contours for the two inlets was the concentrated spillage effects at the bifurcated inlet cowl lip leading edge.

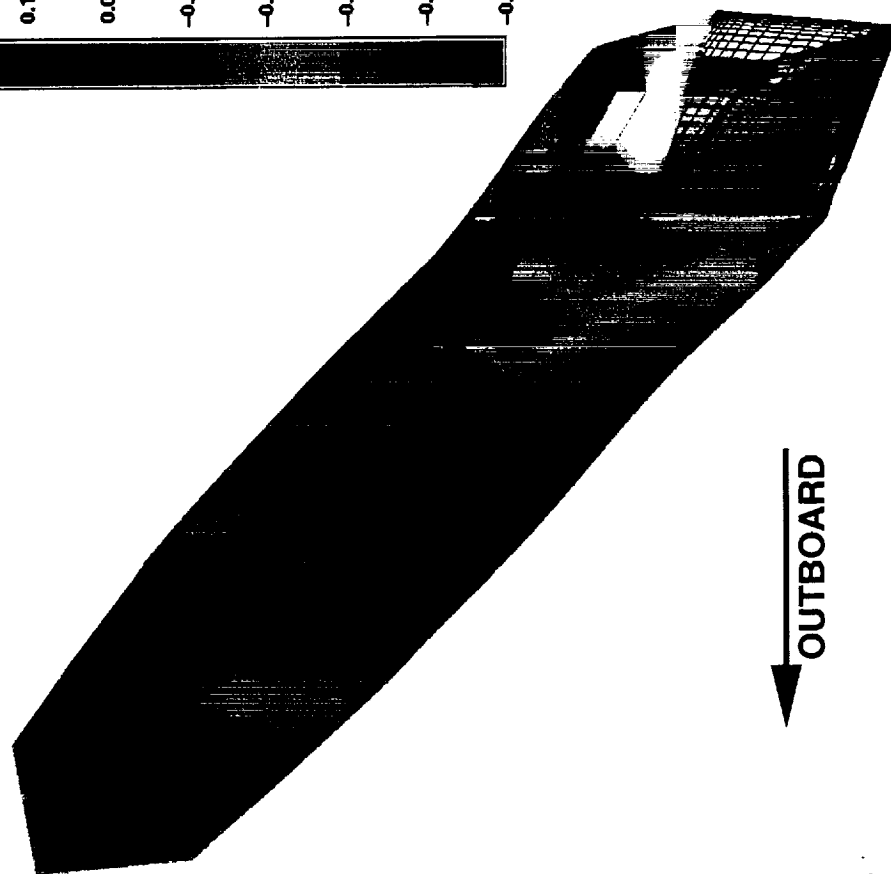
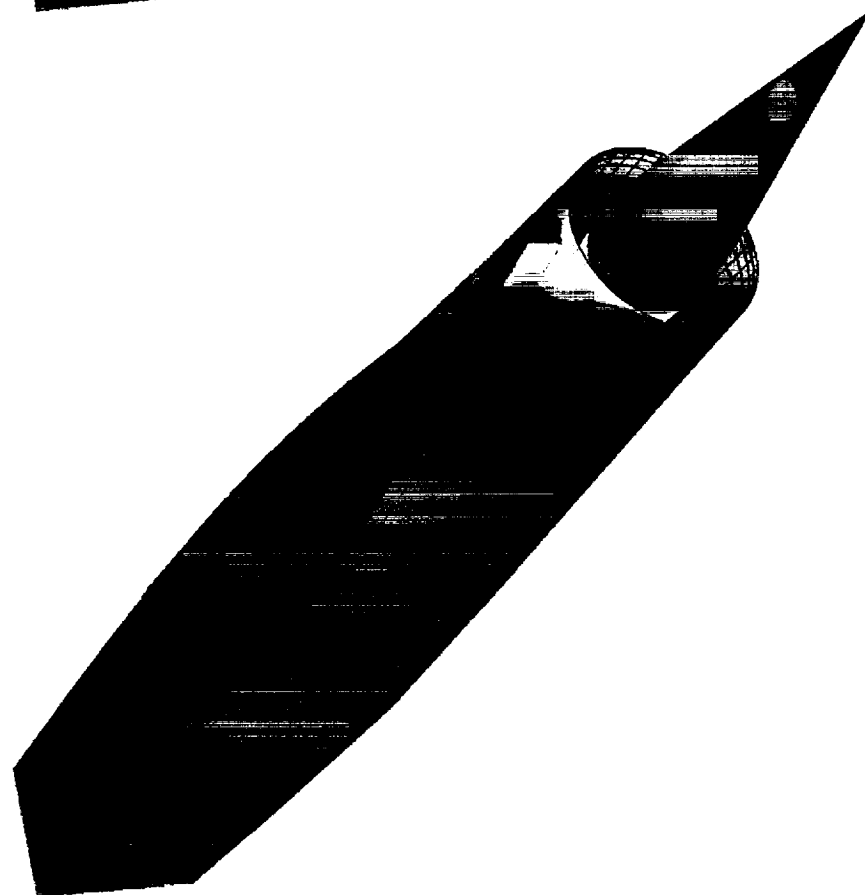


TCA Wing/Body/Nacelle/Diverter Nacelle Pressure Contours

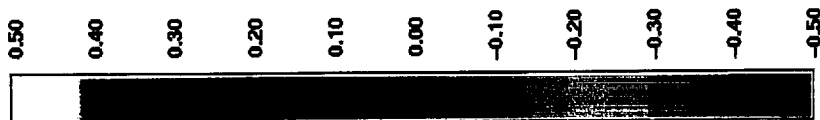
Mach 1.20, $\alpha = 4$ deg, $Re_{MAC} = 11.4$ million, OVERFLOW Solution
 Bifurcated vs. Axisymmetric Inlet, Transonic Climb Spillage (35%)

Axisymmetric Inlet

Bifurcated Inlet



OUTBOARD





---See text for previous page---

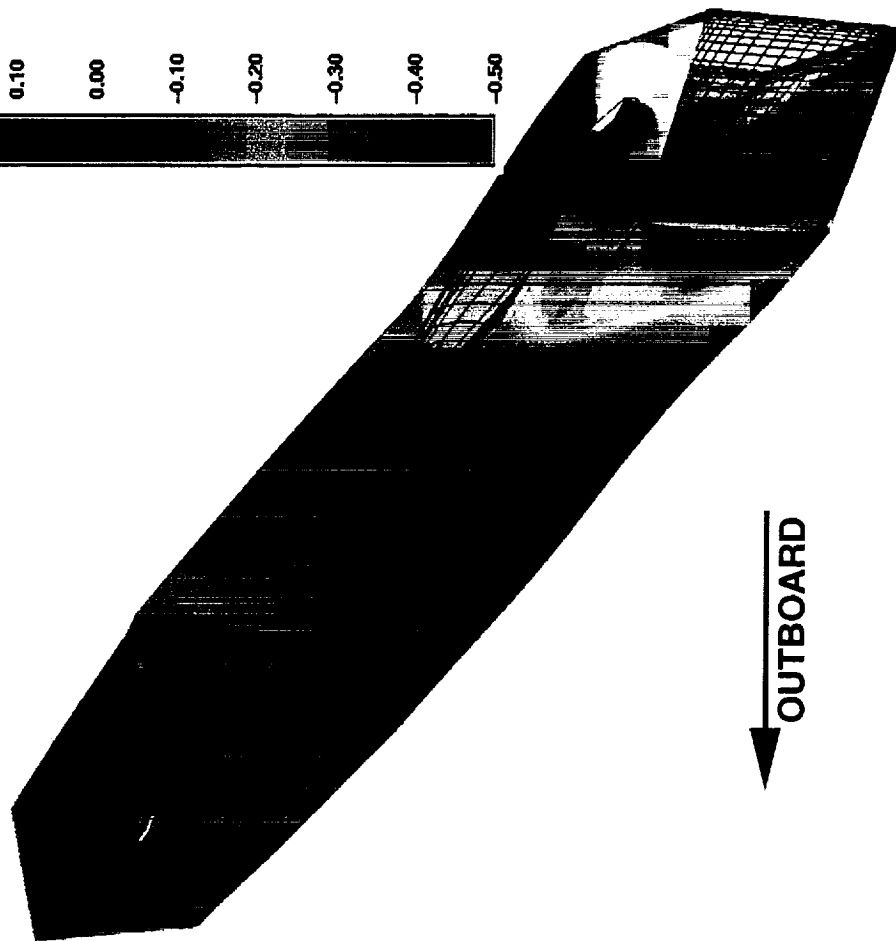
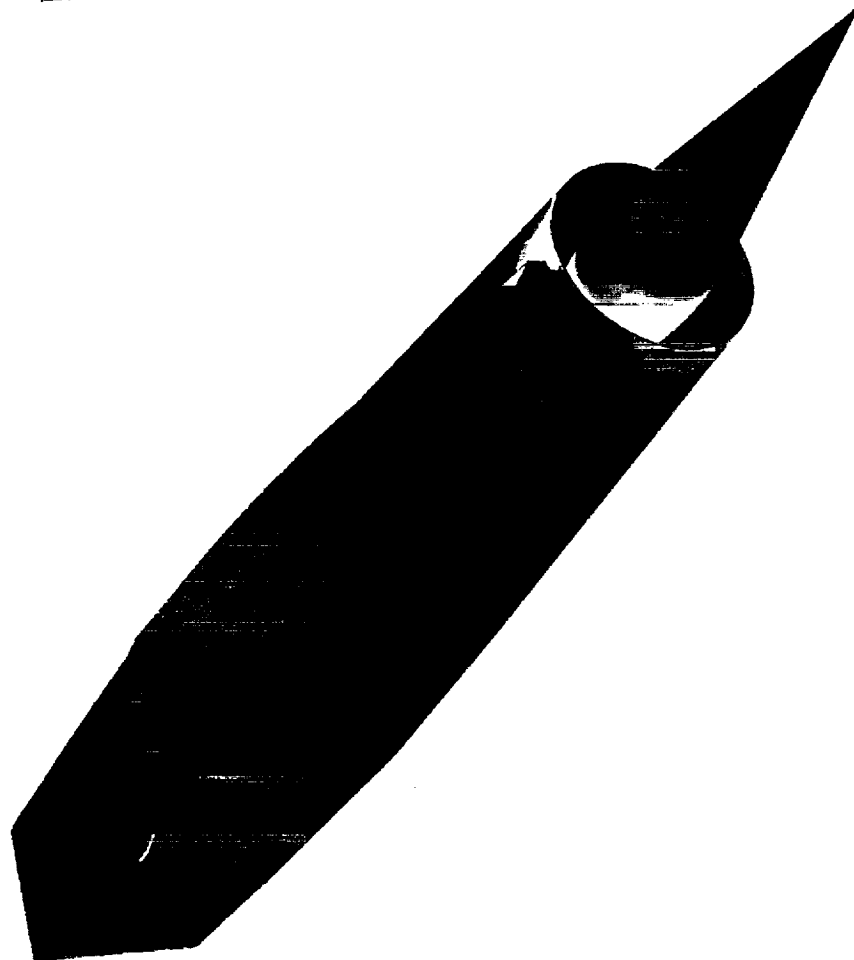


TCA Wing/Body/Nacelle/Diverter Nacelle Pressure Contours

Mach 1.20, $\alpha = 4$ deg, $Re_{MAC} = 11.4$ million, OVERFLOW Solution
 Bifurcated vs. Axisymmetric Inlet, Transonic Climb Spillage (35%)
 OUTBOARD Nacelle

Axisymmetric Inlet

Bifurcated Inlet



OUTBOARD

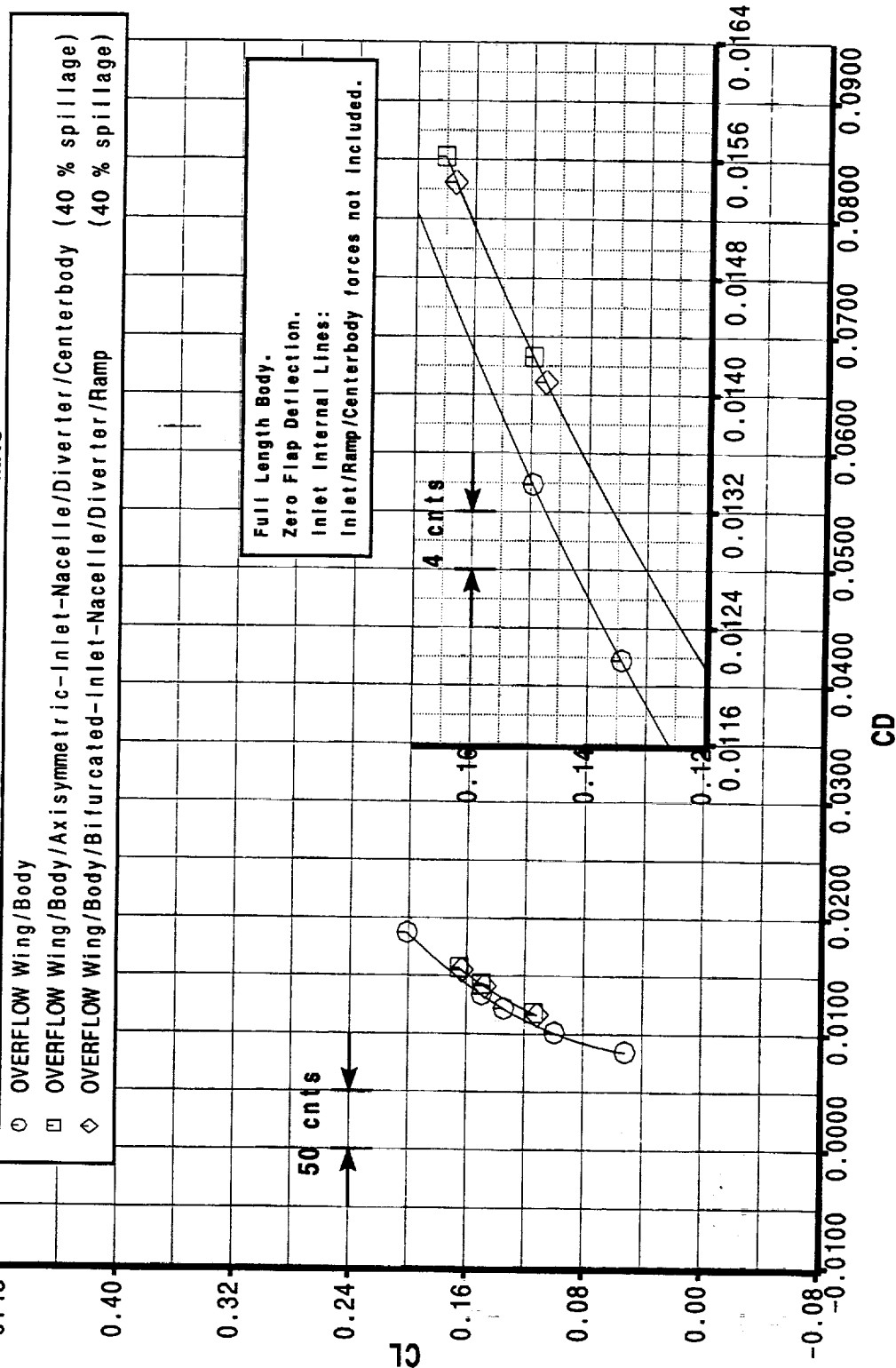


The transonic cruise drag polar for the two inlets is shown. Despite the differences in the pressure distributions shown previously the total installed airplane drag for the two inlet concepts was identical. The bifurcated inlet drag ended up on the same polar as the axisymmetric but for the same angle of attack it had lower lift and lower drag levels. This could be due to the bifurcated inlet lip bevel providing a much larger forward facing surface for the spillage expansion pressures to work on and reduce the drag of the nacelle. Without spillage the lip bevel carried positive pressure on it and was a source of drag (see next figure). The lower lift of the bifurcated installation was the result of the large regions of negative pressure on the wing lower surface more than counteracting the large regions of positive pressure. More investigation is required into component pressures and forces in order to develop a complete understanding of the various lift and drag interference terms and flow physics at work in this complex flow field.



TCA Wing/Body/Nacelle/Diverter Drag Polar, Transonic Cruise Spillage

Bifurcated vs. Axi Inlet, Mach 0.90, $Re_{MAC} = 11$ million





February 1998 HSR Airframe Technical Review

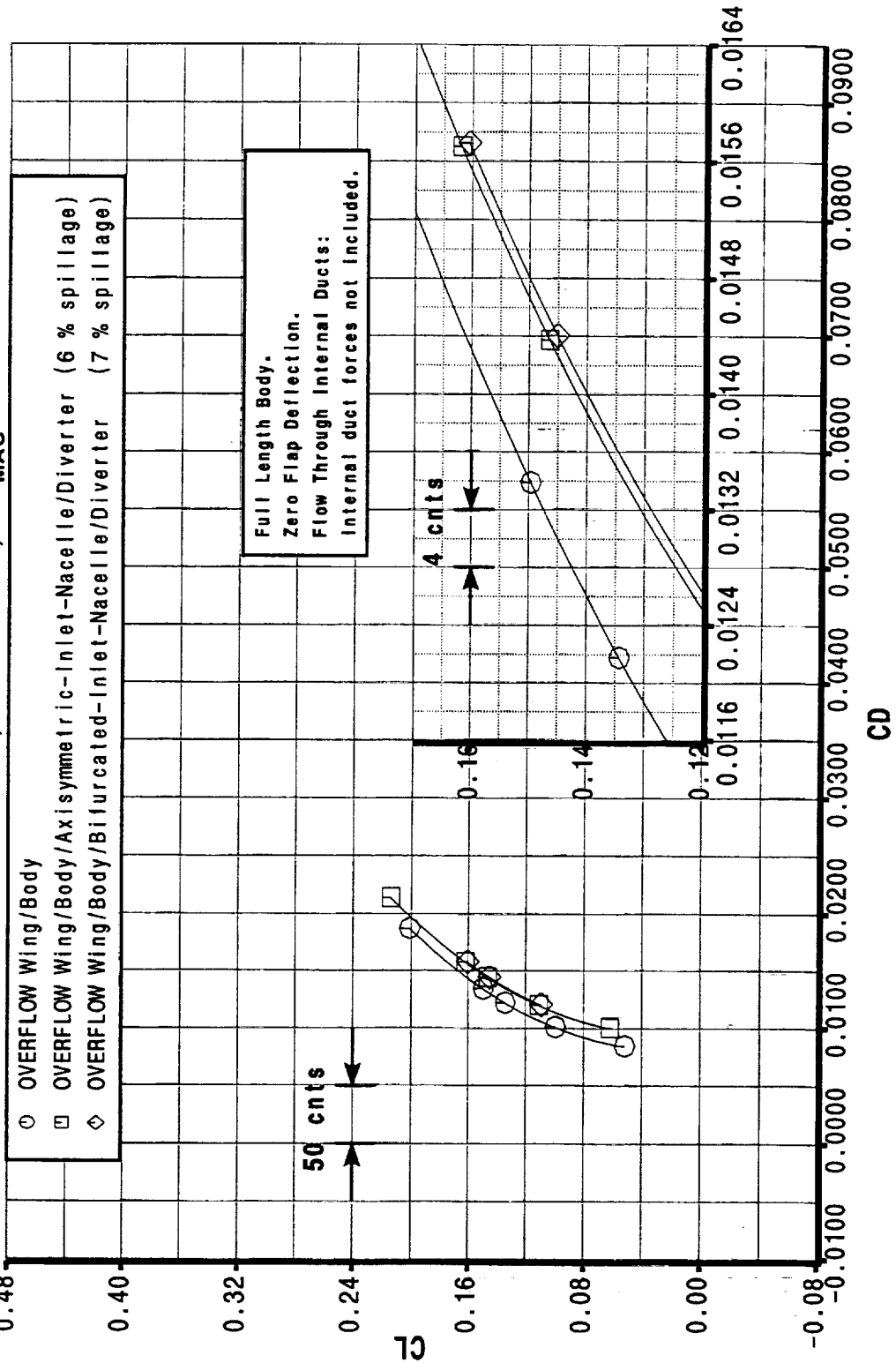
HSCT High Speed Aerodynamics - BCAG



As a reference for the previous figure the two inlets are compared again in this figure at Mach 0.90 but with flow-through ducts. The bifurcated inlet had higher drag than the axisymmetric in this case (~1.5 counts). This was probably due to the bifurcated inlet lip bevel. The comparison is clouded by the higher spillage of the bifurcated (7% vs 6 %) due to the longer internal duct (more boundary layer buildup). This difference is spillage was probably small enough that the drag difference conclusion is not effected.



TCA Wing/Body/Nacelle/Diverter Drag Polar, Flow Through Duct Bifurcated vs. Axi Inlet, Mach 0.90, $Re_{MAC} = 11$ million





February 1998 HSR Airframe Technical Review

HSCT High Speed Aerodynamics - BCAG



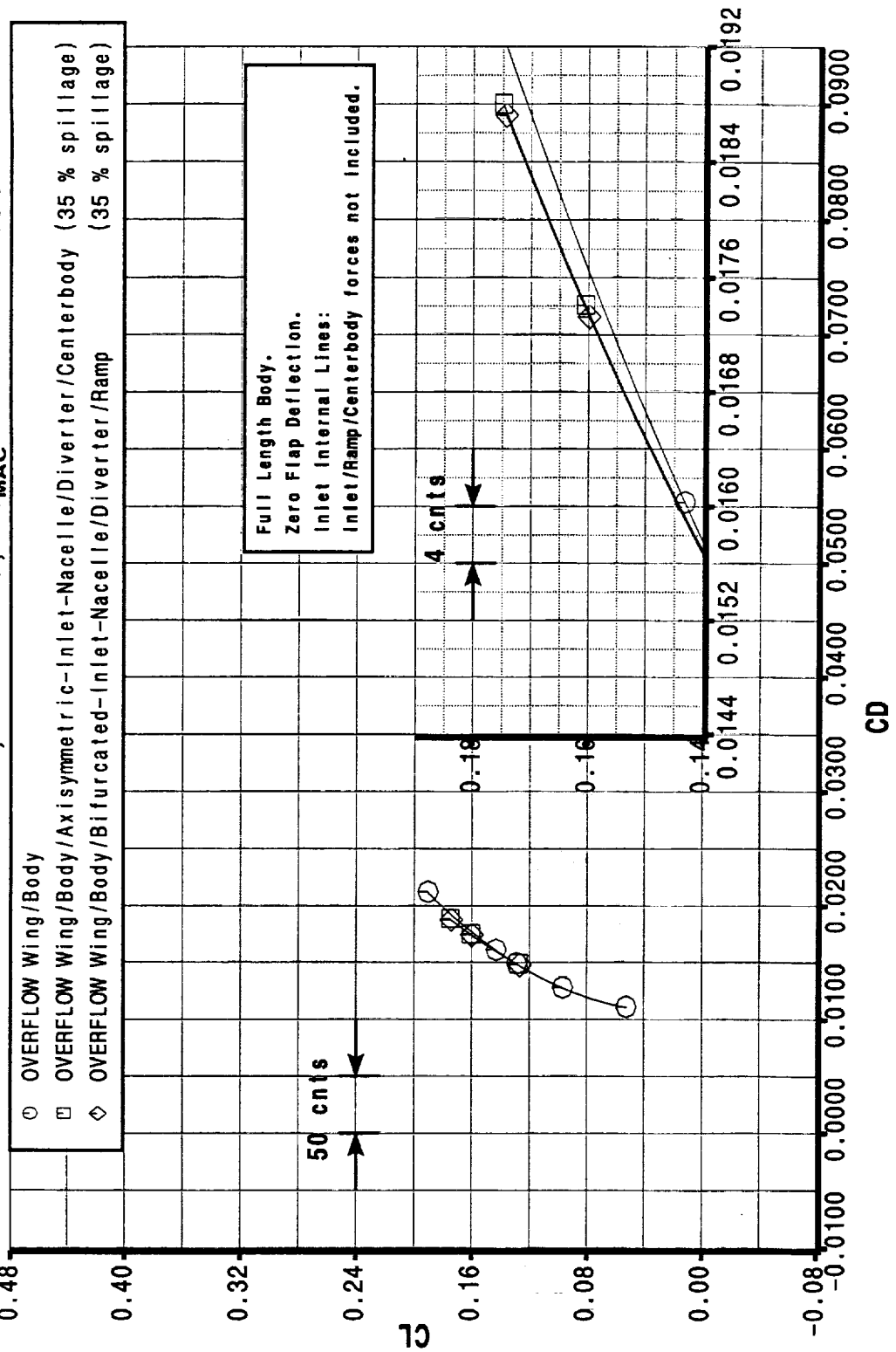
The transonic climb (Mach 1.20) drag polar for the two inlets is shown. Again, despite the differences in the pressure distributions shown previously, the total installed airplane drag for the two inlet concepts was identical. In this case the bifurcated inlet drag was actually slightly less than the axisymmetric drag. Similar to the Mach 0.90 case, for the same angle of attack, the bifurcated had lower lift and lower drag values such that it nearly slid exactly down the axisymmetric polar curve.



HSCT High Speed Aerodynamics - BCAG

TCA Wing/Body/Nacelle/Diverter Drag Polar, Transonic Climb Spillage

Bifurcated vs. Axi Inlet, Mach 1.20, $Re_{MAC} = 11.4$ million





February 1998 HSR Airframe Technical Review



HSCT High Speed Aerodynamics - BCAG

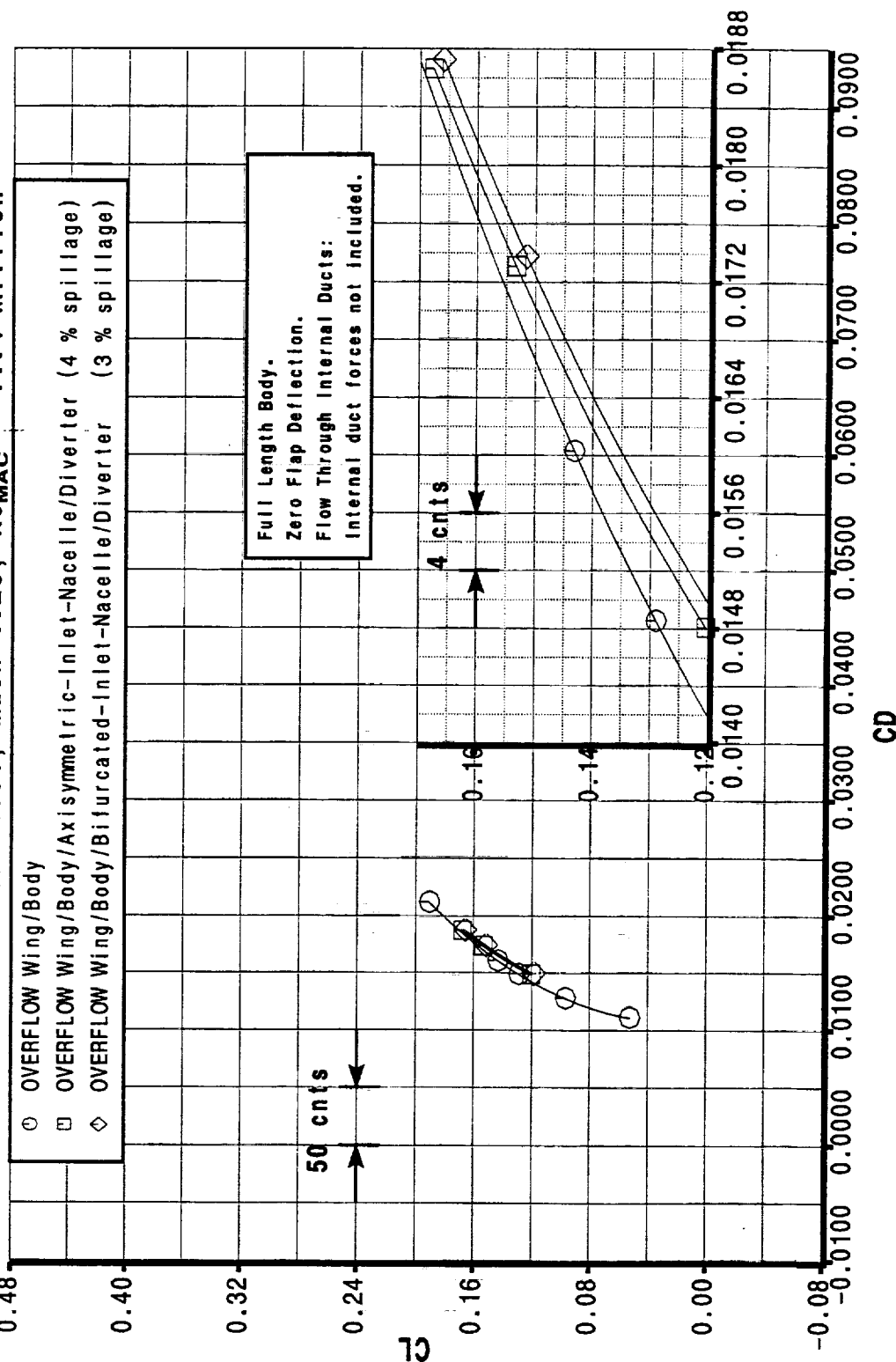
As a reference for the previous figure the two inlets are compared again in this figure at Mach 1.20 but with flow-through ducts. The bifurcated inlet had higher drag than the axisymmetric for this case also (~2.0 counts). The bifurcated inlet spillage was about 1% higher than the axisymmetric spillage as was seen for the Mach 0.90 data.



HSCT High Speed Aerodynamics - BCAG

TCA Wing/Body/Nacelle/Diverter Drag Polar, Flow-Through Duct

Bifurcated vs. Axi Inlet, Mach 1.20, $Re_{MAC} = 11.4$ million





Flight spillage levels have a major impact on the aerodynamic characteristics of the nacelle installation. The implementation of the spillage control boundary condition in OVERFLOW appears to be successful and provided a tool by which these spillage impacts could begin to be ascertained. The spillage increments calculated by OVERFLOW at the PIE wind tunnel condition were relatively close to the flight Reynolds Number data calculated by NGC. A follow-on task will be to run a flight Reynolds Number case with OVERFLOW (or have NGC run a wind tunnel case) to cross-check the two methods.

Although the bifurcated inlet had about 2 counts more drag than the axisymmetric inlet for the transonic flow-through duct cases, the implementation of the flight spillage modeling resulted in identical drag levels for the two inlet concepts. NGC will be calculating the drag of the bifurcated nacelle with spillage at flight Reynolds Number in FY1998.



Spillage Analysis Conclusions

- Flight spillage vs flow-through
- Spillage control b.c. successfully implemented in OVERFLOW
- Flight spillage levels have significant impact on flow field around inlet region and on airplane performance
 - Mach 0.90: Nacelle installed drag reduced by 4 counts
 - Mach 1.20: Nacelle installed drag reduced by 6 counts
- Bifurcated inlet vs axisymmetric inlet nacelle
- Flow-through duct: bifurcated inlet nacelle drag increment over axisymmetric at Mach 0.90 and 1.20 is ~ + 2 counts
- Mach 0.90 / transonic cruise spillage (40%): bifurcated inlet nacelle drag is equal to axisymmetric
- Mach 1.20 / transonic climb spillage (35%): bifurcated inlet nacelle drag is equal to axisymmetric

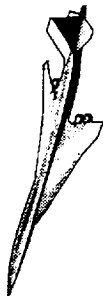


February 1998 HSR Airframe Technical Review

HSCT High Speed Aerodynamics - BCAG



---See text for previous page---



Nacelle Diverter Design and Nozzle Boattail Drag Studies

**P. Sundaram, Chih F. Shieh, Alan E. Arslan,
Hoyt Wallace, and Shreekant Agrawal**

Configuration Aerodynamics

**The Boeing Company
Long Beach, California**

HSR Airframe Technical Review

Los Angeles, California

February 9-13, 1998



This page is intentionally left blank.

Nacelle Diverter Design and Nozzle Boattail Drag Studies

P. Sundaram, Chih F. Shieh, Alan E. Arslan, Hoyt Wallace, and Shreekant Agrawal
The Boeing Company
Long Beach, California 90807-5309

The paper presents the results of the various PAI related effort performed during FY97 at Boeing Long Beach (BLB). One of the important study performed was the TCA nacelle diverter parametric shape modifications carried out to improve the TCA baseline nacelle installation drag. CFL3D Navier-Stokes solutions for wing/body/nacelle/diverter configurations incorporating simple shape modifications to the TCA baseline nacelles and diverters have been obtained at the supersonic cruise Mach number of $M_\infty = 2.4$ for $Re_c = 212$ million. These shape modifications, called N/D cycle 1, kinked the inboard and outboard nacelles to align the local flow at the nacelle inlet face and pitched the inboard nacelle to reduce the diverter volume by lowering the diverter leading-edge height requirement of 0.14% boundary layer run. The N/D cycle 1 design reduced the TCA baseline drag by nearly 1.2 count at the flight Reynolds number and 1.4 counts at the wind-tunnel Reynolds number ($Re_c = 6.36$ million).

The paper also describes the successful completion of the CFL3D Navier-Stokes solutions for the Reference H installed transonic nozzle boattail configurations for axisymmetric and 2-D powered nozzles at both the transonic and reference settings. These installed nozzle computations were obtained on parallel platforms using the CFL3Dhp code with a fast turn-around time. Using these solutions, the jet effects on the aftbody for the axisymmetric nozzles at transonic Mach numbers of $M_\infty = 0.9$ and 1.1 were calculated. Finally, the paper also presents the isolated nozzle study that investigated the effect of turbulence models on the nozzle boattail pressures. This study provided an insight into CFL3D Navier-Stokes solutions for powered nozzle simulations.

Outline

This chart gives the outline of the different topics covered in this presentation.

Outline



High Speed Aerodynamics, Long Beach

- Objectives
- Approach
- TCA nacelle/diverter shaping to reduce drag
- Ref. H installed nozzle computations - revisited
- Jet effects on aftbody drag
- Turbulence model investigation for isolated nacelle
- Summary and conclusions

Objectives

The PAI effort during FY97 were divided into four different topics. These include (a) TCA nacelle/diverter shape modifications, (b) installed nozzle boattail drag calculations for the Reference H axisymmetric and 2-D nozzle geometry, (c) assessing the jet effects on fuselage aftbody, and (d) turbulence model study for powered nozzle simulations.

Objectives



High Speed Aerodynamics, Long Beach

- Reshape the TCA baseline nacelles and diverters to reduce drag
- Assess the capability and efficiency of viscous CFD methods for predicting the isolated and installed configurations including power effects
 - Compare the aerodynamic performance of Ref. H axisymmetric and 2-D nozzle nacelles
 - Determine the jet effect on fuselage aftbody through CFD analyses

Approach

The approach taken to accomplish the different objectives are given in this chart. In general, the present approach is based on the CFL3D Navier-Stokes analysis of the installed wing/body/nacelle/diverter configurations. In addition, to calculate the installation and interference drag values, the CFL3D wing/body and isolated nacelle Navier-Stokes solutions have also been obtained. In particular, for the TCA nacelle/diverter modification study, the TCA wing/body/nacelle/diverter computations were performed at the supersonic cruise $M_\infty = 2.4$ for wind-tunnel and flight Reynolds numbers. The Reference H powered nozzle boattail drag computations involve Navier-Stokes solutions for both the axisymmetric and 2-D nozzles at the transonic Mach numbers of 0.90 and 1.1 for $Re_c = 40$ million. Baldwin-Lomax, Baldwin-Barth, Spalart-Allmaras and $k-\omega$ turbulence models were used in different parts of the present CFD study.

Approach



High Speed Aerodynamics, Long Beach

- Perform parametric nacelle/diverter shape and orientation changes and determine the drag benefits based on CFL3D N-S analysis
- Obtain CFL3D N-S solutions for the Ref. H installed configurations including powered nozzle simulation
- Use the installed powered and flow-through nozzle solutions and obtain the aftbody force increments
- Evaluate the different turbulence models to accurately predict the boattail flap pressures

Nacelle/Diverter Design Procedure

Studies done by BLB in FY96 have shown the potential of a 0.5 count drag reduction due to nacelle shape modification. Other studies by NGC showed the potential of a 1.1 count drag reduction. Consequently, the efforts were continued in that area in FY97 by using Navier-Stokes analyses.

All the modifications to the baseline nacelles were analyzed in the Navier-Stokes mode, using the Baldwin-Lomax turbulence model, at the full-scale Reynolds number of 212 million. Several shape modifications were tried but only the ones yielding a significant drag benefit were included in this process. The initial step was suggested by the FY96 results and consisted of inlet/diverter kinking to align nacelles with the local flowfield. This step is thus used as a baseline from which further nacelle/diverter shape modification studies will be made. Since preserving the diverter leading-edge height required a 3" vertical translation of the inlet/engine part of the inboard nacelle, smoothing/fairing of the nacelle at the engine/inlet location was necessary. Based on the boundary-layer analyses done in FY96, an inboard diverter leading-edge height reduction was achieved by a 0.6 degree complete pitch-up of the inboard nacelle with respect to the wing trailing edge. Studies done by NGC showed that a toe-out of the inboard nacelle will yield a drag benefit. Consequently, a toe-out of the inboard nacelle by 1 degree about the wing trailing-edge was applied. The inboard nacelle pitch-up for diverter leading-edge height reduction with fixed nozzle yielded a much smaller benefit than the one with the full nacelle pitch-up. The nozzle pitch-up seemed to be beneficial and was consequently used for the outboard nacelle. Finally, all of the steps above were combined in the given order and the combined effect configuration was called a N/D Cycle1 design.

Nacelle/Diverter Design Procedure



High Speed Aerodynamics, Long Beach

- TCA full-scale Re N-S analyses of configurations suggested by FY96 studies:
 - Step 1: Inlet/diverter kinking to align both nacelles with local flow
 - Step 2: Inboard LE height reduction (by 3") based on the N-S BL height analyses
 - Step 3: Inboard nacelles toe-out by 1° about wing TE
 - Step 4: Outboard nozzle pitch-up by 0.6°
 - Combination of all the above: gives **N/D Cycle 1**

Results from Nacelle/Diverter Modification Steps

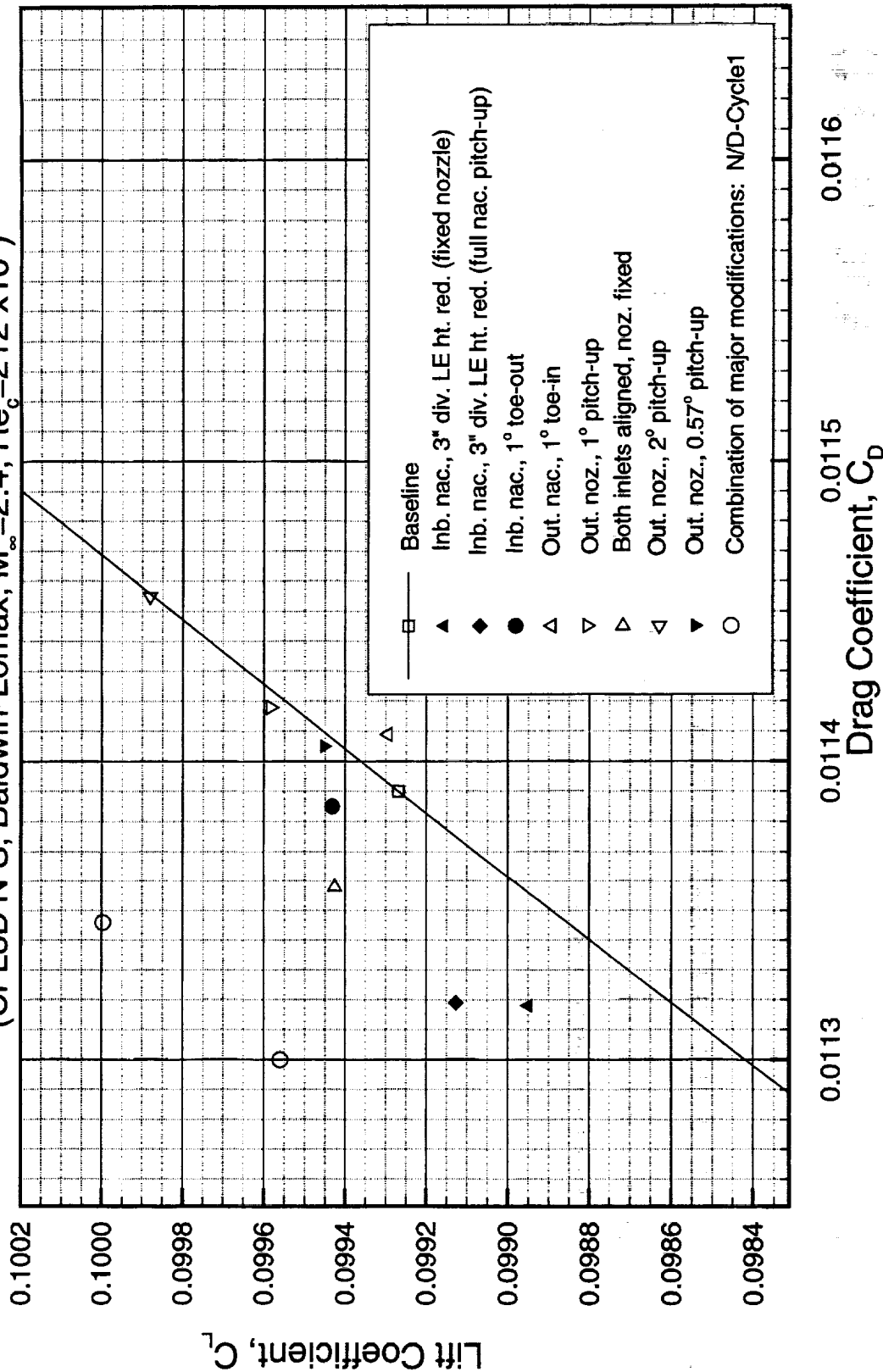
The figure below shows the performance results of the different nacelle/diverter modification steps. The baseline polar is shown by the solid curve. The difference mentioned previously between the complete inboard nacelle pitch-up vs. that with the fixed nozzle can be seen, the first case produced a 0.55 counts drag benefit while the second yielded only 0.35 counts. The inboard nacelle toe-out of 1 degree yielded a 0.2 drag count benefit while the alignment showed a 0.5 counts benefit. On the other hand, the outboard nozzle pitch-up (0.57, 1, and 2 degrees) could not yield more than 0.1 count benefit, achieved approximately at 0.57 degrees pitch-up. The combination of all the above steps, called "final" configuration as well as Cycle1, yielded approximately a 1.2 count drag reduction. All of the above analyses were performed at full-scale Reynolds number.

Results from Nacelle/Diverter Modification Steps



High Speed Aerodynamics, Long Beach

TCA Baseline Wing/Body/Nacelle/Diverter Configuration
(CFL3D N-S, Baldwin-Lomax, $M_\infty=2.4$, $Re_\phi=212 \times 10^6$)



Drag Polars for the TCA Baseline and N/D Cycle1

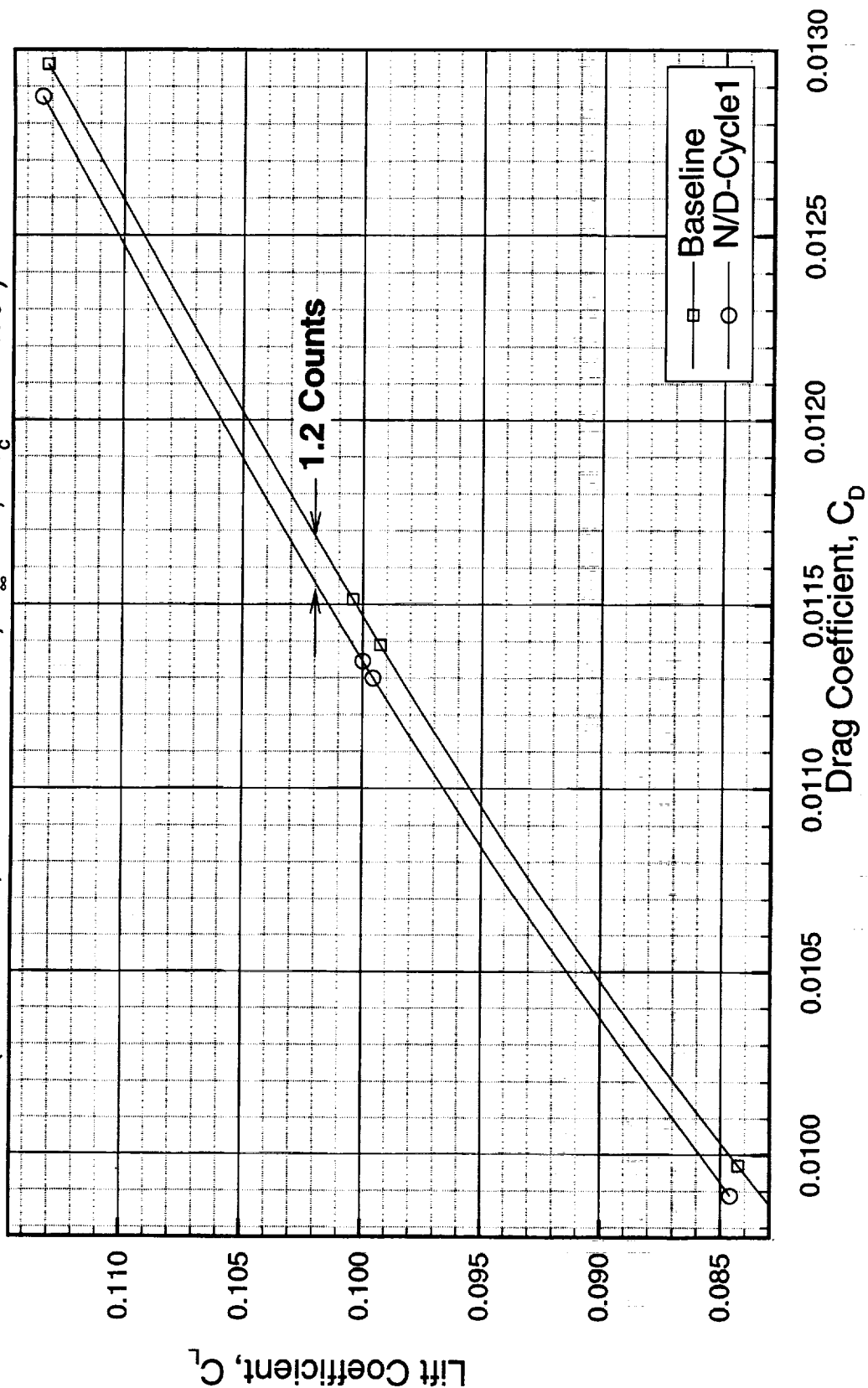
The figure below shows the drag polars for the TCA baseline configuration with the baseline nacelles as well as the final design at Mach 2.4 and flight Reynolds number. Four angles-of-attack were run around the cruise condition and about 1.2 count drag reduction is present at all angles-of-attack.

Drag Polars for the TCA Baseline and N/D Cycle1



High Speed Aerodynamics, Long Beach

Wing/Body/Nacelle/Diverter Configuration
(CFL3D N-S, Baldwin-Lomax, $M_\infty=2.4$, $Re_c=212 \times 10^6$)



Drag Polars for the TCA Baseline and N/D Cycle1

The figure below shows the drag polars for the TCA with the baseline and the modified nacelles. Here again, the drag reduction is present throughout the range of angle-of-attack considered. At the wind-tunnel Reynolds number, it seems that the drag reduction has increased to about 1.4 counts.

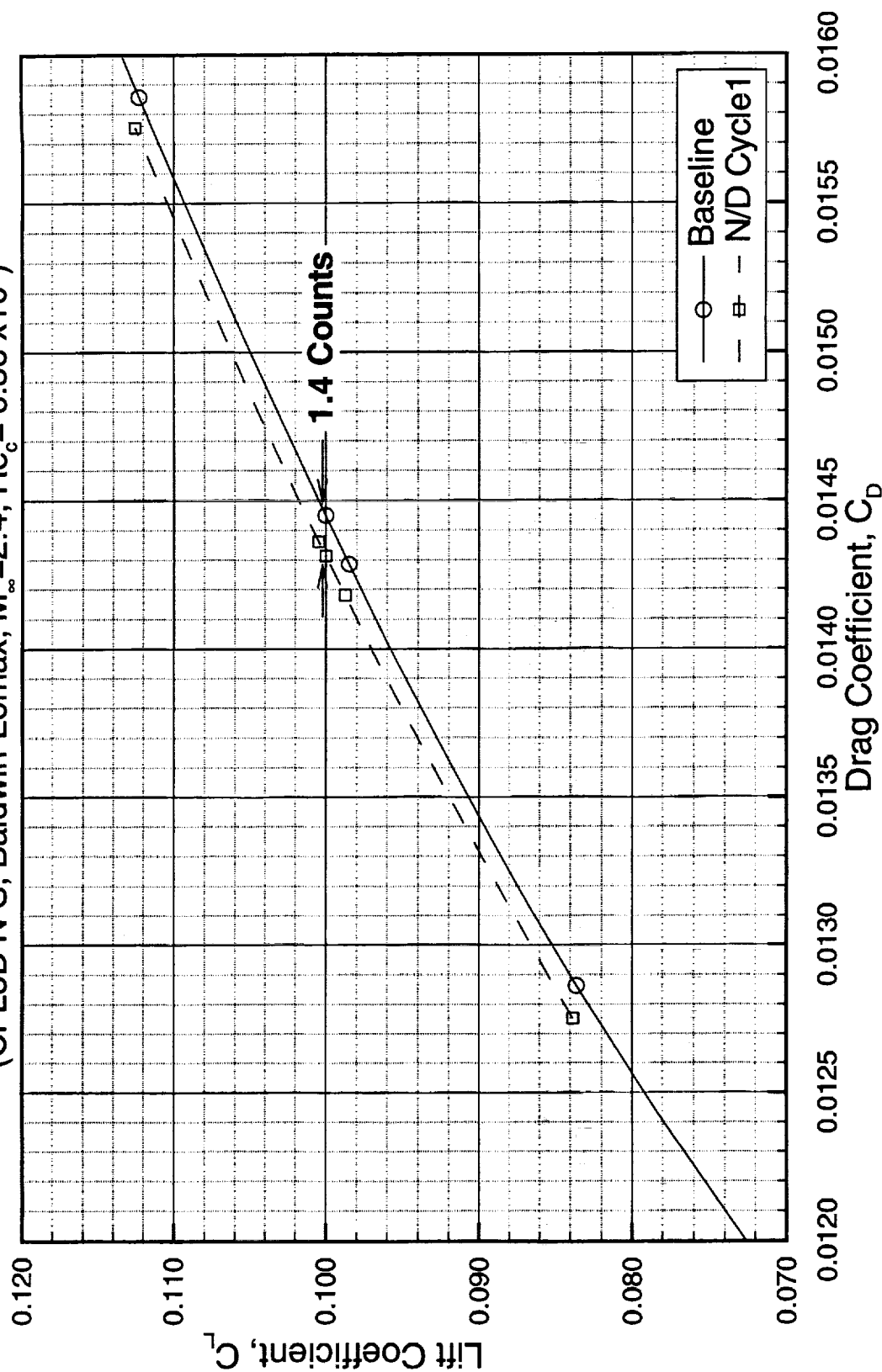
Drag Polars for the TCA Baseline and N/D Cycle1



High Speed Aerodynamics, Long Beach

Wing/Body/Nacelle/Diverter Configuration

(CFL3D N-S, Baldwin-Lomax, $M_\infty = 2.4$, $Re_c = 6.36 \times 10^6$)



Nacelle/Diverter Shaping Results for N/D Cycle 1

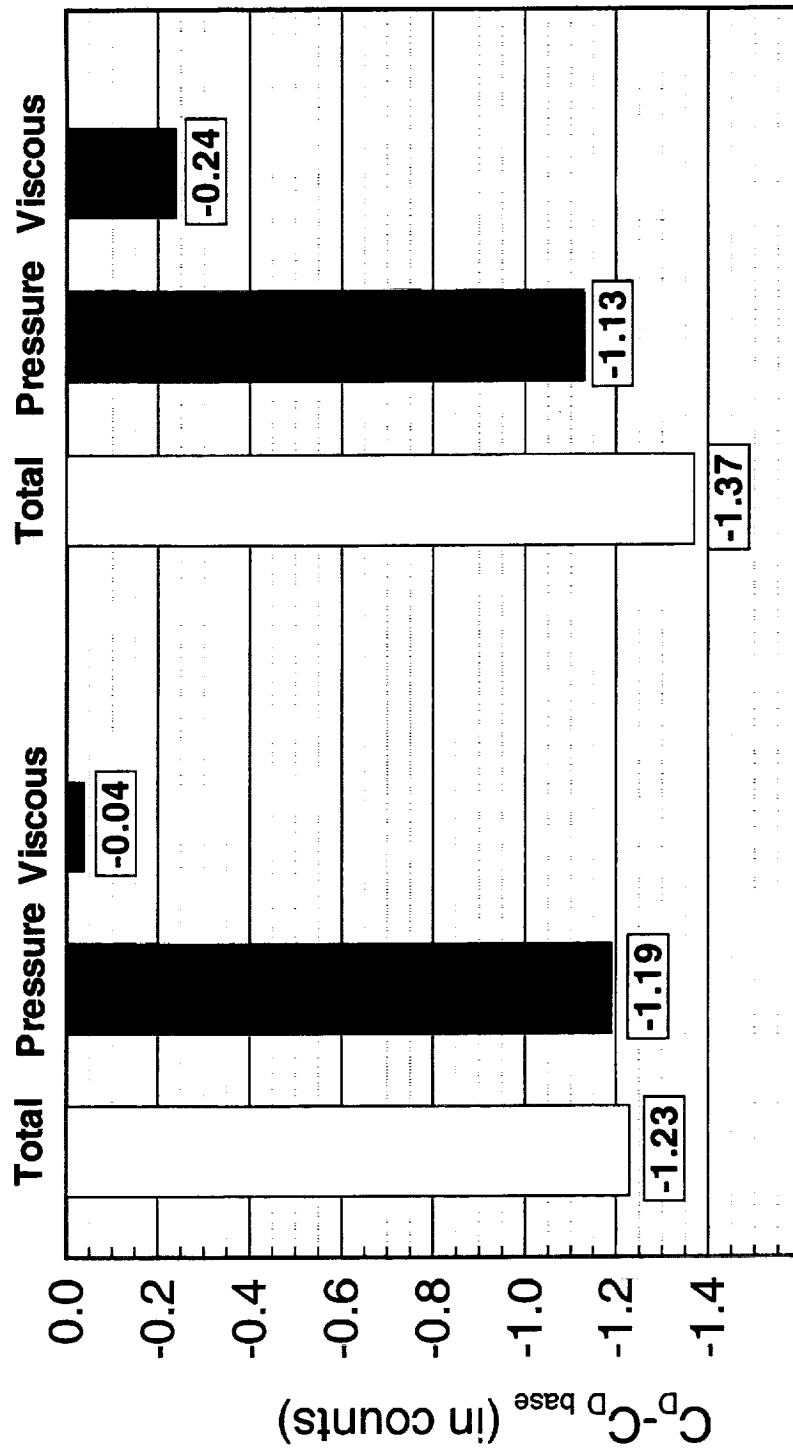
The bar chart below shows a breakdown of the drag benefit in pressure and total drag reduction at both full-scale and wind-tunnel Reynolds numbers. For both cases, it seems that most of the improvement is attributed to the pressure drag reduction. However, at the wind-tunnel Reynolds number, about 0.24 counts of the drag benefit are due to skin-friction. The pressure drag reduction for both cases is approximately 1.2 drag counts.

Nacelle/Diverter Shaping Results for the TCA W/B/N/D Configuration



High Speed Aerodynamics, Long Beach

CFL3D N-S, Baldwin-Lomax, $M_\infty = 2.4$, $Re_c = 212 \times 10^6$, $C_L = 0.1$



$Re_c = 212 \times 10^6$

$Re_c = 6.36 \times 10^6$



Drag Benefit Breakdown for N/D-Cycle1

The table below shows a component drag breakdown for the TCA baseline and N/D cycle 1 design at both flight and wind-tunnel Reynolds numbers. It shows a net pressure drag benefit of about 1 count for the inboard nacelle and 0.5 counts on the wing lower surface.

Drag Benefit Breakdown for N/D-Cycle1

High Speed Aerodynamics, Long Beach



(CFL3D N-S, Baldwin-Lomax, $M_\infty = 2.4$, $C_L = 0.1$)

	Inboard Nacelles		Outboard Nacelles		Wing Lower Surface	
	ΔCD_p (cts)	ΔCD_v (cts)	ΔCD_p (cts)	ΔCD_v (cts)	ΔCD_p (cts)	ΔCD_v (cts)
$Re_c = 212$ million	-0.9	0.0	0.2	0.0	-0.6	0.0
$Re_c = 6.36$ million	-1.0	-0.1	0.2	0.0	-0.4	0.0

Wing Lower Surface Cp Contours

The chart below shows a comparison of the wing lower surface pressure contours for the TCA configuration with the baseline and Cycle 1 nacelles. When considering the region between the two diverters, it seems that the expansion (dark blue) regions are present over a larger surface for the baseline nacelles. Similarly, the bright colors (red and white) corresponding to the high pressure regions are brighter for the baseline. It can thus be inferred that for the Cycle 1 design the shock/expansion interaction is more favorable and would consequently yield some drag reduction observed on the wing lower surface.

Wing Lower Surface C_p Contours for the Baseline TCA and N/D Cycle 1

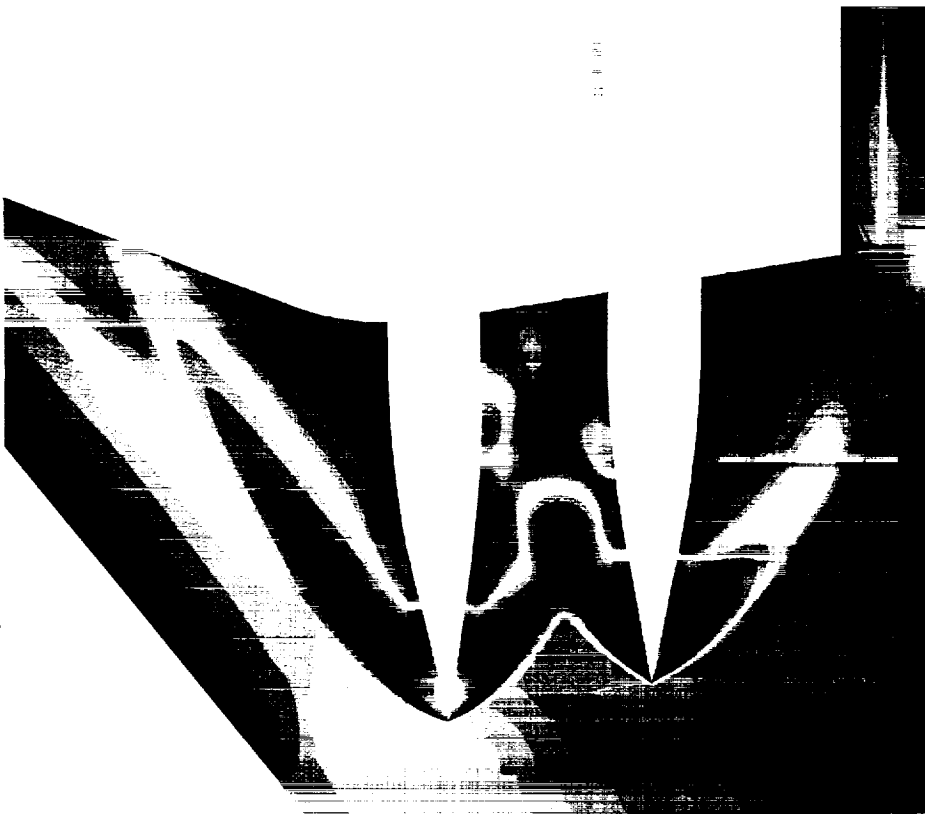


High Speed Aerodynamics, Long Beach

(CFL3D N-S, Baldwin-Lomax, $M_\infty = 2.4$, $Re_c = 212 \times 10^6$, $C_L = 0.1$)



Baseline Nacelles/Diverter



Cycle 1 Nacelles/Diverter



Pressure Distributions for the Baseline TCA and N/D Cycle 1

The chart below shows wing pressure cuts for the TCA configuration with the baseline and Cycle1 nacelles. This chart supports the pressure contour plot shown previously in that the gradients observed for the Cycle1 nacelles are less pronounced than those for the baseline configuration. This explains the more favorable interaction in the channel region.

Pressure Distributions for the Baseline TCA and N/D Cycle1



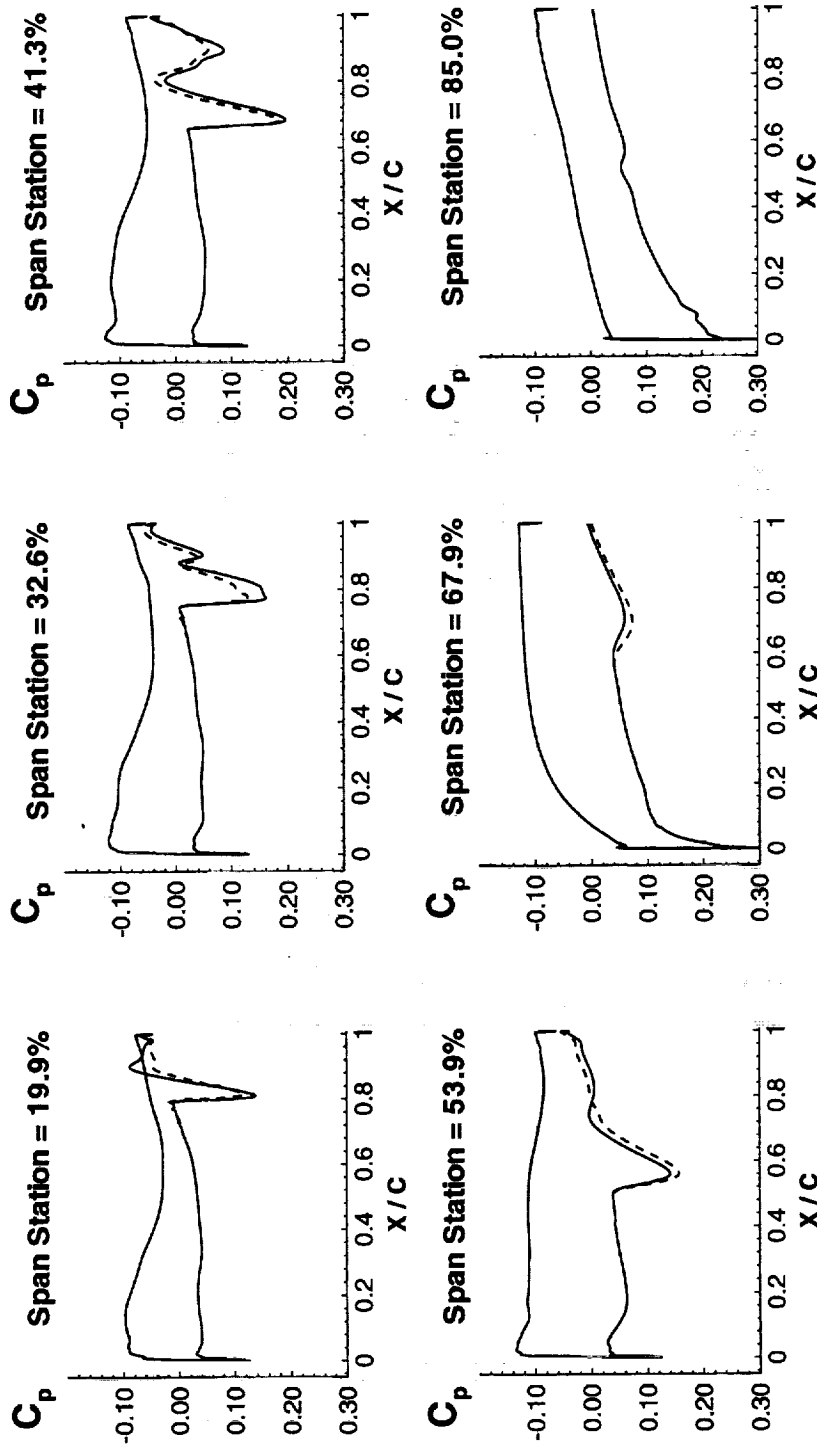
High Speed Aerodynamics, Long Beach

CFL3D N-S, Baldwin-Lomax, $M_\infty=2.4$, $\alpha=3.5^\circ$, $Re_c=212 \times 10^6$

Span Station

85.0 %
68.0 %
53.9 %
41.3 %
32.6 %
19.9 %

— Baseline Nac/Div.
- - - N/D-Cycle1

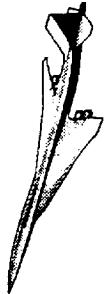


BOEING

Installed Nozzle Boattail Drag

The installed nozzle boattail drag calculations at transonic speeds for the TCA wing/body/nacelle/diverter configuration with 2-D inlets and 2-D nozzles is an important FY98 PAI task. In preparation for this activity, the pending issues pertaining to the Reference H boattail drag studies performed during FY95 and FY96 had to be resolved. The issues remaining were the following. The Reference H installed nozzle boattail computations for powered nozzles performed during FY95 showed significant differences between the solutions obtained by the participating team members using different CFD codes. Also, the CFL3D Navier-Stokes solutions with the Baldwin-Barth turbulence model for the installed 2-D nozzles experienced numerical difficulties. The large amount of CPU and memory requirements for these computations prevented the completion of this study during FY96. The study was further investigated and completed during FY97.

Installed Nozzle Boattail Drag



High Speed Aerodynamics, Long Beach

- An important FY98 PAI activity:-
 - Obtain the installed boattail drag for TCA with 2-D inlet and 2-D nozzles
- Issues on Ref. H installed nozzle boattail drag study
 - Needed axisymmetric nozzle solutions at $M_{\infty} = 1.1$
 - Convergence difficulties experienced for 2-D nozzle solutions
 - Computer resource limitations



Ref. H Installed Nozzle Computations - Revisited

During FY97, an effort was made to revisit the Reference H installed transonic nozzle boattail drag prediction problem and complete the solutions for both the axisymmetric and 2-D powered nozzle configurations. Several modifications to the 2-D installed grid were made to improve the solution convergence. As a consequence, the installed axisymmetric CFL3D Navier-Stokes solutions for both the transonic and supersonic nozzle configurations were also rerun. Solutions were obtained for both the reference supersonic as well as the transonic powered nozzles at $M_\infty = 0.9$ and 1.1 at $\alpha = 4^\circ$. Also, to avoid the large amount of CPU and memory requirements for these transonic computations on the NAS Cray C-90 computer, the parallel version of the CFL3D code, CFL3Dhp, was utilized. Code modifications to include the field-equation turbulence models such as the Baldwin-Barth and Spalart-Allmaras models in the CFL3Dhp parallel code were completed. The isolated powered nozzle study, described later here, recommended the use of Spalart-Allmaras turbulence model, particularly based on the separated flow pattern observed in the nozzle flap region. As a result, the 2-D installed solutions were obtained using the Spalart-Allmaras model.

Ref. H Installed Nozzle Computations - Revisited



High Speed Aerodynamics, Long Beach

- Installed axisymmetric nozzle solutions were completed
- 2-D nozzle installed grid size grew to 9.5 million points
- Parallel version of the CFL3D code was essential
 - Grid too large to fit into a single C-90 processor
 - Multitask version of CFL3D was very inefficient
- Isolated nozzle study recommended the use of S-A model
- 2-D installed N-S solutions obtained using the S-A model
 - 2-D nozzle solutions obtained with rapid turn-around time



Surface C_p 's for Axi and 2-D Installed Ref. H Transonic Nozzles

This color picture compares the surface C_p distributions for the Reference H installed axisymmetric and 2-D nozzle configurations at the transonic setting. CFL3D Navier-Stokes solutions at $M_\infty = 0.9$ and $\alpha = 4^\circ$ for $Re_c = 40$ million have been obtained using the Baldwin-Barth and Spalart-Allmaras turbulence models as shown in the pictures. The wing upper surface pressures for the two nozzle configurations are similar. The nozzle flap regions for the 2-D nozzle shows similar levels of pressures as the axisymmetric nozzle boattail flap region.

Surface Cp's for Axi and 2-D Installed Ref H Transonic Nozzles



High Speed Aerodynamics, Long Beach

CFL3D N-S, $M_\infty = 0.9$, $\alpha = 4.0^\circ$, $Re_c = 40 \times 10^6$



Axisymmetric Nozzle (B-B)



2-D Nozzle (S-A)



Surface C_p 's for Axi and 2-D Installed Ref. H Supersonic Nozzles

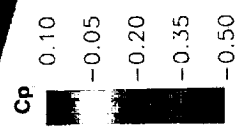
Next, the surface C_p distributions for the installed axisymmetric and 2-D reference nozzles at $M_\infty = 0.9$ and $\alpha = 4^\circ$ for $Re_c = 40$ million are shown. Both the wing and the boattail pressures are comparable and the installed drag values are nearly equal. However, the isolated nacelle drag of the axisymmetric nozzle nacelles are nearly 0.8 counts higher than the isolated 2-D nozzle nacelle which results in a lower interference drag for the axisymmetric nozzle configuration.

Surface Cp's Axi and 2-D Installed Ref H Supersonic Nozzles

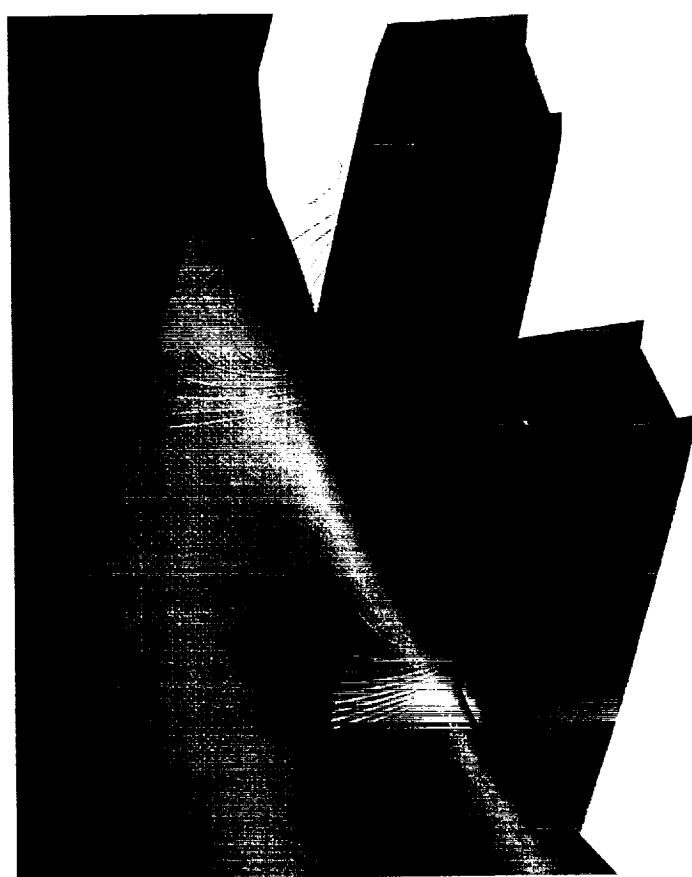


High Speed Aerodynamics, Long Beach

CFL3D N-S, $M_\infty = 0.9$, $\alpha = 4.0^\circ$, $Re_c = 40 \times 10^6$



Axisymmetric Nozzle (S-A)



2-D Nozzle (S-A)



Surface C_p 's for Axi and 2-D Installed Ref. H Transonic Nozzles

The C_p distributions for the installed axisymmetric and 2-D nozzle configurations at $M_\infty = 1.1$ and $\alpha = 4^\circ$ for $Re_c = 40$ million are shown in this chart. The nozzles are set in the transonic configurations. Once again, the wing upper surface pressure distributions for the two nozzles are similar. The axisymmetric nozzle boattail region experiences higher expansion, as evident from the pressure distribution on the outboard side of the inboard nozzle, compared to the 2-D nozzle. This higher expansion in the aft facing boattail flap region is expected to result in higher drag for the axisymmetric nozzle.

Surface Cp's Axi and 2-D Installed Ref H Transonic Nozzles



High Speed Aerodynamics, Long Beach

CFL3D N-S, $M_\infty = 1.1$, $\alpha = 4.0^\circ$, $Re_c = 40 \times 10^6$



Axisymmetric Nozzle (S-A)



2-D Nozzle (S-A)



Surface C_p 's for Axi and 2-D Installed Ref. H Supersonic Nozzles

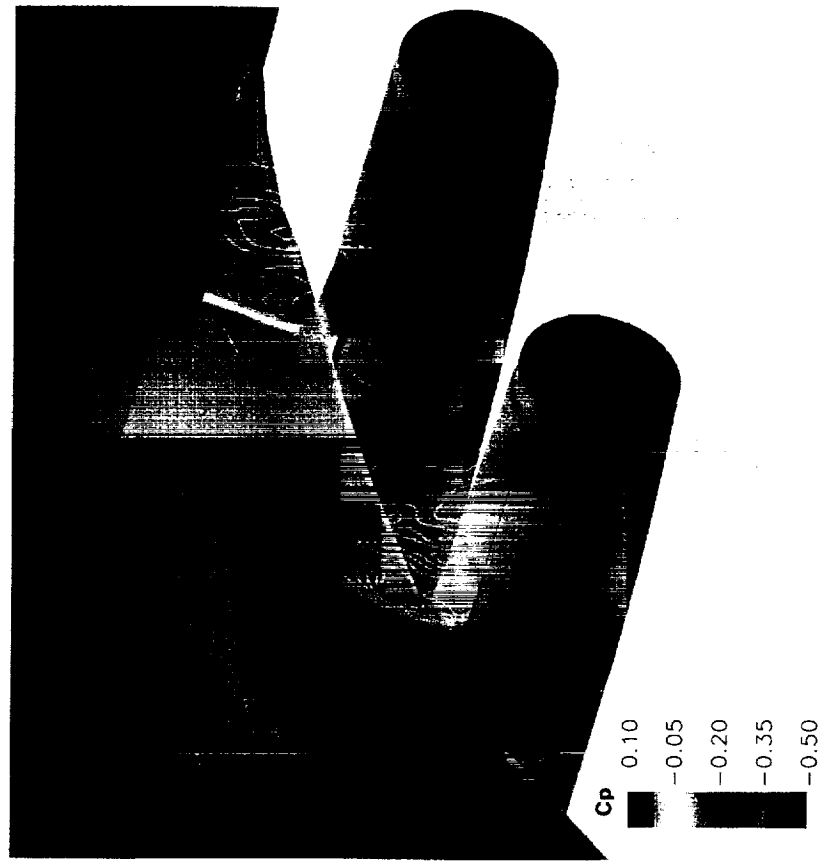
The final flow visualization chart shown here is the surface C_p distributions for the installed axisymmetric and 2-D reference nozzles at $M_\infty = 1.1$ and $\alpha = 4^\circ$ for $Re_c = 40$ million. The boattail surface pressures for the 2-D installed configuration shows a higher level of expansion near the boattail shoulder region compared to the axisymmetric nozzles. Also, the flap shoulder shock is of slightly higher strength near the boattail flap centerline compared to the axisymmetric nozzles.

Surface Cp's for Axi and 2-D Installed Ref H Supersonic Nozzles



High Speed Aerodynamics, Long Beach

CFL3D N-S, $M_\infty = 1.1$, $\alpha = 4.0^\circ$, $Re_c = 40 \times 10^6$



Axisymmetric Nozzle (B-B)



2-D Nozzle (S-A)



Ref. H Installed Nozzle CFL3D Results

This chart shows the CFL3D Navier-Stokes predictions for the installed axisymmetric and 2-D nozzle boattail drag. The Navier-Stokes solutions have been obtained at $\alpha = 4^\circ$ for $Re_c = 40$ million. All viscous drag coefficients excepting the axisymmetric supersonic nozzle at $M_\infty = 1.1$ and axisymmetric transonic nozzle at $M_\infty = 0.9$ were obtained using the Spalart-Allmaras turbulence model. The Navier-Stokes solutions for these two cases have been obtained using the Baldwin-Barth turbulence model. The viscous drag difference between these two models has been verified to be small ($\sim 0.5\%$ of the total drag) for the axisymmetric supersonic nozzle at $M_\infty = 0.9$ and axisymmetric transonic nozzle at $M_\infty = 1.10$.

Ref. H Installed Nozzle CFL3D Results



High Speed Aerodynamics, Long Beach

NPR=5.0, NTR=3.262 ($M_\infty=0.9$); NTR=3.055 ($M_\infty=1.1$)

CDp = Pressure drag; CDv = Surface friction drag; CD = CDp + CDv

$M_\infty = 0.90, Re_c = 40 \times 10^6$				
	Axi/Trans config.	2-D/Tran config.	Axi/Super config.	2-D/Super config.
Turb. Model	B-B	S-A	S-A	S-A
C_l	0.19387	0.19227	0.19317	0.19238
CD_p	0.009382	0.009513	0.008917	0.00892
CD_v	0.007825	0.007655	0.007617	0.00761
CD	0.017207	0.017168	0.016534	0.016527

$M_\infty = 1.1, Re_c = 40 \times 10^6$				
	Axi/Tran config.	2-D/Tran config.	Axi/Super config.	2-D/Super config.
Turb. Model	S-A	S-A	B-B	S-A
C_l	0.21300	0.21361	0.21264	0.21415
CD_p	0.016742	0.016770	0.013967	0.014090
CD_v	0.007454	0.007550	0.007767	0.007490
CD	0.024196	0.024310	0.021734	0.021580

Ref. H Axi and 2-D Nacelle Interference Drag Comparisons

The interference drag comparisons between axisymmetric and 2-D nozzles are given in this bar chart. Both the CFL3D and GCNSfv (Northrop-Grumman's code) Navier-Stokes solutions at $M_\infty = 0.9$ for $Re_c = 40$ million and the NASA LaRC 16-ft TT wind-tunnel test data obtained for the reference flow-through nozzles at $Re_c = 5.6$ million are shown. To calculate the installation drag, the wing/body polar is used to interpolate the wing/body drag at the installed CL value. The 16-ft TT test data results for the reference flow-through nozzle are shown here for an overall comparison only. The jet effects, which would be later shown to be favorable, are absent in the test data. When this favorable interference is added to the test data, the comparison between the test data and the CFL3D Navier-Stokes predictions should improve. The table below shows the details of the installation and interference drag numbers.

	Transonic Nozzle C_L ranges from 0.19 to ≈ 0.193			Supersonic Nozzle C_L ranges from 0.19 to ≈ 0.193		
	2-D nozzle (N-G) [†]	2-D nozzle (BLB)	Axi. nozzle (BLB)	2-D nozzle (N-G) [†]	2-D nozzle (BLB)	Axi. nozzle (BLB)
$\Delta C_{D_{nac-installed}}$	0.00150	0.00135	0.00122	0.00064	0.00068	0.00063
$C_{D_{nac-isolated}}$ (all four)	0.00220	0.00173	0.00156	0.00127	0.00099	0.00108
$\Delta C_{D_{interference}}$	-0.00070	-0.00038	-0.00034	-0.00063	-0.00031	-0.00045
$\Delta C_{D_{isolated}}$ (2D-Axi.) (BLB result)	0.00017			-0.00009		
$\Delta C_{D_{installed}}$ (2D-Axi.)	-0.00004			0.00014		

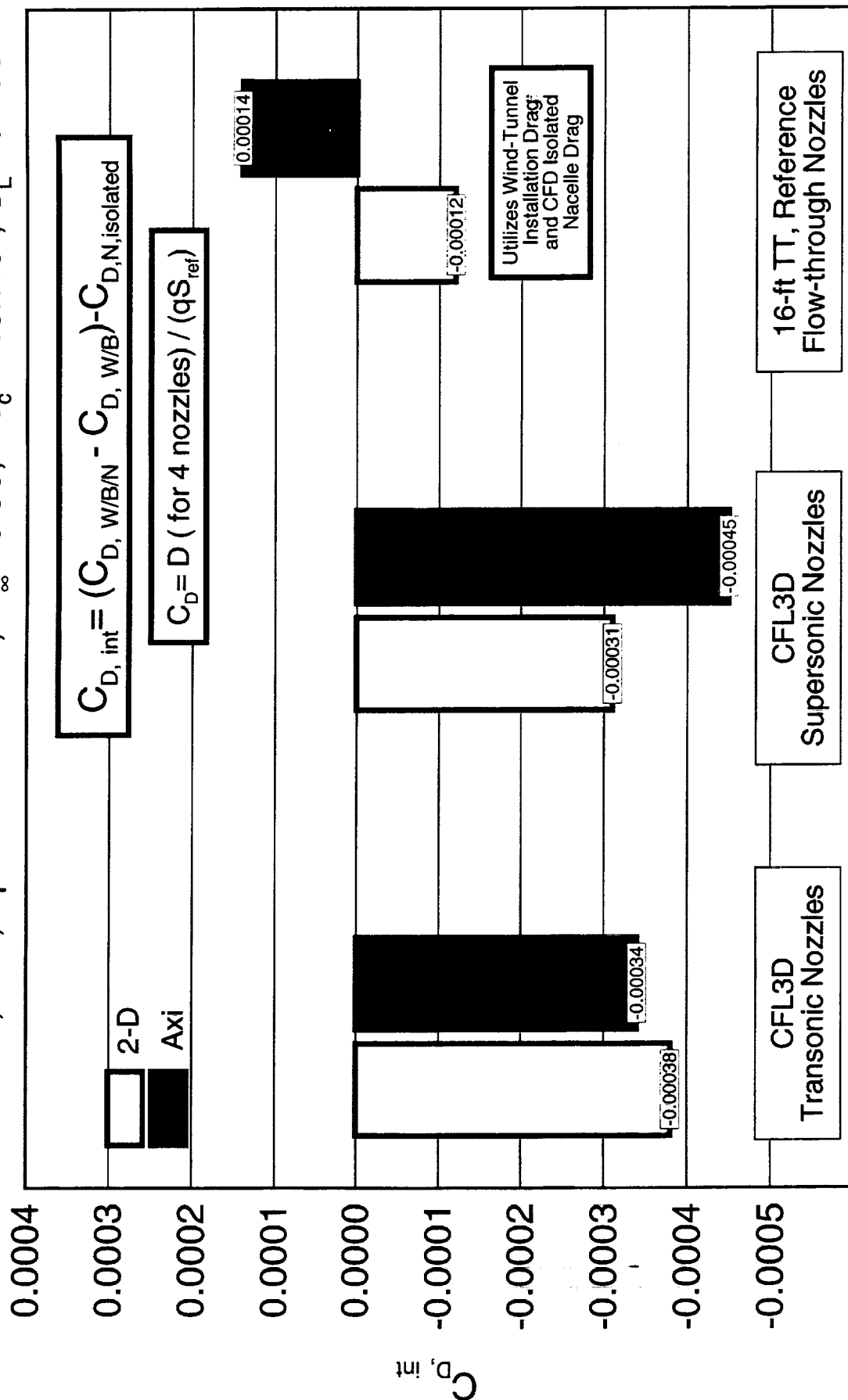
[†] N-G denotes Northrop-Grumman.

Ref. H Axi and 2-D Nacelle Interference Drag Comparisons



High Speed Aerodynamics, Long Beach

CFL3D, N-S, Spalart-Allmaras, $M_\infty = 0.90$, $Re_c = 40 \times 10^6$, $C_L = 0.193$



Ref. H Axi and 2-D Nacelle Interference Drag Comparisons

This chart shows the interference drag value comparison at $M_\infty = 1.1$ for axisymmetric and 2-D nozzles (extracted from the table below). It can be seen that the 2-D nozzle geometry has a more favorable interference for both transonic and supersonic nozzle configurations. The discrepancy between the 16-ft TT reference flow-through nozzle test data at $Re_c = 5.6$ million and the CFL3D-predicted interference drag values are small. When the favorable jet effects on the aftbody is included it would show better agreement between the predicted and test data.

	Transonic Nozzle C_L ranges from 0.206 to 0.214			Supersonic Nozzle C_L ranges from 0.206 to 0.214		
	2-D nozzle (N-G) [†]	2-D nozzle (BLB)	Axi. nozzle (BLB)	2-D nozzle (N-G) [†]	2-D nozzle (BLB)	Axi. nozzle (BLB)
$\Delta C_{D_{nac-installed}}$	0.00260	0.00231	0.00230	0.00049	-0.00059	-0.00016
$C_{D_{nac-isolated}}$ (all four)	0.00460	0.00421	0.00389	0.00176	0.00144	0.00165
$\Delta C_{D_{interference}}$	-0.00200	-0.00190	-0.00159	-0.00127	-0.00203	-0.00181
$\Delta C_{D_{isolated}}$ (2D-Axi.) (BLB result)	0.00032			-0.00021		
$\Delta C_{D_{installed}}$ (2D-Axi.)	-0.00031			-0.00022		

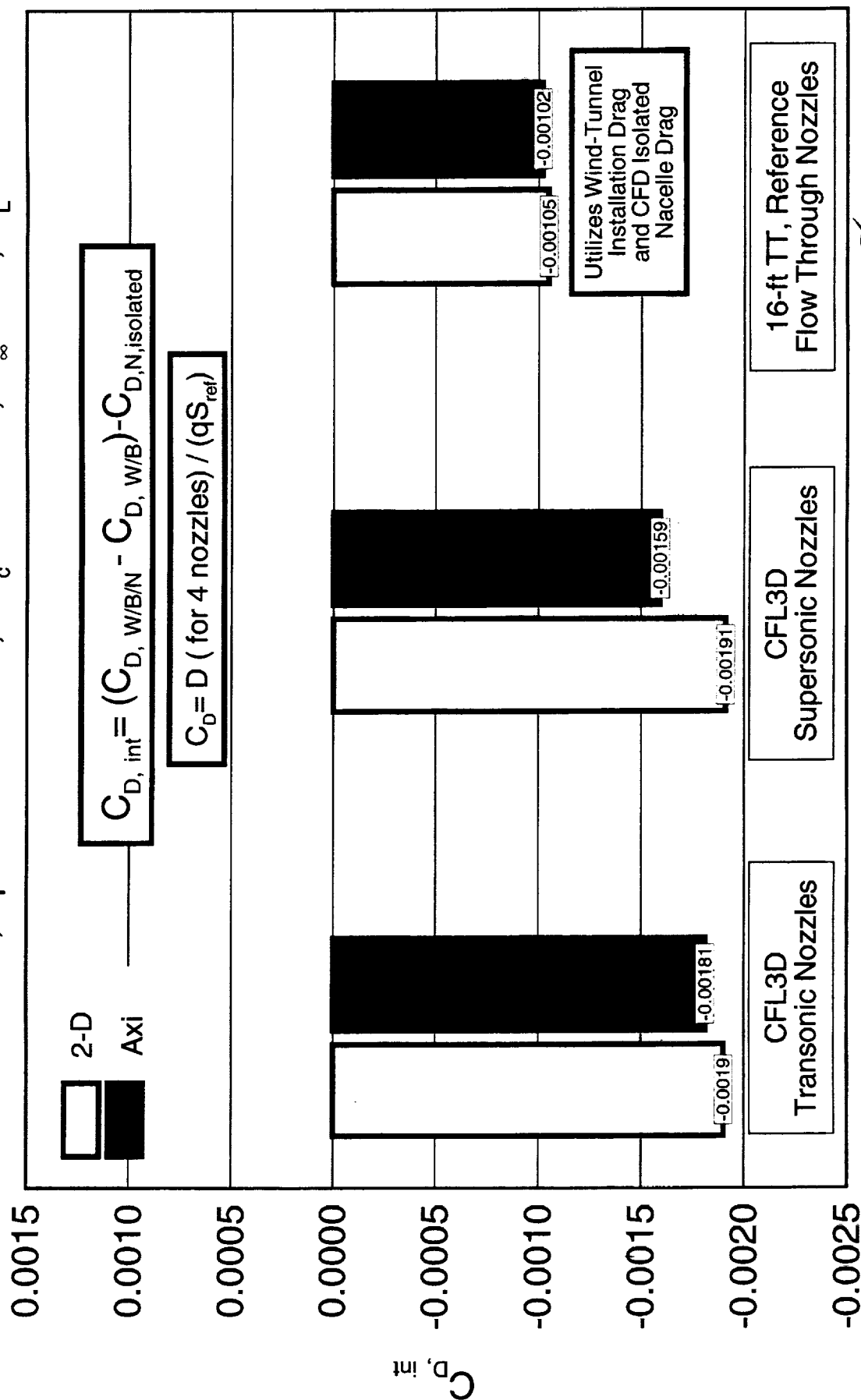
[†] N-G denotes Northrop-Grumman.

Ref. H Axi and 2-D Nacelle Interference Drag Comparisons



High Speed Aerodynamics, Long Beach

CFL3D N-S, Spalart-Allmaras, $Re_c = 40 \times 10^6$, $M_\infty = 1.1$, $C_L = 0.213$



Ref. H Nacelle Interference Drag Increments

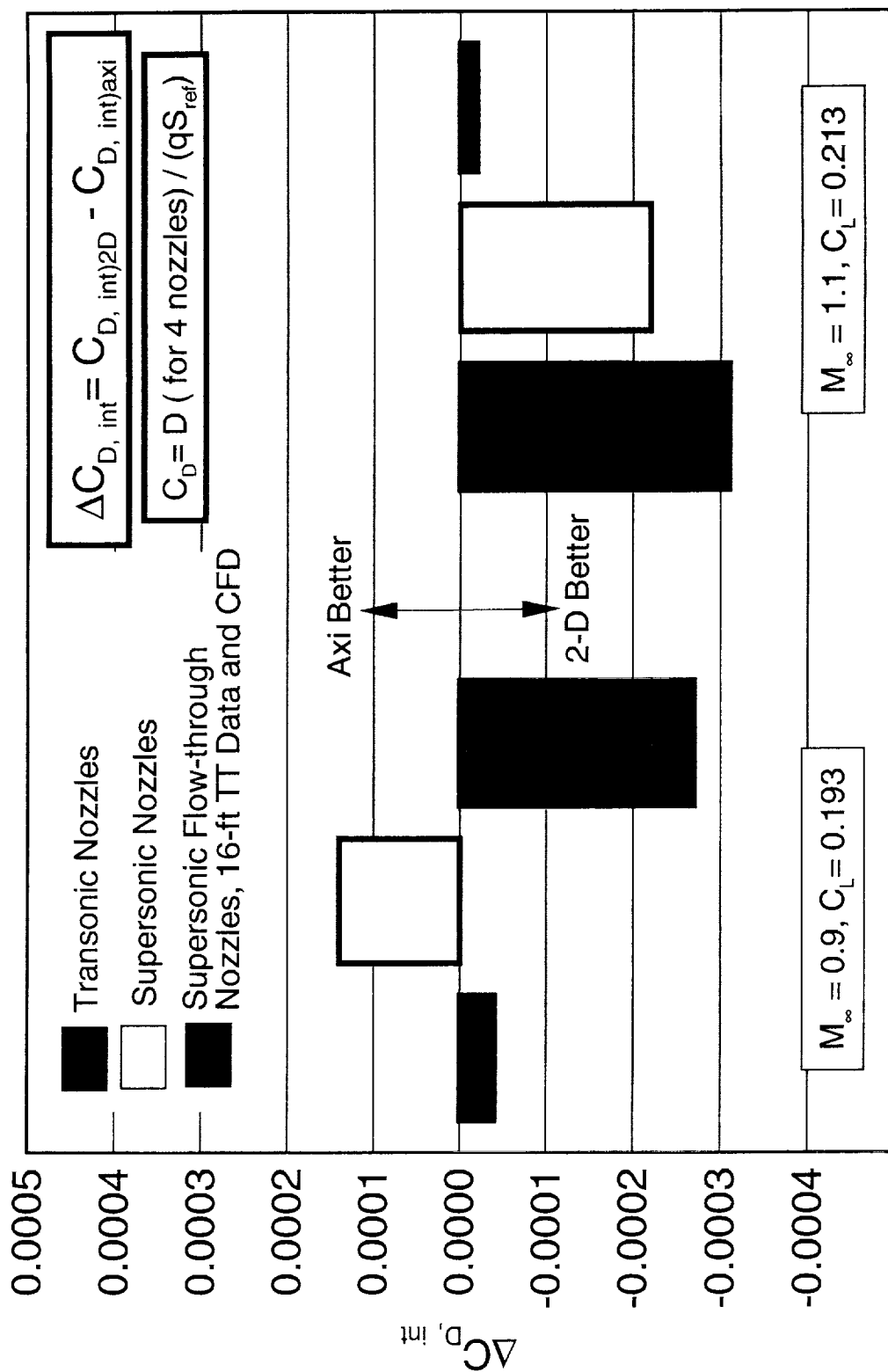
This chart gives the summary of the interference drag increments between the axisymmetric and 2-D nozzles. Except at $M_\infty = 0.9$ for the supersonic nozzle setting, the 2-D nozzle has a desirable favorable interference drag characteristics for all the nozzle settings.

Ref. H Nacelle Interference Drag Increments, 2-D - Axi



High Speed Aerodynamics, Long Beach

CFL3D N-S, Spalart-Allmaras, $Re_c = 40 \times 10^6$



Comparison of CFL3D and IMS Predicted Boattail Drag

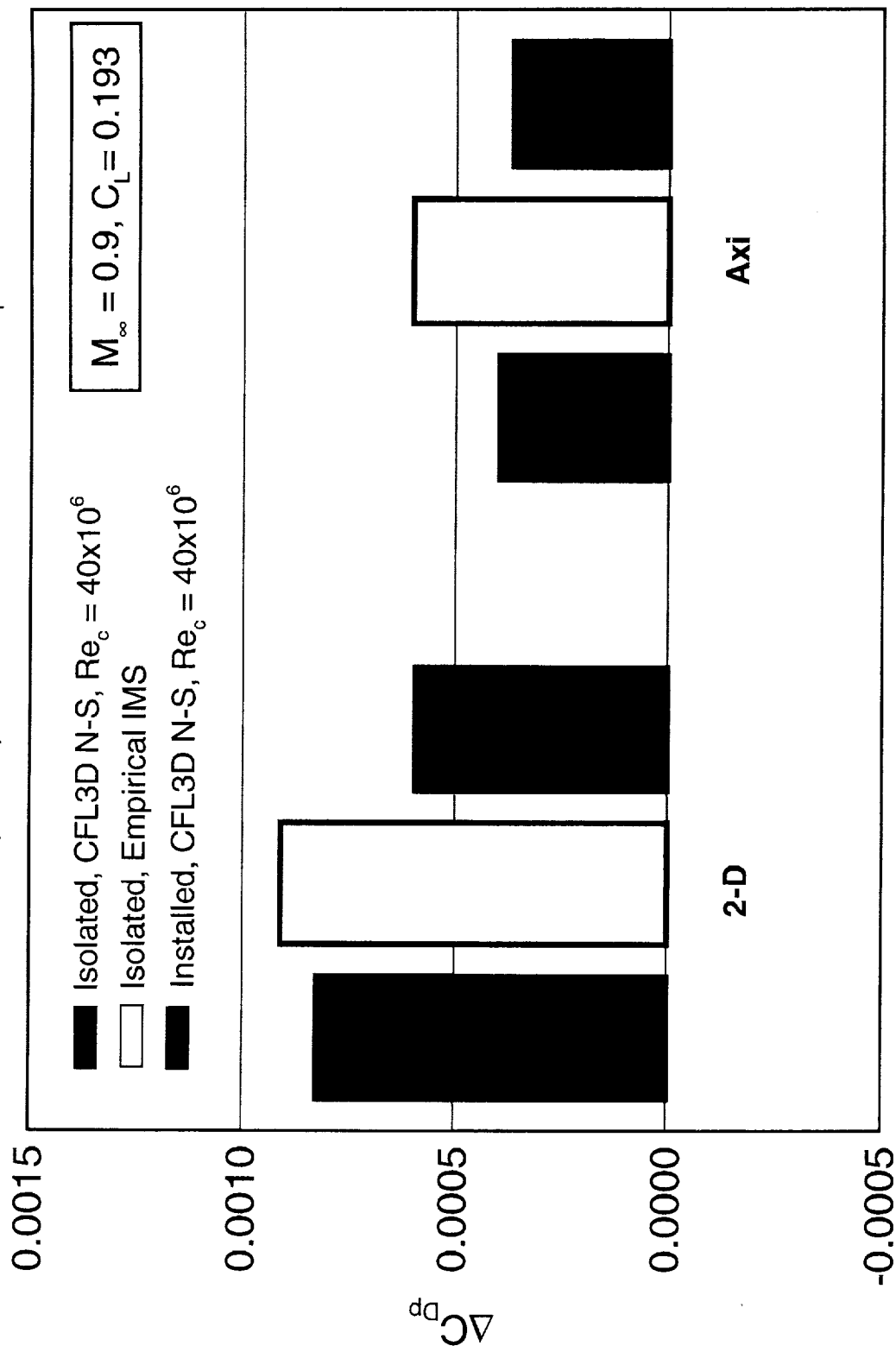
A summary of the Reference H boattail drag predictions for the isolated nacelle results (CFL3D Navier-Stokes), the installed powered nozzle solutions, and the linear-theory-based empirical predictions by the Integral Mean Slope (IMS) method for $M_\infty = 0.9$ is shown. The results show that the IMS predictions are considerably higher than the CFD predictions. However, the isolated nacelle predictions for the axisymmetric nozzles are very close to the installed results obtained from CFL3D.

Comparison of CFL3D and IMS Predicted Ref. H Boattail Drag



High Speed Aerodynamics, Long Beach

Boattail Drag, $\Delta C_{Dp} = C_{Dp}$ (transonic nozzle) - C_{Dp} (reference nozzle)



Comparison of CFL3D and IMS Predicted Boattail Drag

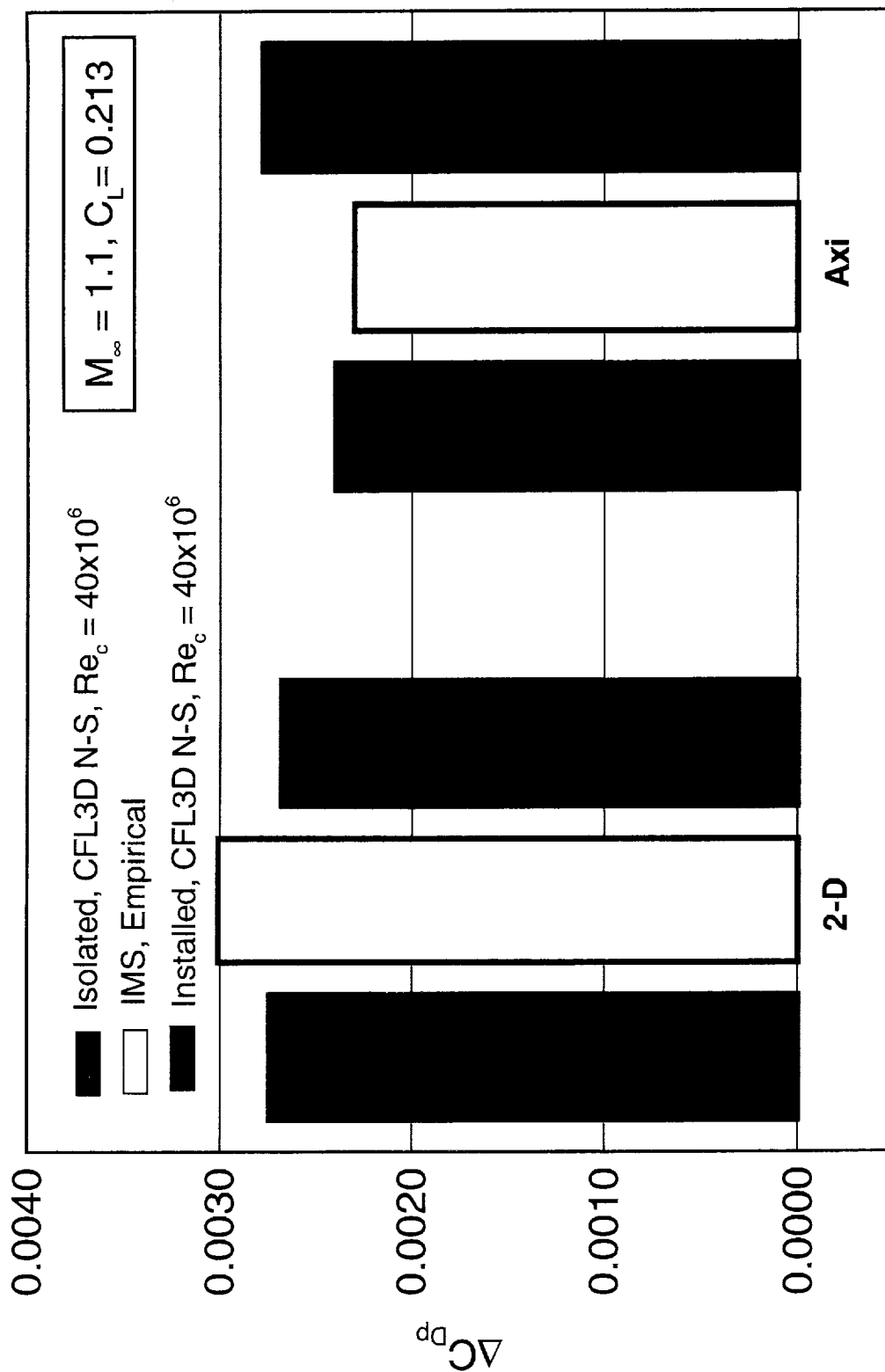
Next, a summary of the Reference H boattail drag predictions for the isolated nacelle results (CFL3D Navier-Stokes), the installed powered nozzle solutions, and the linear-theory-based empirical predictions by the IMS method for $M_\infty = 1.1$ are shown. The results show that the IMS predictions are considerably lower than the CFD predictions for the installed axisymmetric nozzles. However, the IMS and isolated nacelle predictions for the axisymmetric nozzles are very close to each other. Finally, the IMS, isolated, and the installed boattail drag predictions are comparable for the 2-D nozzles at $M_\infty = 1.10$.

Comparison of CFL3D and IMS Predicted Ref. H Boattail Drag



High Speed Aerodynamics, Long Beach

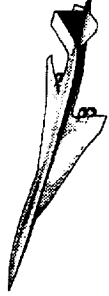
Boattail Drag, $\Delta C_{Dp} = C_{Dp}$ (transonic nozzle) - C_{Dp} (reference nozzle)



Jet Effects on Aftbody Drag

Jet effects on aftbody was studied using CFL3D Navier-Stokes solutions with the Baldwin-Barth turbulence model. Two types of solutions were obtained: the W/B/N/D solutions with powered nozzle jet, and the flow-through solutions. The jet effect is defined as the total drag increments from the flow-through case to the powered nozzle flow case. The aftbody was defined as the fuselage portion downstream of the fuselage station (FS) 2904 for the Ref. H configuration, which is consistent with the fuselage truncated station in wind-tunnel tests. The results are shown for the Ref. H axisymmetric nozzles with transonic and supersonic boattail configurations at $M_\infty = 0.9$ and 1.1 , $Re_c = 40 \times 10^6$.

Jet Effects on Aftbody Drag



High-Speed Aerodynamics, Long Beach

- CFL3D Navier-Stokes solutions
 - W/B/N/D solutions with powered nozzle flow
 - Reference flow-through solutions
- Jet effects on aftbody drag
 - ($C_{D \text{ powered}} - C_{D \text{ flow-through}}$) on aftbody
- Aftbody defined as the body aft of FS 2904
(the Ref. H Wind-tunnel model truncated at FS 2904)
- Results shown for axisymmetric nozzles
 - Ref. H axi transonic/supersonic configurations
 - $M_\infty = 0.9$ and 1.1

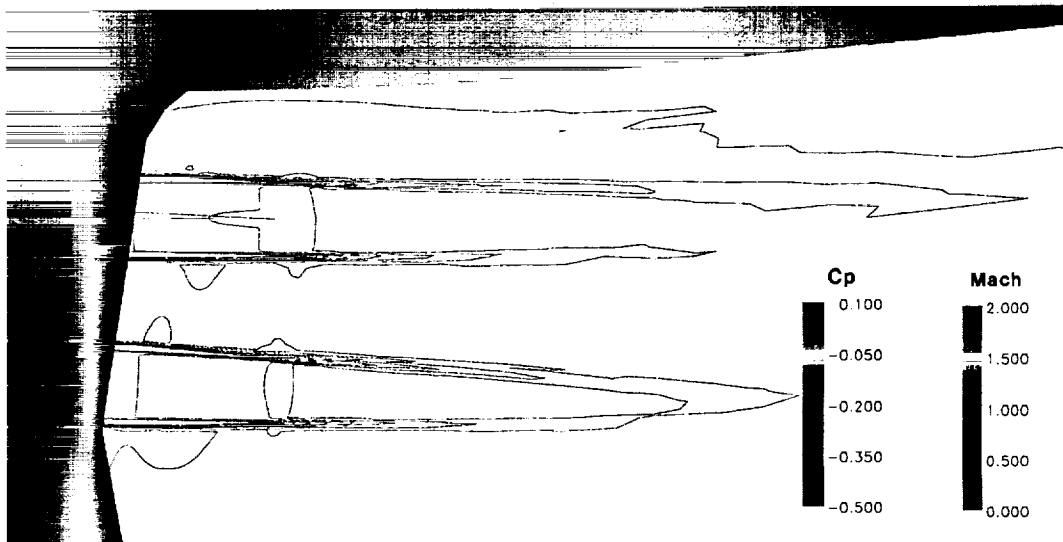
Mach Number Contours with Surface C_p Distributions, $M_\infty = 0.9$

To investigate the jet effect on aftbody, a reference (flow-through) case was created. In the flow-through case, the nacelle external geometry was identical to the axi-supersonic nozzle boattail configuration. However, the nozzle internal geometry was replaced by a constant area duct, exit area of which matched with the nozzle exit area of the axi-supersonic nozzle boattail configuration. Solutions were obtained for $M_\infty = 0.9$, $C_L = 0.193$, $Re_c = 40 \times 10^6$.

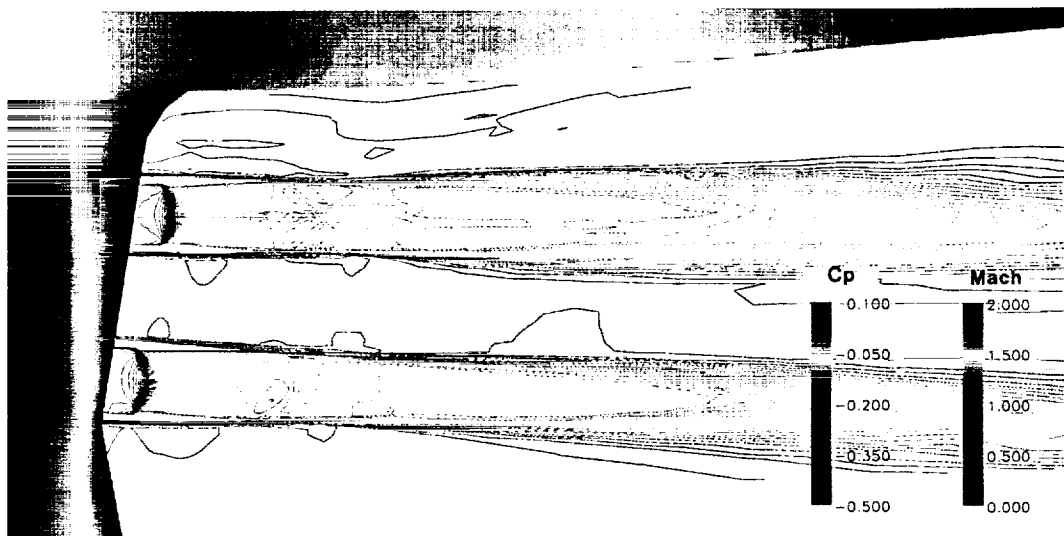
The Mach number contours for the nozzle and the nacelle external flows are shown in this figure. Although the nozzle plume is observed, its effect on at fuselage pressure is negligible. More detailed comparison will be shown in another figure.

Mach Contours With Surface Cp Distributions for the Ref. H with the Flow-through and Supersonic Nozzle Configurations

CFL3D N-S, Baldwin-Barth, $M_\infty = 0.9$, $C_L = 0.193$, $Re_c = 40 \times 10^6$



Flow-through Configuration



Supersonic Nozzle Configuration

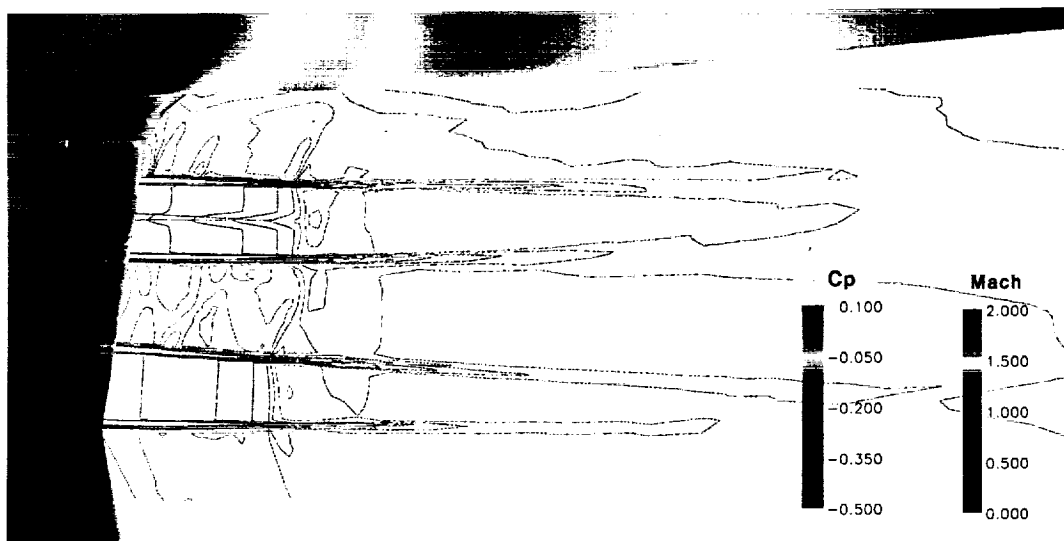
Mach Number Contours with Surface C_p Distributions, $M_\infty = 1.1$

To investigate the jet effect on aftbody, a reference (flow-through) case was created. In the flow-through case, the nacelle external geometry was identical to the axi-supersonic nozzle boattail configuration. However, the nozzle internal geometry was replaced by a constant area duct, whose exit area matched with the nozzle exit area of the axi-supersonic nozzle boattail configuration. Solutions were obtained for $M_\infty = 1.1$, $C_L = 0.213$, $Re_c = 40 \times 10^6$.

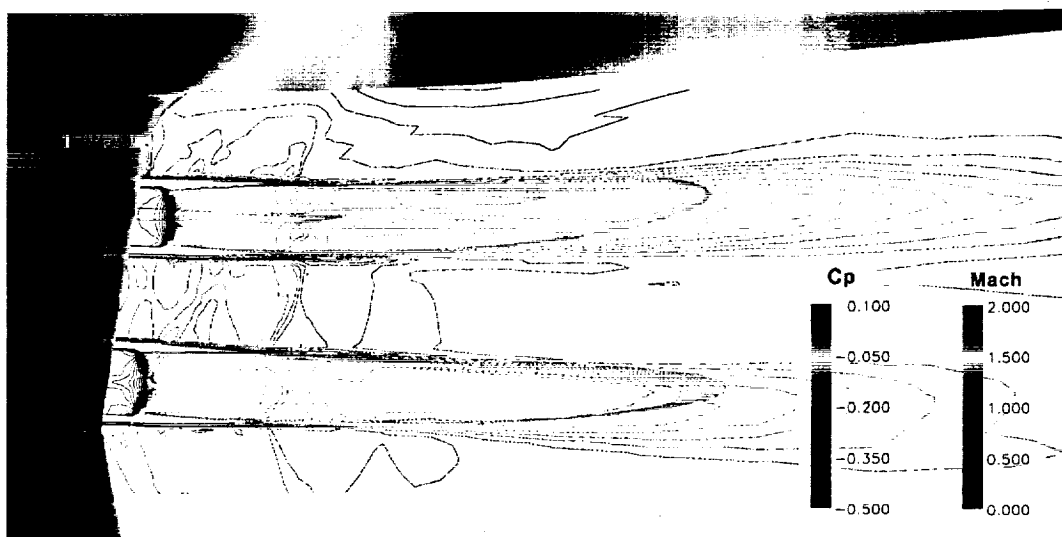
The Mach number contours for the nozzle and the nacelle external flows are shown in this figure. Higher C_p at the fuselage aft portion is observed. More detailed comparison will be shown in another figure.

Mach Contours With Surface Cp Distributions for the Ref. H with the Flow-through and Supersonic Nozzle Configurations

CFL3D N-S, Baldwin-Barth, $M_\infty=1.1$, $C_L=0.213$, $Re_c=40 \times 10^6$



Flow-through Configuration



Supersonic Nozzle Configuration

Pressure Distributions on the Ref. H Aftbody, $M_{\infty} = 0.9$

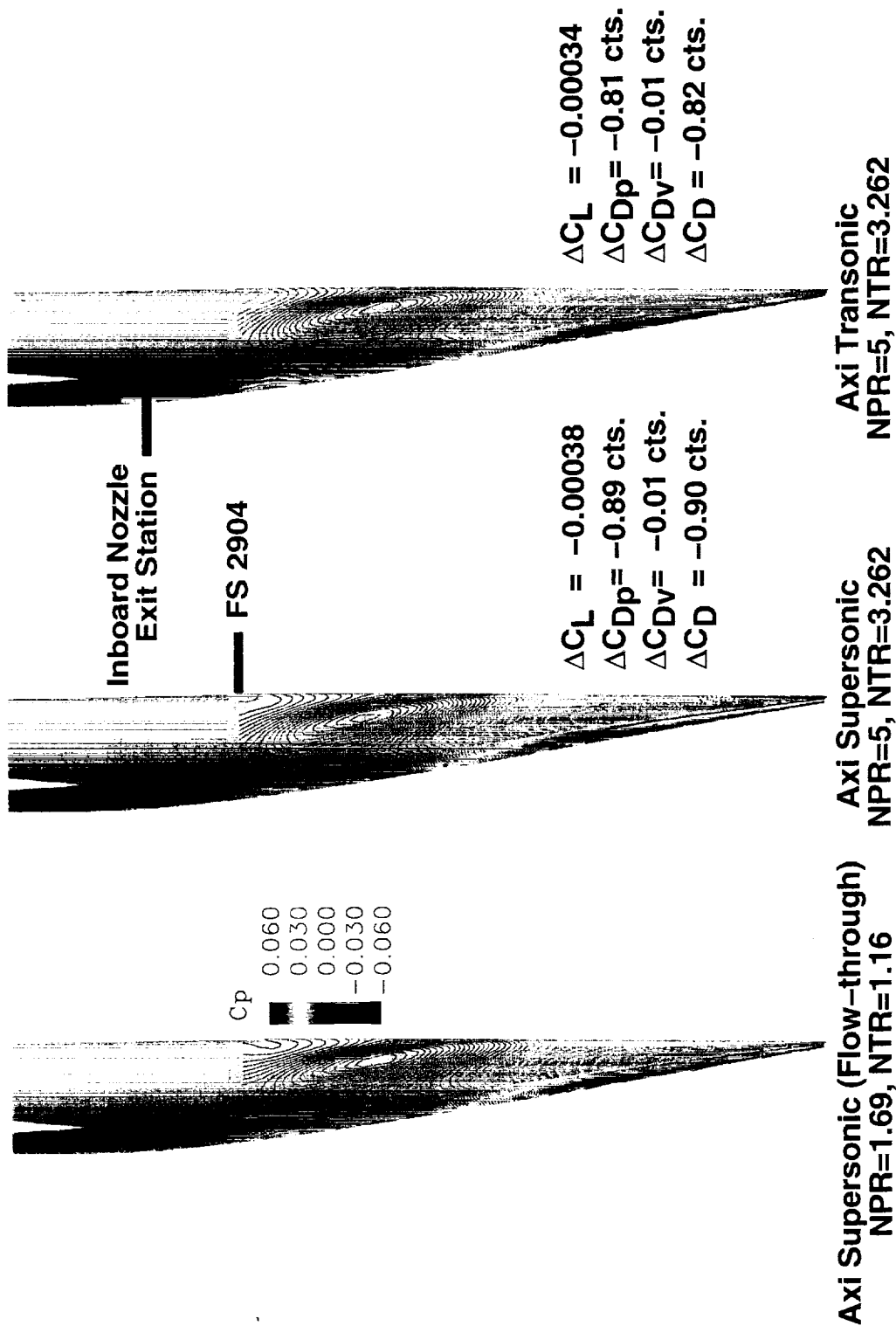
The aftbody pressure distributions for the Ref. H W/B flow-through, axi-supersonic, and axi-transonic nozzle boattail configurations are shown. The aftbody was defined as the fuselage after FS 2904, where the fuselage was truncated in the wind-tunnel test.

For the flow-through case, the freestream condition ($NPR = 1.69$, $NTR = 1.16$) was specified for the constant area duct, while a powered hot flow condition ($NPR = 5$, $NTR = 3.262$) was specified for the installed axi-supersonic and axi-transonic nozzle boattails. The differences in C_L and C_D with respect to the reference flow-through case were shown in the figure. The jet effect on aftbody C_L is seen to be negligible. However, aftbody C_D decreases approximately 0.9 cts. due to the jet effect.

Pressure Distributions on the Ref. H Aftbody, $M_\infty = 0.9$



High Speed Aerodynamics, Long Beach
CFL3D (Baldwin-Barth), $Re_c = 40 \times 10^6$, $\alpha = 4^\circ$ ($C_L = 0.193$)



Pressure Distributions on the Ref. H Aftbody, $M_{\infty} = 1.1$

The aftbody pressure distributions for the Ref. H W/B flow-through, axi-supersonic, and axi-transonic nozzle boattail configurations are shown. The aftbody was defined as the fuselage after FS 2904, where the fuselage was truncated in the wind-tunnel test.

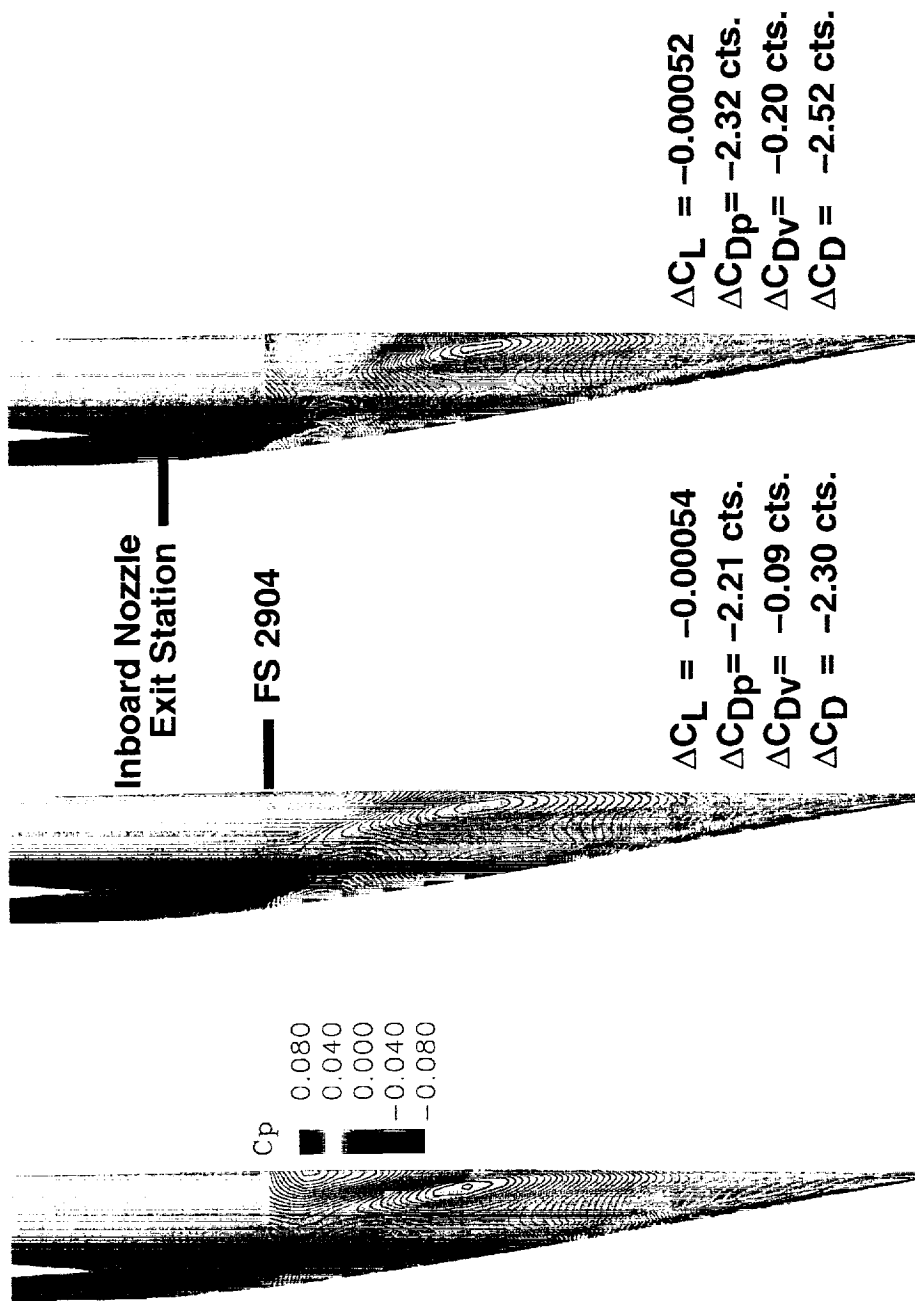
For the flow-through case, the freestream condition ($NPR = 1.69$, $NTR = 1.16$) was specified for the constant area duct, while a powered hot flow condition ($NPR = 5$, $NTR = 3.055$) was specified for the installed axi-supersonic and axi-transonic nozzle boattails. The differences in C_L and C_D with respect to the reference flow-through case are shown in the figure. The jet effect on aftbody C_L is seen to be negligible. However, aftbody C_D decreases approximately 2.3 cts. due to the jet effect.

Pressure Distributions on the Ref. H Aftbody, $M_\infty = 1.1$



High Speed Aerodynamics, Long Beach

CFL3D (Baldwin-Barth), $Re_c = 40 \times 10^6$, $\alpha = 4^\circ$ ($C_L = 0.213$)



Axi Supersonic (Flow-through)
NPR=2.14, NTR=1.24

Axi Supersonic
NPR=5, NTR=3.055

Axi Transonic
NPR=5, NTR=3.055



Jet Effects on Aftbody at Transonic Conditions

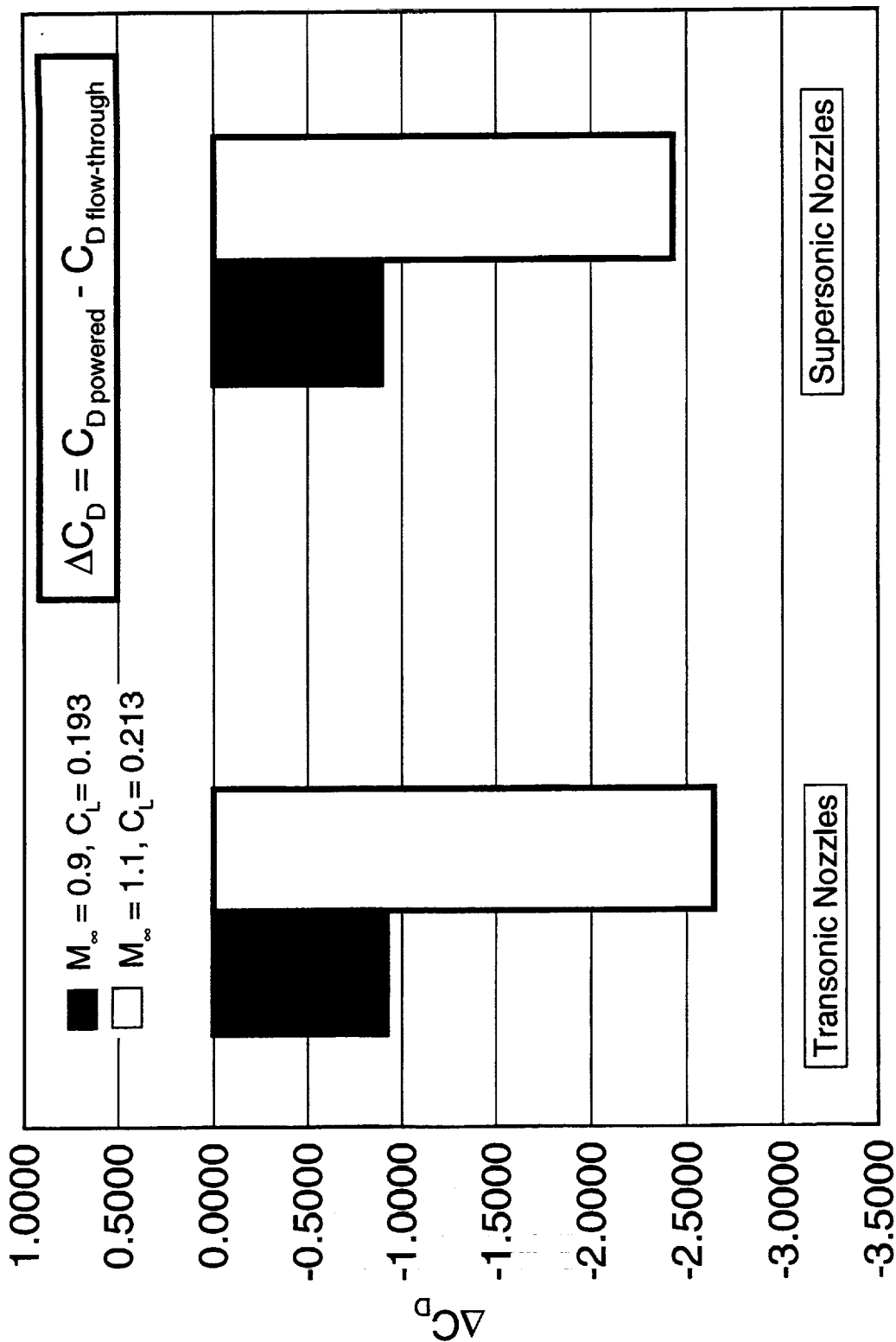
This chart shows the jet effects on aftbody at $M_\infty = 0.9$ and 1.1 for the Ref. H configuration with axi/transonic and axi/supersonic nozzle boattails. The jet causes a total drag reduction for the W/B/N/D configuration by approximately 1.0 and 2.5 cts. for the axi/transonic and axi/supersonic configurations, respectively.

Jet Effects on Aftbody at Transonic Conditions



High Speed Aerodynamics, Long Beach

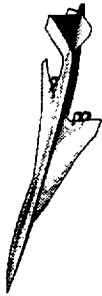
Ref. H Installed Axisymmetric Nozzles, CFL3D N-S, $Re_c = 40 \times 10^6$



Isolated 2-D Nozzle Boattail Analysis

CFL3D Navier-Stokes solutions for an isolated 2-D nozzle boattail are presented now. The solutions were obtained with three turbulence models: the Baldwin-Barth, Menter's K- ω shear stress transport (SST), and Spalart-Allmaras turbulence models. The solutions are compared with NASA 16' TT test data (Test # 477) for an 8.2%-scale model of the nozzle. The configuration selected for CFD validation was the geometry with a nozzle flap angle of 16.4° and nozzle sidewall angle of 4°. The flow conditions analyzed were $M_\infty = 0.9$ and 1.2. The powered nozzle flow conditions were simulated.

Isolated 2-D Nozzle Boattail Analysis



High-Speed Aerodynamics, Long Beach

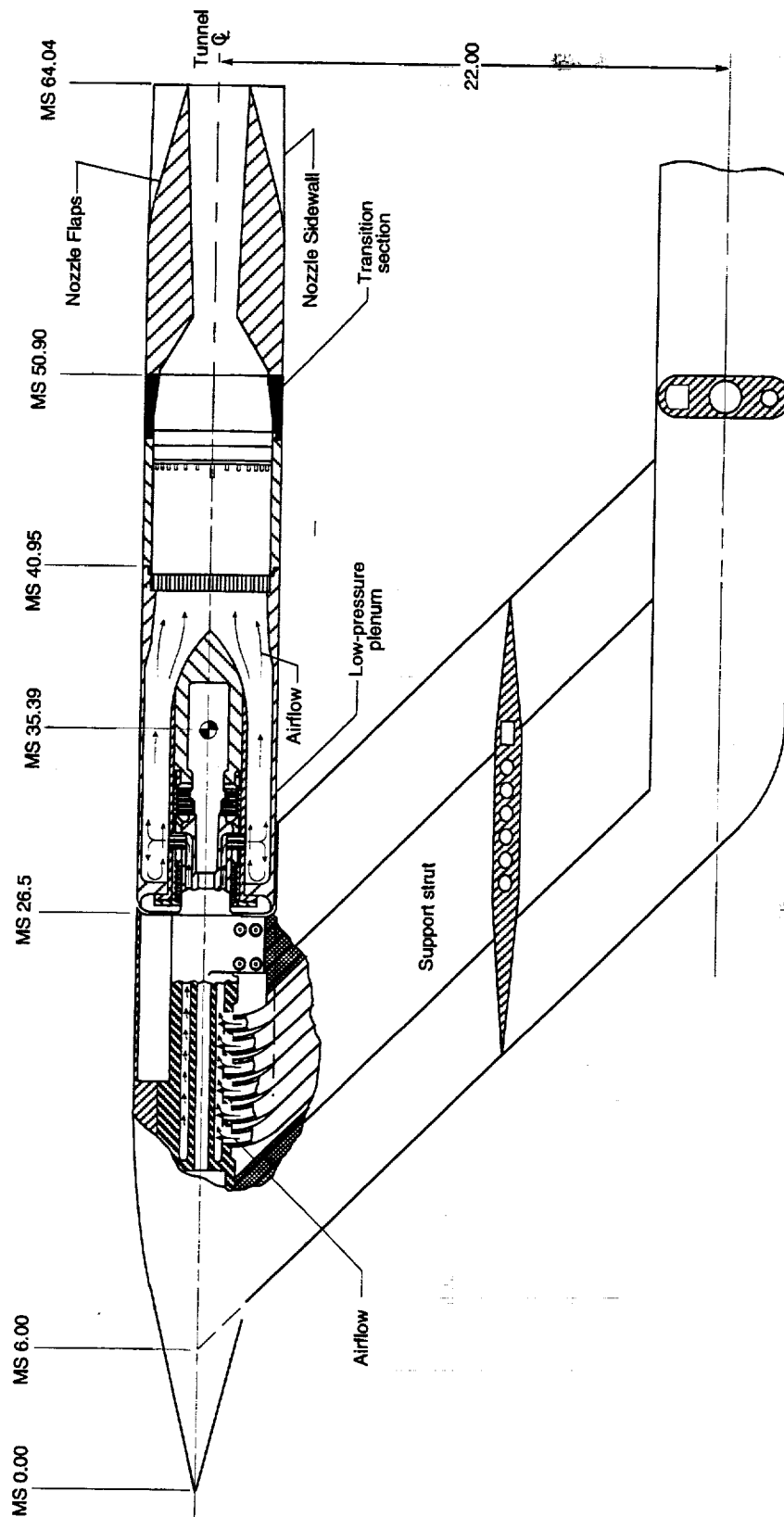
- CFL3D Navier-Stokes solutions
 - Baldwin-Barth, Menter's K- ω (SST), and Spalart-Allmaras Turbulence models
 - Comparisons with the NASA LaRC 16' TT test data
 - 8.2% scale of an HSR 2-D Nozzle Boattail
 - Nozzle flap angle of 16.4°
 - Nozzle sidewall angle of 4°
 - $M_\infty = 0.9$ and 1.2
 - Powered nozzle flow simulations (NPR = 5)

Experimental Arrangement

The experimental results obtained by NASA LaRC at the 16' TT wind -tunnel facility were used to validate the CFD capability for calculating nozzle boattail drag. The arrangement of the test is shown in this figure. The nozzles tested on the isolated, powered nacelle were built at approximately 8.2%-scale so that a correctly scaled internal nozzle geometry and jet could be simulated. The model instrumentation included both the balance measurement of loads on the nacelle and pressure measurement on the nozzle upper and lower flaps with two rows of pressure taps. In addition, there were two rows of pressure taps on one of the nozzle sidewalls.

Experimental Arrangement

High-Speed Aerodynamics, Long Beach



Grid for the Isolated Nozzle Boattail Geometry

The computational grid used for the CFL3D flow solver to simulate the isolated nozzle boattail configuration is shown. The grid, which was originally used in the PAB3D flow code by NASA LaRC, was modified in the present study. The modification was primarily in the nozzle flap zones where the originally patched grid was modified to become point-matched at zone interfaces in order to obtain accurate solutions using CFL3D. Due to flow symmetry, only one quarter of the nacelle/nozzle geometry was used in the computations.

Grid for the Isolated Nozzle Boattail Geometry Tested in LaRC 16' TT



High Speed Aerodynamics, Long Beach

(9 zones, 2.0 million points)



Boattail Region

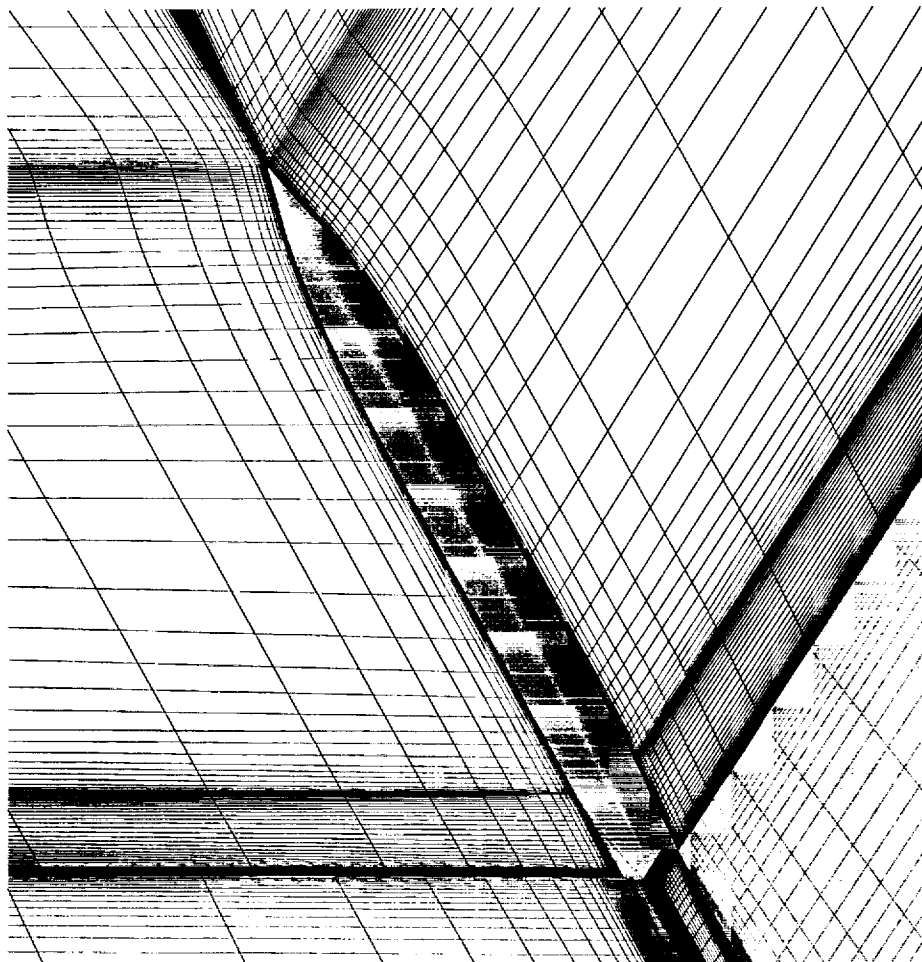


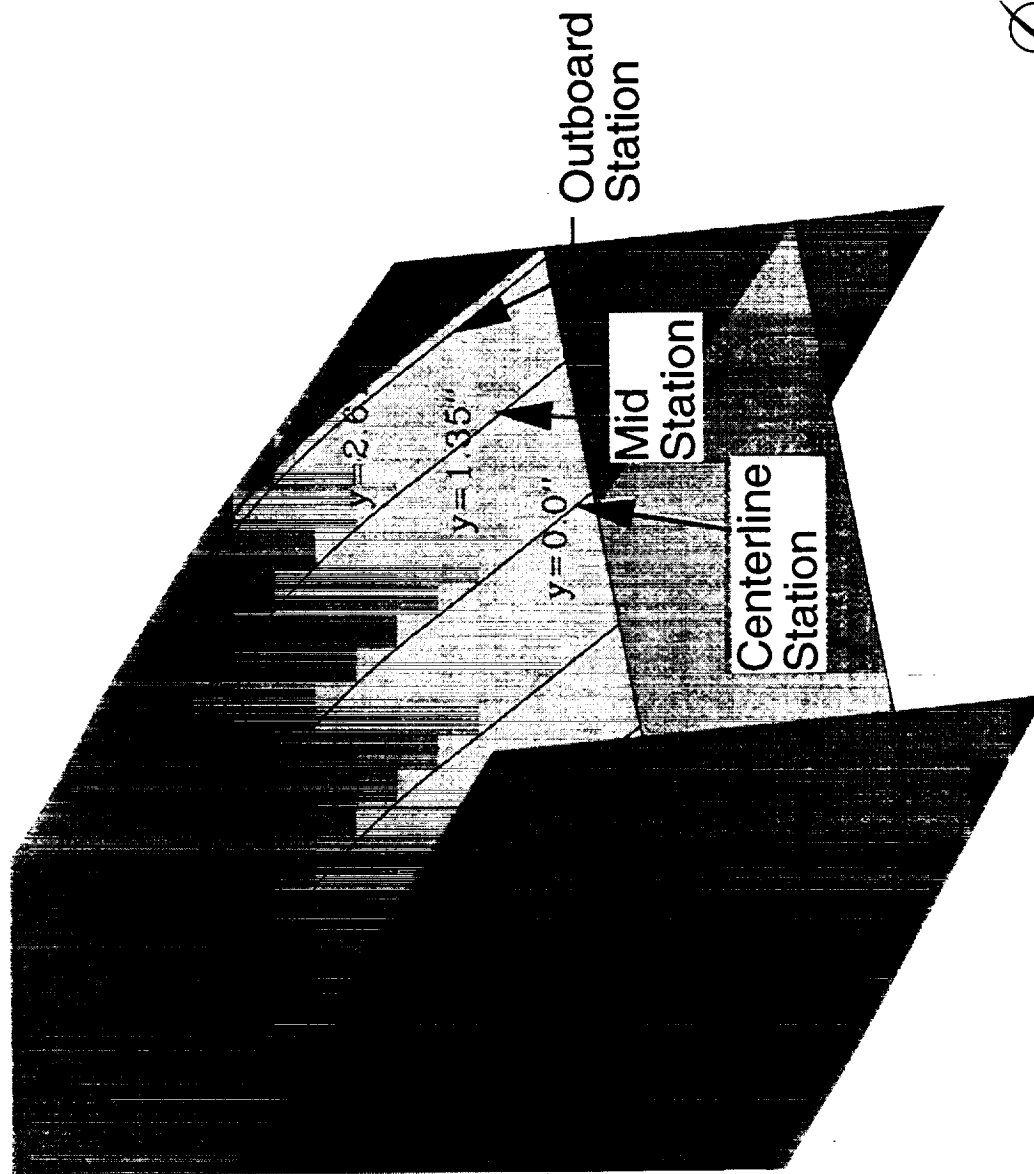
Illustration of the Instrumentation Stations

This figure illustrates the stations where the computed pressures are compared with the test data. The stations $y = 0.0''$, $1.35''$, and $2.61''$ are referred here as the centerline, mid, and outboard station, respectively.

Illustration of the Instrumentation Stations

High Speed Aerodynamics, Long Beach

Isolated Nozzle Boattail Geometry Tested in LaRC 16' TT



BOEING

C_p Distributions on the 2-D Nozzle Flap ($M_\infty = 0.9$) CFL3D, Baldwin-Barth Turbulence Model

This chart shows the C_p comparisons between CFL3D and the test results for $M_\infty = 0.9$, NPR = 5. The CFL3D solutions were obtained using the Baldwin-Barth turbulence model. As shown in the figure, the agreement between these two results are not good. The problem was traced back to the over-prediction of the size of the flow separation region. This will be further discussed in another figure which compares flow patterns obtained by different turbulence models.

C_p Distributions on the 2-D Nozzle Flaps ($M_\infty=0.9$)

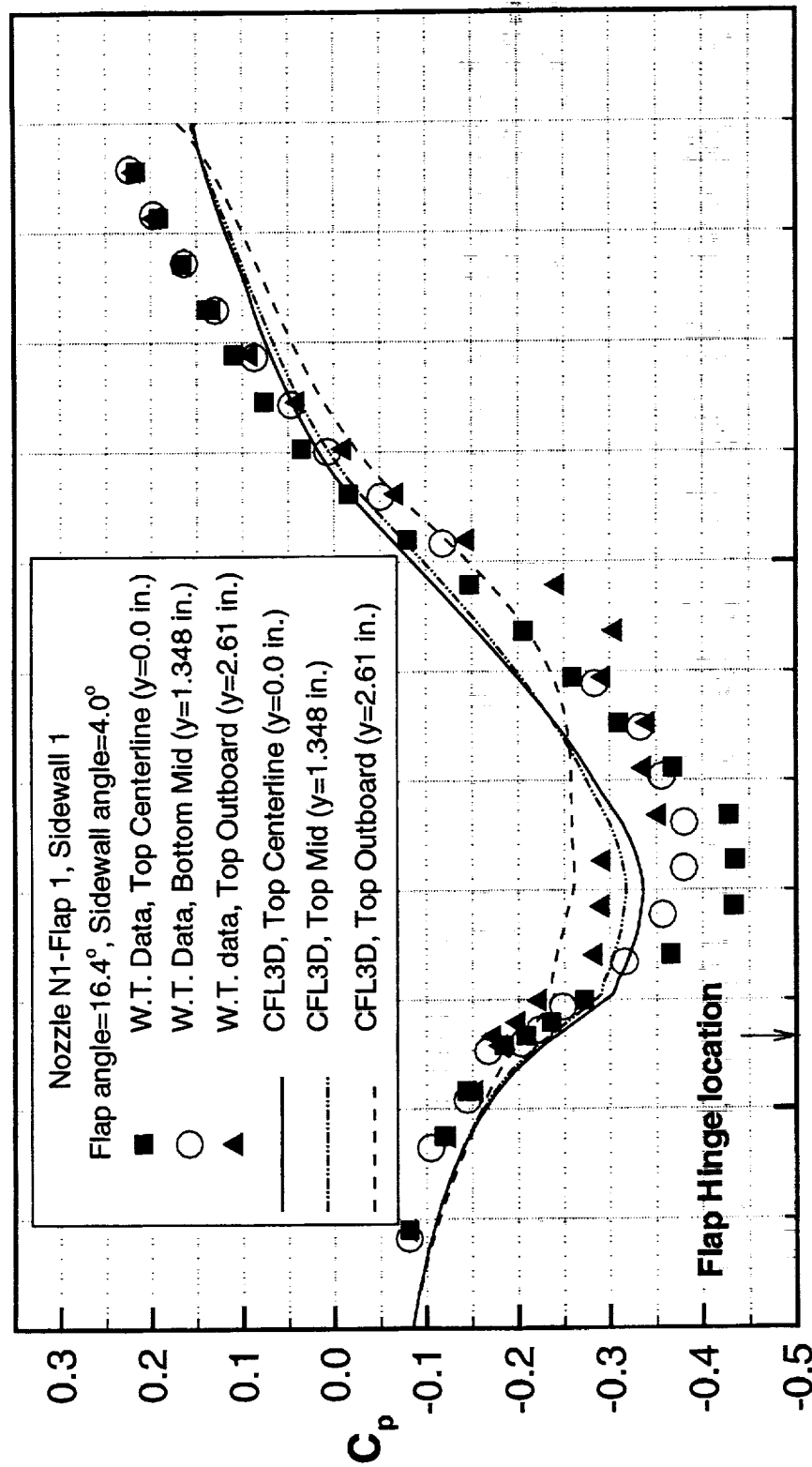
CFL3D, Baldwin-Barth Turbulence Model

High Speed Aerodynamics, Long Beach



Isolated Nozzle Boattail, LaRC 16' TT

$Re_L=21.12 \times 10^6$, NPR=5.0, NTR=1.059



65

X (inches) 60

55

C_p Distributions on the 2-D Nozzle Flap ($M_\infty = 0.9$) CFL3D, Menter's K- ω (SST) Turbulence Model

This chart shows the C_p comparisons between CFL3D and the test results for $M_\infty = 0.9$, NPR = 5. The CFL3D solutions were obtained using the Menter's K- ω (SST) turbulence model. As shown in the figure, the agreements between these two results are much better than the results from the Baldwin-Barth turbulence model.

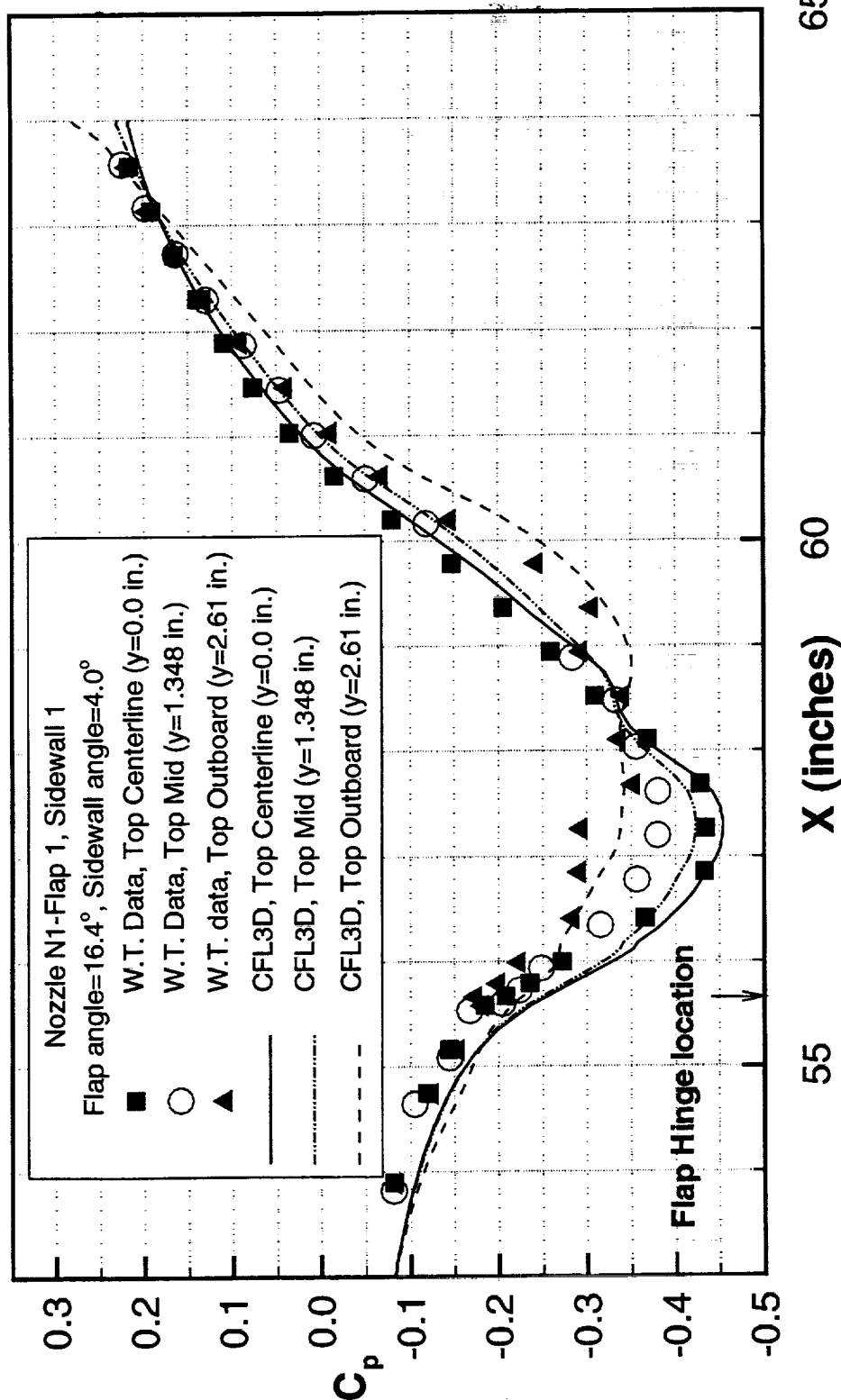
C_p Distributions on the 2-D Nozzle Flaps ($M_\infty=0.9$)

CFL3D, Menter's K- ω (SST) Turbulence Model

High Speed Aerodynamics, Long Beach



Isolated Nozzle Boattail, LaRC 16' TT
 $Re_L=21.12 \times 10^6$, NPR=5.0, NTR=1.059



C_p Distributions on the 2-D Nozzle Flap ($M_\infty = 0.9$) CFL3D, Spalart-Allmaras Turbulence Model

This chart shows the C_p comparisons between CFL3D and the test results for $M_\infty = 0.9$, NPR = 5. The CFL3D solutions were obtained using the Spalart-Allmaras turbulence model. As shown in the figure, the agreements between these two results are much better than the results from the Baldwin-Barth turbulence model, and is similar to the Menter's K- ω (SST) results.

C_p Distributions on the 2-D Nozzle Flaps ($M_\infty=0.9$)

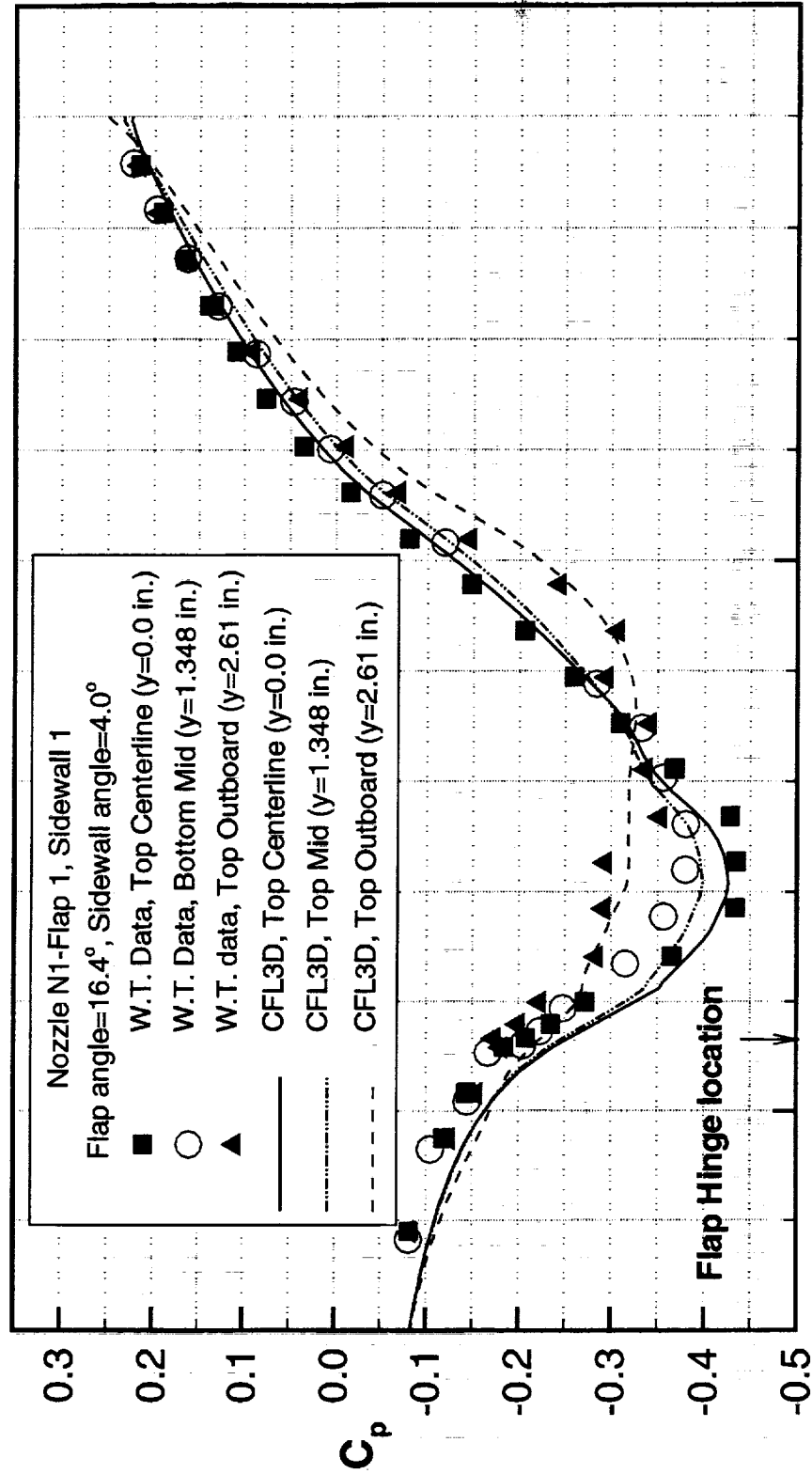
CFL3D, Spalart-Allmaras Turbulence Model

High Speed Aerodynamics, Long Beach



Isolated Nozzle Boattail, LaRC 16' TT

$Re_L=21.12 \times 10^6$, NPR=5.0, NTR=1.059



55 X (inches) 60 65

Surface Particle Traces, CFL3D Solutions ($M_\infty = 0.9$)

The surface particle traces obtained from CFL3D with three different turbulence models for $M_\infty = 0.9$ and NPR = 5 are shown in this figure. The figure shows that the Baldwin-Barth turbulence model predicts flow separation on top of the nozzle flap. However, the flow separation region is significantly reduced and completely eliminated by using the Menter's K- ω (SST) and the Spalart-Allmaras turbulence models. It is observed that the flow pattern at the end of the nozzle flap for the Menter's K- ω (SST) is questionable. Continuing the solution further didn't change the flow pattern at that location. This problem is not a numerical convergence problem. Further discussion will be given in the $M_\infty = 1.2$ case.

Also shown are the boattail drag defined as the drag force acting on the body downstream of the nozzle flap hinge-line. As shown in the figure, the differences of total drag between these three turbulence models are within 0.1 ct. The major effect of the turbulence models is to cause the drag redistribution between the pressure drag, C_{DP} , and the viscous drag, C_{DV} .

Surface Particle Traces, CFL3D Solutions ($M_\infty = 0.9$)

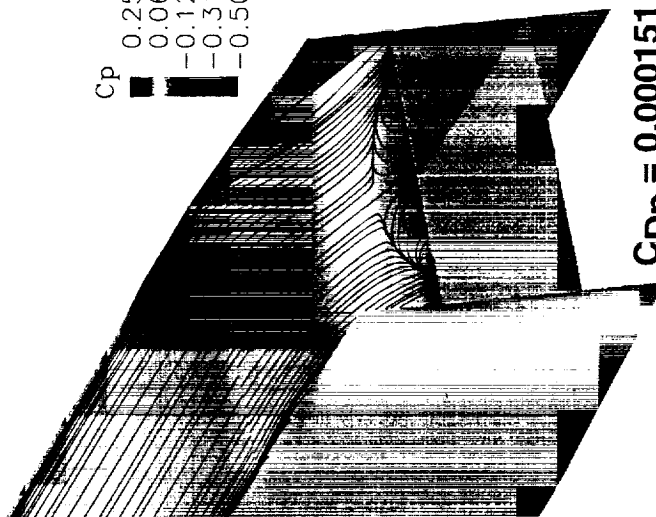
Isolated Nozzle Boattail Geometry Tested in LaRC 16' TT



High Speed Aerodynamics, Long Beach

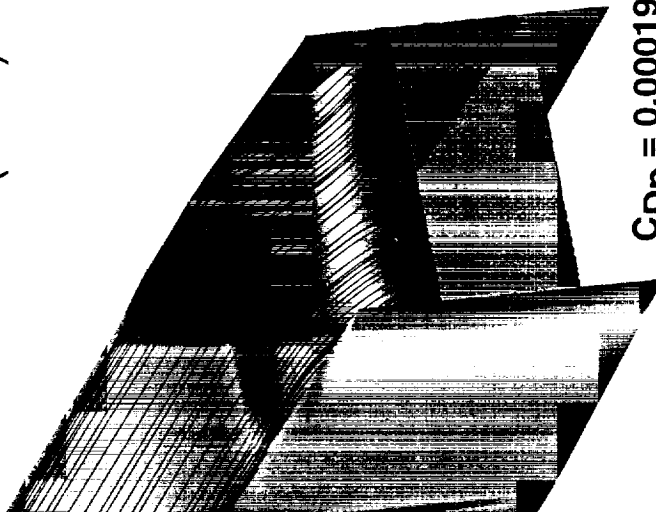
$Re_L = 21.12 \times 10^6$, $\alpha = 0^\circ$, NPR=5.0, NTR=1.059
(9 zones, 2.0 million grid points, Ref. Area = 6824.41 in²)

Baldwin-Barth



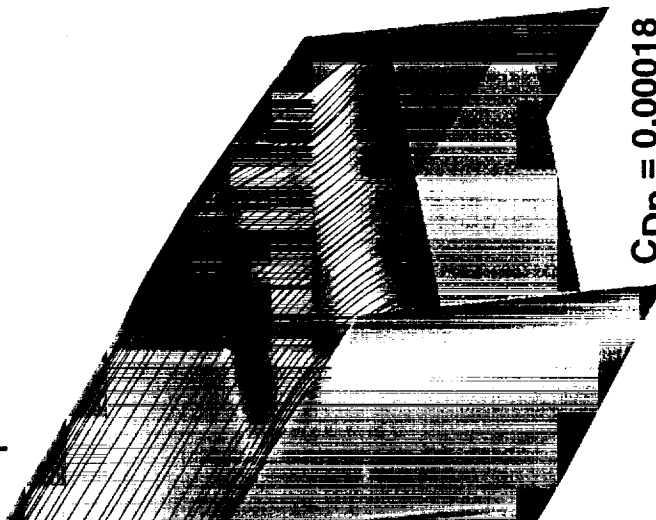
$C_{Dp} = 0.000151$
 $C_{Dv} = 0.000129$
 $C_D = 0.000280$

Menter's K- ω (SST)



$C_{Dp} = 0.000194$
 $C_{Dv} = 0.000093$
 $C_D = 0.000287$

Spalart-Allmaras



$C_{Dp} = 0.00018$
 $C_{Dv} = 0.00011$
 $C_D = 0.00029$



C_p Distributions on the 2-D Nozzle Flap ($M_\infty = 1.2$)

CFL3D, Baldwin-Barth Turbulence Model

This figure shows the C_p comparisons between CFL3D and the test results for $M_\infty = 0.9$, NPR = 5. The CFL3D solutions were obtained using the Baldwin-Barth turbulence model. The CFL3D result shows that the shock location at the outboard station ($y = 2.61''$) is upstream of the shock location at the centerline station ($y = 0.0$). This is opposite to what is seen in the wind-tunnel measurements. This implies that the flow physics for the $M_\infty = 1.2$ case is not properly captured by CFL3D with the Baldwin-Barth turbulence model. The problem is traced back to the flow separation prediction capability. This will be further discussed in another figure which compares flow patterns obtained by different turbulence models.

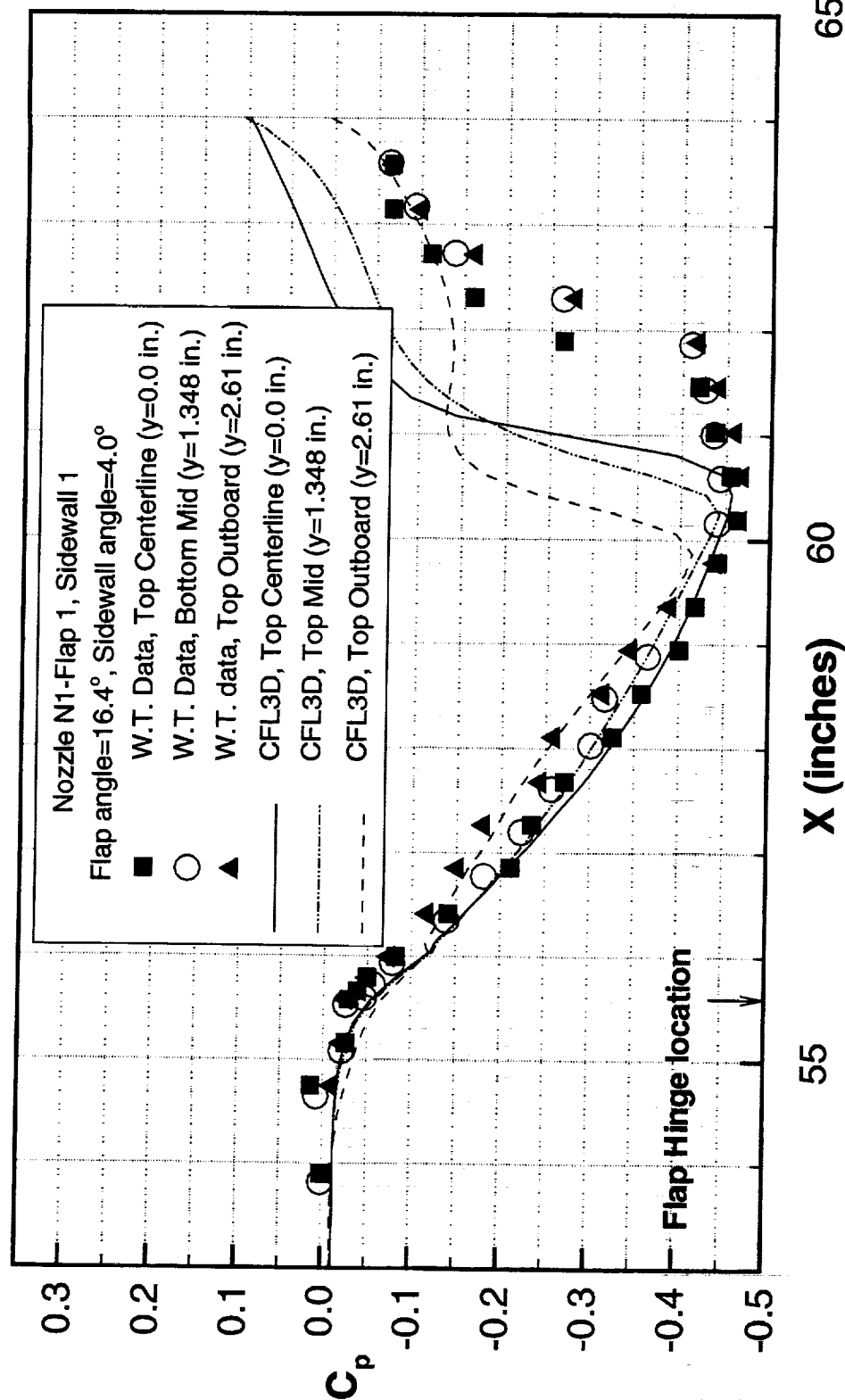
C_p Distributions on the 2-D Nozzle Flaps ($M_\infty=1.2$)

CFL3D, Baldwin-Barth Turbulence Model

High Speed Aerodynamics, Long Beach

Isolated Nozzle Boattail, LaRC 16' TT

$Re_L=21.12 \times 10^6$, NPR=5.0, NTR=1.174



C_p Distributions on the 2-D Nozzle Flap ($M_\infty = 1.2$) CFL3D, Menter's K- ω (SST) Turbulence Model

C_p comparisons between CFL3D and the test results are shown for $M_\infty = 1.2$, NPR = 5. The CFL3D solutions were obtained using the Menter's K- ω (SST) turbulence model. As shown in the figure, the agreement between these two results is the worst among the three turbulence models investigated. The problem is traced back to the flow separation prediction capability. This will be further discussed in another figure which compares flow patterns obtained by different turbulence models.

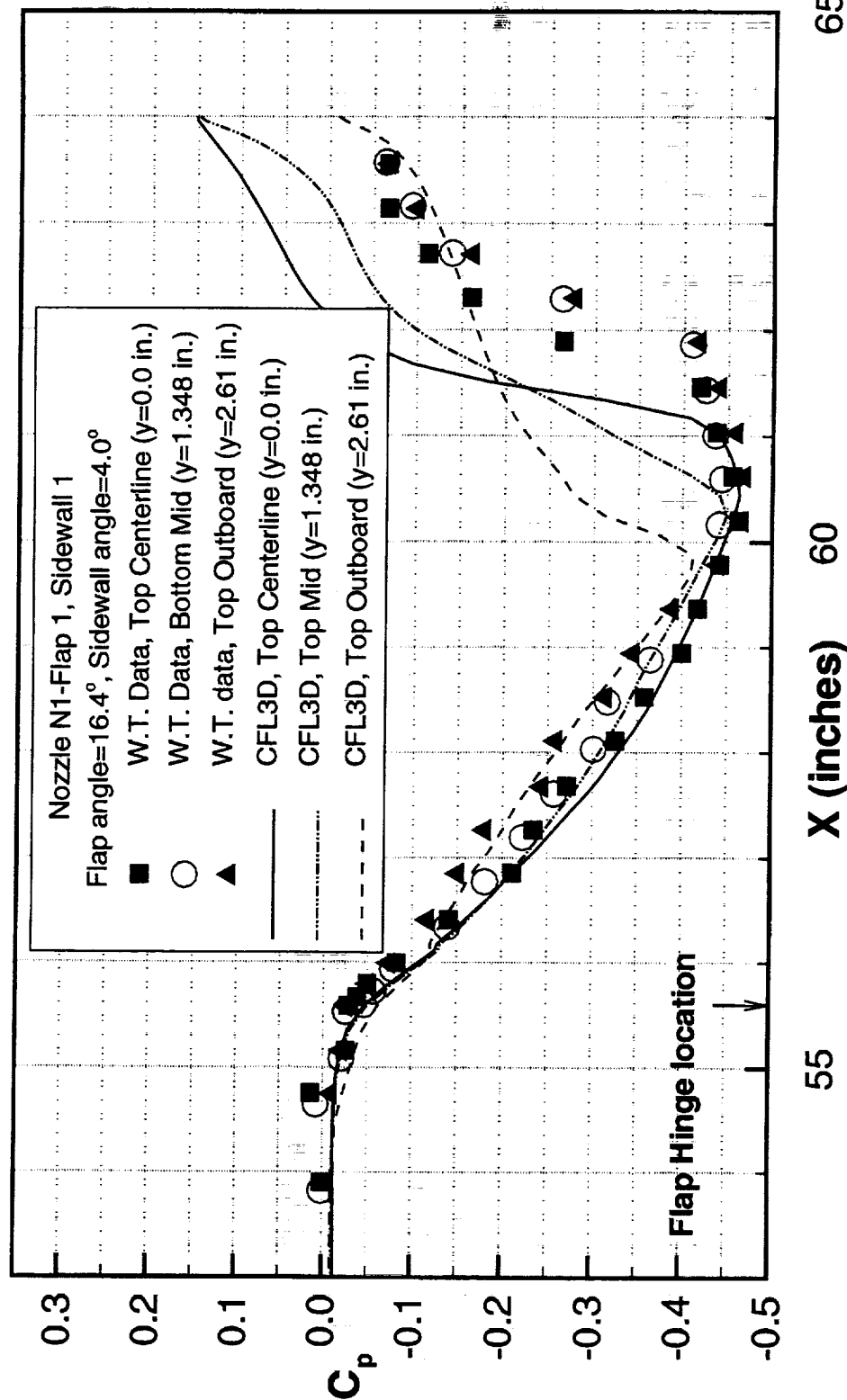
C_p Distributions on the 2-D Nozzle Flaps ($M_\infty=1.2$) **CFL3D, Menter's K- ω (SST) Turbulence Model**



High Speed Aerodynamics, Long Beach

Isolated Nozzle Boattail, LaRC 16' TT

$Re_L=21.12 \times 10^6$, $NPR=5.0$, $NTR=1.174$



55 60 65

C_p Distributions on the 2-D Nozzle Flap ($M_\infty = 1.2$) CFL3D, Spalart-Allmaras Turbulence Model

C_p comparisons between CFL3D and the test results are shown for $M_\infty = 1.2$, NPR = 5. The CFL3D solutions were obtained using the Spalart-Allmaras turbulence model. As shown in the figure, the agreements between these two results are much better than the results from the Baldwin-Barth and the Menter's K- ω (SST) results. Unlike the Baldwin-Barth case, the relative shock locations between different span stations now agree with the test data. However, the predicted shock location upstream of the test data indicates that the predicted flow separation bubble is slightly larger than in the test.

C_p Distributions on the 2-D Nozzle Flaps ($M_\infty=1.2$)

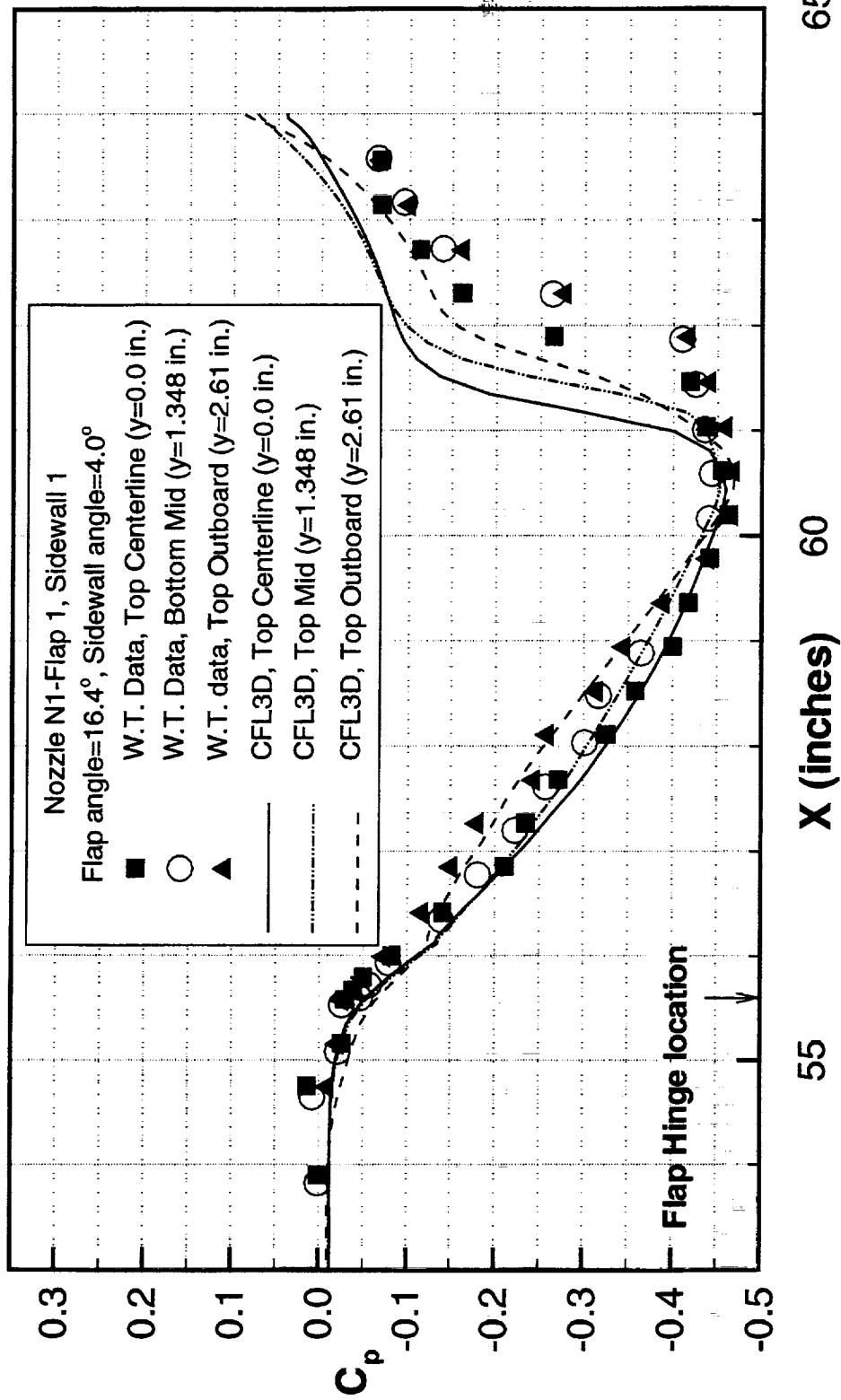
CFL3D, Spalart-Allmaras Turbulence Model

High Speed Aerodynamics, Long Beach



Isolated Nozzle Boattail, LaRC 16' TT

$Re_L=21.12 \times 10^6$, NPR=5.0, NTR=1.174



PAB3D Predicted Pressures Along Flap ($M_\infty = 1.2$)

This figure shows the C_p comparisons between PAB3D and the test results for $M_\infty = 1.2$, NPR = 5. The PAB3D solutions were obtained by NASA LaRC with the Girmaji ASM turbulence model. As shown in the figure, the agreement between these two results are good.

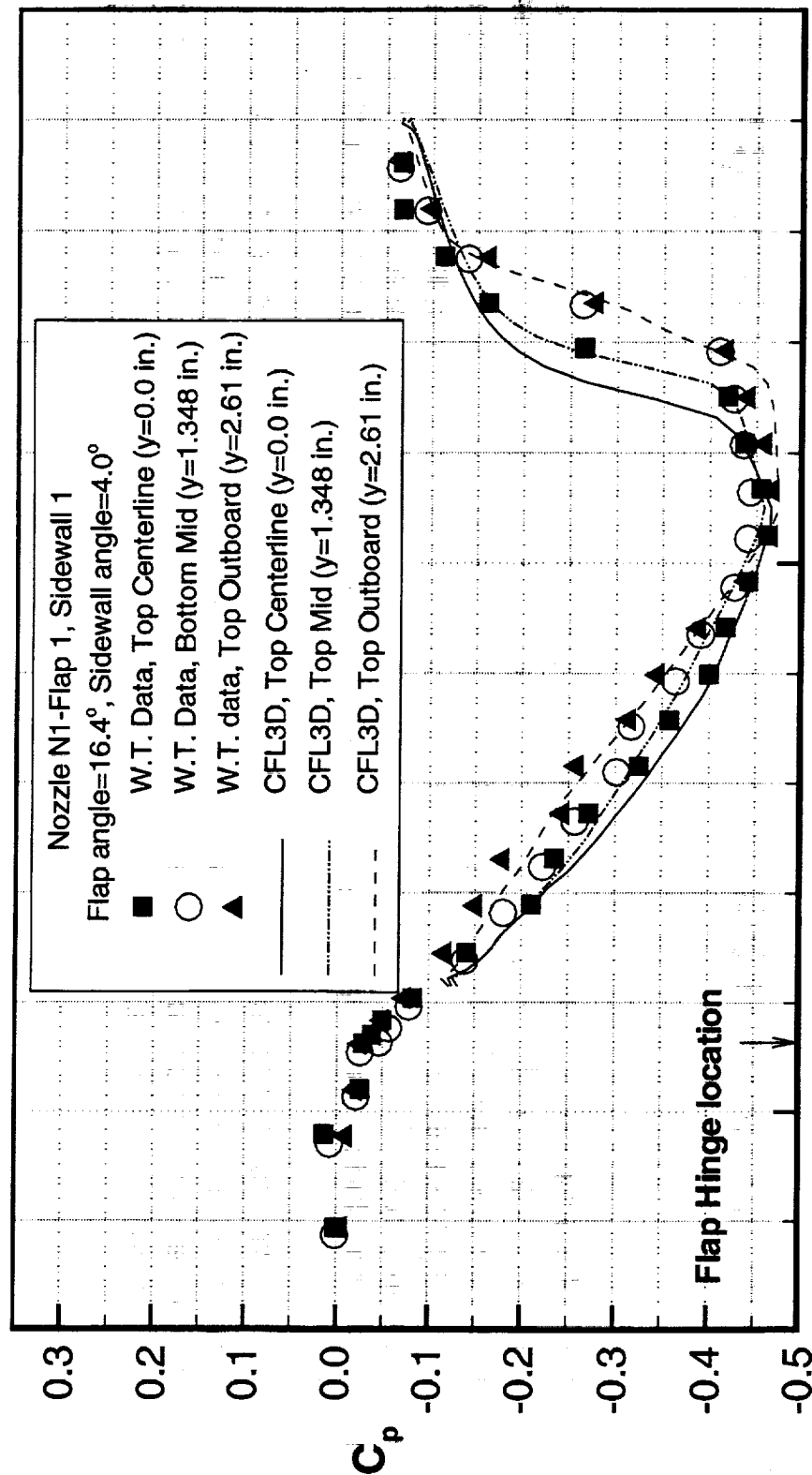
PAB3D Predicted Pressures Along Flap ($M_\infty=1.2$)

NASA LaRC, Girimaji ASM Turbulence Model

High Speed Aerodynamics, Long Beach



Isolated Nozzle Boattail, LaRC 16' TT
 $Re_L=21.12 \times 10^6$, NPR=5.0, NTR=1.174



55 X (inches) 60 65



Surface Particle Traces, CFL3D Solutions ($M_\infty = 1.2$)

The surface particle traces obtained from CFL3D with three different turbulence models are shown for $M_\infty = 1.2$ and $NPR = 5$. The figure shows that the Baldwin-Barth and Spalart-Allmaras turbulence models predict flow separation on top of the nozzle flap. However, the shape of the flow separation regions are different. For the Menter's K- ω (SST) turbulence model, the flow separation region is completely eliminated. From the pressure comparisons between the predicted and the test results, it is concluded that only the Spalart-Allmaras turbulence model predicts flow pattern accurately.

Also shown are the boattail drag values defined as the drag force acting on the body downstream of the nozzle flap hinge-line. As shown in the figure, the differences of total drag between these three turbulence models are within 1.5 cts. The difference is primarily due to the difference in pressure drag value.

Surface Particle Traces, CFL3D Solutions ($M_\infty=1.2$)

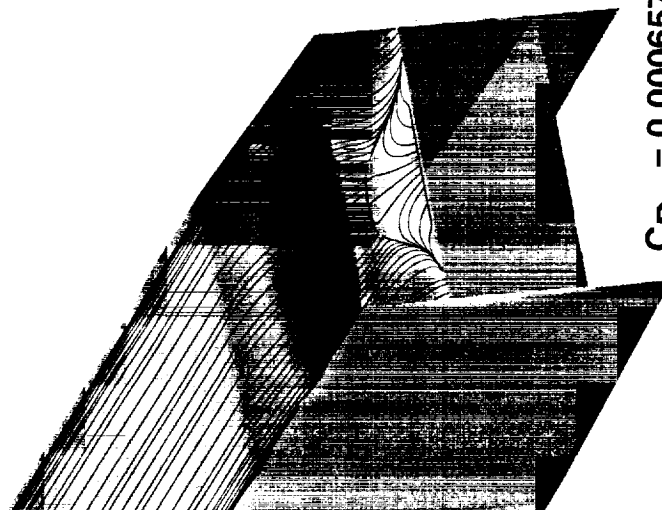
Isolated Nozzle Boattail Geometry Tested in LaRC 16' TT

High Speed Aerodynamics, Long Beach



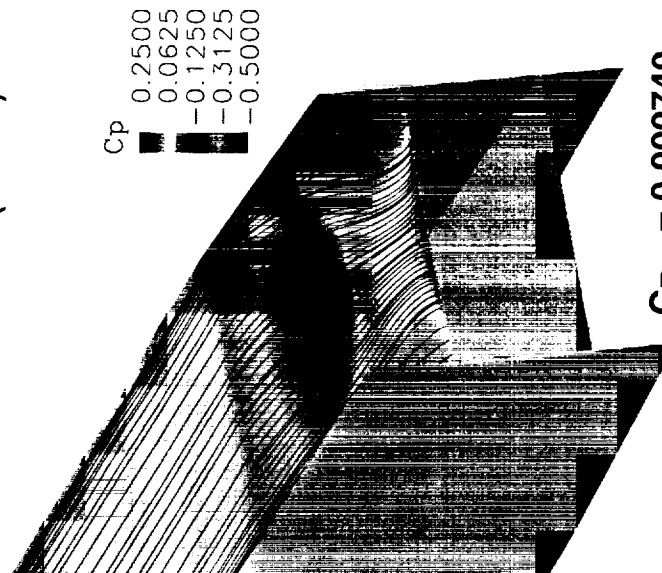
$Re_L=21.12 \times 10^6$, $\alpha=0^\circ$, NPR=5.0, NTR=1.174
(9 zones, 2.0 million grid points, Ref. Area = 6824.41 in²)

Baldwin-Barth



$C_{Dp} = 0.000657$
 $C_{Dv} = 0.000106$
 $C_D = 0.000763$

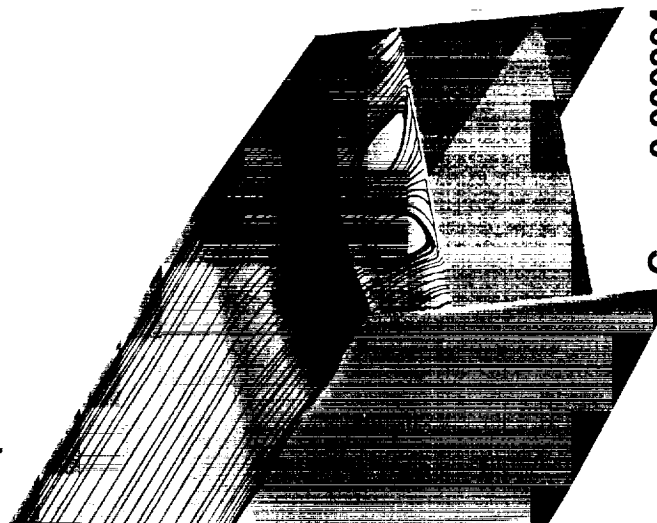
Menter's K- ω (SST)



C_p 0.2500
0.0625
-0.1250
-0.3125
-0.5000

$C_{Dp} = 0.000740$
 $C_{Dv} = 0.000106$
 $C_D = 0.000846$

Spalart-Allmaras



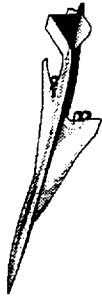
$C_{Dp} = 0.000804$
 $C_{Dv} = 0.000108$
 $C_D = 0.000912$



Summary and Conclusions

The TCA nacelle/diverter re-shaping study resulted in a total drag reduction by 1.2 and 1.4 cts. at full-scale and wind-tunnel Reynolds number, respectively. The interference drag calculations for the Ref. H axi and 2-D nozzles indicate that their interference drag values at transonic speeds are comparable. For $M_\infty = 1.1$, the 2-D nozzle has more favorable interference drag by 3 cts. than the axi nozzle. Jet effect on aftbody drag is favorable at transonic cruise (approximately 1 ct. for $M_\infty = 0.9$, and 2.5 cts. for $M_\infty = 1.1$).

Summary and Conclusions



High-Speed Aerodynamics, Long Beach

- TCA nacelle/diverter re-shaping reduced drag by 1.2 cts. at full-scale Re and 1.4 cts. at wind-tunnel Re
- Interference drag values for Ref. H axi and 2-D nozzles at transonic speeds are comparable
- Jet effect on aftbody drag is favorable at transonic cruise (approximately 1 ct. for $M_\infty=0.9$ and 2.5 cts. for $M_\infty=1.1$)

Summary and Conclusions (cont'd)

CFL3D solutions with the Spalart-Allmaras turbulence model for an isolated 2-D nozzle boattail show good agreements in pressure distributions with the wind-tunnel test data at transonic speeds. The agreement is better than the results from Baldwin-Barth and Menter's $k-\omega$ (SST) turbulence models. Same 2-D nozzle boattail was analyzed at NASA LaRC using PAB3D with the Girimaji algebraic turbulence model. The results for $M_\infty = 1.2$ are better than the Spalart-Allmaras solutions in comparison with the wind-tunnel test data. Implementation of the Girimaji algebraic turbulence model in CFL3D is required to close the gap between CFL3D and PAB3D solutions.

Summary and Conclusions (cont'd)



High-Speed Aerodynamics, Long Beach

- Spalart-Allmaras turbulence model shows good agreement in pressure distributions with W.T. test data for isolated 2-D nozzle boattail
- Implementation of the Girmaji algebraic turbulence model in CFL3D is required to close the gap between CFL3D and PAB3D solutions

This page is intentionally left blank.

HSR

High Speed Research



Configuration Aerodynamics ITD Team Year End Technical Review

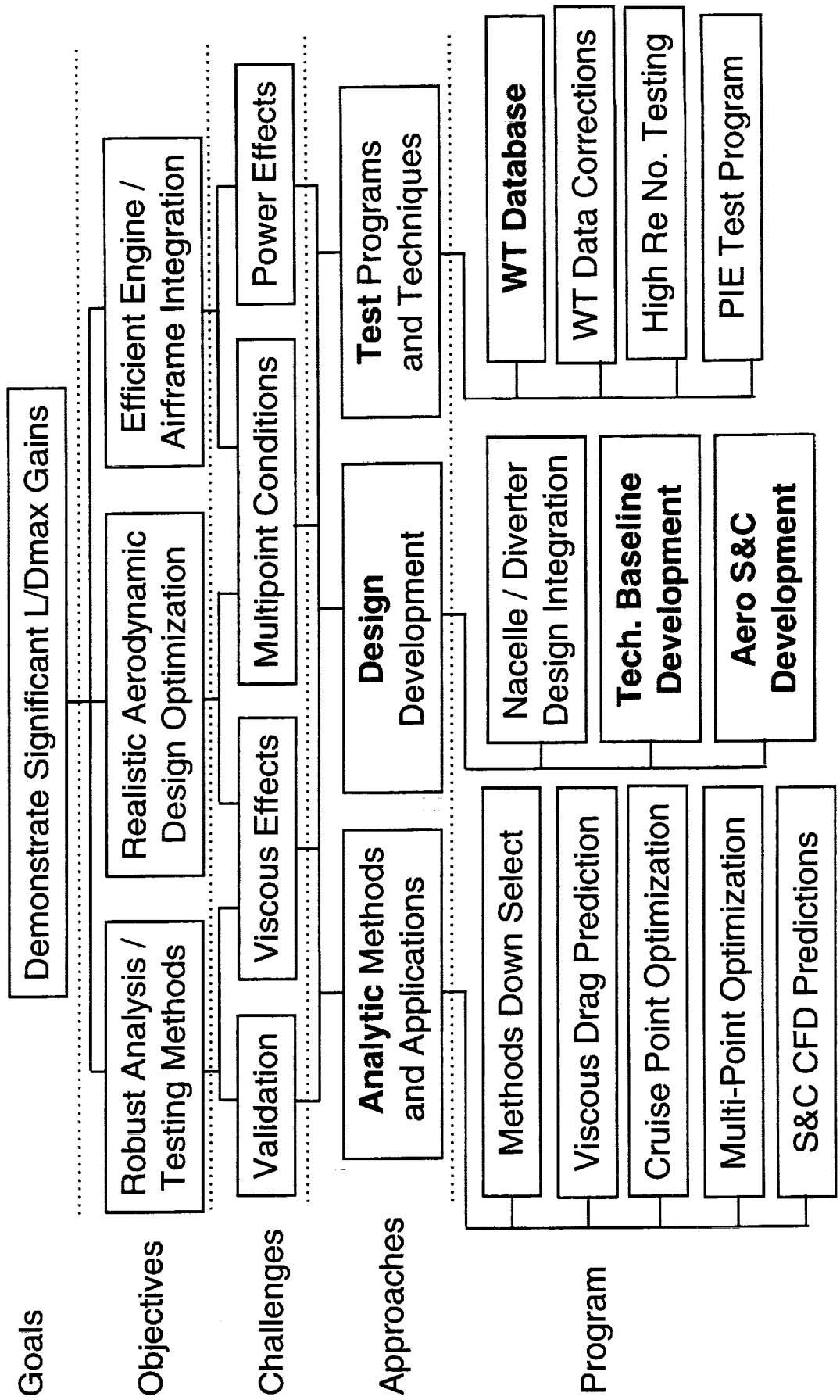
February 9 - 11, 1998

Session 5: Configuration Assessments and Fundamental Studies

Session Chairman: Douglas L. Wilson

Configuration Aerodynamics Technology Development

Session 5: Configuration Assessments and Fundamental Studies



Configuration Aerodynamics Technology Development

Session 5: Configuration Assessments and Fundamental Studies

Objectives:

- **Assess high-speed aerodynamic characteristics**
- **Understand fundamental aerodynamics for HSCT**
- **Support design refinement, baseline updates**
- **Develop appropriate technology metrics**

Issues:

- **Prediction of flight performance from WT and CFD**
- **Aeroelastic effects on S&C, multi-point design**
- **Impact of design features (3-surface config, LE radius)**

Configuration Aerodynamics 1997 Year-End Review

Session 5: Configuration Assessments and Fundamental Studies

8:00 - 8:10	Overview of WBS 4.3.1.4	Doug Wilson, BCA
8:10 - 8:35	Model 2b Test Results	Aga Goodsell, ARC
8:35 - 9:05	NCV Wind Tunnel Test Results	Kevin Mejia, BCA
9:05 - 9:25	Aftbody Closure Model Design - Lessons Learned	Francis Capone, LaRC
9:25 - 9:50	HSR Model Deformation Measurements from Subsonic to Supersonic Speeds	Al Burner, LaRC
9:50 - 10:00	(BREAK)	
10:00 - 10:30	Aeroelastic Assessment of the TCA	GeoJoe Kuruvila, BLB
10:30 - 10:50	S&C Assessment of the TCA	David Blake, BLB
10:50 - 11:10	Initial Predictions of Canard Integration	Todd Magee, BLB
11:10 - 12:00	Panel Discussion	Presenters

HSR Airframe Technical Review
Configuration Aerodynamics

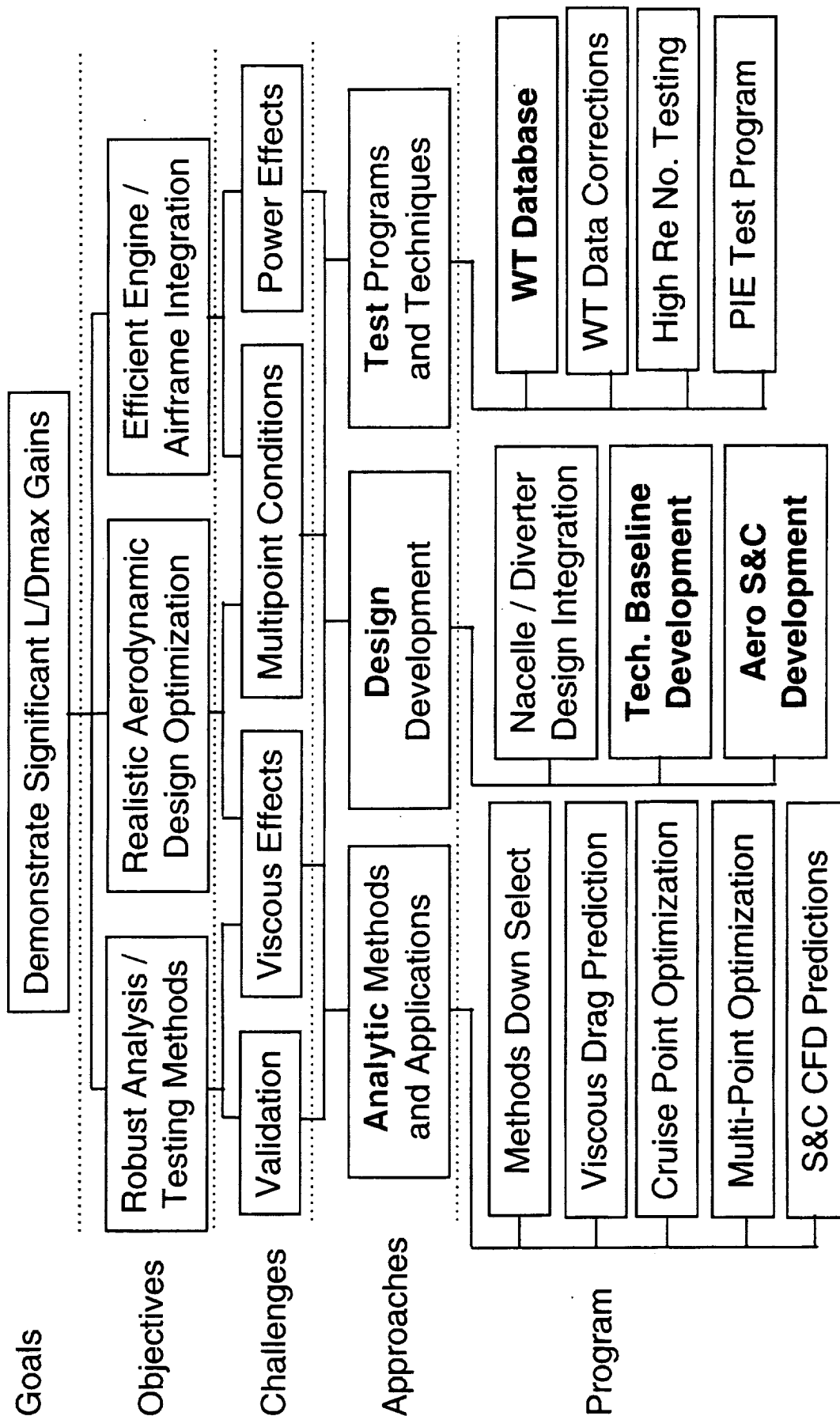
Model 2b Test Results

Aga M. Goodsell
NASA Ames Research Center
February 11, 1998

Viewgraph 1: Session 5: Configuration Assessments and Fundamental Studies

This activity is part of the Wind Tunnel Database and Wind Tunnel Data Corrections Programs. The main purpose of this test was to evaluate the aerodynamic performance of the TCA Baseline configuration around the supersonic cruise point.

Session 5: Configuration Assessments and Fundamental Studies



Viewgraph 2: Test 1679 Summary

This test was conducted at NASA Langley Research Center in Test Section #2 of the Unitary Pressure Wind Tunnel. The test was conducted over a period of five weeks between January 21 and February 25, 1997. Both of the 1.675%-scale TCA Baseline models—Model 2a and Model 2b—were tested. There are two main differences between the models. Model 2a has cutouts for leading and trailing edge flaps and is instrumented with both upper and lower surface pressure taps. On the other hand, Model 2b was built with a solid wing with only two pressure tubes installed to measure nacelle base pressures.

Test 1679 Summary

- Test conducted at LaRC UPWT #2
- Test dates: 1/21/97–2/25/97
- 1.675% Baseline TCA Models tested
 - Model 2a with modular wing
 - Model 2b with solid wing

Viewgraph 3: Test 1679 Objectives

The main objective of test 1679 was to establish Model 2b as a calibration model for future HSR performance tests. Therefore, it was important to obtain high quality performance data at the cruise Mach number of 2.4. As part of this requirement, the goal was to achieve an uncertainty in the measured drag coefficient equal to ± 0.5 counts at 80% confidence. In addition, a comparison of the performance data was made between Models 2a and 2b to evaluate the effects of leading- and trailing-edge flaps and cutouts for pressure tubing on the data.

The second objective of the test was to try to assess the drag due to the trip dots that were applied to the configurations to attain transition from laminar to turbulent flow. To attempt to meet this objective, the dot heights were varied and the resulting aerodynamic forces were measured. Then, sublimation photographs were obtained to observe the resulting transition location in order to determine if the trip dots were effective at tripping the flow.

Test 1679 Objectives

- Establish Model 2b as a calibration model
 - Obtain high quality performance data at $M_{\infty}=2.4$ ($\Delta C_D = \pm 0.5$ cts @ 80% confidence)
 - Compare performance between Models 2a & 2b
- Assess trip drag of Model 2b WB & WBND
 - Measure forces w/ varying trip dot height
 - Obtain sublimation photos; determine transition location

Viewgraph 4: Model 2b upper surface

This is a photograph of the upper surface of Model 2b in the test section. The wing/body configuration consists of three main pieces of hardware: the nose assembly, the wing/strongback with an upper balance cover, and the truncated aft fuselage. All sharp leading and trailing edges were modified to accommodate 0.004 inch thicknesses.

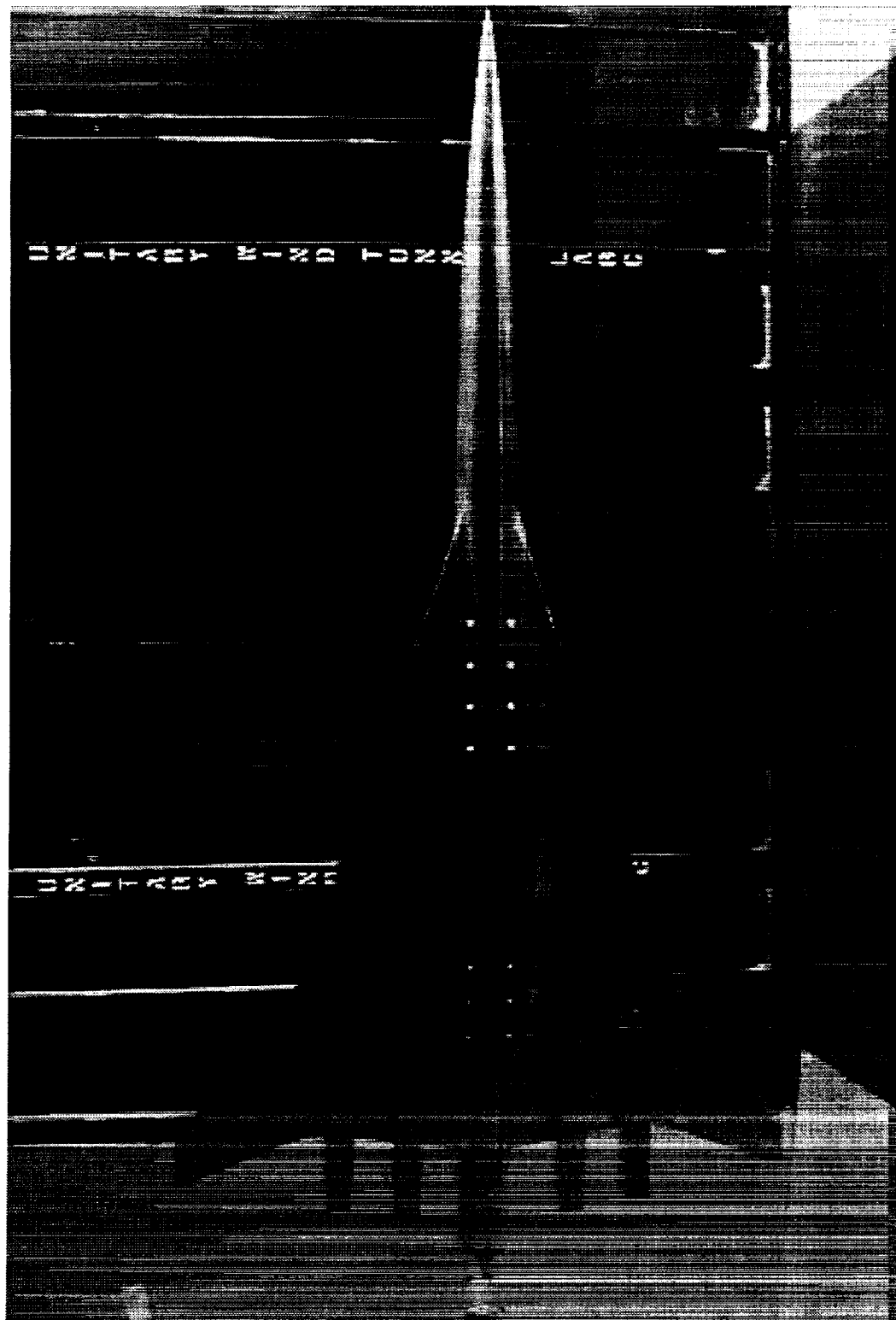
Model 2b Upper Surface



Viewgraph 5: Model 2b lower surface

This photograph shows the lower surface of the model including the nacelles. The diverters were built as an integral part of the nacelles. The lip thicknesses of the nacelles were less than 0.004 inch and the sidewalls of the exit were approximately 0.004 inch thick. The internal duct of the nacelles were fabricated using a wire EDM to save manufacturing time and costs. Therefore, the internal duct was constructed as a linear loft between the circular inlet and the square exit. As a result, the internal duct is different from the OML definition. However, the area of the internal duct varies by less than 0.1%. The two left-hand nacelles were instrumented with four base pressure taps—two on the upper base area and two on the lower base area. The four taps were manifolded into one tube so that an average base pressure was measured during testing.

Model 2b Lower Surface



Viewgraph 6: Data Acquired

Forces and moments were first obtained on Model 2a at freestream Mach 2.4 and 2.7 at two Reynolds numbers— $4 \times 10^6/\text{ft}$ and $3 \times 10^6/\text{ft}$. Since an earlier test entry at UPWT (Test 1671) involved an extensive study on Model 2a, another thorough study of Model 2a was not necessary. Therefore, Model 2a was tested first to make sure that the tunnel was operating consistently, since previous data was available to compare with the current data, and to obtain data for a long-term repeatability analysis. Next, Model 2b was installed in the tunnel. Then, forces and moments were obtained at the same conditions as that of Model 2a. In addition to forces and moments, two flow visualization procedures were conducted. Colored oil flow photographs were acquired at two angles-of-attack— 0° and 3.5° —at supersonic cruise Mach 2.4. As mentioned previously, sublimation photographs were also taken for the different trip configurations at the cruise point.

Data Acquired

- Model 2a (WB and WBNDf)
 - Forces, Moments
 - $M_{\infty}=2.4, 2.7, Re=4 \times 10^6/\text{ft}, 3 \times 10^6/\text{ft}$
- Model 2b (WB and WBNDf)
 - Forces, Moments
 - $M_{\infty}=2.4, 2.7, Re=4 \times 10^6/\text{ft}, 3 \times 10^6/\text{ft}$
 - Colored oil flow
 - $M_{\infty}=2.4$ at $\alpha = 0^{\circ}, 3.5^{\circ}$
 - Sublimation
 - $M_{\infty}=2.4$ at $\alpha = 3.5^{\circ}$ (cruise only)

Viewgraph 7: Drag Data Reduction

In the final data reduction of the forces, several corrections are made to the drag coefficient involving the internal drag of the nacelles, the base pressure acting on the nacelles, and the fuselage cavity pressure.

The internal drag of the nacelles is computed using skin friction coefficients, based on the inlet Mach number from CFD calculations, obtained from Boeing Long Beach "Clutter" charts. These skin friction coefficients are calculated from flat plate theory and corrected for compressibility effects. The skin friction coefficient is applied to the wetted area of the internal duct to obtain the internal drag. This internal drag estimate is then subtracted from the measured drag.

An average base pressure is measured on one inboard nacelle and one outboard nacelle during testing. The base pressure drag due to each nacelle is computed by assuming that the average base pressure acts on the entire base area of the nacelle and is also subtracted from the measured drag.

Finally, two pressure tubes are attached to the sting and are used to measure the cavity pressure inside the aft fuselage. This pressure is applied to the base cavity area and is subtracted from the measured drag.

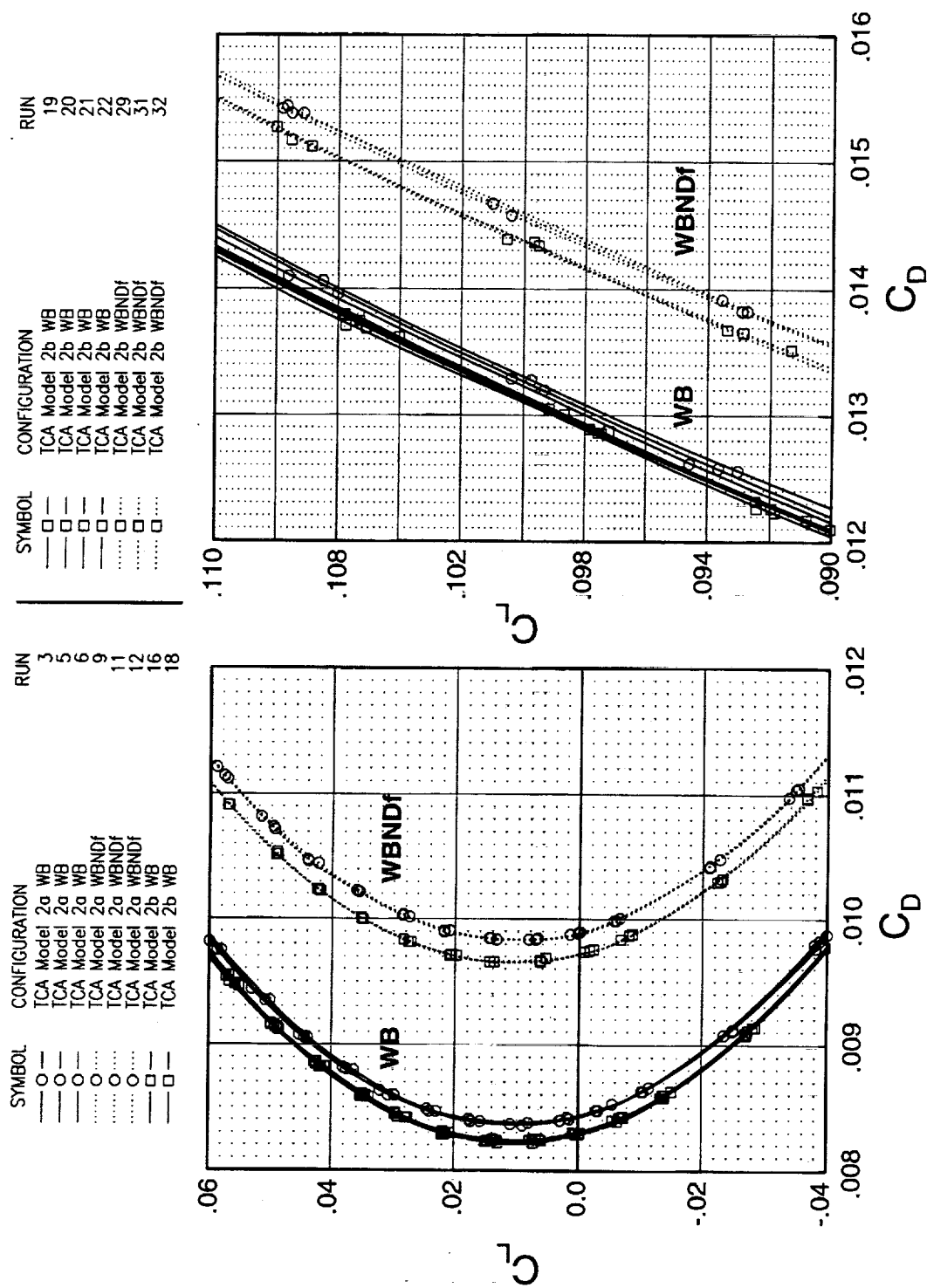
Drag Data Reduction

- Nacelle Internal Drag Correction
 - Skin friction coefficient obtained from BLB “Clutter” charts using inlet Mach number
- Nacelle Base Pressure Correction
 - Base pressure measured during testing
- Fuselage Cavity Pressure Correction
 - Cavity pressure measured during testing

Viewgraph 8: Drag Polars @ $M_\infty=2.4$

The figure on the left gives the drag polar near C_{Dmin} and the figure on the right gives the drag polar near cruise. The lift and drag for both the wing/body (W/B) and the wing/body/nacelle/diverter/fairing (WBNDf) configurations are included in the figures. The drag polars show that Model 2b has less drag than model 2a for both configurations at the two flight conditions.

Drag Polars @ $M_\infty=2.4$



Viewgraph 9: Model 2a/2b Comparison

This chart summarizes the differences in drag between the two wind tunnel models. At cruise conditions, Model 2b produces approximately 1.5 counts less drag than Model 2a for the WB configuration. The WBNDf configuration of Model 2b has about 2.0 counts less drag than that of Model 2a at cruise. The drag increment between the two models is different for the WB and WBNDf configurations because of the differences in the drag increment due to the nacelles. The nacelle increment of Model 2a is slightly greater than that of Model 2b at both C_{Dmin} and cruise as shown in the following chart. This may be a result of manufacturing differences between the two sets of nacelles.

Model 2a/2b Comparison

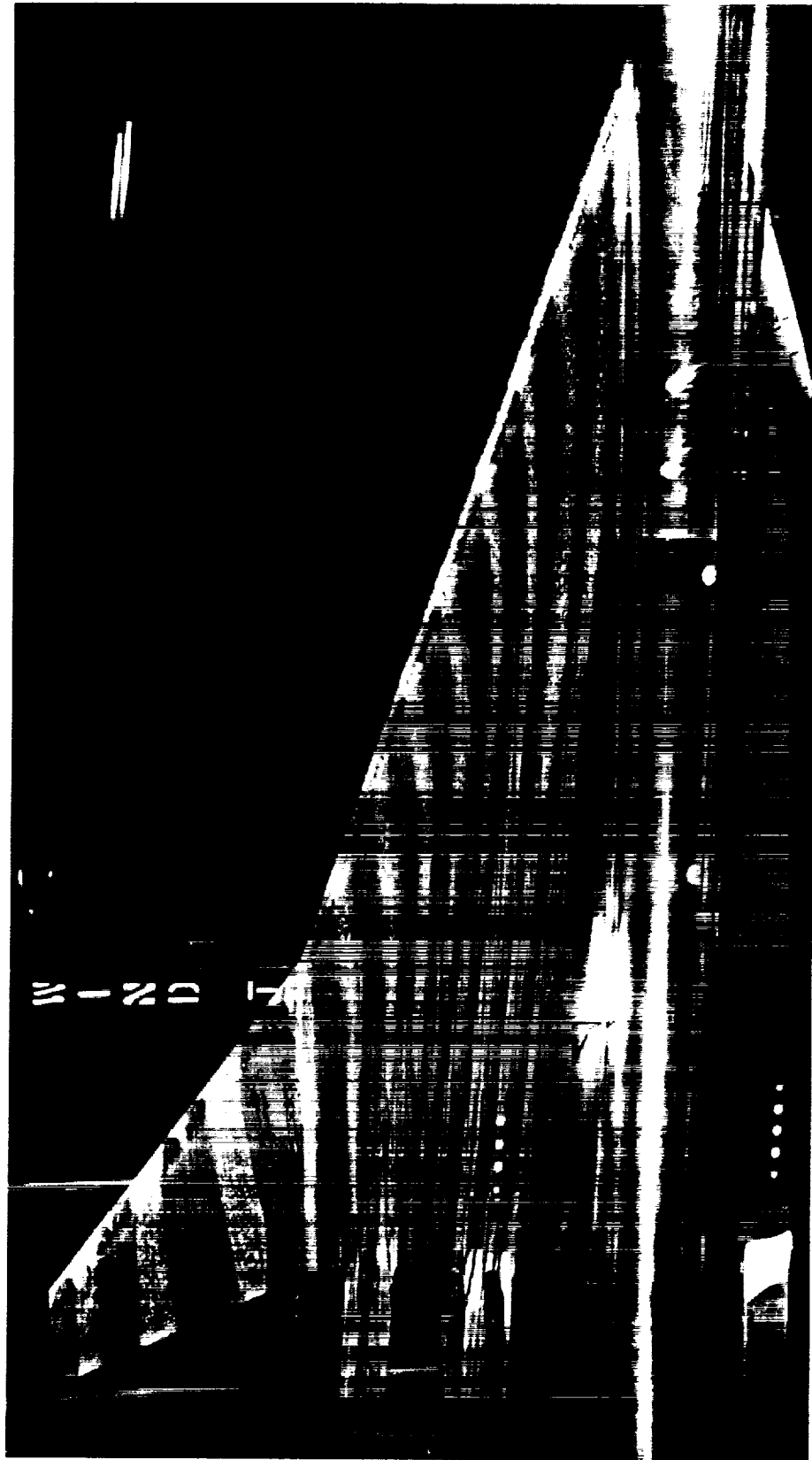
- WB $\Delta C_{\text{Dcruise}} = 1.5 \text{ cts}$
- WBNDf $\Delta C_{\text{Dcruise}} = 2.0 \text{ cts}$
- Model 2a Nacelle Increment
 - @ C_{Dmin} $\Delta C_{\text{D}} = 14.5 \text{ cts}$
 - @ C_{Dcruise} $\Delta C_{\text{D}} = 12.8 \text{ cts}$
- Model 2b Nacelle Increment
 - @ C_{Dmin} $\Delta C_{\text{D}} = 14.0 \text{ cts}$
 - @ C_{Dcruise} $\Delta C_{\text{D}} = 12.5 \text{ cts}$

Viewgraph 10: Colored Oil Flow

This photograph shows the colored oil flow on the upper surface of Model 2b at freestream Mach 2.4 and 3.5° angle-of-attack. The oil flow shows that the flow is attached and that there is only a slight amount of crossflow on the upper surface.

Colored Oil Flow

$M_\infty = 2.4$, $\alpha = 3.5^\circ$, Upper Surface

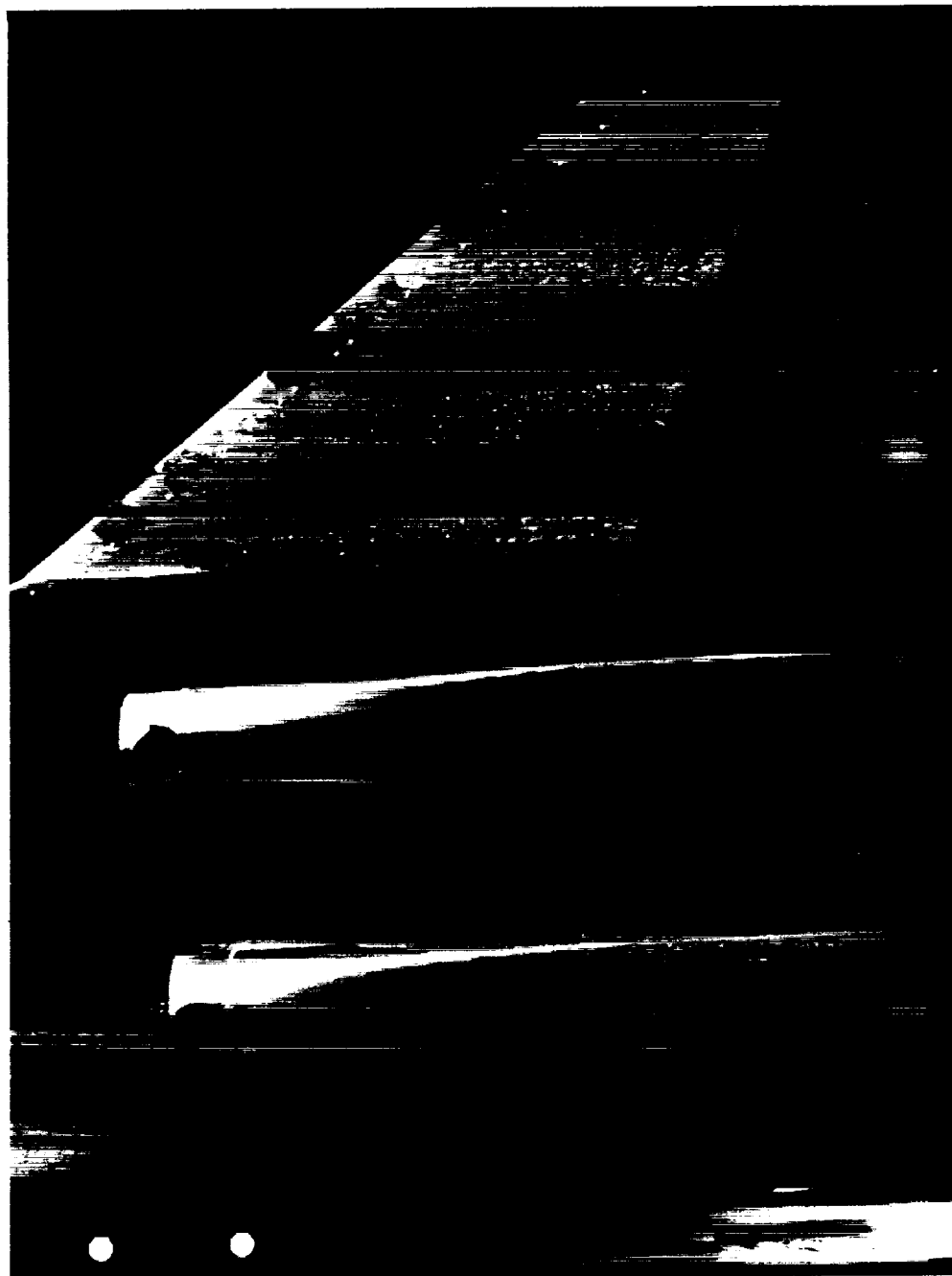


Viewgraph 11: Colored Oil Flow

This photograph shows the colored oil flow on the lower surface of Model 2b at freestream Mach 2.4 and 3.5° angle-of-attack near the nacelles. The oil flow shows that the flow is streamwise over the entire lower surface, except near the nacelles. In this region, the effects of the shock waves from the nacelle inlets on the lower surface flowfield are visible.

Colored Oil Flow

$M_{\infty} = 2.4$, $\alpha = 3.5^{\circ}$, Lower Surface



Viewgraph 12: Trip Drag Study

A trip drag study was conducted by varying the trip dot height on the wing surfaces and the nacelles. The trip dots on the nose remained fixed at a streamwise location of 1.0 inch and were 0.012 inch in height. All of the trip dots on the wing and nacelles were applied at a streamwise location equal to 0.6 inch downstream of the leading edges.

The first part of the study was conducted on the WB configuration and involved changing the trip dots on the entire wing. The following trip dot heights were tested: 0.006", 0.008", 0.010", 0.012", 0.014", 0.017". Sublimation photographs were obtained on both upper and lower surfaces for all configurations.

The second part of the study was again conducted on the WB configuration and involved changing the trip dots on the inboard upper surface only. The same trip dot heights between 0.006" and 0.014" that were used on the entire wing were also used on the inboard upper surface. The remaining wing surfaces were maintained at 0.012". Sublimation photographs were not obtained for these configurations.

Trip Drag Study

- Nose Trip Dot Height 0.012" at $x = 1.0$ "
- WB & Nacelle trip dots at $x = 0.6$ "
- WB Entire Wing Trip Heights:
 - 0.006", 0.008", 0.010", 0.012", 0.014", 0.017"
 - Sublimation obtained on all configurations
- WB Inboard Upper Wing Trip Heights:
 - 0.006", 0.008", 0.010", 0.012", 0.014"
 - Remaining wing at 0.012"

Viewgraph 13: Trip Drag Study, continued

The third part of the study used the WBNDf configuration and involved changing the trip dots on the nacelles only. The trip dots on the entire wing were maintained at 0.012". Three trip configurations were used on the nacelles—0.008", 0.012", and 0.014". Sublimation photographs were obtained on the upper and lower surfaces of the wing including the nacelles.

Various other trip configurations were also tested on the WB configuration. All trip configurations were removed from the wing in order to obtain data for free transition. In addition, 0.0127" glass beads and 0.0117" grit were each applied to the entire wing and tested to observe differences in the transition location. Finally, 0.010" trip dots applied at 0.4 inch downstream of the leading edges on the wing were tested. Sublimation photographs were obtained on all of the alternate trip configurations including free transition.

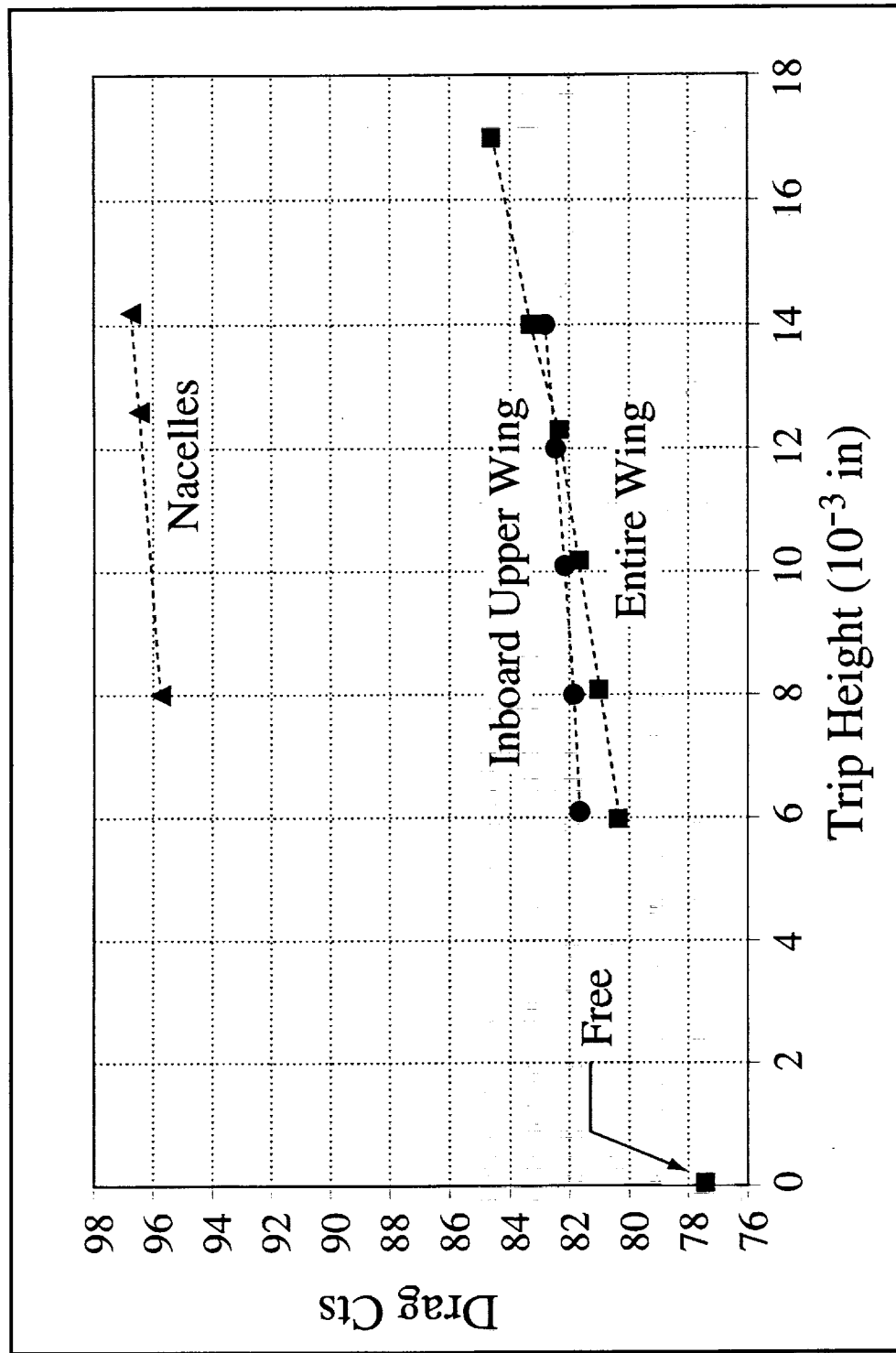
Trip Drag Study

- WBNDf Nacelle Trip Heights:
 - 0.008", 0.012", 0.014"
 - WB trip height 0.012"
- WB Other Trip Configurations:
 - Free Transition
 - 0.0127" Glass Beads at $x=0.6$ "
 - 0.0117" Grit at $x=0.6$ "
 - 0.010" Trip Dots at $x=0.4$ "

Viewgraph 14: Drag vs Trip Height @ C_{Dmin}

This plot shows the variation in the drag of the WB and WBNDf configurations as a function of the trip dot height at C_{Dmin} . The drag of the WB configuration at the free transition condition is also included in the plot. The variation in the drag of the WB configuration which has the same trip configuration applied to the entire wing is linear between trip dot heights equal to 0.006" and 0.012" and between 0.012" and 0.017", but with two different slopes. In addition, the drag of the WB configuration varies nearly linearly over the range of trip dot heights when only the inboard upper wing trip configuration is changed. For the WBNDf configuration, the drag also varies linearly with changes to the trip dot height on the nacelles.

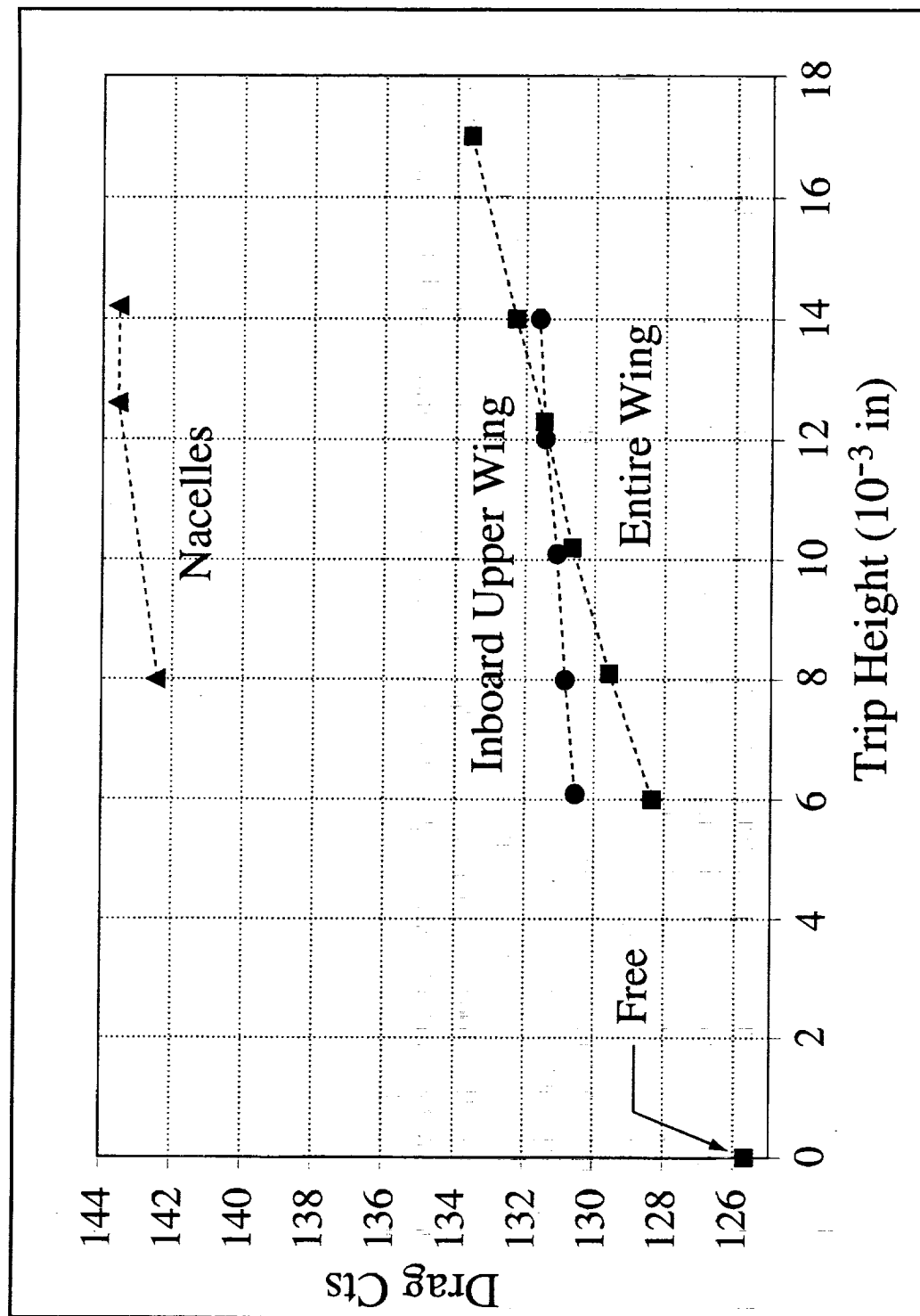
Drag vs Trip Height @ C_{Dmin}



Viewgraph 15: Drag vs Trip Height @ cruise

This plot shows the variation in the drag of the WB and WBNDf configurations as a function of the trip dot height at the cruise condition. Once again, the drag of the WB configuration at the free transition condition is also included in the plot. At cruise, the variation in drag of the WB configuration which has the same trip dot height over the entire wing is no longer linear. In addition, the drag of the WBNDf configuration does not vary linearly with a change in the trip dot configuration of the nacelles. However, the drag of the WB configuration appears to vary linearly when the trip dots are changed only on the inboard upper surface.

Drag vs Trip Height @ Cruise



Viewgraph 16: Sublimation Process

The sublimation material that was sprayed onto the upper and lower surfaces of the model consisted of a saturated solution of fluorene in ethanol, which was run through a coarse filter. The model was installed in a vertical position for the flow visualization runs in order to allow photographs to be taken during the runs. Two cameras were installed, one on each side of the test section, to capture the photographs during the sublimation process. Installation of the cameras to allow optimum visual access was impeded as a result of the steel webs that were part of the windows on each side of the test section. This also made the lighting more difficult to control which resulted in some glare on the bare spots of the model that appeared during sublimation. Once the Mach number and angle-of-attack were attained during each run, pictures were taken every 30 seconds until the majority of the fluorene had sublimed on both surfaces.

Sublimation Process

- Saturated solution of fluorene in ethanol (run through a coarse filter)
- Camera installed on each side of test section
 - Visual access impeded by webs on windows
 - Lighting difficult to control, resulting in glare
- Pictures taken every 30 sec until majority of fluorene had sublimed

Viewgraph 17: Sublimation Photo, Free Transition, Upper Surface

This photograph clearly shows the location of natural transition on the upper surface. Near the wing/body intersection, transition occurs close to the leading edge. The transition location moves further downstream of the leading edge away from the wing/body intersection. The majority of the flow in the outboard region remains laminar.

Sublimation Photo

Free Transition, Upper Surface

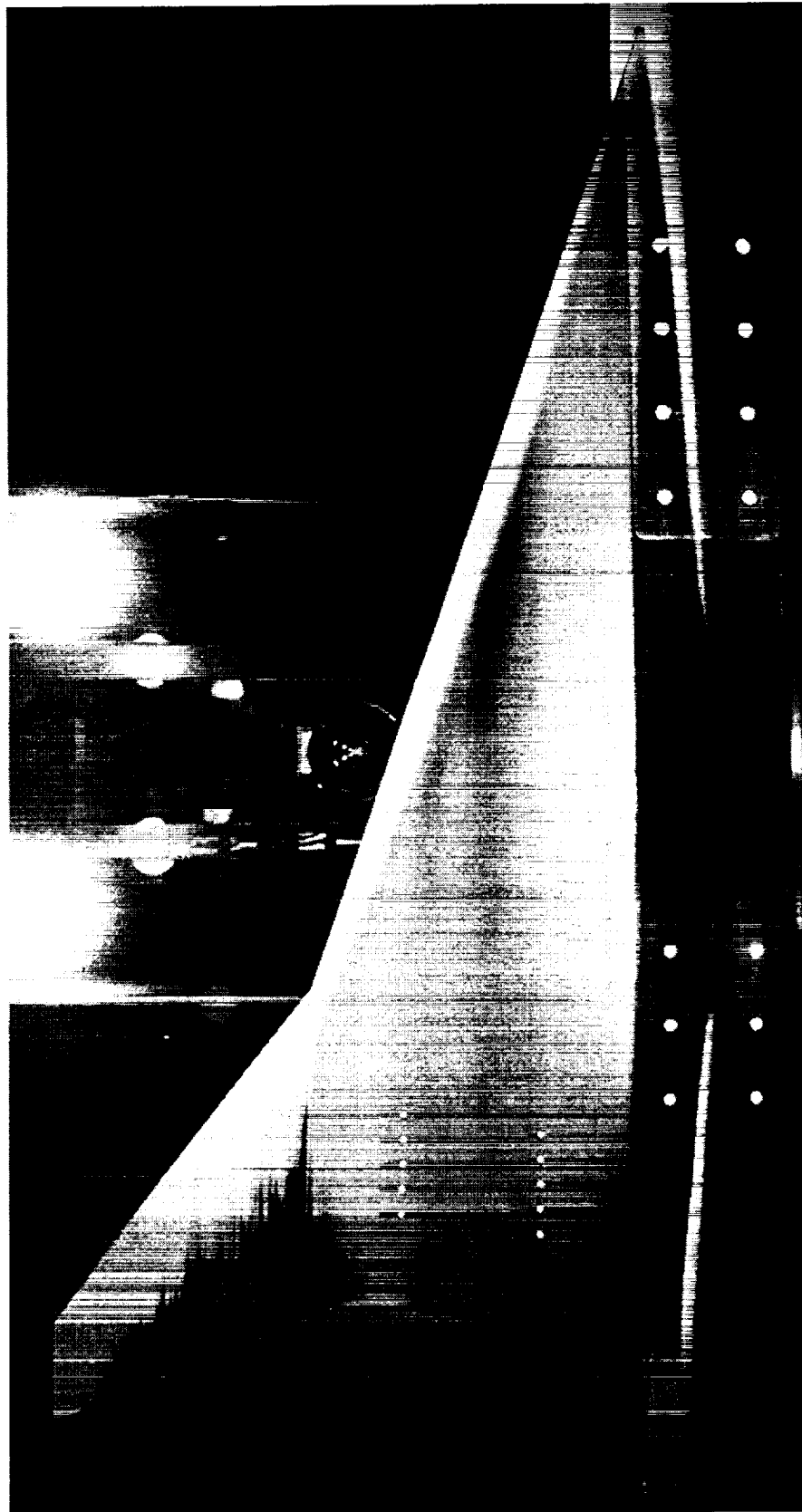


Viewgraph 18: Sublimation Photo, Free Transition, Lower Surface

On the lower surface, natural transition occurs closer to the leading edge than on the upper surface in both the inboard and outboard regions. Nevertheless, the outboard region still maintains a large portion of laminar flow.

Sublimation Photo

Free Transition, Lower Surface



Viewgraph 19: Sublimation Photo, 0.012" Trip Dot, Upper Surface

This sublimation photograph of the wing upper surface with 0.012" trip dots shows that the trip dots are not effective at tripping the flow in the inboard region, but are more effective in the outboard region away from the break in the planform.



Sublimation Photo

0.012" Trip Dot, Upper Surface

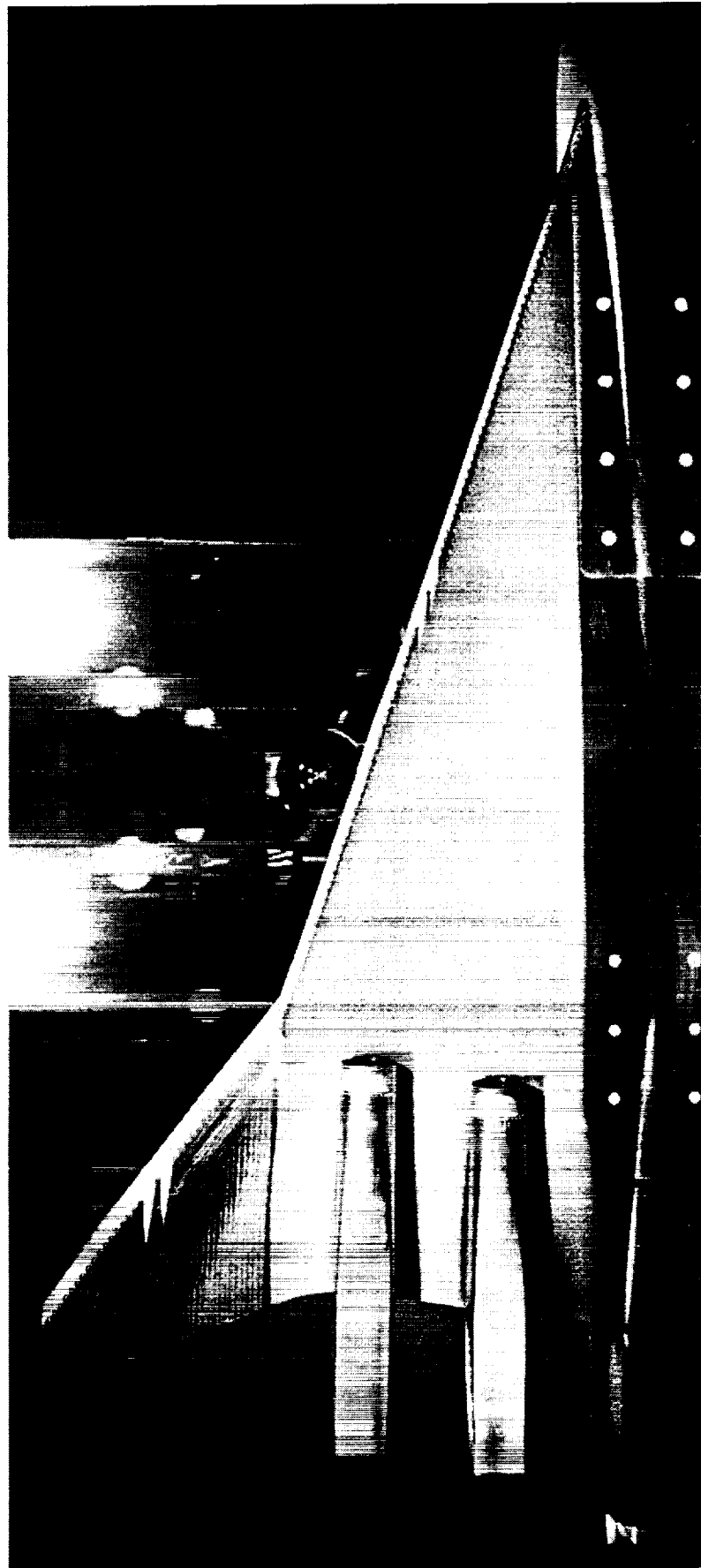


Viewgraph 20: Sublimation Photo, 0.012" Trip Dot, Lower Surface

This sublimation photograph of the lower surface of the wing shows that the 0.012" trip dots are effective at tripping the flow in both inboard and outboard regions. In addition, shock waves produced by the dots are visible in the inboard region.

Sublimation Photo

0.012" Trip Dot, Lower Surface



Viewgraph 21: Further Analysis

In order to attempt a meaningful analysis of the variation in drag with trip dot height and possibly estimate the trip drag, the data must be adjusted to reflect the longer laminar run observed on the inboard upper surface. The actual transition location for each trip dot configuration can be measured from the sublimation photographs obtained during the test. Then, a laminar flow correction can be applied to the drag data. Plotting the "corrected" drag data may produce a plateau which would allow a more accurate estimate of the trip drag as a function of trip height.

Further Analysis

- Obtain transition location from sublimation photos
- Apply laminar flow correction for each trip height
- Evaluate resulting drag curve
- Estimate trip dot drag?

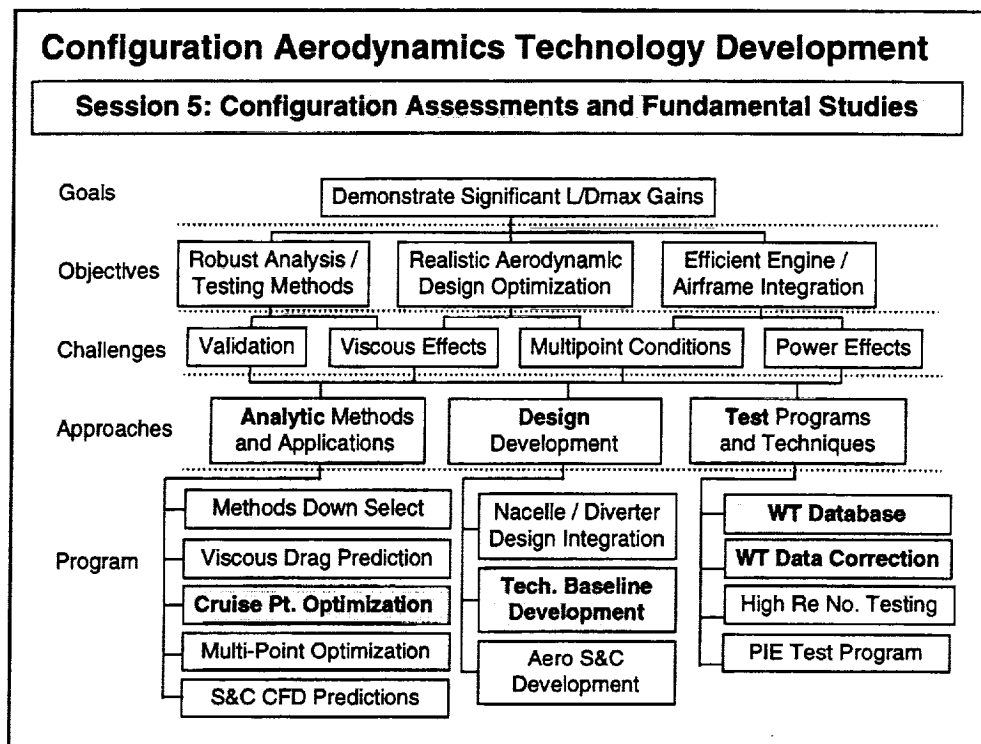
This page is intentionally left blank.

Nonlinear Cruise-pt. Validation (NCV) Model Wind Tunnel Test Summary & Posttest Analysis

Kevin M. Mejia
HSCT Aerodynamics
Boeing Commercial Airplane Group
Seattle, WA

1998 HSR Biannual Airframe Technical Review
February 9-13, 1998
Westin Hotel - Los Angeles, CA

This paper provides the transcript of one of the presentations made during the 1998 HSR Biannual Airframe Technical review on February 11, 1998. This presentation reviews the events of the UPWT 1687 wind tunnel test where the HSR Configuration Aerodynamics Nonlinear Cruise-point Validation (NCV) model was tested to validate one of three nonlinear optimization processes for drag reduction. Also covered are the results of several posttest analysis exercises conducted to understand the differences between test data and pretest predictions.



The work associated with the testing of the NCV model and the post test analysis of the results falls under the "Design Development" and "Test Programs and Techniques" approaches of the CA technology development task. With respect to cruise point optimization, this test serves to enhance the development of the technology baseline, improve the fidelity of the baseline wind tunnel database, and provide more data to aid in the proper correction of current and future wind tunnel test data. All of these activities contribute to the overall goal of Configuration Aerodynamics to "demonstrate significant L/Dmax gains."

Presentation Outline

— High Speed Aerodynamics —



- Objectives of wind tunnel test
- Test entry statistics
- Review of test findings (NCV & TCA)
 - W/B
 - W/B/N/Df
 - Alternate Trip Configurations
- Results summary
- Posttest analysis
- Future work

The following presentation will review the primary objectives of the UPWT 1687 wind tunnel entry and briefly highlight the major events of the test. Most of the presentation will be devoted to a review of the significant results of the test, both nacelles-on and off, and a discussion of alternate trip configurations required to affect a change of flow characteristic on the upper surface of the NCV wing. After a summary of the final wind tunnel results, the second segment of the presentation will review the results of post test analysis studies completed by different groups within Configuration Aerodynamics and Technology Integration which were done to help understand the test data. The last topic covered will elaborate on future work planned to better understand the NCV model and its performance.

NCV Primary Test Objectives

High Speed Aerodynamics



- Validate the W/B increment predicted by CFD at the supersonic cruise condition (wrt TCA.)
- Validate the nacelle increment predicted by CFD at the supersonic cruise condition (wrt TCA.)
- Validate the absolute drag level predicted by CFD for the NCV W/B configuration at the supersonic cruise condition.
- Validate the absolute drag improvement predicted by CFD for the NCV W/B/N/Df configuration at the supersonic cruise condition.

There were four objectives of the NCV wind tunnel test:

- 1) Validate the W/B increment predicted by CFD at the supersonic cruise condition (with respect to the TCA baseline.)
- 2) Validate the nacelle increment predicted by CFD at the supersonic cruise condition (with respect to the TCA baseline.)
- 3) Validate the absolute drag level predicted by CFD for the NCV W/B configuration at the supersonic cruise condition.
- 4) Validate the absolute drag improvement predicted by CFD for the NCV W/B/N/Df configuration at the supersonic cruise condition.

The first two objectives referred to validating the incremental drag level of the NCV configuration relative to the baseline configuration, the TCA. These were considered primary objectives as they only depended upon increments between polars acquired from the two separate models.

The last two objectives focused on using current "best" practices to correct the wind tunnel data to acquire an absolute drag value for comparison to CFD. The corrections to the test data to approximate the "fully turbulent" CFD prediction include: trip drag, laminar run, nacelle internal forces, and nacelle internal skin friction.

NCV Wind Tunnel Test Statistics

High Speed Aerodynamics

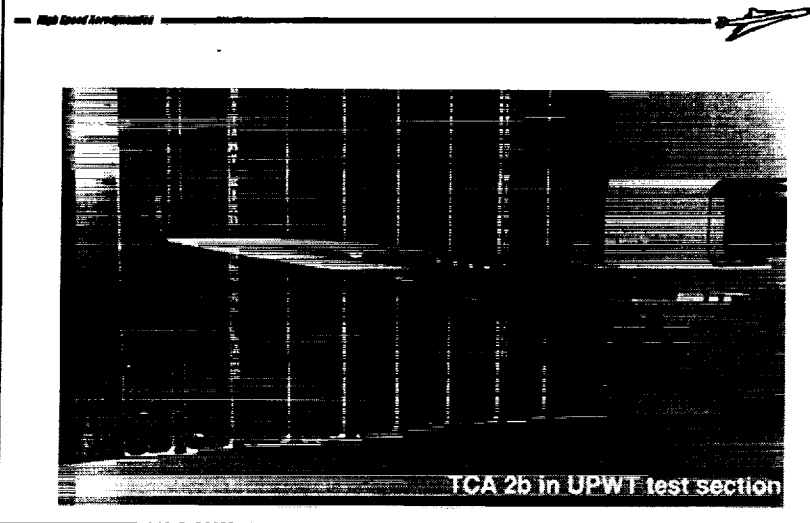


- Test facility: Langley UPWT (test #1687)
- Test duration: Sept. 15 - Oct. 1, 1997
- 55 runs in 130 hrs. of occupancy
 - 2 models, 3 installations, 7 configurations
 - $M = 2.40$, $Re = 4M/ft$, forces & flow visualization
- Test support:
 - HSR Lead Aero Organization**
 - Boeing Aero: Kevin Mejia
 - Boeing Aero: Jeremy Walker
 - Boeing Aero: Chris Vegter
 - Boeing Data Eng: Mark Hansen
 - HSR Lead Test Organization**
 - LaRC Test Eng: Dave Tuttle
 - HSR Test Support**
 - ARC: Mina Cappuccio

The NCV model was tested at the Langley Unitary Plan Wind Tunnel (UPWT) in test section 2. Test number 1687 was run from September 15th through October 1st, 1997 on and extended 1 shift/day operation. 55 valid data runs were completed in 130 hours of occupancy for an average run rate of 0.42 runs/hour. In that time period both the NCV and the baseline Technology Concept Airplane (TCA) models were tested in a total of 7 different configurations. Three separate model installations were required during the test resulting from the need to retest the TCA baseline with an alternate trip configuration.

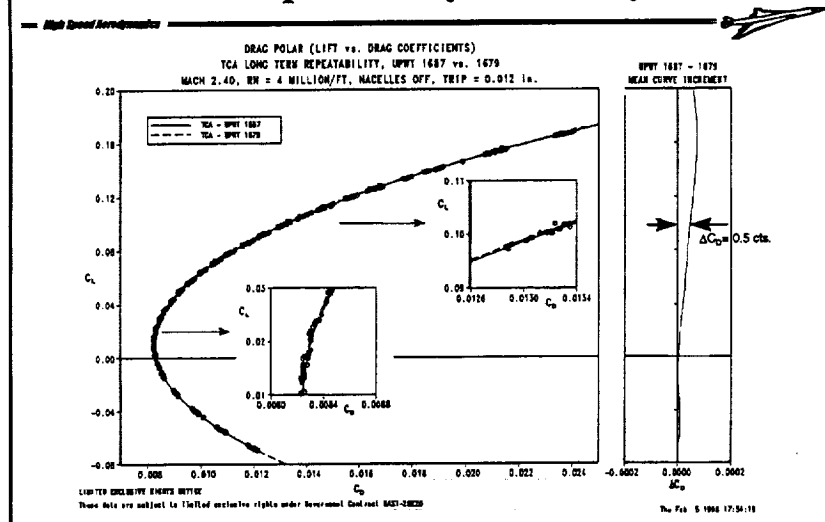
The test condition of prime interest for the majority of the test was Mach 2.40, a Reynolds number of 4×10^6 , and a cruise $C_L = 0.10$. Both force and flow visualization data were acquired throughout the test. Fluorine sublimation and colored oil flow visualization techniques were used to help diagnose and understand the differences between the TCA and NCV models. For this test Boeing, Seattle was the lead aerodynamics organization, LaRC was the lead testing organization, and additional aerodynamics support was supplied by NASA Ames.

Baseline TCA 2b Results (Calibration Model)



Above is a picture of the TCA baseline model as installed in the UPWT test section. The following discussion will focus on the quality and repeatability of the baseline data from the TCA 2b "clean wing" model from which W/B and nacelle increments will be calculated.

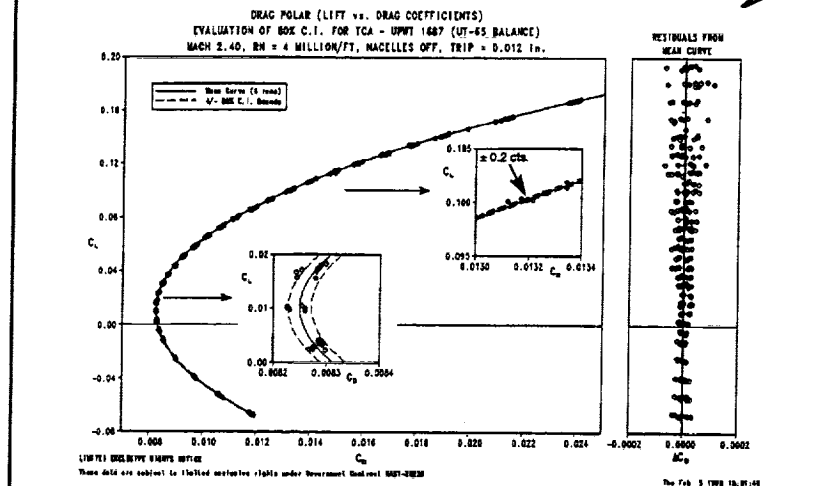
Test to Test Repeatability Was Very Good



One method of evaluating data quality and the accuracy of the reduction equations is to compare the current data to that taken on past tests. The above graph presents a comparison of tests 1679 and 1687, both conducted at the Unitary tunnel using TCA model 2b with nacelles-off. Configuration aerodynamics has an informal goal of matching test-to-test data repeatability to within 0.5 drag counts. The above comparison indicates that the goal has been met, at least over the C_L range of interest (0.0 to 0.10.) Current test data only slightly violates the goal for C_L 's above 0.12.

Although not shown in this presentation, the nacelles-on TCA data shows similar trends in test to test data quality. Over the C_L range of interest (0.0 to 0.10) current test data repeats to within 0.8 cts. and differs from the past test data by a maximum of 1.10 cts. Although some of the above results violate the data quality goal set, some test to test variations in absolute results are expected and for this test where incremental values are most important, the above checks indicate that there are no serious issues with model installation or data reduction.

Confidence Interval Was Within Tolerance

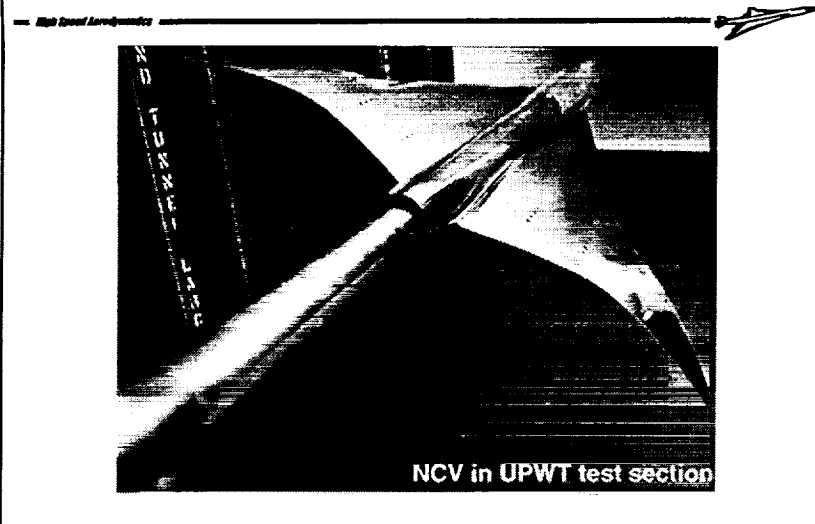


Another method of evaluating wind tunnel test data is to calculate the confidence interval of the drag polar. A second informal data quality goal of the configuration aerodynamics group requires that all data acquired for incremental testing fall within a ± 0.50 drag count tolerance band at 80% confidence. As shown above, the nacelles-off confidence interval is quite tight at ± 0.20 cts. and meets this goal easily. This tight tolerance band about the data is primarily due to the low scatter in the acquired data. Note that the maximum scatter for the nine runs included in this plot is at maximum ± 1.0 cts.

Not included in the above graph are the results for the TCA nacelles-on data. Demonstrating trends very similar to those shown above, the 80% confidence interval was calculated to be ± 0.40 cts. with a maximum scatter in the residual data of ± 1.5 cts. for a total of six runs.

Evaluation of the baseline data showed that the quality was very good and could be used as the baseline values from which the NCV performance increments could be calculated.

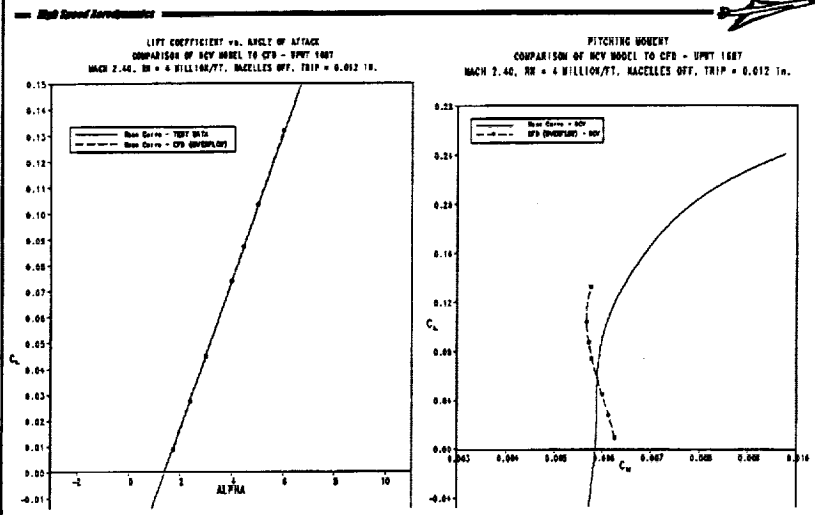
NCV Results (Nacelles-off)



Above is a picture of the NCV optimized model as installed in the UPWT test section without nacelles. Note the “bumps” on the wing near the leading edge and the gull of the outboard wing tips.

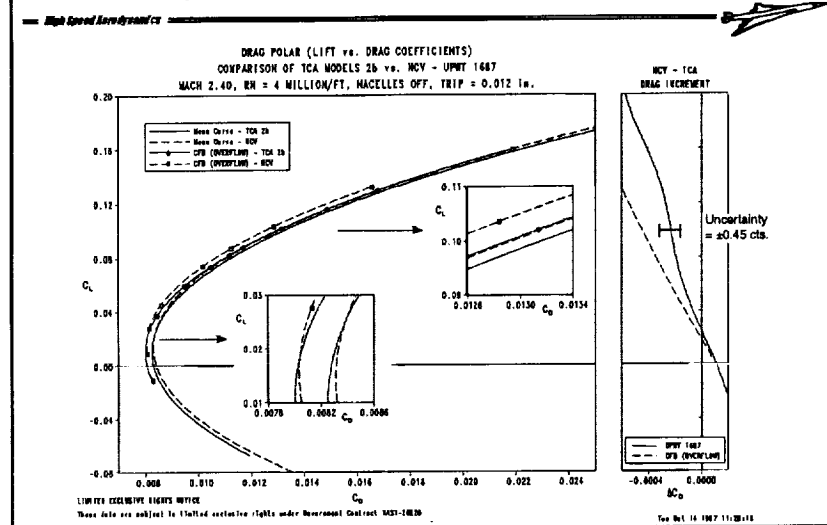
The following discussion will focus on the aerodynamic performance of the NCV model and its comparison to the TCA baseline.

Lift & Pitching Moment Results-Test vs. CFD



The figures above present NCV test data comparisons to CFD pretest predictions for both lift and pitching moment coefficients. Test to theory lift coefficient comparisons are excellent and fall right on top of each other. Pitching moment coefficient comparisons are not as good. Although the moment levels compare well, the characteristics of the two curves do not. It appears that the average slope of the test data indicates that the model is more unstable than predicted by OVERFLOW. Also, the point at which both curves cross the zero lift axis suggests that the NCV would require less tail upload than the CFD prediction which means that the configuration would have slightly more drag in trim.

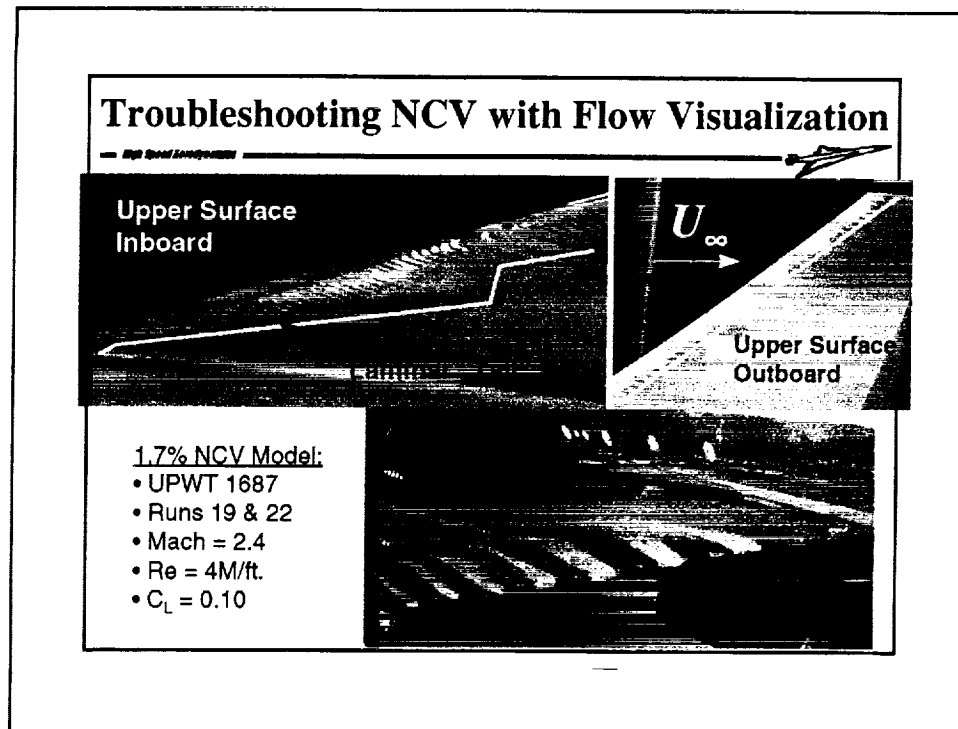
W/B Drag Reduction Less Than Expected



Nacelles-off test (solid) and CFD (dashed) data is presented above. Subtracting NCV wind tunnel data from TCA data shows that at the cruise point, the NCV is 2.3 counts lower drag than the TCA. Pretest CFD calculations predicted that the NCV would be 4.5 counts lower; as denoted by the dashed increment line.

The uncertainty in the calculated increment between experimental polars is only ± 0.45 cts. Because the experimental uncertainty is lower than the calculated increments, the data are considered statistically valid.

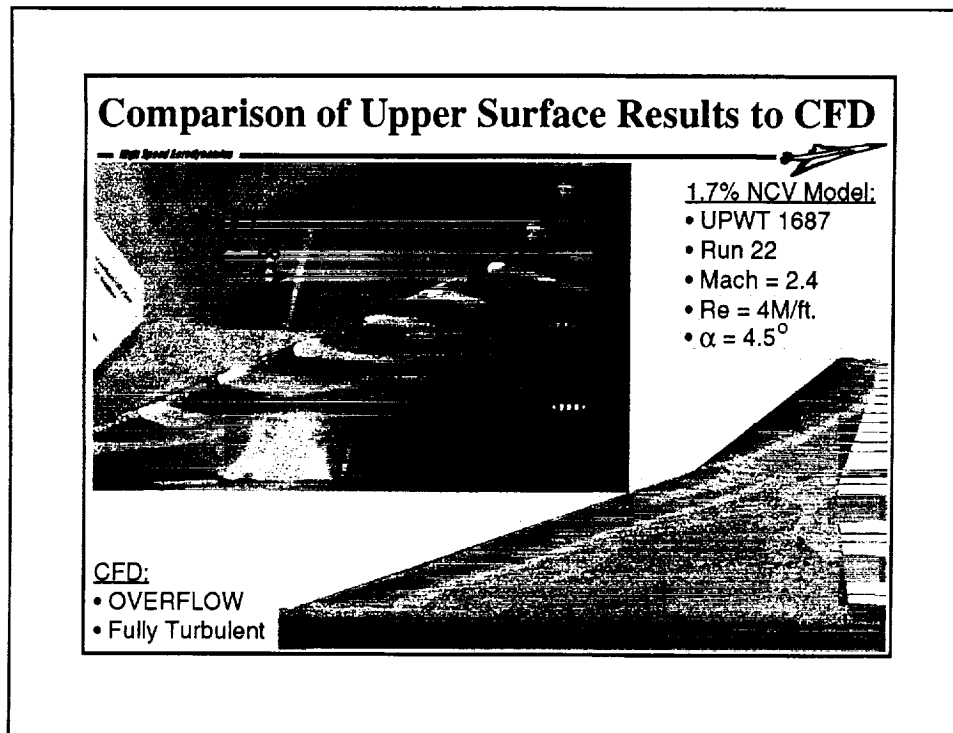
Although not presented above, the NCV with nacelles-off was shown to have only slightly worse data quality compared to the TCA wing/body configuration. It's 80% confidence interval was calculated to be ± 0.40 cts. This slightly larger confidence boundary was due primarily to a larger scatter in drag data for C_L 's greater than 0.12. The scatter at these higher C_L 's was found to be as large as ± 2.0 cts. No explanation was found for this increased scatter.



Given that the wing/body drag increments were approximately 2 cts. less than expected, several flow visualization runs were conducted on the NCV model. It was hoped that if there were any unusual flow characteristics which could be responsible for the performance shortfall, they might be seen.

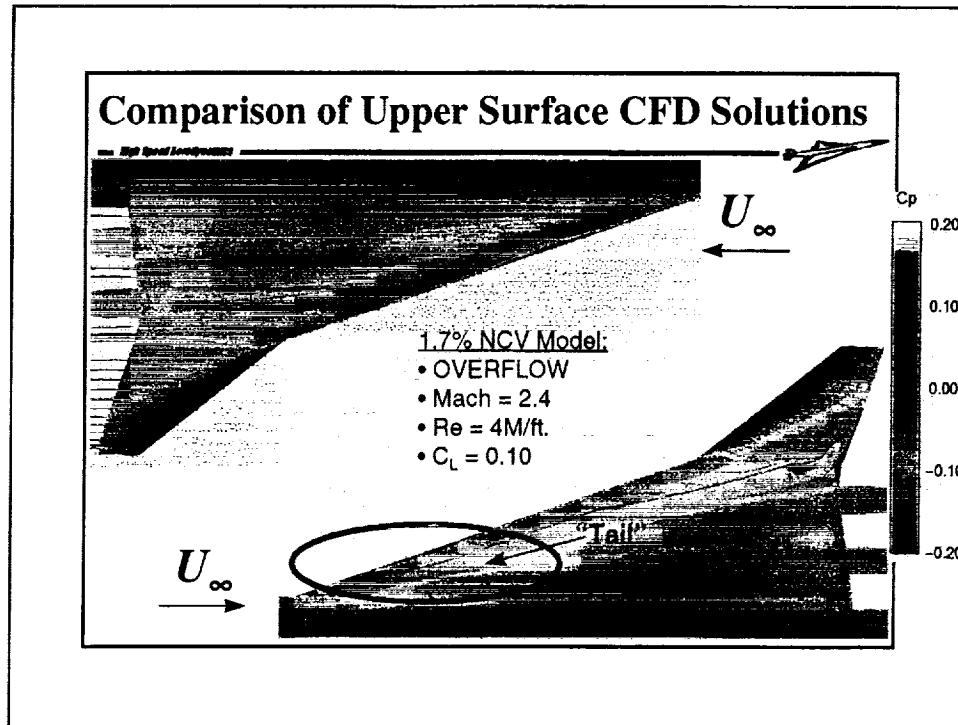
The sublimation run appeared to indicate that for the baseline trip configuration (height = 0.012 in, spacing = 0.20 in, location = 0.6 in streamwise,) the trips were not as effective as they had been on the TCA model. The upper surface, inboard wing segment showed signs of a laminar separation line. There were also signs, on both the inboard and outboard wing segments, that there was more laminar flow present than on the TCA. Neither of these two flow patterns had ever been seen before on previous models.

Colored oil flow visualization runs showed a distinct spanwise flow pattern which was most visible on the inboard half of the wing. The flow at the leading edge of the wing appeared to experience significant spanwise turning which effected the flow streamlines downstream. The outboard supersonic panel also appeared to be affected somewhat by this spanwise turning.



Comparison of the colored oil flow visualization results to the CFD predicted flow patterns further illustrate the flow characteristics previously stated. Below the experimental image is a combination color pressure contour and particle streamline trace graphic from the OVERFLOW force calculation. Comparison of the two images show that streamlines on the wind tunnel model appear to travel farther spanwise than seen on the CFD calculations. Note how streamlines emanating from near the side of body flow well outboard of the inboard nacelle mounting screw holes.

Some insight into possible causes for the flow pattern seen on the NCV model can be gained by observing the interactions between the particle traces and the pressure coefficient distribution of the CFD solution. One can see that near regions of strong negative pressure gradients (green region), the streamlines remain approximately perpendicular to the leading edge. The sharp turning of the streamlines into the streamwise direction occurs only when the flow encounters a higher (less favorable) pressure gradient.



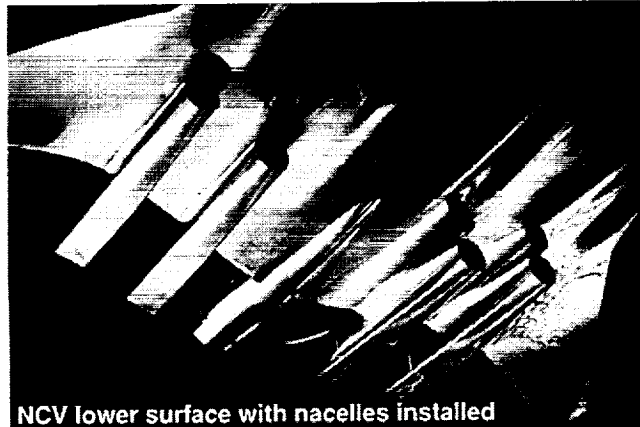
Because the NCV drag performance shortfall was suspected to be related to excessive runs of laminar flow near the wing leading edge, an additional OVERFLOW case was run during the test with a completely laminar boundary layer, starting from the leading edge. Note that the pretest predictions were fully turbulent solutions.

As hoped, the fully laminar solution showed some similar characteristics as the NCV model. The most notable similarity was the tendency of the streamlines to follow along the wing leading edge. A second similarity was the location and length of the "laminar tail" previously seen in the sublimation run. The last significant comparison that can be made between the two solutions is the strength and distribution of the upper surface pressure gradients. Although the turbulent solution appears to have more leading edge suction (as denoted by a lower local pressure coefficient,) the addition of a low C_p 's and a weaker boundary layer appear to combine into a more disruptive flow pattern.

It appeared that the flow witnessed on the NCV model was some sort of hybrid of a laminar and turbulent boundary layer condition.

NCV Results (Nacelles-on)

High Speed Aerodynamics

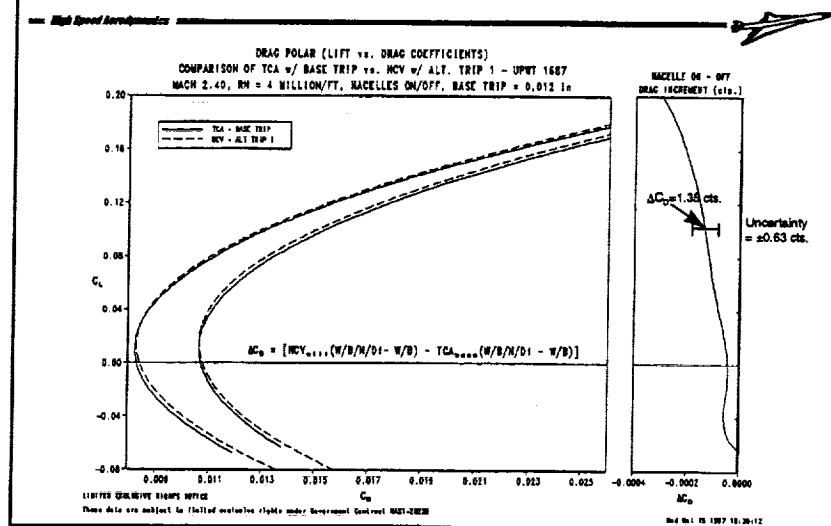


NCV lower surface with nacelles installed

Above is a picture of the NCV optimized model wing lower surface with the baseline axisymmetric nacelles mounted. Note the high quality finish of the model and the "contoured" surface of the wing ahead of the nacelle inlets.

The following discussion will focus on the aerodynamic performance of the NCV model with nacelles-on and its comparison to the TCA baseline.

Nacelles-on Increment Matched Predictions



To calculate the nacelles-on drag improvement increment, differences between TCA and NCV nacelles-on and nacelles-off polars were calculated and then those increments were differenced to arrive at the final NCV performance increment (with respect to the baseline TCA.) At the cruise point evaluation condition of $C_L=0.10$ the NCV with nacelles-on was 1.35 counts lower drag than the TCA. OVERFLOW pretest predictions had anticipated a drag benefit of 1.70 cts. Because this value required a difference between two increments, it is prone to a larger than desired uncertainty value. In this case the uncertainty at 80% confidence is ± 0.63 cts. Because the increment is greater than the uncertainty in the data, the result statistically valid. Taking this fact into account, it can be said that the nacelle increment as predicted by CFD was validated.

Although not presented above, the NCV with nacelles-on was shown to have better data quality compared to the TCA wing/body configuration. Its 80% confidence interval was calculated to be ± 0.20 cts. This smaller confidence boundary was due primarily to a reduced scatter in drag data for C_L 's greater than 0.12 than seen on the TCA.

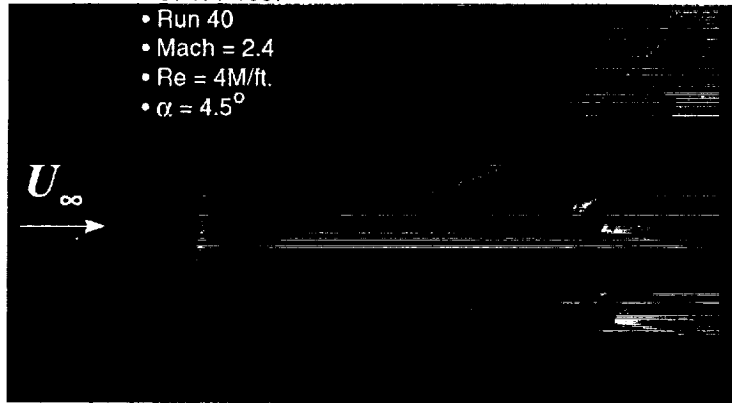
Lift curve slope and pitching moment comparisons between test and CFD data sets was found to have identical characteristics as the NCV wing/body example presented earlier in the presentation.

Nacelles-on Colored Oil Flow Visualization

High Speed Aerodynamics

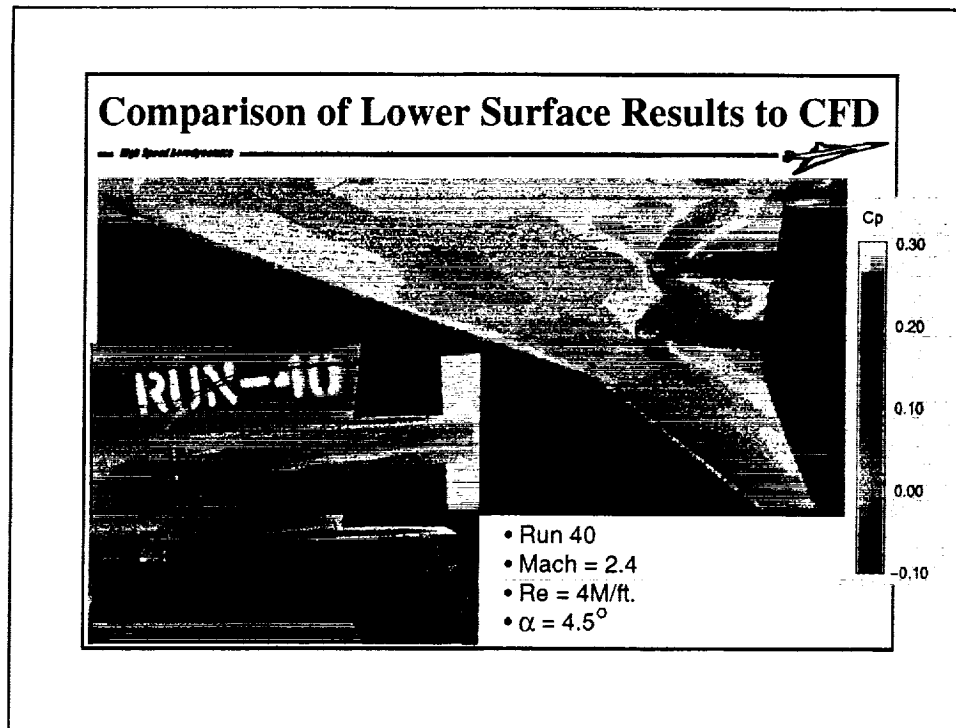
1.7% NCV Model:

- UPWT 1687
- Run 40
- Mach = 2.4
- Re = 4M/ft.
- $\alpha = 4.5^\circ$



A colored oil flow visualization run was made to document the streamline patterns of the wing lower surface with nacelles installed. The flow pattern appeared very well behaved with no notable flow peculiarities.

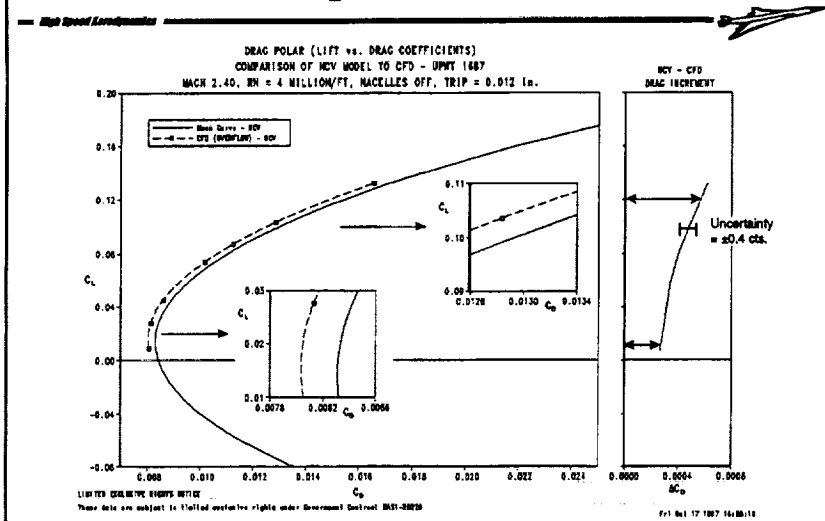
Comparison to wing streamlines as calculated by CFD showed very good agreement (see next page.)



A closer look at the colored oil results near the region around the nacelles shows a very favorable comparison to CFD predictions. Bow shocks caused by the nacelle diverters appear to follow the same path as the CFD results and they seem to coalesce in the same spanwise locations. Although no flow patterns for the external surfaces of the nacelles themselves were calculated, the experimental results indicate that the flow field is benign and well behaved.

Based on experimental force and flow visualization results, nacelle incremental drag benefits as designed into the NCV configuration by the TRANAIR nonlinear optimizer and verified by the OVERFLOW Navier-Stokes code have been validated.


Test vs. CFD Comparison Guided W/B Studies



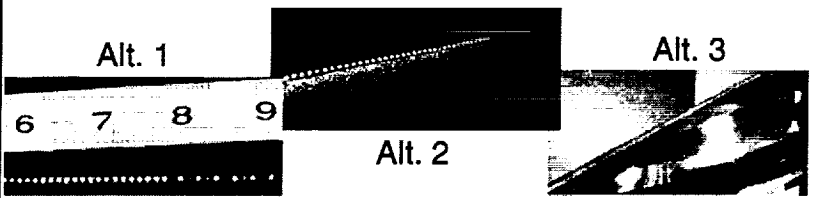
Once the nacelles-on increment for the NCV was validated, work returned to understanding the wing/body results and devising possible experiments which could remedy the performance shortfall. Comparison of the CFD solution to the test data showed that the experimental polar was more "closed" than predicted, as evidenced by differencing the two curves.

The reduced drag benefit as lift coefficient increased was identified as the target of subsequent work for the remainder of the test. Based on the experimental and theoretical data seen up to that point, all indications were that the spanwise flow seen on the wing was caused by excessive laminar flow on the wing. It was hypothesized that if the laminar flow at the leading edge of the wing were eliminated, more streamwise flow would cause the wing to operate as designed and allow it to achieve its performance benefit.

3 Alternate Trip Configurations Were Tested

— *High Speed Aerodynamics* — 

Configuration	Height (in.)	Spacing (in.)	Location (Streamwise, in.)	Grit
Baseline	0.012	0.2	0.6	NA
Alt. 1	0.012/0.0144	0.2/0.1	0.6	NA
Alt. 2	0.012/0.0144	0.2/0.1	0.6/0.0	80
Alt. 3	0.012/0.0144	0.2/0.1	0.6/0.0	50



To trip the leading edge laminar boundary layer, three alternate trip configurations were attempted on the upper surface of the wing. The goal was to affect a change in the force polar by transitioning the boundary layer to fully turbulent from the highlight of the wing leading edge. Details of the baseline and alternate trip configurations are presented above. Alternate trips one and two were only applied to the inboard seven inches of the inboard wing. Alternate three was applied to the entire inboard wing leading edge. Trips two and three extended from the wing highlight, around the leading edge, to the baseline trip dots. The baseline upper and lower surface trips were included as the basis of all three alternate grit configurations.

The effects of alternate trips-one showed up in the drag polar as an increased drag of +0.4 cts. at the cruise point and had no effect at C_{Dmin} . It had no significant effect on the wing streamlines. Alternate trips two and three, utilizing distributed grit, affected a change in the wing streamlines with trip three being the most successful. Alternate two decreased the drag at the cruise point by 0.4 cts. relative to alternate one yielding a net benefit of 0.0 cts.; rats!

Radical Trip Req'd to Fully Transition Flow

High Speed Aerodynamics

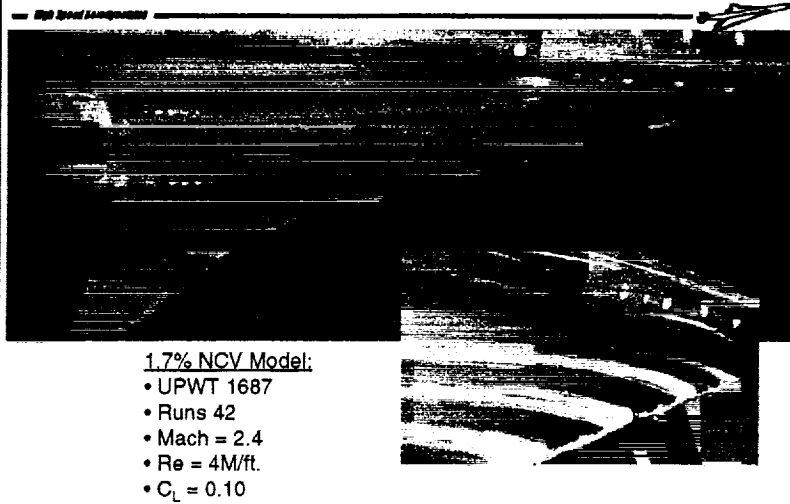


NCV with alt. trip 3 applied to IB wing

Above is a picture of the alternate trip configuration three as applied to the NCV optimized model upper surface. Configuration three was 50 grit applied along the entire inboard wing leading edge, from the leading edge highlight to the baseline trip location on the upper surface.

The following discussion will review the aerodynamic performance of the NCV model with alternate trips.

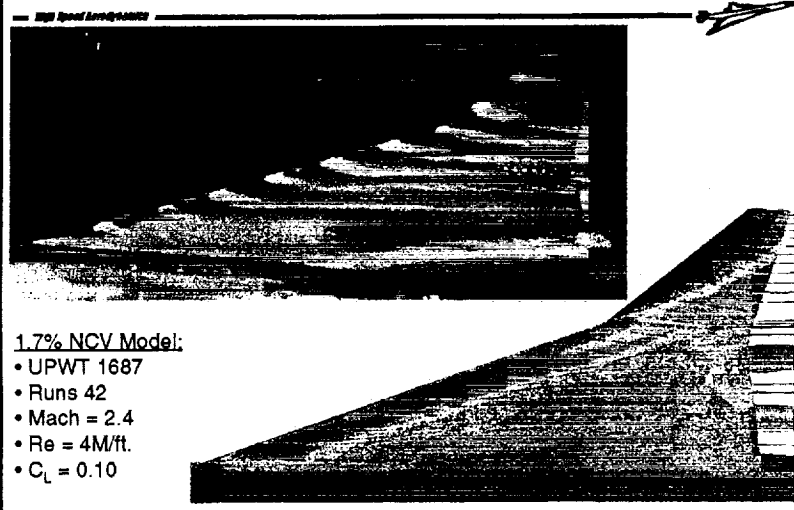
Colored Oil to Evaluate Trip 3 Effectiveness



The effects of alternate trip three on the NCV model streamlines are presented above. It is very easy to see the result of fully transitioned flow starting at the leading edge. There is very little spanwise turning of the flow especially near the inboard wing leading edge.

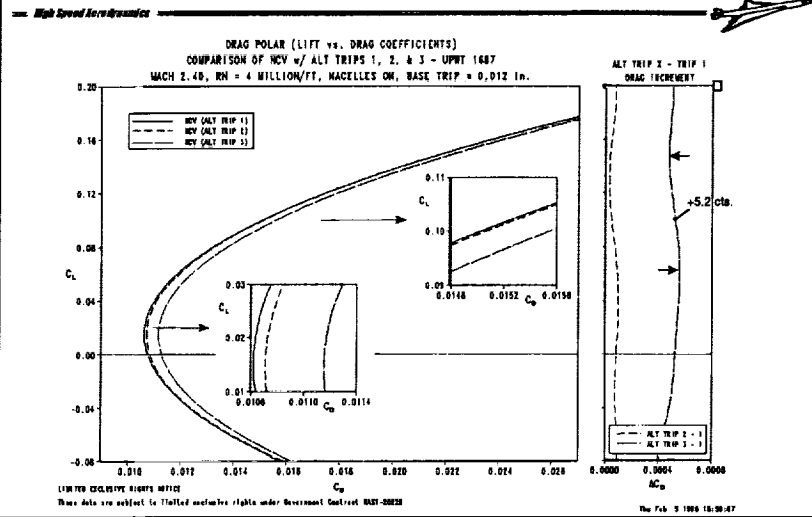
Sublimation images of alternate trip three showed no signs of any laminar flow beyond the baseline row of trips. The heavy grit also removed any signs of the laminar "tail" seen in sublimation images taken earlier in the test with only the baseline trips applied. Because of the benign nature of the sublimation images, they are omitted from the presentation for the sake of brevity.

Comparison to Overflow Streak Lines



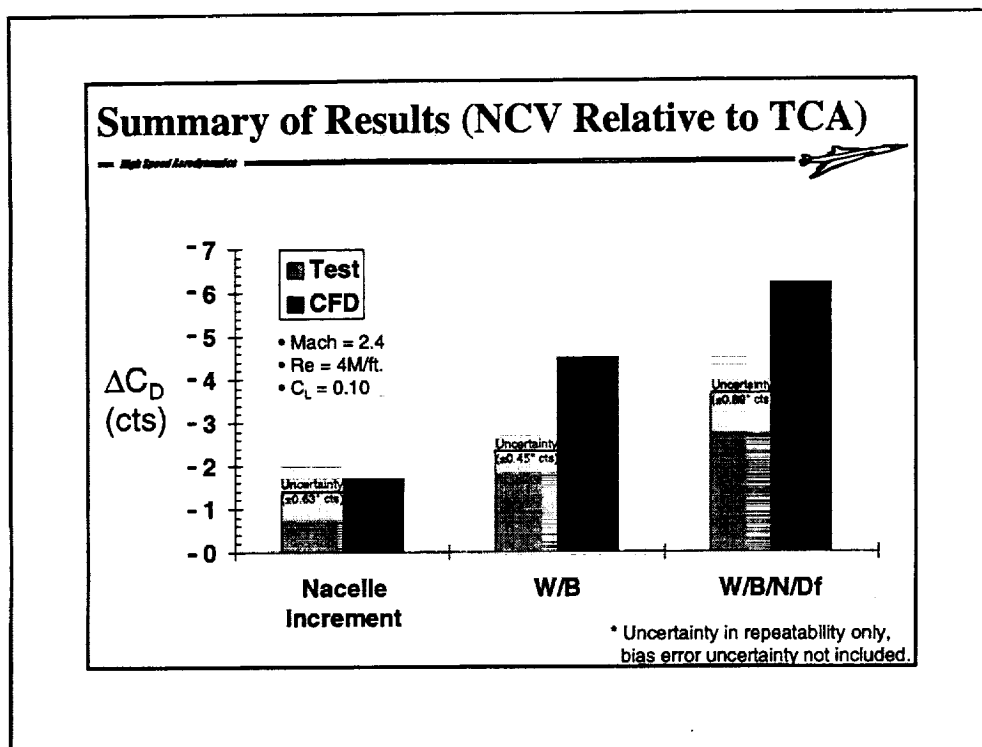
Comparison of the experimental flow visualization results to CFD calculations show that with a fully turbulent boundary layer, the NCV model flow pattern matches predictions exactly. Evidence of radical flow turning near the leading edge is no longer visible.

Alt. Trips Only Slightly Affected Polar Shape



Although the wing streamlines match CFD calculated particle traces with alternate trip three applied, force characteristics did not improve. It was hoped that by applying trips the shape of the polar could be affected, even if a penalty were incurred due to the additional drag of the trips. Like alternate two, trip three affected the polar shape slightly, but it was insufficient to have a significant effect on the NCV wing/body performance increment.

None of the alternate trip configurations had any significant effect on lift or pitching moment results when compared to the baseline NCV trip configuration.



After alternate trip three was attempted with no significant improvement in wing/body results, additional runs were completed to assess trip configuration three effects and short term repeatability on the TCA baseline.

The final results of UPWT 1687 are presented above. As shown earlier, the NCV nacelle increment of -1.35 counts validated CFD calculations (-1.7 cts.) to within the uncertainty of the experiment. NCV wing/body fell short of predictions with only a 2.3 count improvement over the TCA instead of the expected 4.5 drag count benefit. Summing up the total performance improvement for the NCV configuration with nacelles-on, a net 3.65 count improvement was realized over the baseline TCA; a 2.55 count shortfall from the pretest OVERFLOW prediction of 6.2 cts.

NCV Test - Final Observations

- NCV nacelles-on vs. nacelles-off drag increment has been validated (to within experimental C.I.)
- NCV vs. TCA W/B drag improvement was not verified in the wind tunnel.
- Repeatability in LaRC Unitary wind tunnel is good.
 - Test to test = 0.5 to 0.8 cts.
 - Within test = +/- 0.2 to 0.4 cts @80% CI.
- Pressure gradient, laminar flow, trip disks, trip location, and Reynolds number are all possible causes of the NCV performance shortfall.
- NCV successful in highlighting unresolved issues.

As stated earlier, the predicted nacelles-on drag improvement for the NCV configuration was verified in the wind tunnel; to within the experimental accuracy's of the wind tunnel experiment.

The wing/body only drag improvement was not validated in the wind tunnel. Only half of the predicted drag improvement, when compared to the baseline TCA, was realized.

The test data acquired at the Langley Unitary wind tunnel during this test was of very good quality. The test to test repeatability was found to be within 0.5 counts for wing/body only and within 0.8 counts when nacelles were added to the configuration. Within test repeatability was equally good with wing/body runs repeating to within +/-0.2 counts and nacelles-on data repeating to +/- 0.4 counts; both to an 80% confidence interval based on the full drag polar.

After considering all of the information available by the completion of the test, the following factors were prime suspects in the NCV performance shortfall: pressure gradient, laminar flow, trip disks, trip location, and low Reynolds number.

Although the NCV configuration did not meet its expected performance goals, it did serve to bring into the spotlight several unresolved issues in configuration aerodynamics wind tunnel testing. Issues such as: trip drag, laminar run corrections, trip location, and nacelle internal skin friction corrections all need to be addressed in the immediate future in order to improve the fidelity of test to theory comparisons.

Posttest Analysis Results - NCV Summit

High Speed Aerodynamics



- NCV performance workshop held at NASA Ames
 - Laminar NS boundary layer results were puzzling
 - Did we miss something on the forebody?
- Developed a 6 month plan to address NCV prime suspects; trip and transition
 - High Reynolds number test of NCV in BSWT
 - Flow field diagnostics of NCV in UPWT
 - CFD analysis with more representative WT conditions
 - Trip configuration study
 - Boundary layer stability analysis at WT conditions

Shortly after the NCV wind tunnel test was completed, a second CA testing workshop was convened at NASA Ames. The purpose of the November 4-5, 1997 meeting was to review the results of UPWT 1687 and other posttest analysis done on the NCV, then to develop a plan to address the unresolved wind tunnel testing issues highlighted by the NCV test.

Of the topics reviewed during the workshop, additional NS solutions on the NCV configuration with varying runs of laminar and turbulent boundary layers showed peculiar results. It was also noted that the NCV forebody could have a significant effect on the wing, yet little work had been done on understanding its effects.

After 1½ days of discussions, a plan was developed by the workshop attendees to address trip and transition at wind tunnel Reynolds numbers; the most important testing issue requiring immediate attention. The plan only covered the next 6 months, as the results of the early experiments would help guide future studies. The major activities are to include:

High Reynolds number test of NCV in BSWT- to check if a fully turbulent boundary layer at higher Reynolds numbers will effect performance results.

Flow field diagnostics of NCV in UPWT- to help further understand what flow field phenomena could be responsible for the NCV results.

CFD analysis with more representative WT conditions- solutions modeled with boundary layer transition locations as seen in the wind tunnel.

Trip configuration study- alternate trip disk densities and placements.

Boundary layer stability analysis at WT conditions- to help understand what are the major contributors to boundary layer instabilities at WT conditions.

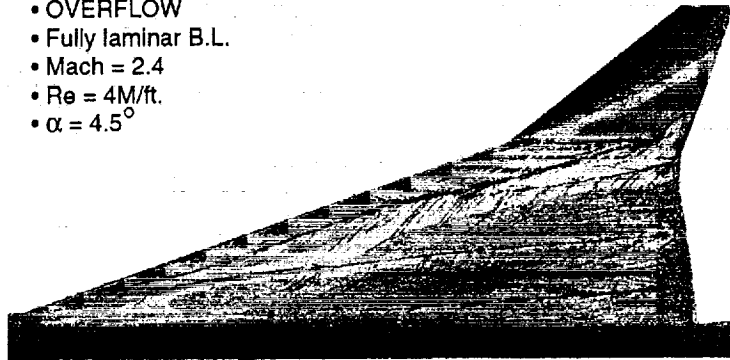
OVERFLOW Solution with Laminar B.L.

High Speed Aerodynamics



1.7% NCV Model:

- OVERFLOW
- Fully laminar B.L.
- Mach = 2.4
- Re = 4M/ft.
- $\alpha = 4.5^\circ$



During the 2nd testing workshop, results were presented showing CFD results with different combinations of laminar and turbulent boundary layer conditions, as well as alternate transition locations. The sum of the results showed that even though the different solutions calculated significantly different streamline patterns than the baseline turbulent solutions, wing pressure drag only changed by 0 to 1 drag counts. Based on these results, one might conclude that the laminar flow on the wing is not the prime source of the NCV performance shortfall.

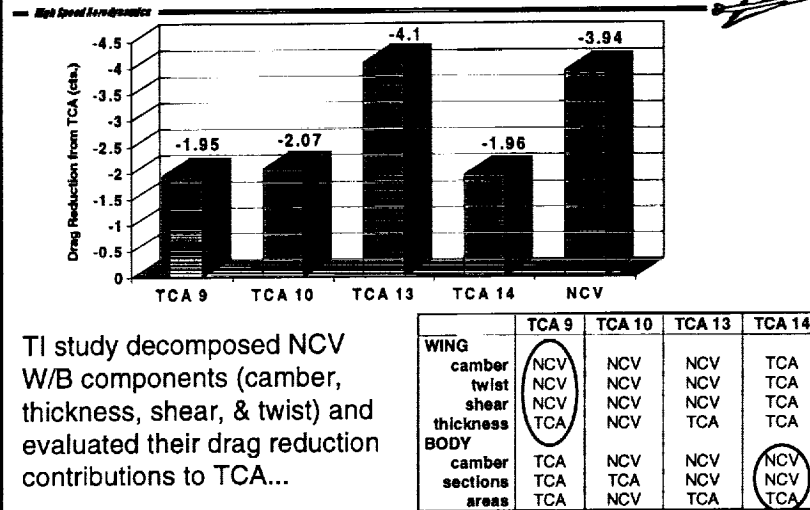
Curvature of Flow on NCV Forebody

High Speed Aerodynamics



The other topic of significant discussion during the workshop was the possible contribution of the NCV forebody to configuration performance improvements. It was known that the forebody was a significant contributor to the optimized wing's performance, but no one understood to what extent one affected the other. Also noted was that during the UPWT 1687 test, very little flow diagnostics were performed on the forebody, thereby leaving a large gap in the database necessary to fully understand the NCV.

Posttest Analysis Results - TRANAIR Study



A parallel study conducted by the Technology Configuration group, took a different approach to understanding the various features of the optimized NCV configuration. The NCV loft was decomposed into its respective camber, twist, shear, and thickness components and then reassembled in a piecewise manner on the baseline TCA loft to quantify the effects of each feature. The above chart presents the highlights of the study.

It can be seen that there two significant contributors to the NCV wing/body performance improvement over the TCA. The first is the wing camber, twist, and shear distribution (TCA 9) and the second is the forebody shape (TCA 14.) Individually, each of these aerodynamic features is worth approximately 2 counts of drag improvement to the TCA. The combination of the two add up to just slightly more than the full NCV wing/body configuration as calculated by TRANAIR. It is worth noting that the signature "gull" of the NCV configuration is approximately 0.7 counts of the 2 counts found in the camber, twist, and shear case of TCA 9.

Posttest Analysis Results - BSWT 644

- 20% of Seattle HSCT aerodynamics IR&D test was devoted to investigating NCV related issues.
- Evaluations of Ref. H and TCA boundary layer characteristics were performed using sublimation & UV oil flow visualization techniques.
 - Trip-off laminar run drag corrections were attempted.
- Trips-on vs. -off drag increments were estimated utilizing three of five different methods ($Re = 4M/ft$ & $8M/ft$ to $14M/ft$)

In preparation for the entry of the NCV model in the Boeing Supersonic Wind Tunnel (BSWT) the Boeing, Seattle high speed aerodynamics group devoted a significant amount of time during an internally funded research and development wind tunnel test (BSWT 644) to understanding Reynolds number effects on boundary layer transition. Both Reference H and TCA were tested over a range of Reynolds number ($8M/ft$ to $14M/ft$) to try to quantify trip drag and laminar run corrections.

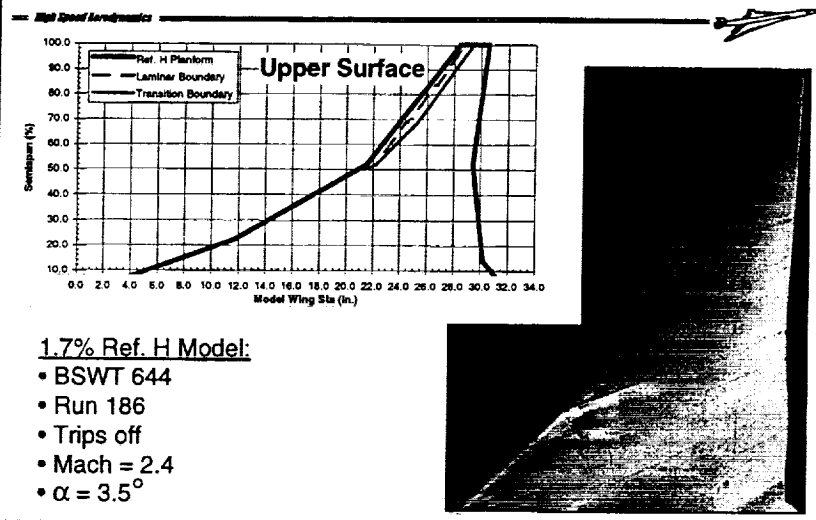
Force data for both models were acquired with and without trips. The trips used for the study corresponded to trip configurations tested on each model in their most recent test at UPWT. Naphthalene sublimation and fluorescent oil flow visualization techniques were used to document boundary layer state.

Five methods are currently available to estimate trip drag corrections:

- 1) Variable trip height extrapolation
- 2) Variable Reynolds number extrapolation
- 3) Excrescence method calculations
- 4) High Reynolds number trips-on/off increments, adjusted for laminar run
- 5) Increment from CFD, adjusted for laminar run

Only methods 2, 3, and 5 are presented here. A FORTRAN 90 code called "Cdf" developed by Robert Kennelly of NASA Ames was used to quantify laminar run corrections to drag based on experimental measurements.

BSWT 644 Test Results - Ref. H @ 9M/ft

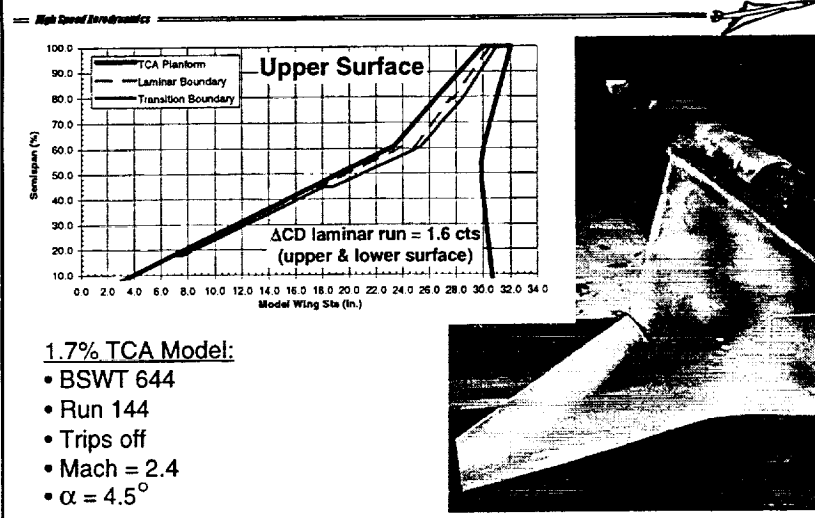


Shown above are the results of sublimation and UV oil flow visualization runs performed on the 1.7% Reference H model in the BSWT wind tunnel at $Re=9M/ft$. The graph presents the measured extent of laminar run as measured after a run on the wind tunnel model upper surface.

As seen above, the maximum extent of streamwise laminar run on the Ref. H configuration was only 1.3 in. aft of the outboard leading edge. Lower surface results show similar trends, with the maximum run of laminar flow equal to 1.1 in. on the outboard panel. Laminar runs on both the upper and lower surface, inboard wing were almost negligible and generally at or forward of the traditional location for trip disks.

A boundary layer flow feature which has only been seen during the BSWT 644 test, is the lighter colored region in the flow visualization image extending 0.5 in. aft of the outboard wing leading edge. It is also partially visible on the inboard segment of the leading edge break. Although labeled "Laminar Boundary" in the graph, the phenomena captured in the image has not yet been well characterized nor explained and merits further discussions.

BSWT 644 Test Results - TCA @ 9M/ft

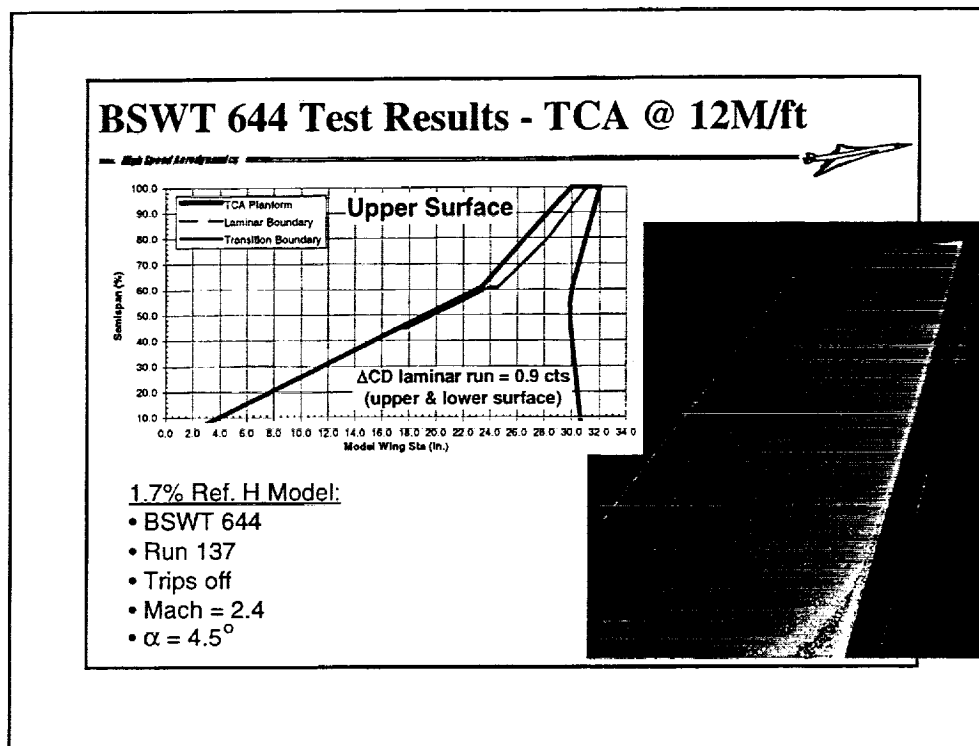


Shown above are the results of sublimation and UV oil flow visualization runs performed on the 1.7% TCA 2b model in the BSWT wind tunnel at $Re=9M/ft$. The graph presents the measured extent of laminar run as measured after a run on the wind tunnel model upper surface.

Comparing the Ref. H data to the TCA transition results, there is an obvious difference in boundary layer state between the two models at the same Reynolds number. While the Ref. H model had little laminar flow on the inboard wing, a significant amount exists on the TCA wing. On the outboard panel, the TCA has a maximum run of laminar flow of 1.8 in.

Although not presented above, the lower surface of the TCA shows a similar pattern as the upper surface. The maximum laminar run, however, is only 0.8 in. at the outboard panel. The TCA at this condition shows a similar "Laminar Boundary" as the Reference H model did. This phenomena is visible in both the sublimation and UV oil results.

Application of the Cdf, mixed boundary layer code calculates the above laminar run to be worth a +1.6 drag count correction to the experimental data. It is worth noting that without trip disks on the model, this small correction is the only one which must be made to the 644 data prior to comparisons with CFD solutions.



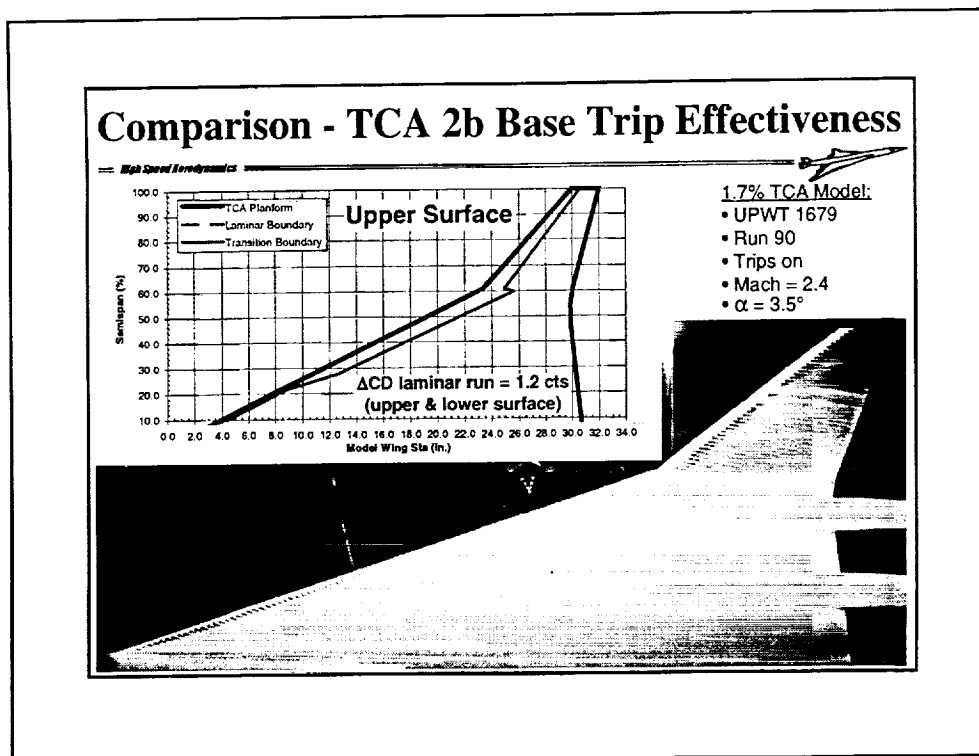
Shown above are the results of sublimation and UV oil flow visualization runs performed on the 1.7% TCA 2b model in the BSWT wind tunnel at $Re=12M/ft$. The graph presents the measured extent of laminar run as measured after a run on the wind tunnel model upper surface.

The most obvious conclusion which can be drawn from this data is that for the TCA to have a similar boundary layer state as the Reference H configuration it requires a significantly higher Reynolds in the wind tunnel. The above data compares favorably to the Ref. H data at 9M/ft.

To help understand the possible sources for this boundary layer performance difference, the primary differences of the TCA from the Ref. H configuration are listed below:

- 1) TCA has a flatter wing (less leading edge camber and twist)
- 2) Its body incidence at cruise is less than the Ref. H
- 3) The TCA body is longer
- 4) The TCA has more leading edge sweep (71° vs. $72^\circ/68^\circ$ inboard and 52° vs. 48° outboard)
- 5) TCA has equal or greater leading edge bluntness

Currently, it is unknown which of the above factors is responsible for the difference in boundary layer state between the two models at the same Reynolds number. The extent of laminar flow measured above indicates that a +0.9 drag count correction need be applied to the test data to simulate a fully turbulent boundary layer.

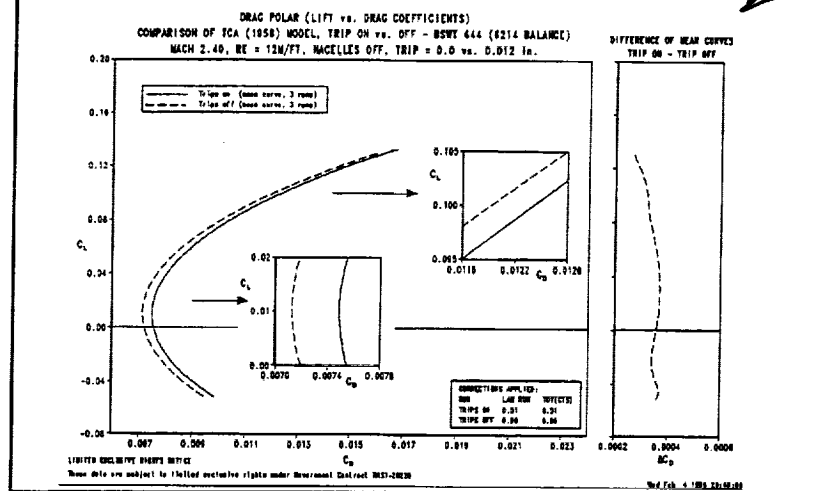


Shown above are the results of sublimation and UV oil flow visualization runs performed on the 1.7% TCA 2b model in the UPWT wind tunnel (test #1679) at $Re=4M/ft$. The graph presents the measured extent of laminar run as measured after a run on the wind tunnel model upper surface.

This data is presented for comparison purposes to TCA data taken at BSWT. Note that no evidence of a lighter "laminar" band can be seen in this data.

The Cdf boundary layer code calculated the correction for this amount of laminar flow to be approximately +1.2 counts. This correction is to be applied to the test data in addition to a trip drag correction. Because it is difficult to accurately determine the exact location of transition for the trips-on condition, an average of two solutions was used where 1) transition occurs at the trips and 2) where transition occurs at the transition boundary outlined above. A thorough understanding of the transition mechanisms associated with placing disks in the model boundary layer flow is required before a more accurate determination of boundary layer transition location can be recommended.

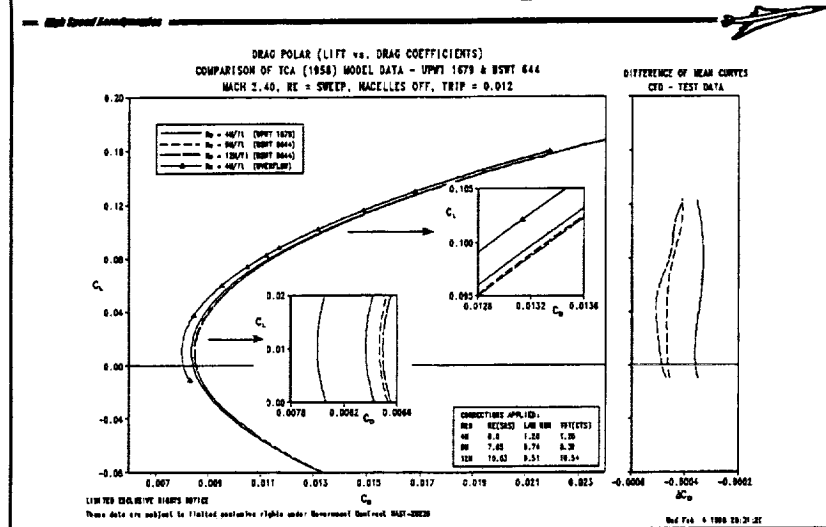
BSWT 644 Test Results - Trip Drag Clues, 1



In an effort to begin quantifying trip drag using the alternate methods mentioned earlier, several attempts were made using experimental data from the BSWT 644 test.

Merged trips-on and off drag polars were differenced for the TCA configuration at a Reynolds number of 12M/ft. Coupled with laminar run corrections calculated by program Cdf, a trip drag correction of 3.2 counts at the cruise condition was determined. The correction appears to vary by ± 0.5 counts over the range of lift coefficients normally tested. Results for data taken at $Re=9M/ft$ show very similar results (3.6 cts., ± 0.4 cts.).

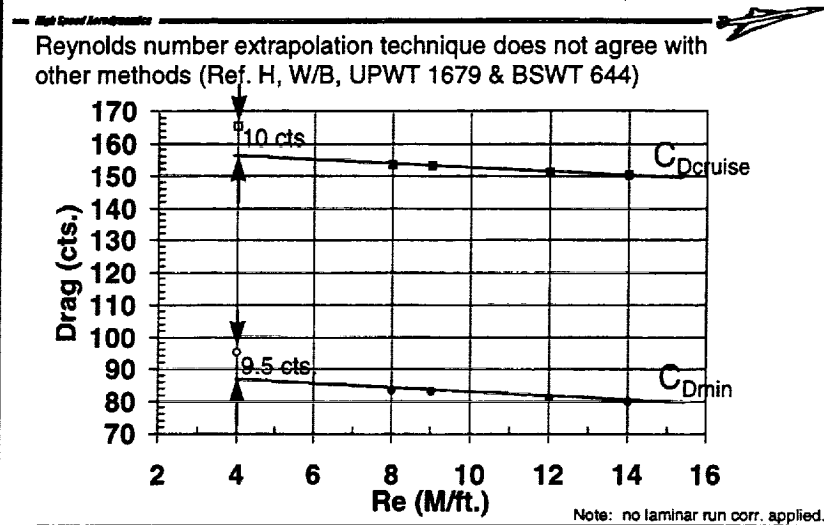
BSWT 644 Test Results - Trip Drag Clues, 2



A second method considered for evaluating the magnitude of trip drag was to subtract experimental, trips-on data corrected for laminar run and Reynolds number effects from a fully turbulent, trips-off CFD force polar. The results of this exercise are presented in the graph above.

The corrected experimental data at a $Re=4M/ft$. utilizing the above method appears to agree well (3.5 cts. +/- 0.2 cts.) with the trip drag value previously calculated at 12M/ft. It is expected that the 9M/ft and 12M/ft experimental data can be made to match the above result if they are incremented from a CFD solution at their corresponding Reynolds number. The large Reynolds number extrapolation necessary for this example appears to be reducing the fidelity of this solution.

BSWT 644 Test Results - Trip Drag Clues, 3



The last trip drag calculation method presented is the Braslow variable Reynolds number extrapolation technique as applied to the Reference H configuration. By extrapolating along the theoretical turbulent line for a "clean" model back to the test Reynolds number, the trip drag is obtained as the difference between the extrapolated curve and the drag measured with trips-on. Because BSWT cannot operate below a Reynolds number of 8M/ft, UPWT 1649 test data were used in this example.

Upon inspection it is quite obvious that the trip drag correction resulting from this method is unreasonable and is significantly different than the results of the previous two methods. However, the method still holds promise as more reasonable trip drag increments have been calculated at other tunnels where they can achieve this wide range of Reynolds numbers. The results may also be affected by the fact that data from two different tunnels (and their associated flow quality differences) were mixed into one solution.

Utilizing all of the methods outlined previously, a full set of well documented low and medium Reynolds number wind tunnel test results, and the Cdf laminar run correction code, it is suspected that a reasonable approximation for trip drag can be had in the very near future. Once at least three of the five methods can be made to agree repeatedly, the riddle of supersonic trip drag at wind tunnel Reynolds numbers can be solved.

Future Work - BSWT 647 (Feb. 16-27, 1998)

— High Speed Aerodynamics



- NCV & TCA models will be tested to 14M/ft
 - Trips on and off
- Sublimation, UV oil, and IR thermography will be used to evaluate laminar run of forebody and wing
 - IR camera allows easier B.L. imaging for a range of alphas
- BSWT 644 test experience valuable for NCV entry
 - Validated previous experiences of natural boundary layer transition at leading edge for higher Re conditions.
 - Identified need for alternate method to visualize forebody
 - Highlighted artificial PM limits due to balance adapter
 - Test will use LaRC 756 balance to alleviate problem

As part of the CA testing team's six month plan, an entry of the NCV model in the Boeing Supersonic Wind Tunnel will be conducted in the second half of February, 1998. The purpose of the test will be to collect force data at higher Reynolds numbers to see if a more turbulent boundary layer can readily solve the configuration's performance shortfall. Also included in the test plan are additional flow visualization runs utilizing several techniques to try and document natural boundary layer transition over a range of alphas and Reynolds numbers.

Experience gathered during the BSWT 644 test entry has been quite valuable in preparing for the 647 entry. It allowed participants to document and verify the effects of high Reynolds number testing on wind tunnel model boundary layer state. It also identified a shortcoming in current flow visualization techniques to document HSCT forebody flow characteristics. This realization allowed the lead aerodynamics organization for test 647 to select another method to visualize what may become a very important piece of the NCV performance puzzle. Finally, the test highlighted the need for a better sting adapter arrangement than tested. Although sufficient for typical research studies, a new configuration utilizing the LaRC 756 balance and larger diameter sting/adapter combination will allow the NCV to fly at the maximum Reynolds number capabilities of BSWT.

It is hoped that with all of the test configuration enhancements outlined above, the performance potential of the NCV model will finally be realized.

This page is intentionally left blank.

HSR

High Speed Research - Configuration Aerodynamics

Langley Research Center

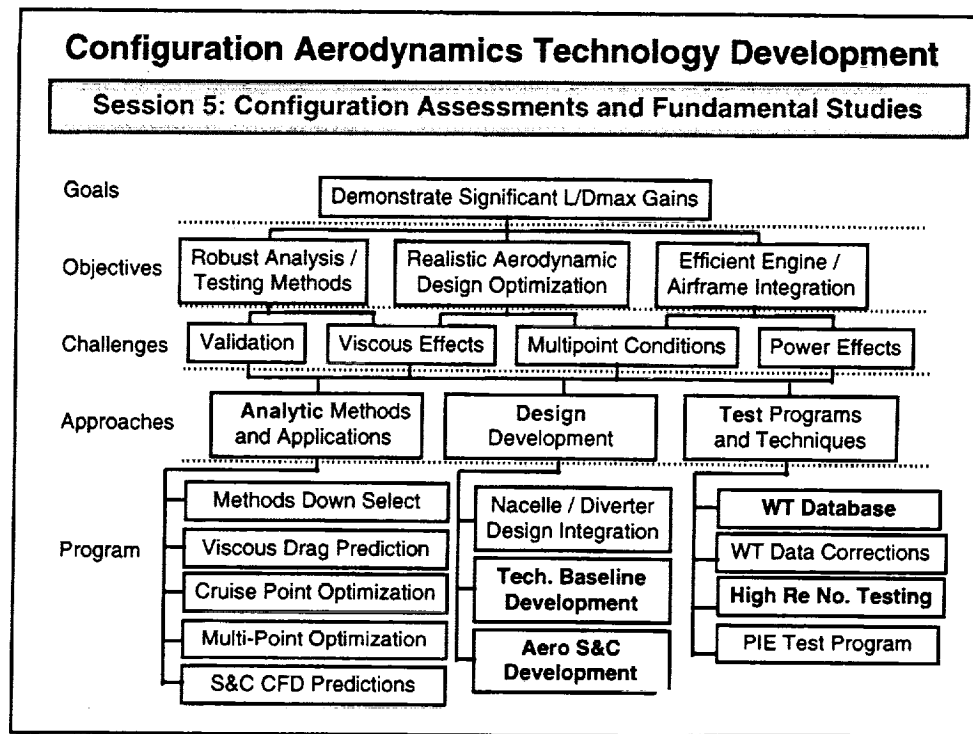


Aftbody Closure Model Design

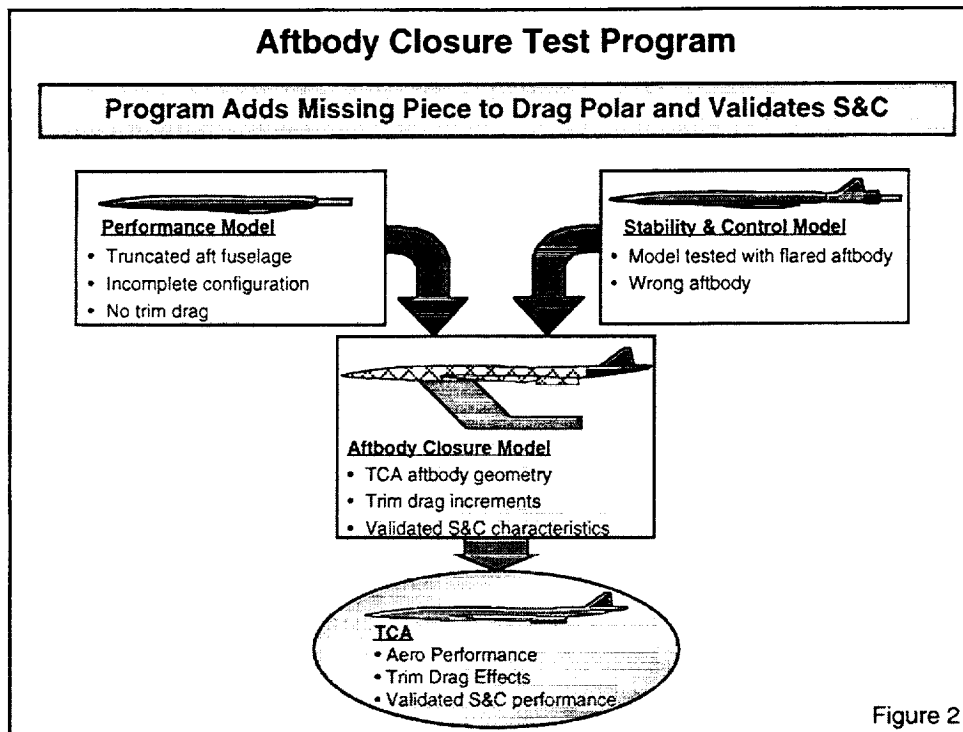
Lessons Learned

Francis J. Capone
NASA Langley Research Center

Aerodynamic Performance Workshop
HSR Annual Airframe Review
Los Angeles, CA
February 9 - 13, 1998

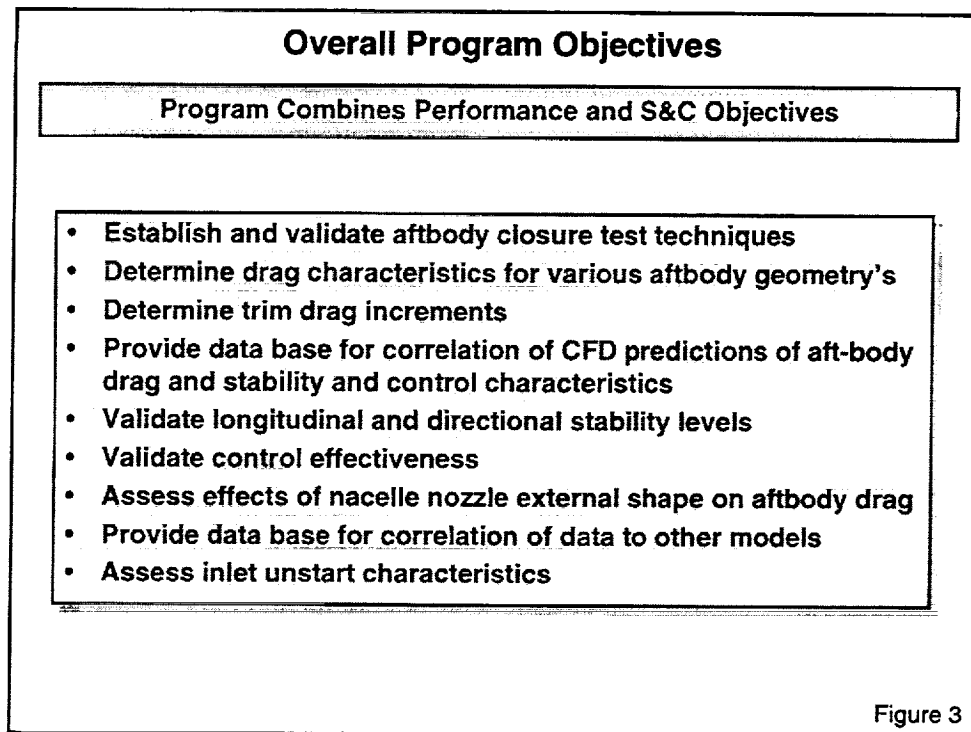


This figure shows the Configuration Aerodynamics "Program on a Page".



An Aftbody Closure Test Program is necessary in order to provide aftbody drag increments that can be added to the drag polars produced by testing the performance models (models 2a and 2b). These models had a truncated fuselage, thus, drag was measured for an incomplete configuration. In addition, trim characteristics cannot be determined with a model with a truncated fuselage.

The stability and control tests were conducted with a model (model 20) having a flared aftbody. This type aftbody was needed in order to provide additional clearance between the base of the model and the sting. This was necessary because the high loads imposed on the model for stability and control tests result in large model deflections. For this case, the aftbody model will be used to validate stability and control performance.



The aftbody closure overall program objectives are a combination of both the performance and stability and control objectives. One prime objective of this program was to establish and validate aftbody closure test techniques. This paper will present the results of study in which the basic model would be wing-tip supported in the wind tunnel. As such, it will show why this particular system was chosen and some of the resulting issues and problems associated with the design of a wing-tip supported model.

Overall Program Requirements

Program Combines Performance and S&C Requirements

Performance Requirements:

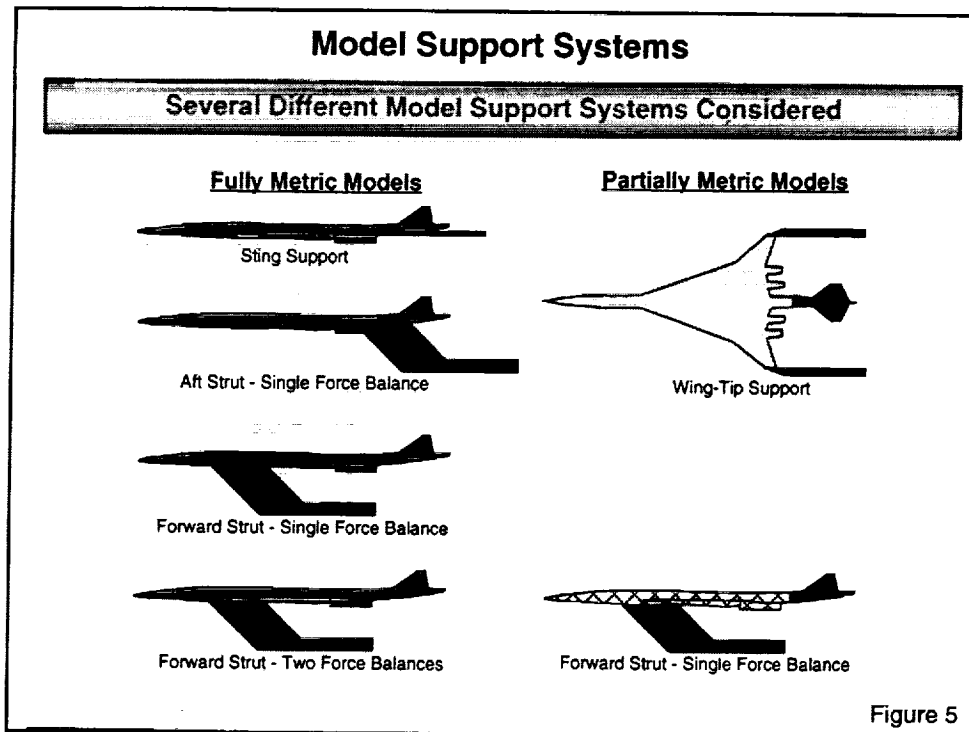
- $M = 0.9, 0.95, 1.2, 2.4$
- $-4^\circ \leq \alpha \leq 8^\circ$
- $\beta = 0^\circ$
- $\delta_i = -6^\circ, -2^\circ, 0^\circ, 2^\circ, 4^\circ, 6^\circ$
- ± 1.5 ct accuracy - Transonic
- $\pm 1/2$ ct accuracy - Supersonic
- Aftbody configurations
 - Baseline TCA aftbody
 - Modified baseline
 - Flared aftbody
- Nacelle shapes

S & C Requirements:

- $M = 0.6, 0.90, 0.95, 1.2, 1.8, 2.4$
- $-4^\circ \leq \alpha \leq 12^\circ$
- $-6^\circ \leq \beta \leq 6^\circ$ - Transonic
- $-3^\circ \leq \beta \leq 3^\circ$ - Supersonic
- $-9^\circ \leq \delta_i \leq 9^\circ$ - Transonic
- $-6^\circ \leq \delta_i \leq 6^\circ$ - Supersonic
- $\delta_r = 0^\circ, 10^\circ, 20^\circ$ - Transonic
- $\delta_r = 0^\circ, 10^\circ$ - Supersonic
- Aftbody configurations
 - Baseline TCA aftbody
 - Flared aftbody
- Nacelle inlet plugs

Figure 4

As with the overall test objectives, the program requirements were also a combination of the performance and stability and control requirements. Note that a wider range of test conditions are necessary for stability and control whereas, one of the more important performance requirements is both a transonic and supersonic accuracy requirement. Model scale was essentially fixed by the need for stability and control data at Mach 1.8. Obtaining data at this Mach number is desirable because of nonlinearities that occur in the various stability parameters. The model scale chosen was 1.5-percent which was the same as Model 20 that was used for stability and control tests. The resulting model length is the longest model that can be tested at mach 1.8 in the Unitary Plan Wind Tunnel (UPWT) at Langley. Tests were also planned for the 16-FT Transonic Tunnel.



The combination of test objectives and requirements generally will have a strong impact on the type of model support chosen for the test. Several support systems can be used for an aftbody closure type test and a study was conducted to determine which support system was best suited to meet the overall test objectives and requirements. For the current test, several support systems were considered and are shown above. These support systems generally fall into two classes; those that are fully metric in which total configuration forces are measured, and partially metric in which forces are measured only on the configuration aftbody. Figures 6 to 11 list the advantage and issues associated with each of the support systems considered in this study.

Fully-Metric Model Support Systems

Sting-Support With Single Force Balance



ADVANTAGES

- Complete aerodynamics measured
- Model can be sized for UPWT
- Could test with truncated fuselage (similar to model 2)
- Could test with extended aftbody (similar to model 20)
- Can test at sideslip

ISSUES

- Aftbody always in presence of sting
- Aftbody increment is difference of two large numbers
- Large balance forces
- Sting interference needs evaluation
- Seal at metric break
- Large internal pressure correction to normal and axial force (corrections based on inaccurate area measurement)
- Cannot be used for HSCT type configurations

Figure 6

Figure 6 shows a sting-supported model. Although this type of support system cannot be used for a HSCT slender configurations, it was included to show advantages and issues for this type support system.

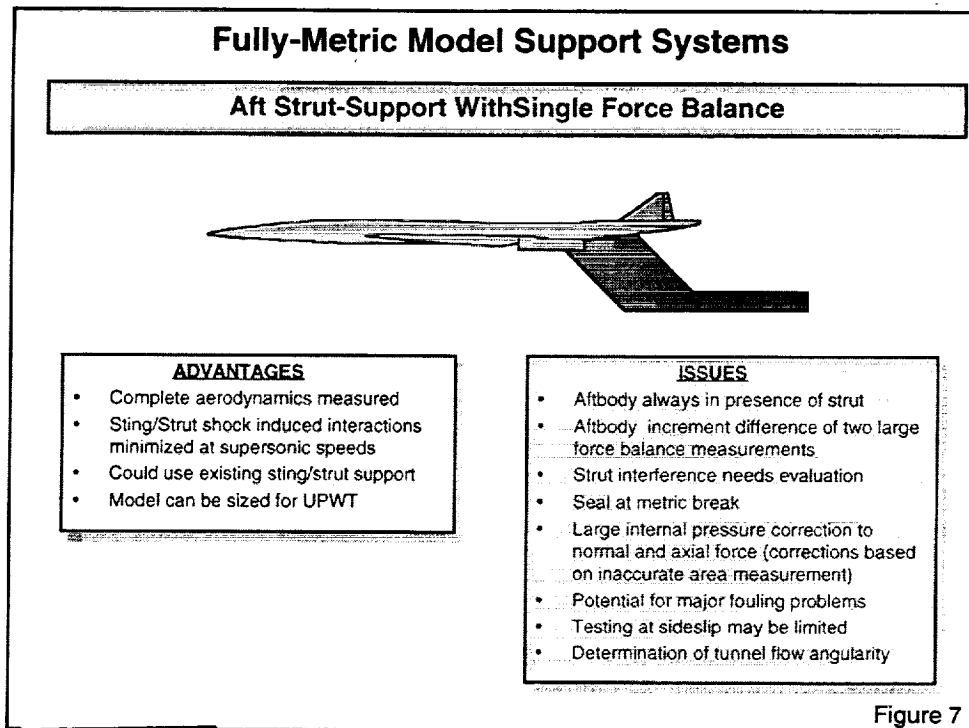
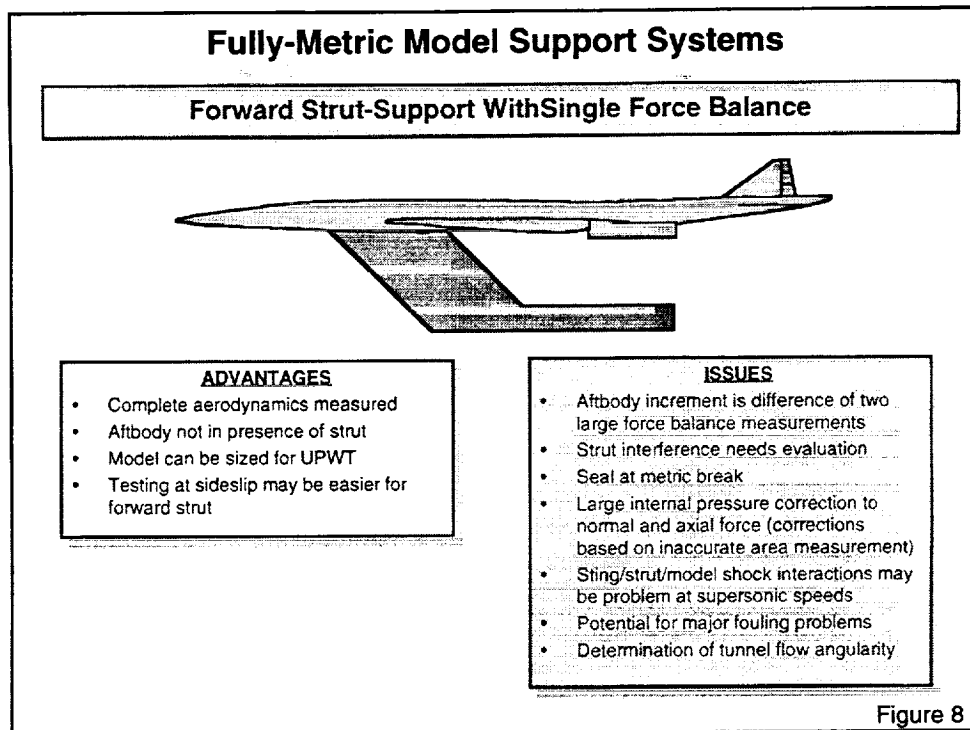
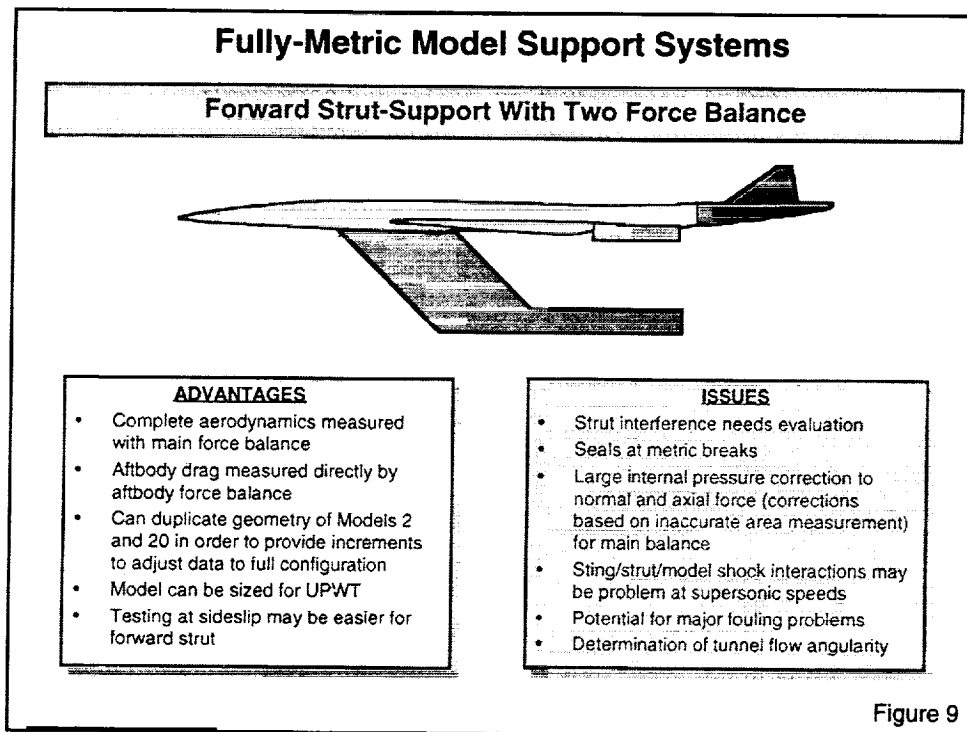


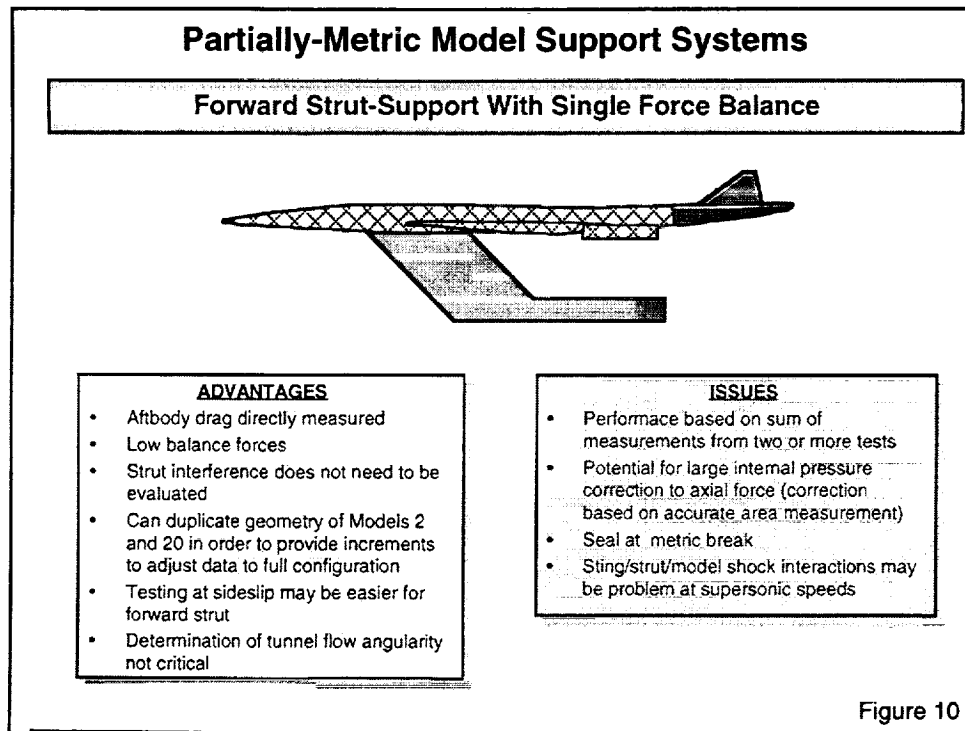
Figure 7 shows a model with an aft strut-support system. This support system was eliminated because the aftbody would always be in the presence of the strut. It was felt that the strut interference effects could not be determined



This figure shows a model with an forward strut-support system. This support system was eliminated because of the need to determine strut interference effects. A large portion of the model fabrication budget would have to be devoted to making alternate position and dummy supports that would be needed to determine support interference. Also, determining support system can take up to 25-percent of the time available to test.



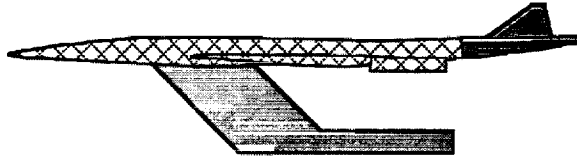
This figure shows a model with an forward strut-support system and a second force balance to measure aftbody forces. While this may be the best support system to use because both total and aftbody forces would be measured, it was also eliminated because of the need to determine strut interference effects.



This figure shows a model with a partially-metric, forward strut-support system in which the force balance measures only aftbody forces. This support system was eliminated because of the uncertainty in sting/strut shock interactions at supersonic speeds that could occur if the same support strut was used in both facilities that tests were to be conducted.

Partially-Metric Model Support Systems

Forward Strut-Support With Single Force Balance



ADVANTAGES

- Aftbody drag directly measured
- Low balance forces
- Strut interference does not need to be evaluated
- Can duplicate geometry of Models 2 and 20 in order to provide increments to adjust data to full configuration
- Testing at sideslip may be easier for forward strut
- Determination of tunnel flow angularity not critical

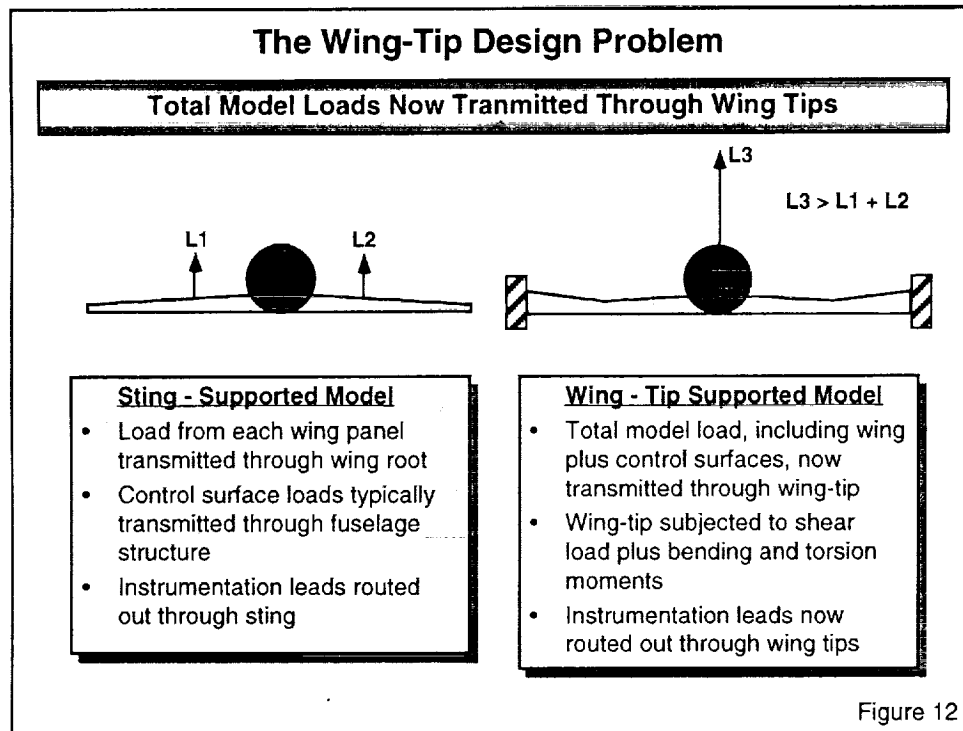
ISSUES

- Performance based on sum of measurements from two or more tests
- Potential for large internal pressure correction to axial force (correction based on accurate area measurement)
- Seal at metric break
- Sting/strut/model shock interactions may be problem at supersonic speeds

Figure 11

This figure shows a model with a partially-metric, wing-tip support system in which the force balance measures only aftbody forces. Although this support system has more issues than the forward strut support shown in figure 10, it was chosen because it was felt that this support system would have the least support interference effects on the aftbody.

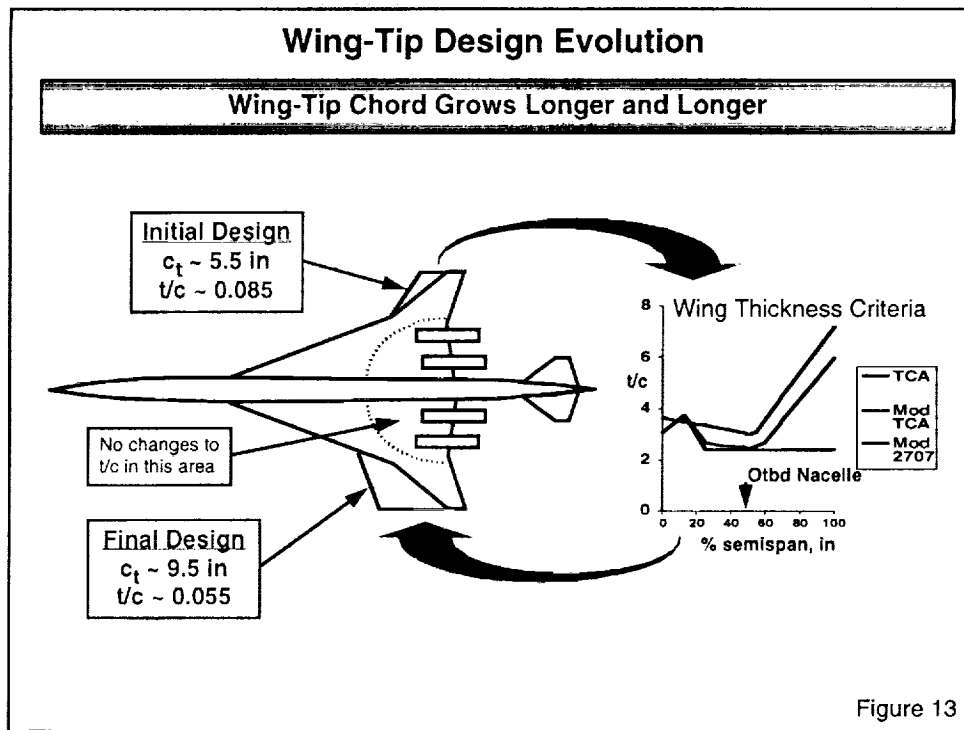
With the support system and model scale chosen, model requirements were issued to designers to proceed with a design of a wing-tip supported model.



This figure has been included to illustrate the main structural problem associated with a wing-tip support model. For a conventional sting-supported model, the main loads are developed on the wings. Typically, the lift load on each wing panel is transmitted through the wing root to a fuselage strongback. The wing root chord generally is longer and thicker than any other wing chord. In addition, control surface loads are transmitted through the fuselage structure. Instrumentation leads are routed out through the sting or a support strut.

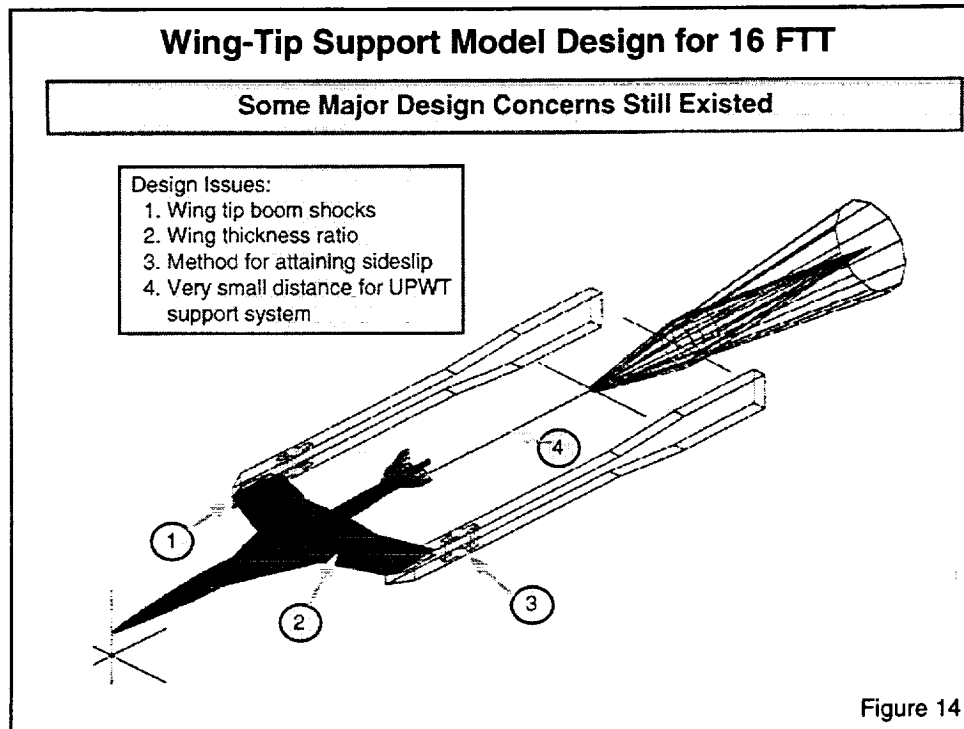
For the wing-tip supported model, total model loads including control surface loads now must be transmitted out through the wing tips. The wing tip is also subjected to shear loads plus bending and torsion moments, the latter which can be quite high. In addition, additional thickness must be made available in order to route instrumentation leads through the wing-tips. These load conditions imposed on the wing tip will result in increases to both the length and thickness of the wing tip chord.

Wing-tip supported model have been in use for many years. Such systems have been used for fighter type configurations at the 16-Ft Transonic Tunnel since 1955. For a fighter type configuration, wing thickness ratio can usually be maintained out to about 50-percent semispan after which the wing is designed to have constant thickness. In addition, a modest increase (15 to 20 percent) in wing tip chord may be required. However, fighter configurations generally have wings with greater aspect ratio and thickness ratio than HSCT configurations. None the less, previous experience in the design of wing-tip support systems had a large influence on the decision to proceed with this type support.



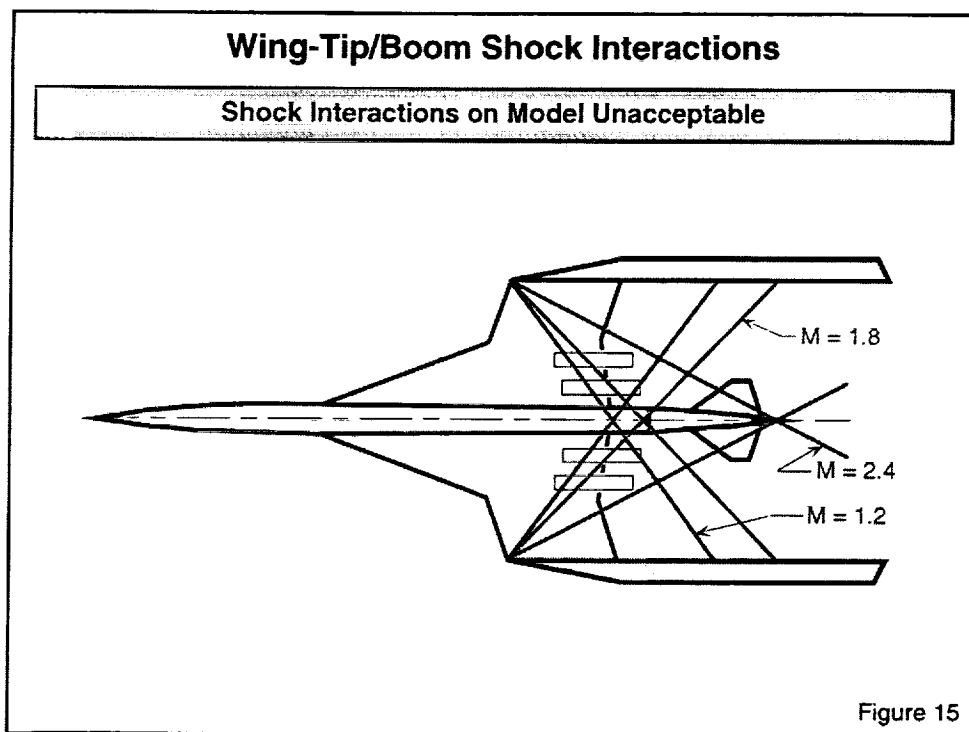
As stated earlier, model design was initiated once the support system, model scale and preliminary loads were known. However, there were no requirements or guidance given to the model designers on how wing thickness ratio may vary along the wing semispan. As a result, the initial design of the wing-tip support model had a tip chord of about 5.5 inches with a thickness ratio of 8.5 percent. This design did however, maintain the thickness ratio of the chord at the break in the wing leading edge. The tip chord for the 1.5-percent model is about 2.2 inches. Thus this first design had a new tip chord that was just over twice as long as the unmodified tip chord.

The model designers were then given wing thickness criteria as shown on figure 13. It was desired that the tip chord thickness ratio not exceed 6 percent. For reference, the wing thickness ratio of a very early supersonic configuration that was tested with a wing-tip support had a 7-percent thick tip chord is also shown in figure 13. As can be seen, the final design that emerged was one that had a tip chord of about 9.5 inches with 5.5-percent thick airfoil. This design also maintained the thickness ratio of the chord at the break in the wing leading edge.



This figure shows a schematic of the wing-tip model as it would be installed in the 16-Ft Transonic Tunnel. Basically, all the hardware shown would have to be built. The wing-tip booms would be about 5 feet long. Sideslip would be accomplished by using incidence blocks in the booms. At this point, the structural design of the support booms did not consider any side loads that would be generated by the forward part of the boom that effectively was at an angle of attack.

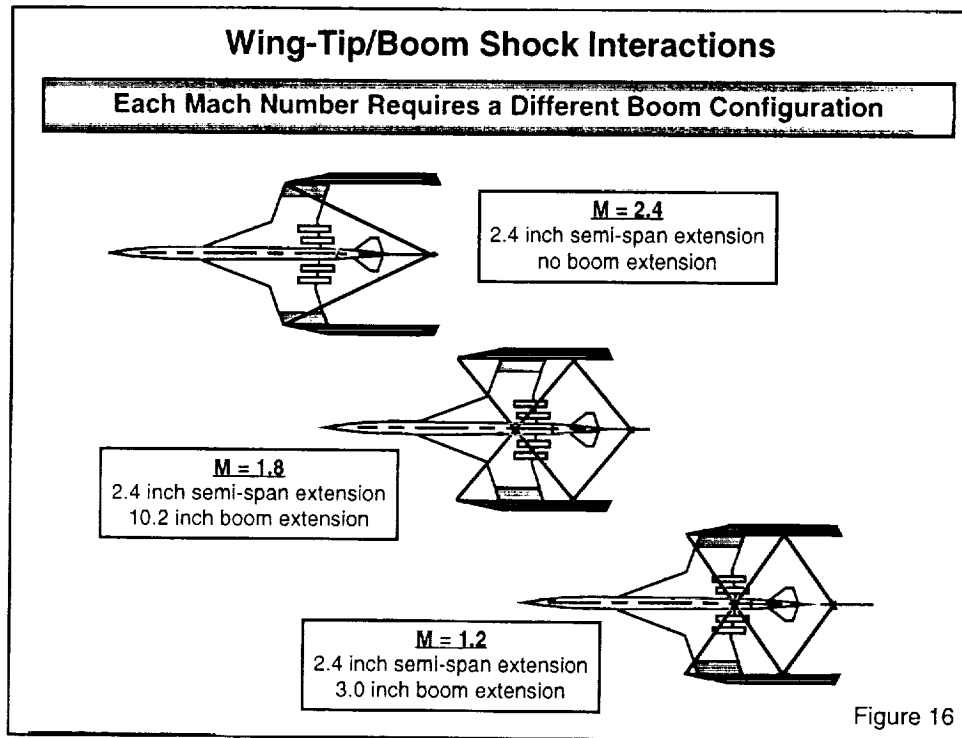
Also shown on this figure are some of the issues that still remained with the wing-tip support that were shown earlier on figure 11. These included wing-tip boom shock interactions on the aftbody portion of the model, wing thickness ratio at about 50 to 60-percent semi-span and the method of attaining sideslip. In addition, there was a concern of the distance between the end of the model and the main tunnel support in UPWT. For the 16 FTT, this distance was fixed at 30 inches whereas in UPWT this distance would be about 6 inches.



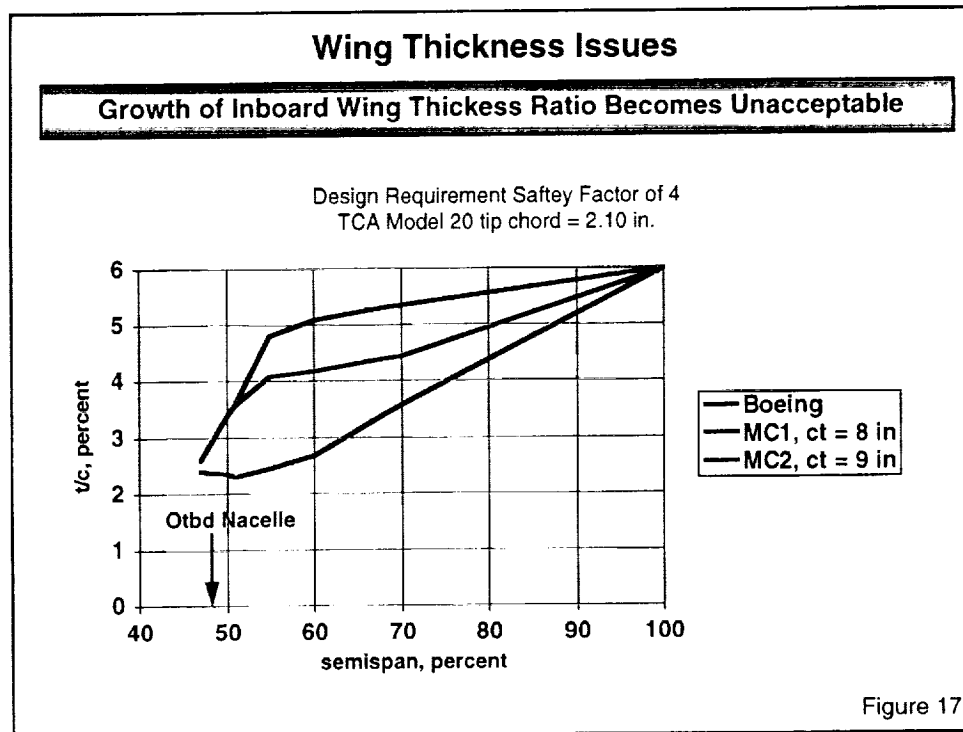
The predicted wing-tip/boom shock intersections on the model at Mach numbers of 1.2, 1.8 and 2.4 are shown in figure 15. At Mach 2.4, shocks from the wing-tip booms can be seen impinging on the aftbody portion of the model which is unacceptable. At Mach 1.8, the shocks intersect on the model near the metric break which also is unacceptable. This is because the shocks may affect the pressure measurements made at the metric break. These pressure measurements are used to correct force data similar to cavity and base corrections for a sting-mounted model. At Mach 1.2, the intersection of the shocks forward of the metric break was also considered marginally unacceptable.

One means of eliminating the effect of the wing-tip boom shock problem is to extend the booms such that the shocks intersect on the nonmetric portion of the model far upstream of the metric break. This method has previously been used. However, this was deemed impracticable for the Mach 2.4 case because the booms would have to be extended forward of the location where the wing leading edge intersects the fuselage. Boom extensions of this length would have resulted in very large loads in the side direction on the booms. The booms would then have to be much thicker to take these loads. In addition, there could be extensive support interference from the flow field of the deflected booms.

The proposed solutions to the above wing-tip boom shock problems are shown in the next figure.



At Mach 2.4, the wing-tip boom shock intersections were moved far downstream of the model by extending the wing semispan by 2.4 inches. A boom extension of 10.2 inches was then required at Mach 1.8 in addition to the span extension in order to move the shock intersections forward on the nonmetric portion enough where the effects of the shocks were considered minimal. At Mach 1.2, a 3.0 inch boom extension was needed. Note, that at these two Mach numbers, no consideration was given to the extra loads imposed on the support booms when the model would be tested at sideslip.



Additional structural analysis were being performed on the wing since the previous analysis shown in figure 13 was done only on the wing tip. The results of this analysis shown on the above figure indicated that the wing thickness ratio had to be at least 4-percent at the 55 to 65-percent semispan stations in order to facility strength and safety factor requirements. This thickness ratio was much higher than the desired thickness of 2.5 percent. This was for the wing with the 9-inch tip chord. The maximum thickness for this portion of the wing that could be tolerated was thought to be about 3 percent.

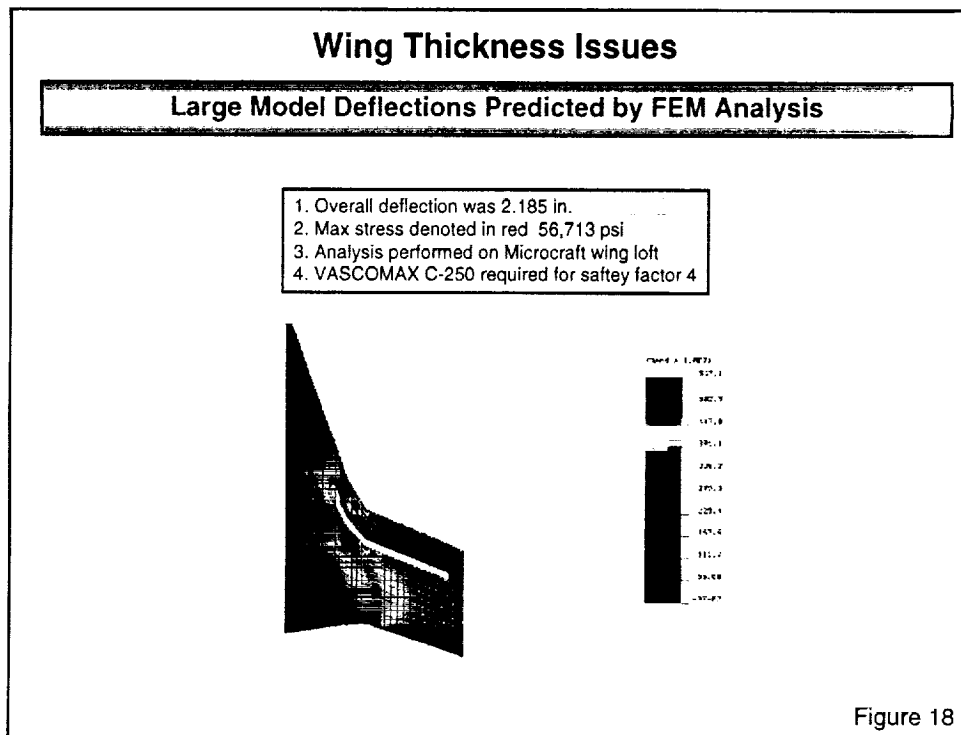


Figure 18 shows the results of a finite element analysis (FEM) that was conducted on the wing-tip support model for the wing identified as MC2 on figure 17. As can be seen, the maximum stresses were about 57 kpsi. This result did check the handbook analysis. However, one factor the handbook analysis could not show were the two areas of high stress concentrations located at the break in the wing leading edge and inboard on the wing at about 25-percent of the chord. Stress concentrations of this type are generally not desirable for primary structure for wind tunnel models. This analysis also showed that the minimum material required was VASCOMAX C-250 which is also a steel that is not generally desirable for fabricating wind tunnel models. However, the most disturbing result from the FEM analysis was the very high predicted model deflection of over 2 inches. This high model deflection was not acceptable.

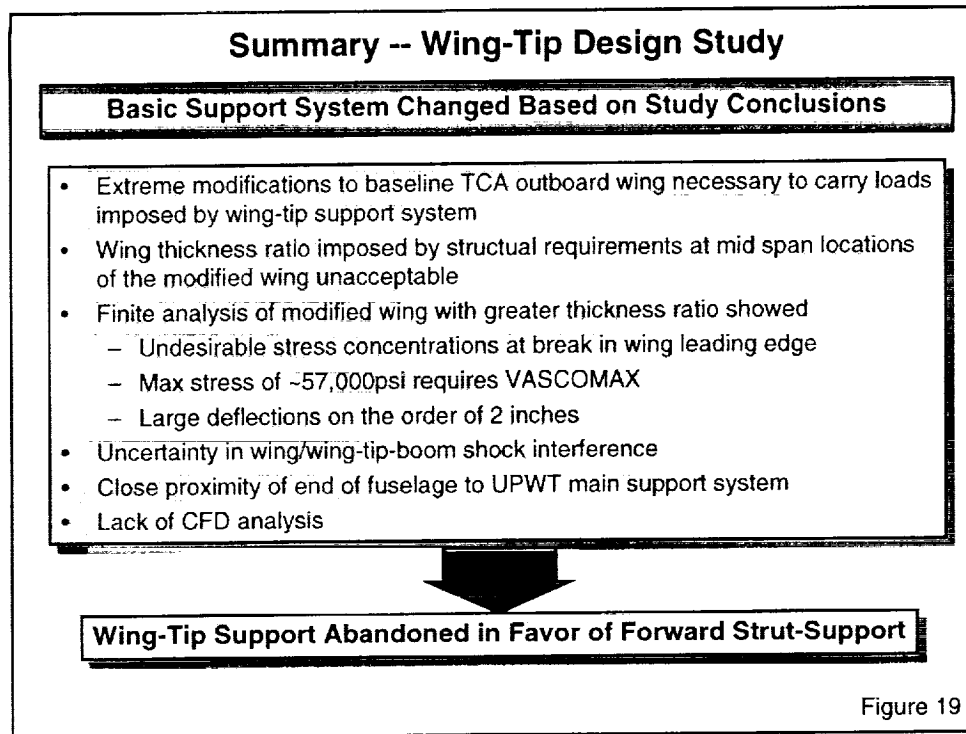


Figure 19

A thorough review was made of all of the results from the wing-tip supported model design. These results are summarized in figure 19. At this point, the wing-tip support was abandoned in favor the forward-strut-support with a partial metric model in which only aftbody forces would be made. This type support system was previously described in figure 10.

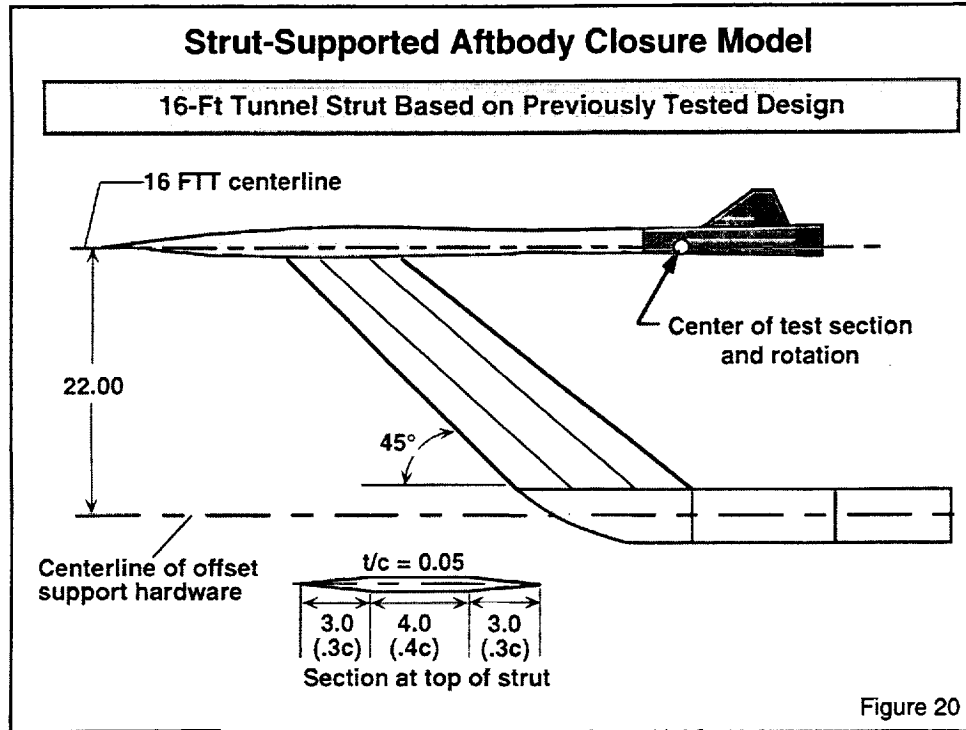


Figure 20 shows a schematic of the model as it will be installed the 16-Ft Transonic Tunnel. The support strut airfoil section characteristics at the top of the strut were similar to a support strut used at 16FTT. The model will be located on the wind tunnel centerline. The aftbody is located basically in the center of the test section.

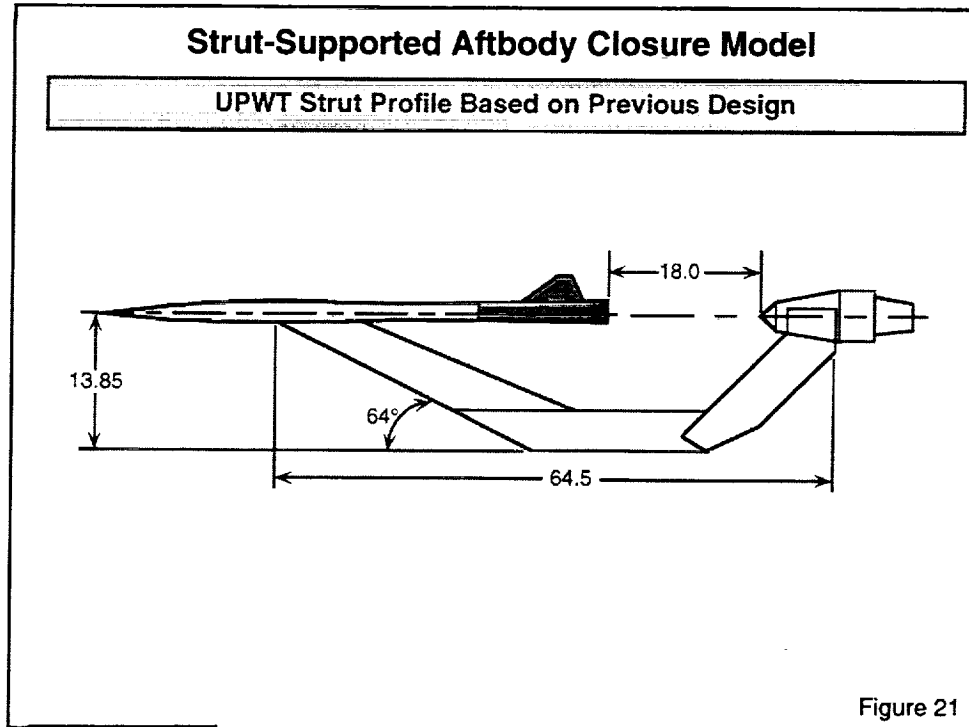


Figure 20 shows a schematic of the model as it will be installed the UPWT. The support strut profile was based on a previous support strut that was tested in UPWT. The blockage characteristics of the current aftbody test are similar to the model previously tested.

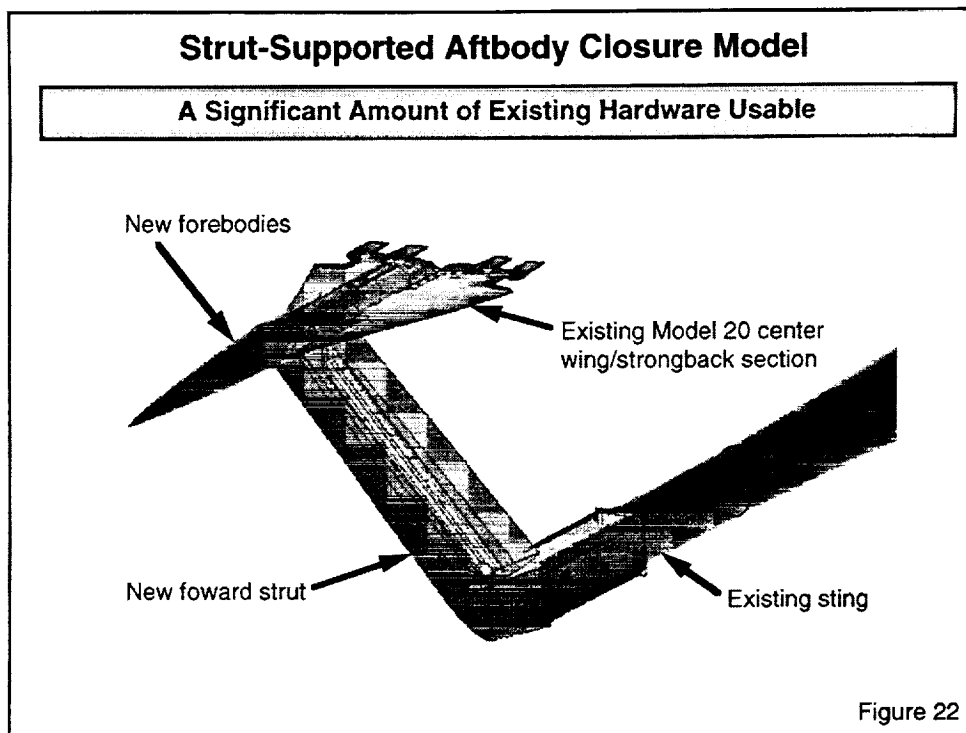


Figure 22 shows another view of the installation for the 16-Ft Transonic Tunnel. One thing to note is that the existing wing/strongback section of model 20 will be used for this investigation. This results in substantial savings in model fabrication time.

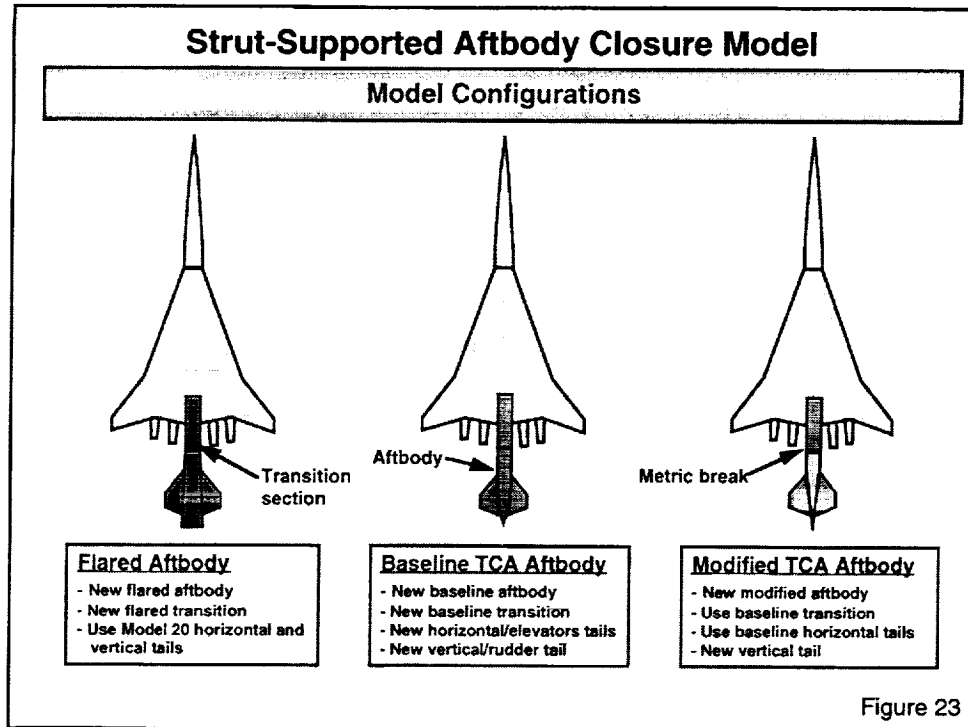


Figure 23 presents the three basic model configurations to be tested. The configuration with the flared aftbody is similar to model 20. The model part labeled transition section will be part of the nonmetric model on which no forces are measure.

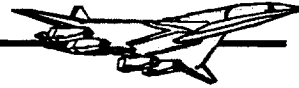
The middle sketch shows the baseline TCA aftbody. It has its own transition sections. As can be seen, all new control surfaces need to be built in order to test this configuration.

The configuration with the the modified TCA aftbody will be used primarily to determine trim characteristics. This aftbody allows the leading edge of the horizontal to remain ported with a $+7^\circ$ setting. The horizontal tail remained ported for the baseline aftbody only to about 2.5° .

HSR

High Speed Research - Configuration Aerodynamics

Langley Research Center

**HSR Model Deformation Measurements from
Subsonic to Supersonic Speeds****A. W. Burner
G. E. Erickson
W. L. Goodman
G. A. Fleming****NASA Langley Research Center****Aerodynamic Performance Workshop
HSR Annual Airframe Review
Los Angeles, CA
February 9 - 11, 1998**

HSR model deformation measurements from subsonic to supersonic speeds at several NASA facilities at Langley and Ames Research Centers are presented. The video model deformation (VMD) method has been used extensively for several years at NASA facilities for deformation measurements for both High Speed Research (HSR) and Advanced Subsonic Technology (AST) tests. Results for HSR models have been presented at two previous Configuration Aerodynamics workshops. Efforts are also underway to develop the projection moiré interferometry (PMI) method that offers potential advantages over the VMD method provided a number of operational difficulties can be overcome. At the current state of development, PMI is not ready for production wind tunnel testing, but after further development may serve to complement the VMD method (especially for measuring the deformation of control surfaces). A. W. Burner of the Experimental Testing Technology Division is the primary contact for the video photogrammetric method for measuring deformation. G. E. Erickson and W. L. Goodman are test engineers at the Langley Unitary Plan Wind Tunnel and 16-Foot Transonic Tunnel respectively of the Aero- and Gas-Dynamics Division. G. A. Fleming of the Fluid Mechanics and Acoustics Division is the primary contact for the projection moiré interferometry (PMI) method.

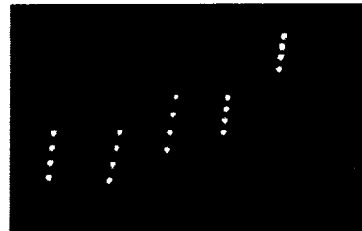
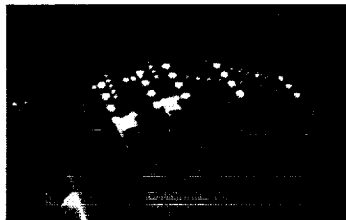
OUTLINE

- **Video Model Deformation (VMD)**
- **Projection Moiré Interferometry (PMI)**
- **Facilities**
- **HSR model deformation measurements**
- **Future work**

This paper describes the video model deformation technique (VMD) used at five NASA facilities and the projection moiré interferometry (PMI) technique used at two NASA facilities. Comparisons between the two techniques for model deformation measurements are provided. Facilities at NASA - Ames and NASA - Langley where deformation measurements have been made are presented. Examples of HSR model deformation measurements from the Langley Unitary Wind Tunnel, Langley 16-foot Transonic Wind Tunnel, and the Ames 12-foot Pressure Tunnel are presented. A study to improve and develop new targeting schemes at the National Transonic Facility is also described. The consideration of milled targets for future HSR models is recommended when deformation measurements are expected to be required. Finally, future development work for VMD and PMI is addressed.

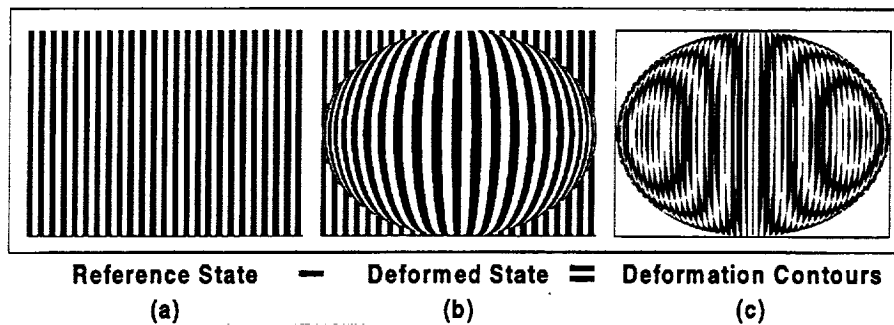
VMD APPROACH

- Single view photogrammetry
- Non intrusive (except targets)
- Automated processing
- Multiple images / data point
- Wind-off polars for calibration
- Angle change due to flow

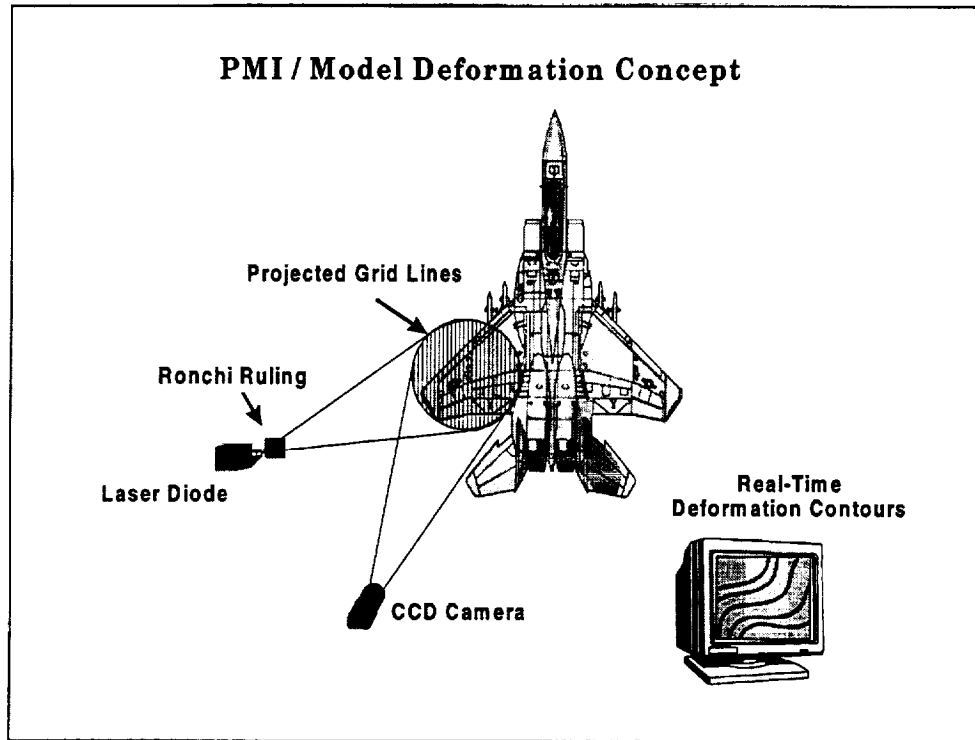


The video model deformation technique (VMD) consists of a single view, single camera photogrammetric solution of targets placed on the wing at known semispan locations. Except for these targets, which may have some minor effects on the aerodynamic data, the technique is non-intrusive. The basic hardware consists of a standard video-rate CCD video camera, light source usually located as close to the camera as possible (except for the National Transonic Facility), frame grabber board, and computer. The computer used at the 16-Ft Transonic Tunnel is shown in the upper right photograph. Targets are typically placed on or near the fuselage to serve as control in addition to a number of semispan locations on the wing. Retroreflective targets applied to the right wing of a TCA model at the Unitary Wind Tunnel are shown in the lower left photograph. A high contrast image of retroreflective targets on the 4% Arrow Wing HSR model at the Ames 12-Ft Pressure Tunnel is shown in the bottom right photograph where the flow direction is upward on the image and the wing tip is to the right. Flat black paint was used to remove glints and increase target contrast. Image processing is used to automatically locate and compute corrected image plane coordinates for each of the targets. Single view photogrammetry is then used to determine the X (streamwise), Z (vertical) coordinates in object space, given the known Y (crossflow) coordinates. Slope angles and vertical displacements at specified chordwise locations are computed by linear least squares for each semispan station along the wing.

Projection Moiré Difference Contouring

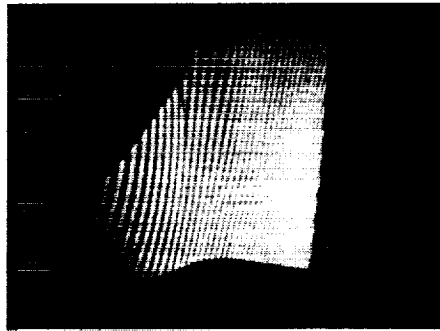


Projection Moiré Interferometry (PMI) is a second video-based model deformation technique under development at NASA - Langley. Based on grid line projection, PMI is an optically simple technique that can measure model deformation over the entire camera field-of-view. With reference to the chart above, assume a series of equispaced, parallel lines are projected onto a perfectly flat test article constituting a reference image (a). Under load, the test specimen will have deformed, and the projected grid lines will appear to lie in different spatial locations compared to the reference state (b). Subtracting images of the object in the reference and deformed conditions produces an image (c) containing moiré fringes (the low spatial frequency bands). Moiré fringes are observable in real time, providing the test engineer immediate video feedback regarding model attitude and deformation. Through off-line image processing and knowledge of the contour interval or *fringe sensitivity constant*, the topology of the deformed surface can be reconstructed.

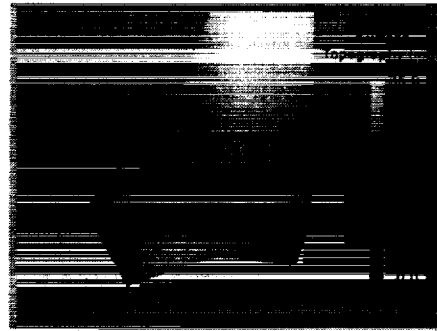


The implementation of PMI as a wind tunnel model deformation instrument is shown schematically above. A pulsed, broad band 800-nm laser diode is used as the illumination source. Light from the diode passes through a Ronchi ruling, a binary grating of etched parallel lines, which causes grid lines to be projected onto the model surface. A conventional RS-170 video camera is used to image the region of interest within 1/10000 second exposure time to effectively *freeze* model position. Images of the model in both wind-off and wind-on conditions are acquired and processed off-line to obtain the deformation profile. Instrument sensitivity is determined by the projected grid line pitch and the angle between the projector and receiver. PMI systems constructed at Langley use laser diode illumination to permit (a) simultaneous operation with other optical instrumentation techniques, (b) lights-on facility operation, and (c) high peak power to investigate large objects. However, any incoherent light source, including white light, can be used. PMI typically requires no surface preparation. The only surface requirement is that some amount of diffusely scattered light be collected by the CCD camera. In some cases, highly polished models would require painting.

Preliminary PMI Data
LaRC UPWT, HSR NCV Configuration



(a) PMI Projected grid lines, HSR NCV Wing



(b) PMI measured surface topology

The first Langley attempt at using PMI to measure model deformation of a fixed-wing aircraft occurred at the LaRC Unitary Plan Wind Tunnel in January, 1998. The model under investigation was a 1.675 %-scale HSR NCV configuration. Preliminary data and intermediate results are shown above for a single 1/10000 second exposure. Image (a) above is a raw PMI data image that has been dewarped to remove optical and perspective distortion. The projected grid lines are apparent. Further image processing of the image in (a) produces a surface topology as shown in image (b). Image (b) is an intermediate processing step, and is shown here only to demonstrate the type of information that can be obtained using PMI. To obtain wind-on model deformation data, the topology of the wing in its reference condition must be subtracted from image (b) above. Currently, image registration and scaling problems are causing difficulties at this stage of the data processing. Algorithms are currently under development to combat these problems and enhance data quality.

COMPARISON OF VMD AND PMI

VMD

- Operational
- 17 tests in 5 facilities
- Alpha sweeps only
- Targets at each semispan
- Data for discrete locations
- Rapid data acquisition
- Near real-time angles
- Rapid final data reduction
- No laser
- 1 window
- Model prep sometimes
- NASA LaRC, ARC

PMI

- Developmental
- 2 tests in 2 facilities
- Alpha & beta possible
- No targets
- Nearly continuous data
- Rapid data acquisition
- Real-time def. Contours
- May be days
- Laser may be used
- 2 windows usually
- Model prep sometimes
- NASA LaRC, DLR (ETW)

The VMD approach has been used to determine model deformation data for 17 tests in 5 NASA facilities over the last 2 years. The PMI approach under development has been used for 2 tests at 2 NASA facilities. While improvements and enhancements to both approaches are still underway, the VMD approach is more mature than the PMI approach for production wind tunnel testing. (The PMI system developed by DLR for the measurement of model deformation at the European Transonic Wind Tunnel (ETW) is also not currently ready for production testing.)

Developments continue on PMI due to the limitations of VMD, not suffered by PMI, such as: (1) data is limited to alpha sweeps only, (2) targets must be applied, and (3) reduced data is only available at discrete locations where targets are located. Both approaches have rapid data acquisition, but at the current developmental stage of PMI, VMD has much faster data reduction with near real time reduction of angles and rapid (in minutes) reduction for twist and bending once wind-off polars are completed. Although a laser is not required for PMI, it does provide operational advantages when selective camera filtering is used. This includes immunity to test section lighting and the capability of simultaneous operation with other optical instrumentation systems. The PMI projector normally requires a window port in addition to the window port required for the PMI camera. It is sometimes necessary to apply flat black paint on regions of the model where glints obscure targets for the VMD approach or to provide a sufficiently diffuse surface for PMI.

NASA FACILITIES DEFORMATION MEASUREMENTS

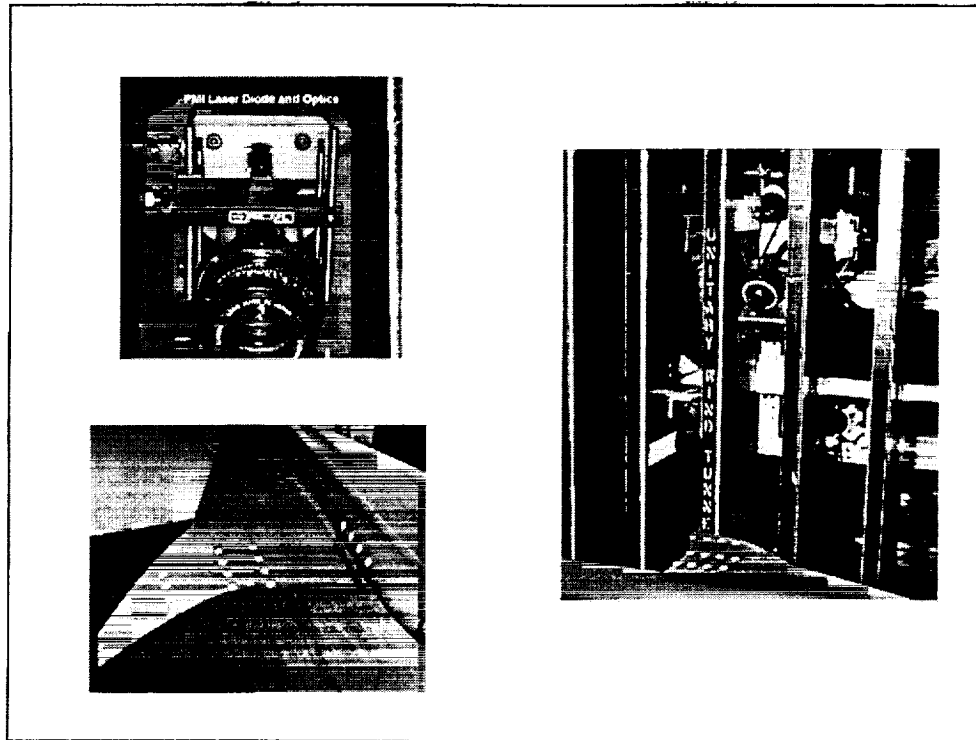
Langley

- **National Transonic Facility**
- **Transonic Dynamics Tunnel**
- **Unitary Plan Wind Tunnel**
- **16-Ft Transonic Tunnel**
- **14-by 22-Ft Subsonic Tunnel**

Ames

- **12-Ft Pressure Tunnel**

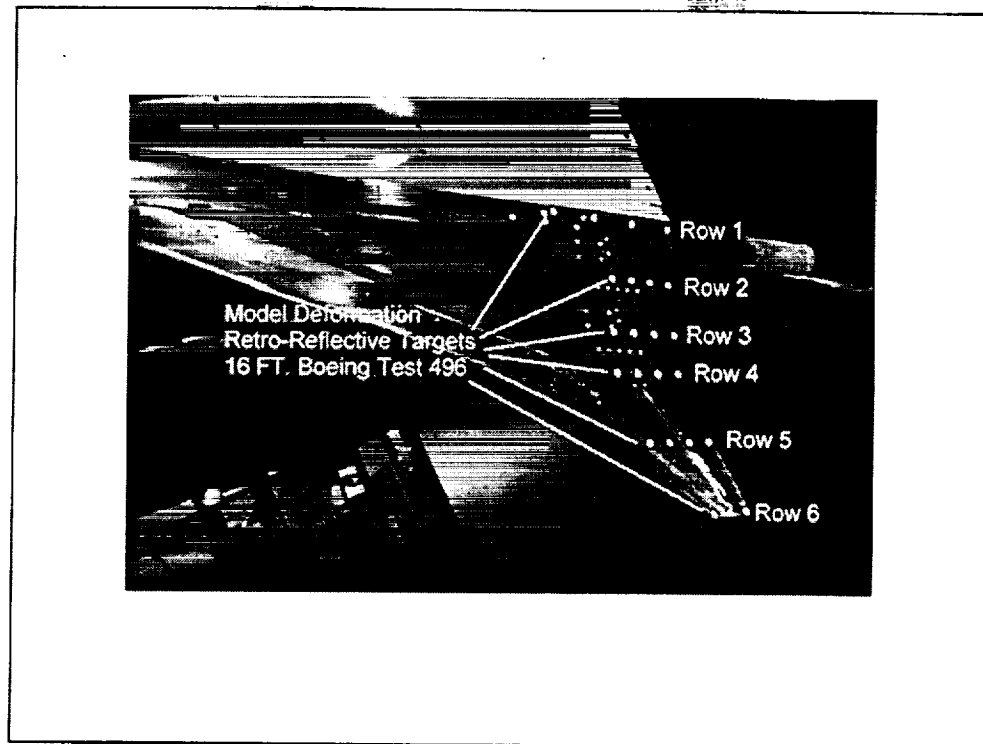
The PMI system has been used to measure rotorcraft blade dynamics at the 14-by 22-Foot Subsonic Tunnel and to measure deformation of an HSR model at the UPWT. Dedicated VMD systems are now operational in 5 tunnels at Ames and Langley. These facilities are the National Transonic Facility (NTF), Transonic Dynamics Tunnel (TDT), Unitary Plan Wind Tunnel (UPWT), and 16-Foot Transonic Tunnel (16-TT) at Langley and the 12-Ft Pressure Tunnel at Ames. Deformation measurements have been made on HSR models at all 5 of these facilities including sting mounted and post mounted full span models and sidewall and floor mounted semispan models. Each of these facilities presents unique challenges to the installation of measurement systems. The most difficult instrumentation challenges occur at the NTF where constraints imposed by operation in a high-pressure environment over a wide range of temperatures (+140 to -250 F) have had a significant impact on the continuing development, improvement, and optimization of instrumentation at the facility (particularly for the measurement of model deformation). For example, retroreflective tape targets have not yet been used at the NTF as in the other 4 facilities due to difficulties in locating a light source sufficiently close to the VMD camera in addition to concerns about the aerodynamic effects due to target thickness. Thus a special polished paint technique for targets has been developed and investigations continue on improved targeting schemes for the NTF.



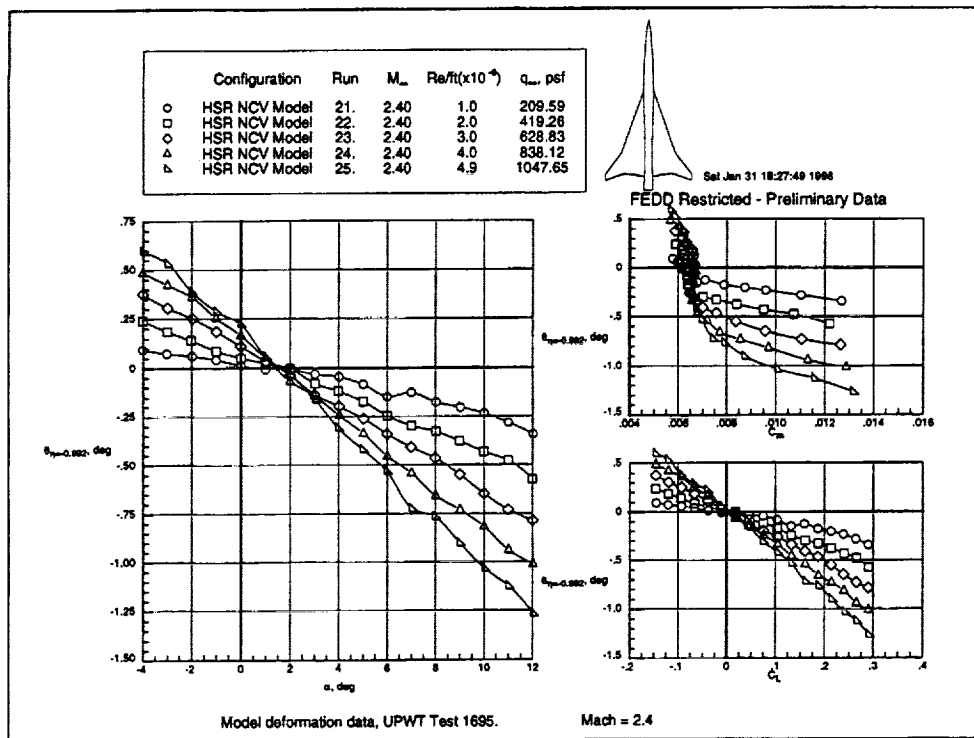
A recent test of the NCV model was conducted in test section #2 at the Langley Unitary Plan Wind Tunnel (test 1695). The primary purpose of the test was for advanced test technique development. Tests were conducted with the video model deformation (VMD) method, projection moiré interferometry (PMI) method, and Doppler global velocimetry (DGV) method. Data were taken for a number of runs throughout the test with simultaneous acquisition of VMD and PMI data. Toward the latter part of the test simultaneous VMD, PMI, and DGV data were acquired at 8 and 12 degree angle of attack. The upper left photograph shows the laser diode and optics of the PMI projector, mounted to the window webbing on the test section door opposite the PMI receiver and VMD camera. The photograph to the right shows the VMD camera with fiber optic ring light (lower) and PMI camera with filter (upper) mounted between the test section window webbing. The two cameras view the left wing of the NCV model which can be seen at the bottom of the right photograph. The mounting stand for the various DGV receivers can be seen in the right photograph behind the window webbing. Another view of the NCV model with retro reflective targets on the upper left wing and body is shown on the lower left. Targets were located on the body ($\eta = -0.084$) and at $\eta = -0.415$, -0.544 , -0.762 , and -0.992 along the wing span. The model was painted flat red to reduce potential specular reflections from the Doppler Global Velocimetry (DGV) system laser in order to improve the signal-to-noise ratio for the DGV measurements.



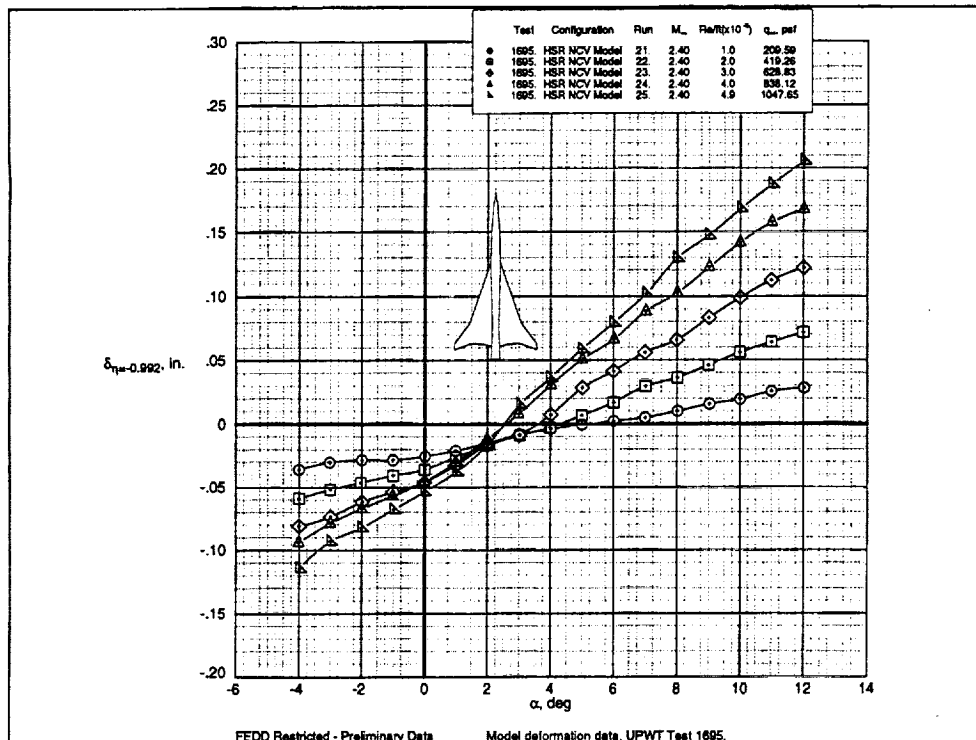
Prior to model installation, a test fixture was placed in the UPWT test section to conduct checkout and comparison tests of the VMD and PMI systems. A formal designed experiment developed by Richard DeLoach of the Experimental Testing Technology Division of NASA Langley was conducted to provide data to assess the relative and absolute performance of the two systems. The test fixture was aligned to be in the approximate location of the left wing of a model. Targets were applied at 5 semispan locations typical for HSR models at the UPWT. Precision accelerometers were used to measure the angle of attack and any accompanying roll of the test fixture which was mounted on a rotation stage and leveling mount. Two of the recently developed angle measurement systems (AMS) developed by the Experimental Testing Technology Division of NASA Langley were used to facilitate the angle measurements. Data were taken with both the VMD and PMI systems simultaneously over a set range of translations and pitch angles. A major concern for optical measurement systems at the UPWT is the large model translation in the flow direction as the pitch angle is changed. This large translation complicates the comparison of flow and no-flow data to determine wing twist and bending. The test fixture was mounted on vertical and horizontal translation stages in order to translate both in the flow direction and vertically to simulate typical motion of a model during testing at the facility. The amount of vertical and horizontal translation was set with gauge blocks.



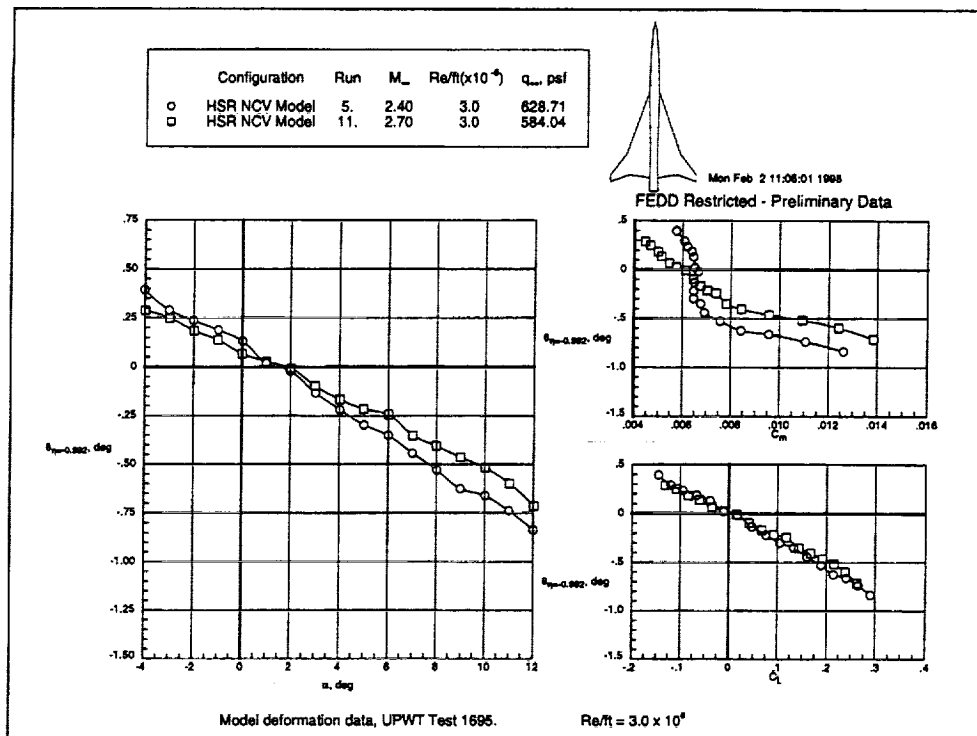
The photograph above shows retroreflective targets placed on the lower right wing of a TCA model at the Langley 16-Foot Transonic Tunnel. The lower surface of the left wing has pressure paint applied with black reference targets. At the Ames 12-Ft, Langley 16-Ft and Langley UPWT a new version of the VMD system, developed by the High Technology Corporation, has been used to track PSP reference targets (using UV light sources) at the same time as PSP data is being taken. The simultaneous acquisition of pressure paint and deformation data would reduce the amount of time required for testing, thus increasing wind tunnel productivity. Currently the low level of fluorescent light from the pressure paint causes poor contrast images on the VMD system, resulting in marginal target tracking robustness. Camera integration times longer than the standard 1/60 second may be necessary to improve the image contrast and hence the reliability of the target tracking. Developments to further unify various advanced optical test techniques is crucial to increased productivity, especially as the number of "competing" optical techniques for various wind tunnel measurements continues to increase.



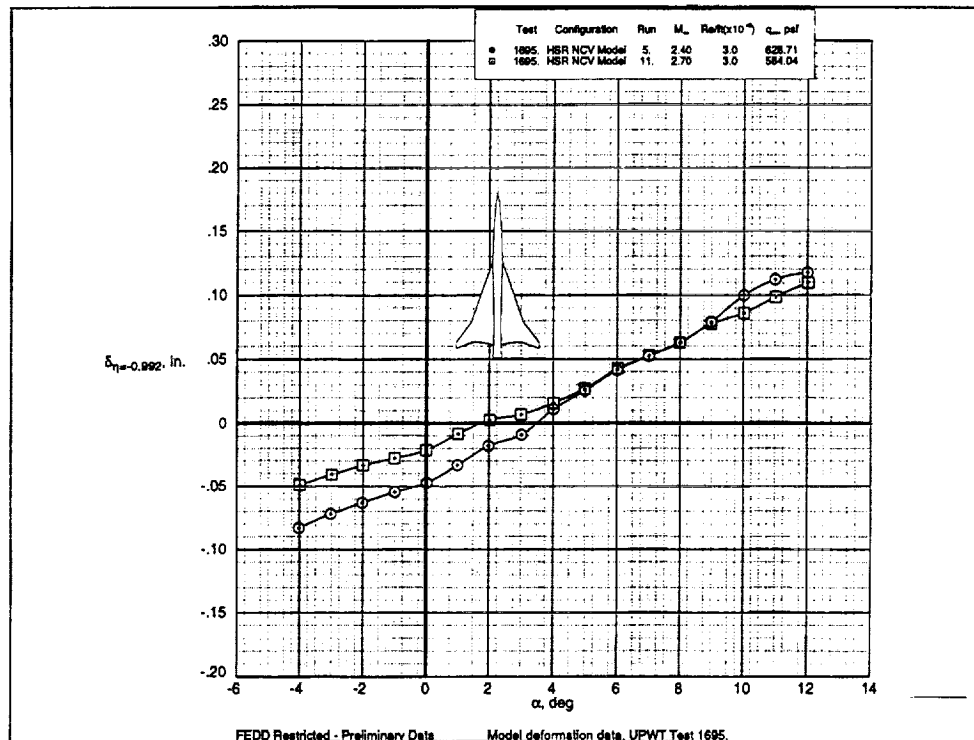
An HSR NCV model was recently tested (test 1695) at the Langley Unitary Plan Wind Tunnel test section #2. Data for the aerodynamically induced wing twist near the wing tip (-0.992 semispan) for Reynolds number sweeps at constant Mach number = 2.4 are plotted above versus alpha, C_L , and C_m . Reynolds number variations are obtained by changing the dynamic pressure, thus the plots above reflect the dynamic pressure effect on aeroelastic wing twist. The maximum wing twist of -1.25 deg at Mach 2.4 occurs at a Reynolds number of 4.9 million. The nearly linear change in twist as a function of alpha has been observed on a number of HSR models.



The vertical displacement near the tip corresponding to the previous plots is shown. For each Reynolds number case, the displacements are nearly equal at $\alpha \sim 2$ degrees with a magnitude of -0.017 inches. Note, however, that zero induced twist and equal twist coincide at approximately 1.5 degrees on the previous plot of wing twist versus angle-of-attack. One might expect that the displacement would be zero when the twist is zero. Whether this discrepancy is an indication of error has not been determined.

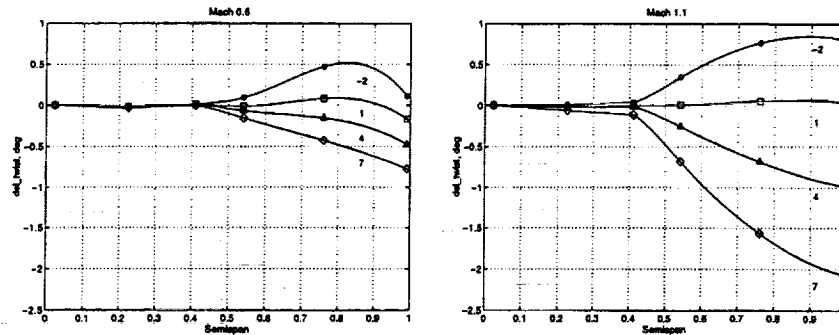


A comparison of the induced wing twist near the wing tip for Mach 2.4 and Mach 2.7 is plotted above for test 1695 at the Langley UPWT. The data also contains a small dynamic pressure effect which tends to increase induced twist for the Mach 2.4 case. However, this does not totally account for the increased twist with decreasing Mach number that has been observed for several different HSR models. Note the C_L plot de-emphasizes the induced twist differences while the differences are accentuated in the C_m plot.



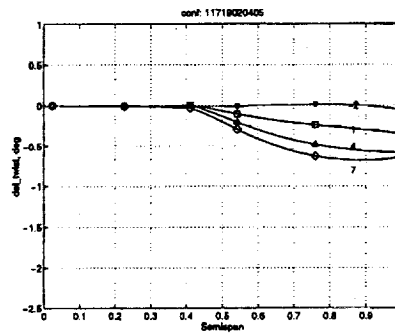
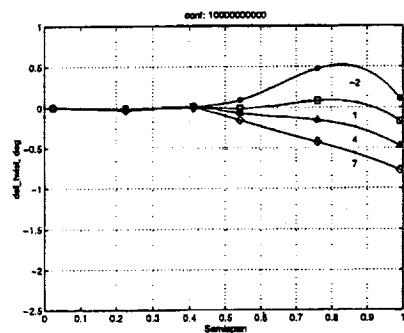
The vertical displacements near the tip corresponding to the twist plots from the previous page are shown above. Note that the zero displacement for the Mach 2.4 plot occurs at 3.5 deg alpha whereas the zero induced twist occurs at 1.5 deg alpha. The zero displacement and twist coincide for the Mach 2.7 data at 2 deg alpha. Comparisons of displacement and twist data may assist in uncovering potential discrepancies in the deformation data.

**TCA MODEL #5
LaRC 16-FT TEST 496
BASELINE CONFIGURATION**

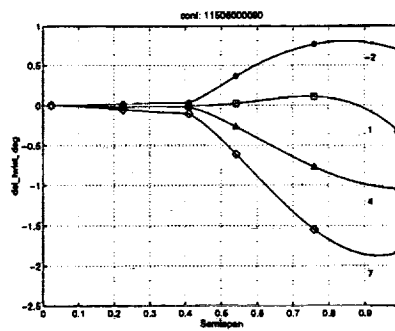
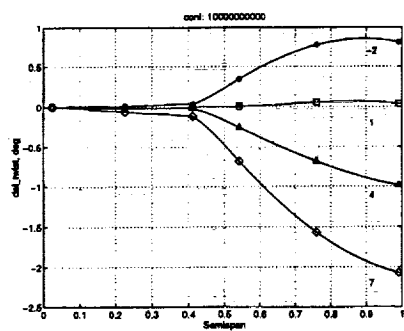


The data above shows load induced wing twist versus normalized semispan for the HSR TCA model #5 tested at Mach 0.6 and Mach 1.1. Testing was performed in the Langley 16-Foot Transonic Tunnel (Test 496). Data for the baseline configuration without deflected flaps is shown for $\alpha = -2, 1, 4$, and 7 degrees. Data were also taken at 0.9 Mach number. Data taken at the test section wall flat settings for the various Mach numbers indicate that the flat setting has little effect on the measured twist, but causes a zero shift in displacement of up to 0.07 inches that varies with semispan station. For the data presented here separate wind-off calibration runs were taken at the appropriate flat setting for each mach number. A comparison of the baseline configuration and configurations with leading and trailing edges deflected at Mach 0.6 and 1.1 for the test 496 are shown on the following plots. Again, the alphas shown are $-2, 1, 4$, and 7 degrees. Note that the smaller chord at the tip (semispan near 1) results in less resolution for angle measurements since the targets at the tip span less distance on the image plane.

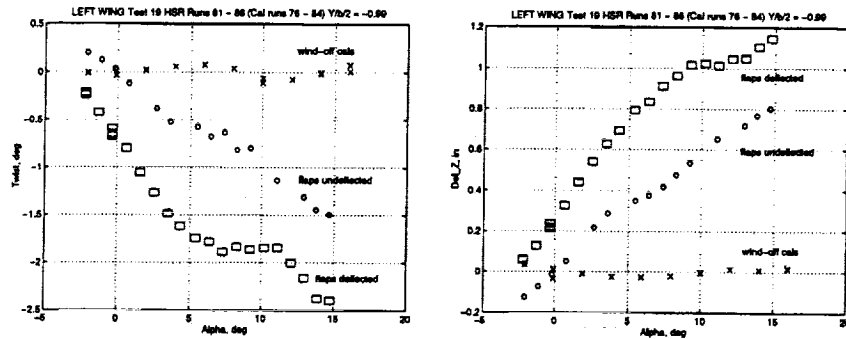
TCA MODEL #5
LaRC 16-FT TEST 496
MACH 0.6



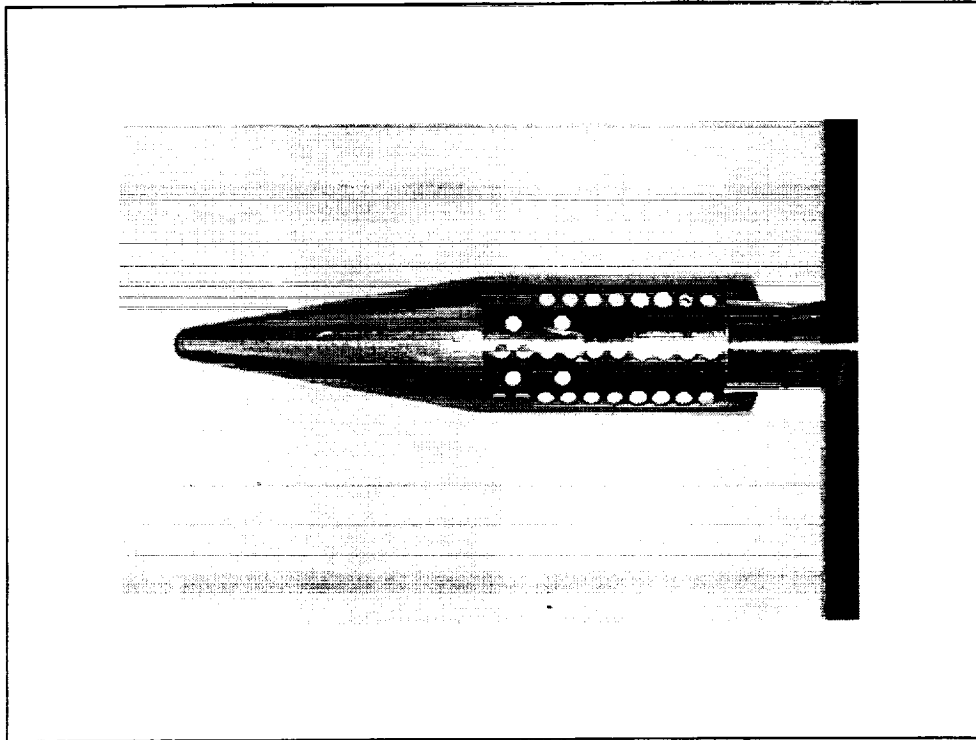
TCA MODEL #5
LaRC 16-FT TEST 496
MACH 1.1



**4% ARROW WING LOW SPEED HIGH LIFT MODEL
AMES 12-FT PRESSURE TUNNEL
MACH = 0.225, $Re = 8.51 \times 10^6$, $Q = 435$ PSF**



Aerodynamically induced wing twist near the wing tip (0.99 semispan) versus alpha for the 4% Arrow Wing HSR model at the Ames 12-Ft Pressure Tunnel is presented above. The change in vertical displacement, Z , versus alpha relative to wind-off is also presented. The Mach number was 0.225, the Reynolds number per foot was 8.51 million, and the dynamic pressure was 435 psf. Data for flaps deflected (squares) and undeflected (circles) are presented. Residuals from wind-off calibration runs (X) are also shown. Wind-off calibration runs use tunnel data for alpha which is not corrupted by sting bending calculations or dynamics associated with wind-on conditions that can lead to bias errors for inertial sensors mounted in the model. Polynomial fits are made to the calibration data to be applied to the wind-on data. The wind-off calibration runs provide an in situ angle calibration near the time that VMD data is taken. Wind-off calibration runs serve to remove the vertical translation that normally occurs due to the model being pitched. Wind-off calibration runs which bracket the wind-on runs also serve as a system stability check. Wind-off calibration runs are especially critical for facilities such as the National Transonic Facility where large temperature and pressure excursions may occur.



An experiment is ongoing at the National Transonic Facility to improve existing methods and develop new methods for applying targets that lessen their potentially negative effect on aerodynamic data. The calibration cone above has been tested at the facility (and will be tested again in April) with a variety of targets including polished paint applied directly to the surface. In addition milled targets have been tested with filler over white paint, retroreflective tape, fluorescent dye and filler mixture, and retroreflective paint. An advantage of milled targets, besides removing the step height, is that permanent targets are available that can be accurately determined with a 3-D coordinate measurement machine prior to testing. Subsequent tests with the model will then already have targets installed at known locations and at the same locations as previous tests. The time to install targets will be essentially eliminated during a test. If retroreflective tape is placed in milled locations, the step height of 0.004 inch is removed, but the surface roughness can be as large as 200 μ inches. There are retroreflective tapes with surface roughness down to 20 μ inches, but light return from these tapes is reduced. For polished paint targets applied directly to the wing surface there is no abrupt step (only a gradual rise to 0.0005 inch with surface roughness of 5 μ inches) compared to the tape targets without milling. Consideration should be given to retroreflective tape (or polished paint) milled targets for future HSR models where deformation measurements are required.

FUTURE WORK

VMD

- Tests at 5 NASA facilities
- Uncertainty analysis
- Robustness and speed
- Reduce and quantify target effects
- Simultaneous measurements with PSP

PMI

- Tests on actively controlled aircraft elements
- Uncertainty analysis and system characterization
- Image processing to increase speed and data quality
- Fully 3-D deformation (long term)

References

- Antcliff, R.R.: **Advanced Measurement Technology at NASA Langley Research Center**. Presented at the RTO (formerly AGARD) Symposium on Advanced Aerodynamic Measurement Technology, Sponsored by NATO 22 – 25 September 1997, Seattle, Washington To be published in CP-601, pp. 2-1 to 2-12.
- Burner, A. W., Wahls, R. A., Owens, L. R., and Goad, W. K.: **Model Deformation Measurement Technique - NASA Langley HSR Experiences**. Presented at the 1st NASA/Industry High Speed Research Configuration Aerodynamics Workshop, Hampton, VA, Feb. 27 - 29, 1996. published in First NASA/Industry High-Speed Research Configuration Aerodynamics Workshop NASA CDDP-1002 (HSR restricted-LEED Conference Proceedings) July 1996 pp 561 - 578.
- Erickson, G. E., Burner, A. W., DeLoach, R.: **Pressure-Sensitive Paint and Model Deformation Systems at the NASA Langley Unitary Plan Wind Tunnel** Presented at the 1997 HSR Aerodynamic Performance Workshop, Hampton, VA, Feb. 25 - 28, 1997. published in NASA CDDP (HSR restricted-LEED Conference Proceedings).
- Burner, A. W.: **Model Deformation Measurements at NASA Langley Research Center**. Presented at the RTO (formerly AGARD) Symposium on Advanced Aerodynamic Measurement Technology, Sponsored by NATO 22 – 25 September 1997, Seattle, Washington To be published in CP-601, pp. 34-1 to 34-9.
- Fleming, G.A., and Gorton, S.A.: **Measurement of Rotorcraft Blade Dynamics using Projection Moiré Interferometry**, to be presented at the Third International Conference on Vibration Measurements by Laser Techniques, June 16-19, 1998, Ancona, Italy.



Effect of Aeroelasticity on the Aerodynamic Performance of the TCA

Geojoe Kuruvila

Peter M. Hartwich

Myles L. Baker

**Configuration Aerodynamics
The Boeing Company, Long Beach**

**HSR Airframe Technical Review
Los Angeles, California
February 9-13, 1998**



This page is intentionally left blank.

Effect of Aeroelasticity on the Aerodynamic Performance of the TCA

Geojoe Kuruvila
Peter M. Hartwich
Myles L. Baker

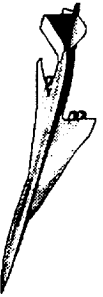
The Boeing Company
Long Beach, California 90807-5309

This paper investigates the effect of static aeroelasticity on the aerodynamic performance of the TCA in the wind-tunnel and in flight. The first part of the paper addresses the impact of wind-tunnel model deformation on the measured and predicted aerodynamic performance of the TCA. The measured model deformations are lofted on to the OML and analyzed using CFD. The results are compared with the wind-tunnel data. The second part of the paper investigates the change in shape and performance of the TCA, during supersonic cruise-climb, due to static aeroelastic effects, using nonlinear aerodynamics and structural interactions. The TCA OML is assumed to be the shape at mid-cruise. Using appropriate correction terms, the need to explicitly know the "jig shape" is alleviated.

Outline

There are two parts to this paper. The first part addresses the impact of wind-tunnel model deformation on the measured aerodynamic performance of the TCA. In the second part, the change in performance of the TCA during supersonic cruise, due to static aeroelastic deformation, is investigated using a nonlinear CFD tool.

Outline



High Speed Aerodynamics, Long Beach

- Part I: Aeroelastic effects in wind-tunnel
 - Objective
 - Approach
 - Results
 - Summary
- Part II: Aeroelastic effects in flight
 - Objective
 - Approach
 - Results
 - Summary



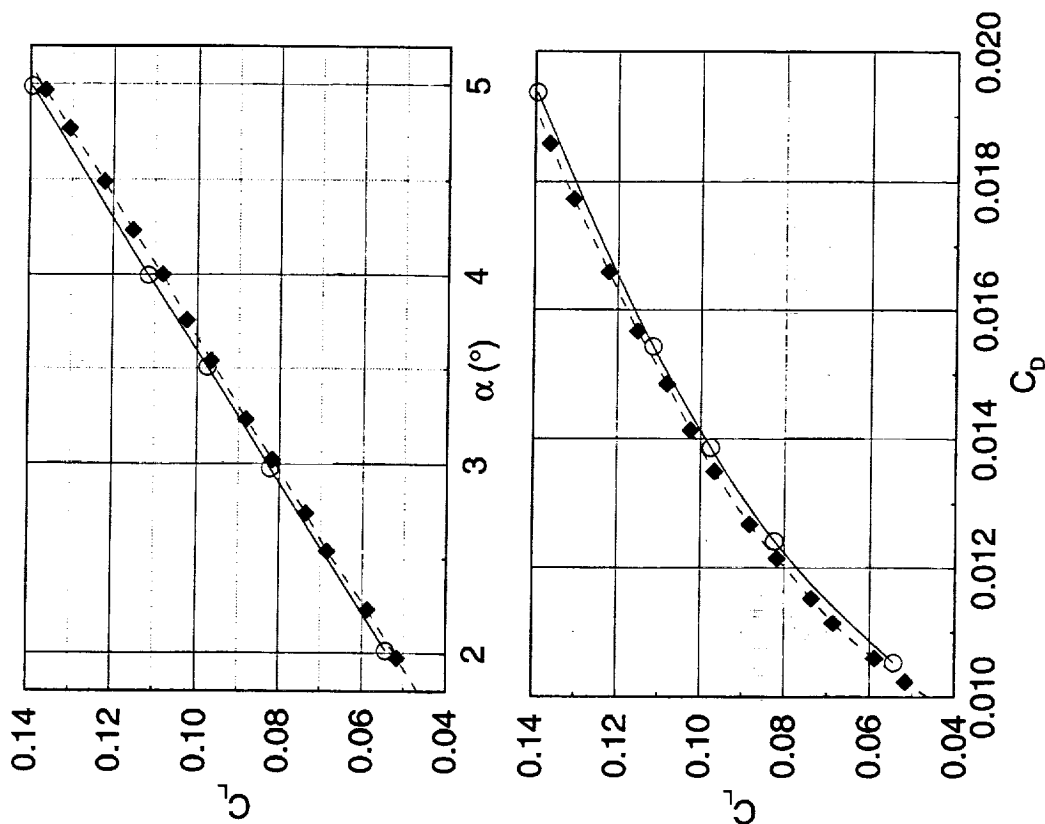
Aeroelastic Effects in Wind-Tunnel

In the HSR program, aerodynamic performances of several HSCT configurations have been predicted using CFD and wind-tunnel test data. The comparison of these data shows discrepancies. Typically, the drag coefficient, C_D , is off by about 3 to 5 counts, the lift-curve slope has a shift and the pitching moment trends do not agree well. These discrepancies may be due to wind-tunnel measurement uncertainties and/or inaccurate CFD simulations. One such uncertainty is due to the aeroelastic effects; most CFD analyses assume a rigid configuration while the model undergoes deformation in the wind-tunnel due to aerodynamic loads.

Aeroelastic Effects in Wind-Tunnel

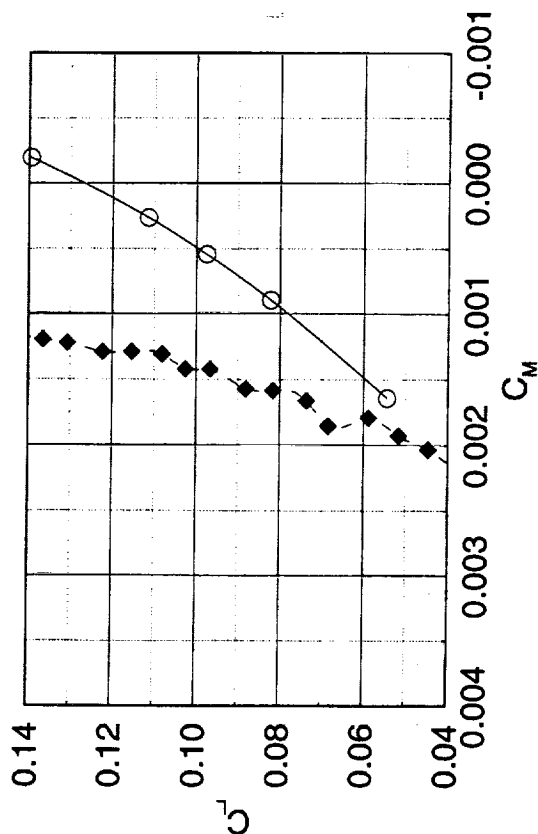


High Speed Aerodynamics, Long Beach



TCA Model 2a W/B/N/D
 $M_\infty=2.4$, $Re_c=6.36 \times 10^6$

—○— Rigid (CFL3D-NS)
 - - -◆- - - UPWT 1671/49



Objective

The objective of this study is to determine the contribution of the wind-tunnel model deformation to the discrepancy between wind-tunnel data and CFD predictions.

Objective

High Speed Aerodynamics, Long Beach

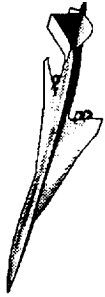


- Determine the impact of wind-tunnel model deformation on the measured aerodynamic performance of the TCA

Approach

First, the deformations of the TCA Model 2a wing/body/nacelle/diverter (W/B/N/D) configuration, at several angles-of-attack, were measured in the Unitary Plan Wind Tunnel (UPWT) at $M_\infty = 2.4$ and $Re_c = 6.36 \times 10^6$. The deformations measured for each of these angles-of-attack were then lofted onto the baseline TCA OML. Navier-Stokes analyses using CFL3D were performed on each of the deformed geometries and the results were compared with the baseline solution and wind-tunnel data.

Approach



High Speed Aerodynamics, Long Beach

- Measure the deformation
 - 1.675% TCA Model 2a
 - UPWT test
 - $M_{\infty}=2.4$, $Re_c=6.36 \times 10^6$
- Loft deformations onto the baseline TCA OML
- Perform CFD analyses of the deformed geometries
- Compare results with the baseline solution and wind-tunnel data

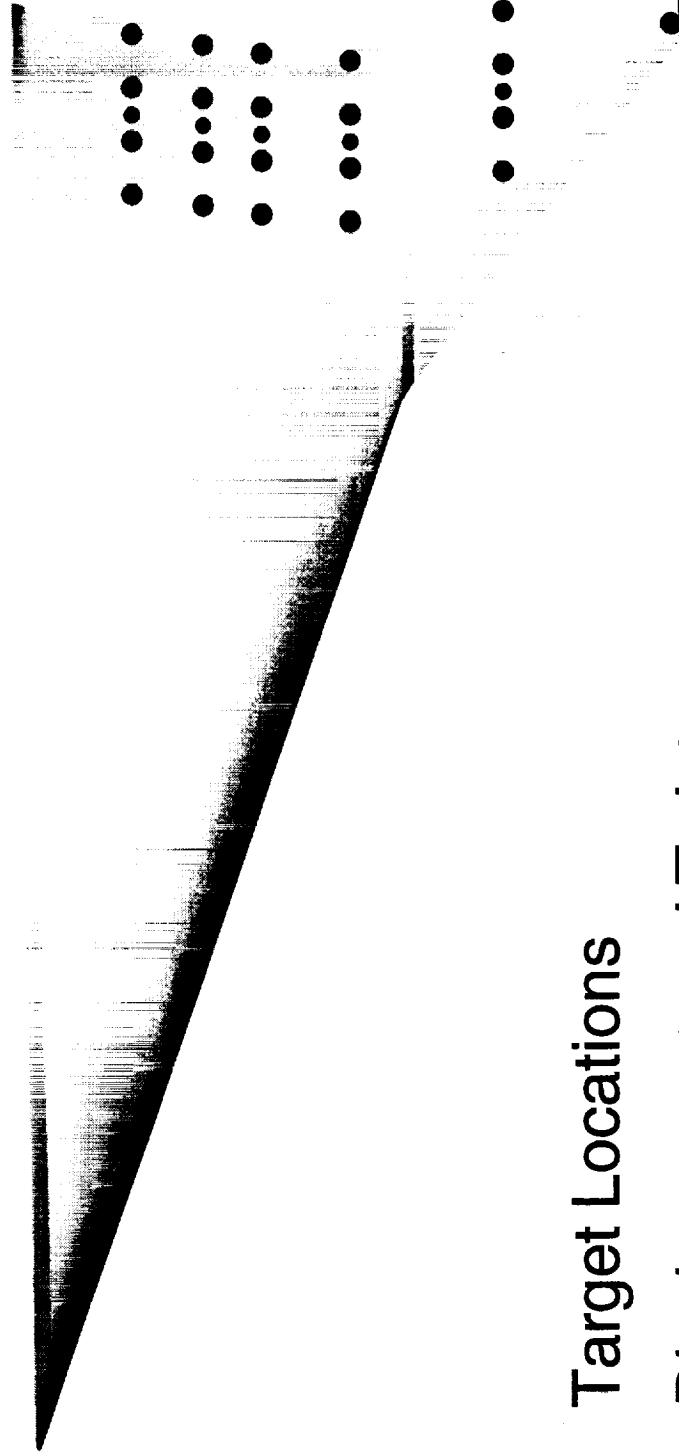
Model Deformation Measurement

The deformation of the model was measured using the Video Model Deformation (VMD) system at NASA Langley Research Center. For VMD measurements, target dots are placed on the model; indicated by the green dots. Images of these targets with wind-off and wind-on conditions are processed and the data is reduced to a set of displacements and twists at the locations indicated by the red dots. The spread of dots on the model is limited by the field of view into the tunnel. Changes in wing camber and deformation of the fuselage were assumed to be negligible.

Model Deformation Measurement



High Speed Aerodynamics, Long Beach



- Target Locations
- Displacement and Twist

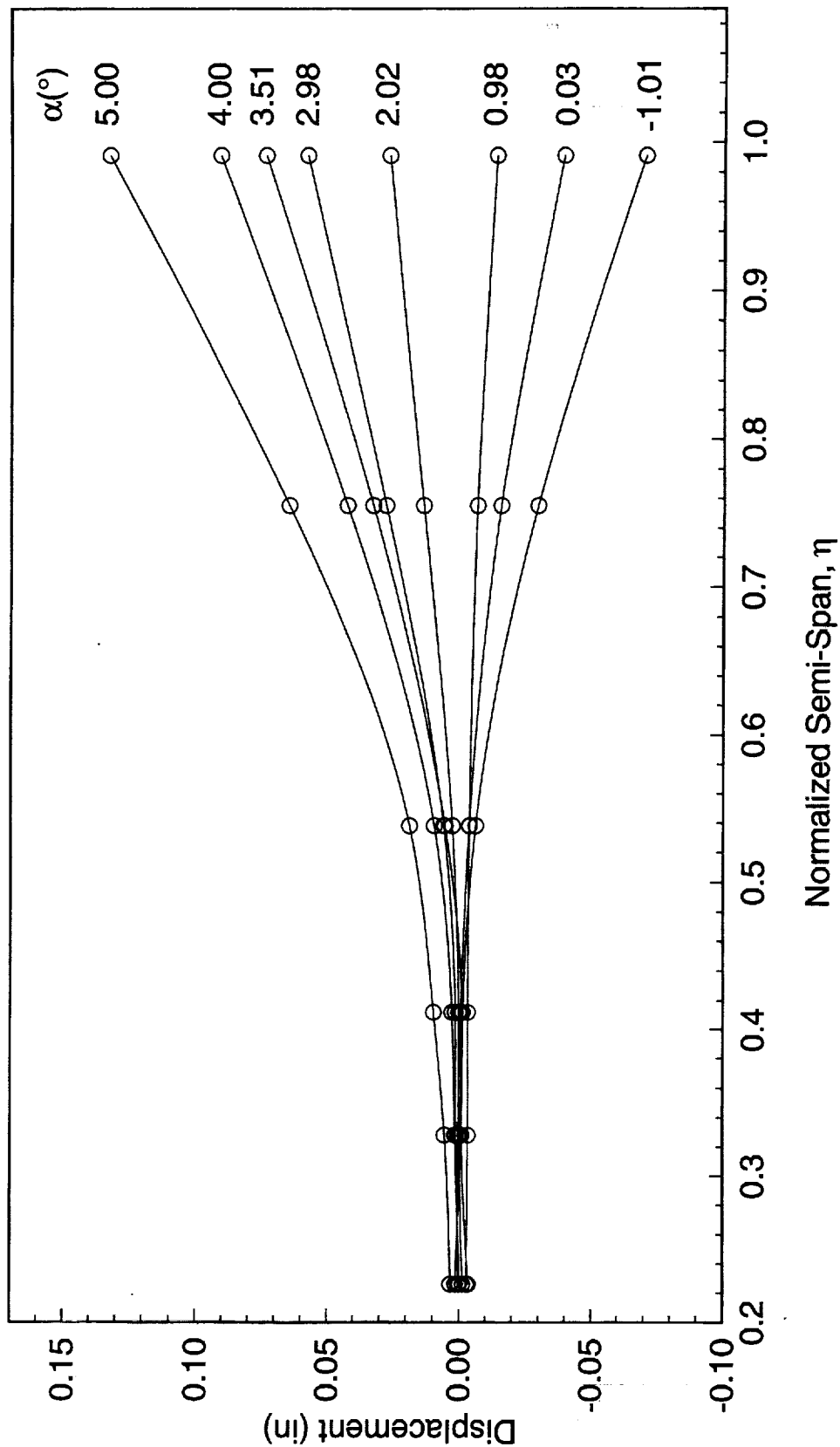


Measured Vertical Wing Displacement

The wing vertical displacements of the TCA Model 2a W/B/N/D configuration, measured during run 1671/85, in the UPWT at $M_\infty = 2.4$ and $Re_c = 6.36 \times 10^6$, are shown. At an angle-of-attack of 5° , the wing-tip deflection is about 0.14 inches. The reason for the crisscross of the data in the inboard wing is not clear. These displacements were interpolated using cubic splines and lofted onto the TCA OML. The use of 3rd order polynomials for interpolation is consistent with the behavior of a cantilever beam bending under load.

In these measurements, the change in camber due to aeroelasticity was assumed to be negligible. Also, the deformation of the fuselage was not measured.

Measured Vertical Wing Displacement, TCA Model 2a W/B/N/D Configuration UPWT Run 1671/85, $M_\infty=2.4$, $Re_c=6.36 \times 10^6$



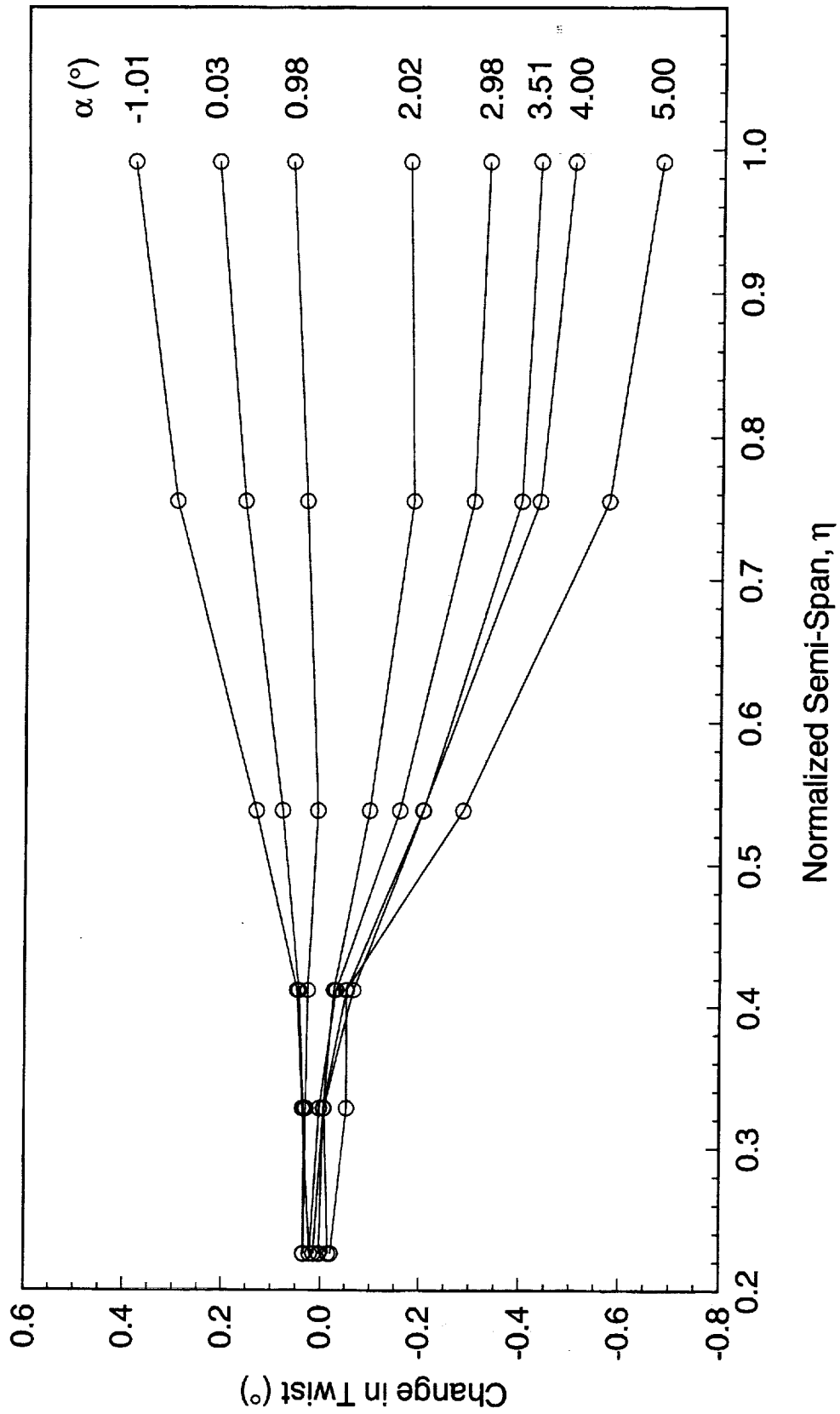
Measured Wing Twist Change

The changes in wing twist of the TCA Model 2a W/B/N/D configuration, measured during run 1671/85, in the UPWT at $M_\infty = 2.4$ and $Re_c = 6.36 \times 10^6$, are shown. At an angle-of-attack of 5° , the wing-tip twists about -0.7° . Again, the reason for the crisscross of the data in the inboard wing is not clear. These twists were interpolated linearly and lofted onto the TCA OML. Linear interpolation is consistent with the behavior of a cantilever beam under torsion.

In these measurements, the change in camber due to aeroelasticity was assumed to be negligible. Also, the deformation of the fuselage was not measured.

Measured Wing Twist Change, TCA Model 2a W/B/N/D Configuration

UPWT Run 1671/85, $M_\infty=2.4$, $Re_c=6.36 \times 10^6$



Geometry and Grid Perturbation

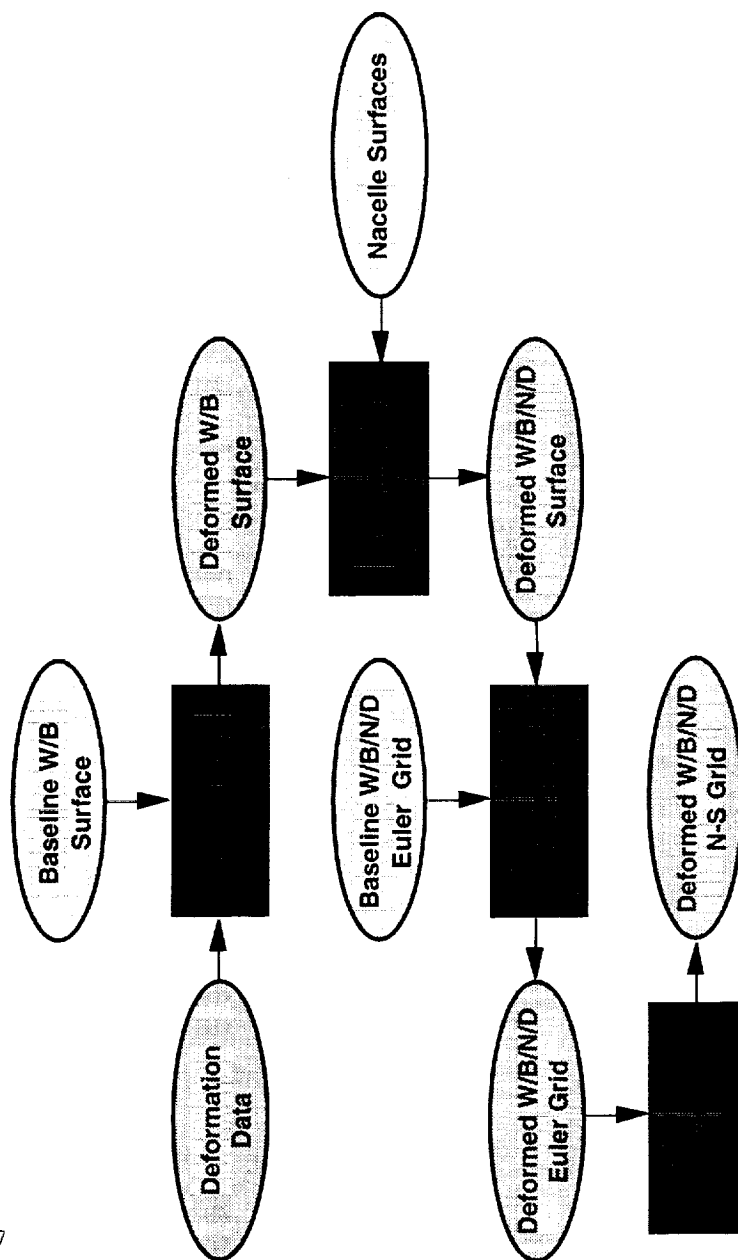
The flow chart shows the process of lofting the measured deformations onto the TCA baseline OML and obtaining a Navier-Stokes grid. This is accomplished in four steps using a suite of codes (represented by the rectangles) connected together using shell scripts. First, the measured deformations are lofted onto the baseline wing/body (W/B) surface. Next, the nacelles are installed on the perturbed W/B surface. The nacelles are allowed to move with the wing. The perturbed wing/body/nacelle/diverter (W/N/D/B) surface along with the baseline W/B/N/D Euler grid is fed to a grid perturbation code (CSCMDO) to obtain the perturbed W/B/N/D Euler grid. Finally, this grid is enriched and clustered to obtain the Navier-Stokes grid.

Starting with a baseline W/B/N/D Euler grid, the time to obtain a perturbed W/B/N/D Navier-Stokes grid is about 15 minutes of wall clock time.

Geometry and Grid Deformation



High Speed Aerodynamics, Long Beach



Process time \approx 15 minutes per angle-of-attack



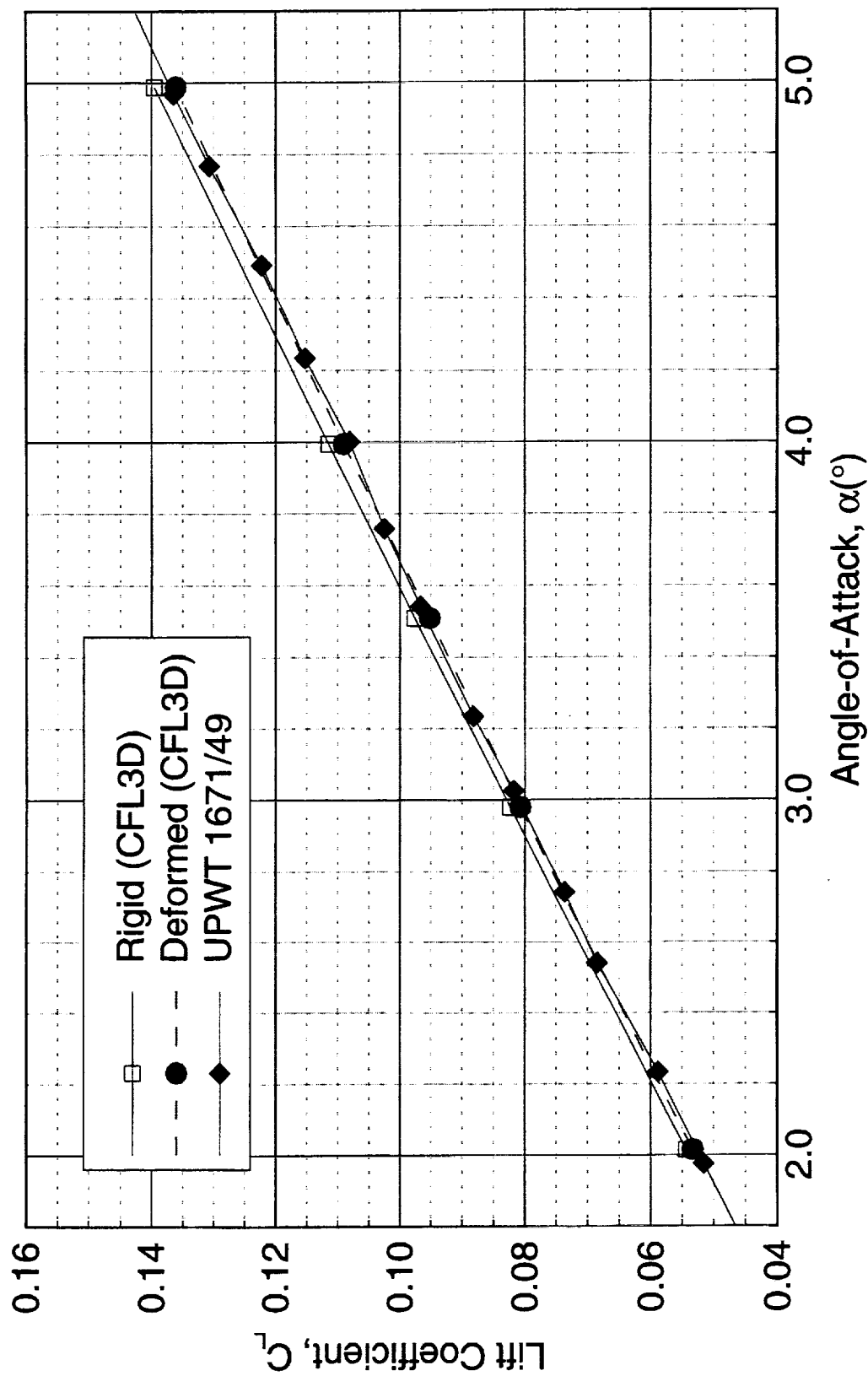
Effect of Deformation, TCA Model 2a W/B/N/D Configuration

The effects of deformation, due to aeroelasticity, on the performance of TCA Model 2a W/B/N/D configuration, at $M_\infty = 2.4$ and $Re_c = 6.36 \times 10^6$, are shown in the next four charts. The Navier-Stokes results obtained using the deformed configurations are compared with the ones obtained for the rigid configuration and wind-tunnel data.

The lift curve slope of the deformed configurations agrees well with that of the test data. At a positive angle-of-attack, the outboard wing unloads reducing the overall lift. Consequently, the pitching moment shows the most significant effect. Due to the unloading of the outboard wing, there is a nose-up pitching moment. The measured and the computed pitching moments agree well when the aeroelastic deformation of the wind-tunnel model is taken into account. The drag polar shows that there is no significant change in drag at a fixed lift due to aeroelastic effects. The unloading of the outboard wing can be easily seen in the pressure cuts shown. However, it is difficult to judge the agreement between the measured and computed pressure of the deformed geometries.

Effect of Deformation, TCA Model 2a W/B/N/D Configuration

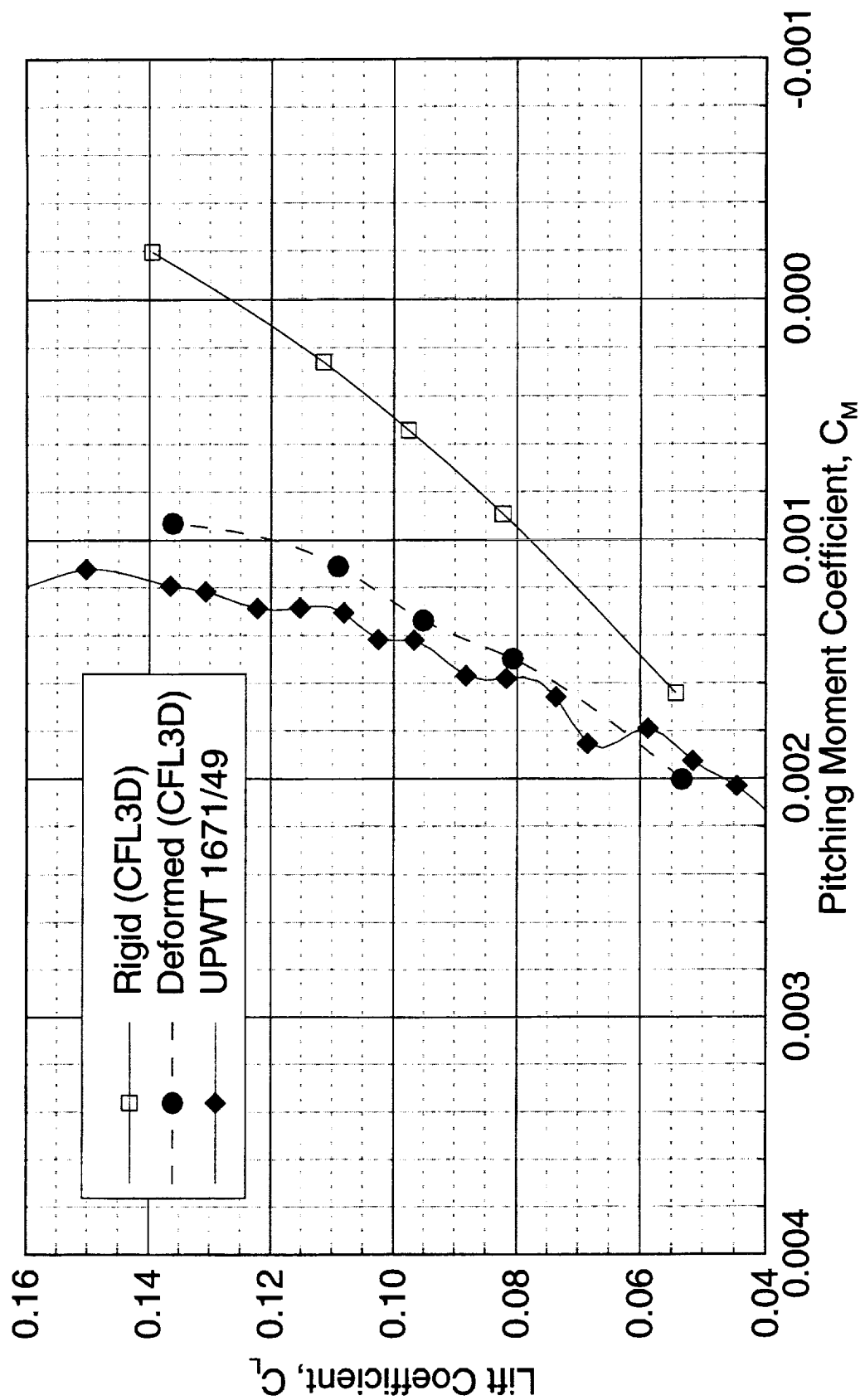
CFL3D N-S (B-L) Solutions and Wind-Tunnel Data, $M_\infty=2.4$, $Re_c=6.36 \times 10^6$



This page is intentionally left blank.

Effect of Deformation, TCA Model 2a W/B/N/D Configuration

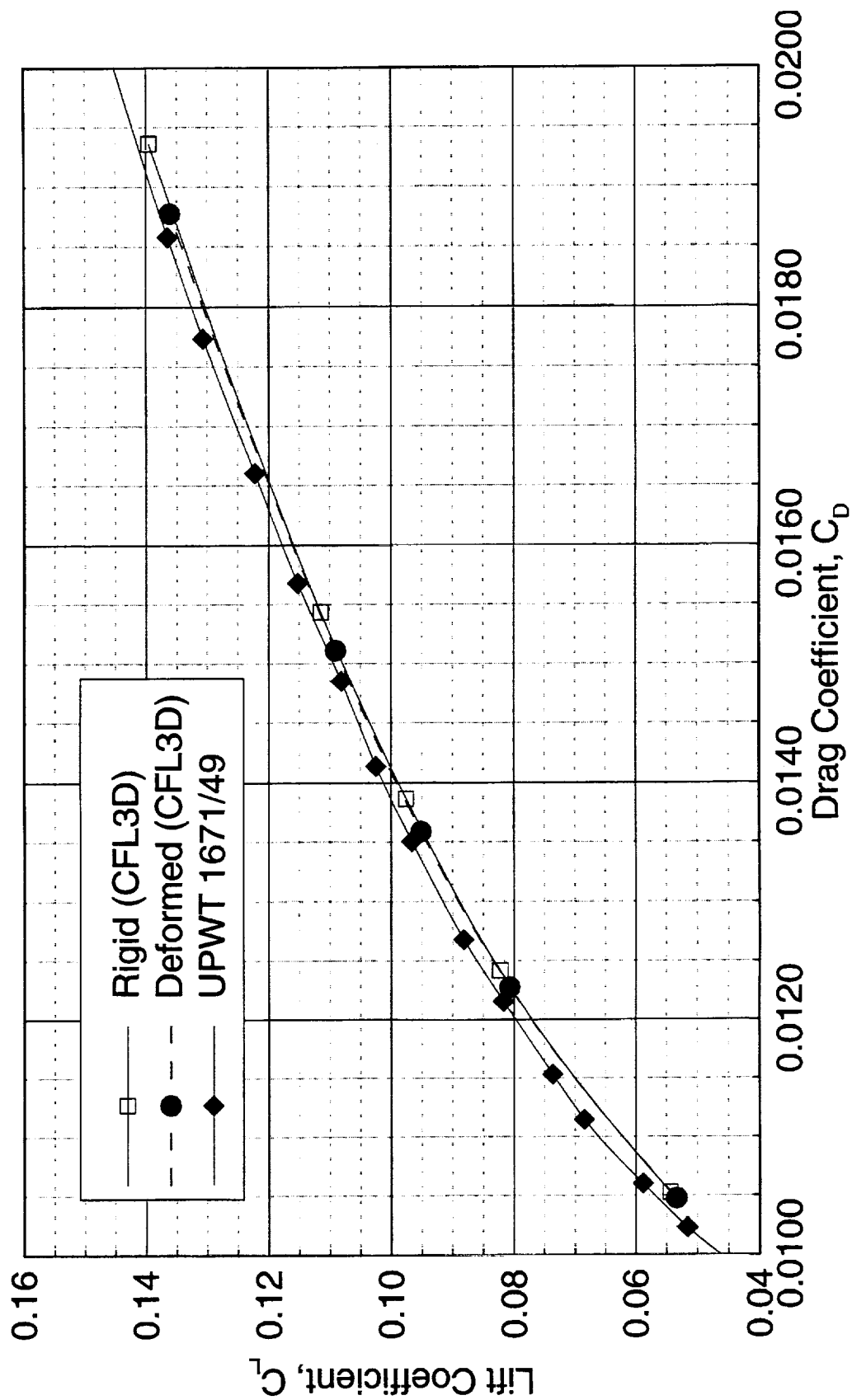
CFL3D N-S (B-L) Solutions and Wind-Tunnel Data, $M_\infty=2.4$, $Re_c=6.36 \times 10^6$



This page is intentionally left blank.

Effect of Deformation, TCA Model 2a W/B/N/D Configuration

CFL3D N-S (B-L) Solutions and Wind-Tunnel Data, $M_\infty=2.4$, $Re_c=6.36 \times 10^6$

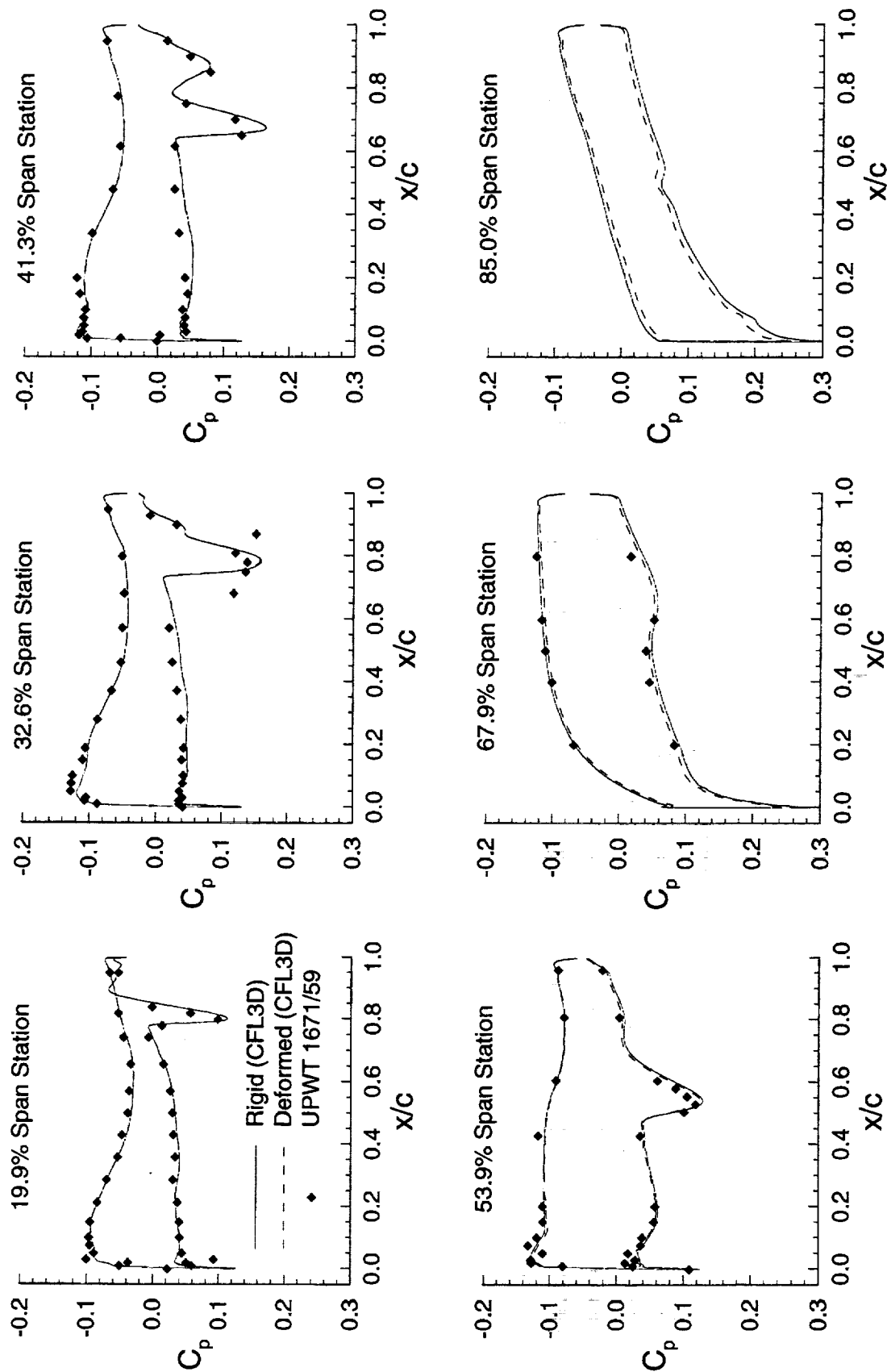


This page is intentionally left blank.

Effect of Deformation on TCA Model 2a W/B/N/D Configuration

CFL3D N-S (B-L) Solutions and Wind-Tunnel Data, $M_\infty=2.4$, $Re_c=6.36 \times 10^6$

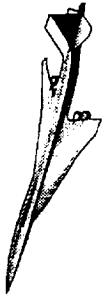
$\alpha=3.5^\circ$, $C_L \approx 0.10$



Summary

From this study, clearly, most of the discrepancies between wind-tunnel data and CFD on the lift curve and the pitching moment of the TCA at $M_\infty = 2.4$ are due to aeroelastic effects. The drag polar shows that the impact of aeroelasticity on the aerodynamic performance is negligible. However the change in pitching moment could affect the trim drag. The discrepancies between wind-tunnel data and CFD in the drag polar may be due to uncertainties in trip drag, turbulence modeling, etc.

Summary



High Speed Aerodynamics, Long Beach

- Most of the discrepancies between wind-tunnel data and CFD in the lift curve and the pitching moment of the TCA Model 2a at $M_\infty=2.4$ are due to the aeroelastic effects
- Negligible aeroelastic effects on the performance

Aeroelastic Effects in Flight

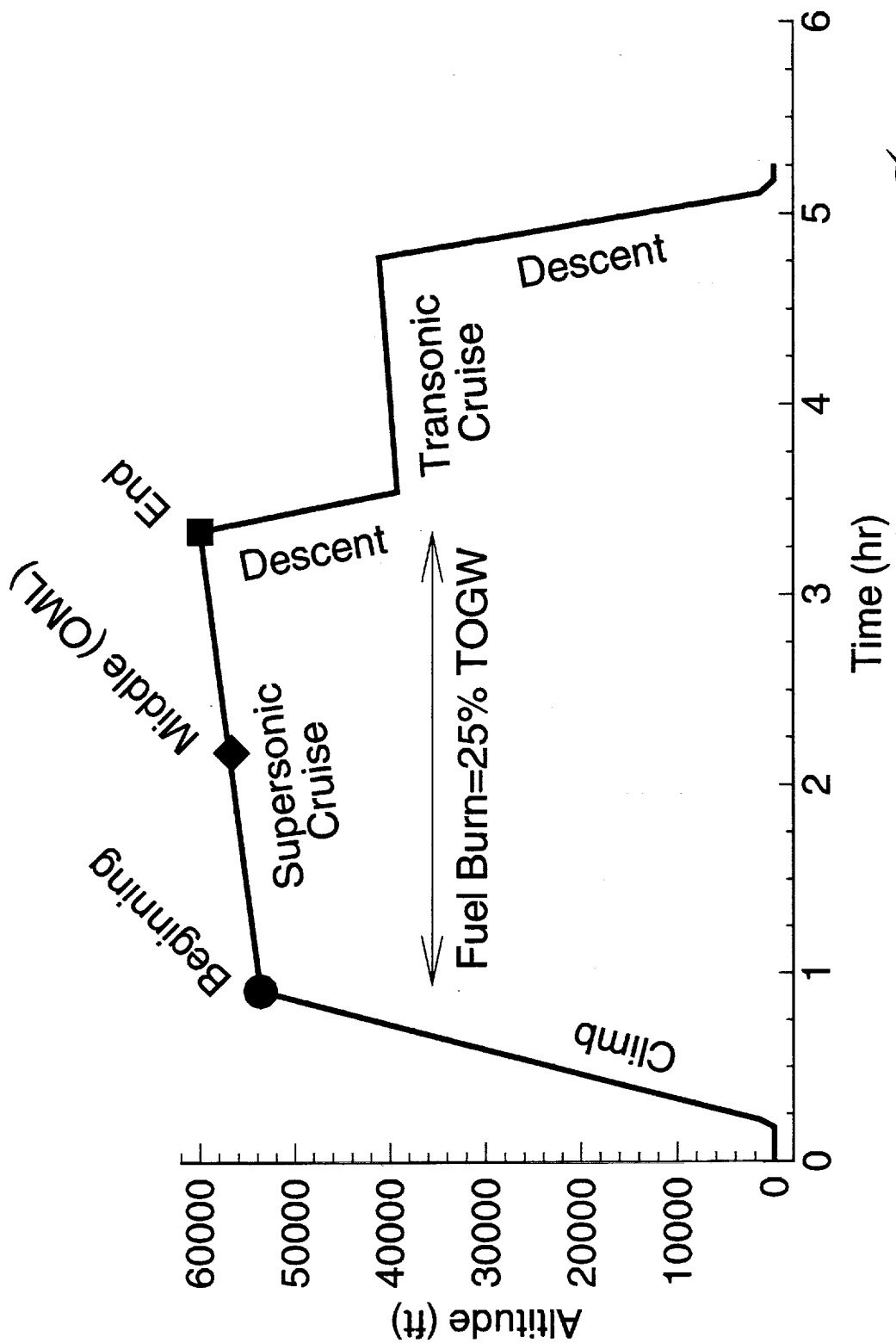
The TCA mission profile is shown. The baseline OML is assumed to be the shape of the airplane at mid supersonic cruise. During the supersonic cruise segment, the airplane cruises from an altitude of 53,600 ft. to 60,040 ft. and burns about 186,000 lbs. of fuel, about 25% of TOGW. The effect of aeroelasticity, on the performance of the TCA, due to the change in weight and dynamic pressure is to be determined.

Similarly, the effect of aeroelasticity on the TCA during the transonic cruise segment also is to be determined.

Aeroelastic Effects in Flight



High Speed Aerodynamics, Long Beach



Objective

The objective of this task is to apply a nonlinear methodology to determine the effects of static aeroelasticity on the aerodynamic performance of an HSCT. While the OML at a cruise point is known, the "jig shape" of the airplane is not known. Given the OML at a cruise point, this method allows the computation of the shape and hence its performance at a different cruise point without explicit knowledge of the "jig shape".

As a first application, this methodology was used to determine the change in shape and performance the TCA, from the beginning to the end of supersonic cruise due to static aeroelastic effects. The shape of the airplane at mid-cruise is assumed to be the TCA OML.

Objective



High Speed Aerodynamics, Long Beach

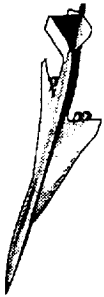
- Apply a nonlinear method to determine the effects of aeroelasticity on the aerodynamic cruise performance of the TCA
 - From beginning to end of supersonic cruise
 - Shape at mid-cruise point is the TCA OML
 - “Jig shape” is not known

Approach

The aeroelastic interactions of the TCA are modeled using the structural equations of motion. The structural responses are modeled using the appropriate number of elastic mode shapes. These mode shapes for the TCA were obtained from a NASTRAN structural FEM model. The aerodynamic forces are obtained by solving the Euler or Navier-Stokes equations. The fact that the "jig shape" is unknown is accounted for by appropriately correcting the right-hand-side of the structural equations of motion. This correction term, also referred to as the "sky-hook" term, is made-up of the effects due the change in force and the change in mass, between the known cruise point and the cruise point of interest.

CFL3D.AE-BA solves the coupled aero/structures model to determine the shape of the airplane and its performance at varying flight conditions.

Approach

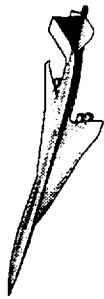


High Speed Aerodynamics, Long Beach

- Use CFL3D.AE-BA to determine the effective shape and aerodynamic performance at the various flight conditions
 - Developed under HSR Task 26 (Materials & Structures)
 - Needs mode shapes
 - Uses “sky-hook” formulation to model jig-shape correction
- Obtain mode shapes from a structural FEM model (NASTRAN)

Aeroelastic Model

Only the vertical displacement of the structure is considered in this study. The generalized amplitude, q_i , of the i^{th} mode shape is obtained by solving the equation of structural motion shown below, where, m_i is the generalized mass, c_i the generalized damping, k_i the generalized stiffness and Q_i the generalized aerodynamic force. The deformation of the structure, in the vertical direction, is given by the summation of the first N mode shapes, h_i , times the corresponding amplitudes, q_i . It is assumed that the aerodynamic frequencies involved in the problem are covered by the frequencies of the N mode shapes. The pressure coefficient, C_p , for computing the generalized forces are obtained by solving the governing equations of the flowfield (Euler or Navier-Stokes equations).



Aeroelastic Model

High Speed Aerodynamics, Long Beach

- Equations of structural motion

$$m_i \ddot{q}_i + c_i \dot{q}_i + k_i q_i = Q_i$$

- Mode shapes

$$\delta(x, y, t) = \sum_{i=1}^N q_i(t) h_i(x, y)$$

- Generalized aerodynamic force

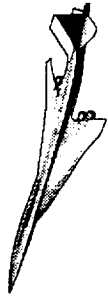
$$Q_i = -\frac{1}{2} \rho_{\infty} U_{\infty}^2 \int_S C_p h_i(x, y) ds$$



Sky-Hook Formulation

Since the objective is to find the static aeroelastic deformation, damping terms are neglected. Therefore, for each mode, the equations of motion at any two cruise points can be written as shown. The stiffness of the structure does not change. However, the mass changes due to fuel-burn. The acceleration due to gravity is denoted by g . The difference of these two equations gives an equation for the change in amplitude, δq_i , from cruise point 1 to 2. The correction term, $Q_{i1} + (m_{i2} - m_{i1})g$, referred to as the "sky-hook" term, alleviates the need to know the "jig-shape".

Sky-Hook Formulation



High Speed Aerodynamics, Long Beach

- At cruise point 1

$$k_i q_{i1} = Q_{i1} - m_{i1}g$$

- At cruise point 2

$$k_i q_{i2} = Q_{i2} - m_{i2}g$$

- Change from point 1 to 2

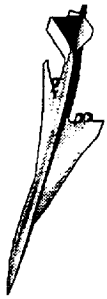
$$k_i \delta q_i = Q_{i2} - [Q_{i1} + (m_{i2} - m_{i1})g]$$

$$\delta q_i = q_{i2} - q_{i1}$$

CFL3D.AE-BA

CFL3D.AE, the aeroelastic version of CFL3D, was developed at NASA Langley Research Center. It was further developed and improved at Boeing Long Beach and named CFL3D.AE-BA (BA stands for the Boeing stock symbol). CFL3D.AE-BA solves the coupled aero/structures model to determine the shape and its performance at varying cruise conditions.

CFL3D.AE-BA



High Speed Aerodynamics, Long Beach

- Compute solution at Point 1
 - Compute “sky-hook” terms, $Q_{i1} + (m_{i2} - m_{i1})g$
 - do
 - Update generalized forces
 - Predict generalized displacements
 - Perturb grid using FlexMesh
 - Update metrics & cell volumes
 - Update flow solution
 - Correct generalized displacements
- enddo

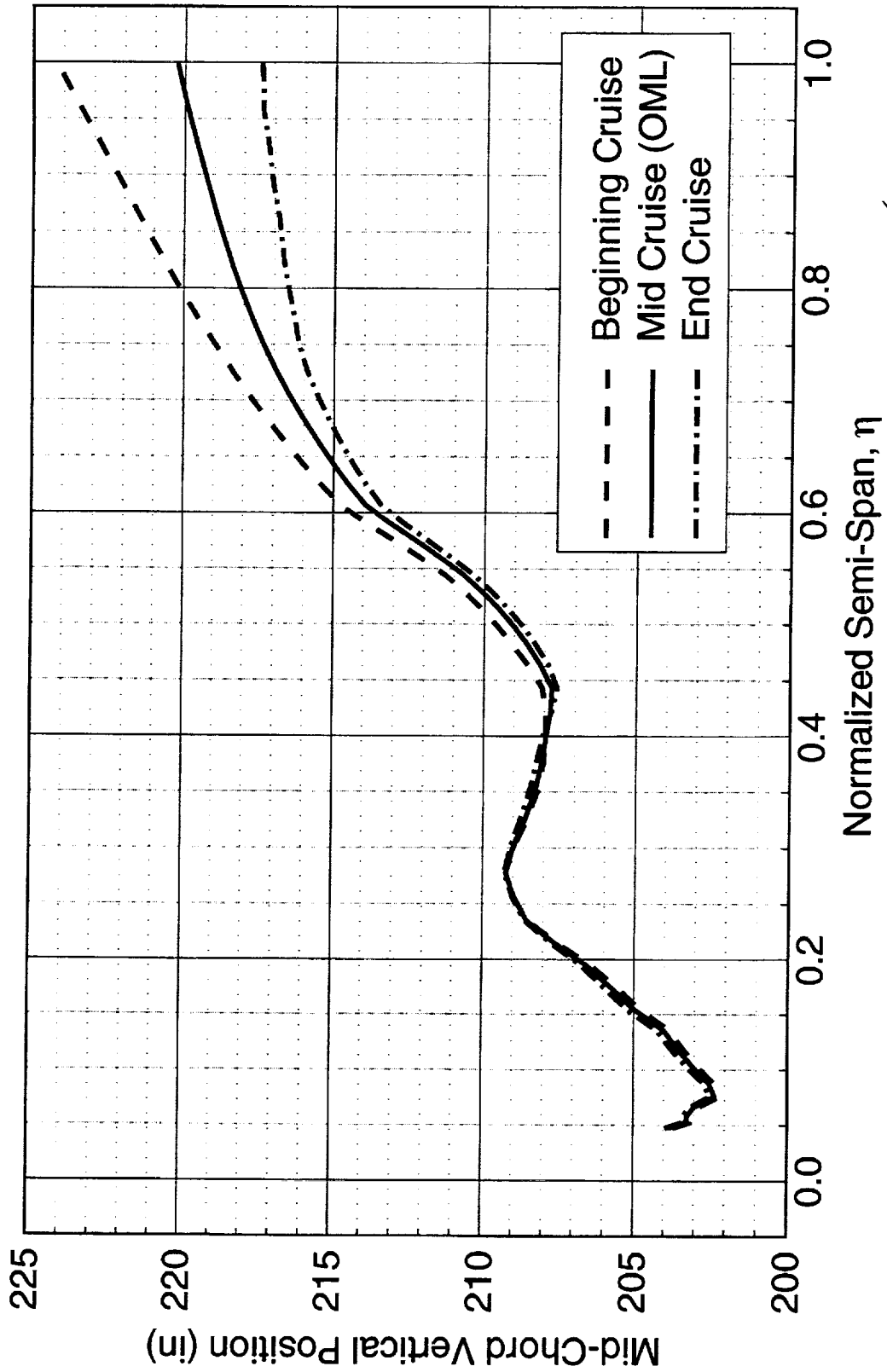
Aeroelastic Effect on TCA Baseline during Supersonic Cruise

The change in shape of the TCA baseline from beginning to end of supersonic cruise, due to static aeroelastic deformation, are presented in the next 3 charts. These calculations were performed using CFL3D.AE-BA in the Euler mode. Although the mode shapes for the W/B/N/D configuration were used, the aeroelastic assessment was performed on the W/B configuration, i.e., the aerodynamic forces due to nacelles have been neglected. The number of mode shapes used were only 22. Therefore, for the reasons given above, these results are considered preliminary. The TCA baseline OML was assumed to be the shape at the mid supersonic cruise point.

Plot of the mid-chord vertical location as a function of the span shows that the wing-tip moves vertically by only about 6 inches from the beginning to the end of cruise. The change in the local incidence of the wing is about -1.1° . Most of the displacement and twist take place on outboard wing. The outboard wing camber also changes due to aeroelastic effects. Since most of the fuel is carried in the inboard wing, which is fairly rigid, it is not very surprising that the overall change in the shape of the airplane is minimal.

Aeroelastic Effect on TCA during Supersonic Cruise

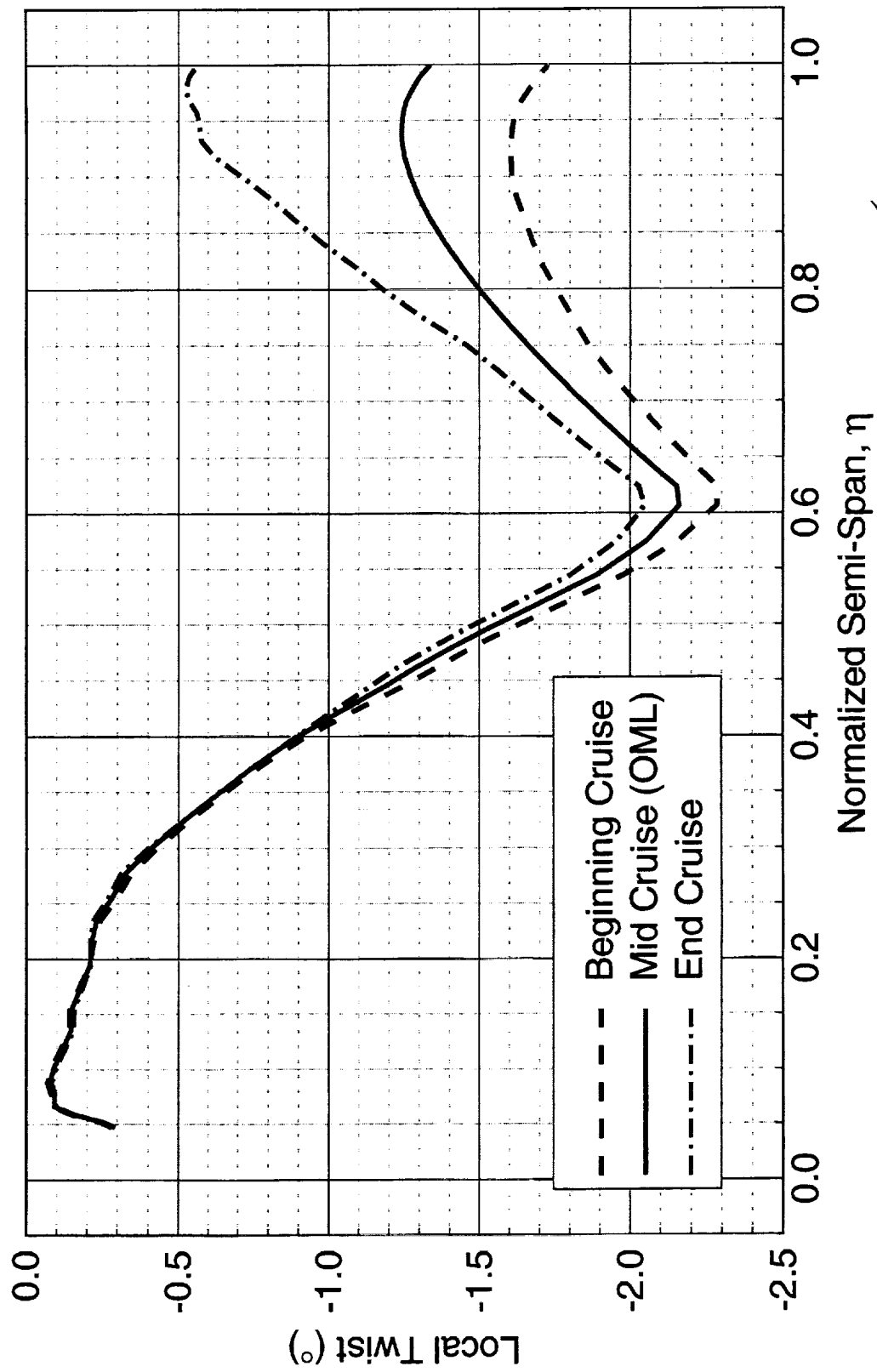
Wing/Body, CFL3D.AE-BA Euler, $M_\infty=2.4$, $\alpha=3.535^\circ$



This page is intentionally left blank.

Aeroelastic Effect on TCA during Supersonic Cruise

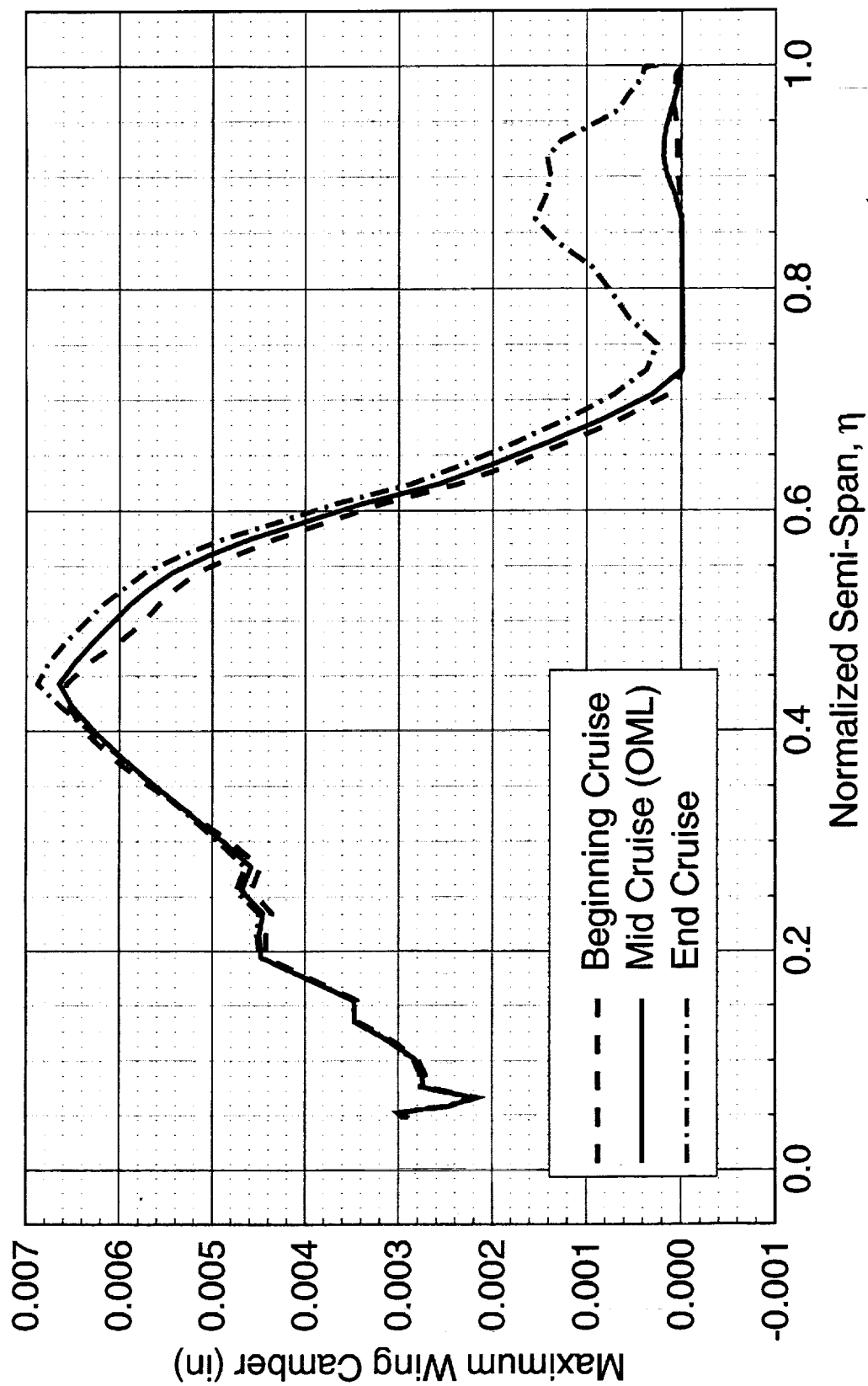
Wing/Body, CFL3D.AE-BA Euler, $M_\infty=2.4$, $\alpha=3.535^\circ$



This page is intentionally left blank.

Aeroelastic Effect on TCA, during Supersonic Cruise

Wing/Body, CFL3D.AE-BA Euler, $M_\infty=2.4$, $\alpha=3.535^\circ$



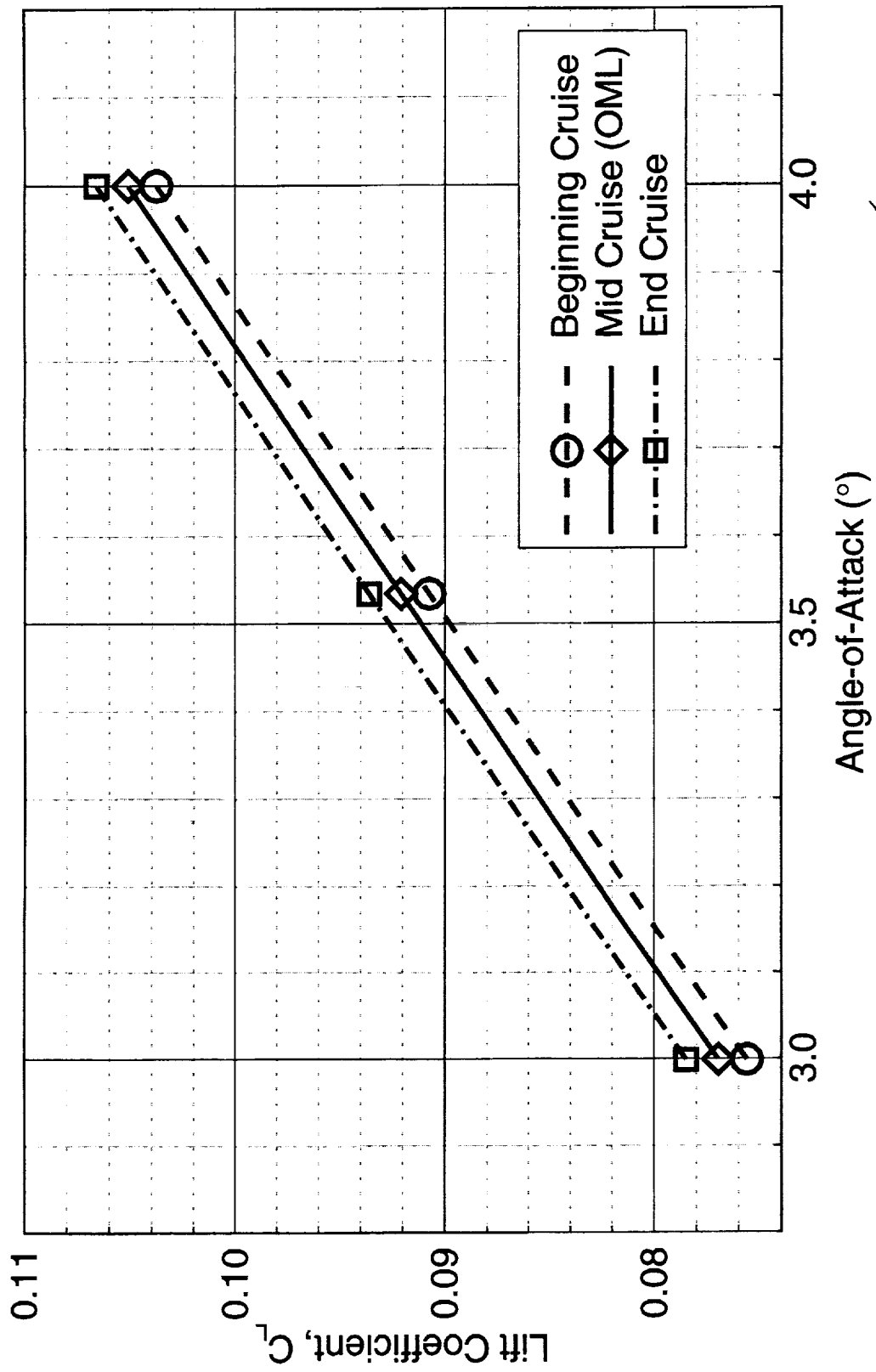
Aeroelastic Effect on TCA Baseline during Supersonic Cruise

The change in aerodynamic performance of the TCA baseline from beginning to end of supersonic cruise, due to static aeroelastic deformation, are presented in the next 3 charts. Again, for the reasons stated earlier, these results are considered preliminary.

It can be observed that as the airplane cruise-climbs, the lift coefficient increases for a given angle-of-attack. There is virtually no change in the drag at a given lift. The pitching moment shows a more nose down moment. However, the stability characteristics of the airplane is virtually unchanged.

Aeroelastic Effect on TCA during Supersonic Cruise

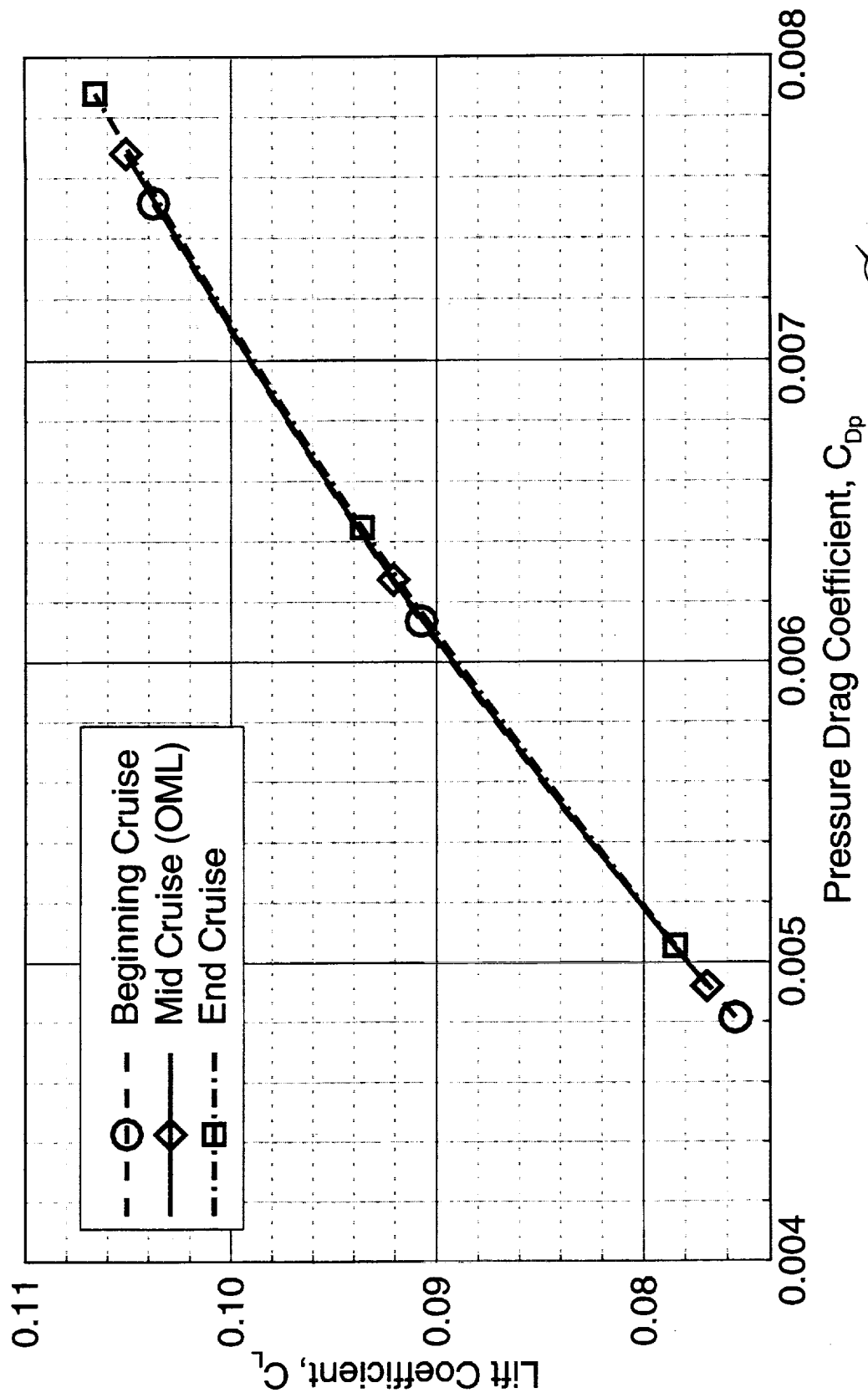
Wing/Body, CFL3D.AE-BA Euler, $M_\infty=2.4$, $\alpha=3.535^\circ$



This page is intentionally left blank.

Aeroelastic Effect on TCA during Supersonic Cruise

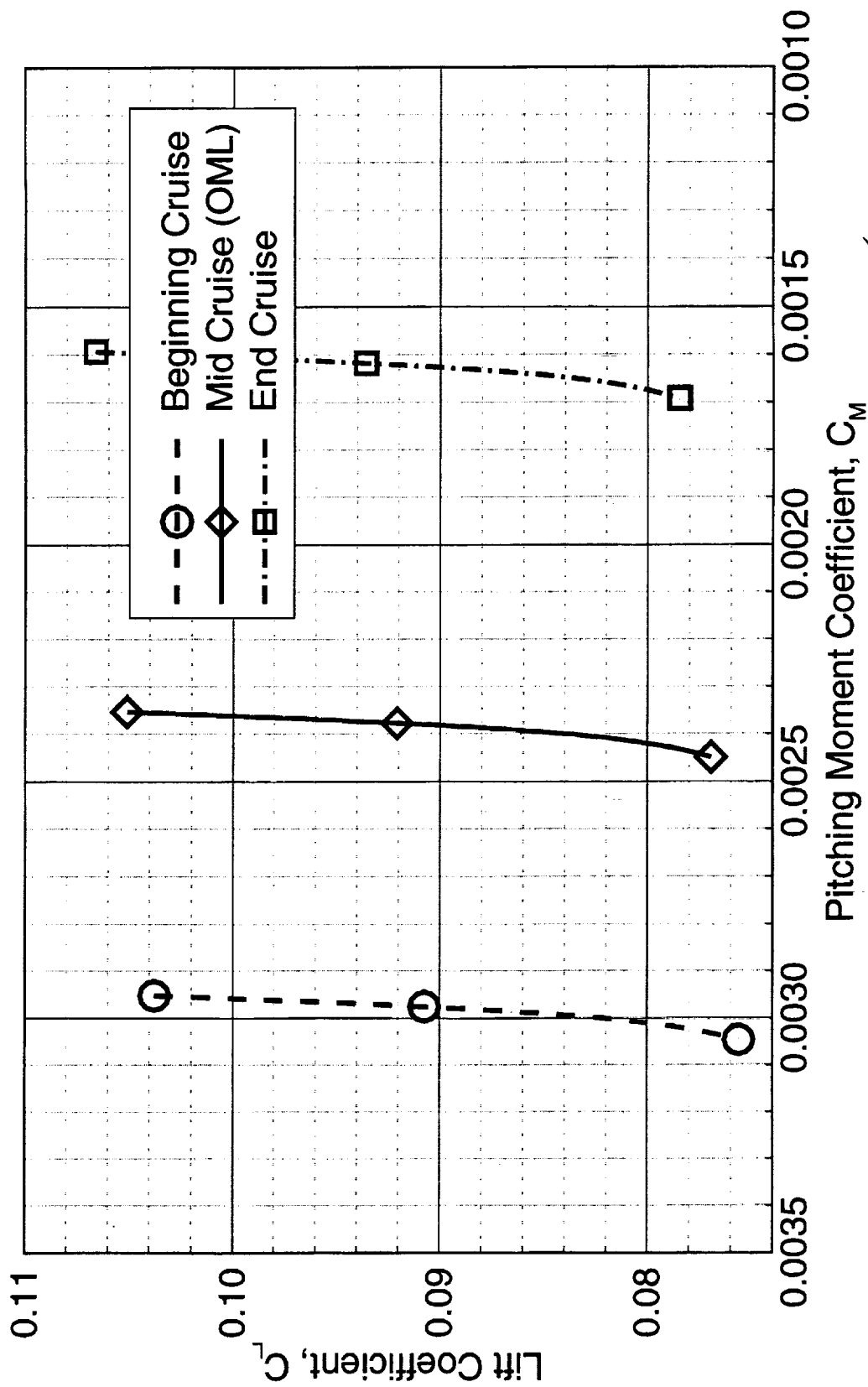
Wing/Body, CFL3D.AE-BA Euler, $M_\infty=2.4$, $\alpha=3.535^\circ$



This page is intentionally left blank.

Aeroelastic Effect on TCA during Supersonic Cruise

Wing/Body, CFL3D.AE-BA Euler, $M_\infty=2.4$, $\alpha=3.535^\circ$

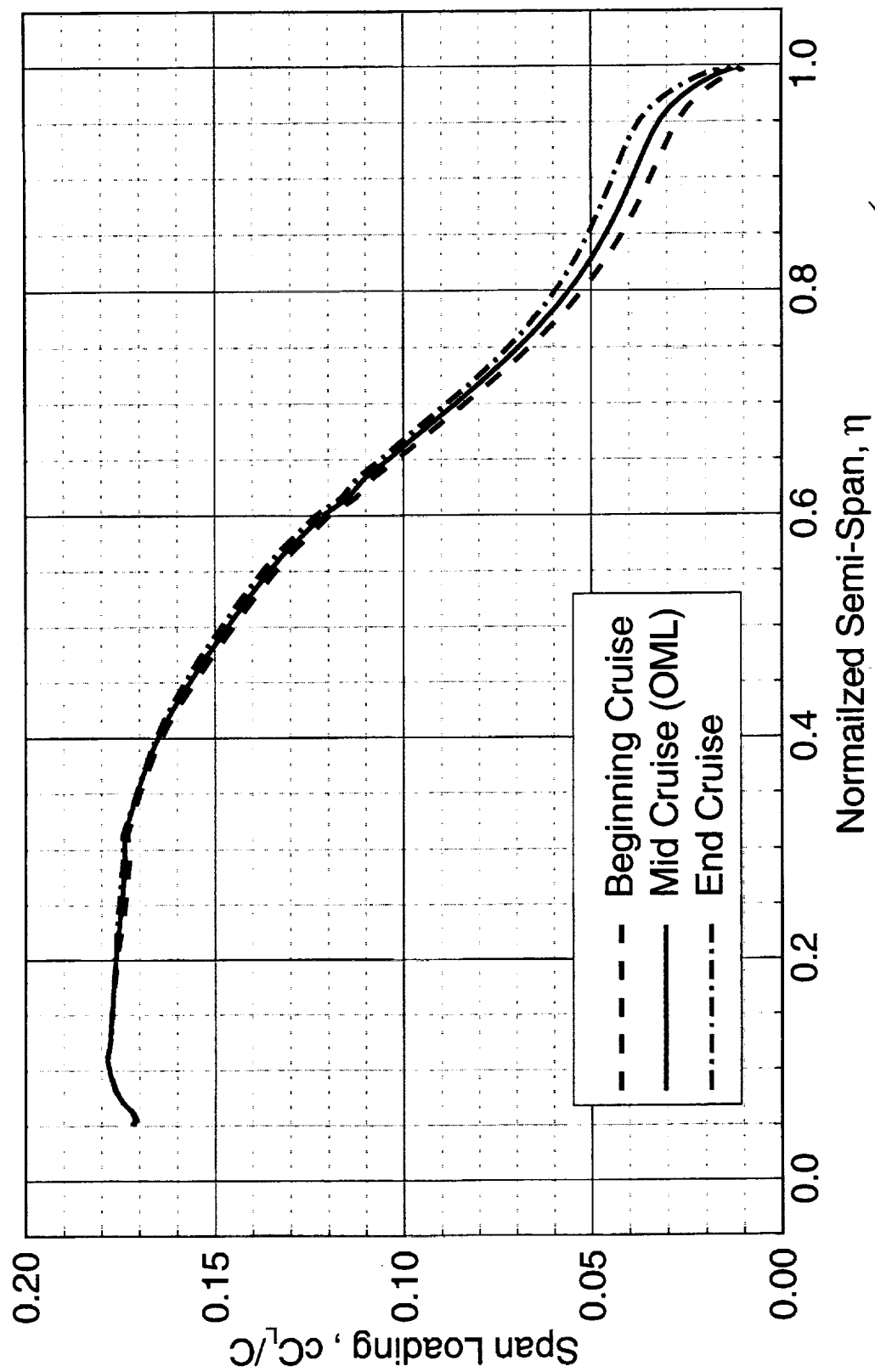


Aeroelastic Effect on TCA Baseline during Supersonic Cruise

The span loading shows that the outboard panel loads up as the airplane cruise-climbs. This is expected since the twist and camber of the outboard wing increases during the cruise-climb.

Aeroelastic Effect on TCA during Supersonic Cruise

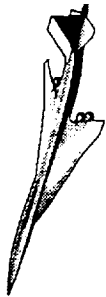
Wing/Body, CFL3D.AE-BA Euler, $M_\infty=2.4$, $\alpha=3.535^\circ$



Summary

Preliminary results indicate that the effect of static aeroelasticity on the performance of the TCA during supersonic cruise is minimal. The Sky-hook formulation alleviates the need to explicitly know the "jig shape".

Summary



High Speed Aerodynamics, Long Beach

- The effect of aeroelasticity on the performance of TCA during supersonic cruise appears to be minimal
- Sky-hook terms alleviate the need for the “jig shape”

Future Work

The results shown here are preliminary. Effects of changing the number of mode shapes, introducing viscosity and adding the nacelles will be studied next. The effect of static aeroelasticity during transonic cruise will also be investigated.

Future Work



High Speed Aerodynamics, Long Beach

- Effect of changing the no. of mode shapes
- Effect of viscosity
- Effect of nacelles
- Effect of aeroelasticity during transonic cruise

This page is intentionally left blank.



Initial TCA S&C Assessment

High Speed Aerodynamics

INITIAL TCA STABILITY AND CONTROL ASSESSMENT

Long Beach

David A. Blake
Paul T. Glessner
Paul Kubiатko

Seattle

Brian A. Nishida
Douglas L. Wilson

HSR Airframe Annual Review held at Los Angeles
February 9-13, 1998



This presentation documents work performed by the Stability and Control groups at the Boeing Company in both Seattle and Long Beach. This work along with the delivery of the corresponding report completed Configuration Aerodynamics Milestone 4-13.

There were two main objectives for this milestone. The first was to assess the high speed Stability and Control (S&C) characteristics of the TCA. The second was to make inputs to help guide future updates of the High Speed Civil Transport.

The approach proposed included the evaluation of flying qualities of the TCA for specific Flying Qualities Requirements. An experimental and computational database would be generated and incorporated into a computer simulation to evaluate the S&C characteristics. Due to proposed configuration changes to the baseline, the Flight Controls ITD team abandoned plans for a full-flight envelope nonlinear simulation. Therefore, both rigid and elastic airplane comparisons between the TCA and Reference H were used in order to perform the assessment.

With regards to pitch stability, two items were of concern. The first involved significant pitch-up at higher angles-of-attack for the TCA while no pitch-up was observed for the Reference H. The second item was the dramatic impact on the Time-to-Double (T_2) values for the TCA. Compared to a T_2 of 6 seconds for the Reference H, the TCA had a T_2 of between 1 and 2 seconds at cruise angle-of-attack and less at higher angles-of-attack.

The TCA appears to have about 80% of the lateral control authority of the Reference H. With new proposed changes to the time-to-bank requirements, the TCA should have acceptable control authority for this critical maneuver.

Similar to the Reference H, the TCA will also not be able to meet the emergency decent requirements using only spoiler slot defectors for the speedbrake function.



Initial TCA S&C Assessment

High Speed Aerodynamics

OUTLINE

- Objectives
- Approach
- Stability and Control Assessments
- Summary





Initial TCA S&C Assessment

High Speed Aerodynamics

OBJECTIVES

- Assess the High Speed Stability and Control characteristics of the TCA
- Make inputs to help guide future updates of the High Speed Civil Transport



The two primary objectives of this milestone (4-13) were to assess the high speed Stability and Control characteristics of the TCA, and to make inputs to help guide updates to the High Speed Civil Transport configuration.

The Initial Stability and Control Assessment of the TCA was performed as part of the NASA contract NAS1-20220, within the Configuration Aerodynamics (Task 32) element.



Initial TCA S&C Assessment

High Speed Aerodynamics

APPROACH

- Initial Approach was Similar to the Reference H Assessment
 - Evaluate specific Flying Qualities Requirements using an Experimental Database, Computational Database, and Simulation Models
- Flying Qualities Requirements selected
 - Pitch Stability and Control, Lateral/Directional Stability and Control, and Emergency Descent Capability
- Experimental Database for TCA
 - Transonic and Supersonic Wind-Tunnel Tests conducted at the NASA LaRC Transonic and Unitary Plan Wind Tunnel with the 1.5% TCA modular controls model (Model 20)



Initially the assessment was going to be done using the same approach as the Reference H assessment. A MATLAB and SIMULINK model would be used to evaluate the Stability and Control Characteristics.

The Flying quality requirements relevant to high-speed conditions were selected from the Flight Control System Requirements document published by the Flight Controls ITD. The requirements selected for the assessment include: pitch stability, pitch control, lateral/directional stability, lateral/directional control, and emergency descent capability. The other requirements were felt to be less critical based on the previous Reference H Assessment.

Experimental data obtained for the TCA was compared to similar results for the Reference H configuration. In addition, aeroelastic increments generated using A502/ELFINI were to be included for selected flight conditions.

The experimental database for the TCA was obtained from wind-tunnel tests performed at both the NASA LaRC Unitary Plan Wind Tunnel (UPWT) and the 16-ft Transonic Wind Tunnel (16' TT). The model used at both facilities was the 1.5% TCA modular controls model. In addition, wind-tunnel data involving the Reference H aircraft tested at the same facilities were used. The model used in both of these tests was the 1.675% modular controls model.



Initial TCA S&C Assessment

High Speed Aerodynamics

APPROACH (continued)

- Computational Database Objectives:
 - 1) Obtain incremental corrections to account for geometric differences
 - 2) Predict stability and control characteristics for transonic flight regime
 - 3) Calculate aeroelastic increments throughout the full-flight envelope in support of the Flight Controls nonlinear simulation effort
- However, since significant changes to the Baseline Configuration were proposed, the plan for a full-flight envelope nonlinear simulation of the TCA configuration was abandoned by the ITD team.
- Thus, for the Computational Database a limited set of geometric corrections was done along with generating elastic corrections for four cases covering a range of Mach numbers and mass distributions.



Before extensive work was completed on the computational database, significant changes to the baseline configuration were proposed within the High Speed Research (HSR) program. These changes included decreasing the outboard wing sweep, increasing the aspect ratio significantly, and adding a possible forward control surface. Since these proposed configuration changes would result in dramatically different aerodynamic and aeroelastic characteristics than for the TCA, the Flight Controls ITD team abandoned plans to develop a full-flight envelope nonlinear simulation of the TCA configuration. This decision meant that it was not necessary to generate aerodynamic data throughout the flight envelope for the TCA.

Since the full TCA simulation was not available, a limited assessment was done at specific points in the transonic and supersonic speed regimes where previous assessments using the Reference H simulation (Cycle 3) indicated problems might exist.

A limited set of corrections was generated using A502 (a linearized potential flow method) to account for the differences between the wind-tunnel model and the actual aircraft.

Elastic corrections were generated at Boeing - Seattle using a combined A502/ELFINI method. This method was also used at Seattle for structural sizing. Data were generated for four mass cases at a range of Mach numbers which covered the flight envelope.

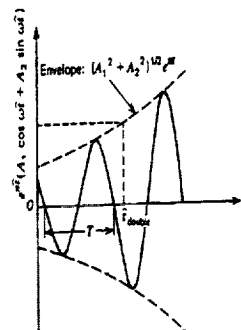


Initial TCA S&C Assessment

High Speed Aerodynamics

PITCH STABILITY

- Static Longitudinal Stability Derivative, $\frac{\partial C_m}{\partial C_L}$
 - This derivative demonstrates the ability of the aircraft to return to its trim angle-of-attack when a disturbance in angle-of-attack has occurred. A negative $\frac{\partial C_m}{\partial C_L}$ is a requirement for static longitudinal stability.
- Dynamic Pitch Stability, Time-to-Double (T_2). This is the time which must elapse during which the disturbance (in this case angle-of-attack) doubles in amplitude. (sample plot from page 168, Etkin, Bernard, "Dynamics of Flight- Stability and Control", Second edition, John Wiley and Sons, New York, 1982.)



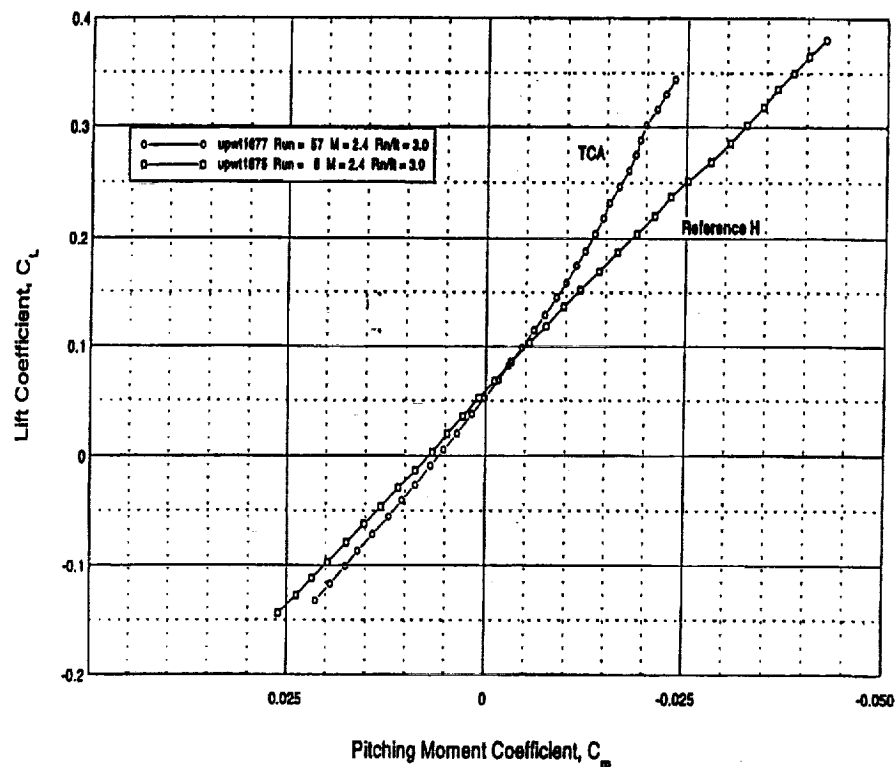
The pitch stability of the TCA was evaluated both qualitatively and quantitatively. A qualitative assessment was made by comparing the nonlinear lift and pitching moment coefficients as well as the linearized longitudinal stability derivatives between the TCA and the Reference H configurations. The quantitative assessment of the dynamic pitch stability was made by combining the results from the qualitative assessment of the static longitudinal stability (both rigid and elastic) and the results of a previous unaugmented pitch stability assessment done using the Reference H full-flight envelope quasi-static aeroelastic simulation.



Initial TCA S&C Assessment

High Speed Aerodynamics

Longitudinal Characteristics Stability Comparison



The data obtained from wind-tunnel tests illustrated that within the transonic Mach regime, significant pitch-up is observed at higher angles-of-attack for the TCA configuration, while no pitch-up is observed for the Reference H configuration.

The figure presented above presents a comparison of the nonlinear pitching moment coefficient vs. lift coefficient of the TCA and the Reference H configurations at Mach 2.4. This figure illustrates the linear characteristics of the Reference H configuration and the nonlinear characteristics of the TCA configuration, particularly at higher values of lift coefficients.

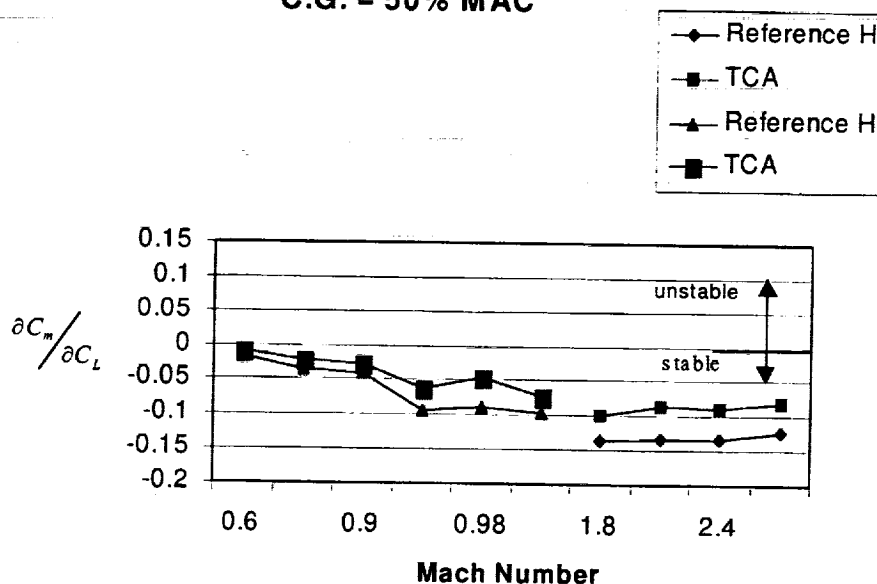


Initial TCA S&C Assessment

High Speed Aerodynamics

TCA and Reference H Comparison of Static Stability Derivative, $\partial C_m / \partial C_L$

Rigid Airplane, $\alpha_i \sim 4$ degrees
C.G. = 50% MAC



BOEING

The values of the longitudinal stability derivative in the figure shown above were linearized about lift coefficients corresponding to 4 degrees of angle-of-attack while the values of the same derivative shown in the next figure were linearized about lift coefficients corresponding to 10 degrees of angle-of-attack. (Note that a 0.01 change in $\partial C_m / \partial C_L$ is equivalent to a 1% MAC change in c.g. location).

The above figure illustrates that at the lower angle-of-attack, both the TCA and the Reference H configurations are stable at all Mach numbers. Additionally, the TCA is less stable (by no more than 5% MAC) than the Reference H configuration at all Mach numbers. However, the next figure shows that at high angles-of-attack, the TCA is unstable for all transonic Mach numbers, whereas the Reference H remains stable (marginally for Mach numbers < 0.9). Also shown is that the TCA is significantly less stable than the Reference H at several Mach numbers, up to values of 10% MAC less stable.

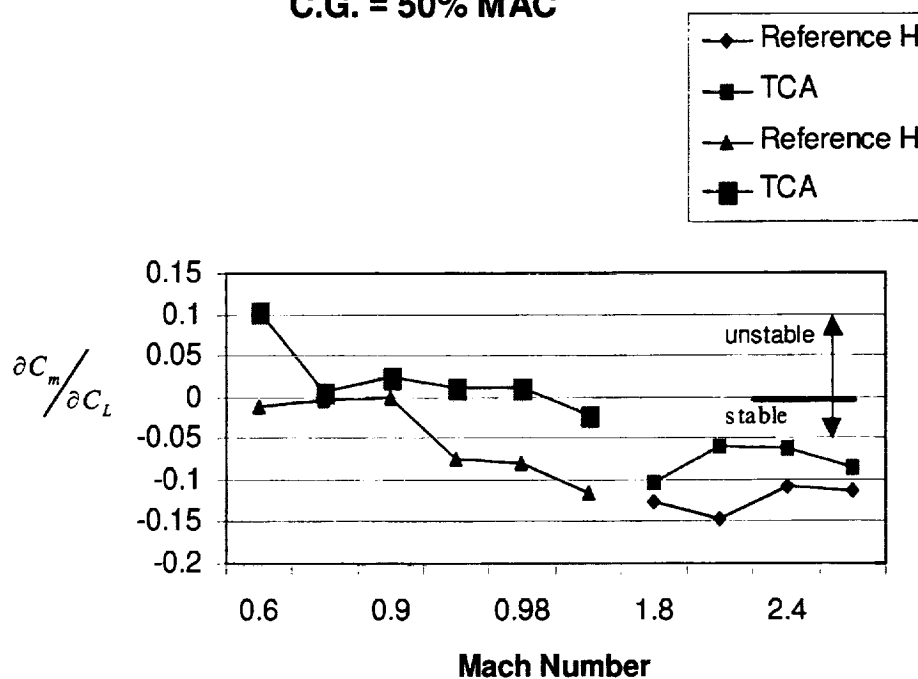


Initial TCA S&C Assessment

High Speed Aerodynamics

TCA and Reference H Comparison of Static Stability Derivative, $\frac{\partial C_m}{\partial C_L}$

Rigid Airplane, $\alpha_f \sim 10$ degrees
C.G. = 50% MAC

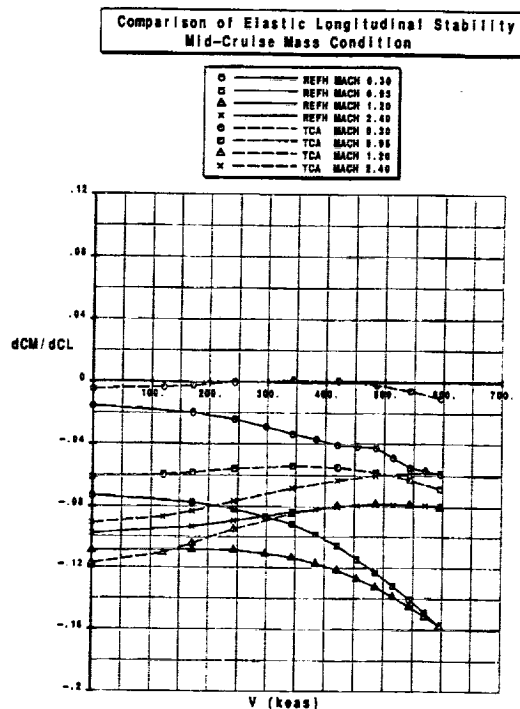


 **BOEING**



Initial TCA S&C Assessment

High Speed Aerodynamics



In addition to the rigid wind-tunnel test data, aeroelastic and aft-body corrections for the TCA have been computed at both the transonic and supersonic cruise points. The aeroelastic increments were computed from ELFINI QSAE data for a selected mass distribution of MCM (Mid-Cruise Mass). The data was computed at an $\alpha_F = 0^\circ$, but it was assumed to be constant for all angles-of attack. The aft-body corrections were calculated by solving potential flow (A502 panel method) over a wind-tunnel and cruise configuration. The aft-body corrections for the TCA reduce the longitudinal stability by 0.3% MAC at Mach 0.9 and 3.3% MAC at Mach 2.4.

Comparing the aeroelastic longitudinal stability derivatives for the TCA and the Reference H configurations at several flight conditions and MCM distribution, it can be concluded that the aeroelastic stability increment between the TCA and Reference H is no more than 2% MAC (TCA being 2% MAC less stable due to aeroelastics) at any of the flight conditions shown. The effects that mass distribution has on the aeroelastic longitudinal stability for the TCA is that as the mass decreases, the TCA becomes more stable. The largest stability increment seen within the operational flight envelope is a change of 2.5% MAC between the initial cruise and final cruise mass cases. This difference occurs at 415 KEAS (Mach 1.2).



Initial TCA S&C Assessment

High Speed Aerodynamics

Dynamic Pitch Stability, Time-to-Double (T_2)

Margin between aft c.g. limit and several T_2 amplitude values

Altitude (feet)	Mach = 0.8		
	$T_2 = 1$ second	$T_2 = 2$ seconds	$T_2 = 6$ seconds
10,000	Ref. H = 9.2	Ref. H = 4.8	Ref. H = 2.4
	TCA = 3.9	TCA = -0.5	TCA = -2.9
20,000	Ref. H = 9.2	Ref. H = 5.2	Ref. H = 0.0
	TCA = 3.9	TCA = -0.1	TCA = -5.3
48,000	Ref. H = 11.4	Ref. H = 0.3	Ref. H = -8.4
	TCA = 6.1	TCA = -5.0	TCA = -13.7



While the specific requirement for dynamic longitudinal stability has not been established by the Flight Controls ITD, an assessment of the time-to-double amplitude, T_2 , of the most unstable root was made for the Reference H at all Mach numbers and altitudes within the high speed flight envelope. The worst case conditions found during this assessment were at Mach 0.8 and 2.4.

The relationship between longitudinal stability and T_2 is assumed to be fixed and invariant between the TCA and Reference H. The unaugmented pitch stability of the TCA can be assessed against the T_2 values determined for the Reference H by adjusting the margins due to stability differences noted between the TCA and the Reference H.

The margins were adjusted for longitudinal stability differences (3.3% MAC for low angles-of-attack to 8.3% MAC for high angles-of-attack), and elastic increments (additional 2% MAC). Additional destabilizing increments to account for aft-body geometry and mass distribution cases are similar between the TCA and Reference H, hence no further adjustments need to be made to the margins.

The data presented shows that at Mach 0.8, and altitudes greater than 20,000 ft, the Reference H has a T_2 between 2 and 6 seconds. At Mach 2.4 and all altitudes, T_2 is greater than 6 seconds; however, the small separation in margin between T_2 values of 1 and 6 seconds indicates that stability levels drop off quickly with aft movement of center of gravity.



Initial TCA S&C Assessment

High Speed Aerodynamics

Dynamic Pitch Stability, Time-to-Double (T_2)

Margin between aft c.g. limit and several T_2 amplitude values

Altitude (feet)	Mach = 2.4		
	$T_2 = 1$ second	$T_2 = 2$ seconds	$T_2 = 6$ seconds
50,000	Ref. H = 5.2 TCA = -0.1	Ref. H = 2.6 TCA = -2.7	Ref. H = 1.8 TCA = -3.5
54,000	Ref. H = 7.7 TCA = 2.4	Ref. H = 5.2 TCA = -0.1	Ref. H = 3.7 TCA = -1.6
60,000	Ref. H = 9.0 TCA = 3.7	Ref. H = 5.7 TCA = 0.4	Ref. H = 4.4 TCA = -0.9

 **BOEING**



Initial TCA S&C Assessment

High Speed Aerodynamics

Pitch Stability Summary

- Significant pitch-up is observed at higher angles-of-attack (AOA) for the TCA while no pitch-up is observed for the Reference H.
- The TCA is less stable in pitch than the Reference H. The TCA remains stable at low AOA, while at high AOA it does become unstable. This analysis was performed "open loop" and no control law augmentation was utilized.
- Due to aeroelastics, the TCA is 2% MAC less stable than the Reference H.
- A dramatic impact on the T_2 values at the aft center-of-gravity results from the reduced longitudinal stability of the TCA configuration. Compared to a T_2 value of 6 seconds for the Reference H aircraft, the TCA has T_2 values between 1 and 2 seconds. The margins at higher AOA would be less than 1 second.
- With lower T_2 values, there is reason for concern regarding pitch stability.



As expected, the reduced longitudinal stability (both rigid and elastic) of the TCA configuration relative to the Reference H configuration has a dramatic impact on the T_2 value at aft center-of-gravity. Whereas the Reference H configuration has T_2 values at 54.8% MAC of 6 seconds, the TCA configuration has T_2 values at 53.1% MAC between 1 and 2 seconds. The margins for higher angles-of-attack were not presented, but it should be obvious that the T_2 values will be less than 1 second nearly everywhere.

This analysis illustrates that there is reason for concern regarding the pitch stability levels of the TCA configuration.



Initial TCA S&C Assessment

High Speed Aerodynamics

Lateral / Directional Control Capability

- Roll Response (Time-to-Bank Maneuver)
- Rudder Effectiveness
- Summary



Two flight requirements are considered which are affected by lateral/directional control capability. The roll response as measured by time-to-bank for the HSCT is primarily determined by lateral control capability. Rudder effectiveness is a good measure of directional control. Control of the inlet unstart involves both lateral and directional control but was not explicitly studied.

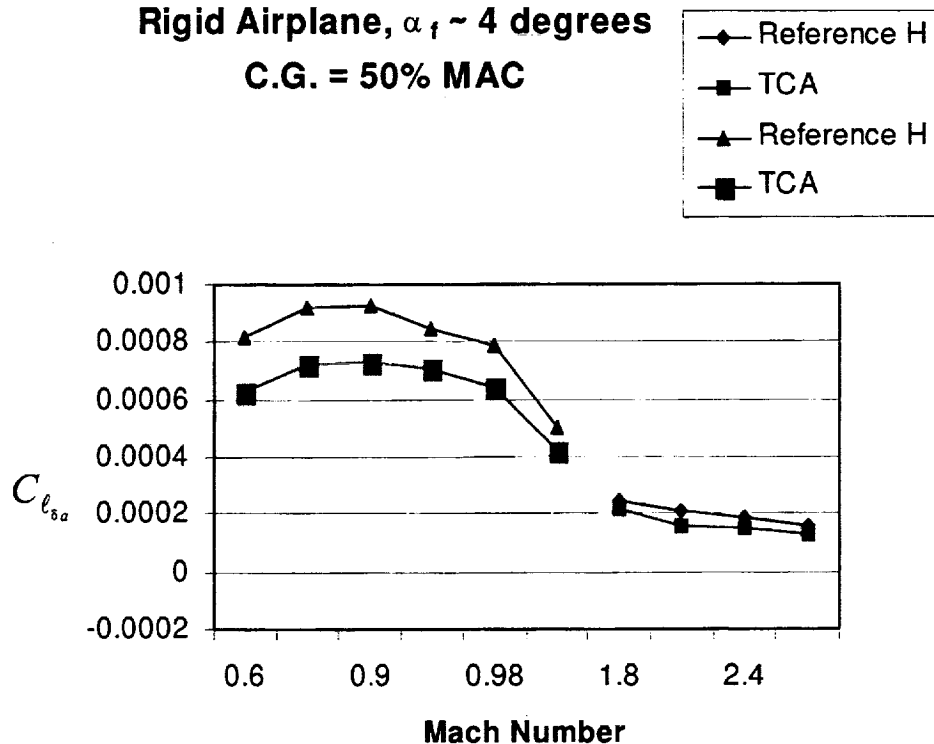


Initial TCA S&C Assessment

High Speed Aerodynamics

TCA and Reference H Comparision of Aileron Effectiveness

Rigid Airplane, $\alpha_f \sim 4$ degrees
C.G. = 50% MAC

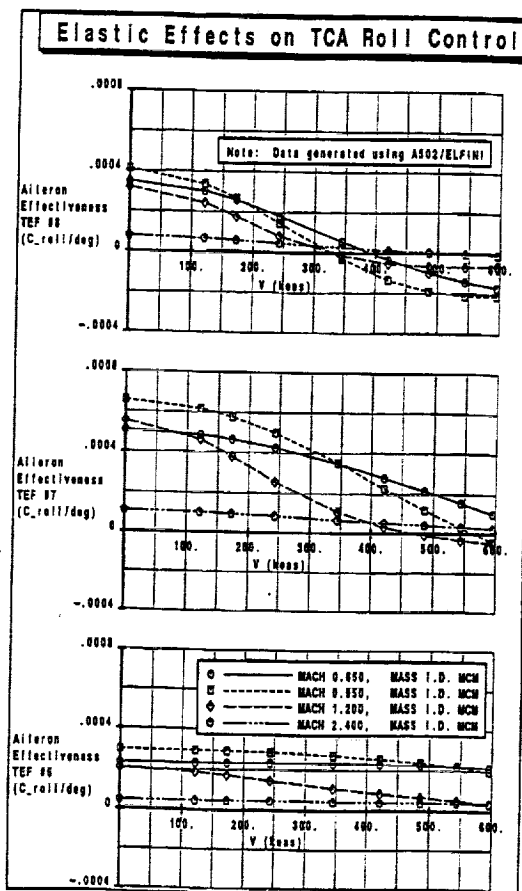


Rigid lateral control effectiveness for the TCA is somewhat less than the Reference H. The values of the aileron effectiveness were taken about the transonic and supersonic cruise angles-of-attack for the rigid configurations. Notice that there are no reversals in effectiveness for the rigid configurations. However, this is not the case for the elastic configurations.



Initial TCA S&C Assessment

High Speed Aerodynamics



Note: The outboard flaps get locked out at speeds greater than 250 KEAS.



The plot shown above illustrates in more depth the aileron reversal characteristics of the TCA configuration. The outboard aileron reversal speeds are somewhat lower than for the Reference H. The aft-body correction is minimal.

The time-to-bank requirement from the "HSCT Flight Control System Requirements Specification" is 2.5 seconds for a 30 degree bank angle change. The Reference H airplane essentially met the roll time-to-bank requirements with actuator hinge moment limits which limited deflection at high-q conditions. The TCA appears to have approximately 80% of the lateral control authority of the Reference H. Therefore, it should come close to meeting the current requirement. In addition, recent evaluations suggest less stringent requirements may be appropriate for the time-to-bank maneuver. The new requirement may be increased to 3.5 seconds. It is therefore felt that the TCA is acceptable with regard to time-to-bank.

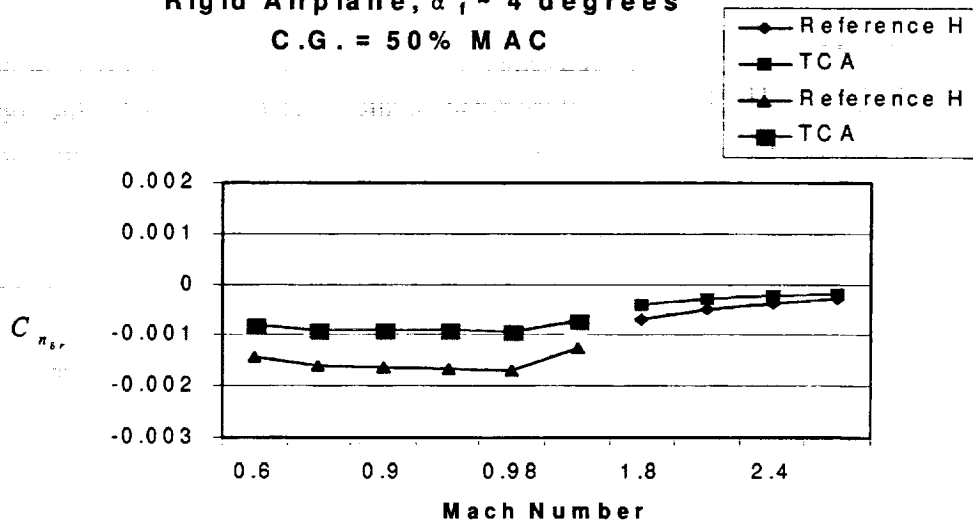
Initial TCA S&C Assessment

High Speed Aerodynamics



TCA and Reference H Comparison of Rudder Effectiveness

Rigid Airplane, $\alpha_i \sim 4$ degrees
C.G. = 50% MAC



The TCA rudder deflections include only the lower two panels compared to all three panels for the Reference H. Adjustments are made for the number of rudder panels deflected and the vertical tail volume.



When making a comparison of the rudder effectiveness, it should be noted that the TCA rudder deflections include only the lower two panels, compared to all three panels for the Reference H. After adjusting for the number of rudder panels deflected and the vertical tail volume, the rudder effectiveness of the TCA and the Reference H are nearly identical at low angles-of-attack.

Using elastic corrections generated from CFD, we were able to conclude that the rudder is 25% less effective transonically while it is 45% less effective supersonically. Correcting for aft-body geometry, in the transonic region, the rudder on the actual airplane geometry is 10% less effective than in the wind-tunnel configuration, while it is about 8% less effective in the supersonic region.

Control of the roll upset associated with an inlet unstart was not explicitly studied. No data were available to define the rolling moment generated on the TCA with an unstarted inlet. The Reference H appeared to have sufficient control to manage a dual inlet unstart, but it has not been determined whether the upset would be similar with the larger TCA inlets, or whether the somewhat lesser roll control available on the TCA would be adequate.

Since the Reference H aircraft did not show any problems with respect to directional control, this aspect of control is not felt to be a major concern.



Initial TCA S&C Assessment

High Speed Aerodynamics

LATERAL / DIRECTIONAL CONTROL CAPABILITY SUMMARY

- Rigid lateral control effectiveness for the TCA is somewhat less than the Reference H. There are no reversals in aileron effectiveness for the rigid configurations, however, there are outboard aileron reversals for the elastic configurations. This is similar to the Reference H.
- The TCA appears to have about 80% of the lateral control authority of the Reference H. Since the time-to-bank requirement may be increased from 2.5 seconds to 3.5 seconds based upon piloted simulation work performed at NASA Ames (by the Flight Controls group), the TCA should be acceptable for this maneuver.
- The rudder effectiveness of the TCA and the Reference H are nearly identical at low angles-of-attack. Thus directional control is not felt to be a major concern.

 **BOEING**



Initial TCA S&C Assessment

High Speed Aerodynamics

Emergency Descent Capability

- As currently defined in Task 36, HSCT Flight Control System Requirements Specification the maneuver is defined as "... a speed brake function shall have sufficient authority [to] achieve a descent rate of 10,000 fpm at V_{MO} and flight idle thrust."
- This statement is intuitively based upon FAR 25.841 which states that the airplane must be designed so that occupants will not be exposed to a cabin pressure altitude that exceeds 25,000 feet for more than 2 minutes or 40,000 feet for any duration following a decompression.
- TCA was not evaluated regarding this, however, comparisons were made between the Reference H and a 1970 Boeing IRAD Study.



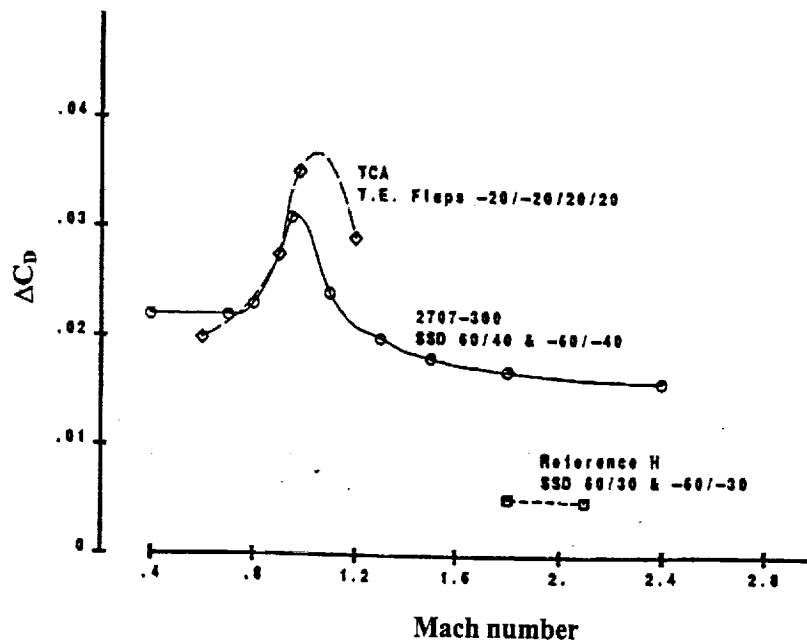
The requirement for descent capability as currently listed in Task 36 - "HSCT Flight Control System Requirements Specification", states that "a speed brake function shall have sufficient authority [to] achieve a descent rate of 10,000 fpm at V_{MO} and flight idle thrust." This statement is intuitively based upon FAR 25.841 which states that the airplane must be designed so that occupants will not be exposed to a cabin pressure altitude that exceeds 25,000 feet for more than 2 minutes or 40,000 feet for any duration following a decompression.



Initial TCA S&C Assessment

High Speed Aerodynamics

Incremental Drag due to Possible Speedbrake Operations



 **BOEING**

The 1970 Boeing IRAD study found that the drag levels provided by the spoiler-slot-deflectors (SSDs) as designed and tested for the 1970 SST 2707-300 configuration were adequate to meet the requirement stated previously. These drag levels are shown in the above plot. The drag levels for the Reference H as tested in the supersonic wind-tunnel test UPWT 1812 indicates that the drag increments for the SSDs on this configuration are ~ 20% of those for the 2707-300 and therefore will not satisfy the requirement. The SSD effectiveness for the TCA configuration has not been determined. However, it is expected to be less than that for the Reference H due to the fact they are slightly smaller per unit wing area and have a larger hinge line sweep angle. Therefore, the TCA will also not meet the emergency descent requirements using spoilers for the speedbrake function.

Also shown in the figure is the effect of differential deflections of the trailing- edge flaps. With the outboard trailing- edge flaps up 20 degrees and inboard trailing- edge flaps down 20 degrees, the required drag levels can be obtained up to the highest Mach number for which data is available. However, several issues must be resolved before using the flaps in this fashion in order to be used as the baseline speedbrake configuration. They include: (1) testing in the critical supersonic condition, (2) the effect of aeroelastics, and (3) the effect on the hydraulic system.



Initial TCA S&C Assessment

High Speed Aerodynamics

Emergency Descent Capability Summary

- Similar to the Reference H, the TCA will also not be able to meet the emergency decent requirements using only spoiler slot deflectors for the speedbrake function.
- Use of alternative flap possibilities such as differential (alternating flaps).





Initial TCA S&C Assessment

High Speed Aerodynamics

Summary

- Pitch stability at higher angles-of-attack may be unacceptable (major concern)
- Lateral / directional control is marginal but is not viewed as a "cliff"
- Incremental drag is inadequate for emergency descent





Initial Predictions of Canard Integration

Todd E. Magee, James O. Hager, and David T. Yeh

**The Boeing Company
Long Beach, California**

Tim Haynes

**Dynacs Engineering Company Inc.
Seattle, Washington**

**HSR Airframe Technical Review
Los Angeles, California
February 9-13, 1998**



This page is intentionally left blank.

Initial Predictions of Canard Integration

Todd E. Magee, James O. Hager, and David T. Yeh
The Boeing Company
Long Beach, California 90807

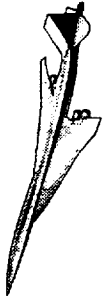
Tim Haynes
Dynacs Engineering Company, Inc.
Seattle, Washington 98055

This paper presents the initial CFD predictions obtained by Boeing Long Beach (BLB) and Dynacs Engineering Company for the integration of a canard on the TCA (Technology Concept Aircraft) wing/body configuration. Each company analyzed different canard configurations. Boeing analyzed the PTC (Preliminary Technology Concept) canard planform, while Dynacs focused on the ACC (Alternate Controls Concept) canard planform. Euler and Navier-Stokes solutions are presented in this paper. The results from both analyses were used to define a wind-tunnel test program, that is outlined in the paper. The results indicate that the PTC planform has a small impact on the wing/body/canard performance. The ACC planform has greater impact on the wing/body/canard performance, because of its close proximity to the wing and its larger planform size.

Outline

The topics listed in this chart outline the preliminary canard integration CFD studies performed by Boeing (Long Beach) and Dynacs Engineering, Inc. (Seattle). This paper is divided into six sections. First, the objectives of the current studies will be defined and the parameters of the study will be discussed. Next, we will look at the two distinct canard configurations that were analyzed. The third and fourth subjects will deal with the Boeing and Dynacs CFD studies, respectively. The approach of each company will be outlined and the results will be shown. The fifth subject will describe the Canard Integration Wind-Tunnel Test that was developed from the CFD results. Finally, the additional work required to prepare for the Canard Integration Test will be outlined.

Outline



High Speed Aerodynamics, Long Beach

- Objectives and Parameters of Canard Studies
- Canard Configurations Analyzed
- BLB CFD Studies
 - Approach
 - Results
- Dynacs CFD Studies
 - Approach
 - Results
- Canard Integration Wind-Tunnel Test
- Future Work

Objectives and Parameters of Canard Studies

There are three main objectives for the canard studies described in this paper. First, there is a need to develop a CFD process to allow fast and efficient analysis of configurations that incorporate a canard, because future HSR configurations will have a canard. This CFD process must be able to incorporate existing grid generation and analysis capabilities for flaps, nacelles, and empennage. The process must also allow efficient nonlinear optimization in the presence of the canard.

The second objective of the canard studies is to provide aerodynamic data to plan the Canard Integration Wind-Tunnel Test. The canard can be integrated with the fuselage in many locations, so it is important to determine which canard integration configurations would be relevant for a wind-tunnel test whose main goal is CFD validation.

The last objective of the canard studies is to determine the influence of the canard integration on performance. An accurate assessment of the aerodynamic performance of various canard mounting locations will allow the aircraft designers to choose the canard integration that maximizes performance.

The canard studies described in this paper will focus on two canard planforms, the PTC (Preliminary Technology Concept) and ACC (Alternate Controls Concept) canard planforms, that will be integrated with the baseline TCA wing/body configuration. The PTC wing/body configuration was not utilized in these studies, since it was not completely defined at the time the studies were performed. The studies do not consider the effect of the nacelles or the empennage. Boeing performed Euler analysis on the PTC canard configurations, and Dynacs performed Navier-Stokes analysis on ACC canard configurations. The freestream Mach number for all of the studies was 2.4. The main parameters that varied throughout the studies were canard mounting location (low, mid, and high), canard dihedral angle (Γ_c), and canard incidence angle (i_c).

Objectives and Parameters of Canard Studies



High Speed Aerodynamics, Long Beach

○ Objectives

- Develop CFD process to model canard configurations
- Provide aerodynamic data for Canard Integration Test planning
- Determine the influence of canard integration on performance

○ Parameters of canard CFD studies

- Baseline TCA wing/body
- PTC and ACC canard planforms
- Low, mid, and high canard mounting locations
- Several canard dihedral and incidence angle settings
- $M_\infty=2.4$, Euler & Navier-Stokes solutions

Canard Configurations Analyzed

The following chart shows the two canard planforms utilized for the studies and their baseline mounting locations on the TCA wing/body. The top view shows that the PTC canard is mounted farther forward than the ACC canard. The PTC planform area (220 ft²) is smaller than the ACC planform area (350 ft²). Both canard planforms have a leading-edge sweep of 54.2°, a trailing-edge sweep of 27.4°, and a bi-convex airfoil cross-section with a 3% maximum thickness to chord ratio. The baseline PTC canard mounting configuration is mid-mounted with $\Gamma_c=0^\circ$ and $i_c=0^\circ$. The baseline ACC canard mounting configuration is low-mounted with $\Gamma_c=-15^\circ$ and $i_c=-2^\circ$.

The front and side views at $\alpha=0^\circ$ and $\alpha=3.5^\circ$ were provided to show the relationship of the two canards with the wing near the minimum drag and cruise conditions, respectively. An important issue in these studies is how the canard wake and canard tip vortex will influence the wing and nacelles. The front view shows what would be seen if you were riding along with the freestream flow. Note that both front views are shown at the same scale. The front view shows that we expect the ACC baseline canard to have an influence on the upper and lower surface of the wing at both the cruise and minimum drag conditions, whereas the PTC canard should mainly have an influence on the upper surface at minimum drag and a lesser influence on the upper surface of the wing at the cruise conditions.

From the location of the two canards it is expected that the ACC canard will have the greatest influence on performance due to its larger planform size and its closer proximity to the wing.

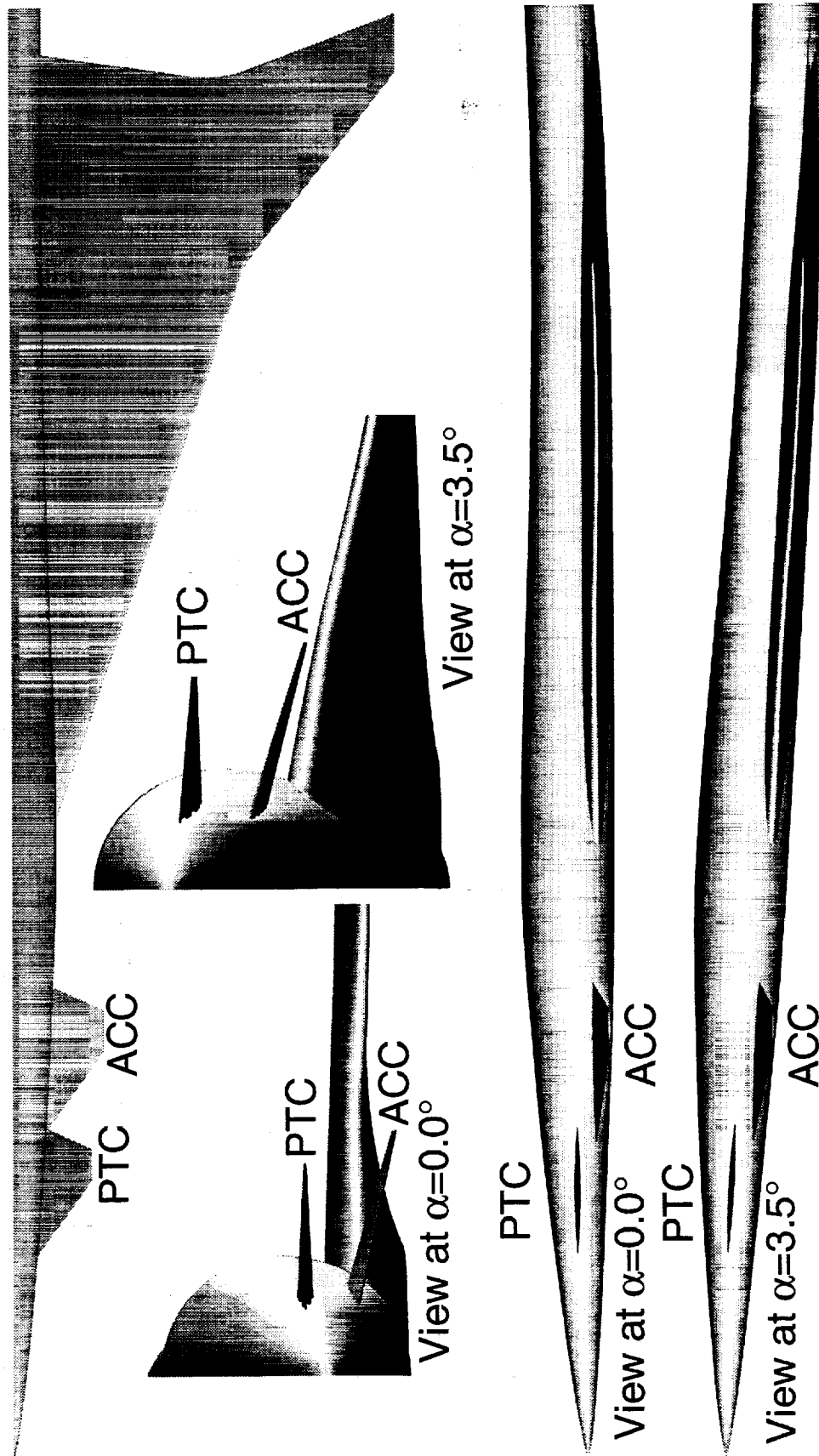


Canard Configurations Analyzed

High Speed Aerodynamics, Long Beach

TCA Wing/Body/Canard Geometry

TCA Wing/Body with ACC ($i_c = -2.0^\circ$) and PTC ($i_c = 0.0^\circ$) Canards



BOEING

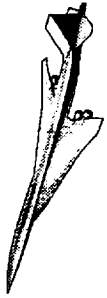
BLB CFD Approach

This chart summarizes the approach taken by the Boeing company to analyze the PTC canard configuration. An overset grid topology was employed to simplify the grid generation and to allow integration of existing grids for additional aircraft components (i.e., nacelles, flaps, and empennage) in the future. A C-O grid topology was used for the wing/body and an H-O grid topology was used for the canard. A total of 1.4 million grid points were used to define the wing, body, and canard. The grid indices are shown for each grid. For the wing/body grid, i is in the spanwise direction, j is in the streamwise direction, and k is in the normal direction. For the canard grid, i is in the streamwise direction, j is in the normal direction, and k is in the roll direction.

An automated canard grid generation routine has been developed by David Yeh of the BLB High-Lift group. It will integrate a canard at any given mounting location (i.e., high, mid, or low) and axial station, and it will rotate and deflect the canard to any dihedral and incidence angles. Once the canard is placed in the appropriate location, an H-O grid is generated by the code. The grid generation on a C-90 takes less than 10 minutes of wall clock time.

The CFL3D version 4.1 flow solver was used in the Euler mode to obtain the CFD solutions. All solutions were generated on a Cray C-90 computer. The FOMOCO (Force and Moment Computation) code was used to get accurate force and moments by generating a zipper grid between the overset grids. These are the same routines utilized by the OVERFLOW code to integrate forces and moments.

BLB CFD Approach



High Speed Aerodynamics, Long Beach

○ Grid generation

- Overset grid topology
 - Wing / body: C-O, (i, j, k): (93, 241, 41)
 - Canard: H-O, (i, j, k): (109, 33, 137)
- David Yeh's automated grid generation code
 - Variable canard mounting positions (i.e., high, mid, or low)
 - Variable canard dihedral and incidence angles
 - Takes less than 10 minutes (wall clock) on C-90

○ Flow Solver

- CFL3D v4.1, Euler
- Solutions obtained on C-90 (vn)

○ FOMOCO used to integrate forces/moments



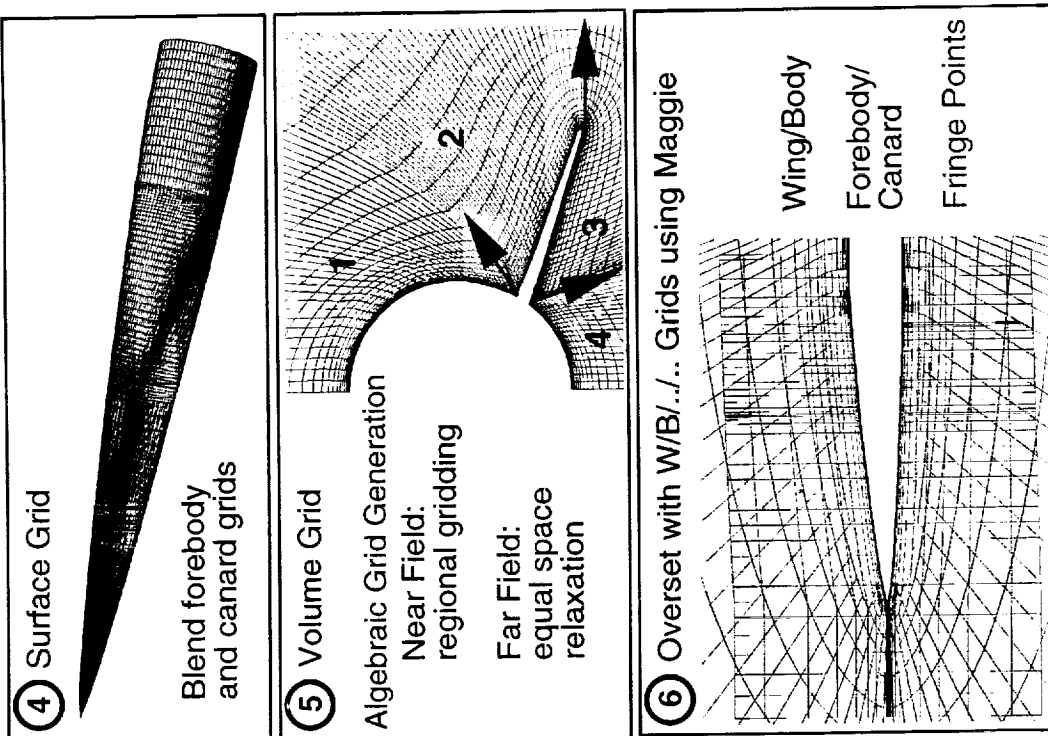
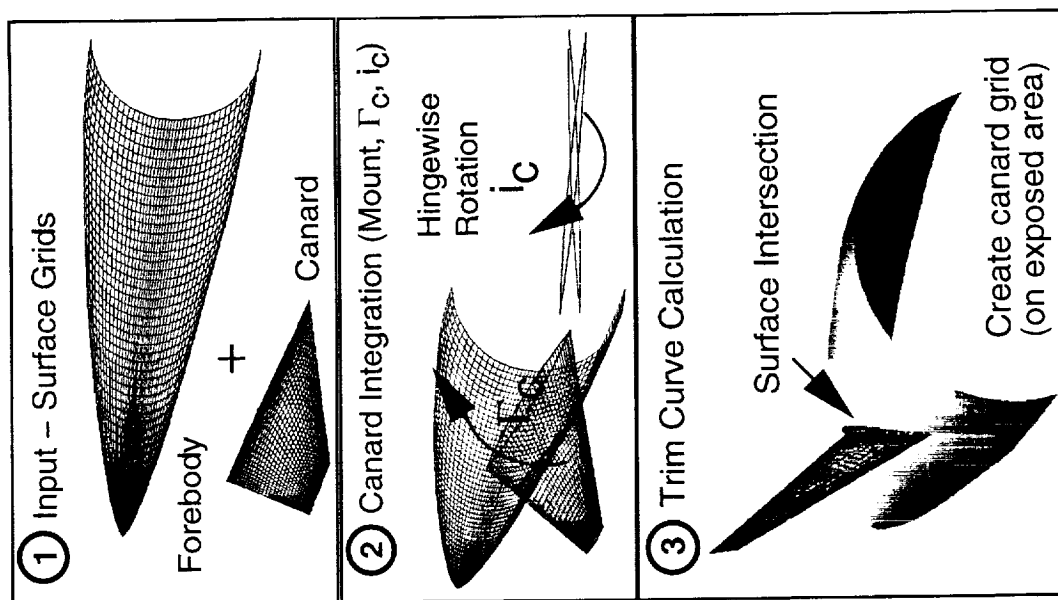
Automated Grid Generation Procedure is Fast and Efficient

The following chart describes in detail the steps involved in the automated grid generation procedure. In step one, existing surface grids for the forebody and the canard are input into the program. In step two, the canard is mounted in the correct position and orientation (high/mid/low, Γ_c , & i_c), and the canard grid is extended to the centerline of the forebody. In step 3, a trim curve is calculated between the canard and the body so that a canard grid can be generated on the exposed area of the canard. In step 4, a blended forebody/canard grid is generated. In step 5, the volume grid is generated using an algebraic grid generation technique. This volume grid is constructed by breaking up the volume into four regions with the interface line between the regions constructed by the surface normals shown in the figure. The spacing of the grid cells conforms to the grid spacing in the near-field, but becomes uniform at the outer boundary. This prevents the formation of cells with crossed sides and negative volumes. Finally, in step 6, interpolation coefficients between the two overset grids are determined from the Maggie code.

Automated Grid Generation Procedure is Fast and Efficient



High Speed Aerodynamics, Long Beach



Canard Manipulation for Parametric Studies

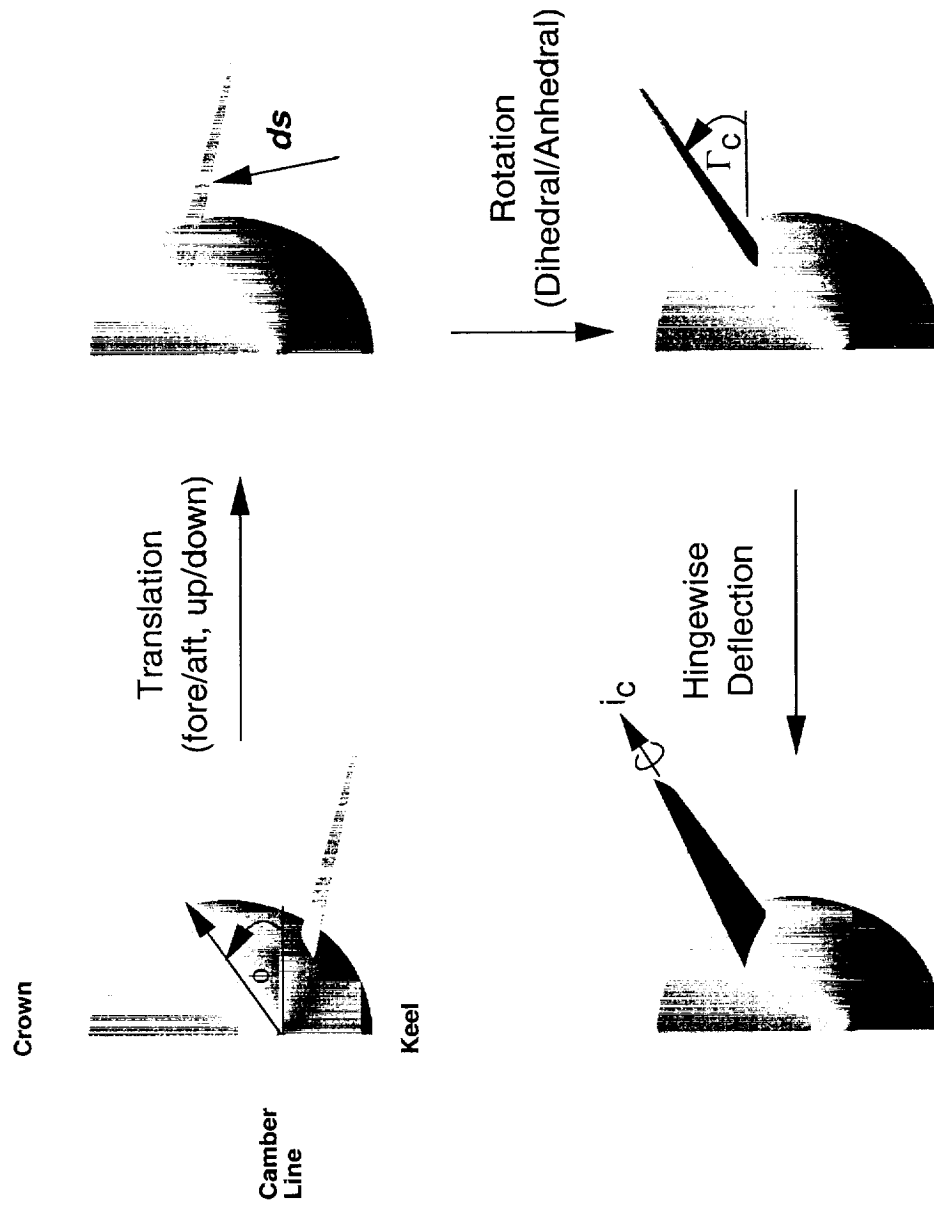
This chart shows how the automated grid procedure moves the input canard grid to the desired mounting location and orientation. This process takes place in step 2 of the automated grid generation process described on the previous page.

First, the input canard grid is translated to the desired mounting location. The fore/aft location of the canard is given by the location of the hingeline at the root of the canard. The up/down location of the canard is given by the angle ϕ measured from the horizontal line drawn from the fuselage camber line. Then, the canard is rotated to obtain the desired dihedral angle, Γ_c . Finally, the canard is given a hingewise deflection to obtain the desired incidence angle, i_c .

Canard Manipulation for Parametric Studies



High Speed Aerodynamics, Long Beach



Baseline TCA Wing/Body/Canard Overset Grid

This chart shows a typical wing/body/canard grid utilized by Boeing in this study. The red region shows the canard grid and the black region shows the wing/body grid. Note that only every other point in the grid is shown in this chart.

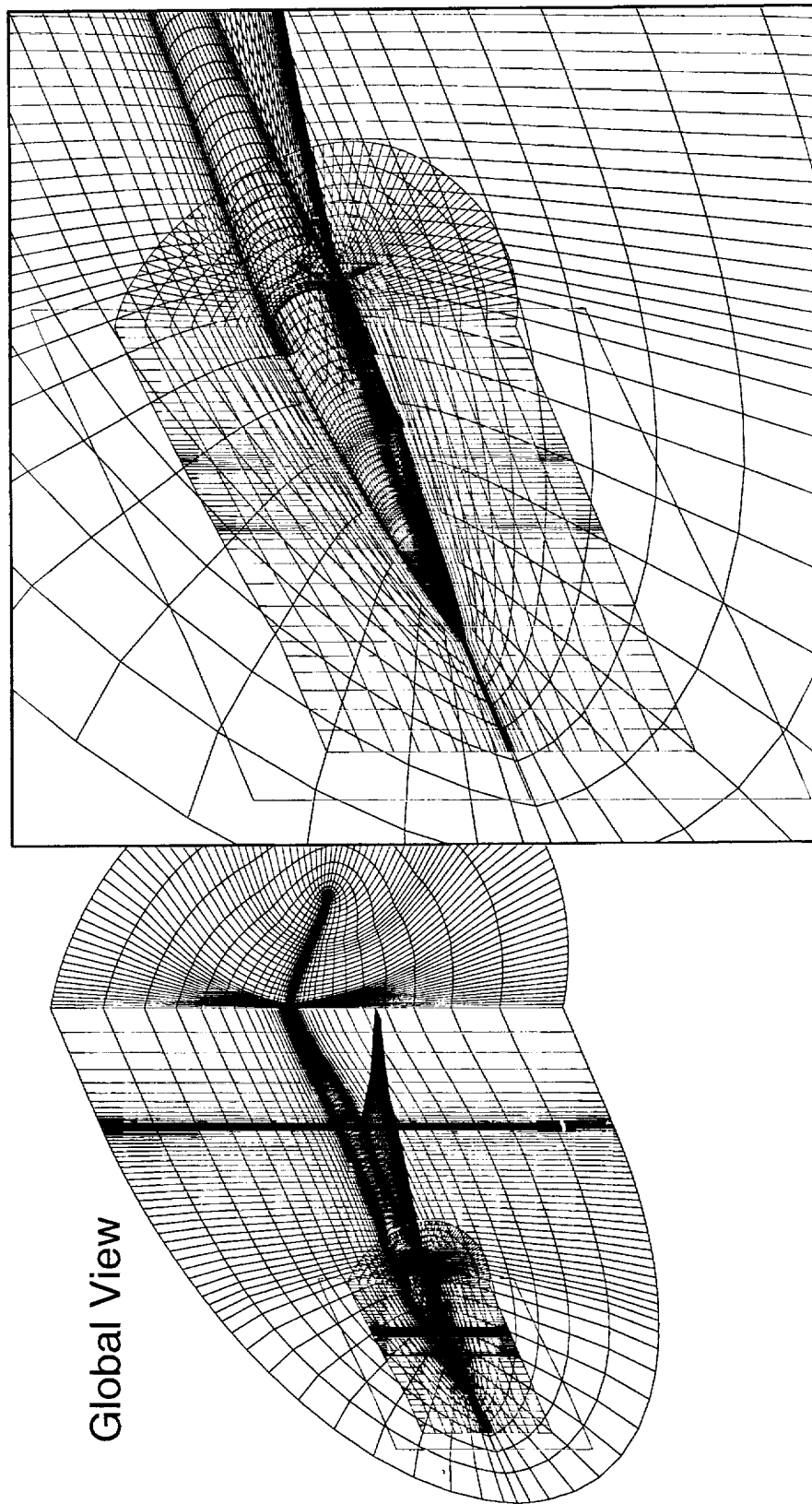
Baseline TCA Wing/Body/Canard Overset Grid



High Speed Aerodynamics, Long Beach

Preliminary Technology Concept Canard Geometry, Every Other Point Shown

Forebody Region



BLB Configurations Analyzed

This chart graphically portrays all of the mounting locations and dihedral angles analyzed by Boeing for the PTC canard configuration. They were selected to bracket the range from a low-mounted canard with anhedral to a high-mounted canard with dihedral. The chart also shows the perspective you would see if you were riding along with the freestream flow when the configuration was flying near the minimum drag and cruise conditions. These perspectives show how the canard may potentially affect the wing. At cruise ($\alpha=3.5^\circ$), the greatest influence is expected to occur on the upper surface from the low-mounted canard. At the minimum drag condition ($\alpha=0^\circ$), it would appear that the wake from the low-mounted canard and the mid-mounted canard ($\Gamma_c=-20^\circ$) would impinge directly on the wing, thus having a significant influence on the upper and lower surfaces of the wing. The other mid-mounted canard configurations would also appear to have some influence on the upper surface of the wing at the minimum drag condition. It should be noted that these ascertions are based only on the relationship of the canard location with respect to the wing at different angles-of-attack, assuming that the wake follows the freestream. It does not consider the upwash or downwash generated from the canard. This will also have an influence on the wing.

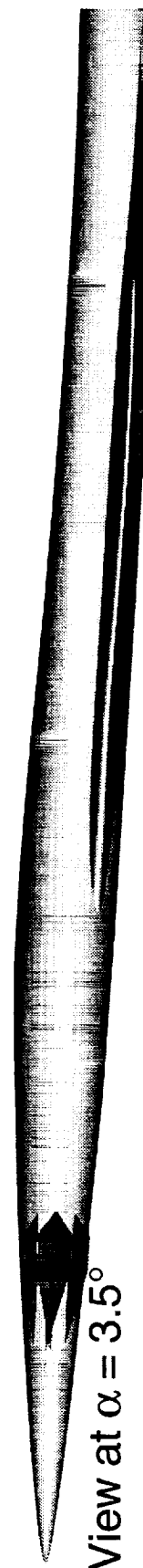
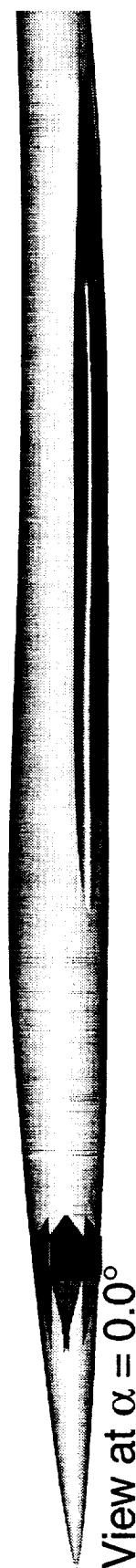
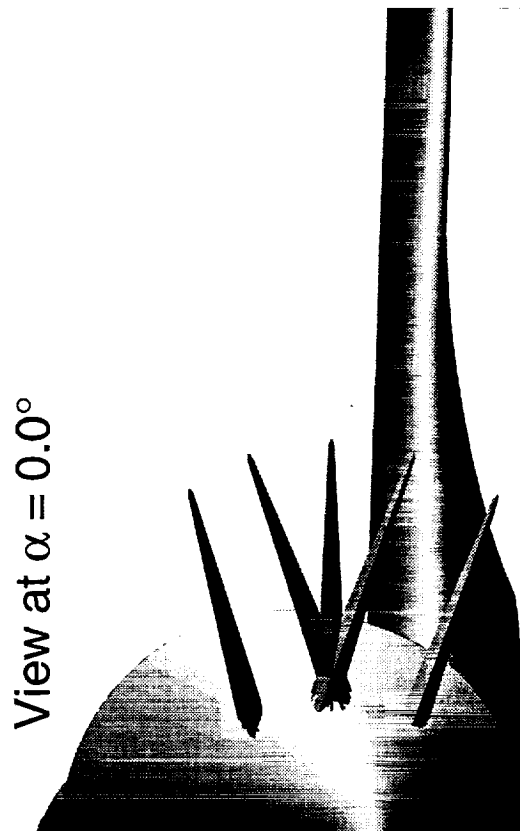
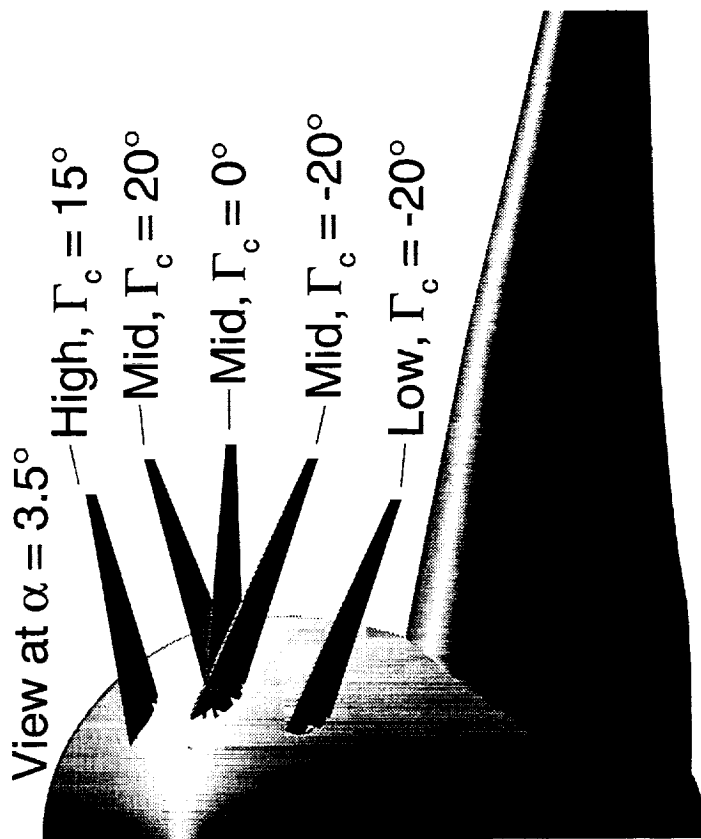


BLB Configurations Analyzed

High Speed Aerodynamics, Long Beach

TCA Wing/Body/Canard Geometry

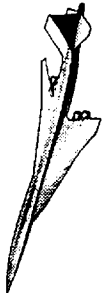
TCA Wing/Body with PTC Canard, $i_c = 0.0^\circ$



BLB Has Generated Many Canard Solutions

This chart shows all of the cases that have been analyzed for the PTC canard by the Boeing Company. A total of 16 Euler drag polars were generated within 3 days. This includes both grid generation and flow solution time. This represents a new benchmark for rapid CFD analysis. The automated grid generation procedure can also generate clustered Navier-Stokes grids and CFL3D can operate in the thin-layer Navier-Stokes mode. We also anticipate rapid response for this type of analysis.

BLB Has Generated Many Canard Solutions



High Speed Aerodynamics, Long Beach

CFL3D Euler Solutions, PTC Canard, $M_\infty=2.4$

Canard Mounting Configuration	Dihedral Angle, Γ_c ($^\circ$)	Incidence Angle, i_c ($^\circ$)	Angle-of-Attack, α ($^\circ$)
Mid (Baseline)	0	-4, -2, 0, 2, 4	0, 1, 2, 3.5, 3.8, 5
	0	-10	1, 2, 3.5, 3.9
Mid	20	-2, 0, 4	1, 2, 3.5
High	-20	-4, 0, 2	1, 2, 3.5
	15	-4, 0, 2	1, 2, 3.5, 3.8
Low	-20	0	0, 1, 2, 3.5, 3.8, 5



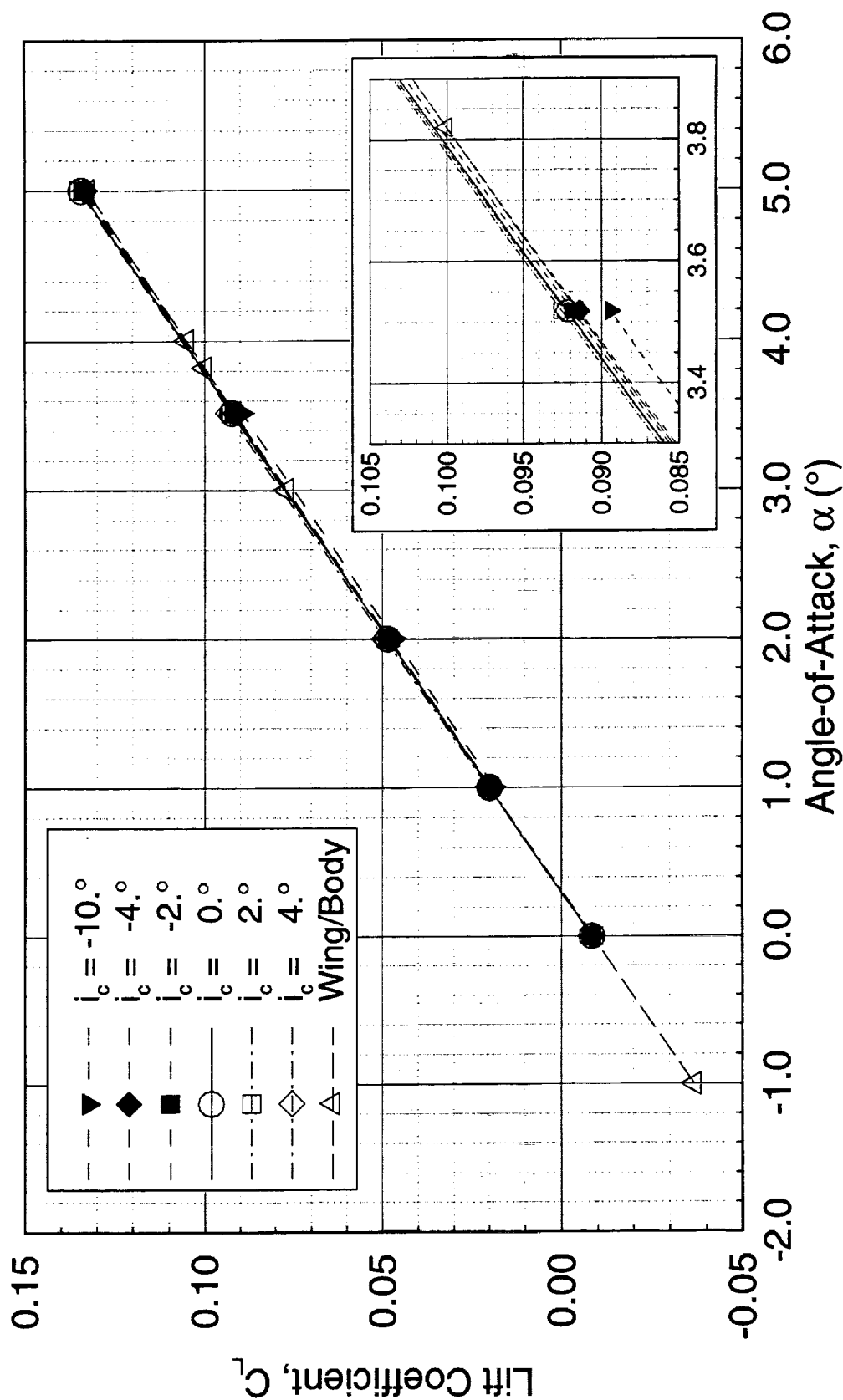
Lift for the TCA W/B/C Configurations

This chart shows lift coefficient as a function of angle-of-attack for the mid-mounted PTC canard ($\Gamma_c=0^\circ$) at variable incidence angles. For comparison purposes, the TCA wing/body results are also shown. For canard incidence angles from -4° to 4° , the slope of the lift curves shown are the same as the wing/body, but at -10° incidence angle there is a slight change in slope. The -10° to -4° data falls to the left of the TCA wing/body lift curve and the -2° to 4° data falls to the right of the lift curve, as expected.

Lift for the TCA W/B/C Configurations



High Speed Aerodynamics, Long Beach
PTC Canard Geometry, Mid Mount, $\Gamma_c=0^\circ$, Variable i_c
CFL3D, Euler, $M_\infty=2.4$



Lift Component Breakdown for the PTC Canard

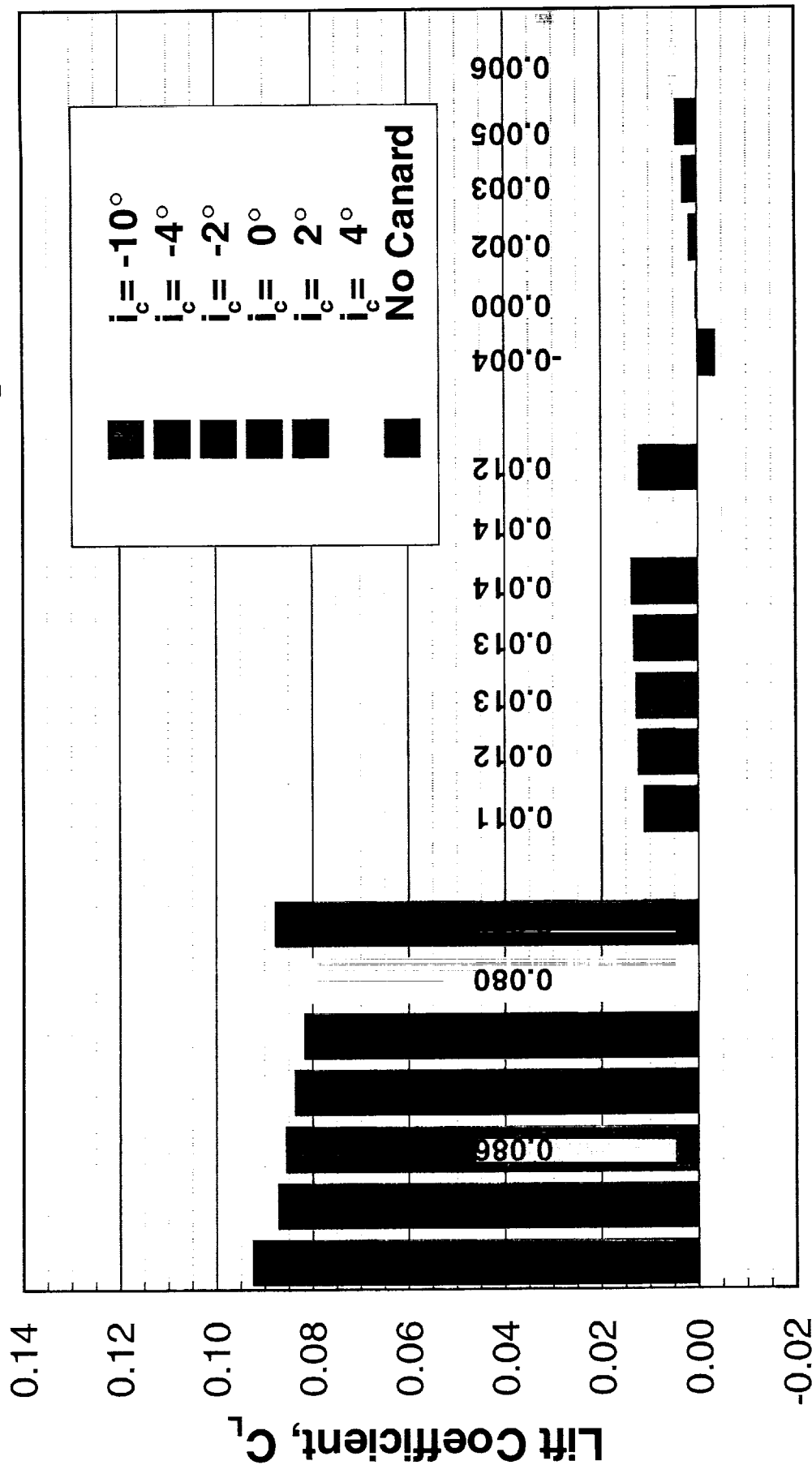
The bar chart on the adjacent page shows the contribution of the wing, fuselage and canard to the total lift coefficient for the PTC mid-mounted canard at variable incidence angles. The total lift coefficient was held to a constant $C_L=0.1$ for this comparison. By deflecting the canard from -10° to 4° , the result is increased lift on the canard and reduced lift on the wing. This same canard deflection range also slightly increases the lift produced by the fuselage. It is observed that approximately -4° of canard deflection is required to achieve a condition of near-zero lift on the canard at a $C_L=0.1$. At this canard deflection the wing lift is nearly the same as the lift on the wing/body without the canard.

Lift Component Breakdown for the PTC Canard



High Speed Aerodynamics, Long Beach

Baseline TCA W/B with PTC Mid Canard, $M_\infty=2.4$, $C_L=0.1$, CFL3D Euler



Wing Fuselage Canard



Drag for the TCA W/B/C Configurations

This chart shows the influence of the mid-mounted PTC ($\Gamma_c=0^\circ$) canard at variable incidence angle on the pressure drag coefficient. As expected, all wing/body/canard drag polars are shifted to the right of the TCA wing/body polar. The lowest impact on pressure drag, at a $C_L=0.1$, is for the canard at $i_c=-2^\circ$. The difference in total pressure drag at this point between the wing/body/canard and the wing/body is less than a count. In general, the PTC canard at the mid-mounted ($\Gamma_c=0^\circ$) location has a very small impact on pressure drag. At cruise ($C_L=0.1$), for small incidence angles ($i_c=-4^\circ$ to 4°) the maximum change in total pressure drag is 4.4 counts with respect to the wing/body.

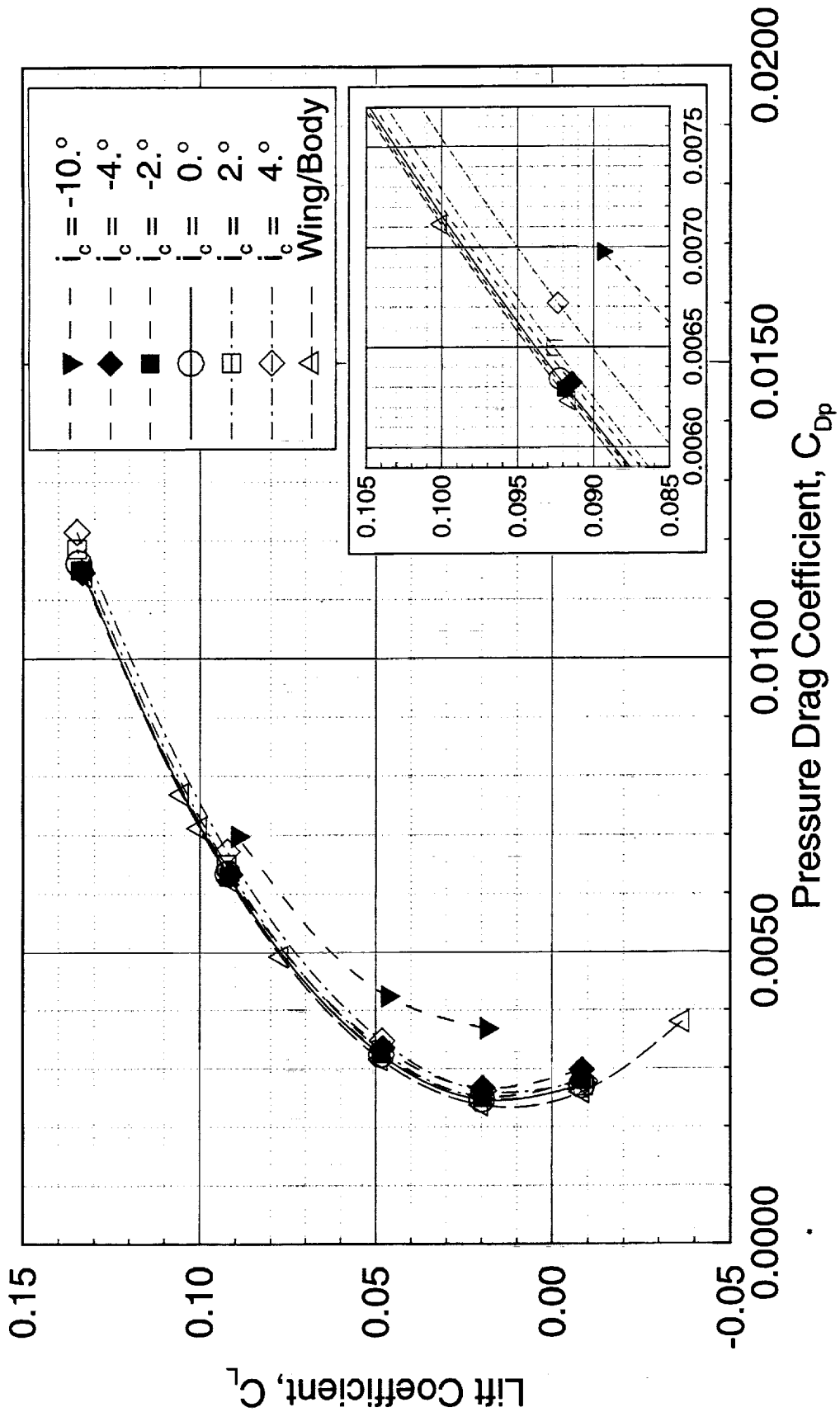
Drag for the TCA W/B/C Configurations



High Speed Aerodynamics, Long Beach

PTC Canard Geometry, Mid Mount, $\Gamma_c = 0^\circ$, Variable i_c

CFL3D, Euler, $M_\infty = 2.4$



Drag Component Breakdown for the PTC Canard

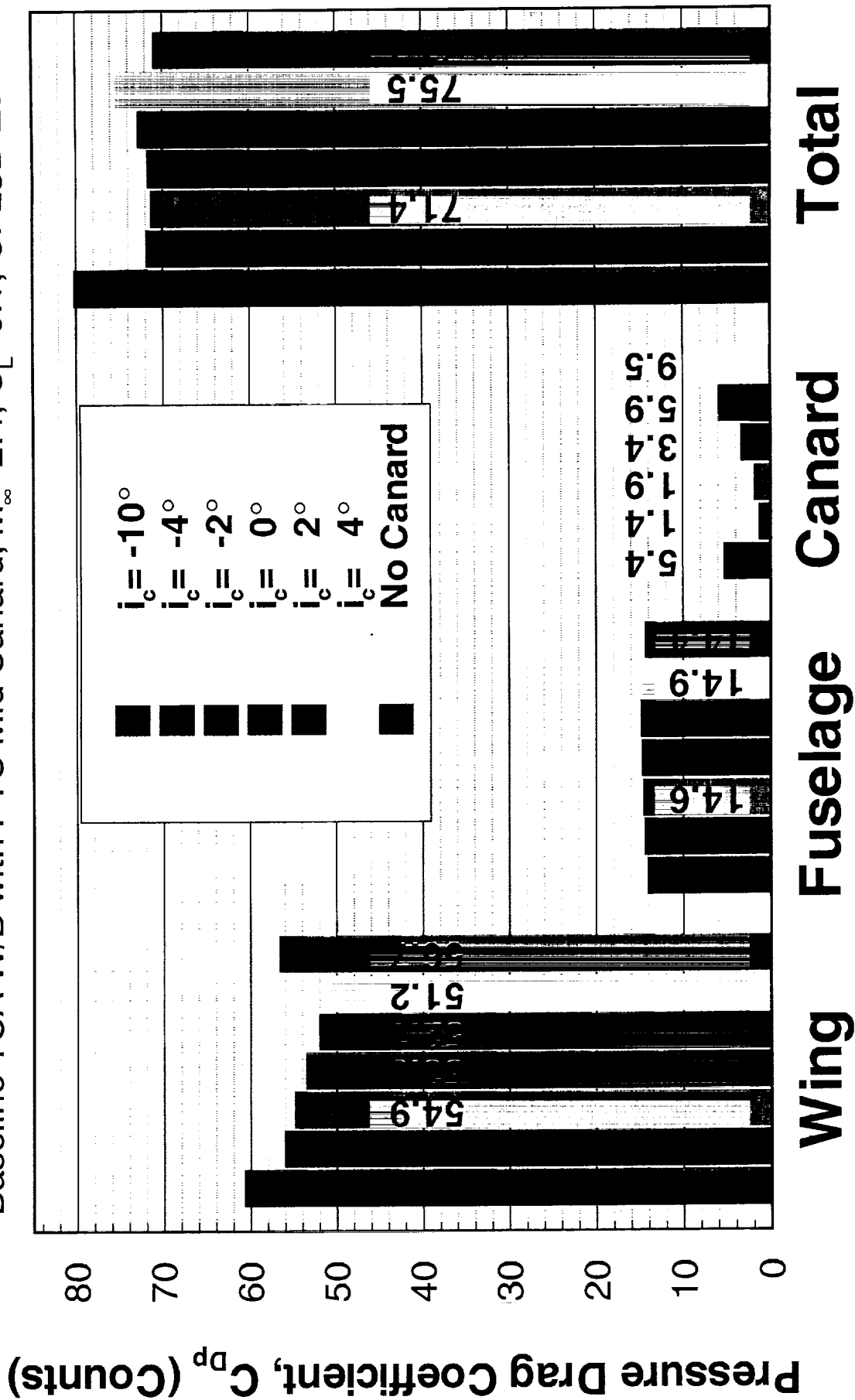
This chart shows the pressure-drag breakdown at $C_L=0.1$ for the PTC mid-mounted canard configuration ($\Gamma_c=0^\circ$) at variable incidence angles. The drag coefficients in this chart are shown in counts. The minimum impact on total pressure drag is 0.3 counts at $i_c=-2^\circ$. The impact on the total wing/body/canard pressure drag coefficient for $i_c=-4^\circ$ to 2° is only 1.8 counts with respect to the wing/body. For $i_c=-4^\circ$ to 4° , the change in total wing/body/canard pressure drag coefficient increases to 4.3 counts. That is an increase of 2.5 counts for a change in incidence angle of 2° . We can see that over the same range of incidence angles the change in wing pressure drag coefficient is a reduction of 5.5 counts, the canard drag coefficient increases 5.9 counts, and the fuselage coefficient increases 0.5 counts. In general, the PTC canard has a small influence on the total wing/body/canard pressure drag coefficient, at a $C_L=0.1$, for small changes in incidence angles, but there does seem to be a significant influence of the canard on the wing.

Drag Component Breakdown for the PTC Canard



High Speed Aerodynamics, Long Beach

Baseline TCA W/B with PTC Mid Canard, $M_\infty=2.4$, $C_L=0.1$, CFL3D Euler



Pitching Moment for the TCA W/B/C Configurations

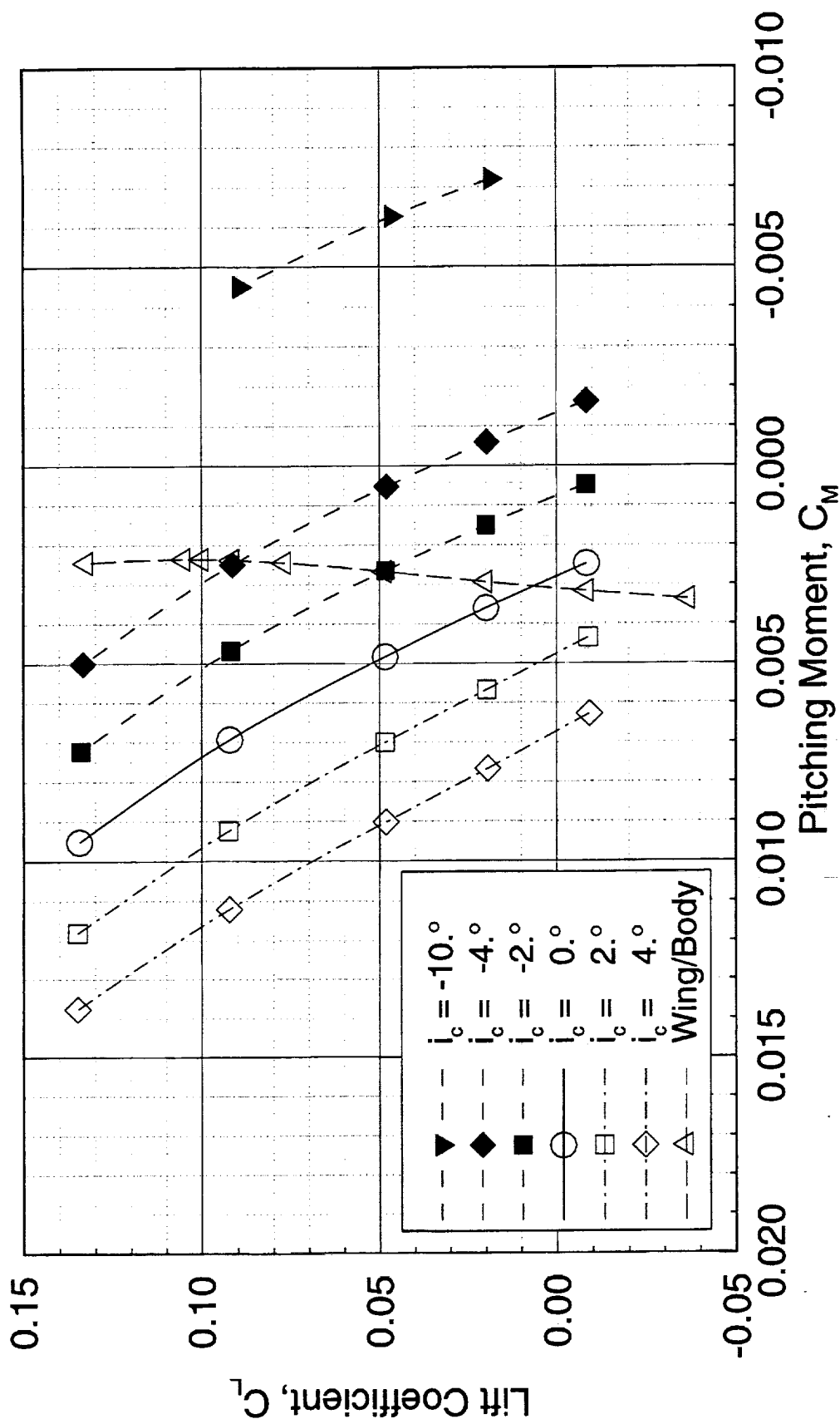
The following chart shows the influence of canard incidence angle on the pitching moment coefficient for a mid-mounted canard with $\Gamma_c=0^\circ$. In general, the small PTC platform provides large changes in pitching moment coefficient with small changes in incidence angle, as expected. It takes approximately $i_c=-4^\circ$ to obtain the same moment coefficient as the wing/body without the canard at a $C_L=0.1$. Interestingly, an $i_c=-6^\circ$ would be required to trim the aircraft without a tail and nacelles, although the stability would be an issue.

Pitching Moment for the TCA W/B/C Configurations



High Speed Aerodynamics, Long Beach

PTC Canard Geometry, Mid Mount, $\Gamma_c = 0^\circ$, Variable i_c
CFL3D, Euler, $M_\infty = 2.4$



Pressure Contours for TCA W/B/C

The following two charts show pressure contours for the mid-mounted PTC canard configuration ($\Gamma_c=0^\circ$) for $i_c=-10^\circ$ to 4° at $\alpha=3.5^\circ$. In general, there are only slight changes in the contours on the wing/body over this range of incidence angles. However, the changes in pressure contours on the canard are dramatic. In these charts, the overset region of the two grids can be seen for the configurations with a canard on them, by the crossed contour lines on the forebody near the apex of the wing.

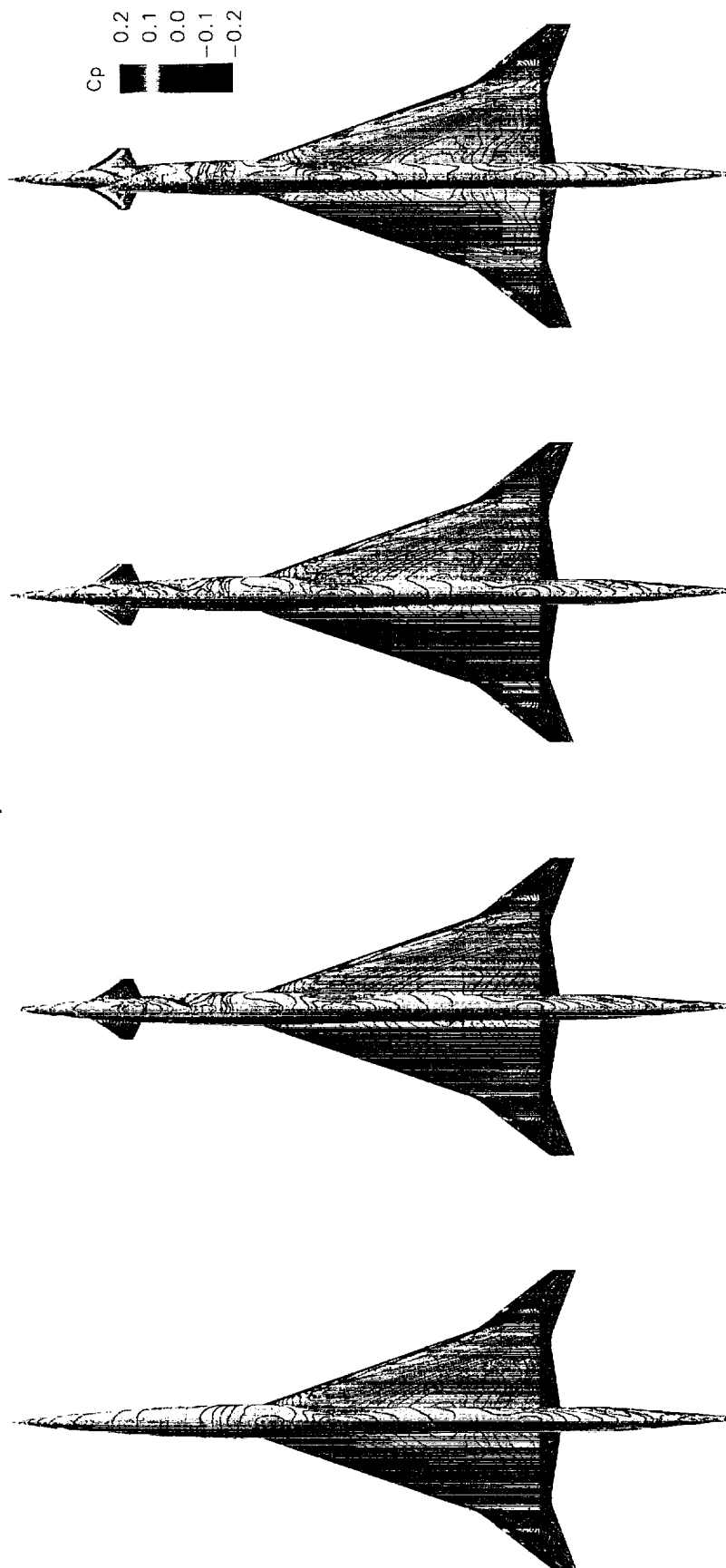
Pressure Contours for TCA W/B/C



High Speed Aerodynamics, Long Beach

CFL3D Euler, $M_\infty=2.4$, $\alpha=3.518^\circ$

Mid Mount, 0° Dihedral



W/B

$i_c=-2^\circ$

$i_c=-4^\circ$

$i_c=-10^\circ$

Top View



(This page intentionally left blank.)

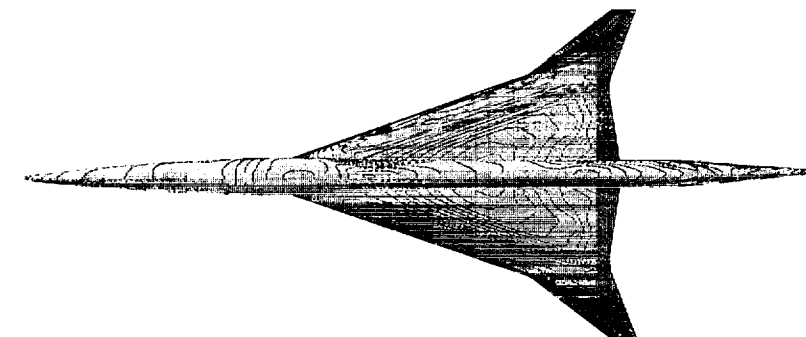
Pressure Contours for TCA W/B/C



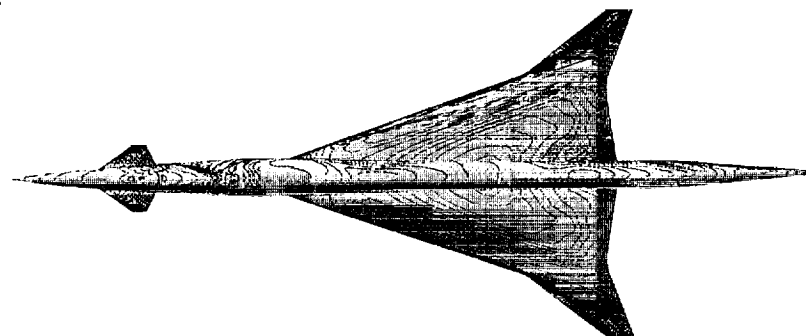
High Speed Aerodynamics, Long Beach

CFL3D Euler, $M_\infty=2.4$, $\alpha=3.518^\circ$

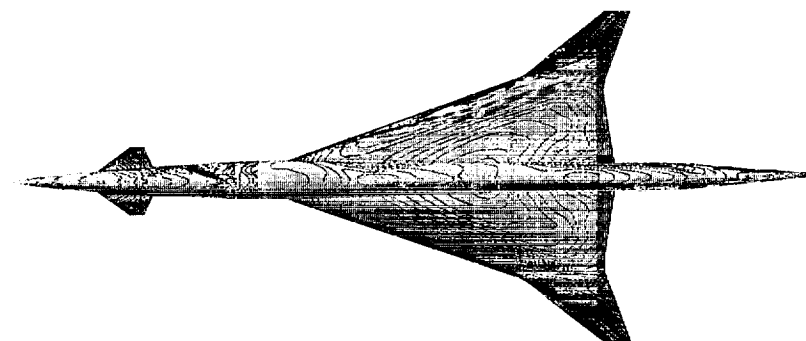
Mid Mount, 0° Dihedral



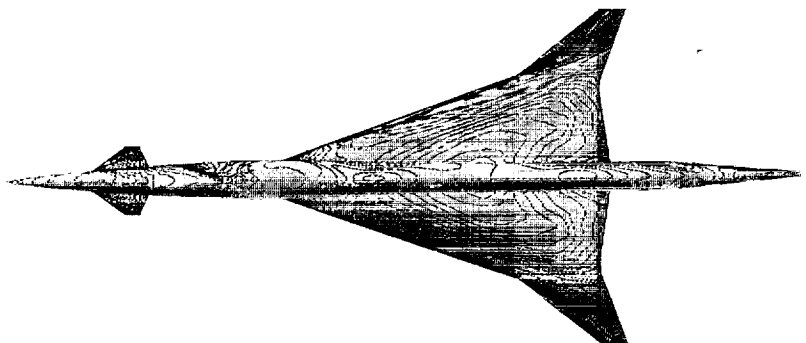
W/B



$i_c=0^\circ$



$i_c=2^\circ$



$i_c=4^\circ$

Top View



Drag Component Breakdown for the PTC and ACC Canard

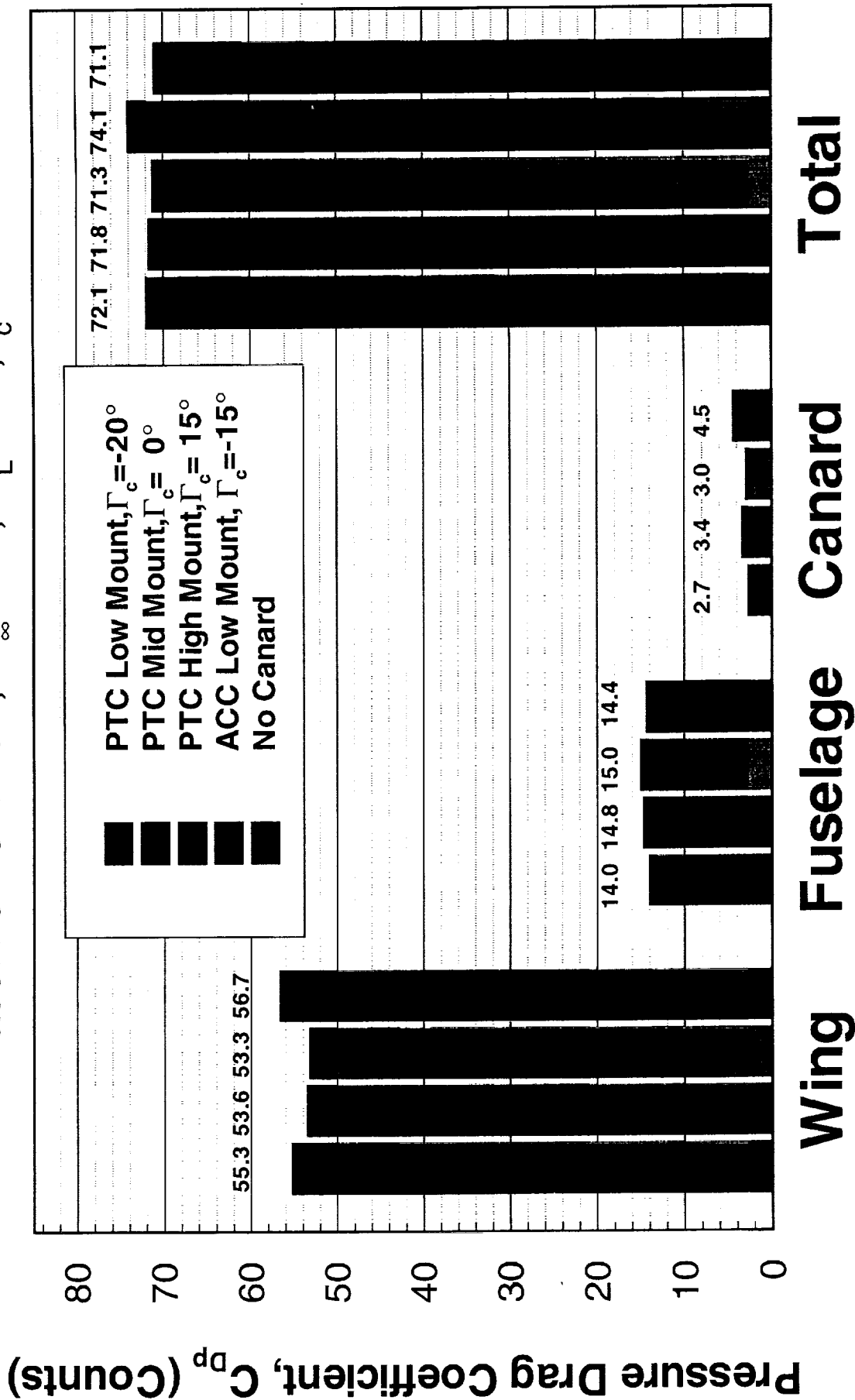
The effect of canard mounting location and planform size on pressure drag coefficient are shown in the adjacent chart. The pressure drag coefficient (in counts) for the wing, fuselage, and canard components, as well as the total pressure drag coefficient are shown for the PTC low-mounted, PTC mid-mounted, PTC high-mounted, ACC low-mounted, and the TCA wing/body configurations. Dynacs provided the ACC low-mounted pressure drag coefficient data. The fuselage and wing components for the ACC low-mount are not shown, because the wing component includes part of the fuselage in Dynacs analysis. All data are shown at $C_L=0.1$ and $i_c=0^\circ$. The chart shows that for the PTC planform a change in mounting location can change the pressure drag on the fuselage by 1 count. The effect of the planform sizes are that the ACC canard planform yields approximately 1.5 more drag counts than the PTC canard planform. It is observed that the canard pressure drag coefficient is nearly insensitive to PTC canard mounting location. For all three PTC mounting locations, the canard pressure drag coefficient is approximately 3.0 counts. The most significant conclusion is that the ACC canard configuration yields 3.0 counts greater pressure drag than the TCA wing/body configuration. This is probably because the ACC canard is closer to the wing than the PTC canard and the ACC canard has a larger planform area. The PTC configuration at $i_c=0^\circ$, yields a count or less of total pressure drag coefficient depending upon the canard mounting location.

Drag Component Breakdown for the PTC and ACC Canard



High Speed Aerodynamics, Long Beach

Baseline TCA W/B, $M_\infty=2.4$, $C_L=0.1$, $i_c=0^\circ$



Pressure Distributions for the TCA W/B/C Configuration

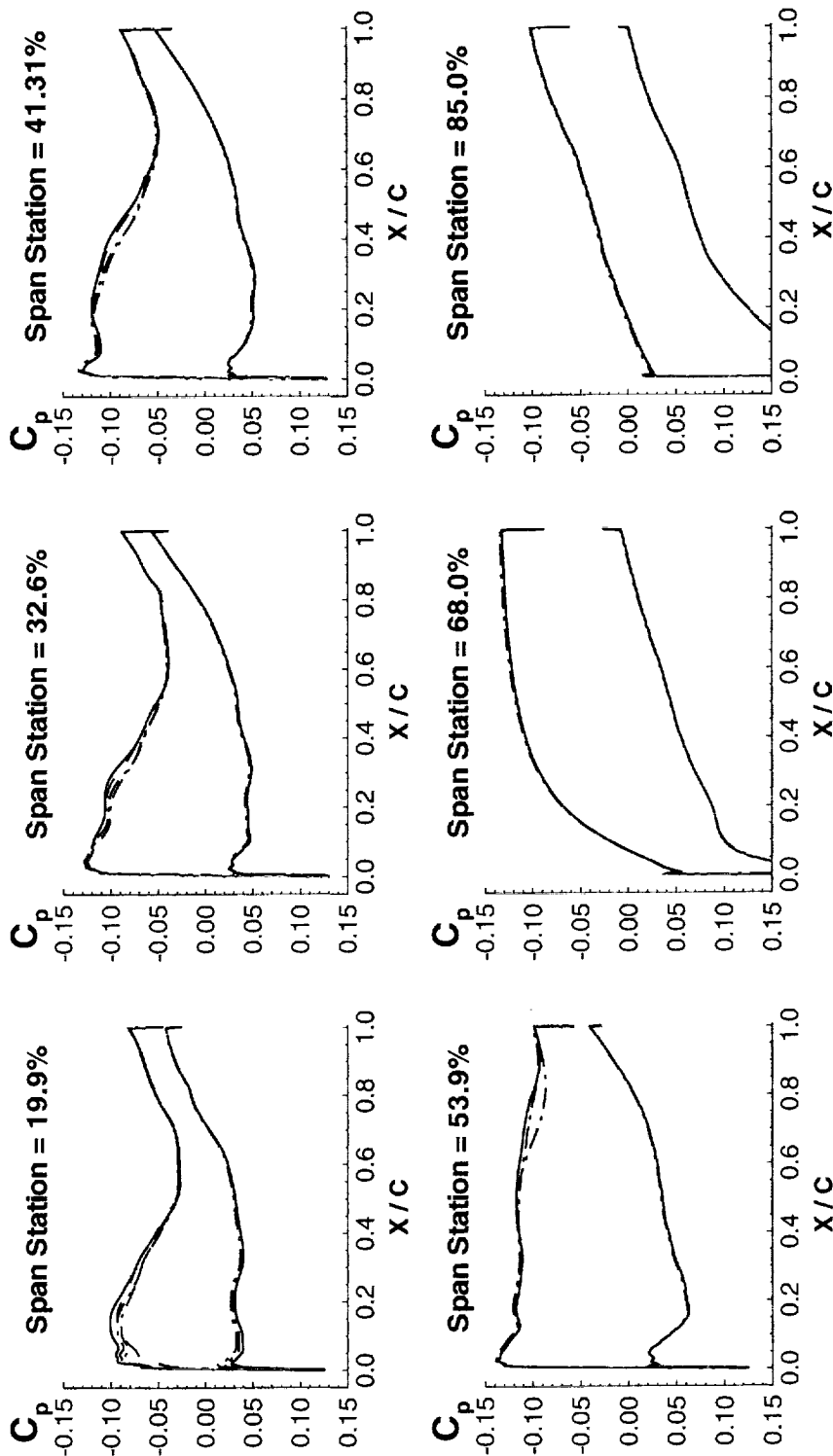
The following chart shows the effect of the PTC canard mounting location on pressure coefficient at $i_c=0^\circ$, $\alpha=3.5^\circ$. Six different spanwise pressure coefficient distributions are shown for the low, mid, and high PTC canard mounting locations and the TCA wing/body. The largest effects are located at the leading edge of the 19.9% span station. The effect on pressure coefficient diminishes with increasing span station and occurs farther from the leading edge. Beyond the 53.9% span station, there is almost no change in pressure coefficient distribution for different PTC canard mounting locations with respect to the TCA wing/body. The 19.9% span station is the only place where significant changes in pressure coefficient are observed on the lower surface of the wing.

Pressure Distributions for the TCA W/B/C Configuration



High Speed Aerodynamics, Long Beach
PTC Canard Geometry, CFL3D Euler, $M_\infty=2.4$, $\alpha=3.518^\circ$ Span Station

Wing/Body	
Low Mount, $\Gamma_c = -20^\circ$, $i_c = 0^\circ$	85.0 %
Mid Mount, $\Gamma_c = 0^\circ$, $i_c = 0^\circ$	68.0 %
High Mount, $\Gamma_c = 15^\circ$, $i_c = 0^\circ$	53.9 %
	41.3 %
	32.6 %
	19.9 %



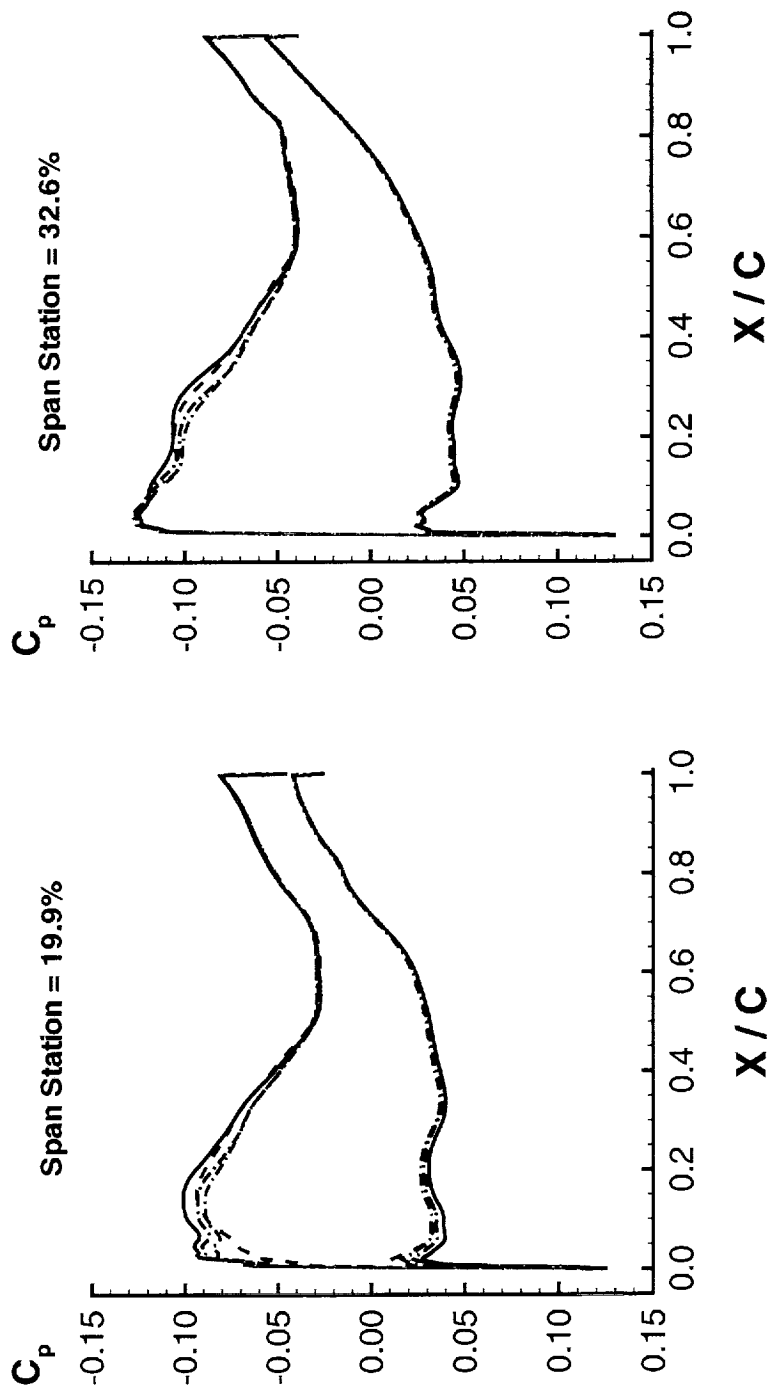
Pressure Distributions for the TCA W/B/C Configuration

This chart shows an enlarged view of the pressure distributions for the 19.9% and 32.6% span stations that were shown on the previous page.

Pressure Distributions for the TCA W/B/C Configuration

High Speed Aerodynamics, Long Beach

PTC Canard Geometry, CFL3D Euler, $M_\infty=2.4$, $\alpha=3.518^\circ$



Pressure Distributions for the TCA W/B/C Configuration

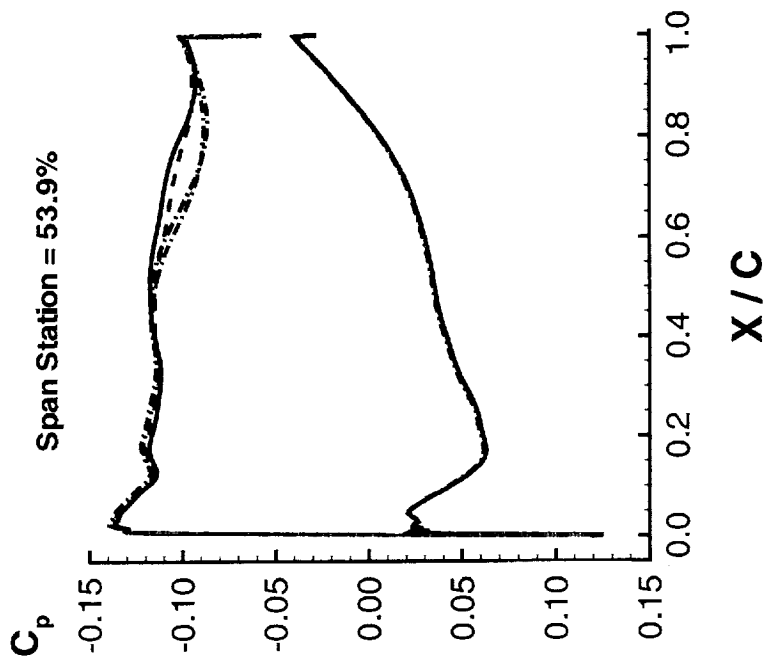
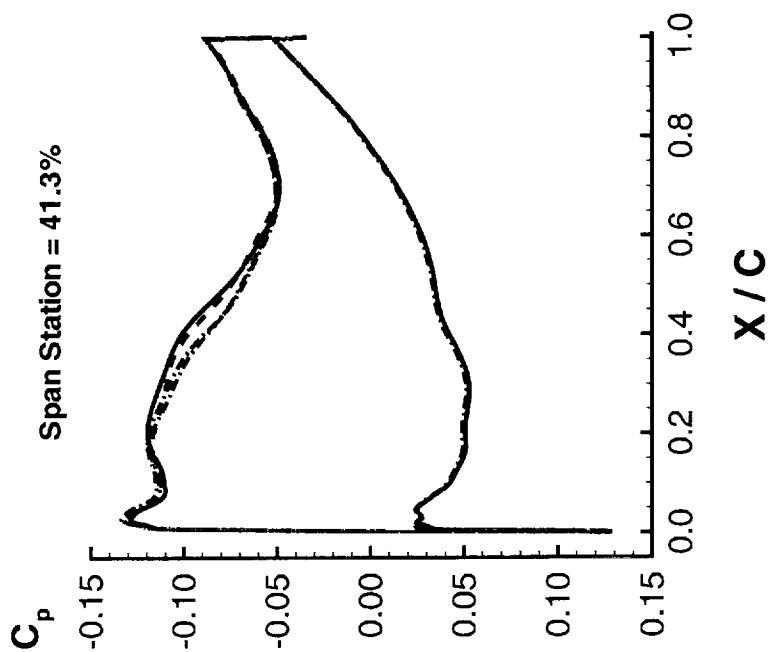
This chart shows an enlarged view of the pressure distributions for the 41.3% and 53.9% span stations that were shown earlier.

Pressure Distributions for the TCA W/B/C Configuration

High Speed Aerodynamics, Long Beach

PTC Canard Geometry, CFL3D Euler, $M_\infty=2.4$, $\alpha=3.518^\circ$

Wing/Body	Span Station
Low Mount, $\Gamma_c = -20^\circ$, $i_c = 0^\circ$	53.9 %
Mid Mount, $\Gamma_c = 0^\circ$, $i_c = 0^\circ$	41.3 %
High Mount, $\Gamma_c = 15^\circ$, $i_c = 0^\circ$	



Pressure Distributions for the TCA W/B/C Configuration

This chart shows an enlarged view of the pressure distributions for the 68.0% and 85.0% span stations that were shown earlier.

Pressure Distributions for the TCA W/B/C Configuration



High Speed Aerodynamics, Long Beach

PTC Canard Geometry, CFL3D Euler, $M_\infty=2.4$, $\alpha=3.518^\circ$

Span Station

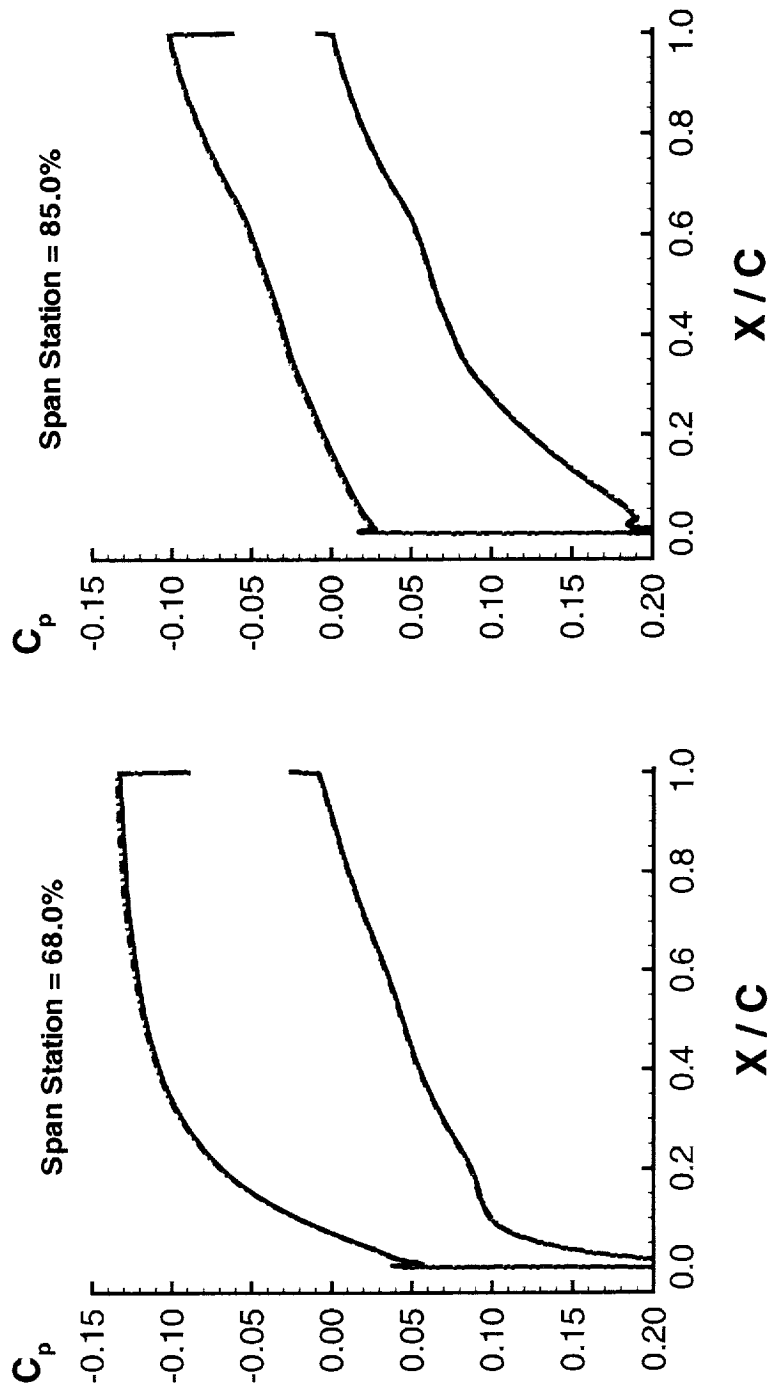
Wing/Body

Low Mount, $\Gamma_c = -20^\circ$, $i_c = 0^\circ$

Mid Mount, $\Gamma_c = 0^\circ$, $i_c = 0^\circ$

High Mount, $\Gamma_c = 15^\circ$, $i_c = 0^\circ$

85.0 %
65.0 %



Streamlines for the TCA W/B/C

This chart shows the streamlines in the wake of the PTC low-mounted canard at $i_c=0^\circ$ near both the minimum drag ($\alpha=0^\circ$) and cruise ($\alpha=3.5^\circ$) conditions. The significance of this chart is that the PTC low-mounted configuration should have the greatest influence on the upper and lower surfaces of the wing over the angle-of-attack range considered. Near the minimum drag condition, the wake passes below the wing. Near the cruise condition, the wake passes over the wing. The PTC low-mounted canard should be a good CFD code validation case because it influences the wing at many conditions. However, to fully understand the influence of the canard wake and tip vortex on the wing, nacelles, and the aircraft performance, a Navier-Stokes analysis should be completed.

Streamlines for TCA W/B/C



High Speed Aerodynamics, Long Beach

CFL3D Euler, $M_{\infty}=2.4$, PTC Low Mount, $\Gamma_c=20^\circ$, $i_c=0^\circ$



$\alpha=0.0^\circ$



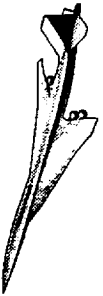
$\alpha=3.518^\circ$

BOEING

Dynacs CFD Approach

This chart outlines the approach taken by Dynacs to analyze the ACC canard configuration. An overset grid topology was utilized, and the surface grids were generated using the Boeing AGPS grid tool. The volume grids were constructed using HYPGEN, a hyperbolic grid generation tool. The grid was clustered near the surface to produce a $y^+ \approx 1$ for accurate viscous solutions. The OVERFLOW flow solver was used to solve the thin-layer Navier-Stokes equations with the Baldwin-Barth turbulence model. This CFD analysis was computed for a Reynolds number, based on mean aerodynamic chord, of 6.4 million. This is a wind-tunnel Reynolds number of 4 million/ft for a 1.675%-scale model. The solutions were run on a Cray C-90 and an SGI R10000.

Dynacs CFD Methodology



High Speed Aerodynamics, Long Beach

○ Grid Generation

- Overset grid topology
 - Surface grids: AGPS
 - Volume grid: HYPGEN
- Viscous grid clustering: $y^+=1$

○ Flow Solver

- OVERFLOW
- Baldwin-Barth turbulence model
- $Re_c=6.4 \times 10^6$ (Wind Tunnel)
- Solutions run on C-90 (vn) and SGI R10000

Dynacs ACC Canard Grids

On the adjacent page, a sketch of the C-grid, used on the canard, and the collar grid, used to resolve the canard-body junction, are shown. The C-grid contains 760,000 grid points, while the collar grid contains 200,000 grid points. These are believed to be sufficient to resolve the canard wake and the canard-body junction.

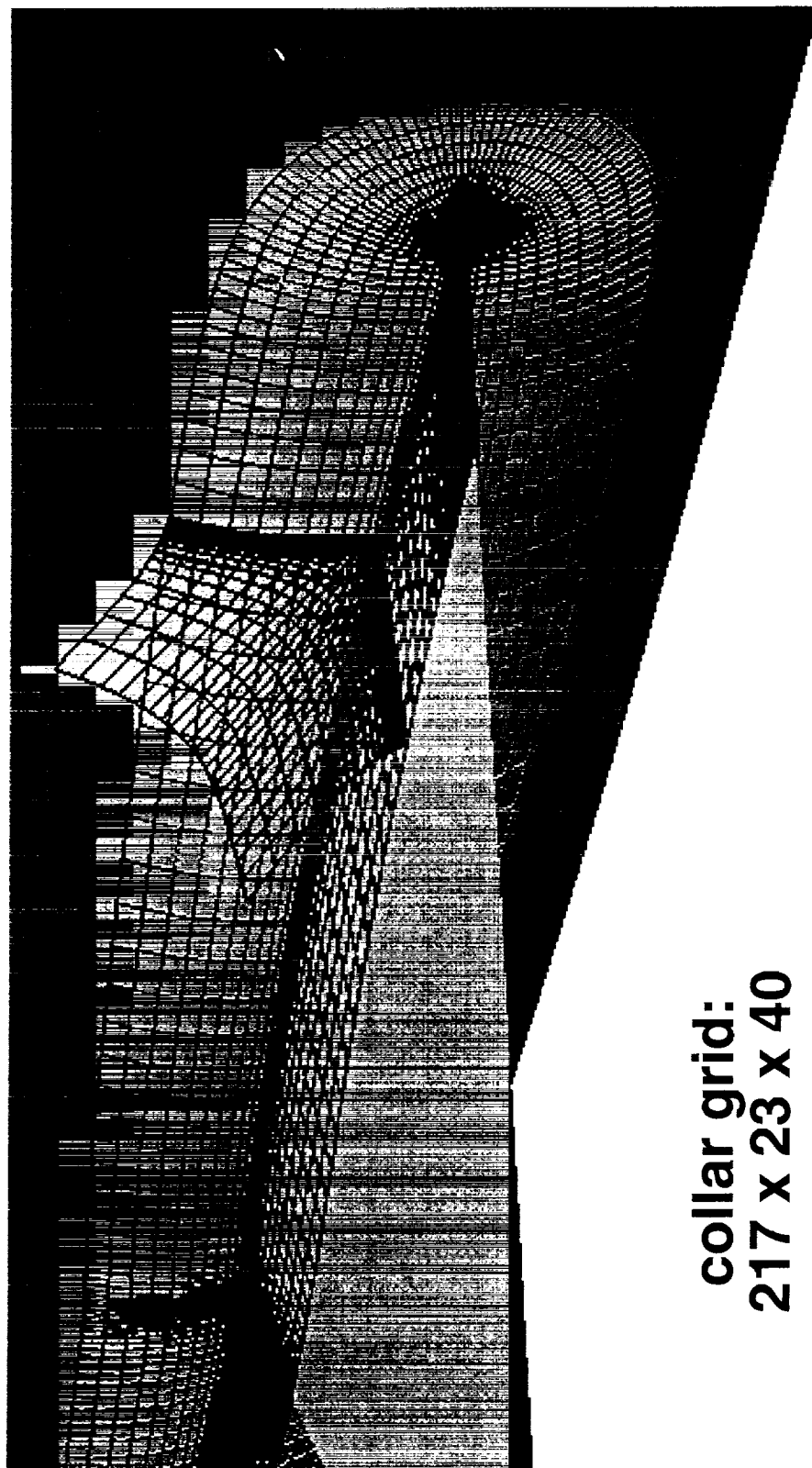


HSR TCA Canard Study



HSCT High Speed Aerodynamics

C-grid used for canards with collar to resolve canard-body junction



collar grid:
217 x 23 x 40

ACC Canard Mounting Positions

This chart shows the mounting locations for the ACC canard considered by Dynacs. The mounting locations consisted of a low mount with -15° dihedral, a mid mount with 0° dihedral, and a high mount with 0° dihedral.

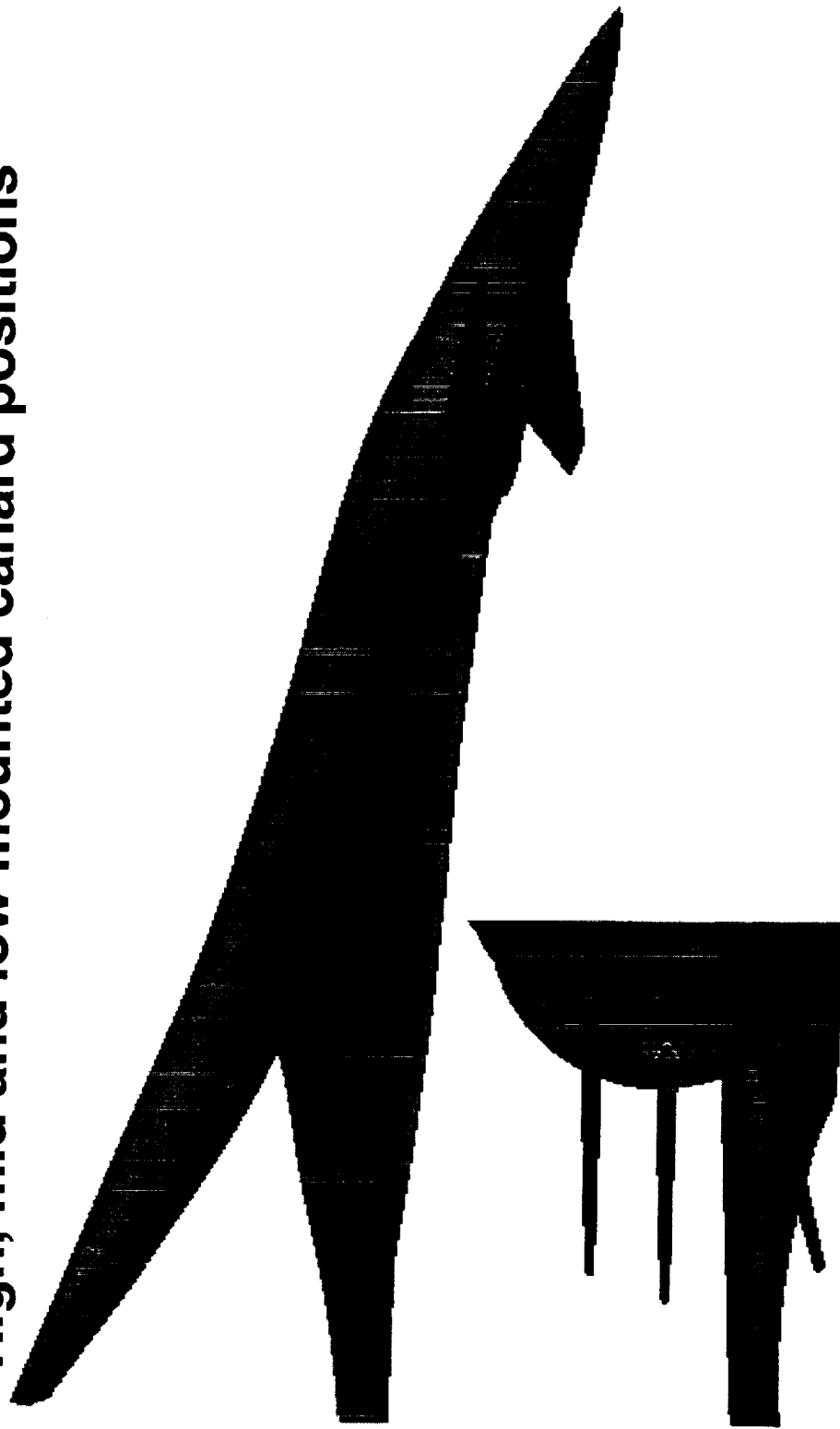


HSR TCA Canard Study

HSCT High Speed Aerodynamics



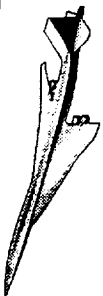
High, mid and low mounted canard positions



Dynacs Navier-Stokes Solutions

Dynacs has generated Navier-Stokes solutions for 9 mini-polars. Three angles-of-attack were considered ($\alpha=2.5^\circ, 3.5^\circ, 4.5^\circ$), at three incidence angles ($i_c=-2^\circ, 0^\circ, 2^\circ$). Note for the low mounted canard, the incidence angle was measured from the baseline value of -2° . Therefore, for the low mounted canard the incidence angles considered, measured from the horizontal, were $-4^\circ, -2^\circ, 0^\circ$. The solutions were computed for a freestream Mach number of 2.4, a Reynolds number of 6.4 million based on the mean aerodynamic chord, and using the Baldwin-Barth turbulence model.

Dynacs Navier-Stokes Solutions



Configuration Aerodynamics

OVERFLOW, Baldwin-Barth, $M_\infty=2.4$ $Re_c=6.4 \times 10^6$, ACC Canard

Canard Mounting Configuration	Dihedral Angle, Γ_c ($^\circ$)	Incidence Angle, i_c ($^\circ$) *	Angle-of-Attack, α ($^\circ$)
Mid	0	-2, 0, 2	2.5, 3.5, 4.5
High	0	-2, 0, 2	2.5, 3.5, 4.5
Low	-15	-2, 0, 2	2.5, 3.5, 4.5

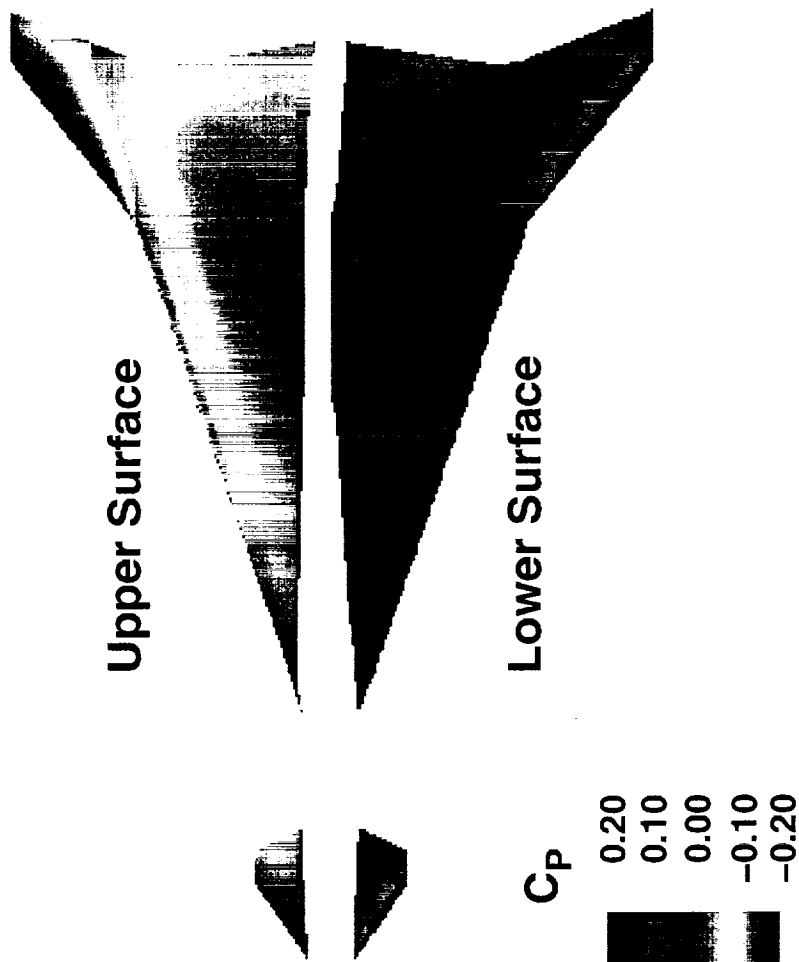
* The incidence angle is measured from the default value of -2° .

ACC Low Mounted Canard C_p

The chart on the adjacent page shows flooded pressure coefficient contours for the ACC low mounted canard and wing at an $\alpha=3.5^\circ$ and an incidence angle from the horizontal of 0° .



Low Mounted Canard ($M = 2.4$, $\alpha = 3.5^\circ$, $\delta = +2^\circ$) Surface Pressure Coefficient (C_p)



ΔC_p on the Wing in the Presence of the ACC

Low-Mounted Canard

The difference between the pressure coefficient on the wing/body/canard and the pressure coefficient on the wing/body is shown on the adjacent page at $\alpha=3.5^\circ$ for a canard incidence angle from the horizontal of 0° . This delta pressure coefficient shows the large influence of the ACC low-mounted canard on the leading edge of the inboard wing. The result is an increased pressure on the upper surface and a decreased pressure on the lower surface, both near the wing apex. There is also some increased pressure on the inboard upper wing extending across the break to the outboard wing trailing edge.

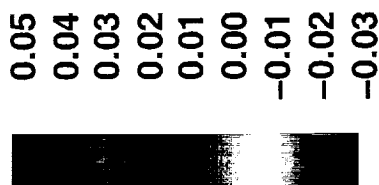


Low Mounted Canard ($M = 2.4$, $\alpha = 3.5^\circ$, $\delta = +2^\circ$) Surface Pressure Coefficient Difference (ΔC_p)

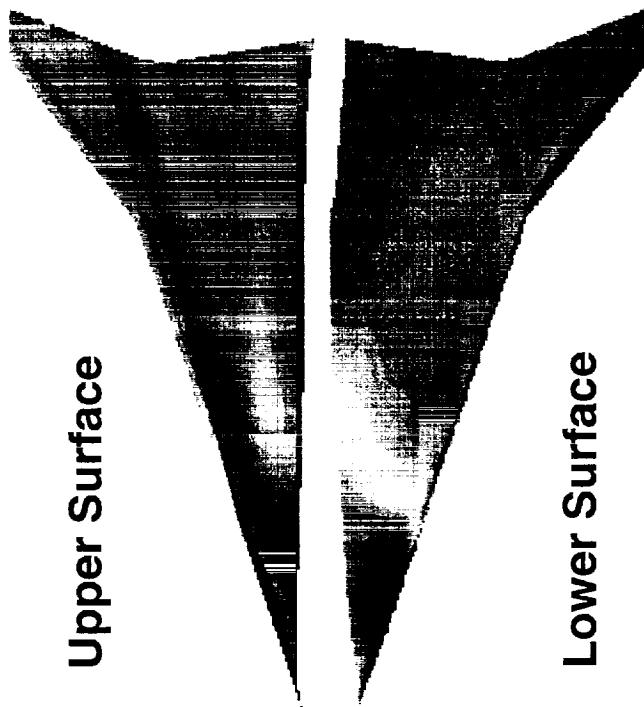
$$\Delta C_p = C_p(WBC) - C_p(WB)$$

Upper Surface

ΔC_p



Lower Surface

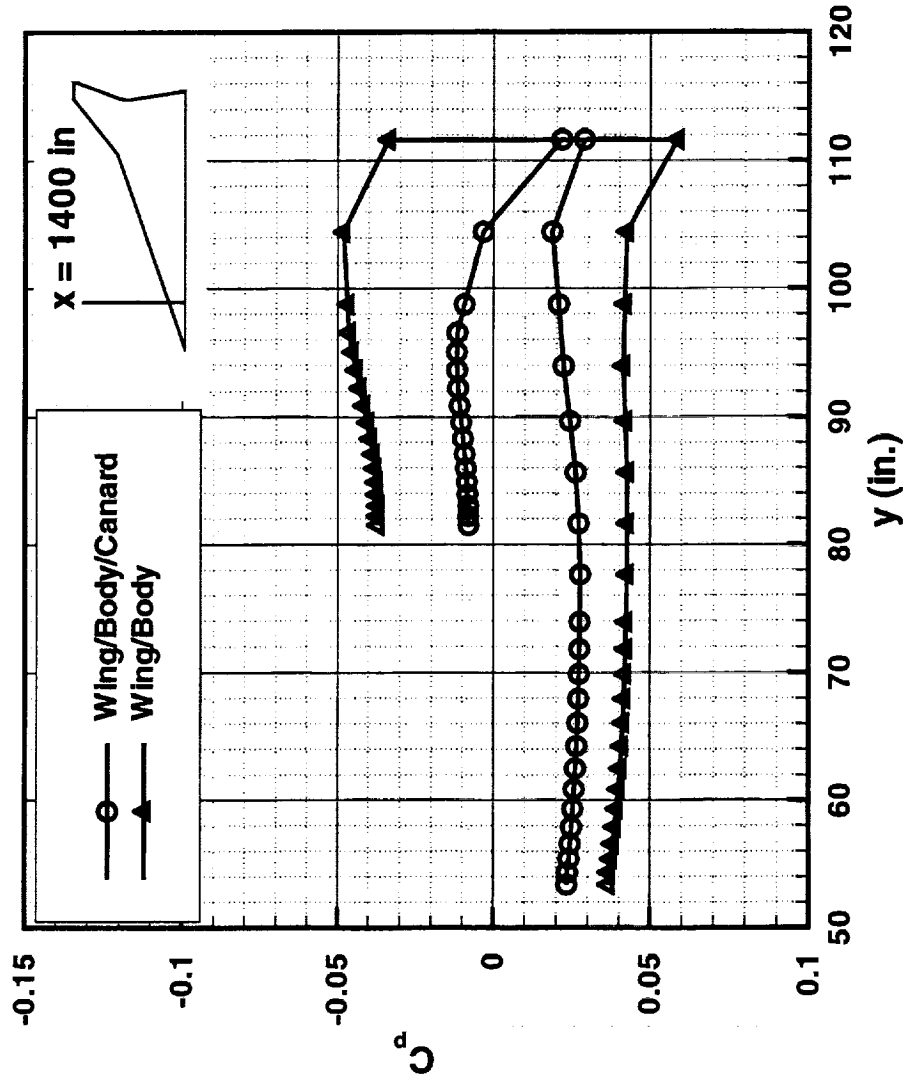


Pressure Distribution Comparisons

This chart shows the pressure coefficient distribution at an axial station of $x=1400$ inches for the wing/body/canard and the wing/body configurations at $\alpha=3.5^\circ$ and a canard incidence angle from the horizontal of 0° . At this axial location, the ACC low-mounted canard produces significant changes in the pressure coefficient on the upper and lower surfaces of the wing. The upper surface of the wing has a higher pressure and the lower surface of the wing has a lower pressure than the configuration without the influence of the canard.



Low Mounted Canard ($M = 2.4$, $\alpha = 3.5^\circ$, $\delta = +2^\circ$) Surface Pressure Coefficient (C_p)

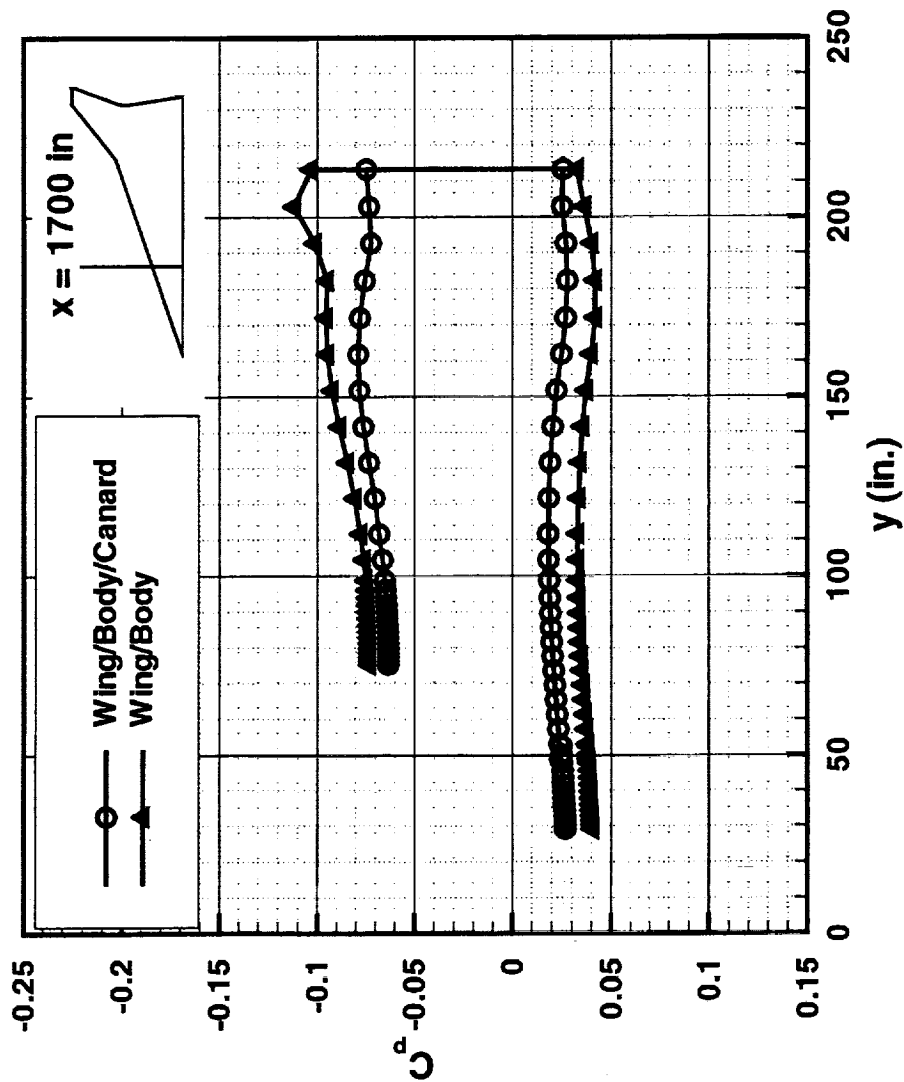


Pressure Distribution Comparisons (Cont.)

This chart shows the pressure coefficient distribution at an axial station of $x=1700$ inches for the wing/body/canard and the wing/body configurations at $\alpha=3.5^\circ$ and a canard incidence angle from the horizontal of 0° . At this axial location, the ACC low-mounted canard produces significant changes in the pressure coefficient on the upper and lower surfaces of the wing, but the changes are not as great as shown on the previous page at the $x=1400$ inch station. Again, the upper surface of the wing has a higher pressure and the lower surface of the wing has a lower pressure than the configuration without the influence of the canard.



Low Mounted Canard ($M = 2.4$, $\alpha = 3.5$, $\delta = +2^\circ$) Surface Pressure Coefficient (C_p)

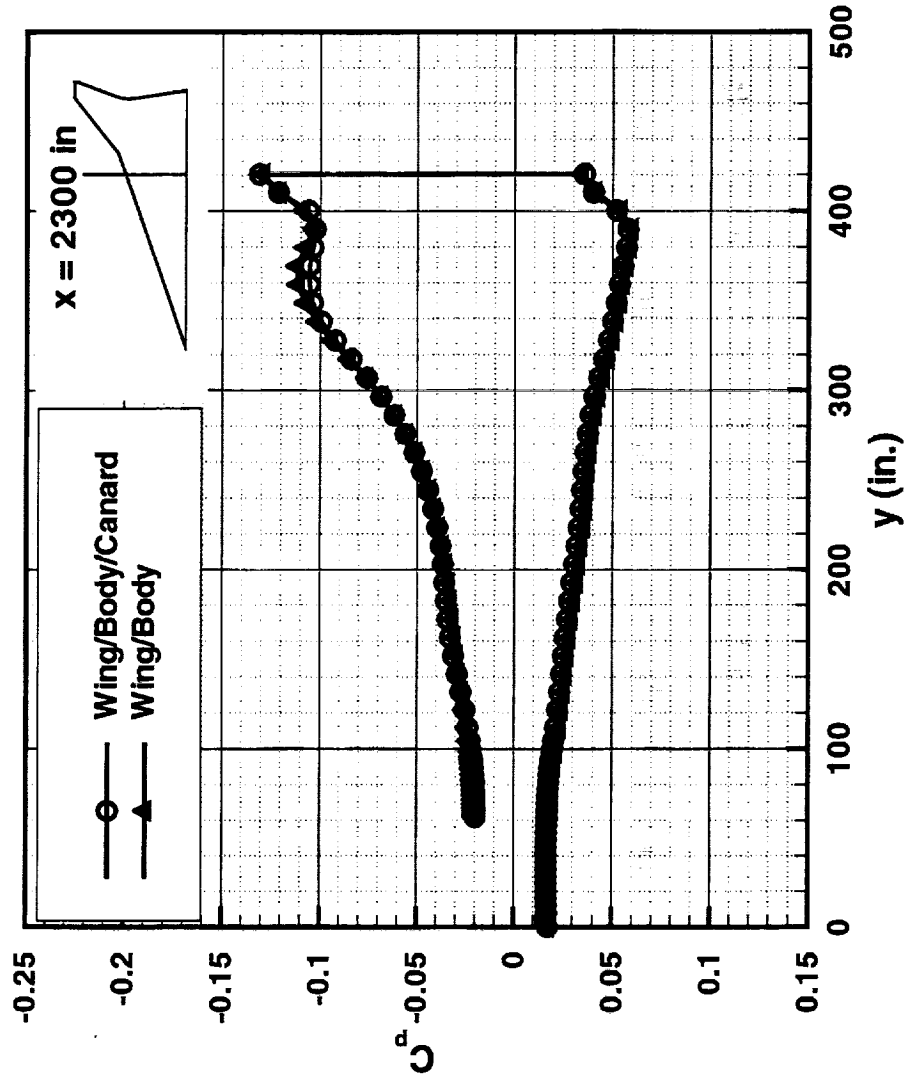


Pressure Distribution Comparisons (Cont.)

This chart shows the pressure coefficient distribution at an axial station of $x=2300$ inches for the wing/body/canard and the wing/body configurations at $\alpha=3.5^\circ$ and a canard incidence angle from the horizontal of 0° . At this axial location, the ACC low-mounted canard produces small changes in the pressure coefficient on the upper and lower surfaces of the wing in comparison to the configuration without a canard.



Low Mounted Canard ($M = 2.4$, $\alpha = 3.5^\circ$, $\delta = +2^\circ$) Surface Pressure Coefficient (C_p)

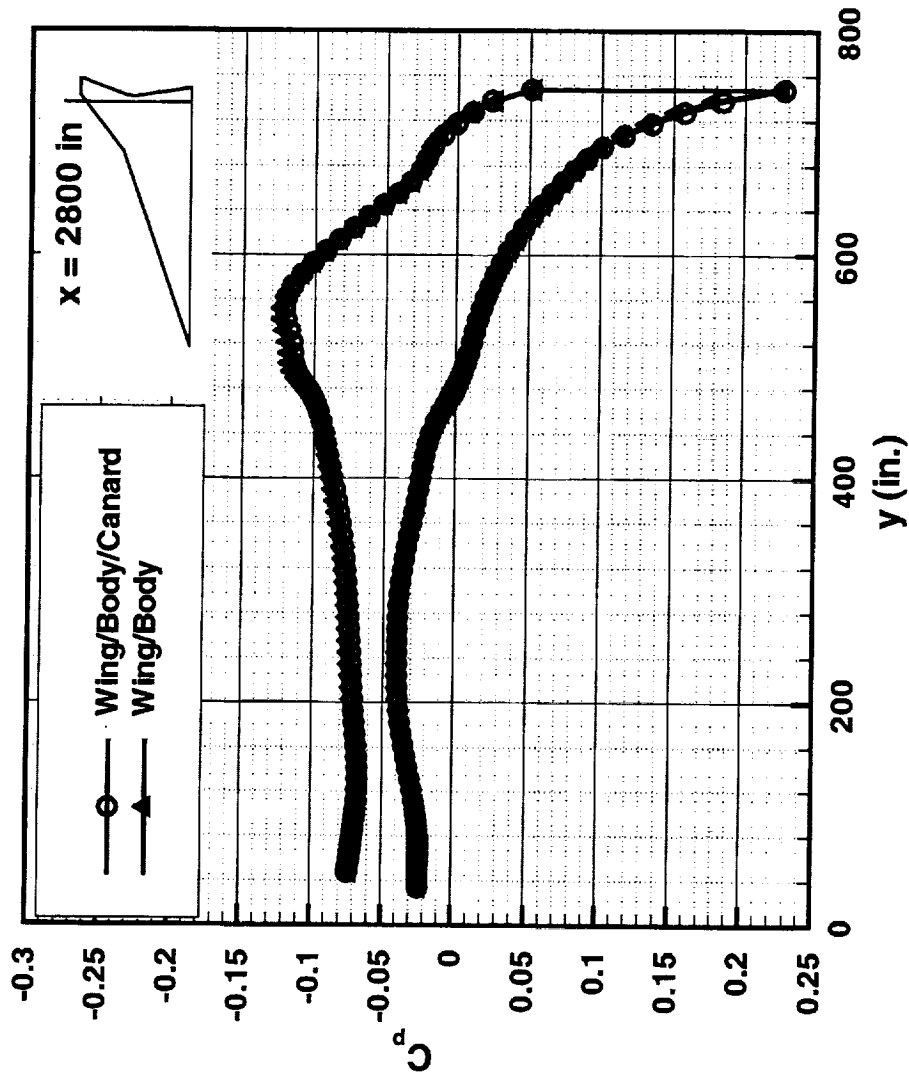


Pressure Distribution Comparisons (Cont.)

This chart shows the pressure coefficient distribution at an axial station of $x=2800$ inches for the wing/body/canard and the wing/body configurations at $\alpha=3.5^\circ$ and a canard incidence angle from the horizontal of 0° . At this axial location, the ACC low-mounted canard produces very small changes in the pressure coefficient on the upper and lower surface of the wing in comparison to the configuration without a canard.



Low Mounted Canard ($M = 2.4$, $\alpha = 3.5^\circ$, $\delta = +2^\circ$) Surface Pressure Coefficient (C_p)



Streamlines for the ACC Low-Mounted Canard

Streamlines seeded in the wake of the low mounted ACC canard show the potential influence of the canard wake on the wing. The streamlines go both above and below the wing. The streamlines are shown for $\alpha=3.5^\circ$ and a canard incidence angle with the horizontal of 0° .

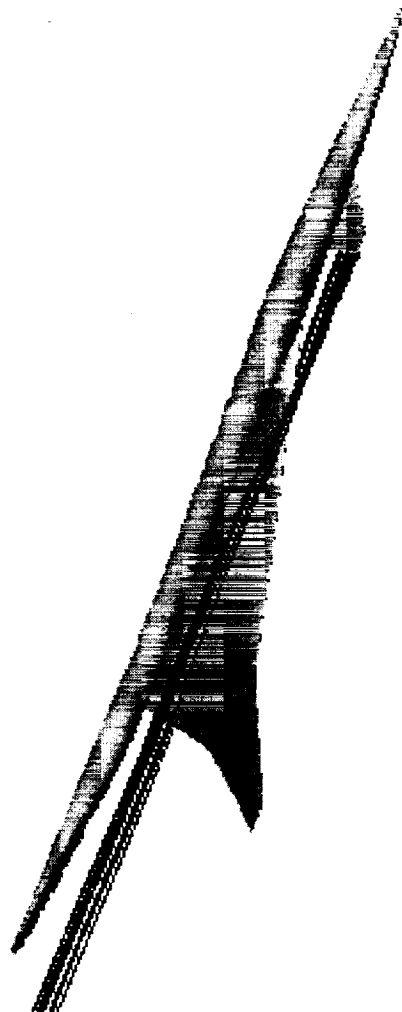


HSR TCA Canard Study

HSCT High Speed Aerodynamics



Low Mounted Canard ($M = 2.4$, $\alpha = 3.5$, $\delta = +2^\circ$) Streamlines



Streamlines for the ACC Low Mounted Canard (Cont.)

This chart shows additional streamline views of the ACC low-mounted canard at $\alpha=3.5^\circ$ and a canard incidence angle with the horizontal of 0° . In the chart, both the side and bottom views are shown.

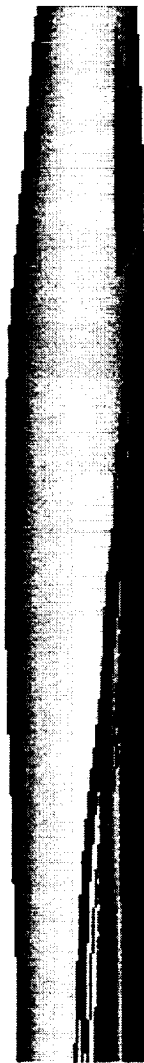


HSR TCA Canard Study

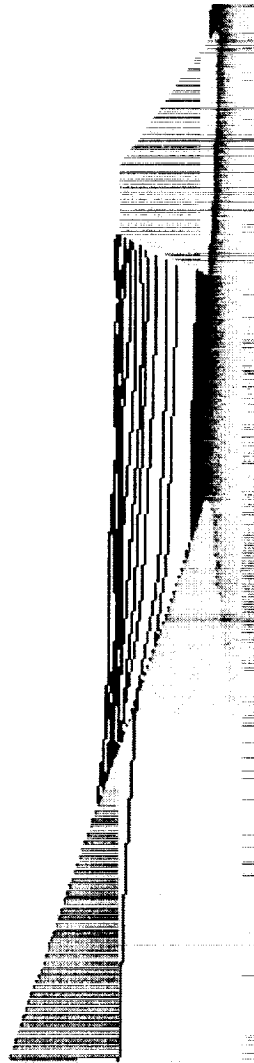
HSCT High Speed Aerodynamics



Low Mounted Canard ($M = 2.4$, $\alpha = 3.5$, $\delta = +2^\circ$) Streamlines



SIDE VIEW



BOTTOM VIEW

The ACC Low Mounted Canard Upwash

The following chart shows the upwash angle at several axial stations for the ACC low-mounted canard configuration at $\alpha=3.5^\circ$ and a canard incidence angle with the horizontal of 0° . The upwash angle is defined as,

$$\text{Upwash Angle} = \tan^{-1} (w/u) - \alpha$$

where, u = streamwise component of velocity
 w = normal component of velocity
 α = angle-of-attack

It can be seen that a significant upwash is created from the low-mounted canard which changes the local incidence of the flow near the apex of the wing/body. This results in the changes observed in pressure coefficient shown on the previous pages for the wing/body/canard configuration with respect to the wing/body configuration.

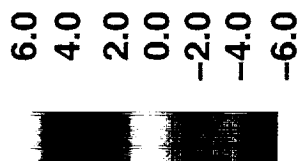


HSR TCA Canard Study



HSCT High Speed Aerodynamics

Low Mounted Canard ($M = 2.4$, $\alpha = 3.5$, $\delta = +2^\circ$) Upwash (degrees)



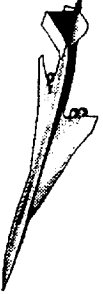
Conclusions from the CFD Studies

The next two charts list the conclusions from both the Boeing and Dynacs CFD canard studies. There are three main conclusions from the CFD studies: 1) The PTC canard has a small impact on the cruise performance of the wing/body/canard configuration with respect to the wing/body configuration, 2) The ACC canard has more influence on the wing than the PTC canard, and 3) Both low-mounted canards have the greatest influence on the wing over the α range considered.

The PTC mid-mounted canard at $i_c=0^\circ$ adds less than 1 count of additional pressure drag to the baseline TCA wing/body configuration at a $C_L=0.1$. Although this is a small performance penalty, the canard does have a significant influence on the wing and fuselage. Over the range of possible canard deflections (-4° to 4°) near the cruise condition ($C_L=0.1$), the canard causes a 5 count change of pressure drag on the wing. This same range of canard deflections results in increased lift on the canard and reduced lift on the wing. The PTC canard mounting location yields a change in the fuselage pressure drag of 1 count at $C_L=0.1$. To better understand the influence of the canard on the wing and fuselage, the upwash/downwash produced by the PTC canard needs to be investigated.

The PTC mid-mounted canard has a significant effect on pitching moment for the incidence angles investigated by Boeing. As expected, approximately -4° of canard deflection is required to yield near-zero lift on the canard. At this deflection angle, the PTC mid-mounted canard configuration provides the same moment coefficient as the baseline TCA wing/body with a pressure drag penalty of only 0.4 counts. Interestingly, only -6° of canard deflection would be required to trim the aircraft without the tail. However, aircraft stability would be an issue.

Conclusions from CFD Studies



High Speed Aerodynamics, Long Beach

○ PTC canard has small impact on cruise performance

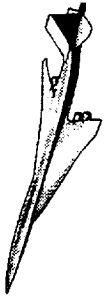
- Less than 1 count in total pressure drag at $i_c=0^\circ$
- At a $C_L=0.1$, a -4° to 4° change in mid-mounted canard deflection angle yields a 5 count change in wing pressure drag
- Canard mounting location can yield a change in fuselage pressure drag of 1 count at $C_L=0.1$
- A mid-mounted canard deflection of -4° is required to yield near-zero lift on the canard
- -4° of canard deflection yields only 0.4 counts of C_{Dp}
- Approximately -6° of canard deflection would be required to trim the aircraft without a tail

Conclusions from CFD Studies (Cont.)

The greater pressure drag penalty, with respect to the PTC canard configuration, provided by the ACC canard configuration is a result of the larger planform and close proximity of the ACC canard to the wing. The ACC low-mounted configuration, at a canard deflection of $i_c=0^\circ$ and a $C_L=0.1$, provides 3 counts more pressure drag than the TCA wing/body. From Dynacs study of the ACC low-mounted canard, significant upwash is produced by the canard that does influence the wing. The upwash produced by the PTC canard, once studied, should show less influence on the wing than the ACC canard, due to the smaller PTC planform size and its further distance from the wing.

Based on the current analyses, it appears that the low-mounted canard, for both the PTC and ACC configurations, provides the greatest influence on the wing over the α range considered.

Conclusions (Cont.)



High Speed Aerodynamics, Long Beach

- **ACC canard has more influence on the wing**
 - Larger planform provides more drag
 - Low-mount configuration ($i_c=0^\circ$) yields 3 counts more total pressure drag than the TCA W/B
 - More influence on wing due to closer proximity
- **Both low-mount canard wakes have greatest influence on wing over the α range considered**

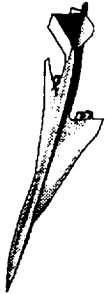
Canard Test Configurations

The results of the canard CFD studies were used to define a Canard Integration Wind-Tunnel Test. Both canard planforms will be tested, because they bracket a range of realistic canard sizes and locations that could be found on future HSR configurations. The ACC canard planform was added because the PTC canard planform and location had small effects on the wing. The larger ACC planform seems to have a significant influence on the wing due to its close proximity and would add additional confidence to any CFD code validation. The test configurations include the PTC low, PTC mid, PTC high, and ACC low-mounted configurations at the dihedral and incidence angles shown on the chart.

For efficient and accurate wind-tunnel testing, two new forebodies will be fabricated for the existing 1.675% Baseline TCA model wing strongback and aftbody (Model 2b). One forebody will have a $\pm 4^\circ$ wiping surface on it to allow sealed deflections for the mid-mounted PTC canard over that range of deflection angles. Unporting will result beyond $\pm 4^\circ$. All other canard configurations will be integrated on the second forebody that does not have a wiping surface integrated into it.

Dynamic Engineering, Inc. (DEI) has been contracted to build the new forebodies and canard model parts for this wind-tunnel test.

Canard Test Configurations



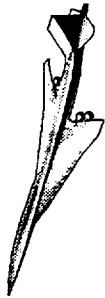
High Speed Aerodynamics, Long Beach

- CFD studies were utilized to define Canard Integration Test configurations
- Decided to test both PTC and ACC canard
 - PTC: Low ($\Gamma=-20^\circ, i_c=\pm 10^\circ$ and 0°)
Mid ($\Gamma=0^\circ, i_c=\pm 10^\circ, \pm 4^\circ$, and 0°)
High ($\Gamma=15^\circ, i_c=\pm 10^\circ$ and 0°)
 - ACC: Low ($\Gamma=-15^\circ, i_c=\pm 4^\circ$ and 0°)
- Decided to fabricate two new forebodies (one with a canard wiping surface)

Test Information

The following is a list of information for the Canard Integration Wind-Tunnel Test. Two models will be tested, Model 2b and Model 52. The only difference between Model 52 and Model 2b will be the new forebodies and canards fabricated by DEI.

Test Information



High Speed Aerodynamics, Long Beach

- **Test facility:** LaRC UPWT Test Section 2
- **Test date:** 4/6/98 - 5/1/98
- **Test duration:** 20 single shift days
- **Models**
 - Model 2b - 1.675% Baseline TCA with truncated aftbody and one-piece nacelle/div
 - Model 52 - Model 2b with two new forebodies to accomodate several canard configurations
- **Test conditions:**
 - $M_{\infty} = 2.4$, $\alpha = -4^{\circ}$ to 12° , $\beta = -6^{\circ}$ to $+6^{\circ}$
 - $Re = 4$ million/ft

Canard Integration Test Objectives

The main objective of the Canard Integration Test is to obtain an experimental database for CFD code validation for W/B/C and W/B/C/N/D configurations. Flow visualization of the canard wake and tip vortex will be conducted to determine how the canard influences the wing and nacelle flowfields. In addition, an assessment of the canard effect on performance and limited S&C characteristics will be performed.

Canard Integration Test Objectives



High Speed Aerodynamics, Long Beach

- Acquire experimental database for CFD code validation on W/B/C and W/B/C/N/D
- Acquire flow visualization data for the canard wake to see how it influences the wing and nacelle flowfields
- Assess the effects of canard location on performance
- Acquire limited S&C characteristics (high alpha, multiple canard deflection angles, and sideslip angles)

Future Work

A great deal of work is still required to prepare for the Canard Integration Wind-Tunnel Test. Navier-Stokes solutions are required to improve the PTC canard wake and tip vortex modeling. This is required because the only dissipation in the recent Euler analysis has been numerical dissipation. To accurately model the canard wake and tip vortex the influence of viscosity is required. In addition, CFD predictions are required for the new forebody with the PTC canard wiping surface to evaluate any differences from the baseline TCA forebody. Pre-test estimates are required for all configurations, as built, in order to make accurate comparisons between test and CFD. Further analyses of existing solutions may also be helpful to obtain increased insight into the effects due to canard integration.

The new model parts need to be fabricated by DEI and a detailed test plan must be created. This test plan will include a run matrix with the proposed number and type of test runs. Finally, the test will be conducted from April 6 to May 1, 1998.

Future Work



High Speed Aerodynamics, Long Beach

- **Additional CFD analyses are required**
 - Navier-Stokes to assess effect of canard wake and canard tip vortex
 - Euler studies for the forebody with wiping surface
 - Pre-test estimates on model parts
 - Further analyses of existing solutions
- **Prepare for Canard Integration Test**
 - Fabricate two new forebodies for Model 2b
 - Test planning
- **Conduct Canard Integration Test**

This page is intentionally left blank.

Overview of Technology Integration Activities Related To Configuration Aerodynamics

**Chester P. Nelson
HSCT Aerodynamics
Boeing Commercial Airplane Group
Seattle, Washington**

**HSR Airframe Technical Review
February 9-13, 1998
Los Angeles, California**

Overview of Technology Integration Activities Related to Configuration Aerodynamics

Chester P. Nelson*
Boeing Commercial Airplane Group
P.O. Box 3707, MS 6H-FK
Seattle, WA 98124-2207

Abstract:

This paper presents a summary of recent and planned activities under the NASA High Speed Research program Technology Integration task (HSR TI) which are of particular interest to the high speed Configuration Aerodynamics (CA) technical element.

The role of high speed aerodynamic design and analysis data supporting the TI sub-tasks is outlined. The contribution of planned trade studies to the definition of an Optimized Aeroelastic Concept configuration (OAC), and the subsequent integration of the Technology Configuration (TC) planned for late 1998 are reviewed. Key trade studies supporting those efforts include those for Alternate Control Configurations (ACC), planform and propulsion system configuration trades, and high aspect ratio wing integration studies.

Results of a typical technology integration sub-task using CFD are shown for the case of assessing the potential excrescence drag penalties of several proposed external configuration features.

* Lead Engineer
HSCT High Speed Aerodynamics, Seattle
Configuration Development Group



An Overview of Technology Integration Activities Related To Configuration Aerodynamics

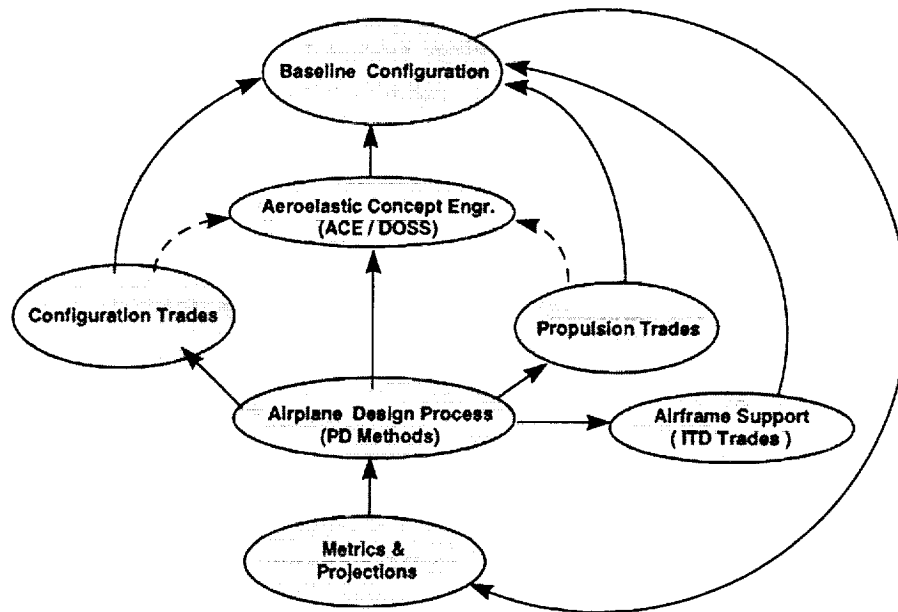
- **HSR Technology Integration sub-task outline**
- **Configuration Trades / "ACE-OAC" => "TC" Baseline**
 - **Alternate Control Configuration ("ACC") trades**
 - **Wing planform, thickness, and integration trades**
 - **Higher order CFD-based aerodynamic loads in ACE (Arslan)**
- **Support of T.I. Propulsion Trades (CFD analysis - Dees)**
- **Airframe Support Trades**
 - **Airplane level impact of non-linear optimized aero geometry (Vegter and Stanislaw)**
 - **NS-based excrescence drag analysis for structures, flight deck (Peterson)**

This paper presents a summary of recent and planned activities under the NASA High Speed Research program Technology Integration task (HSR / TI) which are of particular interest to the high speed Configuration Aerodynamics (CA) technical element.

The role of high speed aerodynamic design and analysis data supporting the TI sub-tasks will be outlined. The contribution of trade studies to the definition of an Optimized Aeroelastic Concept configuration (OAC), and the subsequent integration of the Technology Configuration (TC) in late 1998 will be discussed. Key trade studies supporting this effort include those for Alternate Control Configurations (ACC), planform and propulsion system configuration trades, and high aspect ratio wing integration studies. The work of Arslan, Dees, Vegter, and Stanislaw in providing TI with specific high speed aerodynamics inputs is presented in other papers later in the joint CA-TI technical session.

More than 50 people contribute their efforts in one aspect or another of the Technology Integration effort for HSR. This author particularly thanks those who made direct contributions to the charts presented in this overview paper, including K. Peterson, T. Creighton, E. Adamson, C. Borland, S. Yaghmaee, and P. Dees, of Boeing Seattle, and R. Narducci of Boeing Long Beach. The author also acknowledges T. Haynes of Dynacs Engineering Company who supported TI's ACC study with supersonic Navier-Stokes analysis of baseline and alternate canards.

High Speed Aerodynamic Design / Analysis: Technology Integration Sub-Task Connectivity



High speed aerodynamic design and analysis plays a key role in most of the Technology Integration sub-tasks. The flow of high speed aero data supporting TI is illustrated by the above diagram. At the bottom of the data "food-chain" is the Metrics sub-task and the required input of performance projections and risk assessments from the Configuration Aerodynamics Integrated Technology Development Team (CA -ITD). The performance projections developed with CA directly feed into the Airplane Design Process (ADP) sub-task of TI where they are used to update our the drag polar build-up methods used for airplane performance assessments under the various trade studies and baseline configuration development.

The trade studies conducted by TI are grouped into Airframe Support, Configuration Trades, and Propulsion Trades. The Airframe Support trades element covers airplane level assessments specifically requested by the various technology development ITD teams. Propulsion Trades element supports coupled engine-airframe trades and provides data to guide HSCT engine technology development and Environmental Impact studies. Configuration Trades include alternate controls (canard and 3-surface configurations), elements of Aero Servo Elastic (ASE) analysis, detailed wing integration trades, and parametric wing planform trades. Performance databases developed in the trade studies are augmented by selected higher fidelity (CFD and structural FEM) data in the Aeroelastic Concept Engineering sub-task and run through a Multidisciplinary Optimization process (MDO) to help support the development of the baseline HSCT configuration.



Airplane Design Process (PD Methods)

- **Update test-theory increments from current W.T. database**
- **Improve /adapt performance drag build-ups for new configurations**
 - **3-surface aircraft trim and CG optimization**
 - **Bottoms-up checks of “projected” performance**
 - **Joint high speed / propulsion effort on thrust-drag accounting**
 - **Better accounting of transonic flaps, WT-flight, PIE, aeroelastics**
- **Augment linearized potential flow predictions with higher order CFD**
 - **Canard-wing interference and trim parameters for ACC**
 - **Validate trade study nacelle geometry increments**
 - **Use selected non-linear optimizations (1999 ?)**
- **Process flow-time improvements**

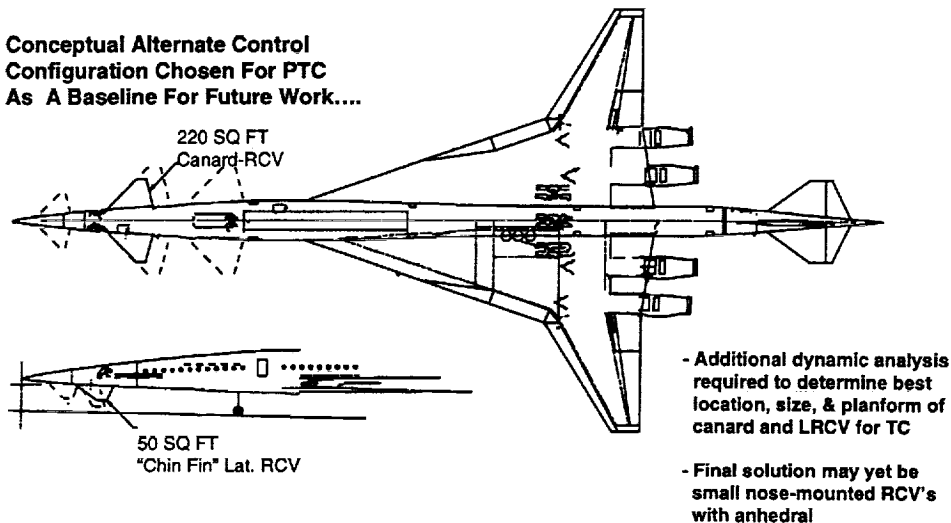
Under the ADP sub-task, the drag prediction methods used to support airplane trades are continually updated. Current wind tunnel results from CA's high speed test program are evaluated annually and used to update test-theory increments. Procedural improvements have provided considerable flowtime reduction for TI trade studies and ACE.

Performance drag methods are also updated as required for the addition of specific configuration features such as 3-surface control arrangements, or 2D bifurcated nacelles. Baseline airplane performance assessments are in-turn used in making performing “bottoms-up sanity checks” of the aerodynamic performance technology projections. A 1998 co-operative effort between the Propulsion community and Aerodynamics is attempting to resolve outstanding issues on thrust-drag accounting (particularly at off-design conditions where the study compliments Propulsion Induced Effects analysis and test planning by CA). CFD-based PIE estimates made under CA have recently been included in the drag build-up process as part of further improving the accounting of “technology projections” and transonic drag elements.

Over the past 2 years, specific trade studies have also been augmented by higher order CFD analysis. During the 1999-2001 period, this is envisioned to grow into the selective use of non-linear aerodynamic optimization using tools currently being developed under CA technology.

"ACC" Alternate Control Configuration Study

**Conceptual Alternate Control Configuration Chosen For PTC
As A Baseline For Future Work....**

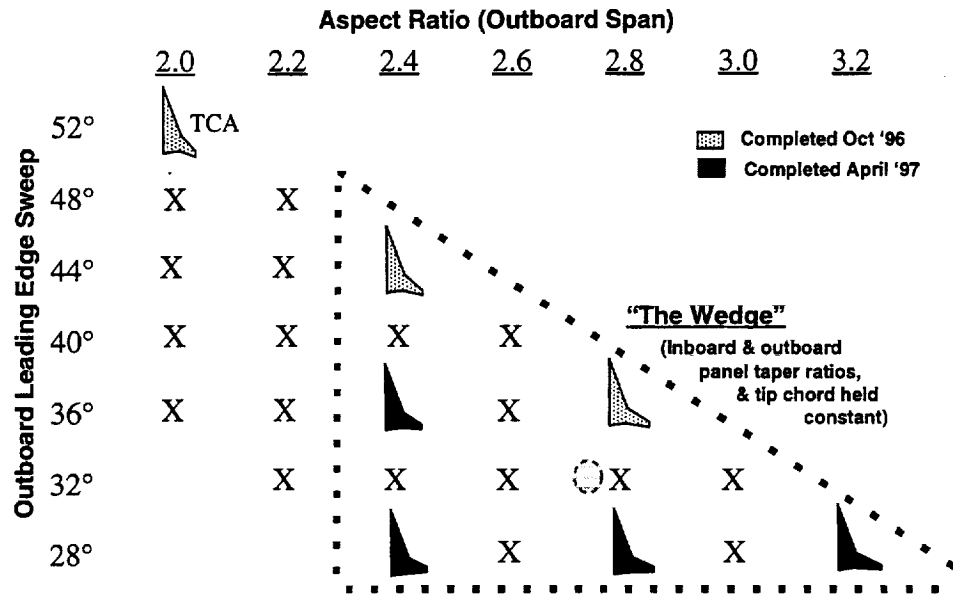


The most obvious result of last year's TI trade studies in terms of changes to the baseline HSCT concept, was the addition of two forward surfaces to the configuration. When the Alternate Controls Configuration (ACC) study began (following on the heels of the previous "LCAP" program) the intent was to identify specific canard-related performance and noise improvements to the baseline. Considering the work being done elsewhere on serious ride quality and pilot handling quality problems caused by the high fineness body, it soon became obvious that some type of forward surface would be required to cope with the airplane's body flexibility.

Subsequent analysis based on the Ref.H configuration confirmed that a set of Ride Control Vanes (RCV's) mounted near the nose had the potential to ameliorate the adverse body dynamics at a net weight penalty far smaller than the penalty for stiffening the body structurally. While an Overflow Navier-Stokes CFD analysis of the initial aft-low-mounted canard showed adverse canard wake interference with the wing (and possibly engine inlets) at Mach 2.4, it appeared that a smaller canard mounted just aft of the flight deck would have a small net favorable effect on aerodynamic performance. On this basis, a medium-sized, mid-mounted forward surface combining canard and longitudinal RCV functions was drawn on the Preliminary Technology Configuration baseline (PTC) in late 1997. An additional forward "chin-fin" was added as a configuration feature "place-holder" in recognition of the fact that some type of Lateral RCV would also be required to solve side-to-side body dynamics issues (see above). While the size of the LRCV was reduced on the final PTC drawing, additional work is needed to properly define the canard / RCV combination for the next baseline.



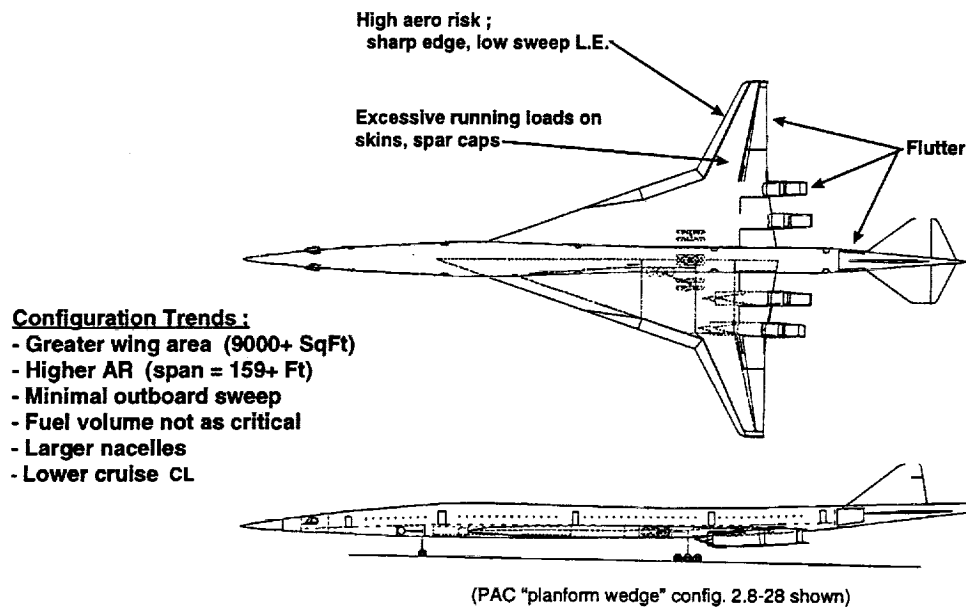
Wing Parametric Planform Trades Off TCA



The wing planform of the PTC airplane is also significantly different the previous HSR baseline configuration (TCA). During 1996-97 significant effort was expended by TI in studying the impact of wing planform on HSCT mission performance, noise, and propulsion system-to-airframe matching.

The aspect ratio 2.0 Technology Concept Airplane (TCA) was initially chosen by HSR as a multi-disciplinary compromise HSCT representation on which to focus technology development in the various disciplines. As shown in the chart above, it falls far outside the planform design space of current interest for heavily noise-constrained configurations. The '96-97 TI planform studies focused on a wedge-shaped region of outboard wing panel sweep and aspect ratio combinations dictated by the need to achieve lower takeoff and approach noise at minimum sized takeoff gross weight using currently projected engine noise levels. This study showed that a configuration of approximately 32 degrees outboard leading edge sweep and an aspect ratio of 2.7-2.8 should satisfy the payload-range requirements at the new minimum takeoff cut-back noise requirement of Stage III-5dB. The combination of 2.73 aspect ratio and 32 degrees outboard leading edge sweep that was subsequently chosen for the PTC definition falls roughly in the middle of the "Wedge" design space covered by the '96-'97 TI trades.

Noise-Sized HSCT Configuration Trends



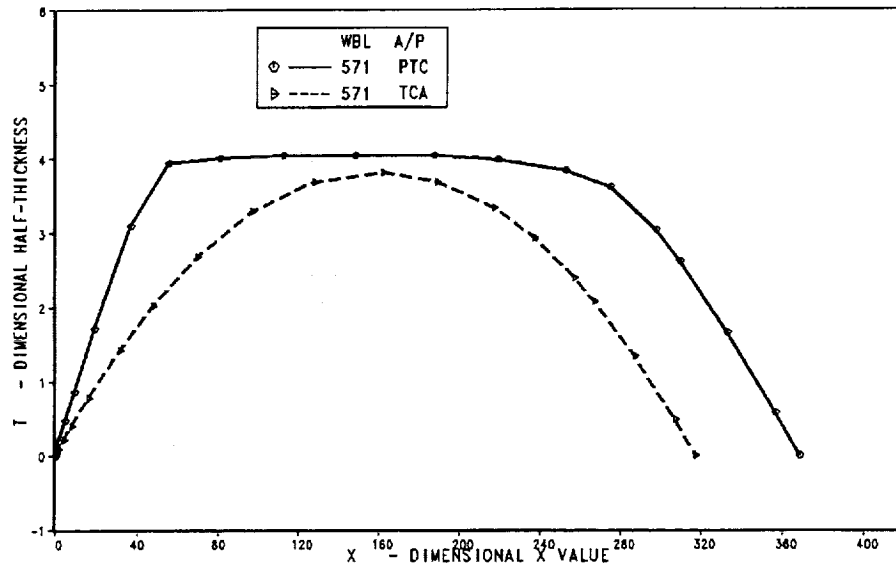
The 1996-97 TI trades further indicated that additional noise restrictions being proposed by the Environmental Impact (EI) team would drive the HSCT wing configuration to even higher aspect ratios and potentially lower outboard sweep angles. Updates to the propulsion system and increases in the computed weight of the engine-nozzle combination have also had a substantial impact on the definition of the PTC.

The general configuration trend is clearly toward bigger nacelles, higher aspect ratio wings (greater span), larger wing areas, and lower cruise altitude (lower CL). These trends also indicate wing structures that are tightly constrained by high running loads, skin thickness limits, and flutter. Along with the larger wing areas comes a simultaneous increase in fuel volume, indicating that the thickness and volume of the wing strake could be reduced, or that the excess volume could be used for future range growth.

The longer outboard panel span and reduced sweeps create some potential risks for High Lift and Stability and Control if simple leading edge flaps have difficulty suppressing flow separation on the thin sharp leading edges (ie.. there may be no organized vortex roll-up when the outboard wing stalls). Early, unstable flow separation on the outboard wing at increased alpha could also increase the severity of subsonic pitch-up. The inboard movement of the leading edge break point in terms of percent semi-span may also bring increased risk of not attaining the projected drag-due-to-lift efficiencies in both the subsonic and supersonic regimes.

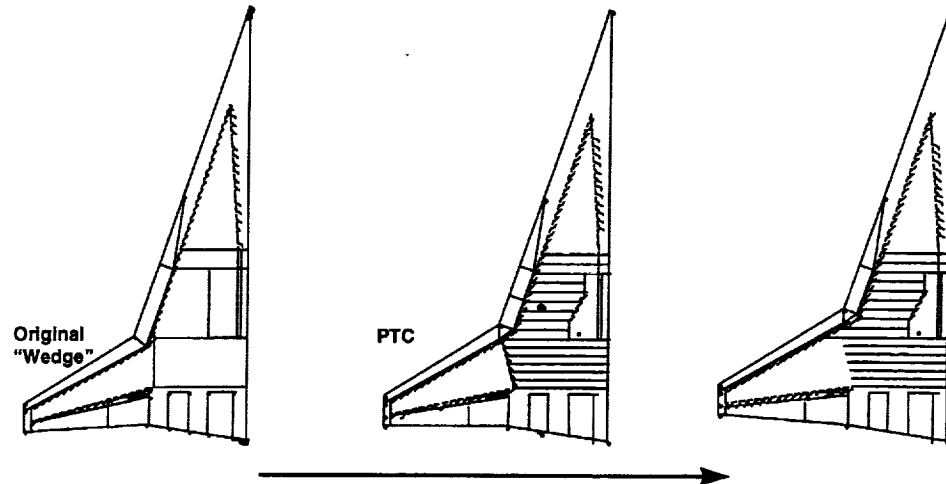


TCA / PTC Outboard Wing Thickness Comparison



In light of the excessively high structural running loads obtained on the FEM structural model of the 2.8 aspect ratio / 28deg. sweep "Wedge" planform, and concern over manufacturability and flutter risk on the outboard wing panel, the PTC was laid out with flat-topped airfoil thickness envelopes outboard of the leading edge break. On the inboard portion of the outboard wing, this design change provides structures with a roughly 50% increase in leading edge spar depth and 30% increase at the rear spar, while minimizing the impact on aerodynamics. The taper ratio of the outboard wing of the PTC was also increased and the leading edge break location moved farther inboard relative to the planforms studied in the "Wedge". The net impact on the PTC wing thickness is shown above for a typical buttock line.

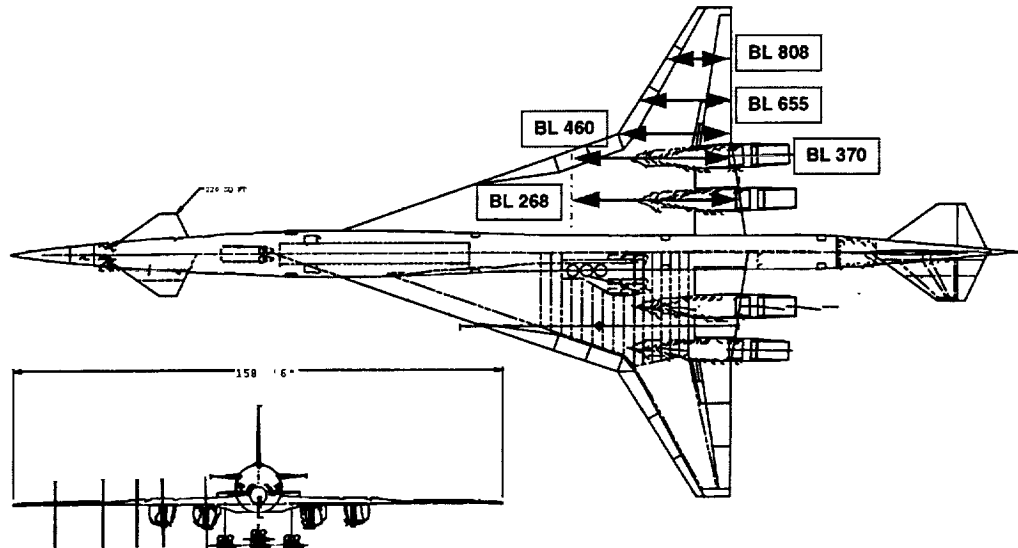
Trend Toward Greater Outboard Panel Taper Ratio



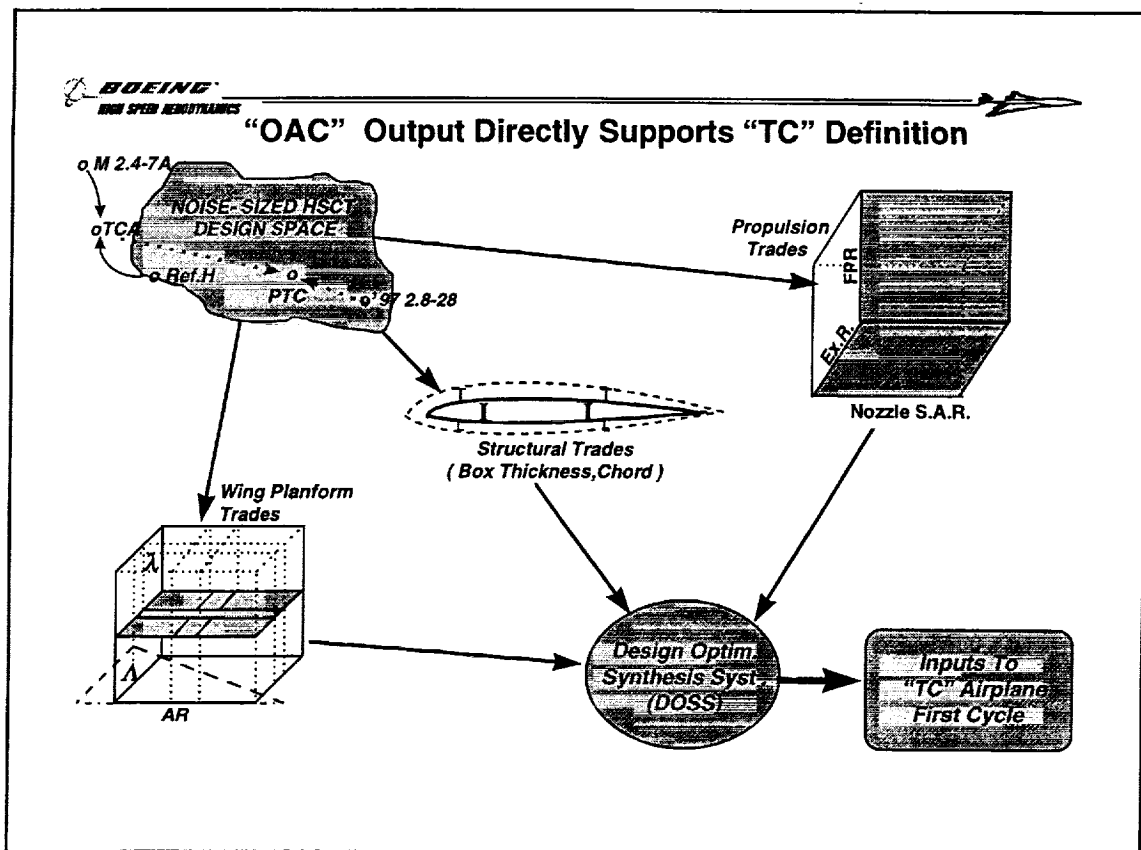
η L.E. Break Moves Inboard As Box Chord ~ BL500 Grows...
 => Reduced Ability to Meet High and Low Speed Aero Projections ?
 (Optimization, Flap Effectiveness, Buffet)

In 1998, the wing planform trade studies leading up to definition of the Technology Concept airplane (TC), cover a design space in which the trend toward increasing outboard taper ratio (break chord/ tip chord) is extrapolated two levels beyond the increase used in the PTC. This provides a significant improvement to the local wing box chord, thickness at constant t/c, and inboard load shift for a given leading edge sweep, span, and tip chord. It is hoped that this will help provide data on the relative structural relief provided compared to the high speed and low speed aerodynamics impact and noise-constrained airplane sizing. Again however, this also moves the leading edge break even farther inboard which may pose increased risk of outboard inlet flow distortion, or shortfall of the projected drag-due-to-lift improvements.

PTC Wing: Critical Structural Thickness Regions



The 1998 TI ACE effort includes an investigation of local wing thickness trades between structures and aerodynamics. Previously identified critical regions of the PTC wing will be perturbed in thickness using “tent function” thickness increments similar to those demonstrated in the Aeroelastic Concept Engineering task’s Preliminary Aeroelastic Concept (PAC) optimization exercise the previous year (see the ACE PAC Final Report). The results of thickness trades on the baseline PTC will be applied through an updated weights estimation code, in incremental drag response surface to other configurations in the planform study.



The DOSS "MDO" program developed under ACE will become an integral part of the configuration development process for the Technology Configuration airplane to be defined in late 1998. The propulsion system trades, structural thickness variations, and planform trades being investigated in TI will all be rolled into a performance database that will be used in DOSS to perform a simultaneous optimization and airplane sizing analysis. The resulting configuration, and the sensitivities around it, should indicate the best combination of global HSCT configuration variables to use as a starting point for the TC airplane. The goal is to allow the TC definition to start in a viable design space that meets the performance and noise requirements while not violating key structural constraints.



T. I. Config. Trades: “Wing Integration”

- **P.D. level assessment of “non-parametric” planform variations**
- **Explore alternate internal structural arrangements for wing-body**
- **Assess impact of alternate landing gear length, location, type**
- **Assess performance /integration trades of Δ span vs. Δ aspect ratio**
- **Assess performance/ integration trades of Δ inboard wing sweep**

Additional variations in wing planform which did not neatly fit in the parametric design space are being investigated separately in the Wing Integration sub-task. The more local or complex types of variations to be studied under this category of work include alternate landing gear concepts, wing internal structural arrangement changes, and identification of high speed versus high lift aerodynamic impacts. The impact of alternate landing gear locations on the structural arrangement and performance will also be assessed.

Performance Drag Build-Up Process

$$\begin{aligned}
 \left\{ \begin{array}{c} \text{T. I.} \\ \text{Performance} \\ \text{Polars} \end{array} \right\} &= \left\{ \begin{array}{c} \text{W.T.} \\ \text{Database} \end{array} \right\} + \left\{ \begin{array}{c} \text{Configuration} \\ \Delta \end{array} \right\} + \left\{ \begin{array}{c} \text{Full-Scale} \\ \text{Airplane } \Delta \end{array} \right\} + \left\{ \begin{array}{c} \text{Tech Proj.} \\ \Delta \end{array} \right\} \\
 &\quad \text{Perf. Config. - W.T. Config.} \\
 &= \text{Full Config. In Linearized Potential flow} + \left[\begin{array}{c} \text{W.T. Test} - \text{Lin. Pot. Flow} \\ \text{Historical "Test - Theory Increment"} \end{array} \right] + \text{CD}_{sf} \left(\begin{array}{c} \text{Graph of } C_{Dsf} \text{ vs } Rn \end{array} \right) \\
 &\quad + \text{CD}_{exo} \left(\begin{array}{c} \text{Graph of } C_{Dexo} \text{ vs } A_{wet} \end{array} \right) + \frac{\text{CD}_{excr}}{\text{CD}_{exo}} \left(\begin{array}{c} \text{Graph of } \frac{\text{CD}_{excr}}{\text{CD}_{exo}} \text{ vs } Mach \end{array} \right) + \text{CD}_{trim} \left(\begin{array}{c} \text{Graph of } C_{Dtrim} \text{ vs } Mach \end{array} \right) \\
 &\quad + \% \text{Tech Proj.} \left(\begin{array}{c} \text{Bar chart of } C_D, C_{Dw}, C_{DL} \text{ vs } Mach < 1, Mach > 1 \end{array} \right) \\
 &\quad \left[+ \Delta \text{CD}_{CFD} \text{ (Non-Lin. Config. } \Delta \text{)} \right]
 \end{aligned}$$

Whether for variations in propulsion system, wing thickness, or planform trades, a complete set of projected airplane drag levels is required by Airplane Performance for each TI trade study element. The drag polar build-up process used will be consistent with the common PD prediction methods discussed at the 1997 High Speed Aerodynamics Workshop at LaRC. This process takes into account model to full-scale geometry differences between the reference wind tunnel models and a given trade study configuration and calculates a strip-wise skin friction value at flight Reynolds number. Table look-ups are added to account for trim drag, excrescence and technology projections. Selected CFD runs are made to determine the magnitude of any expected (or unexpected) non-linear effect not properly captured by the wind tunnel database or linearized potential flow analysis.



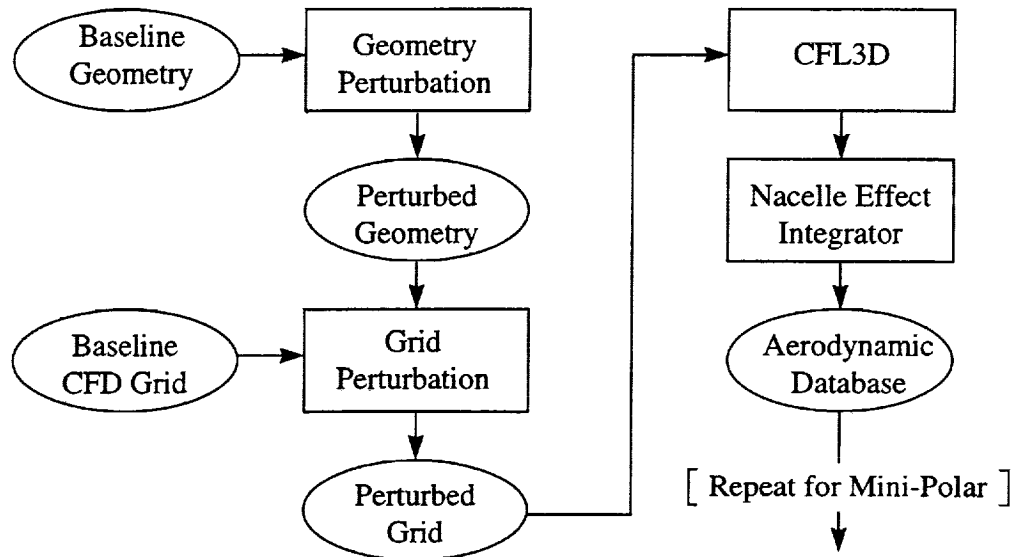
Combined Use Of CFD and Linear Theory for “PAC”

- **Performance polars produced using linear potential code for 720 total possible geometry combinations (on TCA baseline)**
 - Local wing thickness changes
 - Inboard and outboard wing panel twist changes
 - Nacelle size scalars (+/- 100 lb/sec massflow)
- **Drag polar elements and nacelle size scalars fit with n-dimensional response surfaces vs. geometric increments**
- **Selected geometry combinations evaluated in CFL-3D at key Mach / CL conditions to establish non-linear drag effects**
- **CFD-based adjustments fit with drag correction response surface**

A process for selecting, generating, and combining the non-linear CFD results with linear theory drag polars was pioneered under ACE in 1996-97. The MDO demonstration problem (PAC) included the generation of full flight regime linear-aero drag polars for 720 possible wing-nacelle geometry combinations. A very sparse matrix of CFD check cases was selected and run to calibrate the linear theory results. The resulting drag increments between linearized PD methods and the higher order CFD code were fitted with a multi-dimensional response surface as a function of the key geometric variables. The resulting “correction surface” could then be applied within DOSS to adjust the linearized performance polars.

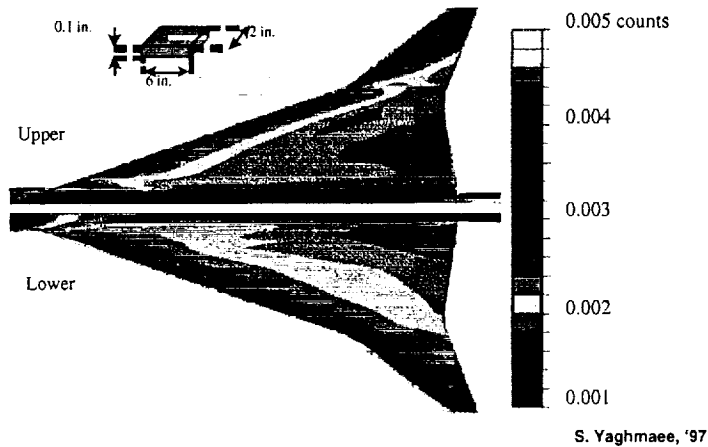


Generation Of CFD-Based Corrections To Polars





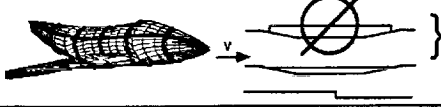
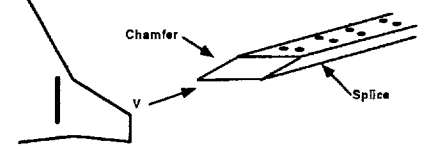
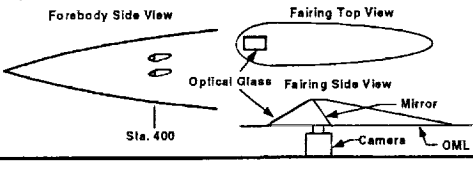
The procedure developed to obtain the non-linear solution data for comparison to the PD drag predictions consisted of perturbing the geometry and CFD grid from the baseline case (wing-body) and then integrating the nacelle pressure field effects on the perturbed wing-body solution. In the PAC demonstration, this process was used to generate a CFD solution database of "mini-polars" for a series of systematic local thickness perturbations at a minimal cost. A similar process will be used to generate CFD "check cases" for selected geometric variations in the 1998 trade studies.

Methods Check: Drag of Generic Excrescence Element Using CFD Flow Properties



Another area where CFD solutions are being applied in TI studies is in the area of excrescence drag assessments under Airframe Support Trades. In the current drag build-up program, the skin friction calculation is adjusted to allow for an excrescence level ("protuberance drag") which approximates that of current metal subsonic transports at incompressible speeds (7% of skin friction). This incompressible value is scaled versus Mach to account for compressibility, and is reduced by 20% everywhere to account for expected HSCT improvements due to smooth composite skins, flush antenna technology, and so on. At the 1997 HSR Aerodynamic Performance Workshop, S. Yaghmaee showed the feasibility of using Navier-Stokes based surface flow parameters together with handbook excrescence drag methods (AGARD, etc.) to compute the drag of individual excrescence drag sources (see above).

Since the 1997 workshop, this method has been used in practice to generate excrescence drag estimates of specific HSCT design features to guide structural and flight deck design concept down-selects and weight metrics.

			
Configuration Feature	Excrescence Description	Drag Penalty (counts)	Airplane Equivalent Δ OEW (lb)
Body Waviness (Pressure Pillowing)  Honeycomb Sandwich Fuselage Skin-Stringer Fuselage	80" and 40" Frame Spacing H/C 20" Frame Spacing Skin-String.	0.0265 0.0405	50 77
Circumferential & Longitudinal Fuselage Splices 	Circumferential Splice Strap with recommended 0.06" chamfered inset. 0.1" Longitudinal Lap Joint Mismatch	0.0618 0.0154	117 29
Wing Box Splices 	0.5" Wing Splice Strap (Assuming 16:1 Chamfer)	0.0210	40
Synthetic Vision System Camera Fairings 	Four fairings for 3-inch diameter fixed XVS cameras, with min. 35deg. window incidence.	1.0	1900

Typical excrescence analysis results are shown above, including an assessment of their drag-equivalent airplane weight penalty--a parameter which has proven easier to communicate to non-aero disciplines. As shown, the excrescence drag assessment for the various structural splice concepts was minimal in terms of airplane weight impact (provided that the protruding fuselage splice concept is avoided).

The impact of the proposed external camera pods for the flight deck XVS technology is more significant, forcing the flight deck community to re-evaluate the potential of using retractable or partly retractable camera pods.

In general the excrescence items which have been calculated so far indicate that the projected excrescence reduction of 20% relative to current subsonic commercial aircraft is a reasonable target for HSCT.

Conclusions

- Increasing use of CFD for higher fidelity “airplane level” trades
 - Wing thickness and nacelle scalars in ACE
 - Canard-wing interference and trim
 - Plans to do selected non-linear optimizations (1999 ?)
- Prediction methods continuously updated (ADP)
 - Bottoms-up checks of projected performance levels
 - Thrust-drag accounting (with propulsion)
 - Concern over “absolute” drag accuracy (W.T., CFD, flight)
- ‘98 trade studies are focused good definition of the “TC”
 - Platform for cross discipline optimization and design process integration during HSR-2a
 - Valid baseline for assessment of continued technology development and alternate concept studies

This presentation has illustrated some of the areas where increased use of CFD analysis, wind tunnel data, and eventually non-linear optimization tools being developed under Configuration Aerodynamics are being applied in airplane level trade studies within the HSR Technology Integration task.

The predictions of “absolute level” aerodynamic performance used in HSCT configuration development are continually being updated and improved through the TI “ADP” sub-task, but the confidence level in these predictions depends directly on the absolute accuracy of wind tunnel data, flight corrections, and CFD validation.

TI efforts for 1998 are focused on providing a good definition of the “TC” airplane which will be used for much of the remaining HSR-II program by all disciplines.

References:

High Speed Civil Transport (HSCT) Technology Concept Airplane Outer Mold Line (OML) Definition, Mc Donnell Douglas and Boeing Commercial Airplane Group, Rev.A March 13, 1996.

High Speed Civil Transport (HSCT) Technology Concept Airplane Configuration Description Document, Mc Donnell Douglas and Boeing Commercial Airplane Group, April, 1996.

High-Speed Research 1997 Aerodynamic Performance Workshop Conference Proceedings Volume 1, NASA Langley Research Center, February, 1997.

1996-97 High Speed Aerodynamic Performance Prediction Methods for the High Speed Civil Transport (HSCT), Boeing Document D6-82095TN, October, 1997.

High Speed Research Program HSR-II Airframe Task 20, Sub-task 2.1.1 Trade Study Summary Deliverable Report, NASA Langley Research Center, October 31, 1996.

High Speed Research Program HSR-II Airframe Task 20, Task 2.1 Technology Integration Deliverable Report, NASA Langley Research Center, October 31, 1997.



Cross-Discipline Evaluation of Optimized Designs and Features

**Chris A. Vegter
Greg S. Stanislaw**

February 12, 1998

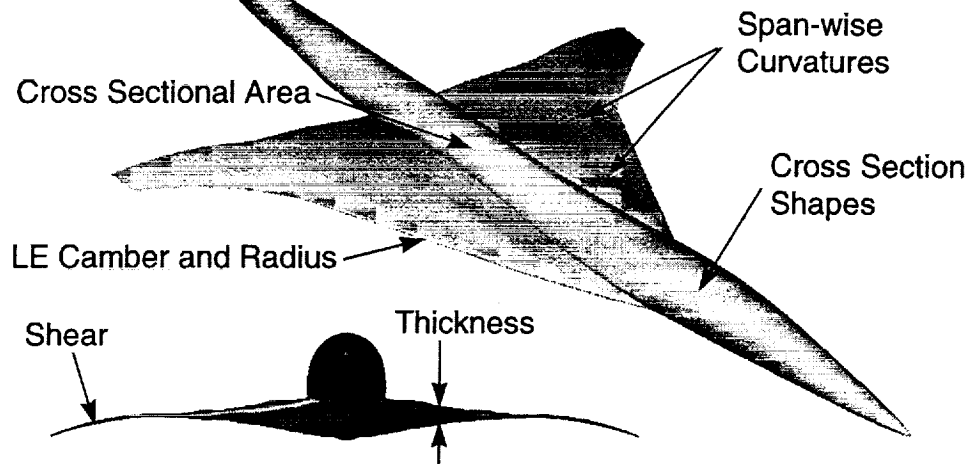
**HSCT Aerodynamics
Boeing Commercial Airplane Group
Seattle, Washington**

1998 HSR Airframe Technical Review

February 9-13, 1998

Los Angeles California

Optimized TCA Features



The purpose of this study was to evaluate the high speed drag benefits of the NCV's features and to get feedback about the features from other disciplines.

The NCV (optimized TCA geometry) contains many features which are different from the TCA. Some of the more obvious differences are the body cross sectional shape changes, the wing shear (or gulling), and the span-wise curvature variations (bumps).

One of the drawbacks of the optimization, is that it proceeds in the direction of lowest drag, whether the shape change results in a large or small drag improvement. Some of the features have impact on other disciplines. It was unknown which of the features were contributing significantly to the drag reduction.

The purpose of this study was to better understand the drag benefits of the various features, and how those features affect the other disciplines.



High Speed Aerodynamic Evaluation of NCV Features

The NCV geometric changes from the TCA can be broken down into the following features:

Wing

- Camber
- Twist
- Shear
- Thickness

Body

- Camber
- Cross Sectional Shape
- Cross Sectional Areas

The features were combined into five wing/body configurations and analyzed using TRANAIR.

By comparing the results with those from the TCA and NCV, conclusions can be drawn about the relative drag benefits of the NCV features.

In order to understand how much drag improvement each of the NCV's features was worth, the TCA and NCV features were mixed and matched into five new wing/body configurations. These configurations were analyzed using TRANAIR.

The wing was broken down into camber, twist, shear, and thickness. The body was broken down into camber, cross sectional shape, and cross sectional area. The body camber was defined as the midpoint between the crown and keel lines.

The resulting wing/body configurations were analyzed using TRANAIR. The nacelles and diverters were excluded as this greatly simplified the setup of the analysis.

In order to truly understand the effect of a geometric feature, the optimization should be repeated with the feature constrained out. Re-optimizing is impractical at this time due to the time and effort required. It is felt that although the exact benefit of a feature may not be determined by mixing and matching geometry's, conclusions can be drawn about the relative drag benefits of the various features.



Grouping of NCV Features for Evaluation

- Body Cross Sectional Shapes, and Body Camber
- Wing Camber, Twist, and Shear
- Body Cross Sectional Area and Wing Thickness

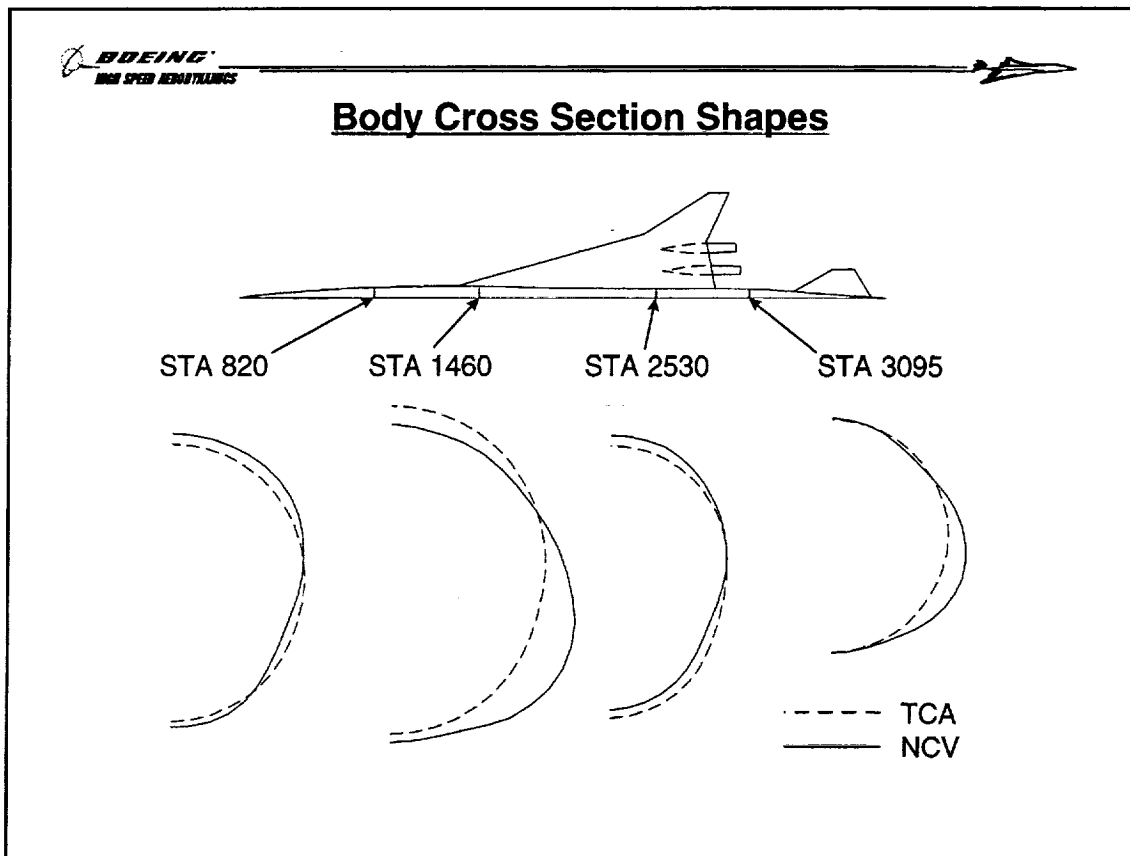
It was not possible to analyze every possible combination of features. The features were grouped to reduce the number of configurations which had to be created and analyzed.

The body cross sectional shape and body camber changes were grouped for analysis.

The wing camber, twist, and shear changes were grouped for analysis.

The body cross sectional area and wing thickness changes were grouped for analysis.

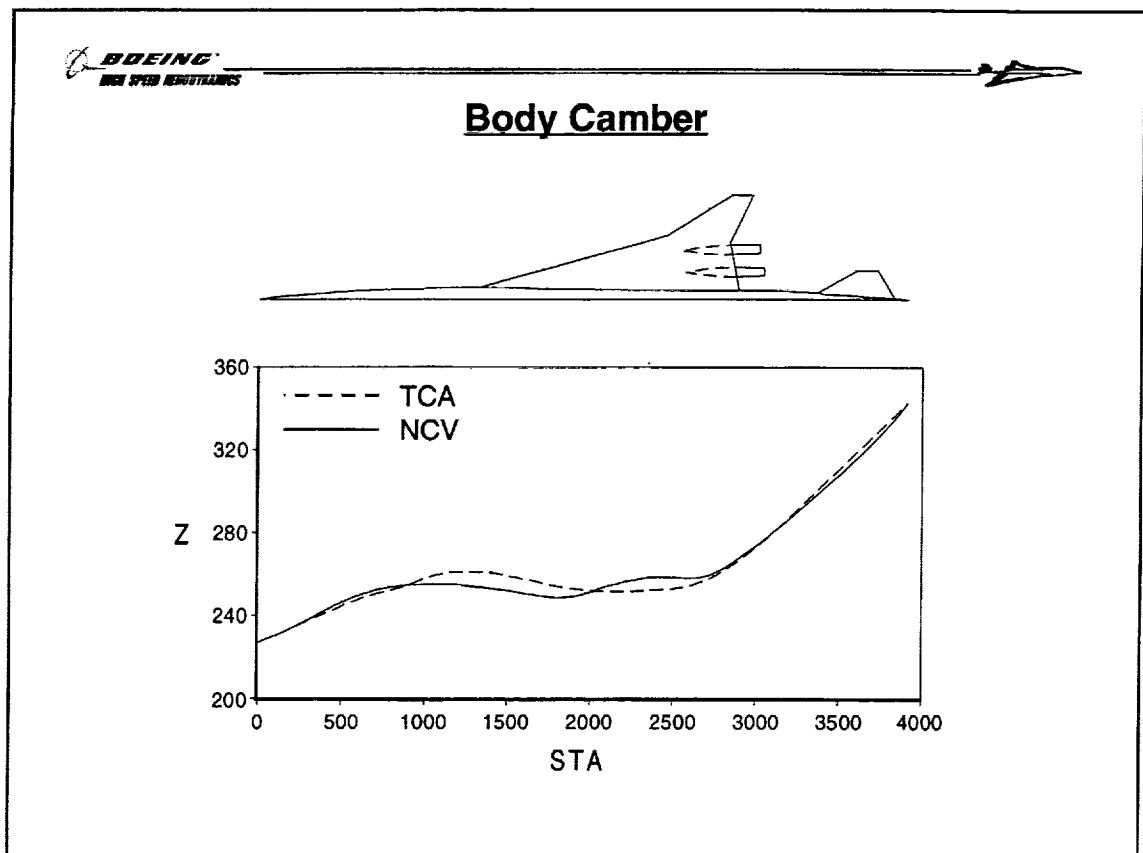
The features will be discussed according to this grouping.



This chart compares the body cross section shapes of the TCA and NCV at four stations along the body.

The NCV body cross section shapes are considerably less circular than the TCA.

During the optimization, the body shapes were required to fit around an internal polygon which represented the minimum cabin interior definition.



This chart compares the body camber of the TCA and NCV.

The body camber line is defined as the midpoint between the crown and keel lines.

The NCV has more camber on the forward body than the TCA.



High Speed Aerodynamic Benefit of Body Cross Section Shapes and Body Camber

Created two new configurations:

	TCA w/ the NCV's Body Shapes and Camber	NCV w/ the TCA's Body Shapes
Wing:		
• Thickness	TCA	NCV
• Camber	TCA	NCV
• Twist	TCA	NCV
• Shear	TCA	NCV
Body:		
• Cross Sectional Area	TCA	NCV
• Cross Section Shapes	NCV	TCA
• Camber	NCV	NCV

In order to evaluate the high speed aerodynamic benefit of the body cross section shapes and body camber, two new configurations were created.

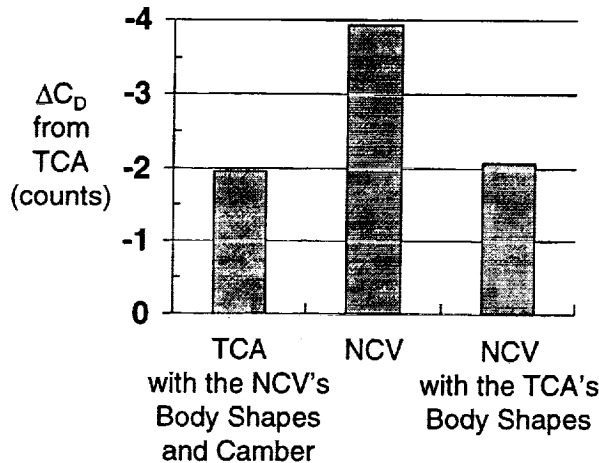
The first configuration was the TCA with the NCV's body cross section shapes and camber applied. The NCV's cross section shapes were scaled to preserve the TCA's cross sectional area.

The second configuration was the NCV with the TCA's cross section shapes applied. As for the first configuration, the TCA's cross section shapes were scaled to preserve the NCV's cross sectional area.

These two new configurations were analyzed using TRANAIR. Comparisons of wing/body TRANAIR results were made with the TCA and NCV.

High Speed Aerodynamic Benefit of Body Cross Section Shapes and Body Camber

TRANAIR Wing/Body Results
Mach=2.40, $C_L=0.080$



- Results in an overall improvement of ~2 counts.
- Body cross section shapes are beneficial independent of the wing.

The wing/body drag increment between the TCA and NCV is approximately four counts.

Applying the NCV body cross section shapes and camber to the TCA yields an approximately two count drag improvement. Applying the TCA body cross section shapes to the NCV results in two of the four count NCV improvement being lost.

The NCV body cross section shapes caused more lift to be carried on the body. The drag on the body also increased. However, the drag on the wing decreased, resulting in two counts of drag improvement.

Because the same drag increment occurred whether the NCV body cross section shapes were added to the TCA or removed from the NCV, it appears that the body cross section shape benefit is independent of the wing.

Cross Discipline Evaluation of the Body Cross Section Shapes

Structures:

- Non-circular fuselage cross section increases cost and weight.
- Detailed structural analysis required to assess the weight impact.
- Worse for skin/stringer than sandwich construction.

Manufacturing Technology:

- Complex shapes may increase difficulty and cost of manufacturing.

Configuration Integration:

- Step down height between door #2 sill and upper wing surface is too high and is an emergency egress concern.

Structures comments:

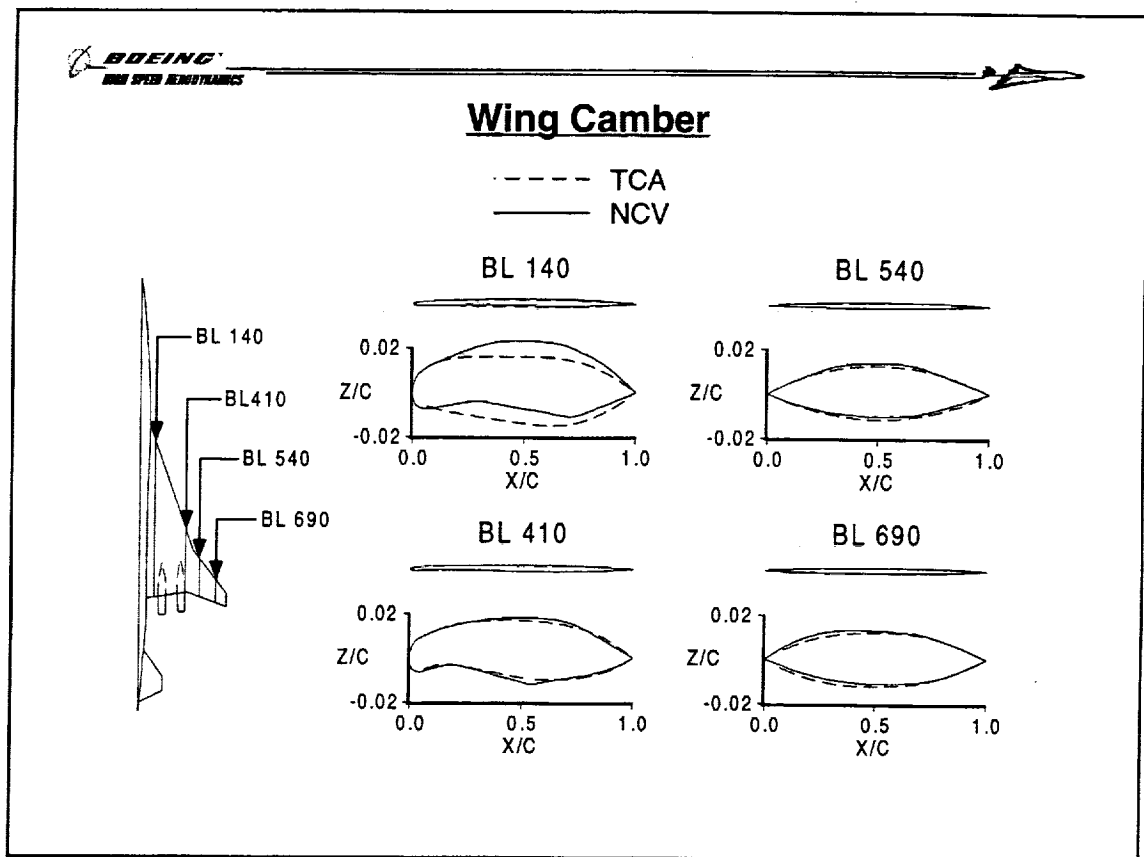
Deviation from a circular cross section in the pressurized sections of the fuselage will give rise to changes to the OML and localized bending moments in the skin panels. Although the sandwich skin panels can be tailored to resist these bending moments, stiffening the skin panels will result in increased cost and weight (magnitude TBD) and in extreme cases could reduce the size of the passenger compartment. Large flat sections in the OML could have a negative impact on frame spacing, decreasing frame pitch to minimize "pillowing" (although, again pillowing is much smaller on sandwich structures than on the TCA skin/stringer baseline). *The skin/stringer panel has almost no ability to resist the bending moments caused by the pressurization of non-circular fuselage.* Deviations from circular cross section give rise to "pillowing" in the skin and increased bending stresses in the frames and stringers of a skin/stringer panel. The frames and stringers need to be stiffer (heavier and more expensive) to control "pillowing". In addition, the frame and stringer spacing may have to be reduced.

Manufacturing Technology's comments:

Complex shapes (those with large curvature variations and/or extreme curvatures) will likely increase the difficulty and the cost of manufacturing (magnitude TBD).

Configuration Integration's comments:

For doors 2 and 3, the step down height from sill to wing upper surface should be no greater than the TCA. The only concern is the excessive sill height of the NCV's door #2 (20" vs. 7" for the TCA). This is unacceptable for safe egress unless an exterior step can be used which would cause a significant drag penalty.



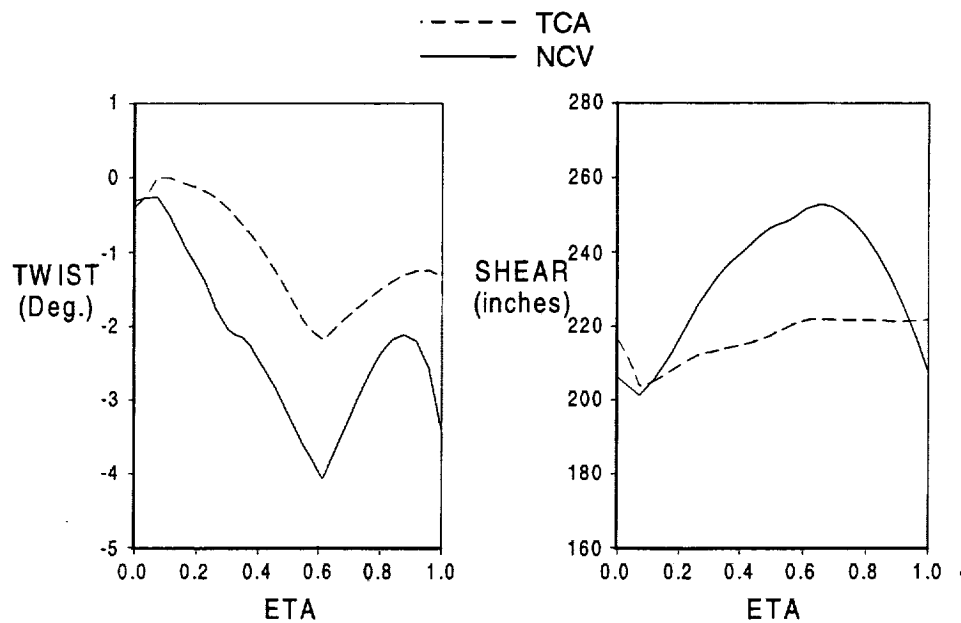
This chart compares the wing airfoil shapes of the TCA and NCV at four span locations.

The airfoil shapes are shown in an enlarged scale so the differences may be seen. The airfoils are shown in 1:1 scale above each enlarged airfoil.

At some sections, the inboard wing of the NCV has more leading edge camber than the TCA. The leading edge of the NCV is also slightly more blunt than the TCA. The outboard wing airfoils have fewer differences.



Wing Twist and Shear



This chart compares the wing twist and shear of the TCA and NCV.

The NCV wing has more leading edge down twist across the entire span. This causes the NCV to fly at an angle of attack approximately one degree higher.

The wing shear is defined as the Z location of the wing trailing edge. The NCV's shear or "gull", which appears in the loft to be most pronounced on the outboard wing, is actually accompanied by a large increase in the dihedral of the inboard wing. As a result, the NCV's wing tip is only 15" lower than the TCA's.

High Speed Aerodynamic Benefit of Wing Camber, Twist, and Shear

Created two new configurations:

	TCA w/ the NCV's Wing Camber, Twist, & Shear	TCA w/ the NCV's Wing Shear
Wing:		
• Thickness	TCA	TCA
• Camber	NCV	TCA
• Twist	NCV	TCA
• Shear	NCV	NCV
Body:		
• Cross Sectional Area	TCA	TCA
• Cross Section Shapes	TCA	TCA
• Camber	TCA	TCA

In order to evaluate the high speed aerodynamic benefit of the wing camber, twist, and shear, two new configurations were created.

The first configuration was the TCA with the NCV's wing camber, twist, and shear applied.

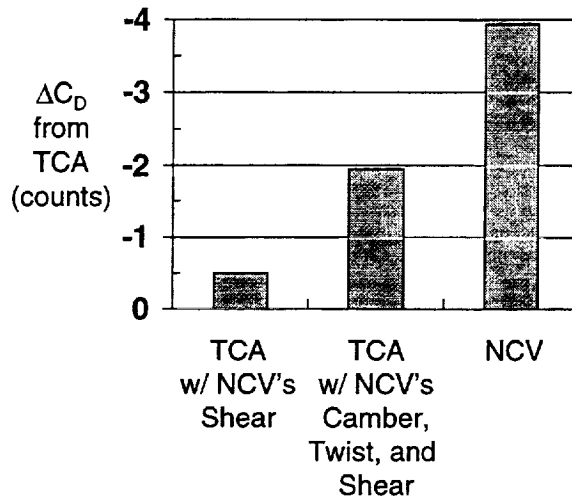
The second configuration was the TCA with only the NCV's shear applied.

These two new configurations were analyzed using TRANAIR. Comparisons of wing/body TRANAIR results were made with the TCA and NCV.



High Speed Aerodynamic Benefit of Wing Camber, Twist, and Shear

TRANAIR Wing/Body Results
Mach=2.40, $C_L=0.080$



- Wing Shear results in 0.5 count improvement.
- Wing Camber, Twist, and Shear result in ~2 count improvement.

The wing/body drag increment between the TCA and NCV is approximately four counts.

Applying the NCV's wing shear to the TCA yields a 0.5 count drag improvement.

Applying the NCV's wing camber, shear, and twist results in a two count drag improvement.

The NCV's camber and twist distribution cause the NCV to fly at an angle of attack approximately one degree higher. The increased angle of attack causes the forward body to carry more lift. This may be beneficial by inducing a flow field which is advantageous to the wing.



Cross Discipline Evaluation of the Wing Camber, Twist, and Shear

Structures:

- Multi-spar design should be able to handle chord-wise and span-wise curvatures with minimal cost or weight impact.

Manufacturing Technology:

- Complex shapes may increase the difficulty and cost of manufacturing.

Configuration Integration:

- Wing tip ground clearance is less than the TCA.

Structures comments:

In the chord-wise direction, the NCV is neither better nor worse than the TCA baseline. Although sharp curvature in the span-wise direction can give rise to out of plane loads, the multi-spar design of the wing and strake will be able to handle the anomalies on the current configuration with minimal cost and weight impact.

Manufacturing Technology's comments:

Complex shapes will likely increase the difficulty and the cost of manufacturing (magnitude TBD).

Configuration Integration's comments:

The NCV's wing tip ground clearance is less than the baseline TCA. Trade studies conducted on the Boeing IR&D baseline reveal increasing ground clearance has some benefits. Ground clearance and pitch-roll trades will need to be developed for any selected non-linear design, but it is not necessary to further constrain the nonlinear optimization designs unless the tip droop increases significantly.



Cross Discipline Evaluation of the Wing Camber, Twist, and Shear (cont.)

Low Speed:

- Span-wise curvature may impact the LE and TE flaps. The flap hinge-lines must be straight.
- Blunter leading edges are better.
- More nose down leading edge camber is better.

Stability and Control:

- Less longitudinally stable than the TCA.
- Inboard and outboard dihedral may affect lateral stability (rolling moment due to beta).

Low Speed's comments:

The outboard wing of the NCV has a considerable amount of curvature in the span-wise direction. This will impact the leading and trailing edge flaps because the hinge-lines of the flaps must be straight.

Blunt airfoils are preferred over sharp airfoils because they perform better at the low mach numbers which characterize the high lift regime.

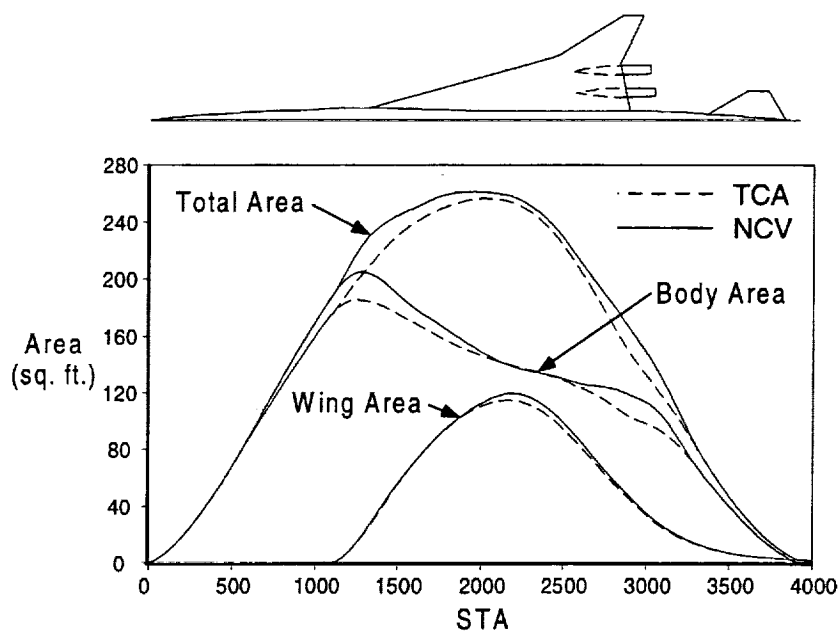
Increasing "nose down" leading edge camber, both inboard and outboard, generally improves high lift performance.

Stability and Control's comments:

The NCV differs from the TCA in its distribution of anhedral and dihedral across the wing. No data is currently available to evaluate the effect of these differences, but it may have a substantial effect on lateral stability (rolling moment due to beta). The TCA has a large coefficient of rolling moment due to beta, and if any wing changes reduce this coefficient it would be viewed as a benefit by stability and control.

Wind tunnel tests have been performed on the NCV and it has been found that it is less longitudinally stable than the TCA. This is a source of concern because the TCA is considered to have marginal longitudinal stability with respect to pitch divergence at the aft C.G. limit. The concern may be offset by the fact that the C_{MO} of the NCV allows the trim C.G. for minimum drag to be approximately 1% farther forward as compared to the TCA. This would allow the C.G. range to be shifted forward offsetting the decrease in longitudinal stability.

Mach 2.4 Cross Sectional Area Distribution



This chart compares the Mach 2.4 cross sectional area distribution of the TCA and NCV.

There are no large cross sectional area distribution differences between the TCA and NCV. The most notable differences occur in the body area just forward and aft of the wing.

During optimization, the wing thickness was constrained to maintain minimum front and rear spar thickness, minimum max.-t/c, and minimum in-spar fuel volume. The body was required to fit around the minimum interior definition.

High Speed Aerodynamic Benefit of Body Cross Sectional Area and Wing Thickness

Created one new configuration:

	NCV w/ the TCA's Body Area & <u>Wing Thickness</u>
Wing:	
• Thickness	TCA
• Camber	NCV
• Twist	NCV
• Shear	NCV
Body:	
• Cross Sectional Area	TCA
• Cross Section Shapes	NCV
• Camber	NCV

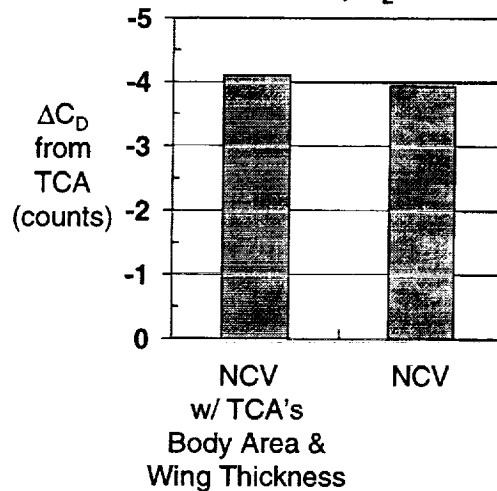
In order to evaluate the high speed aerodynamic benefit of the body cross sectional area distribution and wing thickness, a new configuration was created.

The new configuration was the NCV with the TCA's body cross sectional area and wing thickness applied.

The new configuration was analyzed using TRANAIR. Comparison of the wing/body TRANAIR results were made with the TCA and NCV.

High Speed Aerodynamic Benefit of Body Cross Sectional Area and Wing Thickness

TRANAIR Wing/Body Results
Mach=2.40, $C_L=0.080$



- Thickness changes between the TCA and NCV were not important for the wing/body configuration.
- Thickness variables may be more important for cases with nacelles, because they allow for two surface design.

Applying the TCA's body cross sectional area and wing thickness to the NCV resulted in a negligible change in wing/body drag.

The thickness changes might have been revealed to be more significant if this study had been done with nacelles installed. By changing camber and thickness, the upper and lower wing surfaces can be changed independently. Being able to tailor the lower surface without affecting the upper surface is likely beneficial to nacelle integration.

Cross Discipline Evaluation of Body Cross Sectional Area and Wing Thickness

Configuration Integration:

- Body area checked against minimum interior specifications.
- TCA wing thickness was maintained.
- TCA FEM results revealed the thickness will need to be increased on future configurations.

Low Speed:

- Increased front spar depth is better. Increased spar depth allows for a larger radius of curvature at the flap hinge lines.

Configuration Integration's comments:

The NCV's cross sectional areas were checked against the minimum interior specifications used to develop the TCA. No conflicts were found.

The NCV's wing spar thickness and maximum t/c's were maintained from the TCA. However, results of FEM analysis of the TCA revealed that the wing thickness will need to be increased on future configurations.

Low Speed's comments:

The NCV's front spar depth is slightly greater in some locations than the TCA. Generally, deeper is better because it allows lower hinge-lines and hence a larger radius of curvature when the flaps are deflected.

Summary

Body Cross Sectional Shapes, and Body Camber:

- Worth ~2 counts of drag at Mach 2.4.
- Detailed structural analysis required to assess weight impact.

Wing Camber, Twist, and Shear:

- Together worth ~2 counts of drag at Mach 2.4.
- Wing shear worth ~0.5 counts of drag at Mach 2.4.
- Wing shear may have to be constrained out by flap hinge-line requirements.

Body Cross Sectional Area and Wing Thickness:

- Negligible drag impact.
- Wing thickness (as a variable) is more important for integrating nacelles.
- Wing thickness will probably have to be increased in the future.

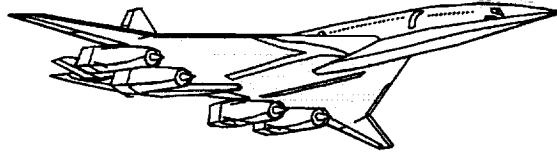
The major findings from this study are summarized.

The NCV's body cross sectional shape and body camber are worth approximately two counts of drag reduction at Mach 2.4. Unfortunately, due to the non-circular nature of the cross section shapes, there will be a structural cost and weight penalty. A detailed structural analysis will be required to determine the weight penalty.

The NCV's wing camber, twist, and shear are also worth approximately two counts of drag reduction at Mach 2.4. The wing shear by itself is worth 0.5 counts of drag reduction at Mach 2.4. In order to integrate the leading and trailing edge flaps, the hinge-line of each flap must be straight. The hinge-line requirement will limit the amount of "gulling" allowed in future optimizations.

The NCV's body cross sectional area and wing thickness had negligible drag impact on the wing/body drag results. The wing thickness changes probably contribute more to drag reduction with nacelles installed, because the lower surface can be tailored independently of the upper surface. Results of FEM analysis of the TCA indicate that the wing thickness will probably have to be increased in the future.

BOEING
HIGH SPEED AERODYNAMICS



TRANAIR Applications For Technology Integration Propulsion Trades

Paul W. Dees
HSCT Aerodynamics
Boeing Commercial Airplane Group
Seattle, Washington
February, 1998

HSR Airframe Technical Review

Los Angeles, CA

February 9-13, 1998

TRANAIR Applications For Technology Integration Propulsion Trades

Paul W. Dees*
Boeing Commercial Airplane Group
P.O. Box 3707, MS 6H-FK
Seattle, WA 98124-2207

Abstract:

Propulsion trade studies often require rapid, inexpensive drag increments between several candidate geometries. Typically a linear potential analysis tool such as A389 is used to get a quick and reasonable drag impact. Some configuration analyses require a tool with the ability to quickly evaluate complex 3D geometry changes. The TRANAIR 3D full potential CFD code offers the capability to evaluate more complex geometry with less cost than the OVERFLOW Navier-Stokes CFD code. It is well validated with experimental test data.

TRANAIR was recently applied as a preliminary design tool to support the TI Task 20 nozzle aspect ratio trade study. This paper compares A389, TRANAIR, and OVERFLOW nacelle pressure drag for the TCA configuration with 2D bifurcated and axi-symmetric nacelles. Several 2D nacelle nozzle aspect ratio analyses will be discussed including the high speed drag results.

Acknowledgements:

Thanks are due to Chet Nelson, Eric Adamson, Robyn Wittenberg, Steve Chaney, and Steve McMahon for their contributions to this work.

*Senior Specialist Engineer
HSCT High Speed Aerodynamics



The Appropriate Tool Must be Selected for
Propulsion Integration Studies.

- Wind tunnel tests: \$60K per/configuration in 1-2 months.
 - + "Complete" answer at multiple Machs & alphas.
 - Requires "mature" designs. Wrong RN, model fidelity & correction uncertainties.
- Navier Stokes CFD: \$17K per/configuration in 150 hr.
 - + Cheaper than testing, accurate results possible.
 - Requires "mature" Lofts. Require dense N.S. grids.
- Inviscid Non-Linear CFD: \$9K per/configuration in 80 hr.
 - + Captures majority of non-lin. effects at lower cost.
 - Requires "mature" designs. May miss something if viscous interactions are strong.
- Linear Analysis (A389): \$500 per/configuration in 5 hr.
 - + Cheap, good results when "non-linear" features minimal.
 - Captures only volume effects and ignores diverter interactions, other 3D effects.

Aerodynamics has four types of tools for configuration analysis. As with many things, greater accuracy costs time and money, so is reserved for mature configurations (or those known to require higher fidelity to capture non-linear flow features).

The benefit of wind tunnel testing is that a complete answer for a range of Machs and angles of attack is provided. The downside is the long lead time and high cost limit the number of configurations that may be tested.

Navier-Stokes CFD is cheaper and gives results that consistently agree with wind tunnel testing. It can only be applied to a limited number of configurations and flight conditions.

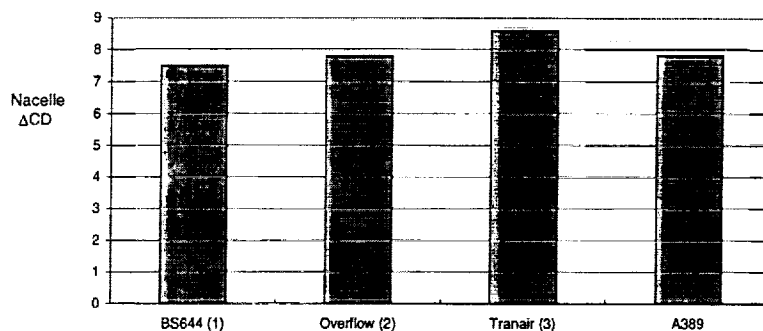
Inviscid non-linear CFD (i.e. Euler or full Potential with non-linear boundary conditions) captures many but not all of the non-linear effects of Navier-Stokes CFD. It is faster and cheaper to run, but it is possible to be led astray by not having the viscous flow physics of Navier-Stokes CFD.

Linear analysis is the least expensive and fastest, but also the least accurate. Many 3D effects such as non-circular nacelles are unable to be evaluated. Linear analysis results are still considered accurate enough for many trade studies not depending on 3D effects.

Comparison Between Methods

For a good low drag installation (baseline TCA) all methods agree to within program experimental uncertainty requirements.

TCA(3570-AR=1.2 Nozzle), Axi Inlets, $Re=9m/ft$
Wind Tunnel Length Body, Internal Duct Forces Removed



- (1) Corrected for -0.8 ct. trip drag, -0.7 ct. ΔCD_p duct from OVERFLOW, and internal skin friction via H349.
- (2) Run at $Re=4$ million/ft and corrected to $Re=9$ million/ft with A389.
- (3) Includes Cd_{skfr} from A389.

The baseline with axi-symmetric inlets and 2D nozzles provides a good geometry to compare the four tools, with OVERFLOW as the Navier-Stokes tool and TRANAIR as the inviscid non-linear tool. All data were corrected to a BSWT wind tunnel truncated aft body and Reynolds number of 9 million per foot. All methods agree to within acceptable program uncertainty requirements. The TRANAIR higher drag level will be discussed in a few charts.

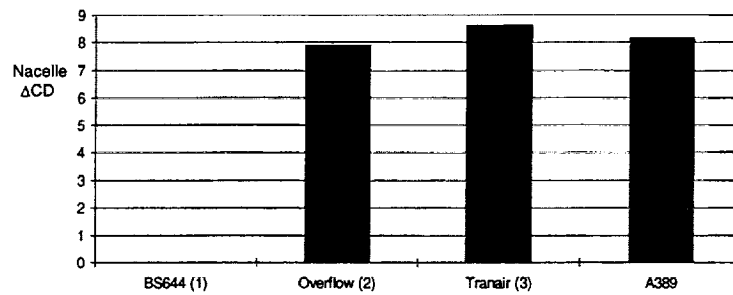
Nacelle ΔCD is defined as the drag for the wing/body/nacelle/diverter minus the drag for the wing/body. It includes skin friction drag and pressure drag. The pressure drag includes nacelle wave drag as well as lift dependent drag (or thrust). Internal duct forces are removed.



Comparison Between Methods

Similar Results Are Obtained For the 2-D Inlet.

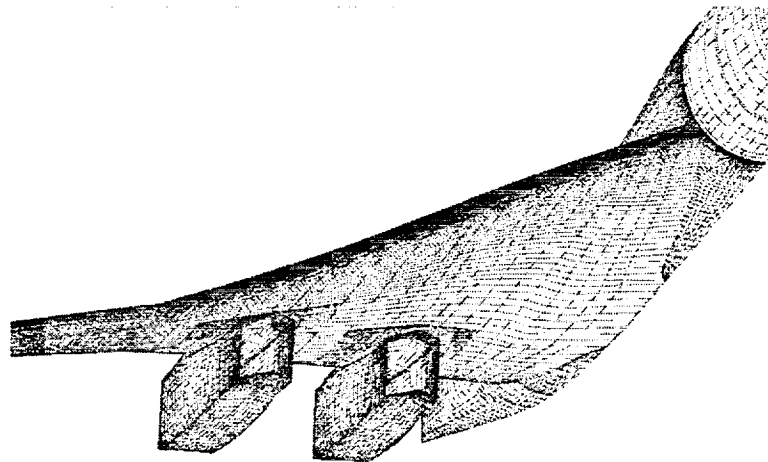
TCA(3570-AR=1.2 Nozzle), 2-D Bif. Inlets, $Re=9m/ft$
Wind Tunnel Length Body, Internal Duct Forces Removed



- (1) Boeing IRAD tests incomplete, HSR tests scheduled.
- (2) Run at $Re=4$ million/ft and corrected to $Re=9$ million/ft with A389.
- (3) Includes C_{dskfr} from A389.

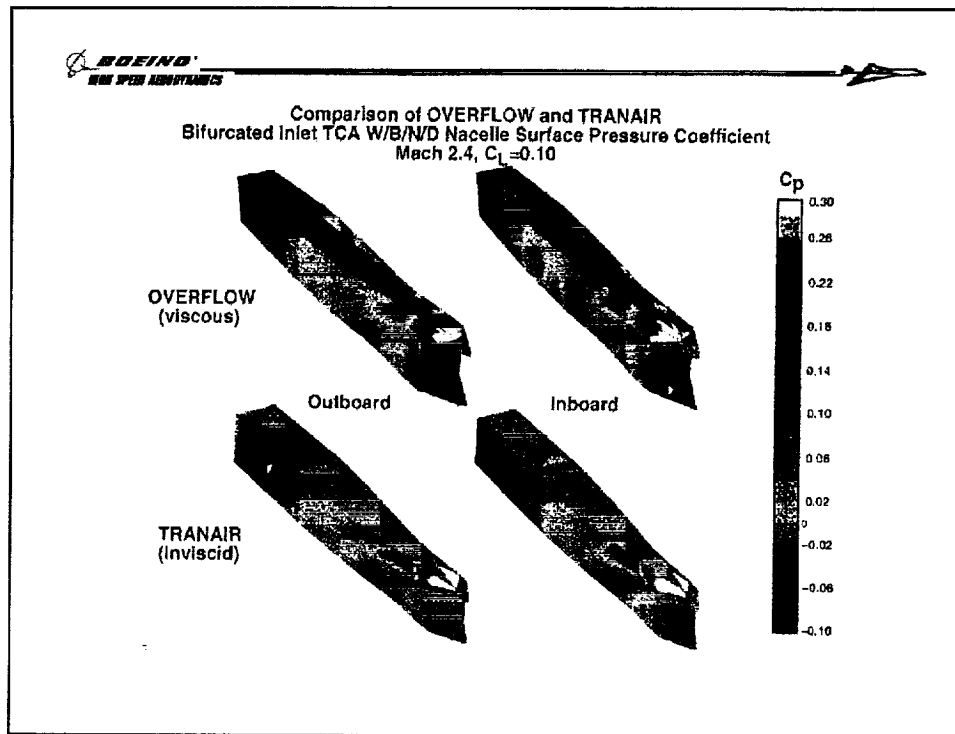
Similar results are obtained for the TCA with 2D bifurcated nacelles, but final Boeing IRAD wind tunnel data are not yet available.

TRANAIR Surface Grid for 2D Bifurcated Nacelles

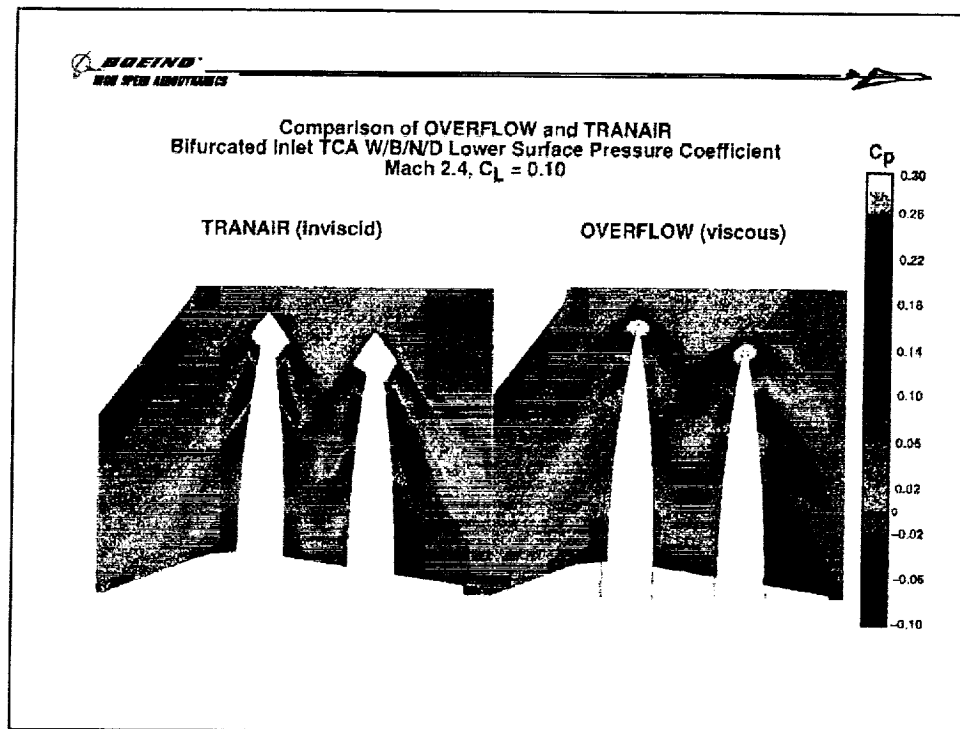


This slide shows typical TRANAIR surface grid (paneling) of the TCA with 2D bifurcated inlets. Creating the surface grid required much time since the previously developed process was inadequate. Flow times are decreasing with a recent case taking less than a week to from initial geometry to final results.

The TRANAIR external lines for the TCA with 2D bifurcated nacelles and diverters were the same as the geometry run in OVERFLOW. Differences in the solutions therefore could be attributed to differences in the flow physics of the codes.

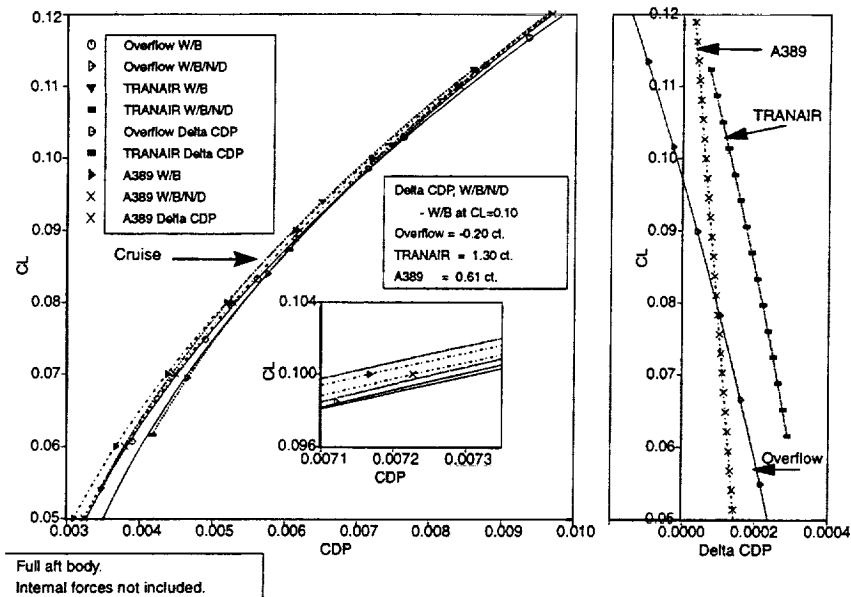


A comparison of TRANAIR to OVERFLOW solutions on the 2D bifurcated nacelles reveals some of the differences due to viscosity. The flow in the boundary layer diverter area is significantly different between the two codes. The diverter shock in OVERFLOW is unswept to the point where the outboard diverter shock interacts with the inlet flow. The re-expansion further downstream is less pronounced than in the TRANAIR solution. The TRANAIR diverter shocks are more highly swept, and the downstream re-expansion more intense. Additionally, TRANAIR indicates further downstream a re-compression that is more intense than OVERFLOW. The OVERFLOW solution is at a wind tunnel Reynolds number of 6.4 million on the MAC.



A comparison of OVERFLOW and TRANAIR on the wing lower surface also reveals significant differences as the diverter shocks influence the wing lower surface. The unswept diverter shock of OVERFLOW dissipates more quickly spanwise than TRANAIR. The wing lower surface pressures between the nacelles are more intense in TRANAIR. OVERFLOW picks up interaction from the inlet leading edge that TRANAIR does not. It stands to reason that nacelle pressure drag increments will differ depending whether they are predicted by TRANAIR or OVERFLOW.

Nacelle Pressure Drag By OVERFLOW, TRANAIR, and A389 TCA With Axi Inlets, Mach 2.4

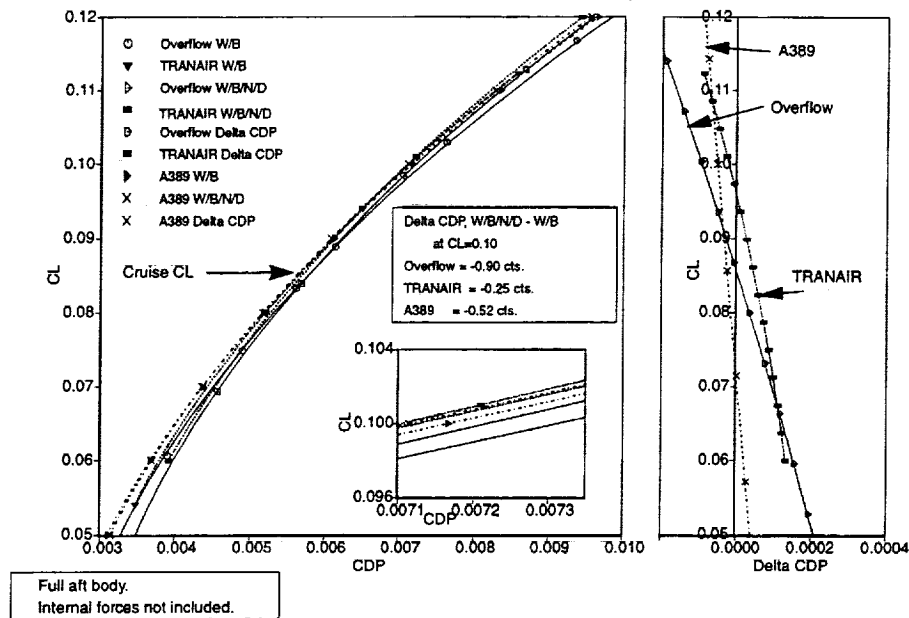


Pressure drag for the TCA W/B and W/B/N/D with axi-symmetric inlets is shown. The polars are all within several counts of each other at a CL of 0.10.

The nacelle pressure drag increments indicate similar trends but differing levels when plotted versus lift coefficient. The nacelles tend to open up the drag polar by providing a beneficial propulsion induced interference, not unlike a mild wing camber. TRANAIR predicts more pressure drag than OVERFLOW with A389 coming in between. A389 tends to underpredict the opening of the drag polar relative to the other two tools because the nacelle lift "footprint" on the wing does not vary with angle of attack.

The full aft body was included in the above data, and nacelle internal forces were removed.

Nacelle Pressure Drag By OVERFLOW, TRANAIR, and A389 TCA With 2D Bifurcated Nacelles, Mach 2.4



Pressure drag for the TCA W/B and W/B/N/D with 2D bifurcated nacelles is shown. The polar opening effect occurs at a lower lift coefficient resulting in less pressure drag than with the axi inlets. As with the axi inlets, TRANAIR predicts more pressure drag than OVERFLOW, but agreement is closer. A389 still tends to underpredict the opening of the drag polar.

The full aft body was included in the above data, and nacelle internal forces were removed.

Tool Selection Results

- OVERFLOW agrees the best with wind tunnel data.
- TRANAIR
 - Overpredicts nacelle pressure drag increments.
 - Good for configuration to configuration increments.
 - Good for 3D details not captured by linearized code.

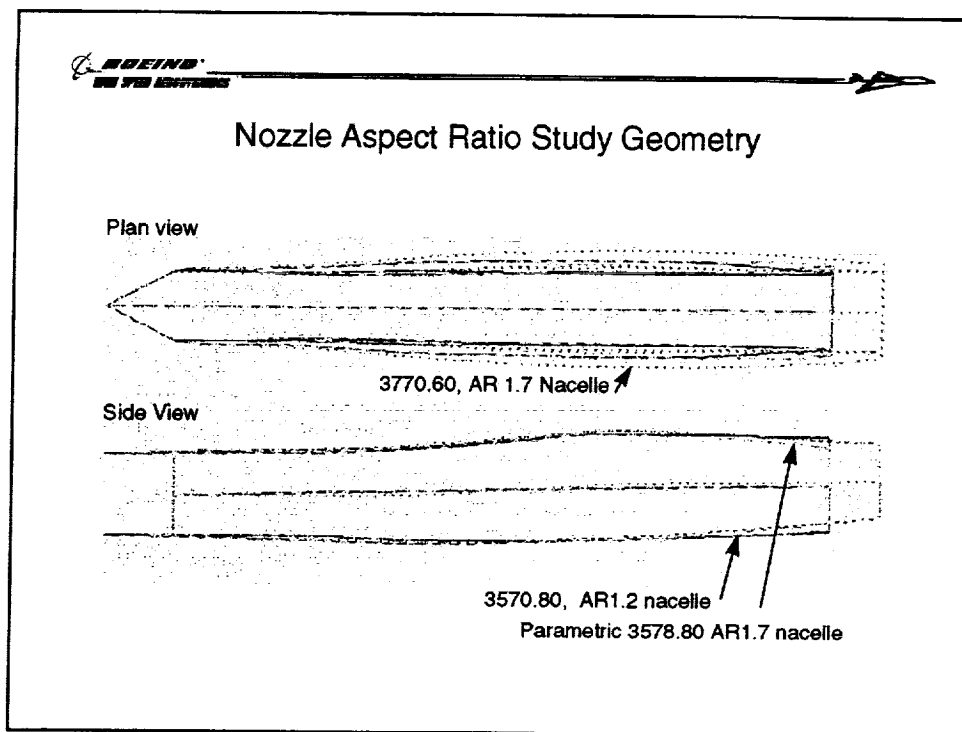
TRANAIR will be used for the nozzle aspect ratio trade study and will continue to be compared with A389 and OVERFLOW for future significant HSCT configurations.

OVERFLOW generally agrees well with wind tunnel data

TRANAIR (and Euler) inviscid codes seem to consistently overpredict nacelle pressure drag increments. Shock/boundary layer interactions in the nacelle diverter area of 2D bifurcated nacelles preclude using TRANAIR or any other inviscid CFD code to estimate absolute nacelle pressure drag increments.

TRANAIR is not considered as reliable as OVERFLOW for estimating absolute levels of nacelle pressure drag increments, but is acceptable for configuration to configuration increments when compared to OVERFLOW and A389.

TRANAIR has the ability to analyze more subtle near-field configuration changes that A389 cannot.



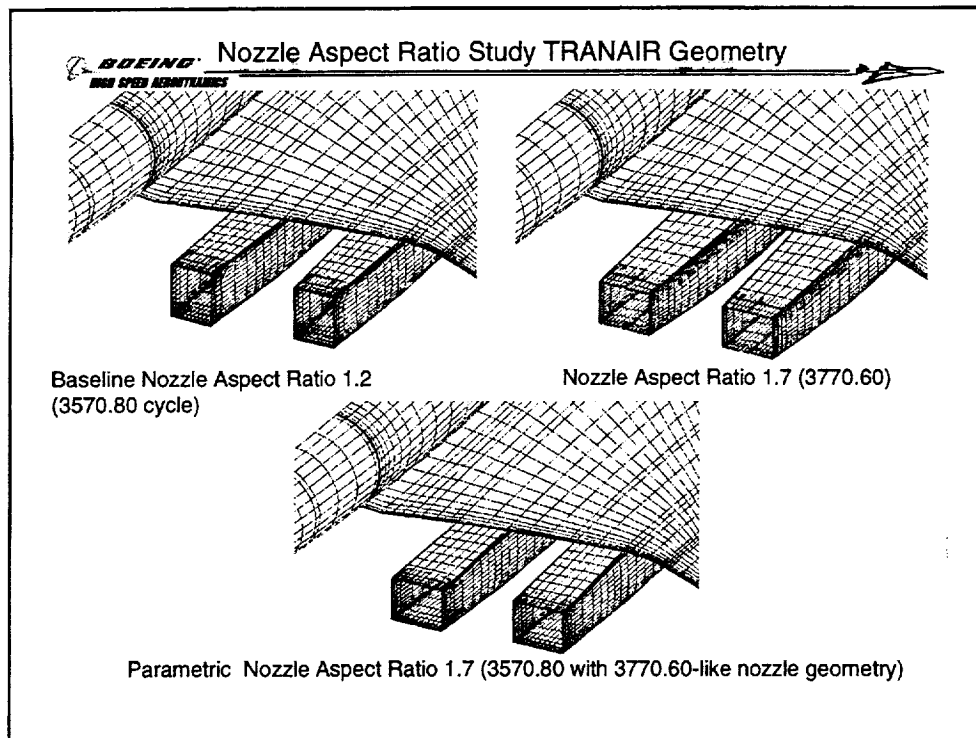
TRANAIR was used to evaluate three distinct nozzle geometries on the TCA wing-body to support the nozzle aspect ratio (AR) trade study. Plan and side views of the nacelle geometry aid in understanding their geometry differences.

The first case was the 2D bifurcated nacelle with a nozzle aspect ratio at cutback of 1.2. The engine cycle is the TCA's 3570.80.

The larger Amax and longer length of the 3770.60, AR=1.7 nacelle is shown. The wider nozzle exit and requirement for straight nozzle sidewalls drove up nacelle Amax.

The nacelle and diverter geometry of the AR 1.7, 3770.60 case changed significantly compared to the AR 1.2, 3570.80 case, making a reason to run a third case, called the parametric nacelle. This geometry had the nacelle forecowl and diverter lines of the first case with a nozzle AR of 1.7 like the second case. The nacelle area distribution was the same as the first case. This "parametric" nacelle was generated to resolve the 3D drag increment of nozzle AR in TRANAIR that A389 is unable to capture. It does not represent a specific "real" buildable nacelle geometry.

Bear in mind that the nozzle aspect ratio listed occurs at the takeoff noise cutback flight condition. At Mach 2.4 the nozzle aspect ratios of 0.814 and 1.275 are equivalent to 1.2 and 1.7 at cutback.



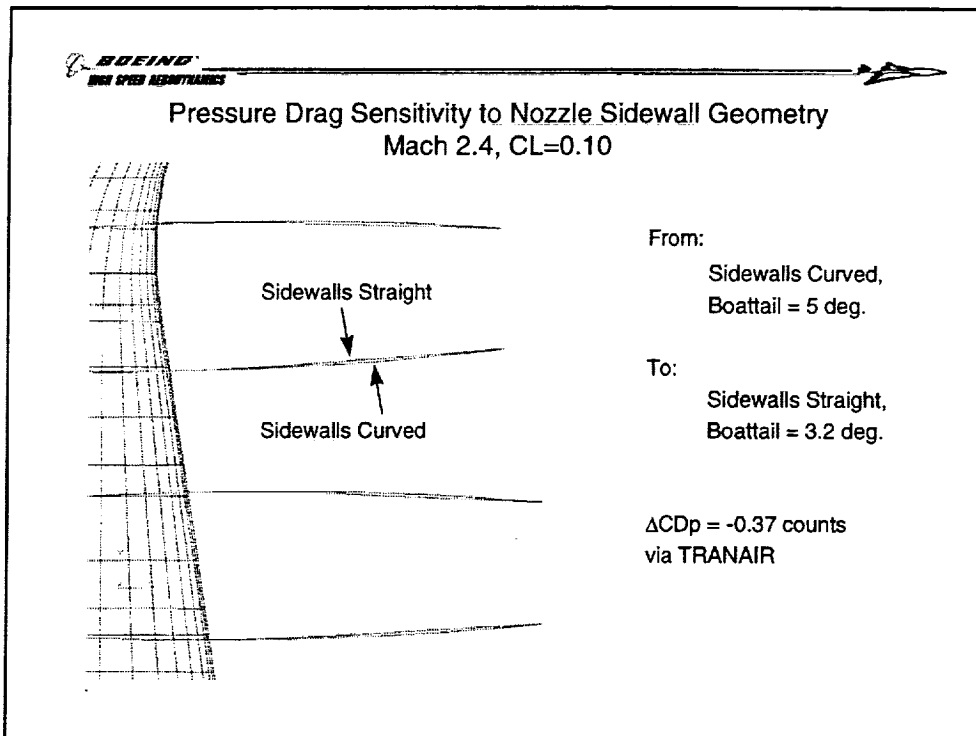
TRANAIR surface grid geometry in the nozzle area is shown for the three cases. The larger nacelle maximum cross sectional area of the 3770.60, AR=1.7 case is apparent, as are the features of the parametric nacelle case.

Details about the engine cycle designations are as follows:

3570.80 = 3.5 fan pressure ratio

0.7 Inlet airflow ratio = cruise mass flow / takeoff mass flow

0.8 bypass ratio = mass flow through fan / mass flow
through core



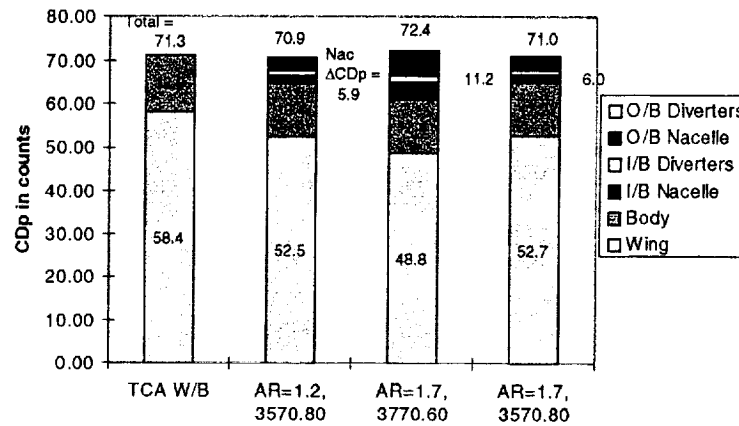
One additional case was run to explore the pressure drag sensitivity to nacelle sidewall geometry.

The 3770.60, AR=1.7 TRANAIR surface Mach distribution indicated an area of accelerating flow on the nozzle sidewalls at the max-half-breadth. The resulting pressure drag reduction was 0.37 counts when the geometry was modified to reduce nozzle sidewall boattail angle and curvature. This appears to be a large drag sensitivity to a small change in geometry, highlighting the need for careful shaping in this area.

Recent IRAD wind tunnel data in the BSWT indicated a similar drag sensitivity with the 3570.80, AR=1.2, although the tested geometry has not been analyzed with CFD. The 3570.80, AR=1.2 nozzle sidewalls are straight with a boattail angle of 3.4 degrees.

TRANAIR ΔCD_p By Component

Mach 2.4, $CL=0.10$



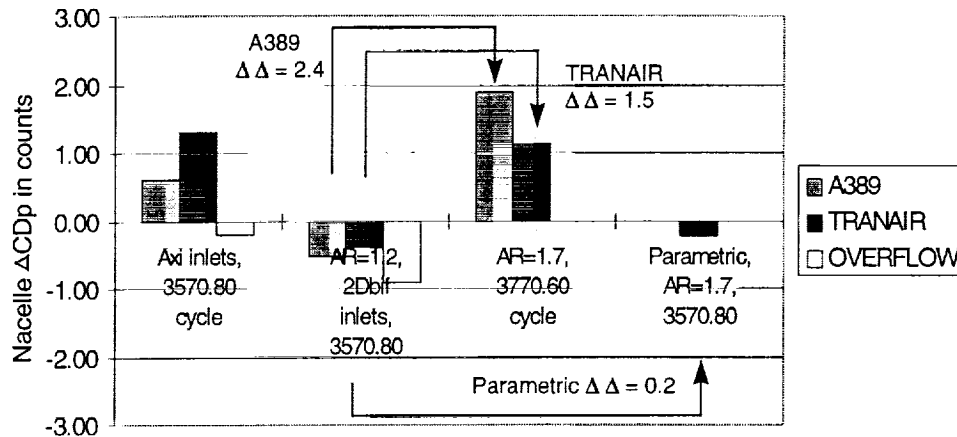
A breakdown of the TRANAIR pressure drag by component is shown to better understand nacelle size impact on the lift dependent drag. The presence of the nacelle reduces the wing portion of the drag by allowing the same CL to be achieved at a lower angle of attack. The nacelles and diverters have their own pressure drag that increases as A_{max} goes up, countering the beneficial lift interference. The wing contributions for all three nacelle-on cases are less than for the wing/body alone case. The wing contribution decreases and nacelle contribution increases further for the 3770.60, $AR=1.7$ case compared to either of the 3570.80 cases.

The parametric nacelle compared to the 3570.80, $AR=1.2$ case has very similar drag components due to having the same area distribution.

The nacelle contributions shown here are not to be confused with $\Delta CD_{nacelle}$, which is $CD_{W/B/N/D} - CD_{W/B}$ alone. It will be shown on the next chart.



Nacelle Pressure Drag Comparison Mach 2.4, CL=0.10



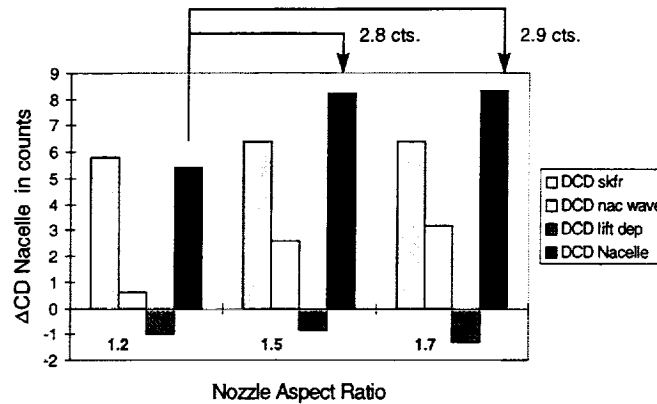
Nacelle ΔCD_p is shown for the various nozzle AR study geometries and prediction tools. The $\Delta \Delta CD_p$ is the difference in nacelle pressure drag between two different configurations.

A389 is predicting a 2.4 drag count $\Delta \Delta CD_p$ between the 3570.80, AR=1.2 and the 3770.60, AR=1.7 cases. TRANAIR predicted only a 1.5 count $\Delta \Delta CD_p$. A389 accounts for the volume effect of the increased A_{max} . TRANAIR is accounting for the 3D effects of the changed forecowl and diverter geometry as well as the lift interference. A389 underpredicts the lift interference, which counters the volume and 3D effects.

The "parametric nacelle" $\Delta \Delta CD_p$ by TRANAIR is 0.2 counts and measures the incremental 3D geometry effects of the nozzle AR change from 1.2 to 1.7.

Thus, a conservative $\Delta \Delta CD_p$ would include both the A389 and the parametric nacelle numbers. The TRANAIR $\Delta \Delta CD_p$ is less conservative. The range of $\Delta \Delta CD_p$ is from 1.5 to 2.6 counts. The average $\Delta \Delta CD_p$ is a logical choice for pressure drag due to the uncertainties of both methods.

Nozzle Aspect Ratio A389 Results



Note: Area distributions updated since 3770.60 TRANAIR analysis.
 $\Delta CDP = \Delta C D \text{ nac wave} + \Delta C D \text{ lift dependent}$

Previous A389 results were for the specific geometries run in TRANAIR rather than for a family of nacelles.

A family of updated nacelle area distributions were used to re-analyze the drag impact of nozzle aspect ratio. Most of the drag penalty is incurred when nozzle AR increases from 1.2 to 1.5, with only a nominal increase from 1.5 to 1.7. These results were combined with the trends from TRANAIR as described in the previous chart to give a drag sensitivity to nozzle aspect ratio.

The drag impact from AR=1.2 to 1.5 represents the drag growth from the HSCT configuration engine update from the TCA to the PTC. Further investigation is underway to understand what portion of this drag growth can be eliminated.

Nozzle AR Bottom Line From Aerodynamics

Nozzle AR 1.2 to AR 1.7

- The ΔCDp varies from 1.5 counts (TRANAIR) to 2.5 counts (A389 + TRANAIR Parametric). Average ΔCDp is 2.0 counts.
- Average $\Delta CDp + \Delta CD$ skin friction of 0.6 counts = 2.6 counts.
- 2.6 counts = 24,800 lb. MTOW for the TCA (9,530 lb. per count).

Nozzle AR 1.5 to AR 1.7

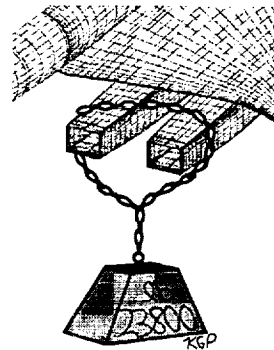
- The $\Delta CD = 0.1$ counts (A389) = 1,000 lb. MTOW.

Nozzle AR 1.2 to AR 1.5

- The ΔCD inferred = 2.5 counts = 23,800 lb. MTOW.

Conclusion:

Multi-discipline re-evaluation needed of AR 1.2



For a nozzle AR 1.2 to AR1.7 the lower bound ΔCDp is the 1.5 counts from TRANAIR. This represents an increment that may be achieved with further design refinement using OVERFLOW to include viscous effects. The upper bound ΔCDp is the 2.3 counts from A389 plus the 0.2 counts of 3D effects from the TRANAIR Parametric $\Delta\Delta$, or 2.5 counts total. An average of the lower and upper bound ΔCDp 's is 2.0 counts. Add the skin friction increment of 0.6 counts to get a total average ΔCD of 2.6 counts. 2.6 drag counts is equivalent to 24,800 pounds of MTOW for the TCA (9,530 lb. per count).

For a nozzle AR 1.5 to AR1.7, the ΔCD from A389 is 0.1 counts, or 1,000 lb. of MTOW.

For the nacelle configurations analyzed, the increment between the one with a AR 1.2 and newer AR1.5 geometry is inferred from the above to be 2.5 counts, or 23,800 pounds of MTOW.

The recommendation drawn from this result is that nozzle aspect ratio 1.2 should be re-evaluated on a more consistent basis with other disciplines to assure selection of the engine installation that is best for the HSCT Technical Configuration airplane. The drag growth from the TCA to the PTC needs to be understood and stopped.



Summary

- TRANAIR a valid PD tool for this study.
 - Can do 3D effects that A389 can't detect.
 - Can evaluate differences between configurations.
 - Cannot capture 2D bif. inlet / diverter / wing viscous interactions.
- Re-evaluation of AR=1.2 needed because of drag-equivalent MTOW penalty of 23,800 lb for AR=1.5.
- Further aerodynamic analysis needed if noise requirements drive us toward an AR=1.7.

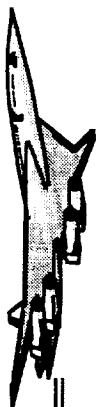
Several conclusions may be made regarding analysis tools choices and engine nozzle aspect ratio. TRANAIR is a valid PD tool when subtle 3D geometry effects that A389 cannot detect may drive a decision. Inviscid codes cannot capture viscous effects like the complex 2D bifurcated inlet / diverter / wing interactions, but can be useful for evaluating differences between configurations.

The true noise-drag trade for a nozzle aspect ratio of 1.2 should be re-evaluated because of the drag penalty observed. The configuration was changed to one with a larger nozzle aspect ratio but which also had a larger nozzle suppressor area ratio (SAR) and maximum diameter. Further analysis of a family of nacelles that only vary in nozzle aspect ratio is needed.

The current PTC configuration as well as the current direction of the noise and engine communities is toward a 1.5 nozzle aspect ratio. Thus, the PTC has this penalty already built in to its sized MTOW and it has the potential to lighten up if the nacelle Amax can be decreased.

Conversely, if noise requirements drive us toward a 1.7 nozzle aspect ratio, the penalty relative to 1.5 may be small. Further aerodynamic analysis would be needed.

This page is intentionally left blank.



CFD Data Generation Process for Nonlinear Loads

Boeing Long Beach: Alan Arslan, Todd Magee,
Eric Unger, Peter Hartwich, Shreekant Agrawal,
Joseph Giesing, and Bala Bharadvaj

NASA Ames: Neal Chaderjian and Scott Murman

NASA/Industry HSR Technology Integration Review
Los Angeles, California
February 9-13, 1998



Ames Research Center



NOTE

This paper was presented in the session entitled "TI Studies related to Configuration Aerodynamics" (CA/TI joint session) on Thursday morning February 12, 1998. The session chairperson was Chet Nelson.

CFD Data Generation Process for Nonlinear Loads

Alan Arslan, Todd Magee, Eric Unger,
Peter Hartwich, Shreekant Agrawal, Joseph Giesing, and Bala Bharadvaj

The Boeing Company
Long Beach, California 90807-5309

Neal Chaderjian, Scott Murman

NASA Ames Research Center
Mofett Field CA 94035-1000

This paper discusses the development of a process to generate a CFD database for the non-linear loads process capability for critical loads evaluation at Boeing Long Beach. The CFD simulations were performed for wing/body configurations at high angles of attack and Reynolds numbers with transonic and elastic deflection effects. Convergence criteria had to be tailored for loads applications rather than the usual drag performance. The time-accurate approach was subsequently adopted in order to improve convergence and model possible unsteadiness in the flowfield. In addition, uncertainty issues relating to the turbulence model and grid resolution in areas of high vortical flows were addressed and investigated for one of the cases.

Outline

This chart gives the outline of the various topics covered in this presentation.



Outline

- ☐ Background
- ☐ CFD Approach for the M2.4-7A
- ☐ Problems encountered
- ☐ Convergence criteria
- ☐ Time-accurate simulation
- ☐ Application to the TCA configuration
- ☐ Sensitivity study by NASA Ames
- ☐ Conclusion

Background

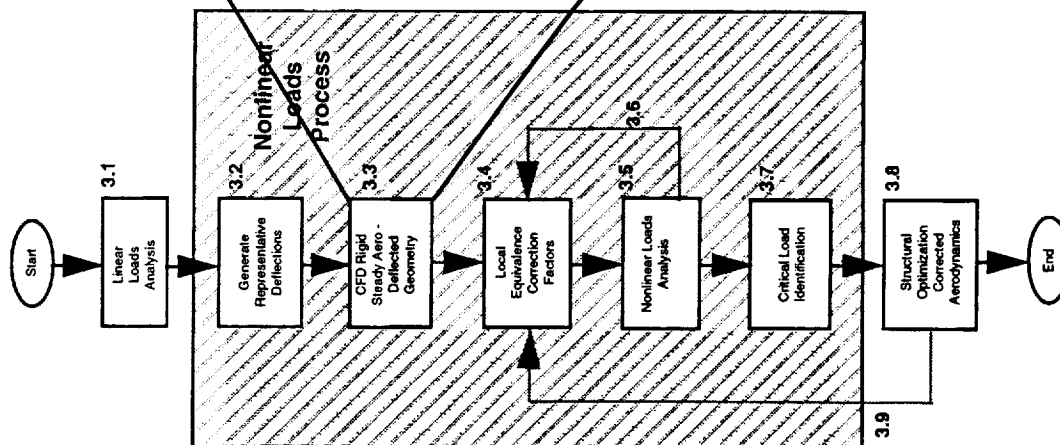
The current NASTRAN process for generating structural loads is based on linear aerodynamics (Doublet Lattice and ZONA) and the critical load conditions must be supplied by the user. A new process has been developed (Local Equivalence Nonlinear Loads Process shown in the flow-chart below) that provides for a nonlinear loads capability in addition to providing a critical loads selection process. This nonlinear loads process uses a fairly small nonlinear aerodynamic database to correct the linear loads process. The database can either be generated using CFD (in which case representative elastic deflections are used) or from wind-tunnel data (in which case a rigid configuration is used); however, only the CFD approach is described here. All of loads cases (not just the critical ones) can then be easily corrected using this procedure and a new set of high-fidelity critical loads selected and used for structural sizing.

The work to be described here pertains only to the generation of the nonlinear aerodynamic database using CFD. High angles-of-attack and Reynolds numbers, plus transonic and elastic deflection effects, pose special challenges in generating this database. Also, the convergence criteria must be tailored to loads rather than the usual aerodynamic performance.

Initially, the only configuration for which an extensive validated CFD database at transonic regimes was available was the M2.4-7A Opt5 (obtained from nonlinear optimization on the baseline arrow wing). Consequently, the current approach used the later configuration to develop the CFD process for loads applications. Afterwards, the process was applied to the TCA configuration.



Background



□Objective:

- Develop process to generate a CFD database for use in the local equivalence correction procedure for the nonlinear loads process

□Approach:

- M2.4-7A: Learning Process
- TCA application

CFD Approach for the M2.4-7A Configuration

Most of the process development was done with the M2.4-7A wing/body configuration. The optimized M2.4-7A Opt5 configuration was selected because of the extensive validation work done on it under Configuration Aerodynamics (Tasks 3 & 32). Five wing/body configurations were obtained, each corresponding to representative deflections discussed earlier. These configurations correspond to the deflected wing/body shapes as a result of the loads at a given angle-of-attack.

CFD analyses were performed for a single Mach number during the methods development phase of this task. Analysis was done at Mach 0.6 for five representative angles-of-attack ranging from -14° to 23° . The grid consisted of a single-block C-O topology with 93 points in the spanwise direction, 237 in the streamwise, and 89 in the normal directions. The Euler grids for the configurations with representative deflections were generated by perturbing the baseline rigid wing/body grid using a package (CSCMDO) acquired from GEOLAB at NASA Langley. After perturbation, the grids were manually improved and then clustered for Navier-Stokes analyses.

The CFL3D code was used for the N-S analyses. The numerical scheme consisted of flux-difference splitting with multigrid acceleration. The flow was assumed to be fully turbulent and the Baldwin-Lomax algebraic turbulence model with the Degani-Schiff option was used. The Reynolds number used for the simulation was the flight Reynolds number of 301 million (based on the mean aerodynamic chord).



CFD Approach for the M2.4-7A Configuration

☐ Configuration:

M2.4-7A Opt5 wing/body

☐ Grid-Topology:

C-O grid of 93x237x89

☐ Geometries:

Obtained from deflected shapes for cases ranging from -1g to 2.5g at five angles-of-attack

☐ Grid Generation:

Perturbation of a rigid baseline Euler grid (CSCMDO/FLEXMESH) and clustering for N-S

☐ Analysis:

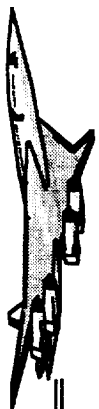
CFL3D N-S, steady flow, Baldwin-Lomax turbulence model (Degani-Schiff option turned on for higher angles-of-attack)

☐ Flight Conditions:

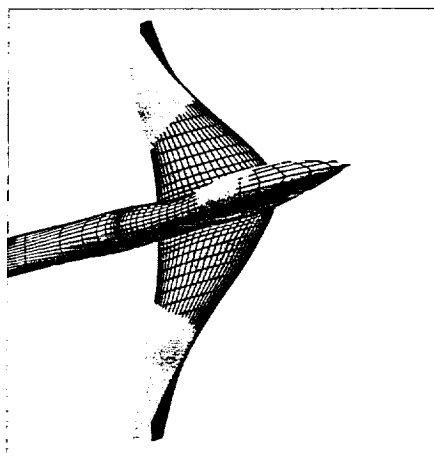
Mach= 0.6, $Re_c = 300$ million. angles-of-attack of -14, 1.8, 12, 18, and 23 degrees

M2.4-7A Opt5 Wing/Body Shapes

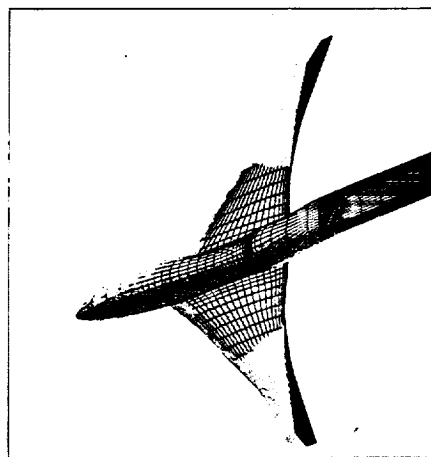
The chart below shows two of the geometries used for the CFD analyses. The rigid geometries are shaded while the C-O grid topology is shown for the deflected shapes. The figures below show the wing/body configuration with the fuselage attached to a wind-tunnel sting. Note that the fuselage is also structurally deflected.



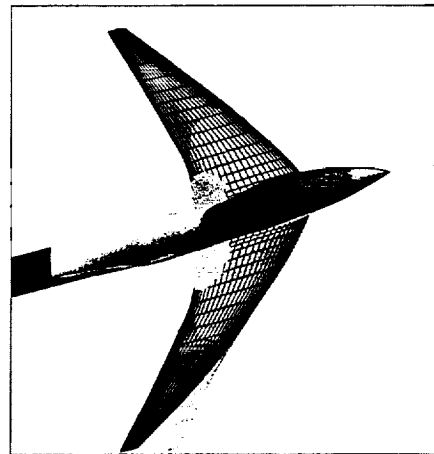
M2.4-7A OPT 5 Wing/Body Shapes
Baseline and Deflected Configurations for the Database
 $\alpha = -14^\circ$ $\alpha = 23^\circ$



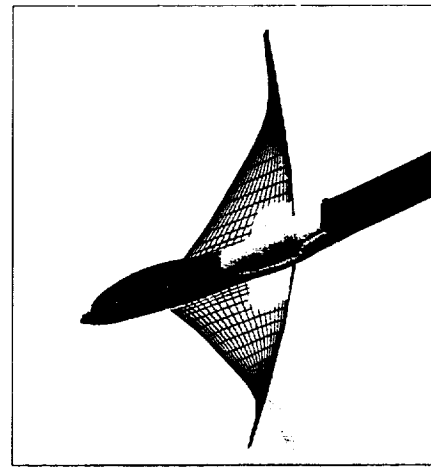
Front View



BackView



Front View



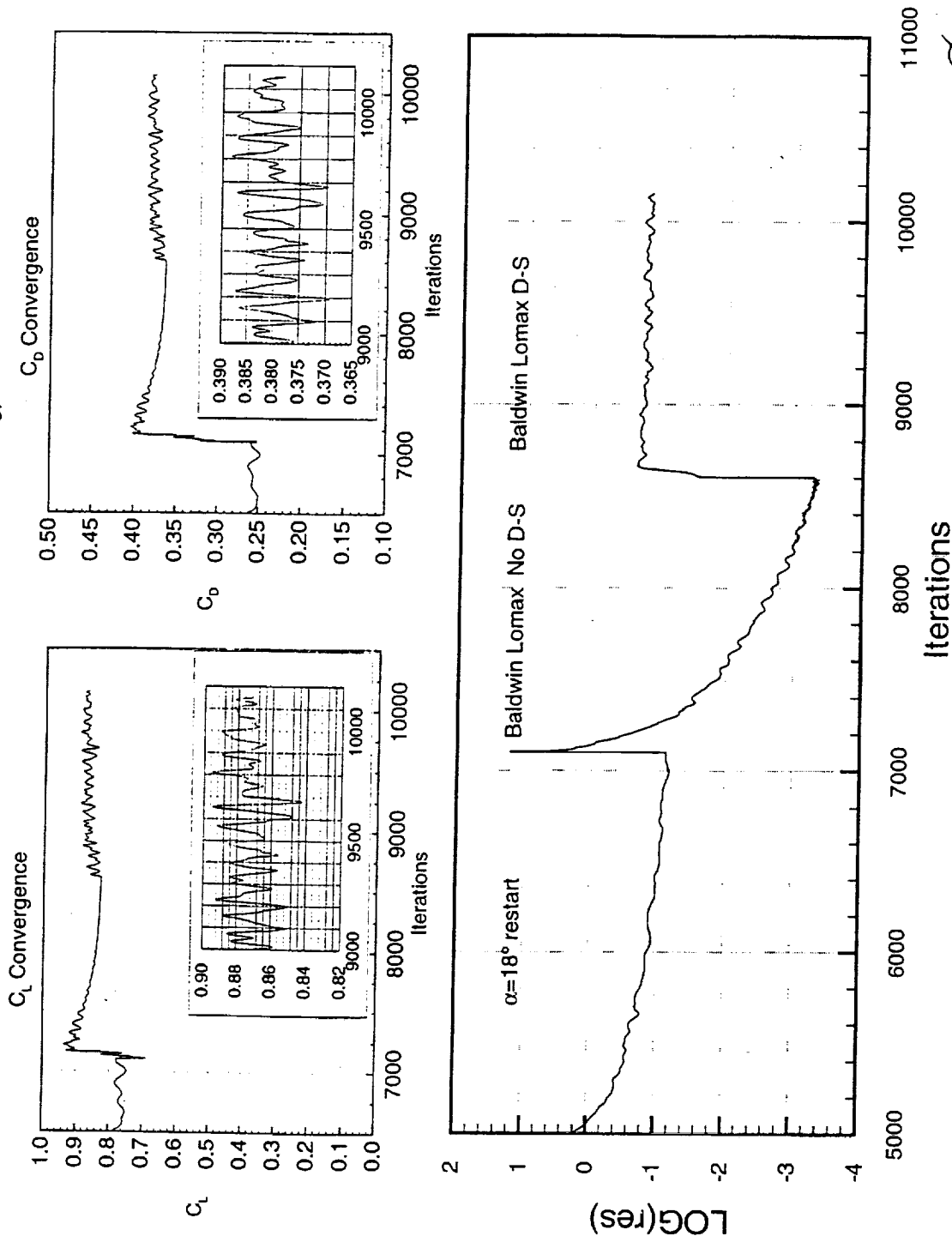
BackView

Convergence History for the M2.4-7A Opt5

When the steady-state formulation in CFL3D is used for the higher angles-of-attack, the solution does not converge smoothly. For example, the solution for the representative geometry corresponding to the 22.9° angle-of-attack is shown above. The residual seems to “hang up” with lift and drag fluctuating in a range of 4 to 5%. The reason for this fluctuation is believed to be the highly separated flow with separation lines coincident with the strong vortices formed at the nose and wing apex.

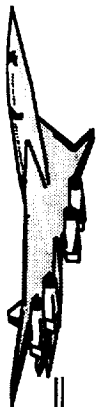


Convergence History for M2.4-7A Opt5 Configuration with Deformation
CFL3D N-S (B-L, D-S); $Re_c = 301 \times 10^6$; $M = 0.60$; $\alpha = 23.050^\circ$; C-O(93x237x89)
(2 Level Multigrid; Integration w/ full sting)



M2.4-7A Opt5 W/B Surface Flow Traces

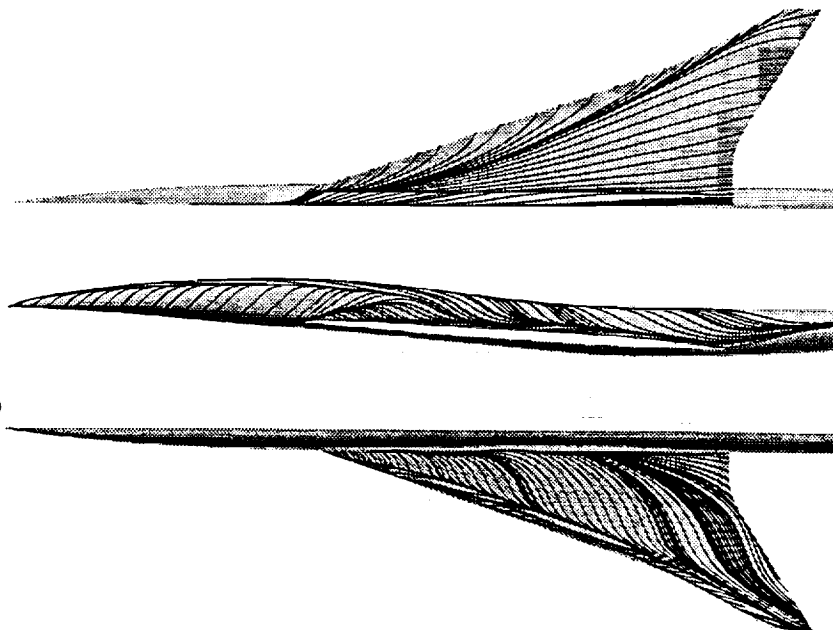
The surface streamlines at the end of 10,100 iterations are shown in the figure on the left. There is an indication of flow separation on the upper surface which is most likely contributing to the unsteadiness in the solution.



M2.4-7A Opt5 W/B Surface Flow Traces

CFL3D N-S, 10100 Iterations, $M_\infty=0.6$, $\alpha=23.05^\circ$

$Re_c = 301 \times 10^6$



Top View Side View Bottom View

Convergence Summary for the Opt5 Wing/Body

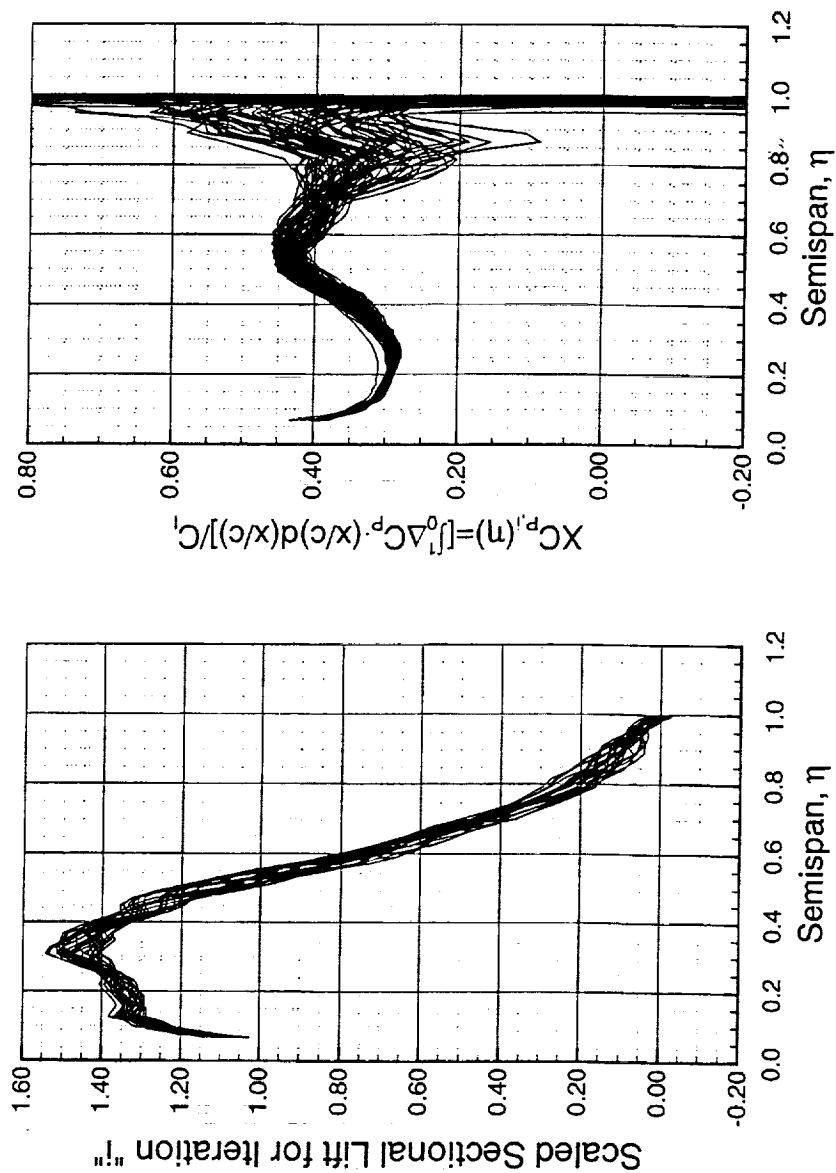
The two plots below, correspond to the -14° angle-of-attack case. The figure on the left hand side shows the sectional lift (scaled by the total lift coefficient at a given iteration) for the last 100 iterations. The values show a significant scatter. The figure on the right shows the axial location of the center-of-pressure X_{cp} as a function of span. This plot indicates that the X_{cp} varies significantly over the outboard wing. Since these results indicate a lack of convergence, new criteria need to be developed in order to establish convergence for CFD solutions in support of non-linear loads.



Convergence Summary for M2.4-7A Opt5 Wing/Body Wing with Representative Deflections

CFL3D N-S, $M_\infty=0.60$, $\alpha=-14.0$ deg., $Re/ft=3.21$ million, 93x237x89 C-O Grid

$XC_{P,i}$ = Local Center-of-Pressure at Iteration "i"



Convergence Criteria for Loads

Convergence criteria were established by monitoring several quantities of interest:

- (a)- The “mean” lift coefficient (integrated over wing/body) and its % deviation. The mean value is computed by a “moving average” technique. In other words, the values of C_L are averaged over the total number of iterations as the solution progresses, with an update every 10 iterations. This is a useful parameter, but the % deviation could become quite large when the mean value approaches zero.
- (b)-The actual value of the fluctuation between the latest available peak and trough is computed.
- (c)-The spanwise distributions of the sectional lift and center-of-pressure are also monitored at each iteration. The sectional loads (cC_l/c_{bar}) are scaled by C_L at each iteration to give insight not only on the magnitude of the fluctuation but also on shape changes (i.e., spanwise shifting of the load).
- (d)-The variations in the quantities of interest were quantified by the use of σ and ϵ , which are the respective rms values of the difference between the scaled sectional loads and center-of-pressure curves at local peaks and troughs.



Convergence Criteria for Loads

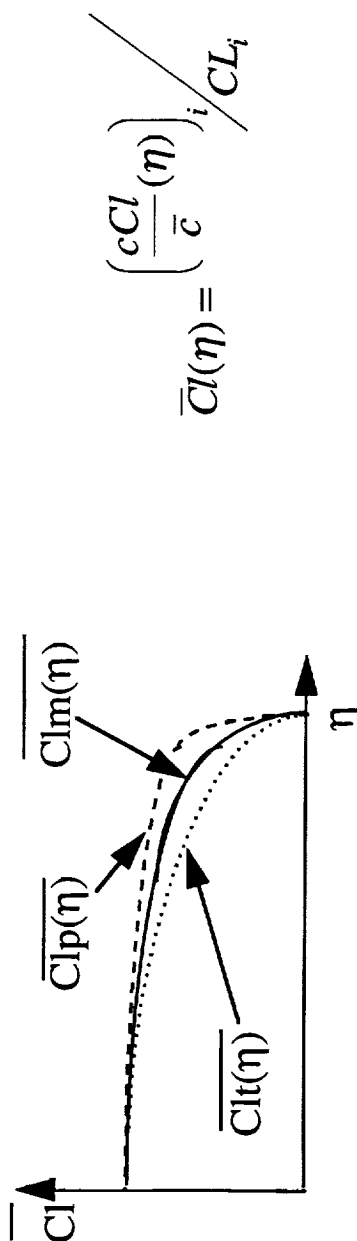
- % Deviation from mean (moving average):

$$(CL_n - CL_m) / CL_m$$

- Difference between peaks & troughs:

$$\Delta(C_L) = |CL_p - CL_t|$$

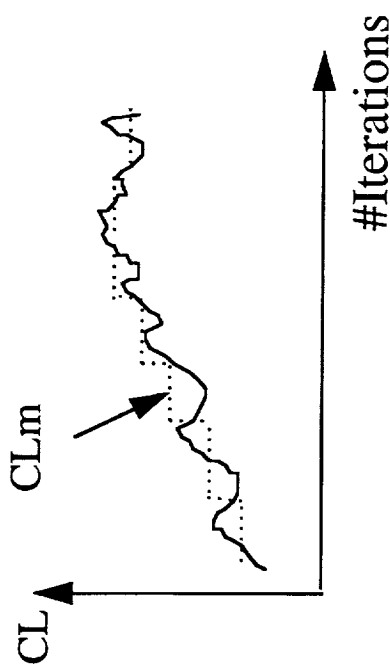
- Non-dimensional sectional lift:



- Mean values of the relevant shape variations:

$$\sigma = \sqrt{\int_0^1 (Cl_p - Cl_t)^2(\eta) d\eta}$$

- Similar approach for the center-of-pressure



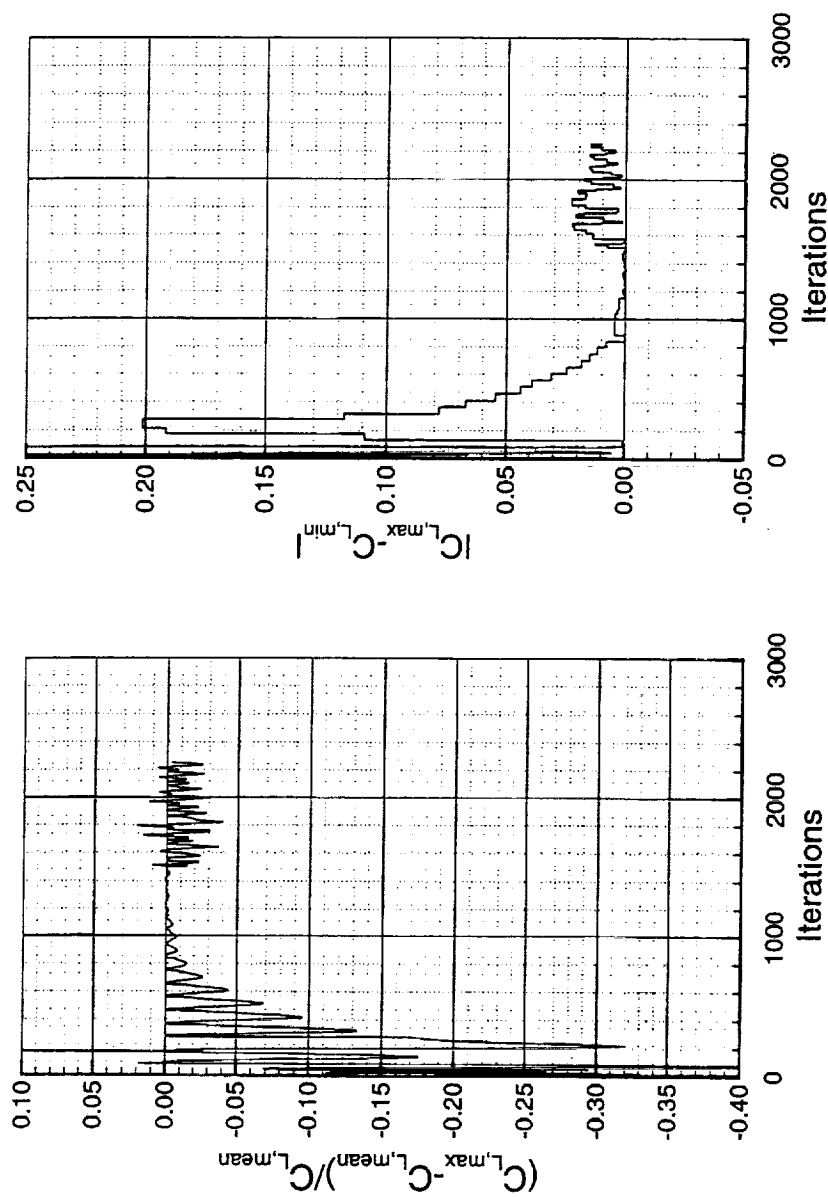
Convergence Summary for the Opt5 Wing/Body

The figures below show the convergence criteria applied to the $\alpha = -14.0^\circ$ case. The lift quantities monitored, are varying within 2 to 5% of the respective mean values.



Convergence Summary for M2.4-7A Opt5 Wing/Body Wing with Representative Deflections

CFL3D N-S, $M_\infty=0.60$, $\alpha=-14.0$ deg., Re/ft=3.21 million, 93x237x89 C-O Grid



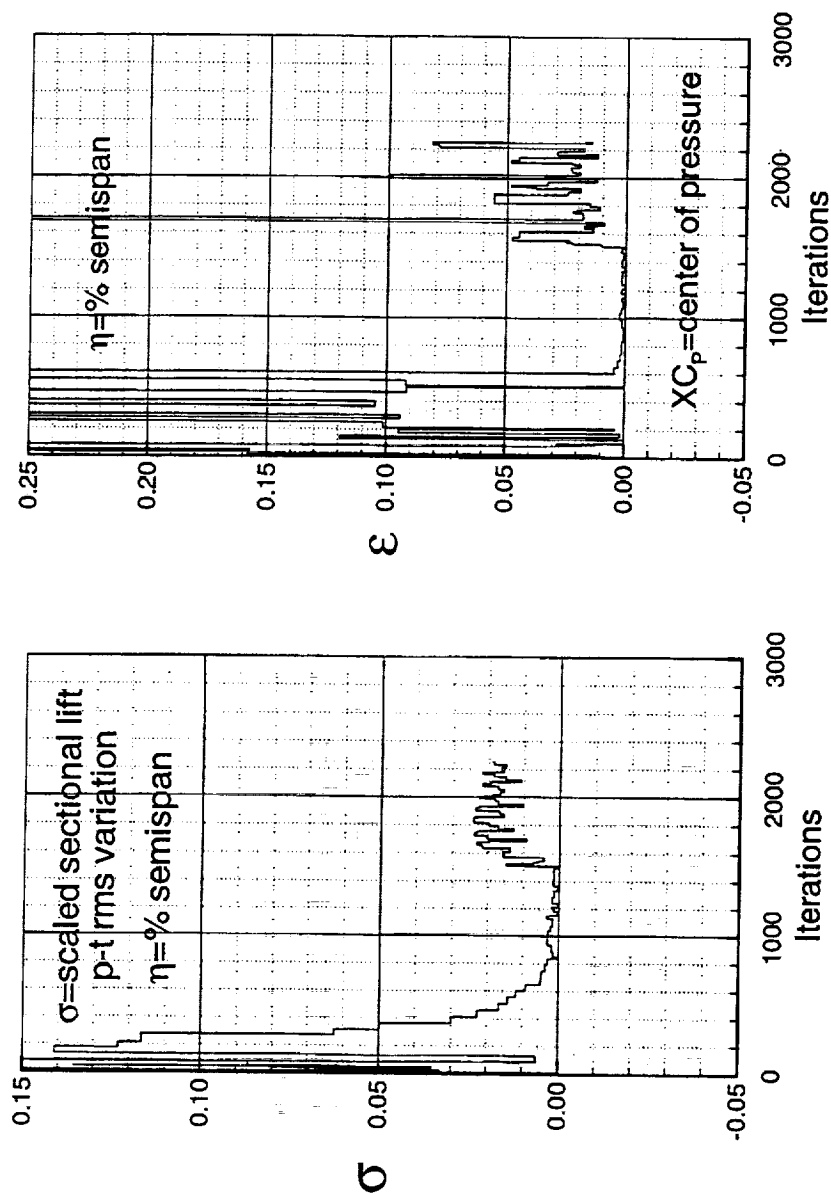
Convergence Summary for the Opt5 Wing/Body

The figures below show the convergence criteria applied to the $\alpha = -14.0^\circ$ case. The sectional loads quantities monitored, are varying within 2 to 3% for σ and 5 to 8% for ϵ . Consequently, the large variations of the sectional loads and X_{Cp} curves observed are reflected in the monitored quantities. These fluctuations reflect flow unsteadiness patterns that are either numerically induced or actual features of the highly separated flowfields.



Convergence Summary for M2.4-7A Opt5 Wing/Body Wing with Representative Deflections

CFL3D N-S, $M_\infty=0.60$, $\alpha=-14.0$ deg., $Re/ft=3.21$ million, 93x237x89 C-O Grid



Time-Accurate Simulation

The answer to the question of numerical vs. flowfield unsteadiness can be provided by a time-accurate simulation. In fact, the time-accurate analysis to perform the steady high angle-of-attack simulations was suggested by Scott Murman and Neal Chaderjian from NASA Ames based on their experiences with delta wings and F-18 flight tests.

The $\alpha = -14^\circ$ case was used as a test-bed for the time-accurate simulations because of its particular "lack" of convergence. The time-accurate approach used with the implicit scheme present in CFL3D consisted of the τ -TS second-order-in-time method. The use of three sub-iterations per time-step allowed the lowest computational cost (the code manual recommended five). In this case, each time-accurate step will be equivalent to 3 steady-flow iterations. It was estimated that the flowfield can be covered by 1000 time-steps which yields a non-dimensional time-step of 11.25 (~ 0.001 sec). The time-accurate solutions assume a pseudo-time CFL of 10.



Time-Accurate Simulation

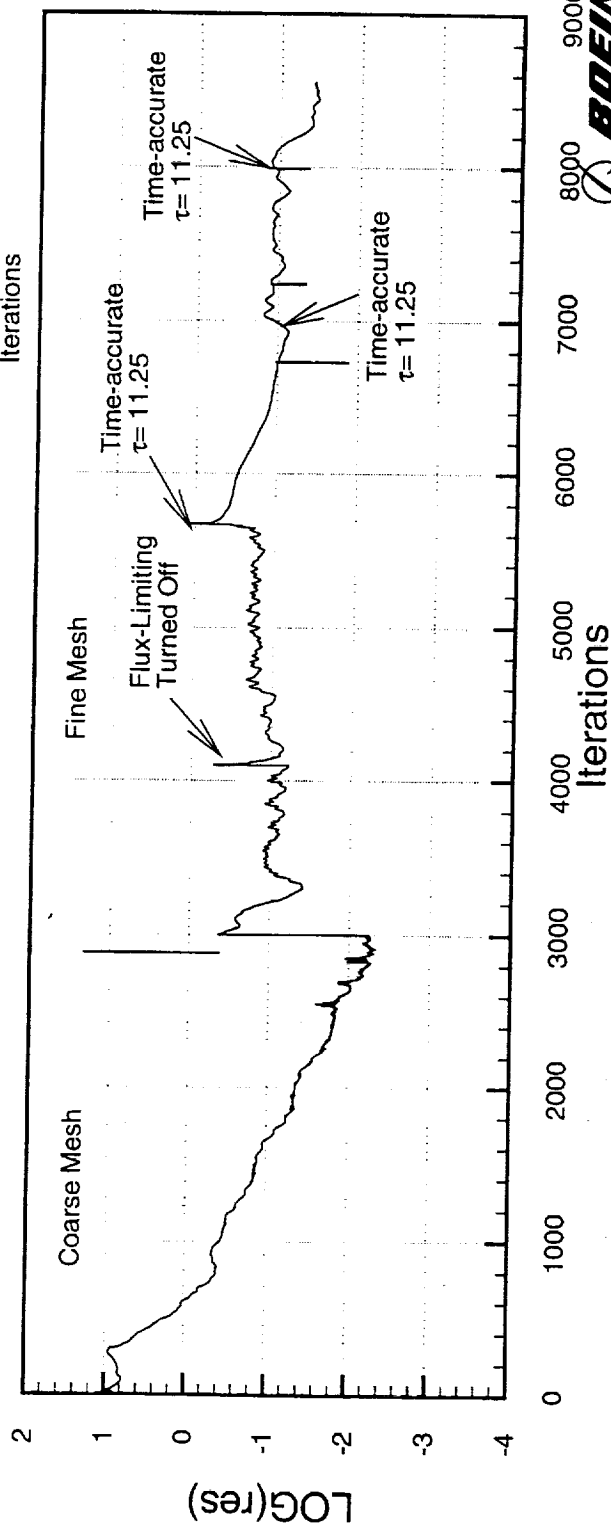
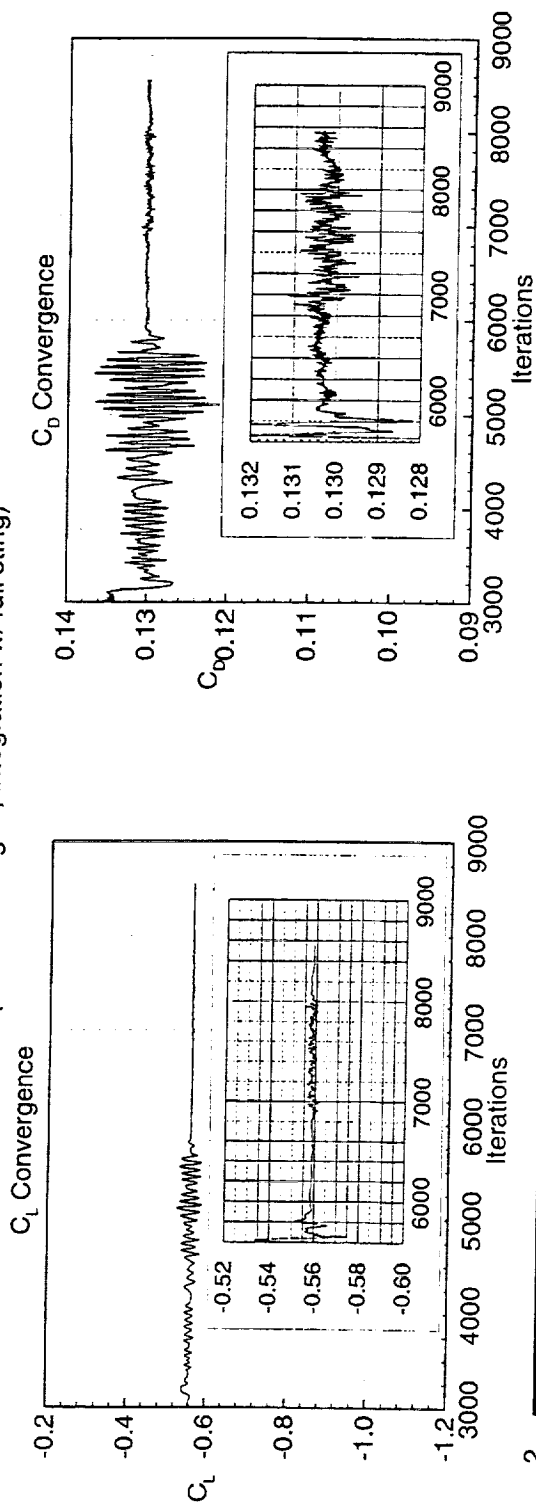
- ☐ Restart from steady-state solution: $\alpha = -14$ deg.
- ☐ Approach:
 - τ -TS method
 - 3 subiterations
 - Estimated # of iterations to cover flowfield $\sim 1000 \rightarrow dt = 11.25$
 - Attempts to increase time-step
- ☐ Improved overall convergence with a 20-30% increase in CPU cost

Convergence History for Opt5 with Deformation

The figure below shows the convergence history before and after the use of time-domain computations. The overall residual seems to monotonically decrease once the time-accurate mode is initiated at iteration #5600 and the amplitude of C_L oscillation went down by about an order of magnitude. However, the use of a larger time-step did not seem to help the convergence with the given number of sub-iterations.

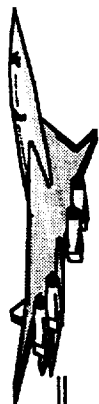


Convergence History for M2.4-7a Opt5 Configuration with Deformation
CFL3D N-S (B-L, D-S); $Re_c = 301 \times 10^6$; $M_\infty = 0.60$; $\alpha = -14.565^\circ$; C-O(93x237x89)
(2 Level Multigrid; Integration w/ full sting)



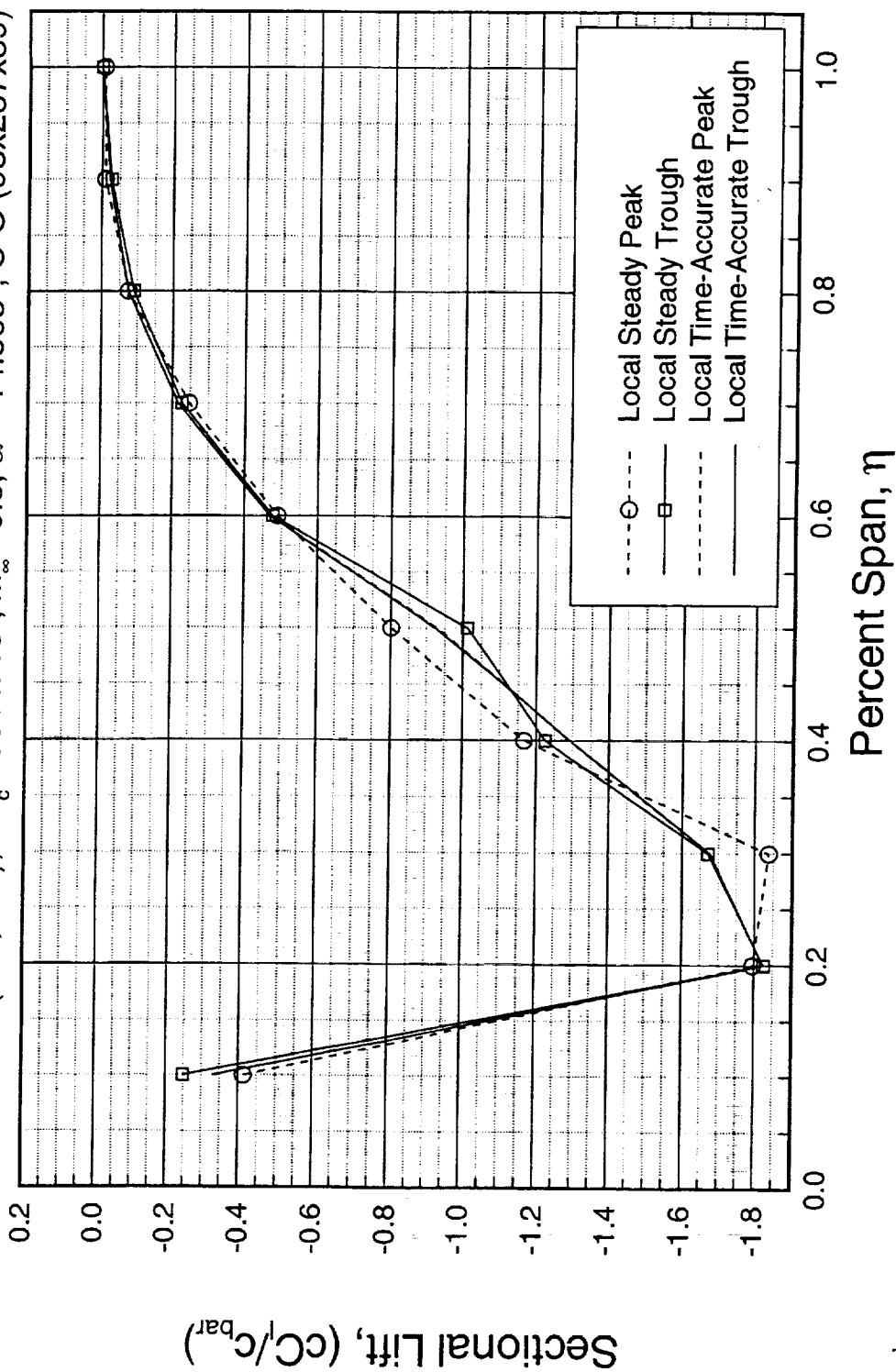
Loads Calibration Study, Sectional Lift

As shown in the figure below, the decrease in oscillations was also seen at the sectional load level, the amplitude of oscillations around a mean curve has been significantly reduced. In fact, very little difference is observed between the time-accurate peak and trough curves.



Loads Calibration Study, Sectional Lift M2.4-7A Opt5 W/B Configuration with Deformations

CFL3D N-S (B-L,D-S); $Re_c = 301 \times 10^6$; $M_\infty = 0.6$; $\alpha = -14.565^\circ$; C-O (93x237x89)



Lessons Learned from CFD Analysis of M2.4-7A

When clustering the CFD grids for the deflected shapes (obtained from perturbation of the rigid baseline grid) for the flight Reynolds number (about 300 million), many problems were encountered and manual improvement of the grid quality was needed. Consequently, the use of a lower Reynolds number (~40 million for example) was suggested to simplify the grid generation process.

The flowfield at higher angle-of-attack is very unsteady and no particular periodicity of the monitored quantities for convergence was observed. Due to the complex flow mechanism at high angles-of-attack, steady-state equations are inadequate and time-accurate solutions are needed.

Special convergence criteria have been established for loads calculations. Quantities, such as spanwise lift, its rms fluctuation from peak to trough, and fluctuation from mean of the total lift coefficient, are monitored for convergence. These convergence criteria are better suited for CFD loads analysis, as opposed to those used in typical attached flow cases normally encountered for aerodynamic performance (e.g., drag).



Lessons Learned from CFD Analysis of M2.4-7A

- ☐ **Grid generation must be simplified (use of flight Reynolds numbers created highly clustered grids)**
- ☐ **Very unsteady-like behavior for higher angles-of-attack, no particular periodicity**
- ☐ **Need special loads convergence criteria**
- ☐ **Steady-state equations inadequate, need time-accurate solutions**

Application to the TCA Configuration

The approach for the TCA configuration was similar to that used for M2.4-7A with the exception that the grid was preprocessed for both leading and trailing-edge flaps. Here, the C-O topology used more points in the streamwise direction and a smaller number of points in the viscous direction. The process that takes a clean wing/body grid and does the actual flap deflection and relevant grid perturbation has been developed and validated in the high-lift group under HSR Task 33 (High-Lift). The rigid configuration, had the outboard leading-edge flaps deflected by 8° to represent the range of Mach numbers, since the generation of the grid for different flap settings for every Mach number would require considerably more effort. The grid perturbation process for the deflected shapes has been improved significantly and fewer difficulties were encountered than for the M2.4-7A grid. In order to ease the clustering and facilitate convergence it was decided to use a lower Reynolds number of 40 million. The expectation is that the solution based on a Reynolds number of 40 million would be adequately representative of the full-scale flowfield. However, additional work on this topic is being done by NASA Ames and is reported in section 4.7. As in the M2.4-7A arrow wing, the CFL3D N-S code with the Baldwin-Lomax (Degani-Schiff) turbulence model was used. Based on the M2.4-7A experience, it was decided to use the time-accurate mode of analysis with the established convergence criteria for all cases. Since the grid used was three-level multigridable, steady-state solutions with coarse and medium meshes were obtained first and time-accurate simulations were started with the very first iteration of the fine grid (with a few exceptions).



Application to the TCA Configuration

☐ Configuration:

TCA wing/body

☐ Grid-Topology:

C-O grid of 93x281x69

☐ Geometries:

Obtained from representative deflections

☐ Grid Generation:

Preprocess for flaps / flap deflection

Perturbation of a rigid baseline Euler grid (CSCMDO) and clustering for Navier-Stokes analyses

☐ Analysis:

CFL3D N-S, time accurate, Baldwin-Lomax turbulence model (Degani-Schiff option turned on for higher angles-of-attack)

Reynolds number of 40 million (based on the mean aerodynamic chord)

Cases Analyzed

The simulations were performed at four different Mach numbers, 0.8, 1.2, 2.0, and 0.95 in increasing order of difficulty. The five angles-of-attack were -10.5° , 2.83° , 12.11° , 18.3° , and 22.9° . However, only Mach 0.8 included the 23° case and Mach 2.0 did not include the 18° case. Consequently, four cases were eliminated. The table below shows the flow conditions and angles-of-attack that were analyzed for the TCA wing/body/LE flap configuration. Among the matrix of 20 cases to run four cases were omitted. It was decided that computations at an angle-of-attack of 23° will not be necessary for the nonlinear loads database at Mach numbers above 0.95. As a matter of fact, even the 18° angle-of-attack case was not necessary for Mach 2.0.

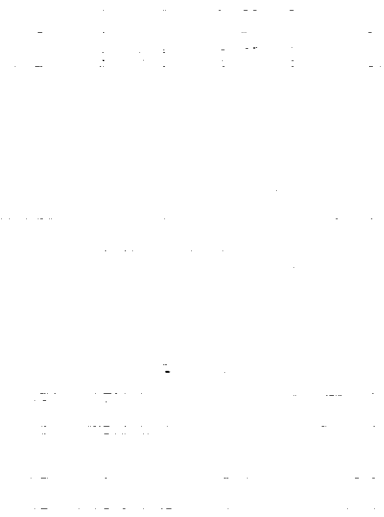


Cases Analyzed

	Deflected Shape				
	$\alpha = -10.4^\circ$	$\alpha = 2.83^\circ$	$\alpha = 12.1^\circ$	$\alpha = 18.3^\circ$	$\alpha = 22.9^\circ$
Mach 0.8	✓	✓	✓	✓	✓
Mach 1.2	✓	✓	✓	✓	N/A
Mach 0.95	✓	✓	✓	✓	N/A
Mach 2.0	✓	✓	✓	N/A	N/A

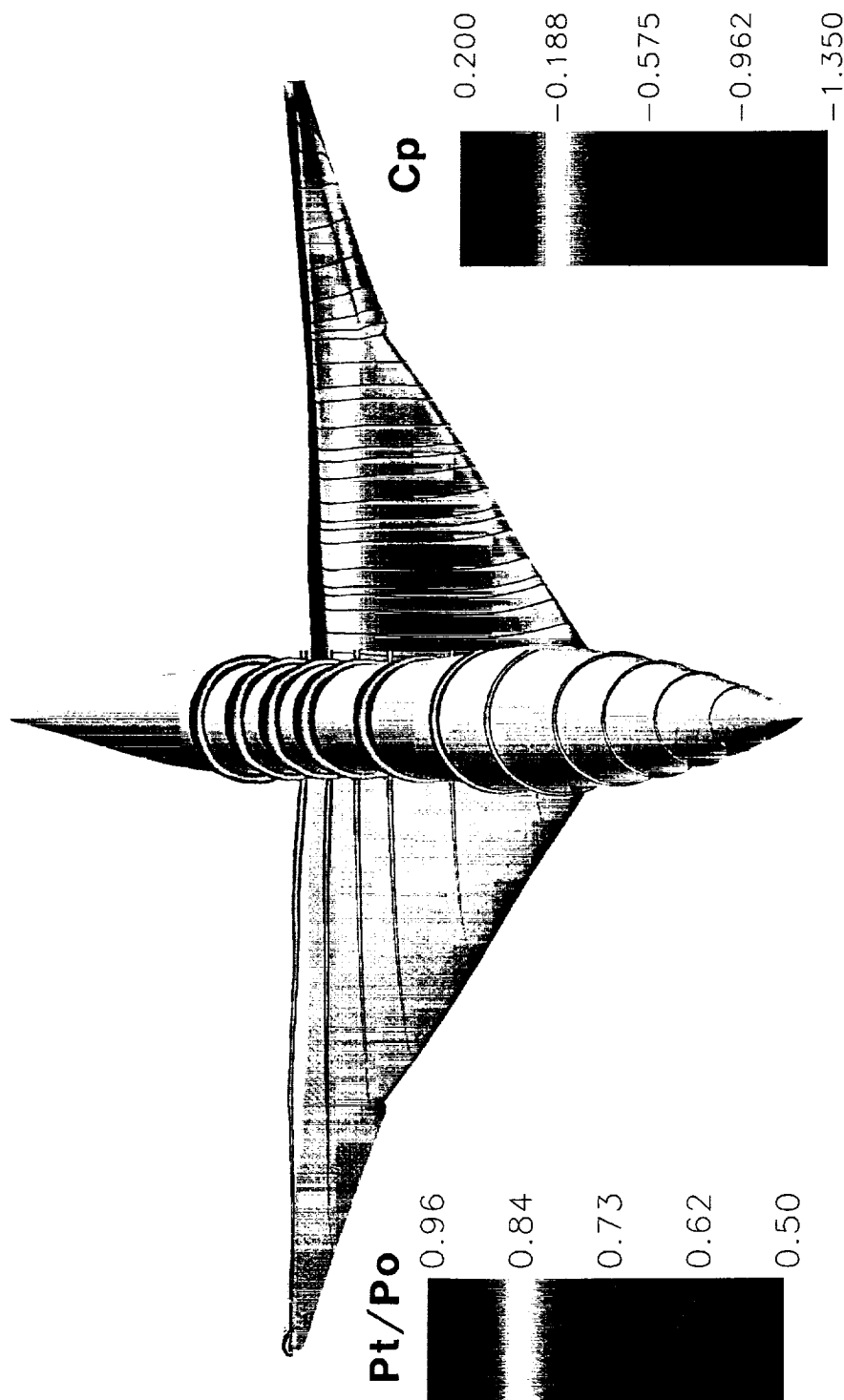
Flow Analysis of the TCA Wing/Body/LE Flap

An example of a benign (low α) transonic flowfield ($\alpha=2.83^\circ$, $M_\infty=0.95$) is shown in the chart above. The left side of the figure shows the normalized total pressure cuts along several span stations while the right side displays the surface pressure coefficients on the wing with field streamlines. The flow is benign as expected and no separation pattern is observed. In spite of the higher spanwise component of the streamlines near the tip, significant flow acceleration/expansion is observed along the flap edge.





**Flow Analysis of the TCA Wing/Body/Leading-Edge Flap
Configuration with Representative Deflections**
Streamwise Total Pressure cuts, Surface Cp Distributions and Streamlines
CFL3D, N-S, Baldwin-Lomax D-S, $M_\infty = 0.95$, $\alpha = 2.83^\circ$, $Re_c = 40$ million
(C-O Grid 93x281x69)

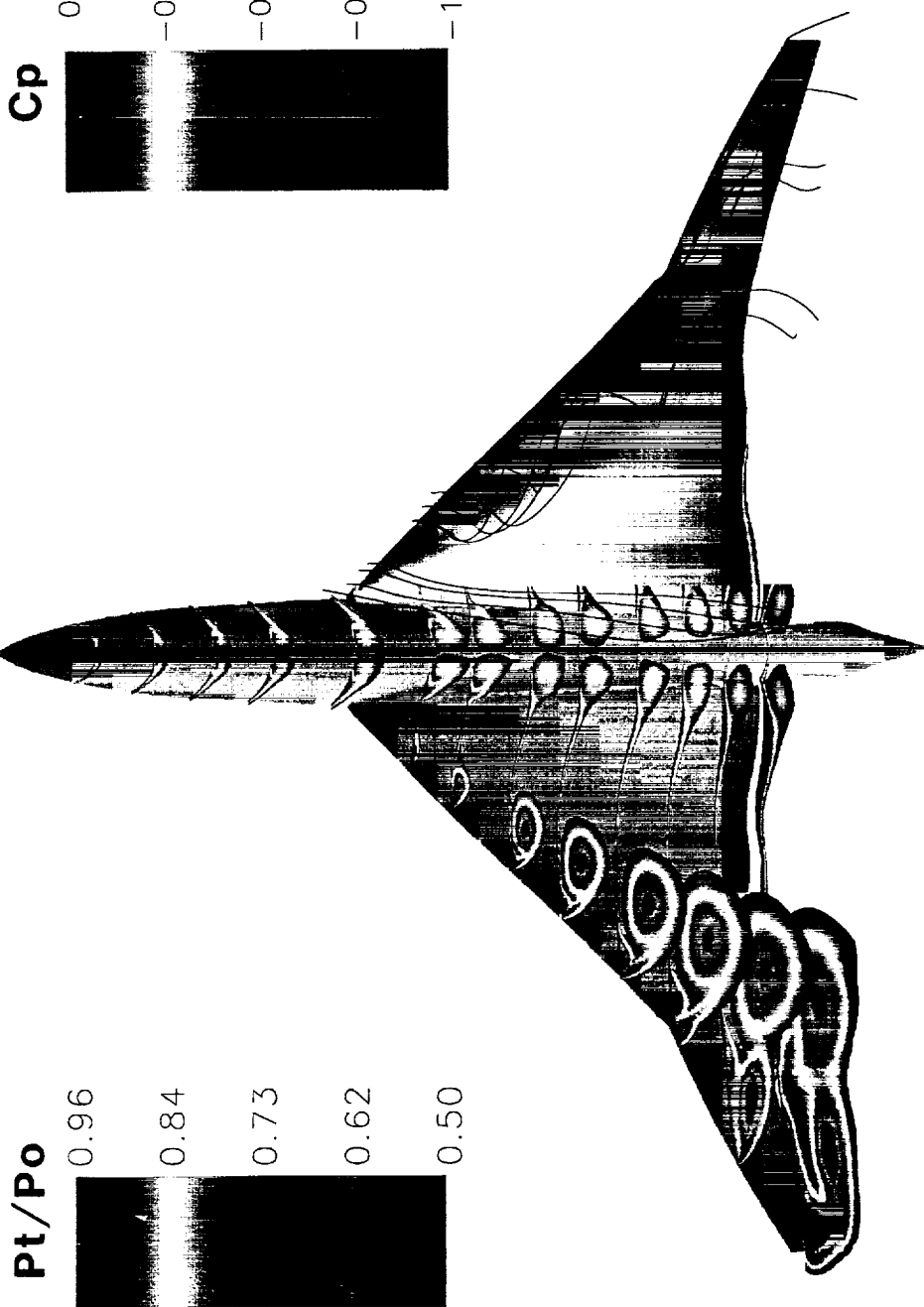


Flow Analysis of the TCA Wing/Body/LE Flap

The flowfield for this negative angle-of-attack case ($\alpha = -10.44^\circ$, $M_\infty = 0.95$) is not as benign as shown in the figure below. The left side of the plot indicates three types of vortices. The first one would be the forebody vortex which remains significant up to the wing trailing edge. The second type of vortex gets started at the wing apex and dominates the wing lower surface flowfield. When examining streamwise cuts from the apex, a secondary vortex is observed starting at the sixth streamwise cut from the wing apex. This flow feature cannot be captured without the use of the Degani-Schiff option in the turbulence model. The third type of vortex is the wing leading-edge break vortex which tends to be stronger because of the 8° outboard leading-edge flap deflection.



**Flow Analysis of the TCA Wing/Body/Leading-Edge Flap
Configuration with Representative Deflections**
Streamwise Total Pressure cuts, Surface Cp Distributions and Streamlines
CFL3D, N-S, Baldwin-Lomax D-S, $M_\infty = 0.95$, $\alpha = -10.44^\circ$, $Re_c = 40$ million
(C-O Grid 93x281x69)



Flow Analysis of the TCA Wing/Body/LE Flap

The flowfield for the 18.3° angle-of-attack at Mach 0.95 case is shown in the figure below. Here, the forebody vortex bursts halfway through the fuselage since the upper surface vortex interactions with the fuselage causes the vortex to burst sooner. The wing upper surface pressure contours show a "shadow" of the apex vortex. When looking at the fifth streamwise normalized total pressure cut from the wing apex, three types of vortices are observed. The main apex vortex is followed by a secondary vortex at the verge of bursting. Finally, the leading-edge break vortex moves away from the surface allowing the wing-tip vortex to be seen at the last cut. For these higher positive angle-of-attack cases, higher Mach numbers show similar results. Also, vortices tend to be flatter with higher Mach numbers.

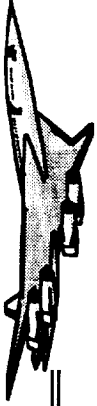


**Flow Analysis of the TCA Wing/Body/Leading-Edge Flap
Configuration with Representative Deflections**
Streamwise Total Pressure cuts, Surface Cp Distributions and Streamlines
CFL3D, N-S, Baldwin-Lomax D-S, $M_\infty = 0.95$, $\alpha = 18.3^\circ$, $Re_c = 40$ million
(C-O Grid 93x281x69)



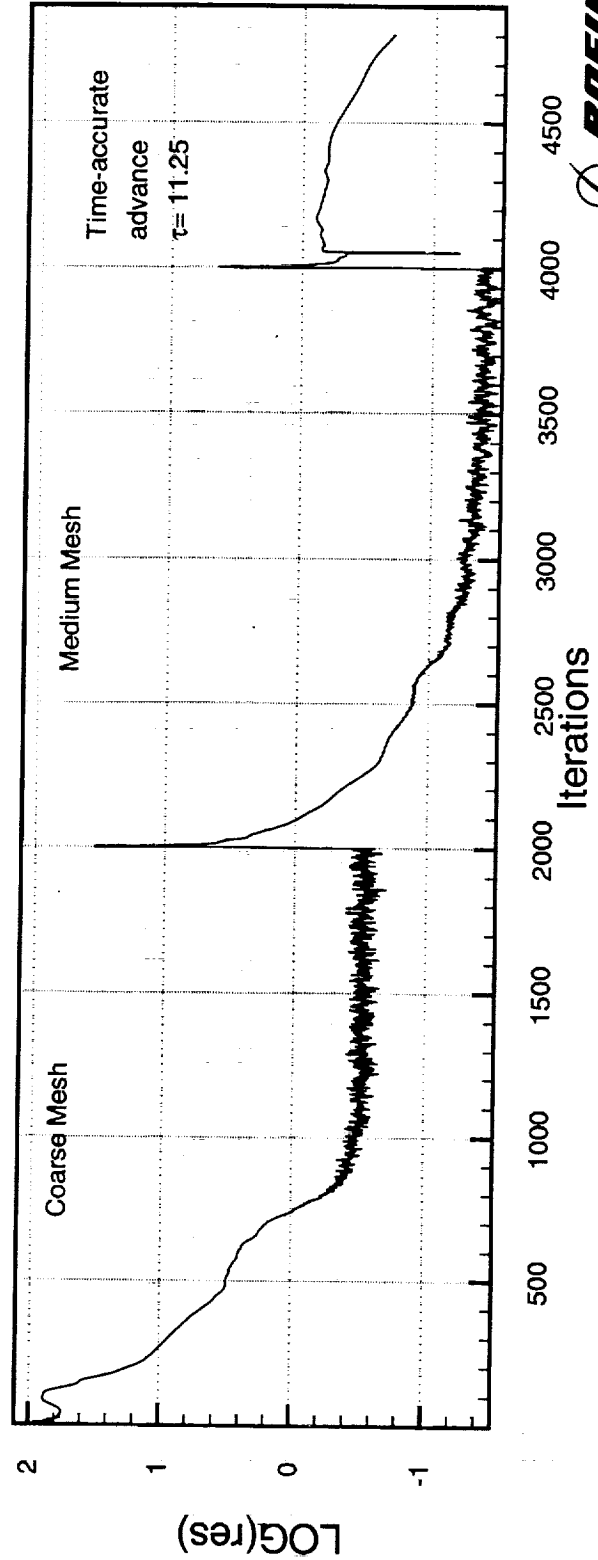
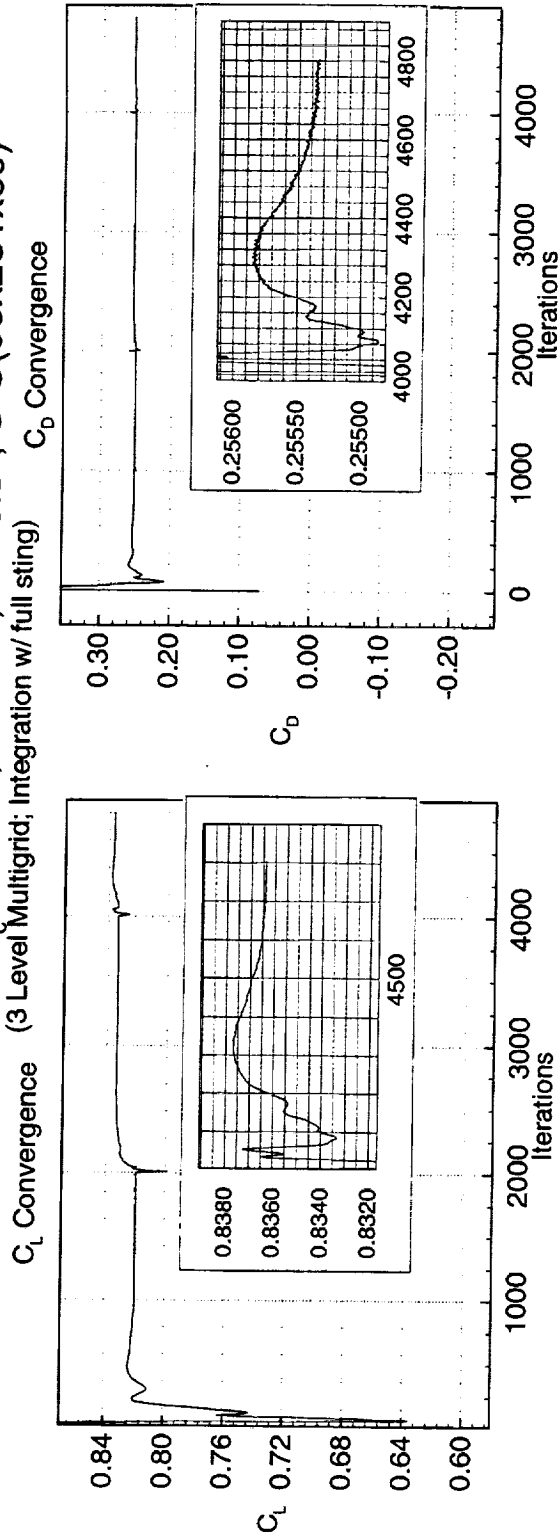
Convergence History for the TCA W/B/LE Flap

Convergence results for the 18.3° at Mach 0.95 case are shown in the figure above. This is one of the most difficult case to converge. In fact, when looking at the residual history, more iterations were needed for this case. Lift and drag had one last oscillation of 0.1%.



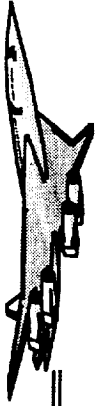
Convergence History for the TCA W/B/LE Flap Configuration with Deformation

CFL3D N-S B-L D-S; $Re_c = 40 \times 10^6$; $M = 0.95$; $\alpha = 18.3^\circ$; C-O(93x281x69)



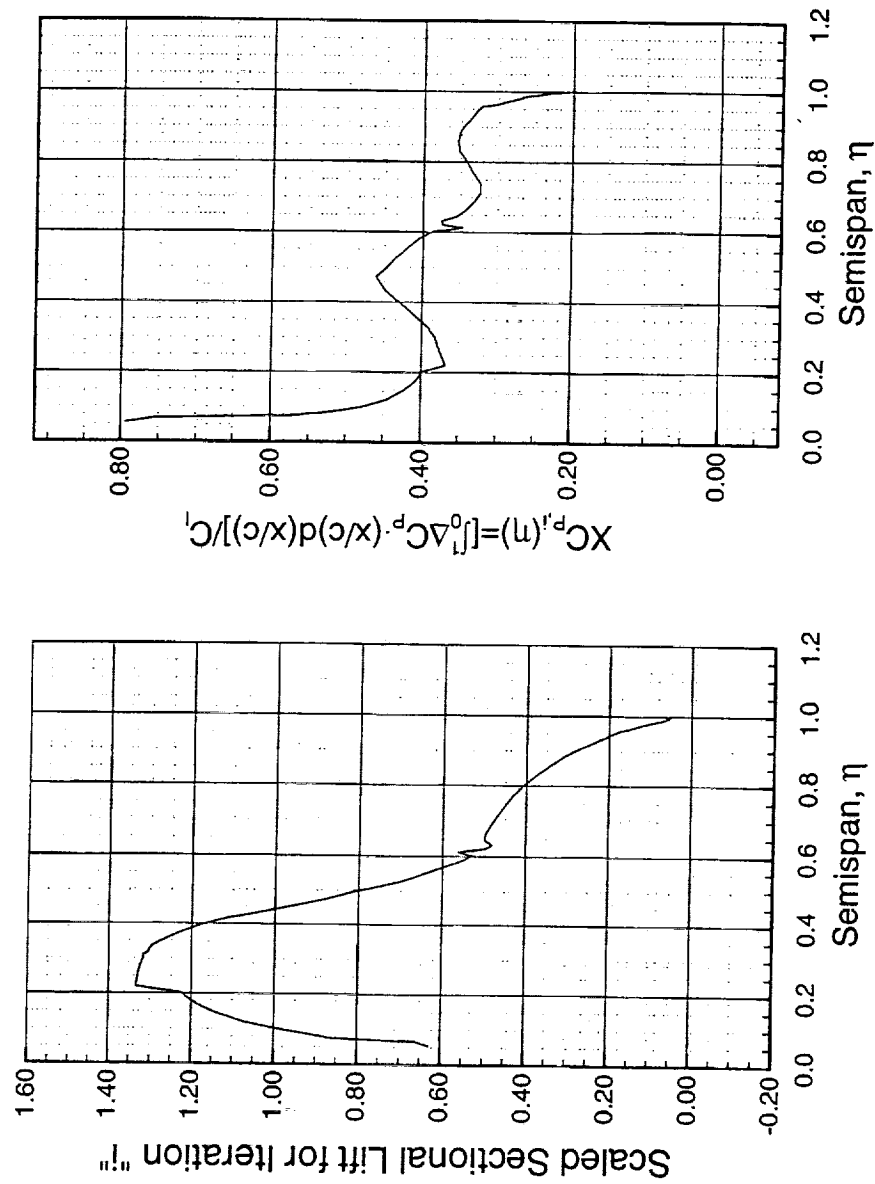
Convergence Summary for the TCA W/B/Out LE Flap

The quantities observed for the convergence criteria are all varying within less than 0.1%. However, when looking at the sectional properties for the last 200 iterations no variation is observed in both the scaled sectional lift and the center-of-pressure curves. Since, the thickness of the band is small with respect to the actual values, the solution was stopped at this level. It is worthy to note that every 565 iterations required 8 hours of CPU time on the C-90. Therefore, unless absolutely needed, further time steps are avoided.



Convergence Summary for the TCA Wing/Body/Out LE Flap Wing with Representative Deflections

CFL3D N-S, Baldwin-Lomax D-S, $M_\infty = 0.95$, $\alpha = 18.0$ deg., $Re_c = 40$ million, 93x281x69 C-O Grid



Sensitivity Study by NASA Ames

The 18° angle-of-attack case discussed previously did not show significant fluctuations and was actually one of the better behaved cases. Other flow regimes showed much larger fluctuations. In fact, the uncertainties related to the turbulence model effect, grid density and resolution in the areas where strong vortices are formed, and Reynolds number effect, remain to be assessed.

The emphasis here is solely on the loading due to lift forces, and not on the drag forces which would require more sophisticated (and time-consuming) schemes. The loads analysis calculations were all performed on a single configuration at the same flow conditions as the previous three charts. As a first step, the objective of this assessment will address the effect of three main components on loading: effect of turbulence model, resolution of the fuselage forebody, and the density in regions of off-surface vortices. It was attempted to analyze the effects of each of these components individually by computing incremental changes from a baseline configuration. In this way, while it can't be claimed which method is the most accurate (due to a lack of experimental data), the effect of each component investigated, as well as the cumulative effect of all, can be stated in terms of percentage change. The CFD code used for this sensitivity study was OVERFLOW.



Sensitivity Study By NASA Ames

❑ Issues: Uncertainty Assessment by NASA Ames ACE teammates

- Turbulence model
- Grid density/resolution
- Reynolds number

❑ Objective: Assess the influence of the following on the CFD loads prediction for the deflected TCA configuration at $\alpha = 18^\circ$, $M_\infty = 0.95$, $Re_c = 40$ million:

- Turbulence model (production vs. “True” Degani-Schiff)
- Forebody grid resolution (effect on forebody vortex)
- Off-surface, wing vortex grid resolution



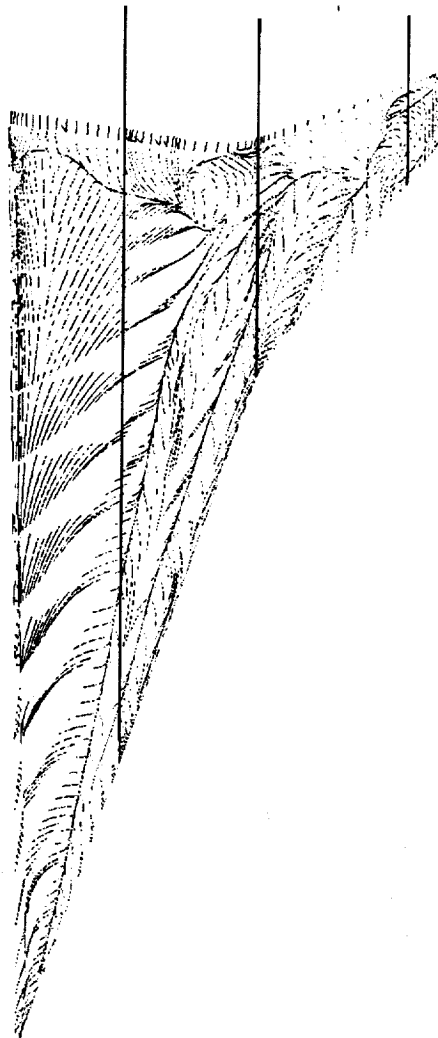
Effect of Turbulence Model on Pressure Distributions

The figure below shows the computed surface flow pattern over the wing for two computations with different versions of the Degani-Schiff modification. The blue lines in these figures represent spanwise stations that will be used to examine the wing loading more closely. In both computations, on the inboard wing sections the flow separates from the wing leading edge, reattaches near the wing root, and then induces a boundary layer flow outboard from the wing root. This induced boundary layer separation is in a similar manner to a crossflow separation, and reattaches near the leading edge. A tertiary separation is also present between the secondary separation and reattachment lines. Over the outboard section of the wing, the flow again separates at the leading-edge and induces a secondary flow which also separates at about the quarter chord location. Comparing the two turbulence model implementations, the OVERFLOW version has a delayed secondary separation and, in general, a tighter bunching of the secondary/tertiary separation region. The OVERFLOW implementation is predicting a higher value of the turbulent eddy viscosity near the separation locations, which in turn delays the onset of the flow separation. These computations were performed at a freestream Mach number near unity where the flow would form a shock wave near the wing trailing edge. The OVERFLOW implementation is producing a distinct shock-induced separation line near the wing trailing edge, as expected. The modifications which follow, show a more complicated separation pattern near the trailing edge, which does not correspond to a sharp shock wave. It is felt that the logic of the Degani-Schiff modifications as originally reported in Degani's paper (1986), which was designed solely for crossflow separation, is being confused by the streamwise shock-induced separation of this case, and leading to erroneous results. In both implementations of the turbulence model, a complicated flow structure is visible near the wing tip. It is felt that this is a result of unsteadiness in the computations.

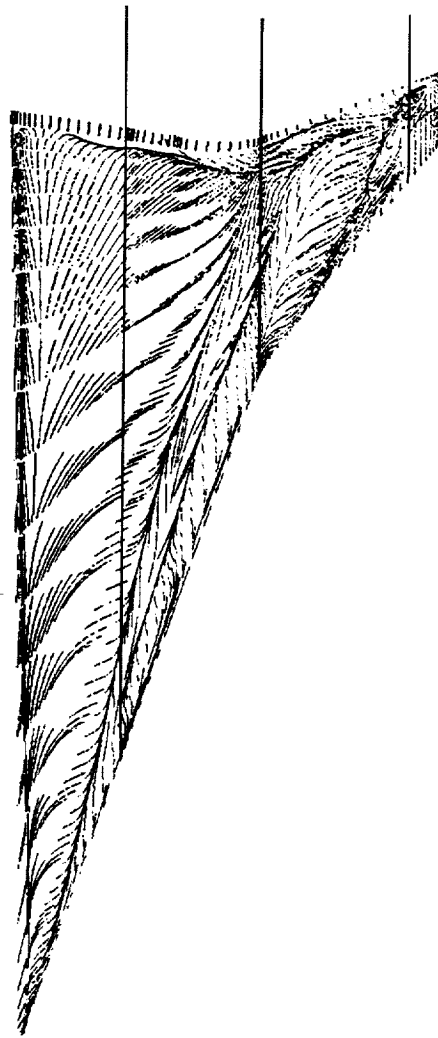


Effect of Turbulence Model on Pressure Distributions and Wing Upper Surface Flow Pattern

(TCA Wing/Body/LE Flap Configuration $M_\infty = 0.95$, $\alpha = 18.3^\circ$, $Re_c = 40$ million)



"True" Degani-Schiff



Production Degani-Schiff

Effect of "True" Degani-Schiff/Grid-Modification

The summary of the computed lift and drag for each computed configuration is given in the table below. The cumulative difference in lift force from applying all of the changes, the turbulence model, refined forebody region, and wing-vortex grids, is 2.4%. That these changes in lift are small is possibly due to the excessive amounts of dissipation that were required to compute the solutions using the given grid system. While the trends appear rational, the quantitative differences cannot be stated with any certainty.

At the three labeled spanwise stations in the chart below, the pressure distributions for both computations are compared. These stations correspond to $y/b = 0.31$, $y/b = 0.61$, and $y/b = 0.93$ all referenced to the body centerline. Examining the first inboard station, $y/b = 0.31$, the OVERFLOW implementation is predicting a primary vortex suction peak at $x/c = 0.25$, and a small induced secondary vortex suction peak at about $x/c = 0.10$. The original implementation of the Degani-Schiff modifications is predicting a weaker primary vortex suction peak located closer to $x/c = 0.3$, but also a strong distinct secondary suction peak at $x/c = 0.10$ and a small tertiary suction peak at $x/c = 0.175$. The OVERFLOW implementation predicts a shock near the trailing edge, while the original implementation is obviously having problems in this region. At the wing break, $y/b = 0.6$, the two implementations are showing similar behavior. The original Degani-Schiff implementation is better able to capture the distinct suction peaks from the different primary and secondary vortices which combine in this section. At the outboard section, $y/b = 0.93$, there are relatively large differences between the predicted pressure distributions for the two implementations. This is due to the presence of unsteadiness in the computations. All of the computations were run in a non-time-accurate mode in order to accelerate the convergence in the inviscid flow regions. This was done primarily due to time constraints within the study.

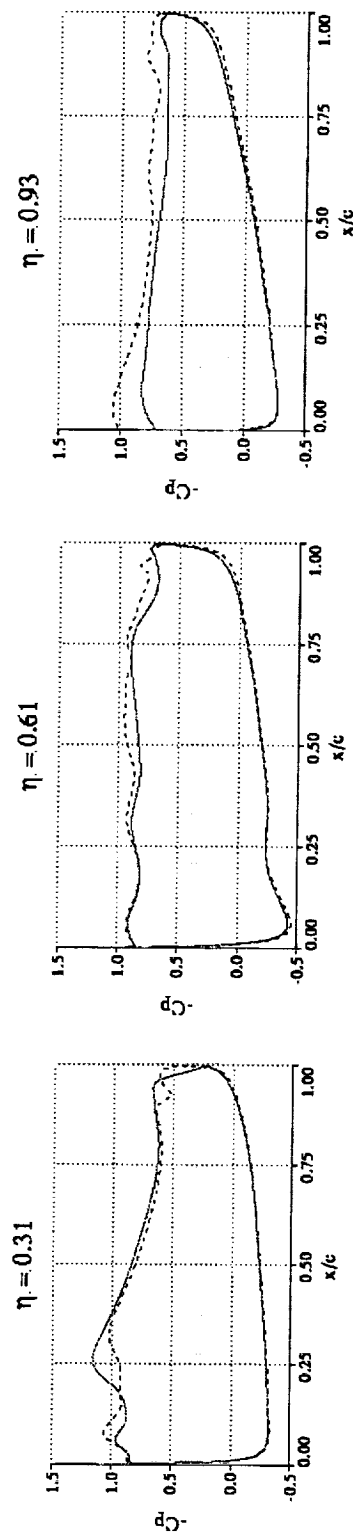
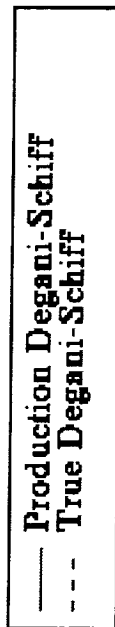


Effect of "True" Degani-Schiff/Grid-Modification

- 2.4% Increase in lift with change in turbulence model:

Case	C_L	$C_{L_{wing}}$	C_D	L/D
Production	0.823	0.717	0.25	3.28
True D-S	0.829	0.718	0.25	3.32
Fuselage Grid	0.835	0.717	0.25	3.36
Fuse + Vortex Grid	0.841	0.723	0.26	3.23

- Variation in pressures:



Summary/Conclusion

A process has been established for CFD data generation for the nonlinear loads database. The process was initially developed on the M2.4-7A configuration and applied subsequently to the TCA configuration

Convergence criteria for loads were established and quantities describing the variations of sectional properties were monitored.

The use of time-accurate simulations alleviated some of the numerical unsteadiness that caused large variations in sectional loads, especially at the outboard wing section.

However, the flowfield for higher angles-of-attack seems to be dominated by the wing primary vortex. Therefore, the uncertainties associated with the turbulence model and grid resolution could not be quantified with certainty since the variation in the integrated quantities were rather small (2.4%) compared to the strength of the wing primary vortex.



Summary/Conclusion

- ☐ Process established for CFD data generation for nonlinear loads database
- ☐ Loads convergence criteria were established
- ☐ Use of time-accurate simulations improved convergence
- ☐ Some uncertainty of turbulence model/grid - flowfield dominated by the wing apex primary vortex

Possible Further Studies

The use of larger time-steps will help a faster convergence of the solutions. However, the use of more sub-iterations would be necessary. The Reynolds number effects are to be investigated in order to establish confidence in the database obtained at 40 million. The same turbulence model comparison study that was performed for Mach 0.95 needs to be done for supersonic Mach numbers where boundary layers are thinner and vortices flatter. The use of smoother grids (in other words grids that have less spanwise stretching due to flap segments) is highly recommended. Finally, in the framework of assessing the effect of turbulence models modifications to the Spalart Allmaras turbulence model for vortical flows should be investigated.



Possible Further Studies

- ☐ Use of larger time steps (with more sub-iterations?)
- ☐ Assess effects of Re number
- ☐ Turbulence model comparison study at supersonic Mach numbers
- ☐ Smoother grids (less stretching at flap segments)
- ☐ Modifications to the S-A model for vortical flows for further uncertainty assessments

REPORT DOCUMENTATION PAGE			Form Approved OMB No. 0704-0188	
Public reporting burden for this collection of information is estimated to average 1 hour per response, including the time for reviewing instructions, searching existing data sources, gathering and maintaining the data needed, and completing and reviewing the collection of information. Send comments regarding this burden estimate or any other aspect of this collection of information, including suggestions for reducing this burden, to Washington Headquarters Services, Directorate for Information Operations and Reports, 1215 Jefferson Davis Highway, Suite 1204, Arlington, VA 22202-4302, and to the Office of Management and Budget, Paperwork Reduction Project (0704-0188), Washington, DC 20503.				
1. AGENCY USE ONLY (Leave blank)		2. REPORT DATE December 1999		3. REPORT TYPE AND DATES COVERED Conference Publication
4. TITLE AND SUBTITLE 1998 NASA High-Speed Research Program Aerodynamic Performance Workshop <i>Volume I—Configuration Aerodynamics</i>			5. FUNDING NUMBERS WU 537-07	
6. AUTHOR(S) S. Naomi McMillin, Editor				
7. PERFORMING ORGANIZATION NAME(S) AND ADDRESS(ES) NASA Langley Research Center Hampton, VA 23681-2199			8. PERFORMING ORGANIZATION REPORT NUMBER L-17758B	
9. SPONSORING/MONITORING AGENCY NAME(S) AND ADDRESS(ES) National Aeronautics and Space Administration Washington, DC 20546-0001			10. SPONSORING/MONITORING AGENCY REPORT NUMBER NASA/CP-1999-209692/ VOL1/PT2	
11. SUPPLEMENTARY NOTES				
12a. DISTRIBUTION/AVAILABILITY STATEMENT Unclassified—Unlimited Subject Category 02 Distribution: Nonstandard Availability: NASA CASI (301) 621-0390			12b. DISTRIBUTION CODE	
13. ABSTRACT (Maximum 200 words) NASA's High-Speed Research Program sponsored the 1998 Aerodynamic Performance Technical Review on February 9–13, in Los Angeles, California. The review was designed to bring together NASA and industry High-Speed Civil Transport (HSCT) Aerodynamic Performance technology development participants in areas of Configuration Aerodynamics (transonic and supersonic cruise drag prediction and minimization), High-Lift, and Flight Controls. The review objectives were to (1) report the progress and status of HSCT aerodynamic performance technology development; (2) disseminate this technology within the appropriate technical communities; and (3) promote synergy among the scientists and engineers working HSCT aerodynamics. In particular, single- and multi-point optimized HSCT configurations, HSCT high-lift system performance predictions, and HSCT simulation results were presented along with executive summaries for all the Aerodynamic Performance technology areas. The HSR Aerodynamic Performance Technical Review was held simultaneously with the annual review of the following airframe technology areas: Materials and Structures, Environmental Impact, Flight Deck, and Technology Integration. Thus, a fourth objective of the Review was to promote synergy between the Aerodynamic Performance technology area and the other technology areas of the HSR Program.				
14. SUBJECT TERMS High-Speed Research; High-Speed Civil Transport			15. NUMBER OF PAGES 953	
			16. PRICE CODE A99	
17. SECURITY CLASSIFICATION OF REPORT Unclassified	18. SECURITY CLASSIFICATION OF THIS PAGE Unclassified	19. SECURITY CLASSIFICATION OF ABSTRACT Unclassified	20. LIMITATION OF ABSTRACT UL	